V. Edwin Geo
Fethi Aloui   *Editors*

Energy and Exergy for Sustainable and Clean Environment, Volume 2

Springer

Green Energy and Technology

Climate change, environmental impact and the limited natural resources urge scientific research and novel technical solutions. The monograph series Green Energy and Technology serves as a publishing platform for scientific and technological approaches to "green"—i.e. environmentally friendly and sustainable—technologies. While a focus lies on energy and power supply, it also covers "green" solutions in industrial engineering and engineering design. Green Energy and Technology addresses researchers, advanced students, technical consultants as well as decision makers in industries and politics. Hence, the level of presentation spans from instructional to highly technical.

Indexed in Scopus.

Indexed in Ei Compendex.

V. Edwin Geo · Fethi Aloui
Editors

Energy and Exergy for Sustainable and Clean Environment, Volume 2

Springer

Editors
V. Edwin Geo
Department of Mechanical Engineering,
Faculty of Engineering and Natural
Sciences
Istinye University
Istanbul, Turkey

Fethi Aloui
INSA Hauts-de-France
Université Polytechnique Hauts-de-France
(LAMIH UMR CNRS 8201)
Valenciennes, France

Contents

Contents

Advancement in Refrigeration Systems

Wind Energy Technologies

A Novel Fuzzy Logic-Controlled Vienna Rectifier to Extract Maximum Power in the Grid-Connected Wind Energy System Applications

Hari Charan Nannam and Atanu Banerjee

Abstract In this paper, a novel fuzzy logic-controlled Vienna rectifier to extract maximum power at variable wind speed is proposed. Vienna rectifier consists of three switches and four diodes with an input inductor and performs both AC/DC and DC/DC conversions in a single stage. A permanent magnet synchronous generator (PMSG) coupled with wind turbine system is used in this paper. The tracking of the maximum power is a real challenge in wind energy systems. In this paper, the variable speed of the wind turbine generator system and the power output of the permanent magnet synchronous generator are chosen as inputs to the fuzzy logic controller to track the maximum power according to the change in wind speed by following 27 set of rules formulated in the fuzzy rule base. The pulse width modulated signals from the fuzzy logic controller initiate the three switches in the Vienna rectifier. The proposed control scheme not only tracks the maximum power from the wind but also enhances the input DC voltage, ensures sinusoidal nature at input mains and balances the voltage across the two capacitors. The Vienna rectifier is interfaced to the grid through space vector pulse width modulated voltage source inverter. The MATLAB/Simulink environment is utilized in order to observe the optimum performance of the system. The proposed control algorithm is experimentally validated using a real-time simulator OPAL RT 4200. The experimental results are in agreement with simulation results and prove the robustness of the control scheme.

Keywords Boost-type rectifier · Fuzzy logic controller · 6 Maximum power point tracking · Variable speed wind energy system · Vienna rectifier

H. C. Nannam (✉) · A. Banerjee
National Institute of Technology Meghalaya, Shillong, Meghalaya, India
e-mail: harichararan@nitm.ac.in

1   Introduction

According to renewable global status report 2018 update REN21 (2018), a noticeable interest in the utilization of wind energy sources has been increased in the renewable markets due to remarkable and administrator changes in policies, which have driven many industries to take up this privilege before the favourable schemes expires, a swift decrease in wind power price in both onshore and offshore, clean and many environmental benefits. According to status report, an increase of 11% from the previous year (2016) has been noticed (an increase of 52 GW), and at present (2017), the total capacity of wind power all around the world is risen to 539 GW. In the early stage of wind power generation, a fixed speed wind turbines was used and the generated wind power is directly integrated to the grid. There arose a lot of issues like less energy conversion efficiency (wind turbine extracts energy at a single speed, and in other speed, it remains inactive), sub-synchronous oscillations between generator and turbine shaft, huge mechanical stress, etc. According to [1], a multi-stage geared squirrel cage induction generator (SCIG) was used as a generator for fixed speed wind turbines. A soft starter which is composed of power electronic switches was implemented in order to mitigate high in-rush currents at the initiation of the system, and the wind energy system requires no power electronic converter under normal operation [2]. At the end of 1990s, the technology has driven towards variable speed wind energy conversion systems due to its dominant merits over fixed speed wind energy systems. The enhanced efficiency of energy conversion, a lower stress on the mechanical parts, lower maintenance and extended life cycle due to less failures in gear box and as well as in bearing, less noise and accepted quality of power made the technological world to pursue after variable speed wind energy systems. The entire history and present trends of variable speed wind energy conversion system have been explained clearly in [3]. At the early stages of variable speed wind energy technology, a wound round induction generator (WRIG) with rotor resistance control has implemented to achieve partial variable speed operation of wind energy system as the manipulations in rotor resistance reflect on torque and speed of the generator. The power electronic switches provided the necessary control to change the value of external rotor resistance. This setup can be implemented for limited speed range (approximately 10% more the synchronous speed), and this system suffers from resistive losses. Later, doubly fed Induction generator (DFIG) with the same above-mentioned configuration except the replacement of external rotor resistance by grid connected power electronic converter with no soft starter was proposed [4]. The power electronic converter which was implemented at the rotor circuit has to undertake only 30% of rated generator power. The enhanced power conversion efficiency, amplified speed range (approximately 30%) and improved dynamic performance are the advantages of the DFIG-based wind energy system. Direct-driven wind turbine generator system (gearless mechanism) has become a new alternative for the designers and manufacturers to overcome the gear mechanism failures and to ensure low maintenance. The drawbacks prevailed in DFIG-based wind energy

became auspicious situations for direct-driven wind energy systems. The dissipation of excessive heat in the gear system and wear due to friction, the requirement of oil for free movement of gears, noise pollution, unable to meet the entire reactive power requirement of the grid, disturbances in the generator system during grid fault conditions like transients in stator currents can be considered as drawbacks of DFIG-based wind energy system [5]. During the early days of direct-driven wind energy system technology, electrically excited wound round synchronous generator (WRSG) has extensively used as wind turbine generator [1, 5]. The main stumbling block of the emerging direct-driven technology is the requirement of large torque. Since the size of the machine being determined by the rating of torque required, low-speed large torque direct-driven technologies has a bulky structure which is so many times (approximately 60%) bigger than wind energy system with geared technology. This impediment can be repressed by utilizing permanent magnets for excitation in synchronous generator [4, 5]. The detailed explanation of different types of generator used in fixed and variable speed wind turbines (with gear and direct driven) can be seen in [6, 7]. In this paper, a direct-driven (gear less) wind turbine with permanent magnet synchronous generator is used as a wind turbine generator system. The organization of the paper is as follows: Sect. 2 consists of basic features of wind turbine system which consists of constructional features and mathematical modelling of wind turbine generator system. The operating principle of PMS-based wind energy system is explained in Sect. 2. The basic operation of Vienna rectifier is explained in Sects. 3 and 4. The detailed explanation of maximum power point tracking (MPPT) algorithms is explained in Sect. 5 and proposed, fuzzy logic control algorithm (FLC) is explained in Sect. 6. The results and discussion is explained in Sect. 7. Finally, Sect. 8 consists of conclusion and is followed by acknowledgement and references.

2 Basic Principle of Wind Energy Conversion System

The wind energy conversion system converts the amount of available kinetic energy in the wind to usable electrical energy. The major parts in direct-driven wind turbine-generator system consists of blades mounted on the hub, shaft (for direct-driven gear mechanism is not required) and permanent magnet synchronous generator (PMSG). The kinetic energy per unit time of an undisturbed wind when passing through the area of cross-sectional turbine A, having the velocity V_0 (undisturbed wind) and density of the air as ρ is given as

$$P_w = \frac{1}{2}\rho A V_0^3 \tag{1}$$

According to theory of linear momentum and principle of Bernoulli, the amount of power extracted by wind turbine or the mechanical power output can be given as [8]
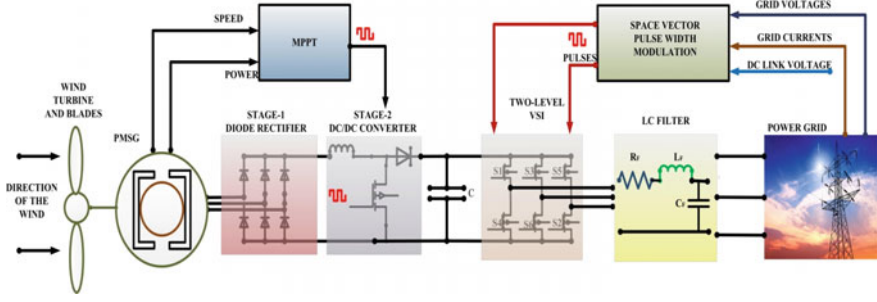
Fig. 1 complete representation of conventional Grid-connected wind energy system

$$P_T = \frac{1}{2} C_p(\gamma, \lambda) \rho A V_0^3 \tag{2}$$

The pitch angle control had no dominion in controlling the wind turbine during the speeds between cut-in and rated, so it can be zero.

The tip speed ratio (λ) is defined as ratio of speed of the tip of blade to speed of the wind,

$$\lambda = \frac{\omega_b * R_r}{V_w} \tag{3}$$

According to (2), the mechanical power (P_T) is directly proportional to coefficient of power (C_p). So, the maximum power drawn from the turbine ($P_{T,\max}$) depends on maximum value of power coefficient ($C_{p,\max}$). The coefficient of power C_p depends on angle of pitch blades and tip speed ratio (λ, γ). The maximum value of coefficient of power ($C_{p,\max}$) occurs at certain value of tip speed ratio (λ), and this corresponding tip speed ratio is constant for a turbine blade. The conventional block diagram representation of grid-connected wind energy conversion system is shown in Fig. 1.

2.1 Mathematical Modelling of Permanent Magnet Synchronous Generator (PMSG)

In this paper, a non-salient or surface pole-mounted permanent magnet generator is used as a wind generator due to its less cost of construction and equal distribution of air gap. In this paper, the synchronous generator is modelled in rotor frame of reference due to its simplicity in framing the equations. Since the PMSG consists of permanent magnets, the rotor field current can be modelled as a current source (Is) with a fixed magnitude. The equations of voltage for permanent magnet synchronous generator according to [2], are given as follow:

$$V_{ds} = -R_s I_{ds} + \omega_r L_{qs} I_{qs} - L_{ds} \frac{d}{dt} I_{ds} \tag{4}$$

$$V_{qs} = -R_s I_{qs} - \omega_r L_{ds} I_{ds} - L_{qs} \frac{d}{dt} I_{qs} + \omega_r \lambda_{rf} \tag{5}$$

The electromagnetic torque (T_e) developed by the PMSG is given as

$$T_e = \frac{3P}{2} \lambda_{rf} I_{qs} \tag{6}$$

Since the system considered here is non-salient machine, so $L_{ds} = L_{qs}$, and hence, the development of electromagnetic torque purely lies on I_{qs}.

3 Operating Principle of Three-Phase /Three-Level/Three-Switch Vienna Rectifier

Though the diode bridge rectifier which act as grid side converter in Fig. 1. has the merits like cost-effective and reliable, it undergoes a few drawbacks like introducing harmonics into the mains current, lack of dominant power factor control, torque ripples which reduces the efficiency. In order to address this issues, researchers worked out, and after many transformations in the actual circuit, Vienna rectifier was proposed [9]. The different modes of transformation of circuitry have been clearly explained in [10]. Vienna rectifier is an AC/DC/AC converter device which can convert alternating quantity (AC) to direct quantity (DC) and at the same time which can boost the input DC voltage to the desired DC voltage level. Vienna rectifier consists of three switches, one for each phase, and it generates three voltage levels, namely V_{dc}, 0 and $-V_{dc}$. Simplified control, less cost, less harmonic distortion, reduced voltage blocking stress on power semiconductor switches, unity power factor operation, reliable and efficient are the merits of the Vienna rectifier [9, 10]. The proposed topology of Vienna rectifier along with fuzzy logic-controlled maximum power tracking algorithm is shown in Fig. 2. The operation of Vienna rectifier in all states (000–111) and its operation as boost rectifier are clearly explained in [9–11].

4 Maximum Power Point Tracking Techniques in Wind Energy Systems

Since the availability of wind is patchy and random, the expeditious tracking of peak power point is indispensable for wind energy conversion systems. Once the static friction has been overcome by the rotor, it starts to rotate and achieves a possible stable zone. If the load torque increases simultaneously with the speed of the rotor,
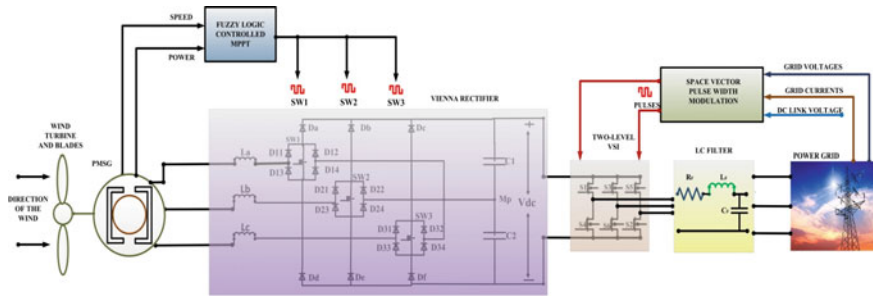
Fig. 2 Proposed fuzzy logic-controlled MPPT Vienna rectifier for a grid-connected wind energy system

the rotor operates in the stall region and accelerates to a feasible speed of operation though the possible highest wind speed is achieved. The energy extracted in this condition is significantly low as a result of stalled operation of rotor. In other case, if the increase of load torque is sluggish with the speed of the rotor, then the rotor rotates with speed more than the operating speed and the result is poor extraction of optimum energy from the wind. Hence, the system has to be operated somewhere between these two loading limits so as to obtain an optimum rotational speed to transfer maximum power from the wind. The characteristics of mechanical power against the rotor rotational speed shown in Fig. 3, and Eq. (2) explains that for every
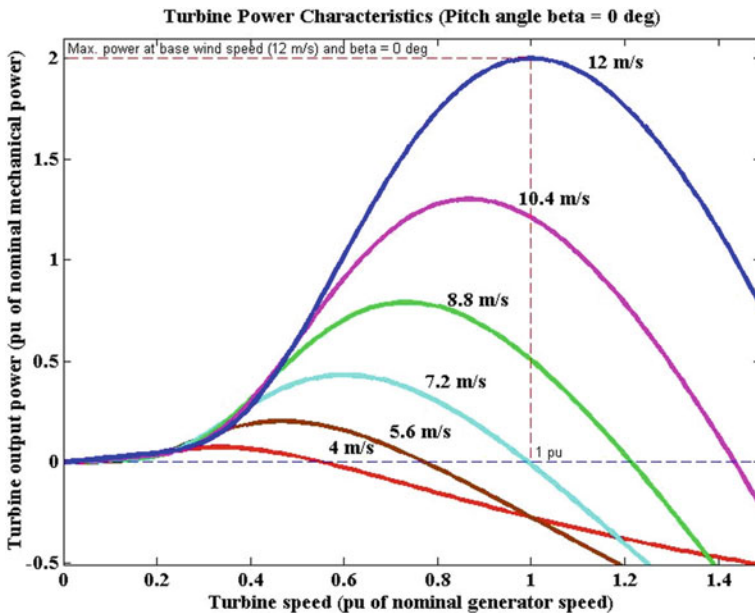
Fig. 3 Mechanical output power versus speed of the turbine

speed of the wind the maximum power of a wind turbine depends on maximum coefficient of power ($C_{p, max}$), and this maximum coefficient of power occurs only at one value of tip speed ratio ($\lambda = \lambda_{optimum}$) which is optimum. So, if the rotor of the wind turbine is operated at $\lambda_{optimum}$, whatever may be the speed of the wind, there is a possibility of extracting peak power [12, 13].

Basically, the MPPT techniques which are wide spread from the past are tip speed ratio control [13], power signal feedback control [12], optimal torque control [14] and hill climbing search control [15], advanced hill climbing search method [16] where a lookup table is implemented for hill climbing search method, and several different kinds of optimal power tracking methods are explained in [17]. Most of the MPPT methods described above has implemented proportional–integral–derivative (PID) controller to extract maximum power out of wind energy. In [18], for controlling the speed, a PID tuner has been implemented. In [19], in order to extract the optimum power, a simple V/Hz control method was proposed. In [20], it was declared that the comparative analysis of PID controller and V/Hz controller was done and it was proven that classic controllers like V/Hz controller can provide better performance over PID controllers. The main drawbacks of conventional PID controllers is a laborious process of tuning the parameters for swift and desired dynamic response, operational amplifiers (op-amps), which are used in the implementation of PID tuners and which have the negative effects, like ageing and temperature dependency and the system performance can be debased [21]. A new control scheme based on sentences in a simple language and simple if–then rules which is different from conventional control schemes and user-friendly was proposed in Zadeh in 1973 [22]. The merits of fuzzy logic controllers are, a rigorous mathematical modelling is not essential, easy to execute, endurable performance of the system as it is independent on ageing and atmospheric conditions. So, in this paper a fuzzy logic based MPPT algorithm has been implemented to acquire the above-mentioned benefits. According to Zadeh [22], fuzzy logic controller schemes is a three-step process: (i) the inputs have to be expressed in linguistic variables based on fuzzy set theory which is called fuzzification, (ii) the conditional statements based relation between linguistic variables, and (iii) conversion of rule-based fuzzy logic linguistic variables with member functions into analogue signal which is called defuzzification. When there is change in wind speed, the rotor of generator has to track it for extraction of the optimum power, and this control scheme is executed by fuzzy logic controller (FLC).

5 Proposed Controller Scheme

In this paper, a FLC controller is considered to track the maximum power. The FLC operates as a fundamental block to generate necessary control signal to balance voltage across the capacitors for Vienna rectifier. The sinusoidal current nature of input current mains also depends on the FLC signal. The inputs considered for the FLC are output power of PMSG and speed of the rotor of generator. As the unknown value of wind speed changes, FLC changes the speed of the rotor of generator and
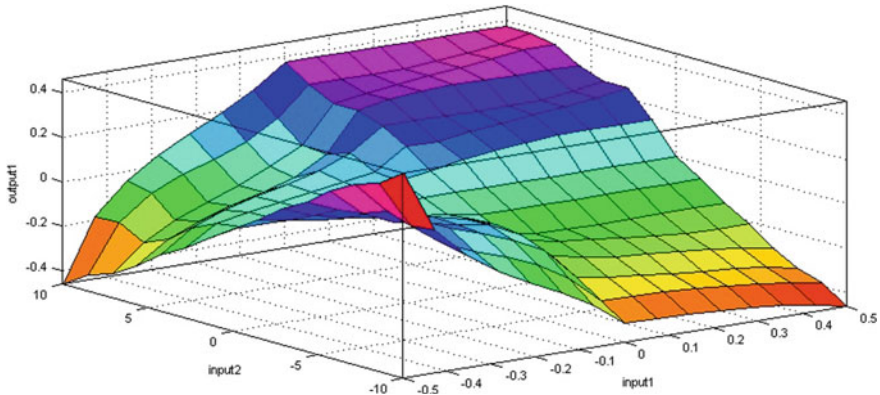
Fig. 4 Surface viewer of FLC

increments the power of the PMSG. If the change in power is positive, the peak power is in the right side and again FLC increases the speed of the rotor of generator. If the change in the power of the PMSG is negative, then maximum power is towards the left side and the FLC decreases the speed. This process continues until the maximum power is reached. The surface viewer of FLC is shown in Fig. 4.

The rules for FLC are shown in Table 1. The variable N + + shows negative very big, NB shows negative big, NM shows negative medium, NS shows negative small, ZZ shows zero, PS shows positive small, PM shows positive medium, PB shows positive big, and P + + shows positive very big.

The speed signal generated by FLC at maximum power point is considered as a reference speed signal. The reference speed signal is compared with actual speed of the permanent magnet synchronous generator (PMSG,) and the difference is fed through a well-tuned proportional plus integral) (PI) tuner [23, 24]. The PI tuner generates the required torque reference. The reference torque is compared with the calculated torque according to (6) to generate a reference quadrature current, where reference quadrature current ($i_{q,ref}$) is given as

$$i_{q,ref} = \frac{T_{e,ref}}{{}^3/_2 * p * \lambda} \tag{7}$$

Table 1 Rules for the fuzzy logic controller

	N ++	NB	NM	NS	ZZ	PS	PM	PB	P ++
N	P ++	PB	PM	PS	ZZ	NS	NM	NB	N ++
Z	NB	NM	NS	NS	ZZ	PS	PM	PM	PB
P	N ++	NB	NM	NS	ZZ	PM	PM	PB	PB

By using parks transformation, $i_{q,\,ref}$ and $i_{d,\,ref}(=0)$ are converted into i_a, i_b, i_c. The i_a, i_b, i_c signals are added with capacitor voltage balance signal generated by a voltage balance controller of Vienna rectifier. The voltage balance controller consists of half of the total voltage across the capacitor (V_{total}) and voltage across capacitor C_2, as shown in Fig. 2. The difference between these two quantities is tuned by a PI regulator, which generates reference waveforms for pulse generation. The reference waveform is compared with triangular carrier to generate necessary pulse width modulation signal.

6 Experimental Validation

The entire simulation work is validated by a real-time simulator OPAL RT. The real-time simulator used in this paper is OP 4200. The OP 4200 is one of the OPAL-RT real-time simulators. It consists of a system on chip combining an ARM CPU and a KintexTM-7 FPGA. It is also equipped with signal conditioning for 128 input–output lines. This design provides four signal-conditioning cassettes. Op4200 contains PentaLinux version 4.0.0 Xilinx operating system with a CPU speed of 1 GHz. It requires a DC supply of 24 V, and it can generate an output signal of $+/-16$ V. The real-time setup to validate the simulation result is presented in Fig. 6. The real-time setup consists of a PC with installed RT-LAB software, a real-time simulator OP4200, DSO and power analyzer and connected wires to capture the required results (Fig. 5).

Fig. 5 Real-time simulator OP4200
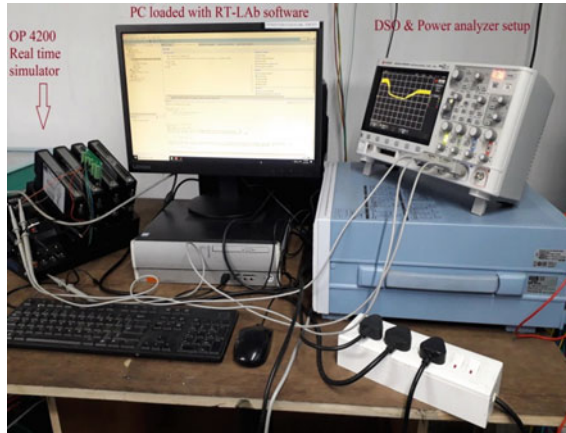
Fig. 6 Rreal-time setup with host PC and OP4200

7 Results and Discussion

The system is simulated using MATLAB/Simulink software. The rotor speed of PMSG at variable wind speeds is shown in Fig. 7. According to change in wind speed, the rotor speed also changes. As per change in the rotor speed, the output power of PMSG also changes and is represented in Fig. 8. The FLC tracks the peak power and varies the rotor speed at each wind speed. The Vienna rectifier increases the sine nature of the input AC current. The change in wind speed is reflected on the Vienna rectifier input current and is represented in Fig. 9. The voltage balance control balances the voltage across the capacitors. As a result, the voltage stress
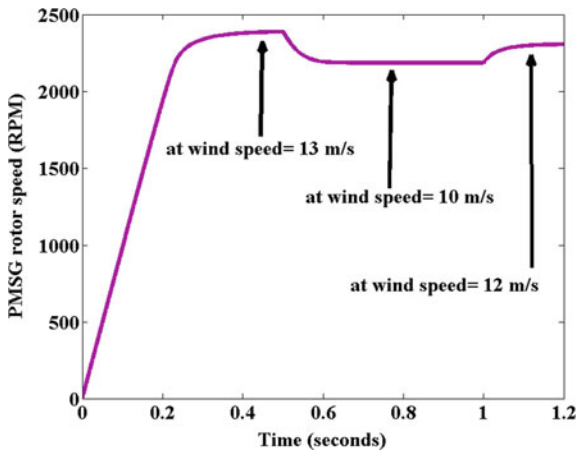
Fig. 7 PMSG rotor speed versus time
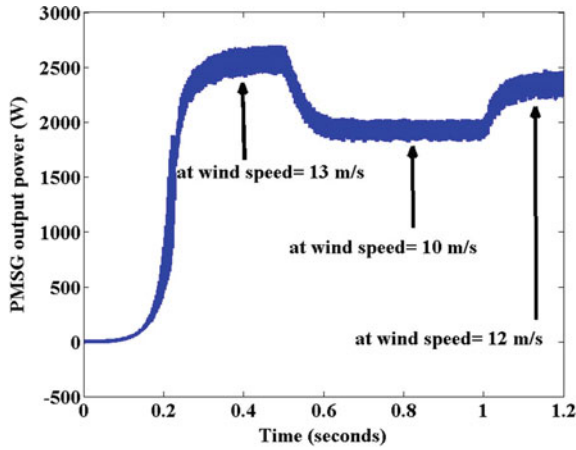
Fig. 8 PMSG voltage versus time
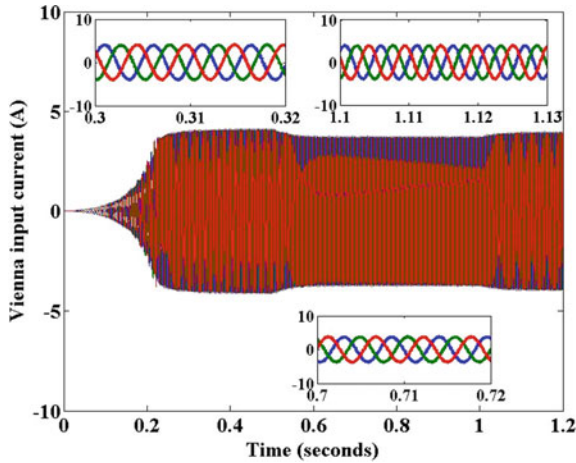
Fig. 9 Input current of Vienna versus time

across each switch is decreased by a factor of 2. The voltage across each capacitor is shown in Figs. 10 and 11. The total DC link voltage which is an input to inverter is represented in Fig. 12. The Vienna rectifier generates a three-level voltage and is shown in Fig. 13. In order to validate the simulation results, the entire system is operated using OP4200. The change in rotor speed according to change in wind speed in real-time environment is presented in Fig. 14. The actual wind speed is scaled to + /−16 V in OP4200 while configuring the input and outputs. The PMSG output power result using OP4200 is shown in Fig. 15. The mains current waveform should be in sinusoidal when Vienna rectifier is used. The sinusoidal nature of input current mains is shown in Fig. 16. The comparative analysis of input current waveform with
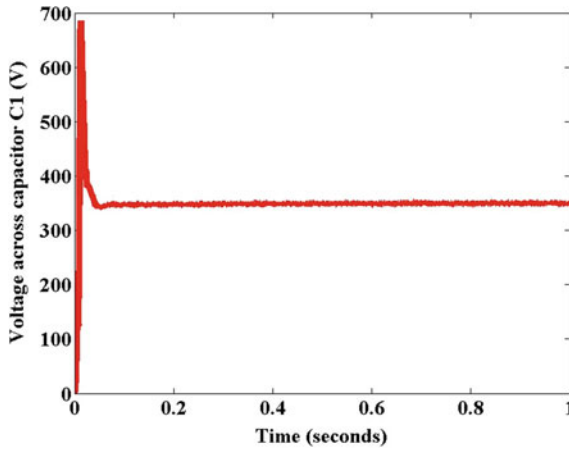
Fig. 10 Voltage across the capacitor C_1 versus time
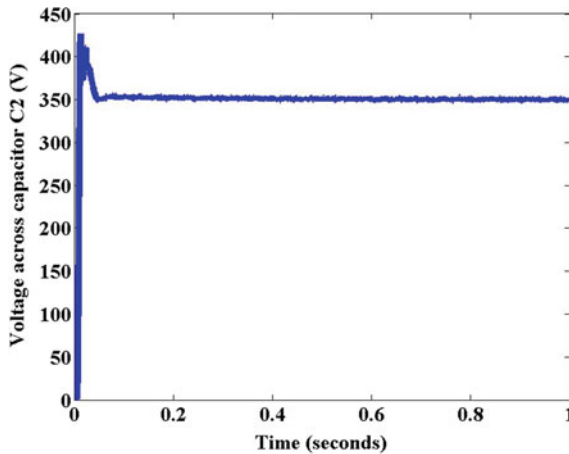
Fig. 11 Voltage across the capacitor C_2 versus time

and without Vienna rectifier is shown in Fig. 17. The current waveform without Vienna rectifier consists of dominant harmonics and is evident from Fig. 17. Vienna rectifier consists three-level line-line voltages. The representation of DC link voltage and three-level voltage is shown in Fig. 18. The inverter voltage and currents using OP4200 are shown in Figs. 19 and 20. Figure 21 represents the power flow from the source to grid. The capacitor voltages, DC link voltage and Vienna rectifier current are shown in Fig. 22.
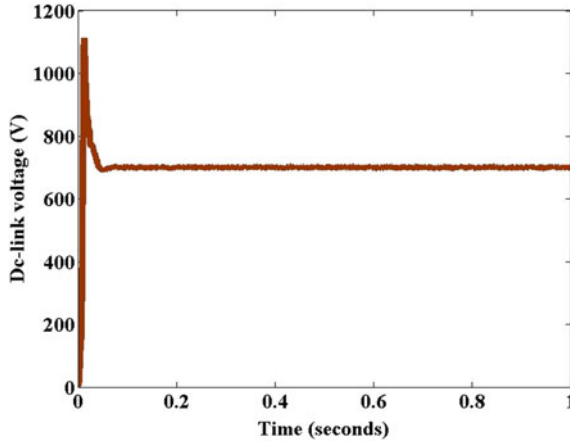
Fig. 12 Voltage across the capacitors (DC link voltage) versus time
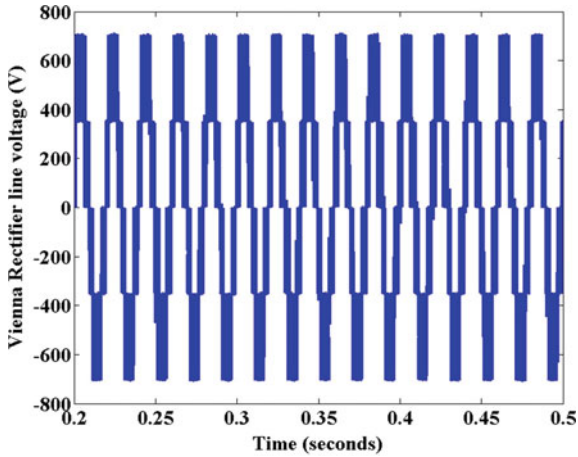
Fig. 13 Three-level voltage of Vienna rectifier versus time

8 Conclusion

In this work, a new controller for wind energy system to ensure power quality and to track peak power is proposed. The controller consists of an adaptive fuzzy logic controller to track maximum power and a DC voltage regulator to assure balance voltage across the DC link terminals. The controller is proved to be robust enough to track the maximum power at variable wind speeds. A balanced voltage control which reduces the voltage stress across the power electronic switches is proposed, and the real-time simulator results prove its optimum performance at variable wind speeds.
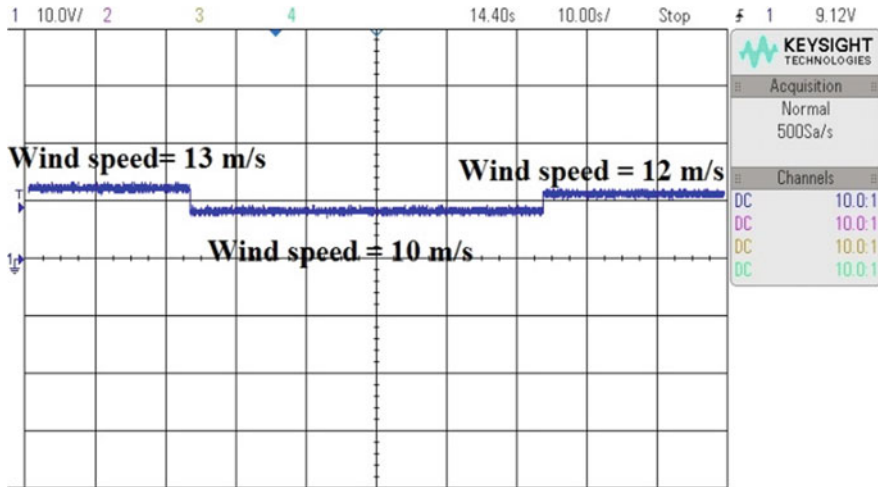
Fig. 14 Input current of Vienna versus time
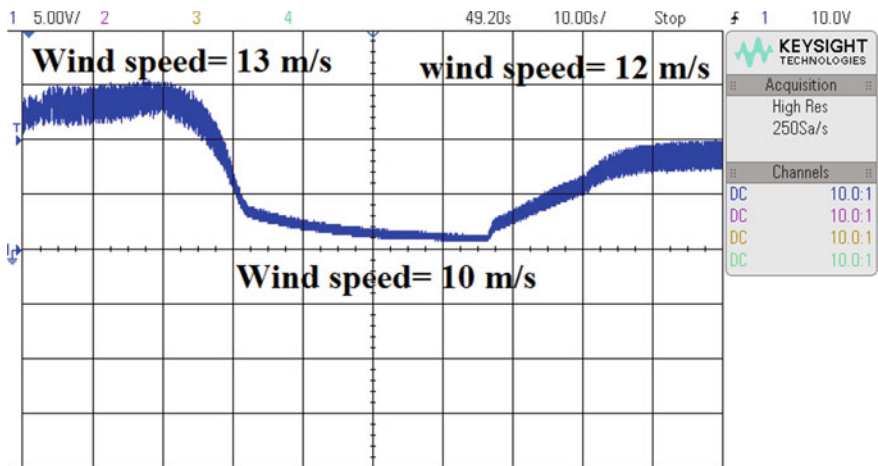
Fig. 15 PMSG output power versus time

An improved power quality at the input mains can be seen from the real-time results which are an evident of optimum performance of the proposed control scheme.
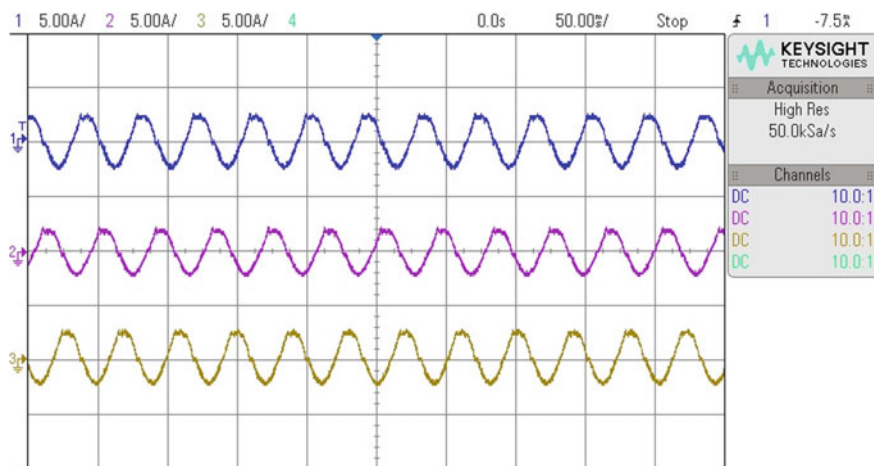
Fig. 16 Input current of Vienna versus time
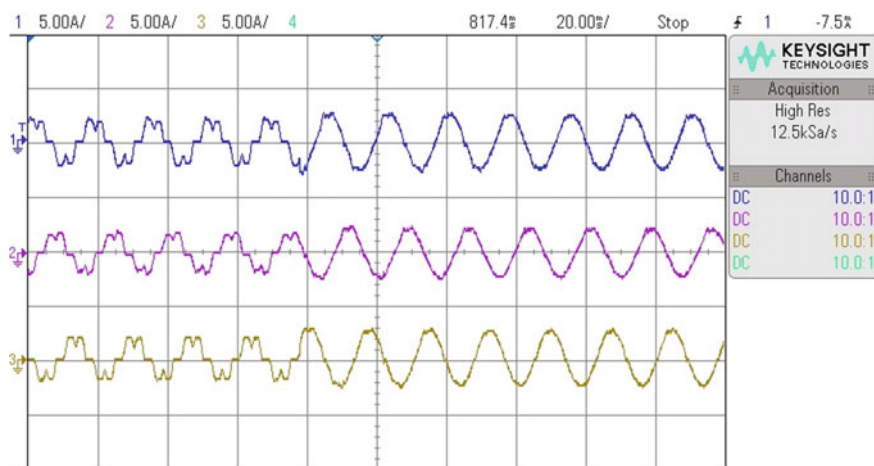
Fig. 17 Input current with and without Vienna versus time
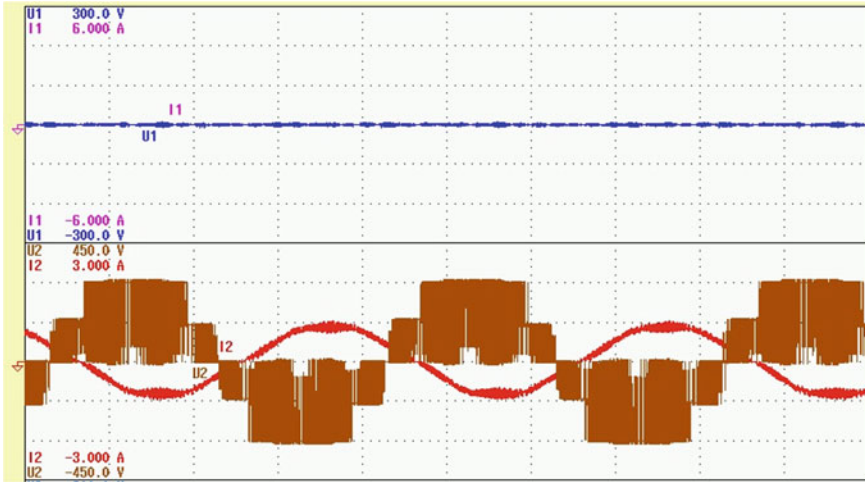
Fig. 18 Dc link voltage and three-level voltage versus time
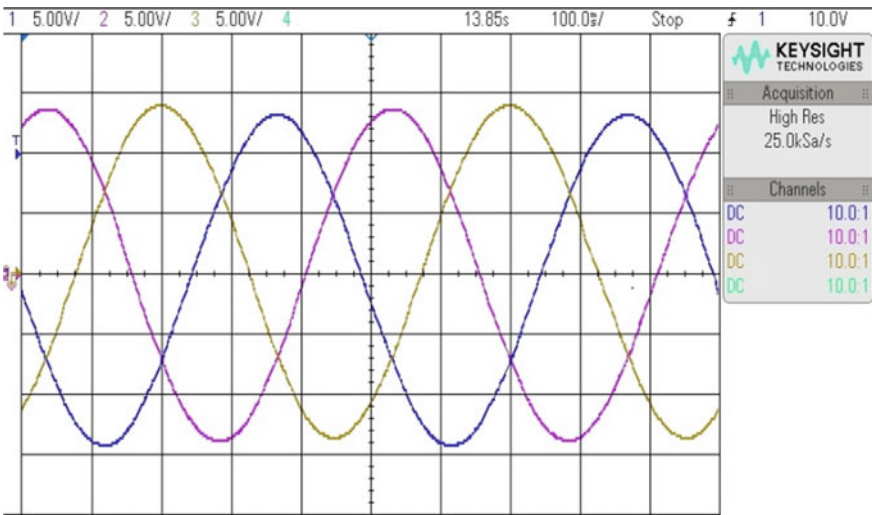
Fig. 19 Inverter output voltage versus time
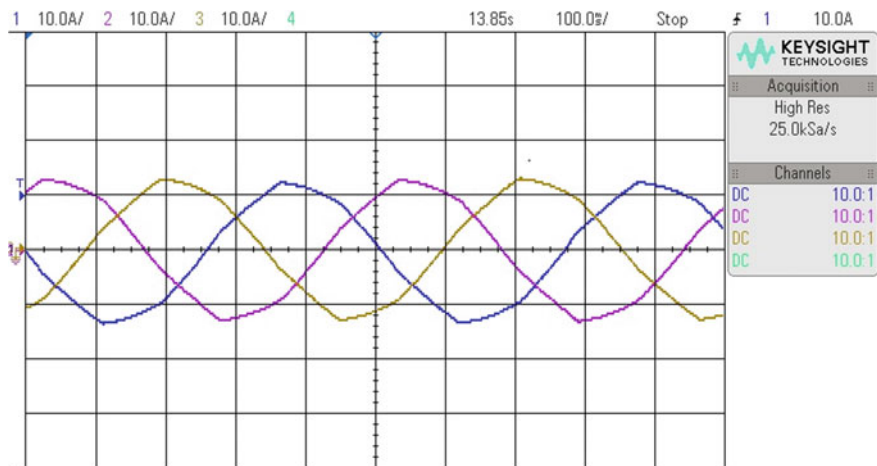
Fig. 20 Inverter output current versus time
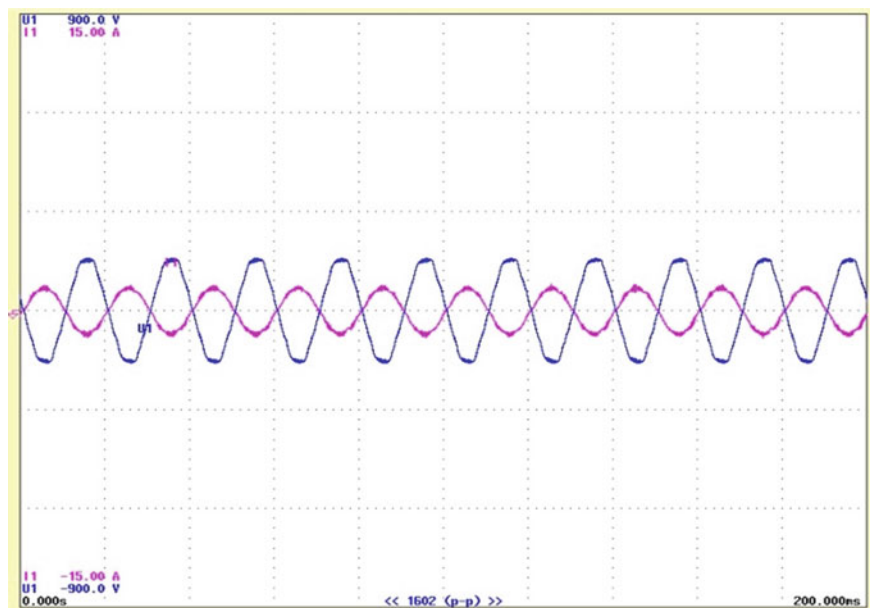
Fig. 21 Voltage and current of Vienna versus time
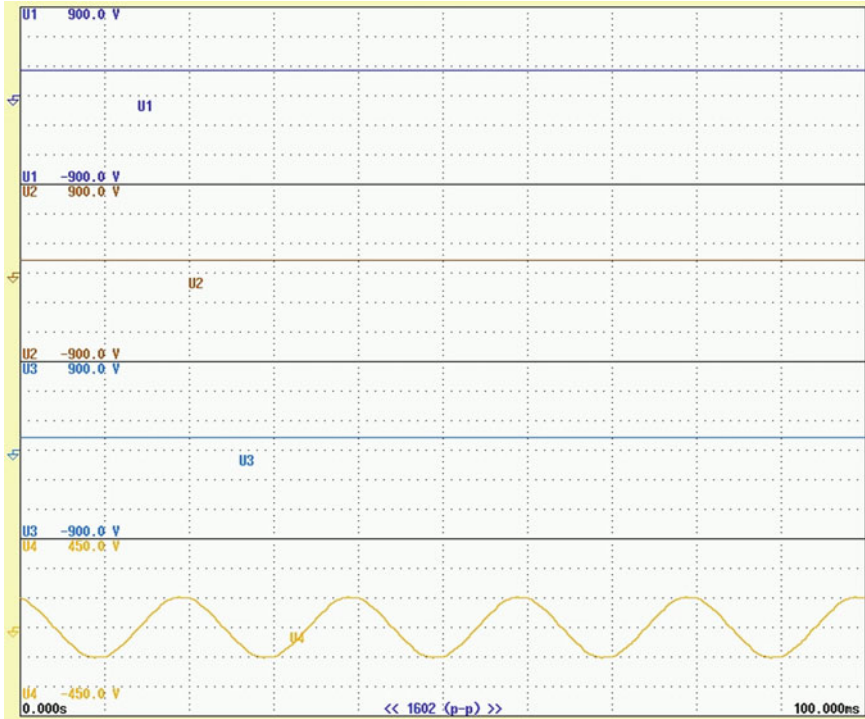
Fig. 22 V_{c1}, V_{c2}, $V_{dc\ link}$, Vienna input current versus time

References

1. Polinder H, Van der Pijl FF, De Vilder GJ, Tavner PJ (2006) Comparison of direct-drive and geared generator concepts for wind turbines. IEEE Trans Energ Conver 21:725–732
2. Wu B, Lang Y, Zargari N, Kouro S (2011) Power conversion and control of wind energy systems, John Wiley & Sons, Inc., Hoboken, New Jersey
3. Carlin PW, Laxson AS, Muljadi EB (2001) The history and state of the art of variable-speed wind turbine technology, Technical report. National Renewable Energy Laboratory (NREL), Colorado
4. Pena R, Clare JC, Asher GM (1996) Doubly fed induction generator uising back-to-back PWM converters and its application to variablespeed wind-energy generation. IEE Proc Electr Power Appl 143:231–241

5. Dubois MR (2004) Optimized permanent magnet topologies for direct driven wind turbines, Ph.D. dissertation, The Netherlands
6. Hansen LH, Madsen PH, Blaabjerg F, Christensen HC, Lindhard U, Eskildsen KA (2001) Generators and power electronics technology for wind turbines. In: 2001 27th annual conference of the IEEE industrial electronics society, 2000–2005.
7. Blaabjerg F, Ma K (2017) Wind energy systems. Proc IEEE 105:2116–2131
8. Twidell J (2006) Tony weir renewable energy sources, 2nd edn. Taylor & Francis group
9. Kolar JW, Zach FC (1997) A novel three-phase utility interface minimizing line current harmonics of high power telecommunication rectifier modules. IEEE Trans Ind Electron 44:456–467
10. Nannam HC, Banerjee A (2018) A detailed modeling and comparative analysis of hysteresis current controlled vienna rectifier and space vector pulse width modulated Vienna rectifier in mitigating the harmonic distortion on the input mains. IEEE Int Conf Industr Eng Eng Manage (IEEM) 2018:371–375
11. Nannam HC, Misra P, Banerjee A (2018) Harmonic analysis of state vector pulse width modulated Vienna rectifier. In: 2018 2nd international conference on power, energy and environment: towards smart technology (ICEPE), pp 1–6
12. Buehring IK, Freris LL (1981) Control policies for wind energy conversion systems, 128:253–261
13. Koutroulis E, Kalaitzakis K (2006) Design of a maximum power tracking system for wind energy conversion applications. IEEE Trans Ind Electron 53:486–494
14. Morimoto S, Nakayama H, Sanada M, Takeda Y (2005) Sensorless output maximization control for variable speed wind generation system using IPMSG. IEEE Trans Industr Appl 41:60–67
15. Datta R, Ranganathan VT (2003) A method of tracking the peak power points for a variable speed wind energy conversion system 18: 163-168
16. Wang Q, Chang L (2004) An intelligent maximum power extraction algorithm for inverter based variable speed wind turbine system. IEEE Trans Power Electron 19:1242–1249
17. Kazmi SM, Goto H, Guo HJ, Ichinokura O (2010) Review and critical anlysis of the research papers published till date on maximum power point tracking in wind energy conversion systems. IEEE Energ Convers Congr Exposition, 4075–4082
18. McIver A, Holmes DG, Freere P (1996) Optimal control of a variable speed wind energy turbine under dynamic wind conditions. In: 1996 IEEE industry applications conference thirty first IAS annual meeting, 1692–1698
19. Zinger DS, Muljadi E, Miller A (1996) A simple control scheme for variable speed wind turbine. In: 1996 IEEE industry applications conference thirty first IAS annual meeting, 1613–1618
20. Chedid R, Mrad F, Basma M (1999) Intelligent control of a class of wind energy conversion systems. IEEE Trans Energy Convers 14:1597–1604
21. Hilloowala RM, Sharaf AM (1996) A rule based fuzzy logic controller for a PWM inverter in a standalone wind energy conversion scheme. IEEE Trans Ind Appl 32:57–65
22. Zadeh LA (1973) Outline of a new approach to the analysis of complex system and decision process. IEEE Trans Syst Man Cybern 3:28–44
23. Nannam HC, Banerjee A, Guerrero JM (2021) Analysis of an interleaved control scheme employed in split source inverter based grid-tied photovoltaic systems. IET Renew Power Gener 15:1301–1314
24. Nannam HC, Banerjee A (2021) A novel control technique for a single-phase grid-tied inverter to extract peak power from PV-Based home energy systems. AIMS Energy 9:414–445

Performance Analysis of UPFC and DPFC in a Grid-Integrated Hybrid Solar–Wind System

Haricharan Nannam, Abhilash Sen, and Atanu Banerjee

Abstract In this work, a relative inspection is performed with distributed power flow controller (DPFC) and unified power flow controller (UPFC) connected to a solar–wind hybrid system. The hybrid system consists of dual sources for renewable energy as solar and wind. Solar generation system followed by a boost converter is useful to raise the level of DC power from the solar energy. On the other hand, wind generation system followed by a diode rectifier and boost converter amplifies the energy received from wind source. Now DC obtained from both the sources is coupled to a common DC bus to get the DC link voltage which eventually is applied as input to the grid side two-level voltage source inverter (VSI). The grid side demands control actions and monitoring perfectly due to the presence of distortions, noise, power losses, etc. Reactive elements reduce these problems up to a certain extent, but it increases the possibility of sub-synchronous resonance phenomenon and extra inductive and capacitive losses. Moreover, the power factor is also affected considerably. Thanks to the emerging FACTS technology, which controls as well as increases the utilization of transmission lines to its full thermal limits. Unified power flow controller (UPFC) is one of the latest FACTS devices available today. It controls the power flow through the lines by varying line inductances, transmission angles and voltage magnitude. The disadvantage of UPFC is its immensely high rated three-phase series–shunt converters and the increased ripple content in output grid voltages and currents. These problems are overcome by a newly invented FACTS device, namely distributed power flow controller (DPFC), which uses small single-phase series and shunt converters. The paper studies the effect of incorporating UPFC and DPFC to hybrid solar–wind system. Additionally, working principle of both the devices was presented. At the end, results from MATLAB simulation are used to support the claim of DPFC being superior to UPFC.

H. Nannam · A. Banerjee
Electrical Engineering, National Institute of Technology Meghalaya, Shillong, Meghalaya 793003, India

A. Sen (✉)
Electrical Engineering, National Taiwan University of Science and Technology, Taipei, Taiwan 10607
e-mail: abhilashsen0070@gmail.com

Keywords Renewable system · FACTS devices · DPFC · UPFC · Solar PV system · Wind energy system · Hybrid generation system

1 Introduction

It is very well known and well documented that the emissions due to carbon combustions are affecting the environment at a global scale [1]. Global warming and fossil fuel depletion are forcing to change the focus from thermal-based generation to renewable-based generation [2]. It is clearly noted by the International Renewable Energy Agency the increase in production of power by renewables in the twenty-first century. It is also stated that the overall production of wind energy has gone up to 487 GW, which is 7 times the amount it was ten years ago. The overall production of solar system also increased up to 302 GW, which is 43 times as it was ten years ago. Developing countries are also setting up renewable targets to improve their overall power at the grid level. China is one of the leading countries as far as renewable power generation is concerned. In China by the end of the year 2016, the total photovoltaic power and wind power capacity was around 77.42 and 168.69 GW, respectively [3]. European countries are not far behind. European Union (EU) has a target in mind to reach power production using renewables by 20% of its total energy consumption by the year 2025. The European nation Germany has further ideas of reaching renewable use up to 30% by 2020 and 60% by 2050 [4].

Out of all the renewables in market, solar, wind and hydro power are the most dominant ones. With decreasing day-to-day cost of these technologies, it is now easily available with the common people. These renewable technologies, especially solar and wind, are called variable renewable energy (VRE), and in the coming years, these will be dominant over the conventional sources as well. In the past decades, many researches were performed on renewable systems, especially to increase the overall efficiency of the whole system. On view of this, the hybrid generation system came up the market. In [5], the behaviour of hybrid solar–wind generation system is analysed. The authors stated that the complementary nature of these two sources makes them the best choice for co-generation or hybrid generation. Both solar and wind systems completely depend on weather conditions. They are present in abundance, non-polluting and free of cost available, which makes it perfect alternative to the existing conventional sources. The hybrid generation system can feed power to the main grid as a grid-integrated system or it can work independently supplying power to a load. During independent operation, the voltage and current have to be according to the rating of the load. In case of grid integration, the voltage and current should be according to the grid standards [6]. So both the operations deal with challenges. [7] described the issues with grid integration of renewable sources. The authors focused mainly on power quality issues which emerge due to penetration of renewable sources. With arising power quality issues, changes in fault level also occur. Different positioning of renewables at the line results in different fault levels and hence different protection schemes [8]. Another approach performed in

[9] concluded that voltage fluctuations, frequency fluctuations and harmonic distortions are very common problems in grid-connected system. As defined by IEEE std. 929–2000, voltage flicker, frequency fluctuation and harmonic distortion are the major factors to affect the power quality of a grid-connected renewable system. In other words, monitoring of power at the output side is appreciable. In the process, transmission lines have a major role to perform, which opens up ways for flexible AC transmission system (FACTS) to improve the power level and to mitigate some of the problems mentioned above.

The most dominant and popular FACTS device was introduced in [10], namely unified power flow controller (UPFC). The incredible capability of this device was to control all parameters of transmission lines in order to control the power flow through it. It can control the voltage magnitude and angle as well as the transmission angle. The authors also discussed some disadvantages of UPFC, firstly, the complexity. Two high rated three-phase converters are joined using a common DC link. Secondly, the device is not portable; there should always be a connection between the two converters for complete operation. In the year 2010, Yuan et al. [11] introduced yet another FACTS device, namely distributed power flow controller (DPFC), which according to the authors is an advanced version of UPFC. The function and capability of DPFC are same as that of UPFC, but the operation is quite different. It uses small rated single-phase full wave converters. Moreover, the connection between series and shunt converters is not present which makes installation and upgradation very easy. It also uses the third harmonic frequency component for the power flow control operation. The paper starts with the main system model in Sect. 2. The next two Sects. 3 and 4 deal with the operating principles of UPFC and DPFC, respectively. Section 5 presents the results obtained from MATLAB/Simulink and observations. Section 6 consists of the paper conclusion followed by Acknowledgement and References.

2 System Description

2.1 Photovoltaic System

The solar generation system rated at 1000 W consists of a solar panel, followed by perturb and observe (P&O)-based DC–DC boost converter. The solar panel used is Mitsubishi PV with only parallel connected module and five number of series connected module. The detailed specifications are shown in Table 1. The VSI is controlled using state vector pulse width modulation (SVPWM) technique [12]. The VSI controller takes voltage at grid Vg, current at grid Ig and DC link voltage Vdc as the inputs and correspondingly generates six pulses to maintain the DC link voltage constant at the given reference quantity.

Table 1 Uncompensated source-side system parameters

Variable	Values
PV OC voltage(V_{oc})	30.8 V
PV SC current(I_{sc})	8.23 A
Maximum power(P_{max})	200 W
DC link reference(V_{dc})	500 V
Transformer rating	440 V/25 kV, 1000VA, 50 Hz
Grid voltage	25 kV
TSR	0.2
Cpmax	0.59
Torque constant (PMSG)	0.912
Wind speed	12 m/s^2
No. of phases (PMSG)	3
Pole pairs (PMSG)	2
Inertia	25 kgm^2
Viscous damping	0.0003035
Vdc link capacitor	4000uF
L filter	0.135 H
R filter	0.001 Ω

2.2 Wind Energy System

Wind energy conversion system consists of direct-driven permanent magnet synchronous generator (PMSG) with a turbine followed by a diode bridge rectifier to convert alternating quantity (AC) into direct quantity (DC) and a DC–DC converter to track the maximum power at an enhanced output voltage level. In order to track maximum power, a simple perturb and observe (P&O) algorithm is utilized due to its simplicity and reduced complexity. The values of PMSG which has been utilized in the system are shown in Table 1. The enhanced DC output of the chopper is directly connected to the main DC link point or the point of common coupling of the solar system, resulting in the hybrid model (Fig. 1).

3 Unified Power Flow Controller

Unified power flow controller abbreviated as UPFC belongs to the category of combined devices. Two three-phase converters make the most part of it. The converters are joined in continuation using a DC link. The series converter injects desired voltage of desired magnitude and angle to the line. The DC link is used to transfer the active power from the shunt converter to the series converter. Subsections explain the detailed working of both the series and shunt controllers.
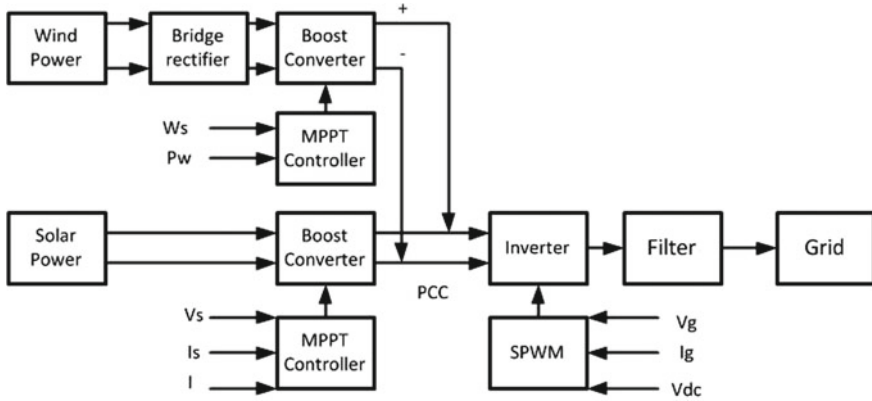
Fig. 1 Block representation of the entire system

3.1 UPFC Shunt Controller

The shunt controller functions like a normal static shunt compensator (STATCOM). Its main function includes charging of the DC link capacitor voltage, which could be utilized by the series converter for its own operation and maintaining constant voltage at the point of connection. It accepts Vdcref (desired value for DC capacitor voltage) and V1ref (the desired value for line voltage) as references. The error term of Vdcref with DC voltage (Vshdc) is regulated using PI controller which gives result Idref. Likewise, Iqref equals to the output obtained using tuned PI controller, regulating the inaccuracy between desired voltage and grid voltage.

3.2 UPFC Series Controller

The series control utilizes the voltage stored by the capacitor to inject the power quantities in accordance with the references as depicted in Fig. 2. The system provides two references: Pref and Qref. With the help of conventional PI tuner, Idref and Iqref
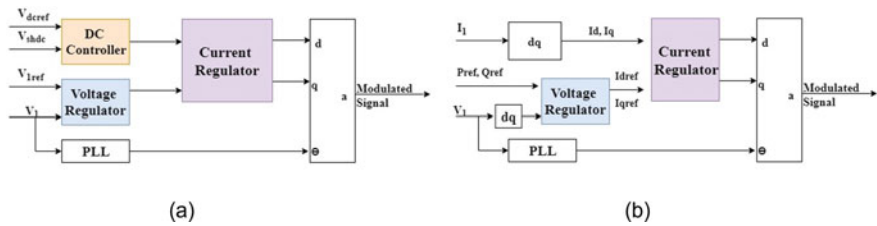
Fig. 2 Controller diagrams of UPFC **a** series, **b** shunt

(current references) can be obtained by utilizing values of P_{ref}, $V_{d,g}$, Q_{ref} and $V_{q,g}$ as shown by Eqs. (1) and (2):

$$I_{dref} = \frac{\left(V_d * P_{ref}\right) + \left(V_q * Q_{ref}\right)}{\sqrt{(V_d)^2 + (V_q)^2}} \tag{1}$$

$$I_{qref} = \frac{\left(V_q * P_{ref}\right) - \left(V_d * Q_{ref}\right)}{\sqrt{(V_d)^2 + (V_q)^2}} \tag{2}$$

4 Distributed Power Flow Controller

Distributed power flow controller (DPFC), proposed in [11], is a modified variety of unified power flow controller (UPFC). It is basically the combined result of UPFC and DSSC or distributed static series controller [13]. The idea is to upgrade the UPFC in such a way that the new device overcomes all the disadvantages of UPFC.

The DC link connection between shunt and series converter in UPFC acts as a constraint for further upgradation. Hence, the DC link is eliminated to increase flexibility of the system. The high-voltage transmission line itself is used as the connection path between shunt and series converter. The interesting fact which makes DPFC different from other devices is the use of the third harmonic current component. The DPFC set-up comes with a pair of star–delta transformers. These transformers are used to inject third harmonic component in the line and later reject the harmonic component through it. The reason for using third harmonic and not the other higher harmonics is the fact that it can be easily filtered out from the line using a low-pass filter. The low-pass filter can be eliminated using the star–delta transformer itself. As delta appears to be open for the third harmonic component, joining the neutral of star to ground actually passes the entire third harmonic component to the ground. Moreover, the line inductances are also lowered using third harmonic and not the higher harmonics. Another problem of UPFC is its high rated converters. This problem is solved using multiple small rated series converters. The number of series converters depends on the desired real and reactive power. UPFC faces another problem as if any one of the converters becomes useless, the operation is stopped. In case of DPFC, all the converters have separate control blocks and separate capacitors, that is why the failure of one will not affect the operation of the other converters. The structure of DPFC is shown schematically in Fig. 3.
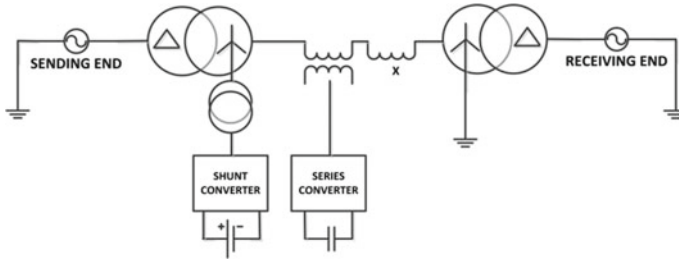
Fig. 3 Schematic diagram of DPFC

4.1 DPFC Shunt Controller

The shunt controller performs at third harmonic frequency. Its main function is to support the working of series converters. The block diagram of shunt control structure is shown in Fig. 4. Its main work is to deliver the third harmonic component, which will be utilized for charging the series capacitors. The controller accepts two references: the third harmonic direct axis reference and third harmonic quadrature axis reference as Id3ref and Iq3ref, respectively. A single-phase coupling transformer is also used through which the third harmonic current is injected into the neutral of the star–delta line transformer. The injected current is broken into its corresponding dq parameters (Id3 and Iq3) using single-phase abc to dq transformation block. The actual dq components Id3 and Iq3 are compared with the references Id3ref and Iq3ref for getting the Vd* and Vq*. The angle ωt is obtained through a PLL block and is multiplied with a gain of 3 for getting the required $3\omega t$. These three parameters Vd*, Vq* and $3\omega t$ give the modulated signal using single-phase dq to abc transformation.
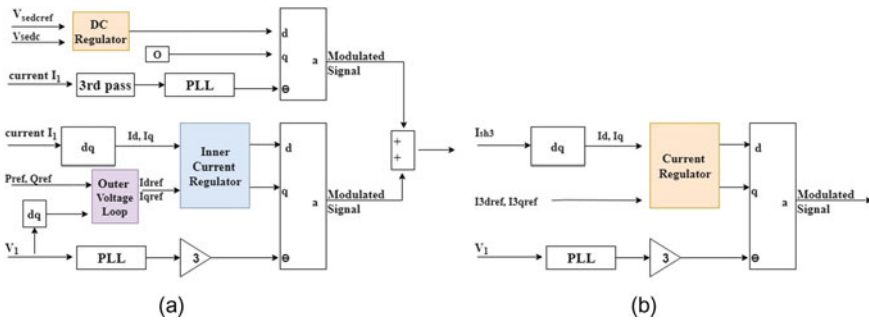
Fig. 4 Schematic diagrams of DPFC controllers **a** series controller, **b** shunt controller
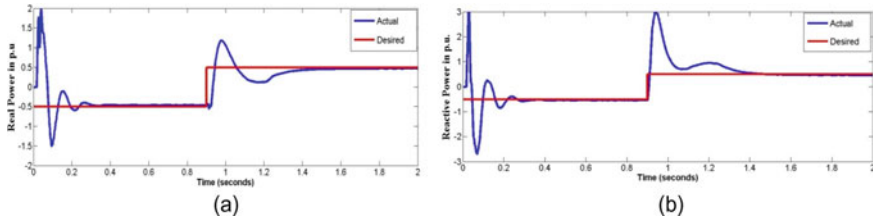
Fig. 5 Power tracking using UPFC **a** real power, **b** reactive power

4.2 DPFC Series Controller

The series converter performs the main function of DPFC, i.e. the control of power flow through the line. The series converter in DPFC is a standard four switch full controlled single-phase converter. The series converter is connected with the transmission line through a single-phase coupling transformer. The converter performs two actions: firstly, it charges its own capacitor, i.e. acts as a rectifier, and secondly, it injects the desired voltage which in turn affects the power parameters, i.e. it also functions as an inverter. The third harmonic content in the line is utilized for charging the capacitor. At the same time, it injects the required voltage at fundamental frequency. As the function is performed at two different frequencies, two different control structures are needed. The modulated signals from both the controllers are added to get the final modulated signal for the series converter. The controller implements vector current control strategy. The control structure of the series converter is shown in Fig. 4.

The third harmonic frequency control charges the capacitor up to the reference voltage value Vdcseref as given by the operator. The actual voltage Vdcse and reference voltage Vdcseref are compared, which gives the error signal. The error signal is passed through a PI tuner which gives the Vd*. The Vq* is kept zero. The line current (i) contains 50 Hz signal as well as 150 Hz signal. As this is the third harmonic frequency control, the line current (i) is filtered out using a high-pass filter, to get the third harmonic content of the line. The output of HPF is passed through a single-phase phase-locked loop (PLL) which gives phase angle $3\omega t$. The three components Vd*, Vq* and $3\omega t$ act as the input for single-phase dq to abc transformation block. This transformation block generates the modulating signal for third frequency control. The fundamental frequency control's primary function is to inject required voltage of desired magnitude and angle into the line, which in turn controls the real and reactive power flow through the line. It follows the direct power control (DPC) strategy. The references are given as real power reference (Pref) and reactive power reference (Qref). The input voltage of DPFC, in this case the output voltage of the inverter, is broken into its corresponding dq parameters [14].

Table 2 Uncompensated grid-side system parameters

Parameters	Values
Vgrid (kV)	25
Igrid (amps)	0.03
Vinv (volts)	440
Iinv (amps)	5.58
Real power (p.u)	0.71
Reactive power (p.u)	0.38
Voltage THD (%)	4.42
Current THD (%)	5.02
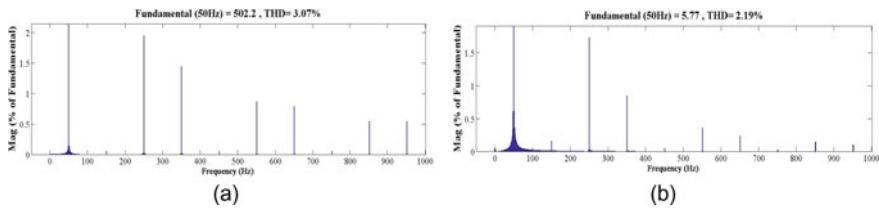
Fig. 6 Total harmonic distortion with UPFC **a** line voltage, **b** line current

5 Results and Discussion

The results for uncompensated system are depicted in Table 2. Uncompensated system means the FACTS devices (UPFC and DPFC) are connected but are not enabled. It is observed that the real power rests at around 0.71 p.u and the reactive power at 0.98 p.u. The voltage and current THD are 4.42% and 5.02%, respectively.

The FACTS is connected after the grid side main inverter. The targets of reactive and real power are taken as − 0.5 p.u. and 0.5 p.u. For UPFC shunt controller, KP = 1.2 and KI = 400. For series controller, KP = 0.3 and KI = 22. V1ref is 1p.u., and Vdcref is 500 V. Likewise, DPFC comprises a shunt converter and a set of three series converters. The variables for shunt controller are as follows: Ishref3 = 3A and Kp, KI values are 0.05 and 0.5, respectively. Similarly, for the series controller, Vsedcref = 50v, power references Vref and Iref are −0.5 and 0.5 p.u. Kp and KI values are 0.5 and 20, respectively. The results are depicted from Figs. 6, 7 and 8.

6 Conclusion

The conclusions of the study are drawn based on the total harmonic distortion and power tracking capabilities of both the devices. Table 3 presents the detailed simulation results obtained through MATLAB/Simulink platform. The uncompensated
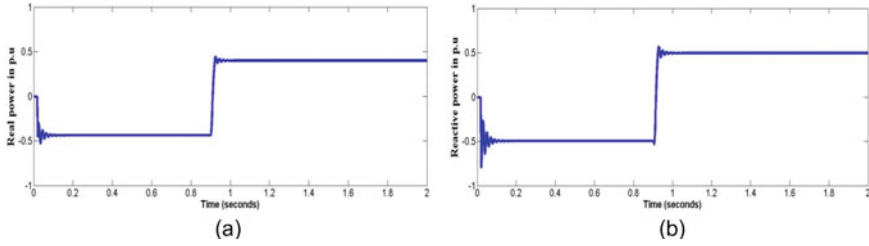
Fig. 7 Power tracking using DPFC **a** real power, **b** reactive power
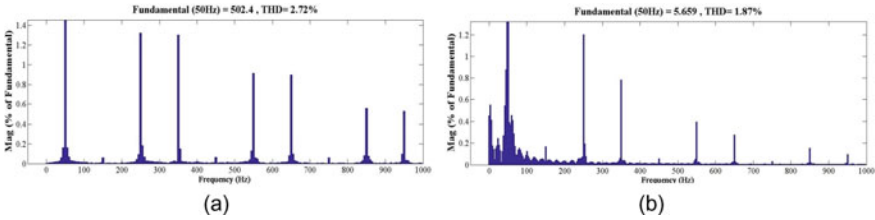
Fig. 8 Total harmonic distortion with DPFC **a** line voltage, **b** line current

Table 3 Line powers and THD results

Parameters		UPFC	DPFC
Real power	Ref: −0.5	−0.46	−0.49
	0.5	0.44	0.44
Reactive power	Ref:−0.5	−0.55	−0.48
	0.5	0.46	0.49
Voltage THD (%)		3.07	2.72
Current THD (%)		2.19	1.87

voltage and current THD were 4.42% and 5.02%, which is reduced using UPFC to 3.07% and 2.19%, respectively, and further reduced using DPFC to 2.7% and 1.8%, respectively. In addition, the paper also describes the control structure and working of the power controllers in detail. At the end of the analysis, it is clear that DPFC outperforms UPFC in accuracy as well as robustness.

References

1. Kroposki B, Johnson B, Zhang Y, Gevorgian V, Denholm P (2017) Achieving a 100 percent renewable grid: operating electric power systems with extremely high levels of variable renewable energy. IEEE Power Energ Mag 15(2):61–73
2. Du E, Zhang N, Hodge BM, Wang Q, Kang C, Kroposki B, Xia Q (2018) The role of concentrating solar power towards high renewable energy penetrated power systems. IEEE Trans Power Syst 33(6):6630–6641
3. [REN21 Secretariat. Renewables 2017: Global status report. http://www.indiaenvironmentportal.org.in. 2017.
4. Moreira A, Pozo D, Street A, Sauma E (2017) Reliable renewable generation and transmission expansion planning: co-optimizing system's resources for meeting renewable targets. IEEE Trans Power Syst 32(4):3246–3257
5. Sarkar S, Ajjarapu V (2011) MW resource assessment model for a hybrid energy conversion system with wind and solar resources. IEEE Trans Sustain Energ 2(4):383–391
6. Wu Y-K, Lin J-H, Lin H-J (2017) Standards and guidelines for grid-connected photovoltaic generation systems: a review and comparison. IEEE Trans Ind Appl 53(4):3205–3216
7. Telukunta V, Pradhan J, Agrawal A, Singh M, Srivani SG (2017) Protection challenges under bulk penetration of renewable energy resources in power systems: a review. CSEE J Power Energ Syst 3(4):365–379
8. Brahma SM, Girgis AA (2004) Development of adaptive protection scheme for distribution systems with high penetration of distributed generation. IEEE Trans Power Delivery 19(1):56–63
9. Liang X (2017) Emerging power quality challenges due to integration of renewable energy sources. IEEE Trans Ind Appl 53(2):855–866
10. Gyugyi L, Schauder CD, Williams SL, Rietman TR, Torgerson DR, Edris A (1995) The unified power flow controller: a new approach to power transmission control. IEEE Trans Power Delivery 10(2):1085–1097
11. Yuan Z, de Haan SW, Ferreira JB, Cvoric D (2010) A facts device: distributed power flow controller (DPFC). IEEE Trans Power Electron 25(10):2564–2572
12. Liu Y-C, Ge X-L, Zhang J, Feng X-Y (2015) General SVPWM strategy for three different four-switch three-phase inverters. IEEE Electron Lett 51(4):357–359
13. Divan D, Johal H (2007) Distributed FACTS-a new concept for realizing grid power flow control. IEEE Trans Power Electron 22(6):2253–2260
14. Sen A, Banerjee A, Nannam H (2020) A comparative analysis between two DPFC models in a grid hybrid solar–wind generation system. IEEE PESGRE, Cochin, India.

Design and Fabrication of a Lighter than Air Wind Turbine

Saket Singh, Samridh Mehta, Rishi Jain, K. Vishnu Kiran, Utkarsh Bajpai, and K. B. Ravichandra Kumar

Abstract The Lighter than Air (LTA) Wind Turbine system utilizes the stronger wind currents at higher altitudes to generate electricity. Suspended in the air with the help of tethers, this system is capable of rotating about its axis which further actuates an onboard AC generator that transfers the current to the ground, where the alternating current is transformed into useful direct current. The envelope and wing design of the system is such that it can operate under conditions with wind flow from two directions and a spherical envelope further increases the balloon's stability in turbulent weathers due to an acting Magnus effect. Such systems have the efficacy of being used very efficiently in metropolitan cities where the establishment of conventional wind turbines is not feasible due to space constraints. Such lighter than air systems have a huge latent potential in building a sustainable future and this project works towards the manifestation of the same. This paper offers an alternative which can be further worked upon to make a viable solution for this concept.

Keywords Lighter than air · Wind energy · Sustainability · Fabrication · Design

Nomenclature

g	Gravitational constant (m.s-1)
p	Pressure (N.m-2)
L	Lift (N)
r	Radius (m)
h	Altitude (m)
I	Moment of Inertia (m4)

S. Singh (✉) · S. Mehta · R. Jain · K. V. Kiran · U. Bajpai · K. B. R. Kumar
SRM Institute of Science and Technology, Chennai, India
e-mail: singhsaket625@gmail.com

Greek letters

α   Angular Acceleration (rad/sec2)
ρ   Density (kg/m3)
μ   Viscosity (Pa.s)
τ   Torque (Nm)

Subscripts

s   Static

1   Introduction

Wind is the fastest growing energy source in the world and one of the lowest priced renewable energy technologies today, at a cost of 4–6 cents per kW hour. "There is enough energy in high altitude winds to power civilization 100 times over; and sooner or later we're going to learn to tap into the power of winds and use it to run civilization." The life cycle for the energy gained from wind turbines is simple if the physical parts last. The generation of electricity from wind power takes place in several steps. It requires a rotor, usually consisting of 2–3 blades, mounted atop a tower; wiring; and "balance of power" components such as converters, inverters and batteries Wind turbines at ground level produce at a rate of 20–25%, but when placed at altitudes from 600–1000 feet, energy output can double.

The existing methods of efficiently harnessing wind energy to electrical energy primarily involve a wind turbine.

Horizontal and Vertical axis wind turbines are the two dominant classes of wind turbines. Small turbines are predominantly utilized as auxiliary power units for battery charging of low power equipment like traffic warning signs, streetlights, and consumer vehicles. Larger turbines can contribute to the domestic power supply while excess power can be returned to the utility by net metering. Wind farms-arrays of exceptionally large turbines are an important source of intermittent renewable energy. These are strategically deployed by many nations at scale to reduce fossil fuel consumption. One assessment claimed that, as of 2009, wind had the "lowest relative greenhouse gas emissions, the least water consumption demands and the most favorable social impacts" compared to coal, gas and even renewable resources like—photovoltaic, geothermal energy and hydro power.

Airborne wind turbines are conceptualised as a wind turbine that has its rotor supported in the air without a tower. Such a design benefits from higher velocity and persistence of wind at high altitudes, diverse mechanical and aerodynamic options, reduction in overall cost due to lack of tower construction or the need for slip rings

or yaw mechanism. While the caveats include safely suspending and maintaining the turbine at altitudes of hundreds of meters in turbulent winds, transferring the generated power back to earth, and interference with aviation.

Airborne wind turbines are part of a wider class of Airborne Wind Energy Systems (AWES). They may operate in low or high altitudes or on top of skyscrapers. Tethering is a core part of AWESs. A non-conducting tether may be used when the generator is ground-based. But when the generator is aloft, then a conductive tether would be used to transmit energy to the ground. AWESs suffer from some disadvantages—Kites and helicopters are grounded when there is insufficient wind; kytoons and blimps may resolve the matter. Other disadvantages for our system are: Bad weather like lightning or thunderstorms could temporarily suspend use of the machines, requiring them to be brought back down to the ground. Some schemes may require a long power cable and that may interfere with aircraft operations.

2   Design Inspiration

Several profound disadvantages make it harder to implement the technology as the go to energy harnessing source. These include:

- Wind turbines can be large, reaching over 140 m (460 ft) tall and with blades 55 m (60 yd) long, and people have often complained about their visual impact.
- Environmental impact of wind power includes effect on wildlife Thousands of birds, including rare species, have been killed by the blades of wind turbines.
- Energy harnessed by wind turbines is sporadic and not a "dispatchable" source of power; its availability is based on whether the wind is blowing, not whether electricity is needed.
- Turbines can be placed on ridges or bluffs to maximize the access of wind they have, but this also limits the locations where they can be placed.
- To maximize the energy output enough to power a city, a large area of land (known as wind farm) needs to be acquired. Due to the large length of wind blades, two windmills cannot be located at proximity. Hence, a much larger land area is required to accommodate a greater number of windmills.
- Lighter than Air Wind Turbines mitigates most of the technological disadvantages mentioned above. Some of the advantages of LTAs over traditional windmills are:
- Unlike the traditional windmills, the design of Lighter than air wind turbines are such that they are capable of rotation irrespective of the wind direction i.e. they are aerodynamically efficient.
- LTAs are usually suspended in the air with tether cables. They don't require large independent structural towers. The structural requirements of LTAs are less as compared to windmills.
- LTAs are cheaper and easier to manufacture and transport. They also require less maintenance due to less mechanical parts involved in the design.

- LTAs are smaller in size and therefore, does not require huge acres of wind farm to generate electricity. Instead, many LTAs can be placed close to each other. LTAs can also be placed individually over tall skyscrapers.
- It is a known fact that at higher altitudes, wind blows more faster than at low altitudes. It will be easier for a tether attached LTA to harness the wind energy at those higher altitudes when compared with tower mounted traditional windmills.

3 Generator Selection and Output

3.1 Generator Selection

The generator selected for the final design is a 12–24 V 36 W Mini Wind Turbine Generator. Due to the low weight of the generator, and the subsequent performance with large torque, this generator perfectly suits our necessities for the balloon to generate adequate electricity (Fig. 1 and Table 1).

Fig. 1 12–24 V 36 W mini wind turbine generator

Table 1 Specifications of 12–24 V 36 W mini wind turbine generator

Power	40 W
Speed	12V3000 turn/24V5000 transfer
DC generator time by	Maximum 36 W (DC)

3.2 Generator Output

As simulated using Simulink, a graphical programming environment for modelling, simulating and analyzing multidomain dynamical systems, the following data was collected (Fig. 2) (Tables 2 and 3).

Practically, the data that was collected from the generators are.

4 Transmission Mechanism

The objective of the mechanism is the transmission of power from the LTAWT to the generator.

The LTAWT was fabricated using PVC material. It is completely sealed to prevent any leakages of gas molecules. As the cost of Helium was exorbitant, the Lighter than Air Wind Turbine had to be tested in front of the Open Jet Wind Tunnel in
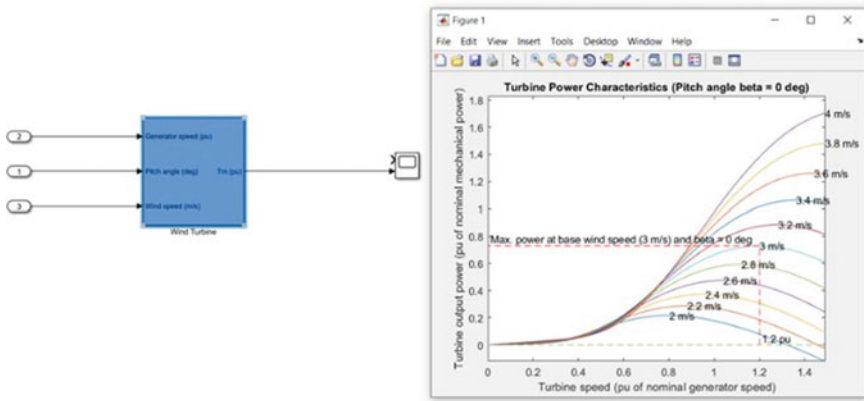
Fig. 2 Simulink analysis showcasing the generator output

Table 2 Theoretical data collected using simulink analysis of 12-24 V 36 W mini wind turbine generator

Torque	0.1 N-m
Maximum RPM	3000RPM
Power generated (2 generators)	80 W

Table 3 Practical data collected of 12 V–24 36 W mini wind turbine generator

Generator current	4A
Generator Voltage	23 V
RPM	2950RPM
Calculated power	92 W

the Aerospace Hangar at SRM Institute of Science and Technology. However, tether cables would be unable to keep the LTAWT in place in front of the wind tunnel. To mitigate this problem, a platform was design and fabricated for the sole purpose of testing the LTAWT in front of the open jet wind tunnel.

4.1 Shaft and Platform

The shaft design is inspired from the Twin Spool arrangement which is like the Jet Engines. A Stainless-Steel shaft is kept stationary and is concentrically mounted to a 3D Printed Pipe (Fig. 3) (Table 4).

This entire shaft with pipe mounting is coupled to the balloon. This entire structure is further mounted to a platform with the help of Ball Bearings (Table 5).

Fig. 3 The 3D printed pipe incorporated with the stainless-steel shaft

Table 4 Dimensions of the shaft design

Stainless steel shaft diameter	8 mm
3D printed pipe inner diameter	19 mm
3D printed pipe outer diameter	25 mm

Table 5 Dimensions of the interior ball bearing

Inner diameter	8 mm
Outer diameter	19 mm

Table 6 Dimensions of the platform ball bearing	Inner diameter	25 mm
	Outer diameter	37 mm

The supporting platform was made 1150 mm high from the ground. The platform has Ball Bearing to hold the pipe (Table 6).

The Ball Bearing was push fitted inside the Plywood which is directly crafted on the platform. The Generator is mounted with a 3D Printed Hub as shown in the Figure. 3D Printed Gears were used with a gear ratio of 3:1 to proliferate the RPM Output (Figs. 4 and 5) (Table 7).

The mechanism can be segregated into two divisions:

(1)   Stationary parts: The 8 mm Stainless-steel shaft which passes through the LTAWT holds the complete body. The tethers are attached to both the ends of this shaft. The Generator is also stationary which is mounted on the shaft with the 3D printed mount.

Fig. 4 Gear 1
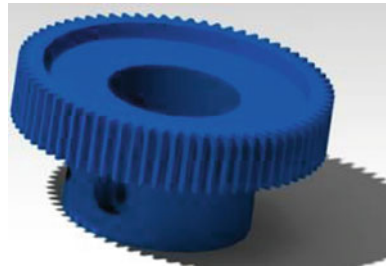
Fig. 5 Gear 2

Table 7 Dimension of the gears	Gear 1		Gear 2	
	Inner diameter	25 mm	Inner diameter	8 mm
	Outer diamter	60 mm	Outer diamter	20 mm

Fig. 6 3D printed pipe and the stainless-steel shaft mounted on the balloon, generator in its mount, CAD model for the translation mechanism

Fig. 7 Translation mechanism for mark III
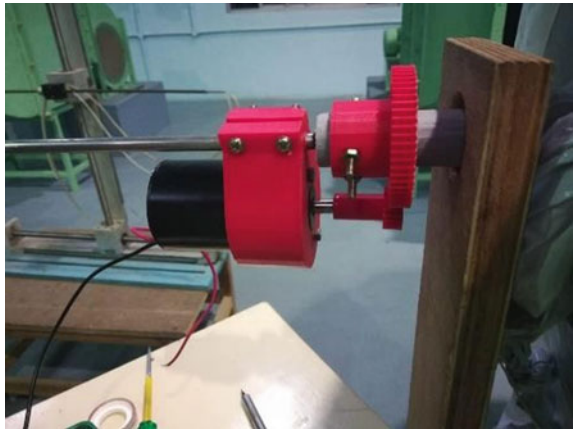
(2)   Dynamic parts: All other parts of the design exhibit motion. The inside plate in the platform has ball bearings attached to it. The inner plate is stationary and outer plate is rotating. The inside plate is attached to the rubber gasket, 3D printed coupler. The coupler couples the inside plate with the pipe.

This pipe is concentric with the stationary shaft. The Spur gear is mounted on this pipe which transmits the power to the Generator.

The gear on the pipe is meshed with another gear on the generator.

Thus, the power is transmitted from the rotating balloon to the generator and energy is produced (Figs. 6 and 7).

4.2 Structural Analysis of the Shaft

The stainless-steel shaft is a crucial component of the mechanism as it carries the complete load of the balloon and the Generators. A detailed structural analysis on the shaft is conducted in ANSYS Workbench 15.0 (Structure).

Given parameters:

- 1600 mm long Stainless-Steel Shaft
- Uniformlydistributedloadswherethe generator is mounted
- 50 mm-300 mm
- 1300 mm-1450 mm
- Fixed Supports at 300 mm and 1300 mm, where Ball Bearings are mounted.

After successfully running the solver, the results obtained are (Figs. 8 and 9).

1) Maximum Deflection = **0.3mm**
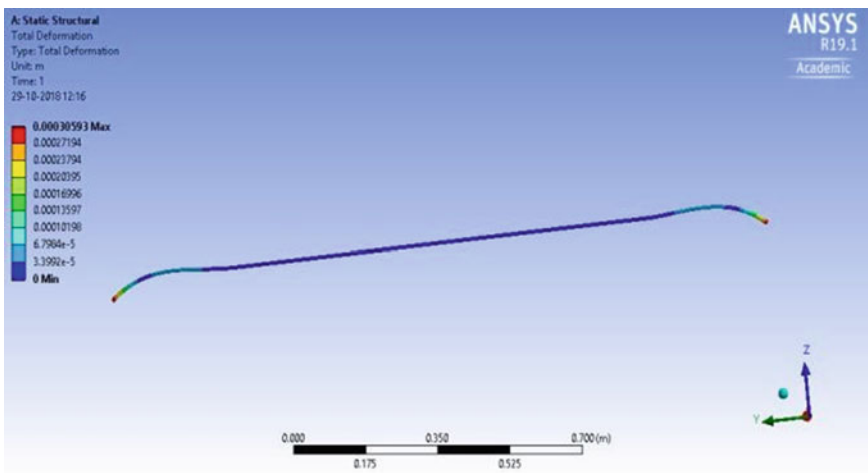
Fig. 8 Total deformation on the shaft

2) Maximum Stress = 5.4178e7 Pa
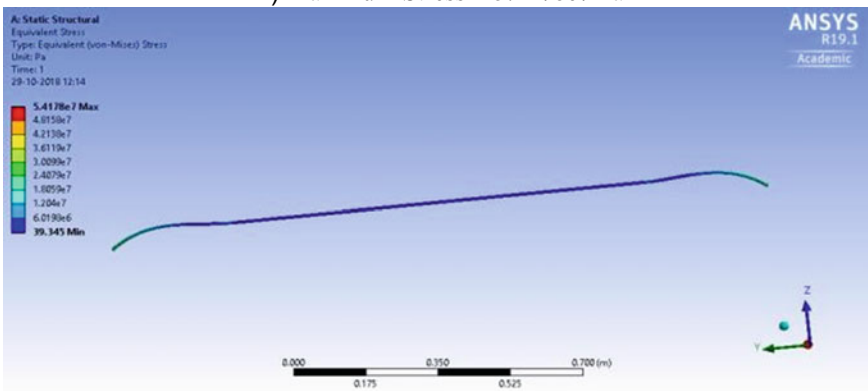
Fig. 9 Maximum stress on the shaft

5   Windspeed Calculations and Baloon Sizing

5.1   Windspeed Calculations

The design of the lighter than air wind turbine will majorly be dictated by operating wind conditions at the operating altitude. The subsequent wing design and the lift generated by them to create a rotating torque is also governed by the wind speed and hence deciding an operating altitude is an integral part of the design phase.

As environmental wind flow over cities and other terrains are also shear flows in nature, there exists a wind gradient as we move upwards. Much like a traditional boundary layer over external geometries, a planetary boundary layer is seen to form over Earth's surface. This is naturally caused because of a shear layer with the terrain and vertically extends up to the point where the gradient of flow velocity is the same as the freestream. In addition to this, daytime heating from the sun leads to increased mixing of the boundary layer and the freestream. This mixing leads to a significant increment in the boundary layer thickness and must be taken into consideration.

For Wind Turbine Engineering, a polynomial variation between the altitude and wind speed can be defined by,

$$\left(\frac{v}{v_0}\right) = \left(\frac{H}{H_0}\right)\alpha$$

where,

α Hellman's Constant = Friction Coefficient
v Windspeed at operating altitude
v_0 Windspeed on ground (i.e. 10 m)
H Required Altitude
H_0 10 m

The Hellman exponent is parametrically derived from various environmental constraints such as the location of the coast, if there are peaks in the terrain below and also the stability of the air around. Considering the application to be over the coastal area of Chennai, India, we can consider a Hellman's Coefficient of 0.4 for the subsequent wind speed calculations.

After due literature surveys, it was judged that an operating altitude of 300 ft would be apt for the design. This decision was made after considering trade-off that although a higher altitude would provide very lucrative operating conditions, such an operating height would exponentially demand a bigger balloon size due to the added tether weight. An exponentially bigger envelope size would then cubically demand more lifting gas volume to lift the enter system up. Finally, as Helium is one of the primary and ideal lifting gases and happens to be one of the rarest on earth as well, its use becomes very constrained. Hence, it is a penultimate task of selecting an operating altitude that is optimum from the sizing as well as cost point of view.

The average wind speed on ground in Chennai is 8 kmph or 2.22 m/s as per the metrological department. The wind speed at 300 ft is found with the help of the relation given above.

$$\frac{v_{300\text{ft}}}{2.22} = \left(\frac{91.44}{10}\right)^{0.4}$$

Hence, $v_{300\,\text{ft}} = \mathbf{5.38\,m/s}$

The subsequent wing calculations and design have been done in accordance to this wind speed. This wind speed is streamlined as compared to planetary flow near the surface as there are no disturbances to distort it. This will facilitate better lift generation over the wings.

5.2   Weight Estimation and Baloon Sizing

To find an optimum size for the envelope enough to lift the entire setup, it is imperative to estimate the weight of the envelope, the wings attached to it, the onboard payload and the tether along with an additional extra static lift. The total lift needs to be quantified to ensure enough buoyancy for the envelope to pick the entire system up. Once an initial total system weight has been estimated, the balloon is sized and iterated for until an optimum value has reached. An initial benchmark for the onboard payload was taken as 3 kg and the envelope and wing weight as 2 kg.

The envelope was chosen to be spherical in shape because of its high volume to surface area ratio. A high volume to surface area ratio is preferred in order to facilitate the largest lifting gas volume possible to lift up as much weight as possible. A higher volume to surface area ratio also implies a lower surface area that means that the envelope weight also is towards the lower end. This is another important aspect as a lower surface area would directly reduce the mass of the envelope material. The Surface Area to Volume ratios of various 3d geometries are given as follows (Table 8).

The sizing of the envelope is governed majorly by the Archimedes Principle and the fundamentals of buoyancy. This can be simply done by equating two known physical aspects for any floating object. Since for such a floating wind turbine, the buoyant force comes from the displacement of its weight, and lift being a difference between this buoyant force and displaced gas, the sizing relationship is.

$$L_s = B - W_{\text{gas}}$$

$$L_s = W_{\text{air}} - W_{\text{gas}}$$

$$L_s = V_g(\rho_{\text{air}} - \rho_{\text{gas}}) \tag{1}$$

Table 8 Surface area to volume ratios of various 3D geometries

Shape		Characteristic Length a	Surface Area	Volume	SA/V ratio	SA/V ratio for unit volume
Tetrahedron		side	$\sqrt{3}a^2$	$\dfrac{\sqrt{2}a^3}{12}$	$6\sqrt{6} \approx \dfrac{14.697}{a}$	7.21
Cube		side	$6a^2$	a^3	$\dfrac{6}{a}$	6
Octahedron		side	$2\sqrt{3}a^2$	$\dfrac{1}{3}\sqrt{2}a^3$	$3\sqrt{6} \approx \dfrac{7.348}{a}$	5.72
Dodecahedron		side	$3\sqrt{25+10\sqrt{5}}a^2$	$\dfrac{1}{4}(15+7\sqrt{5})a^3$	$\dfrac{12\sqrt{25+10\sqrt{5}}}{(15+7\sqrt{5})a} \approx \dfrac{2.694}{a}$	5.31
Capsule		radius (R)	$4\pi a^2 + 2\pi a \times 2a = 8\pi a^2$	$\dfrac{4\pi a^3}{3} + \pi a^2 \times 2a = \dfrac{10\pi a^3}{3}$	$\dfrac{12}{5a}$	5.251
Icosahedron		side	$5\sqrt{3}a^2$	$\dfrac{5}{12}(3+\sqrt{5})a^3$	$\dfrac{12\sqrt{3}}{(3-\sqrt{5})a} \approx \dfrac{3.970}{a}$	5.148
Sphere		radius	$4\pi a^2$	$\dfrac{4\pi a^3}{3}$	$\dfrac{3}{a}$	4.83515
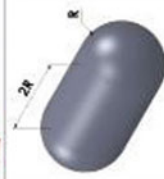
where, $V = 4/3\,\pi r^3$.

It should be noted that for windy operating conditions, the current floating wind turbine must have a net positive lift. The reason for this is to prevent the turbine from dropping its altitude due to any possible downward push from the turbulent or windy freestream. This net positive aerostatic lift should allow for a stable recovery of the original operating altitude of the wind turbine. For the tethered aerostat system, this design condition can be met by the following equation.

$$L_s = W_{env} + W_{tether} + W_{payload} + L_{excess} \tag{2}$$

From Eqs. (1) and (2), we get

$$V_g(\rho_{air} - \rho_{gas}) = W_{env} + W_{tether} + W_{payload} + L_{excess}$$

$$\frac{4}{3}\pi r^3 g(\rho_{air} - \rho_{gas}) = W_{env} + W_{tether} + W_{payload} + L_{excess}$$

Here, W_{tether}, $W_{payload}$ and L_{excess} are fixed values. The Only variables are the volume of the lifting gas (V) and W_{env} that are cubically and exponentially dependent on the radius of the envelope, respectively. The volume of the wings has been neglected as they are accountable for little lift generation. That is,

$$\frac{4}{3}\pi r^3 g(\rho_{air} - \rho_{gas}) = (k.4\pi r^2) + W_{fixed}$$

$$W_{env} = W_{tether} + W_{payload} + L_{excess}$$

Here, k is the mass per square meter (kg/m2) of the envelope material and hence multiplying this with the surface area of the sphere will give us W_{env}.

ρ_{air} and ρ_{gas} are found for the operating altitudes of 300 ft (91.44 m). Air density variation with altitude can be derived as follows:

$$T = 59 - (0.00356 \times h)$$

$$P = 2116 \times [(T + 459)] \times 5.256$$

where the temperature is given in Fahrenheit degrees, the pressure in pounds/square feet, and h is the altitude in feet. Finally,

$$\rho = \frac{P}{[1718 \times (T + 459.7)]}$$

On calculating further,
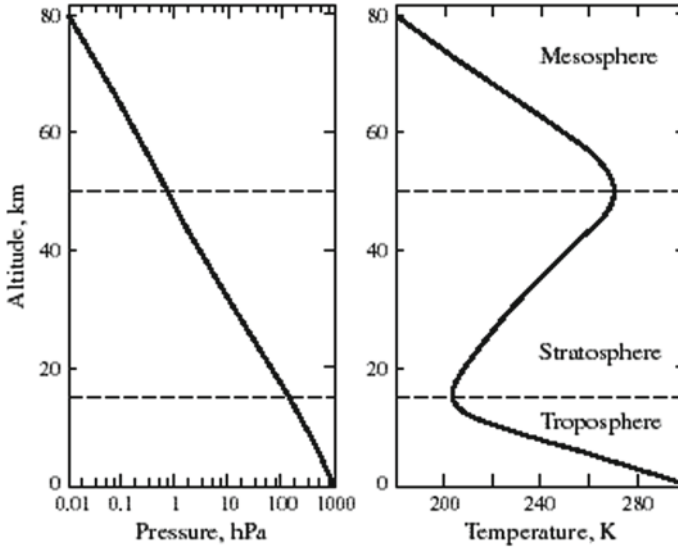
Fig. 10 Graphs representing pressure and temperature variation with altitude

$$\rho_{\text{air}} = 1.218 \, \text{kg/m}^3 \text{ at 300ft.}$$

Similarly,

$$\rho_{\text{helium}} = 0.16085 \, \text{kg/m}^3 \text{ at 300ft}$$

Conversely, these values can simply be found by referring to the already established charts of the respective temperature, pressure and density variations with respect to altitude (Fig. 10).

Substituting the values of ρ_{air} and ρ_{helium}, we get,

$$49.7614r^3 = \left(k^4 . \frac{\pi}{3} r^2\right) + W_{\text{fixed}}$$

The selected material for the envelope has a gram per square centimetre value of $450 \, \text{g/cm}^3$ which represents the value 'k'. Also, W_{fixed} represents the sum of weights of the tether and payload.

W_{tether} can be found by multiplying the rope's mass per meter with the altitude that it needs to cover. Standard breaking strengths and mass per unit length of commercial ropes can be found on their data sheet itself. A ¼ inch diameter nylon rope seems to be a viable option considering its failure load of 56.167 kg after a Factor of Safety of 12. With a mass per unit length value of 0.023, the mass of such a tether comes out to be,

$$W_{\text{tether}} = 0.023 \times 91.44$$

$$W_{tether} = \textbf{4.103kg for two tethers}$$

$W_{payload}$ was estimated to be 2 kg after design on CAD platforms. The design has been discussed extensively on in the subsequent chapters.

Hence, $W_{fixed} = 2.103 + 2$

$$W_{fixed} = 6.206 \, \text{kg for two tethers}$$

Substituting the value of W_{fixed} and 'k', we get,

$$49.7614 \, r^3 = 5.652 \, r^2 + 8.206$$

Solving this cubic equation for 'r', we get,

$$r = \textbf{0.588\,m}\sim\textbf{0.6m}$$

6 Wing Design

Two wing designs were considered based on the feasibility and ease of fabrication, cost, torque generation and wing efficiency. The two options that were considered were a fixed wing and a drag bucket. However, manufacturing the fixed wing and mounting it on the envelope wasn't feasible and demanded a lot of time and money. Hence, to make things easier and equally effective, a drag bucket type wing was made and directly pasted on to the envelope. Once wind flows into the bucket, a lot of parasitic and form drag is created and this enables the balloon to spin about its axis.

This drag bucket has a diameter of 0.62 m and has a thin sheet of fabric behind it. The design was tested using CFD tools and a total drag of 1.524 N. For a moment arm of 0.7 m, the torque being generated comes out to be (Fig. 11).

Fig. 11 The drag bucket designed on a CAD platform
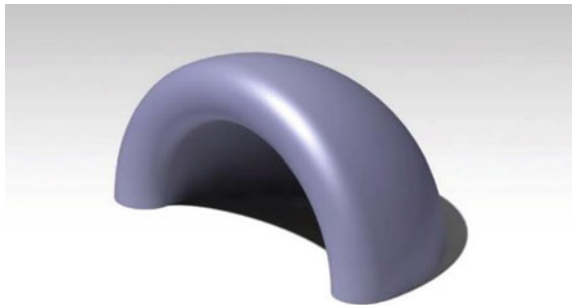
$$\text{Torque} = \text{Drag} \times \text{Moment Arm}$$

$$\text{Torque} = 1.524 \times 0.7$$

$$\textbf{Torque} = \textbf{1.067Nm}$$

Hence, for 4 such drag buckets,

$$\text{Total torque} = 1.067 \times 4$$
$$= \textbf{4.268N} - \textbf{m}$$

At 4.268 N-m, the balloon rotates at,

$$\alpha = \frac{4.268}{1.48872}$$

Since,

$$(\alpha = \tau)$$

Hence, **Angular Acceleration = 2.8669 rad/sec².**
Also,

$$n = \frac{(\alpha \times t \times 30)}{\pi}$$

Therefore,

$$n = \frac{(2.8869 \times 5 \times 30)}{3.14}$$

n = **136.9 rpm** (considering torque from all four buckets)

7 Fabrication

7.1 *Material Selection*

The project is related to Lighter than Air mechanisms. Hence, for the fabrication only the lightest weighted material possible with enough rigidity to support the entire weight of the mechanism had to be selected. To achieve this rationale for the LTAWT,

Table 9 Physical properties of polyvinyl chloride (PVC)

Density	1.35~1.45 specific gravity
Economics	PVC is readily available and cheap
Melt temperature	100–260°C
Tensile strength	• Flexible PVC: 6.9–25 MPa (1000–3625 PSI) • Rigid PVC: 34–62 MPa (4930–9000 PSI)

we selected Polyvinyl Chloride (PVC) sheets to be the material for the balloon, the reasons for which are stated as follows (Table 9).

7.2 Fabrication

The fabrication for the LTAWT was separated into two distinct domains:

(1)   Balloon Fabrication,
(2)   Mechanism Fabrication.

7.2.1   Fabrication of Baloon

The word balloon gives a general image in mind but here we are talking about a turbine. Using the balloon designing and sizing explained in V: Balloon Design and Sizing, we fabricated the balloon using various methods and came across several iterations.

Since the balloon is the wind turbine itself, we needed to take great care while selecting the fabricating methods for it. The balloon is analogous to the propeller in the design. The major factors on which the design was based are;

(1)   Low surface area of the balloon to use minimum material for lowest possible weight,
(2)   High volume of the balloon to fill maximum amount of helium gas for maximum possible lift force,
(3)   Balloon shape for Magnus Effect to act on it for stability.

The major factors for fabrication of the balloon are;

(1)   Light weight material,
(2)   Material requires strong adhesion as balloon must be fabricated in parts to be joined together,
(3)   Material should have enough strength to be able to hold the air pressure inside it without bursting.

Hence, the method of heat sealing was decided as the primary method to fabricate the balloon, as it was the best way to encompass all the adjourning factors required for the balloon (Fig. 12).

Fig. 12 Mark III inflated
with compressed air

7.2.2   Fabrication of Transmission Mechanism

The mechanism's main objective was transmission of power from the balloon to
the generator. We had decided to use gears for power transmission. Based on our
calculations we came up with the gear ratio to be 3:1. The components required for
mechanism are:

(1)   Ball bearing
(2)   Stainless-steel shaft
(3)   3D Printed Hollow pipe with Surface Coupling
(4)   Gears
(5)   Generator
(6)   Generator Mount
(7)   Circlips
(8)   Inner and Outer Circlip Plier
(9)   Nuts and Bolts

The gears, hollow pipe with surface coupling and generator mounts were
fabricated using 3D Printing technique (Fig. 13).

Fig. 13 CAD Models of the
mount and the hollow pipe
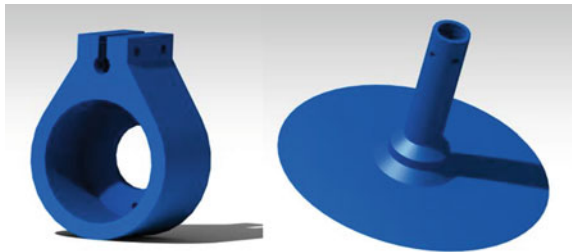
Fig. 14 Mark III

The shaft was divided into two parts which is mounted on both the sides forming a cantilever. To support this cantilever, we have provided 2 supports with ball bearings. The final mechanism was coupled with the balloon with the help of anabond adhesive and was very strong without any slippage between the balloon and the mechanism (Fig. 14).

8 Fabrication

The testing of the LTAWT was done in front of the Open Jet Wind Tunnel inside the Aerospace Hangar of SRM Institute of Science and Technology. In an ideal case, helium would be used to inflate the balloon for it to rise in the air and rotate at an altitude, which was the basic case for the design which was proposed. Although, after a lot research, helium was found to be expensive and hydrogen is too volatile to be used for this purpose. Hence an improvised stand was fabricated for the balloon to be tested in front of the Open Jet Wind Tunnel in the Aerospace Hangar, with the balloon being inflated using compressed air (Table 10).

Table 10 Results derived from testing

Distance of the balloon from the ground	1500 mm
Distance of the balloon from the wind tunnel	2000 mm
Wind speed	~ 20 m/s
RPM of the balloon	36
RPM of the generator (3:1)	108
Electricity produced by 2 generators	2 V

9 Future Scope

The prototype was built to utilize the powerful winds blowing at higher altitudes for the purpose of generating electricity. The balloon works the way it is supposed to. The aim was to check if the design truly worked as per the standards and as the report suggests, good results have been acquired. However, there exist certain deficits in the prototype which did not produce practical results similar to the ones produced theoretically.

Talking about the scope, there exists a much bigger picture than the existing prototype's, which is but the starting point and a substantial success towards an even better future of electricity generation. The succeeding prototype can be iterated on a number of parameters.

1. **A bigger balloon size**: a bigger balloon will be heavier hence can support better generators and ensure the utilization of a greater volume of the blowing winds, thereby permitting the model to produce greater amounts of electricity.
2. **A more versatile transmission system**: Presently only two gears are being used. The prototype can be levelled up to implement planetary gear systems in entirety, which will further facilitate a feature of toggling the RPM produced by the gears when the model is stationary. This will enable operating the prototype to work more efficiently in accordance to the wind patterns to produce an increased throughput. A versatile translation system will also ensure increased torque even if the balloon is operating on a lower RPM.
3. **Increased gear to teeth ratio:** The greater the ratio, the greater the rpm and hence the greater the torque. This will ensure better performances and increased electricity generation.
4. **Incorporating smart devices**: Using raspberry pi with smart generator technology the prototype can be taken to whole new levels,
a. This will enable smart toggling of rpm even when it is operational, however the mechanical aspect will be quite arduous to make this possible, as every gear would need a variety of connections;
b. Relevant sensors can help to analyse the temperature at different heights and record the corresponding speed of the winds, thereby allowing the prototype to adjust to the current conditions and working in accordance to the most suited functionality for a given condition;
c. Integrating the mechanical aspect to the tech-driven ones by making a user-friendly application that can enable the developer to make changes to the behaviour of the operational prototype at any time, from the ground level.

The parameters listed above have been devised only theoretically. While some seem doable, others may require more knowledge (which may be out of the current scope) to up the current levels to a whole new high. Fixing and bettering the mechanical aspect of the prototype shall be the topmost priority of the successor.

Initially, the aim of the project will be to ensure an increase in the throughput by working on the gear systems which are the major setbacks to good electricity generation as per the most recent observations.

From there, putting the renewed prototype to a challenging testing environment in order to test its durability, in case the weather goes south, will be the following step. If everything goes well, the prototype should be able to power at least one complete household as its lower bound.

Analysis of Different Geometrical Impacts on Wind Turbine Blades

N. Aravindhan (ID)**, Chidambaranathan Bibin, S. Murali, M. Marimuthu, Siddi Harsha Vardhan, and Santhosh Varma**

Abstract Renewable power production is getting advancement as an alternative to conventional type power generation. The design of wind turbine blades getting advanced to be efficient, further it needs to exhibit lightweight, durability, high fatigue strength, damage tolerance, the potential of recycling, and stiffness. A lot of efforts were made to upsurge the effectiveness of the wind turbine blades like adding triplets at the edges, biplane blades, blades with moving surfaces. In this work, we tried three different methods for validating the performance of the blades by inducing a hole near the tip of the blades, a material reduction in the tip of the blades with the standard profile of NACA 4415. The results indicated that the standard profile performed better compared to the modified profiles as the velocity at the tip decreases and the pressure on the tip of the blades increased drastically.

Keywords Wind turbine blades · Triplets · Biplane · Hole · Material reduction

1 Introduction

The minimal effort, proficiency, consistency, and wide accessibility, wind energy has arisen as perhaps the most remarkable sustainable power source lately. In the performance of wind turbines, blades are a vital part. An optimal design of small-scale blades can easily outperform a shape that can outperform the unoptimized large-scale blades [1]. Ansal Muhammed et al. studied the performance of wind turbine blades made of various materials, including the AW 106 Epoxy/E-Glass fiber/nano clay Composite. They examined the viability of using nanocomposites in wind turbine blades at different working conditions [2]. Blades made by hand lay-up, which includes mixing various percentages of Montmorillonite nano clay into an AW 106 Epoxy/E-Glass fiber composite, are stronger. A comparative analysis of the proposed four materials blades suggests that the composite with 1% Montmorillonite

N. Aravindhan (✉) · C. Bibin · S. Murali · M. Marimuthu · S. H. Vardhan · S. Varma
Department of Mechanical Engineering, RMK College of Engineering and Technology, Puduvoyal, Tiruvallur 601206, India
e-mail: aravindhn25389@gmail.com

had exhibited higher tensile stress with optimum hardness comparing other compositions [3]. The researchers investigated the properties of regular fiber-supported polymer composites in wind turbines, with different approaches and different compositions. They identified that the normal fiber built compositions are exciting good mechanical properties and will be biodegradable [4].

2 Different Shaped Edges for Improving the Performance of Wind Turbine

Pengfei Li et al. made a mathematical investigation of lightning connection to wind turbine edge. They proposed a technique that exploits electrostatic recreation to inspect the conception of the line lightning connection qualities of wind turbine sharp edges [5]. The lightning association normal for a turbine cutting edge and a descending pioneer is examined utilizing a three-dimensional electromagnetic recreation dependent on the limited component measure. Our recreations show that the weakest territory for lightning strikes on a breeze turbine cutting edge is inside 6 m of the tip, with the initial 1 m being especially helpless as shown in Fig. 1 [6].

Shi-Zheng et al. generated a high-devotion dimensional decrease model of composite breeze sharp edge by the variational asymptotic multistage strategy. The thermoplastic variational articulation of a three-dimensional composite breeze cutting edge was developed by utilizing the construction's intrinsic little boundaries, the thermoplastic energy utilitarian was then asymptotically extended to a succession
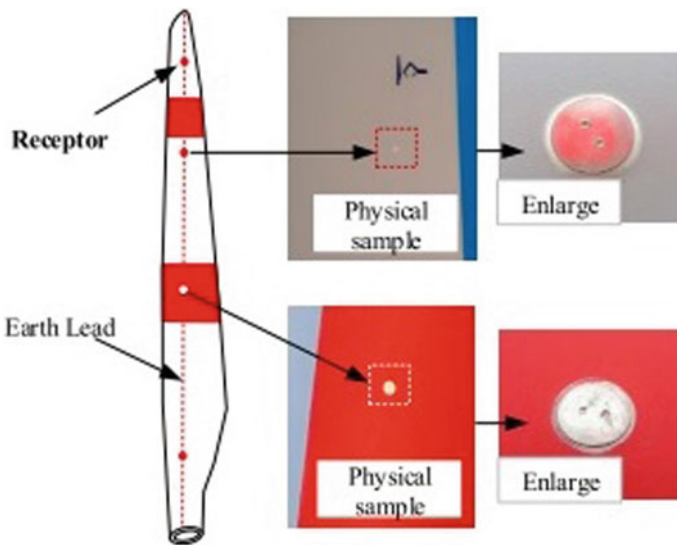
Fig. 1 Enlargement of receptors for improving the blade efficiency [6]

of 2D energies. The proposed setup generated the robust movement of blades and the loads are disturbed in all segments [7].

Bhupinder Singh et al. generated a wind turbine sharp edge idea for inducing a low rotational velocity at variable rates with various turning points utilizing Q-Blade programming. The edge component energy model was utilized to assess the lift, drag, just as pressing factor coefficients of air profiles utilizing QBlade programming. Two optimal profiles were identified for the conditions on which the NACA0012 performed better comparing the NACA008, due to the expanded harmony thickness [8]. Suresh et al. formulated a little even pivot wind turbine for rustic applications with low wind speeds. They proposed that the force coefficient (Cp) fluctuated for all aerofoils chosen comparable to the Tip Speed Proportion (k).

As shown in Fig. 2, Mohammad et al. [9] attempted mechanical recycling and reusing of life-ended wind turbine blades. They used 3D printing to regenerate the model and reuse the useful constituents of scrap cutting edges in a Melded Fiber Manufacture (FFF) measure to improve the piece edges' mechanical properties.

Nachtane et al. developed another hydrofoil idea for marine current turbines and led a hydrodynamic execution test on it. They formulated a numerical investigation on another hydrofoil for marine flow turbines that were fabricated and tried under submerged conditions. The XFLR5 code and QBlade, an Edge Component Energy solver with a sharp edge configuration include, is utilized to assemble the turbine edge. The performance is simulated in CFD and the results indicated that the proposed edge is capable of an undeniable degree of execution [10].
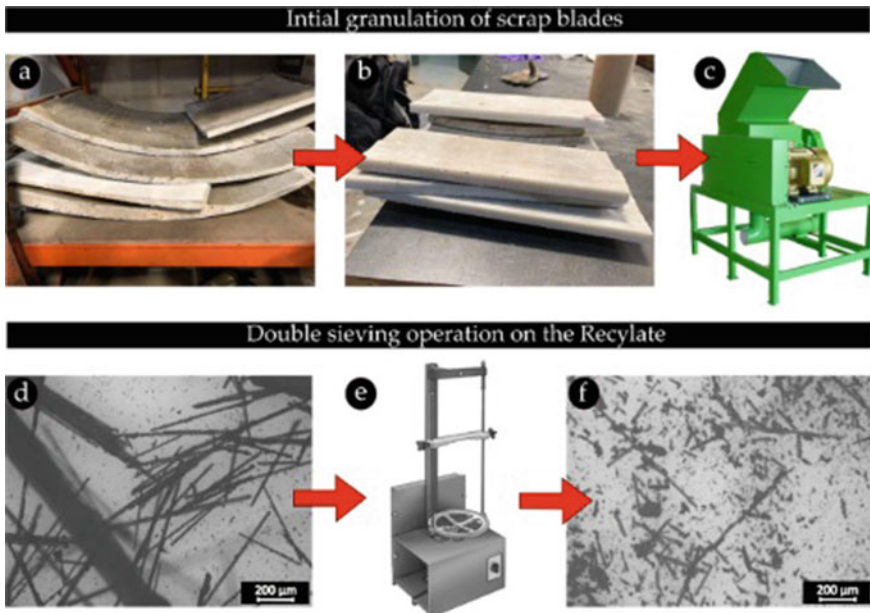
Fig. 2 Recycling of wind turbine blades [9]

Ajay et al. reviewed the wind turbine analysis of blades for improving the theoretical and numerical efficiency of blades. The optimal modification of the angle of attack will improve the aerodynamic efficiency. They analyzed the various loading forces under dynamic operating conditions on a wind turbine are presented. The power and efficiency of small-scale wind turbines are evaluated under different velocities [2].

Roadman et al. proposed the thermoplastic composite breeze turbine edges. The edges are made as joining of thermoplastic sap made breeze turbine cutting edges. The fabrication complexity is taken over by thermoplastic resin. It overcame the conventional welding methodology to join two edges with a greater exhibition of strength to weight ratio [11].

Xin Shen designed a little wind turbine with adaptable cutting edges. They mathematically examined the acceptability of transforming bladed turbine. The flexible edges have improved the efficiency of the turbine considerably [12]. The Composite rotor cutting edge aeroelastic was developed recently. In which the composite edge with a run-of-the-mill profile with a high degree of angle of blades for a parametric demonstrating measure [13].

Schubel et al. analyzed the mathematical performance of rotor-cutting edge yield for a little flat pivot wind turbine. It explores the presentation of two kinds of level hub wind turbine edges, one of which was displayed utilizing the sharp edge component force hypothesis for improving the performance of wind turbine blades [14].

Raj Oak et al. the adaptable breeze turbine sharp edges streamlines the flow and aeroelastic properties under incidental insecure inflows. The aeroelastic model is dependent on the mathematically cutting edge component energy framework. The streamlined and Aeroelastic properties of the NREL 5WM adaptable breeze turbine edge are concentrated under intermittent temperamental inflow the results show that as the cutting edge passes by the pinnacle, the Breeze shear prompts huge varieties in the fold diversion and yaw second, while the Pinnacle shadow impact makes intense changes in the, push energy, and yield strength [15].

3   Innovative Blade Shapes for Improving the Efficiency

Salimipour et al. proposed a moving surface of a seaward wind turbine fan which improves mathematically as shown in Fig. 3. The blade segmented as a stream control gadget, the surface has thrived with a streaming surface. The impacts of position and speed of the moving surface on the stream attributes were researched to accomplish the best mechanical effectiveness of the airfoil at each approach. A computational liquid elements method was utilized to reproduce the stream. 30, 62, 131, and 152% increment in proficiency, separately [16].

Chiu et al. developed a biplane wind turbine with sharp edges which improved underlying proficiency, streamlined execution, and diminished streamlined burdens. Interestingly, the impact of these factors on cutting-edge mass is evaluated for identifying the mass of biplane wind turbine edges. The weight reserve funds are generous,
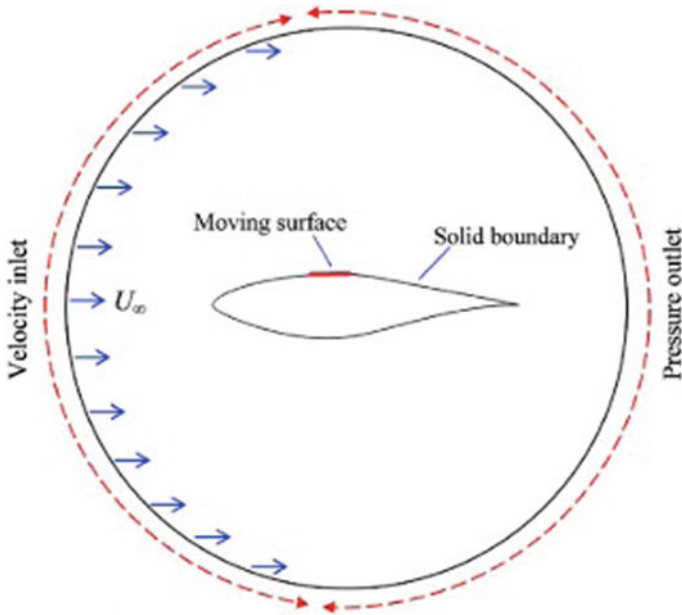
Fig. 3 Moving surface blades [16]

with ideal biplane sharp edges being more than 45% lighter than a comparably streamlined monoplane edge. This is to a great extent because of the biplane cutting edges' better opposition than fold shrewd avoidance when contrasted with monoplane edges, considering altogether less fight cap material to be utilized. Biplane edges have additionally been demonstrated to be more impervious to consumption in Fig. 4 [17].
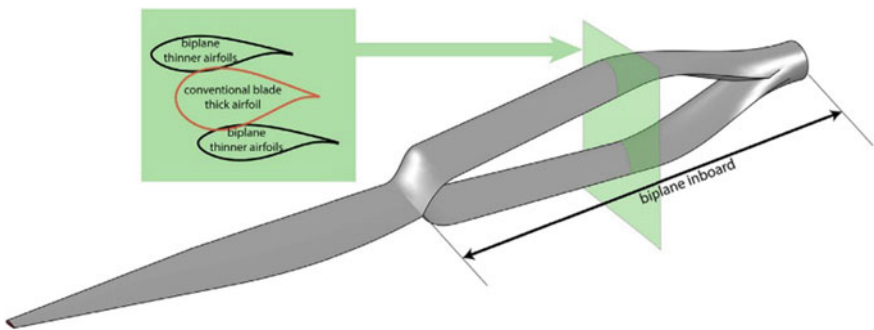
Fig. 4 Blades with biplane edges [17]

4   Performance Analysis of Composite Blades to Improve Their Characteristics

Ganesh R Kalagi the investigated mechanical properties of common fiber built-up polymer composite materials for wind turbine edges. They reported the utilization of regular fiber-supported polymer composites as their properties, constituents, producing innovations, and imperfections. The best illustration of a sustainable power source is wind energy. In nature, the materials utilized in wind turbines are likewise non-biodegradable [17]. An adaptable multibody approach was utilized to advance the state of low-speed wind turbine edges.

Monteiro [18] performed a wind tunnel testing with a wind turbine blade of length 1.2 m and compared it with numerical results generated by Q Blade element momentum codes. The experiments were conducted at 2 X 2 m open chamber closed circuit for a wind speed of 3–8 m/s. They calculated the rotation of the shaft with varying tip speed ratios. The wind speed has a significant impact on the power coefficient as speed increases power coefficient decreases.

Imraan et al. [19] evaluated the performance of telescopic blade wind turbines with a prototype of chord length 0.6. Under different wind speeds, they have measured the performance of rotor speed, shaft twisting force, and thrust. The 20% of the extended step-change in the blade chord has resulted in a reduction of the power coefficient. But using telescopic blades has overcome the power losses for all blade extensions. The plotted correlations for both experimental and numerical results have acted as a gap for bridging the losses due to the step-change in the chord.

Usabiaga et al. [20] presented an automated procedure for principal stress and strain analysis on wind turbine blades at different locations. They performed a two-and-a-half dimensional aeroelastic analysis and identified the pressure distribution due to variations on wind turbine loading.

Le et al. [21] carried out wind tunnel experiments for predicting the behavior of wind turbines under abnormal conditions. They examined velocity measurements at multiple heights with the flow device capable of generating a gust of a non-stationary outflow. The experiments are carried out on a tall building model and compared with numerical results. They indicate that a multi-blade flow device is capable of generating the gust from present wind turbines with huge modifications to the present wind turbines.

Guo et al. [22] developed vertical axis wind turbine blades with an inclined pitch axis. The blade performance was measured under low speeds wind tunnel. They identified that the inclination of 8° produced maximum power coefficients at a wind speed of 7.28–9.16 m/s. Beyond the fold angle of 8° in any direction the maximum coefficient of power decreases. The blade pitch angle influences the power output more comparing the blade diameter and rotor area.

5 Role of Profiles on Wind Turbine Blades

Hirahara et al. [23] developed a unique small-scale turbine with a 500 mm rotor diameter for functioning in the urban environment. They used the National Aeronautics and Space Administration (NACA) 2404 cross-sectional profile for turbine blades. They visualized the airflow around the turbine with particle flow velocimetry. They have shown better performance when operating under the range of wind speed 8 m/s to 12 m/s.

The three blades setup is proved to be more efficient with high rotational speed for small-scale wind turbines even at a speed range of 2.5–3.5 m/s. Pambudi et al. [24] developed a nozzle lens to improve the rotational speed of the rotor. And it's evident that from the experimental results the larger diameter lens increased the wind speed which in turn increased the power output also.

6 Proposed Modification on Wind Turbine Blades

The three models have been integrated and analyzed for better performance. The NACA 4415 non-twisted profile is selected due to its ability to exhibit a high speed ratio at low speeds and three models proposed are described as follows.

Model 1:Standard NACA 4415 Profile

Model 2:Standard NACA 4415 Profile with the hole at the tip

Model 3:Standard NACA 4415 Profile with material reduction at the tip

7 Results and Discussion

7.1 Performance of Standard National Advisory Committee for Aeronautics (NACA) 4415

The performance of standard NACA 4415 is shown in Fig. 5. We have chosen to plot the velocity contour of NACA 4415 at a wind speed of 12 m/s. The results interpolated that the velocity at the tip reduces drastically within the range of 6–9 m/s. The power coefficient will not be as expected due to the reduction in the tip speed ratio. The results are intercepted in the following Fig. 6.

Though the velocity contour profile has been equivalent on the blade throughout the tip shows the major change. It creates a lot of effects as the tip acts as the major source for deciding the Power coefficient value. The pressure analysis of sure NACA 4415 was performed under the pressure of 101.325 Pa. The results interpolated that the pressure at the tip increases drastically within the range of 25–43 Pa. The power
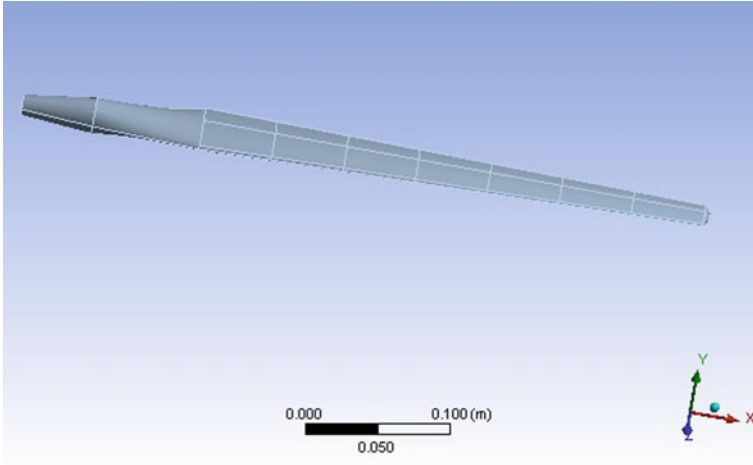
Fig. 5 NACA 4415 profile
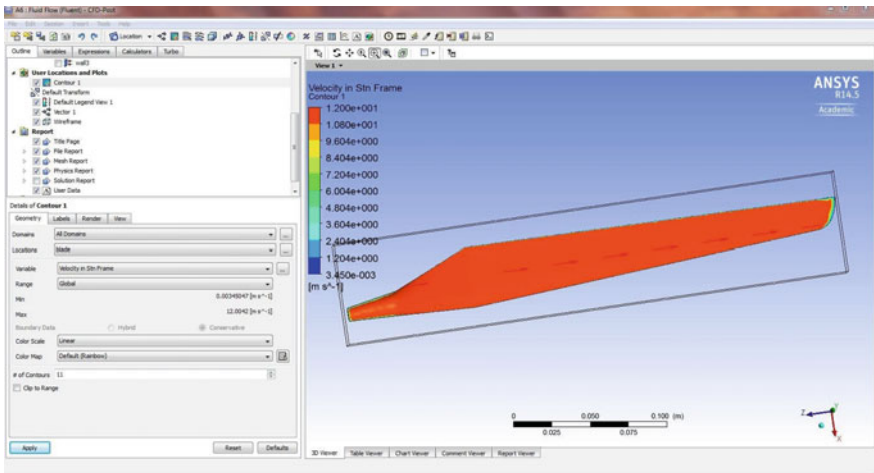
Fig. 6 NACA 4415 velocity contour profile

coefficient will not be as expected due to the reduction in the tip speed ratio. The results are intercepted in the following Fig. 7.
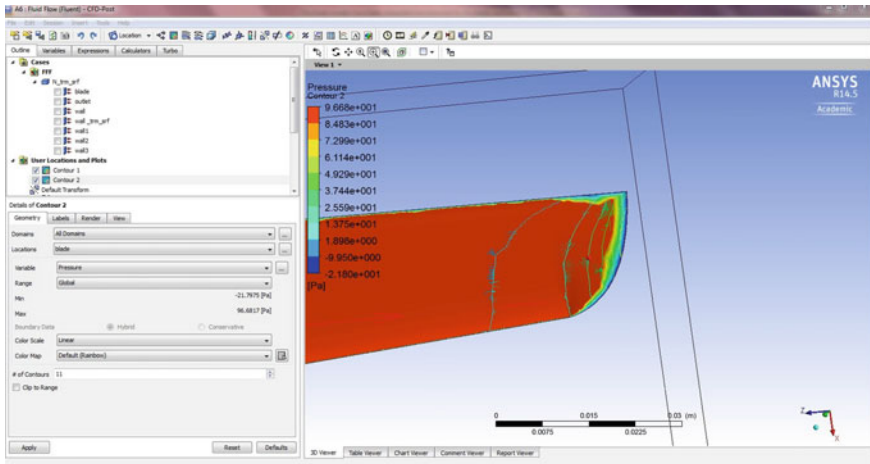
Fig. 7 Pressure contour profile of standard NACA 4415

7.2 Standard NACA 4415 Profile with the Hole at the Tip

A hole is made behind the tip of the blade for reducing the material on that tip. As same as the standard model we analyzed the velocity contour of NACA 4415 Profile with the hole at the tip under wind speed of 12 m/s. The velocity analysis of NACA 4415 was performed under wind speed of 12 m/s. The results interpolated that the velocity at the tip reduces drastically within the range of 3–7 m/s. The power coefficient will not be as expected due to the reduction in the tip speed ratio. The results are intercepted in the following Fig. 8. The hole at the tip on the blade for a reduction on a velocity on the blade. Though the velocity contour profile has been equivalent on the blade throughout the tip shows the major change. It creates a lot of effects as the tip acts as the major source for deciding the Power coefficient value. The pressure analysis of sure NACA 4415 Profile with the hole at the tip performed under the pressure of 101.325 Pa. The results interpolated that the pressure at the tip increases drastically within the range of 25–80 Pa. The power coefficient will not be as expected due to the reduction in the tip speed ratio. The results are intercepted in the following Fig. 9.

7.3 Standard NACA 4415 Profile with Material Reduction at the Tip

As a part of our new approach, we tried to have a material reduction at the tip, and its velocity contour of NACA 4415 Profile with material reduction at the tip is analyzed under the same constraints as shown in Fig. 10. The results interpolated
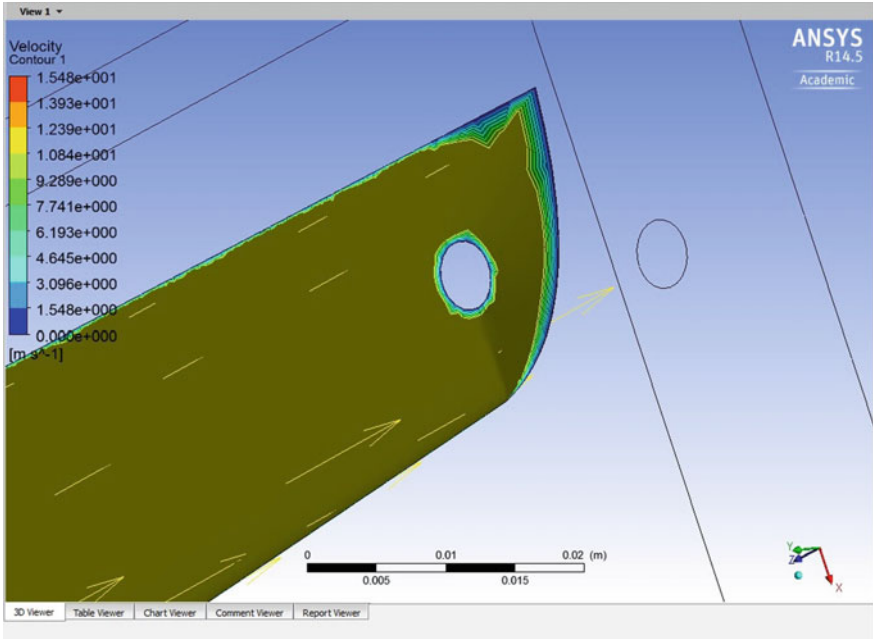
Fig. 8 Blade with the hole at the tip
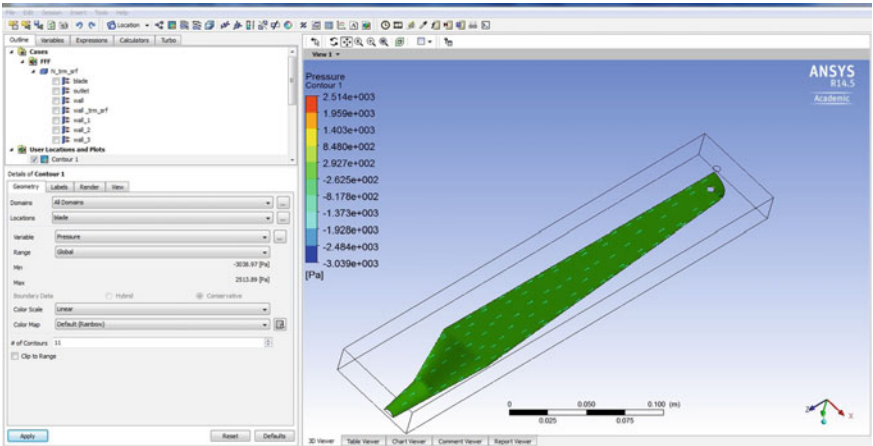
Fig. 9 Pressure contour profile of NACA 4415
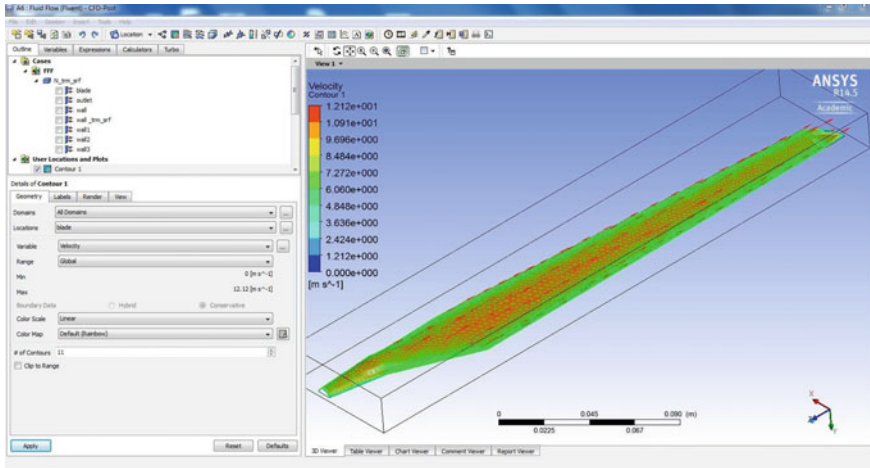
Fig. 10 Velocity contour analysis for model 3

that the velocity at the tip reduces drastically within the range of 3–8 m/s. The power coefficient will not be as expected due to the reduction in the tip speed ratio. The pressure analysis of sure NACA 4415 Profile with the material removed at the tip performed under the pressure of 46–96 Pa as shown in Fig. 11. The results interpolated that the pressure at the tip increases drastically within the range of Pascal in Fig. 12. The power coefficient will not be as expected due to the reduction in the tip speed ratio. The results are intercepted in the following Fig. 13.
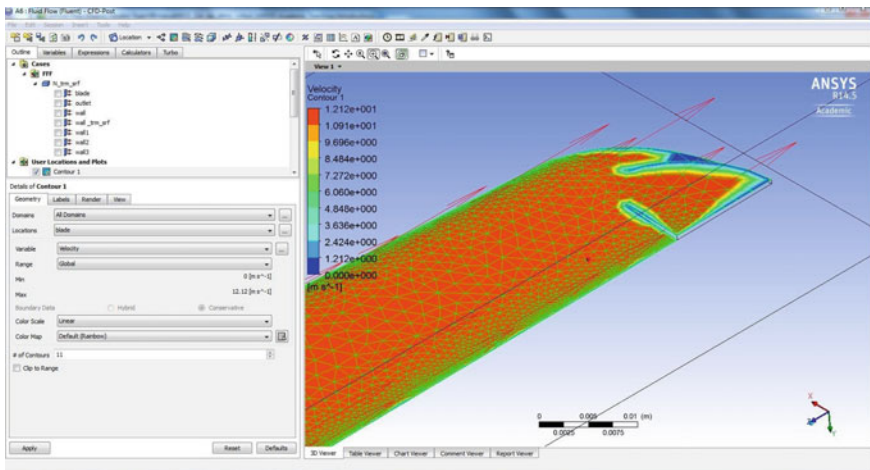
Fig. 11 Velocity contour NACA 4415 profile with material reduction at the tip
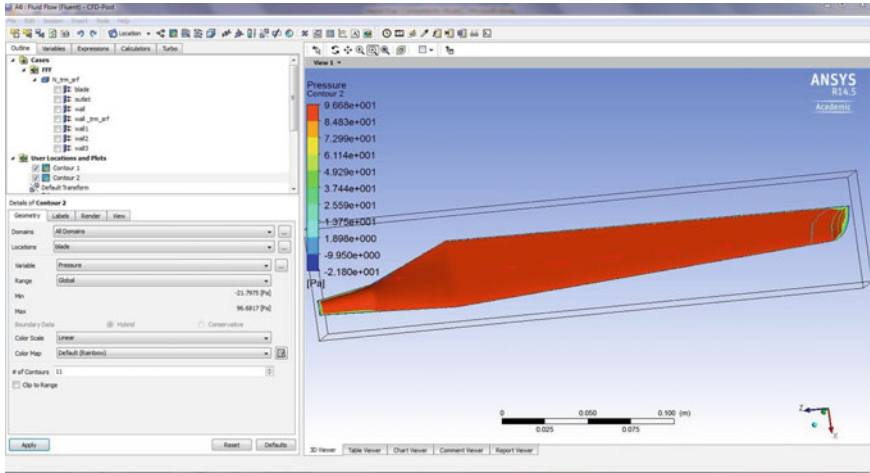
Fig. 12 Pressure contour profile at the tip
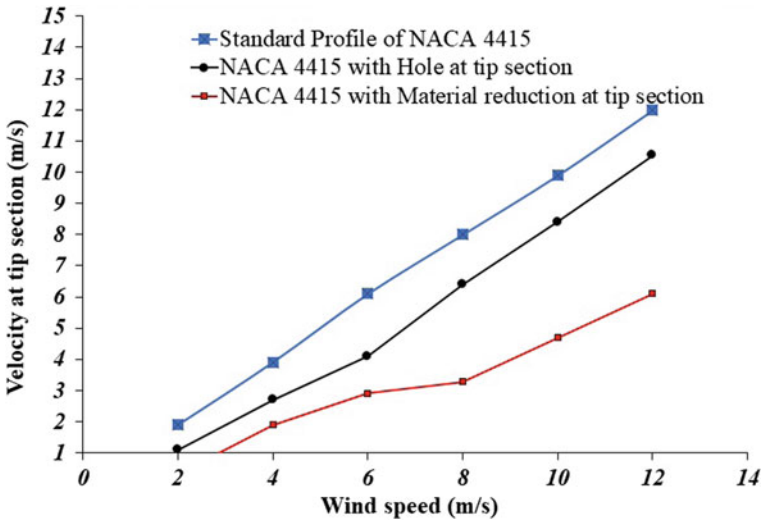
Fig. 13 Comparative performance of NACA 4415 various profiles

The material reduction at the tip on the blade for a reduction on pressure on the blade. Though the pressure contour profile has been equivalent on the blade throughout the tip shows the major change. It creates a lot of effects as the tip acts as the major source for deciding the Power coefficient value.

8 Conclusion

For improving the concert of wind turbine researchers have tried a lot of pioneering approaches have employed but still, the standard forms of turbines are efficient and existing on practical usages. In this work, we tried two different approaches apart from the conventional behavior but it performed considerably low than the present turbines as shown in Fig. 13. The results indicate the velocity deceleration on modifications 1 and 2 comparing the standard profile this is mainly due to the pressure increase on the tip of the blades due to hole and material reduction on the surface of the blades.

References

1. Tummala A, Velamati RK, Sinha DK, Indraja V, Krishna VH (2016) A review on small scale wind turbines. Renew Sustain Energy Rev 56:1351–1371. https://doi.org/10.1016/j.rser.2015.12.027
2. Ajay V, Venkateshwarlu B, Vishnu Vardhan T (2018) A review on fabrication and performance evaluation of small wind turbine blades. Int J Mech Eng Technol 9:240–265
3. Ansal Muhammed K, Ramesh Kannan C, Stalin B, Ravichandran M (2020) Experimental investigation on AW 106 Epoxy/E-Glass fiber/nano clay composite for wind turbine blade. Mater Today Proc 21:202–205. https://doi.org/10.1016/j.matpr.2019.04.221
4. Mishnaevsky L, Branner K, Petersen HN, Beauson J, McGugan M, Sørensen BF (2017) Materials for wind turbine blades: an overview. Materials (Basel) 10:1–24. https://doi.org/10.3390/ma10111285
5. Bibin C, Seenikannan P (2013) Experimental analysis of energy recovery from an internal combustion engine exhaust using rankine cycle. Adv Mater Res 768:158–163. https://doi.org/10.4028/www.scientific.net/AMR.768.158
6. Li P, Lv D, Li C, Yue X, Cao H (2019) Optimized design of wind turbine blade receptors based on electrostatic field theory. Electron 8:1–13. https://doi.org/10.3390/electronics8121418
7. Aravindhan N, Chidambaranathan B, Rokesh D, Jagadesh D, Pravin S, Ramkumar N (2020) Performance of statistical control tools in identifying the defect on plunger-a review. In: IOP conference series: materials science and engineering vol 906. https://doi.org/10.1088/1757-899X/906/1/012012
8. CEA (2020) Installed Capacity (in Mw) 29:4991–4999
9. Rahimizadeh A, Kalman J, Henri R, Fayazbakhsh K, Lessard L (2019) Recycled glass fiber composites from wind turbine waste for 3D printing feedstock: effects of fiber content and interface on mechanical performance. Materials (Basel) 12. https://doi.org/10.3390/MA12233929
10. Nachtane M, Tarfaoui M, Saifaoui D, Rouway M (2019) Hydrodynamic performance evaluation of a new hydrofoil design for marine current turbines. Mater Today Proc 30:889–898. https://doi.org/10.1016/j.matpr.2020.04.346
11. Murray RE, Roadman J, Beach R (2019) Fusion joining of thermoplastic composite wind turbine blades: lap-shear bond characterization. Renew Energy 140:501–512. https://doi.org/10.1016/j.renene.2019.03.085
12. Shen X, Yang H, Chen J, Zhu X, Du Z (2016) Aerodynamic shape optimization of non-straight small wind turbine blades. Energ Convers Manag 119:266–278. https://doi.org/10.1016/j.enconman.2016.04.008
13. Jia L, Hao J, Hall J, Nejadkhaki HK, Wang G, Yan Y, Sun M (2021) A reinforcement learning based blade twist angle distribution searching method for optimizing wind turbine energy power. Energy 215:119148. https://doi.org/10.1016/j.energy.2020.119148

14. Schubel PJ, Crossley RJ (2012) Wind turbine blade design. Energies 5:3425–3449. https://doi.org/10.3390/en5093425
15. Ageze MB, Hu Y, Wu H (2017) Wind turbine aeroelastic modeling: basics and cutting edge trends. Int J Aerosp Eng https://doi.org/10.1155/2017/5263897
16. Salimipour E, Yazdani S (2020) Improvement of aerodynamic performance of an offshore wind turbine blade by moving surface mechanism. Ocean Eng 195:106710. https://doi.org/10.1016/j.oceaneng.2019.106710
17. Chiu PK, Roth-Johnson P, Wirz RE (2020) Optimal structural design of biplane wind turbine blades. Renew Energ 147:2440–2452. https://doi.org/10.1016/j.renene.2019.08.143
18. Monteiro JP, Silvestre MR, Piggott H, André JC (2013) Journal of Wind engineering wind tunnel testing of a horizontal axis wind turbine rotor and comparison with simulations from two blade element momentum codes. Jnl Wind Eng Ind Aerodyn 123:99–106. https://doi.org/10.1016/j.jweia.2013.09.008
19. Imraan M, Sharma RN, Flay RGJ (2013) Wind tunnel testing of a wind turbine with telescopic blades: the influence of blade extension. Energy 53:22–32. https://doi.org/10.1016/j.energy.2013.03.008
20. Usabiaga H, Vandepitte D (2018) An efficient procedure for the calculation of the stress distribution in a wind turbine blade under aerodynamic loads. 172:42–54. https://doi.org/10.1016/j.jweia.2017.11.003
21. Le V, Caracoglia L (2019) Generation and characterization of a non-stationary flow field in a small-scale wind tunnel using a multi-blade flow device. J Wind Eng Ind Aerodyn 186:1–16. https://doi.org/10.1016/j.jweia.2018.12.017
22. Guo J, Zeng P, Lei L (2019) Performance of a straight-bladed vertical axis wind turbine with inclined pitch axes by wind tunnel experiments. Energy 174:553–561. https://doi.org/10.1016/j.energy.2019.02.177
23. Hirahara H, Hossain MZ, Kawahashi M, Nonomura Y (2005) Testing basic performance of a very small wind turbine designed for multi-purposes. Renew Energ 30:1279–1297. https://doi.org/10.1016/j.renene.2004.10.009
24. Pambudi NA, Pristiandaru DL, Wijayanto DS, Sriwardani N, Rahman N, Bugis H, Wahyudi BD, Sudibyo C, Karno MW (2017) Experimental investigation of wind turbine using nozzle-lens at low wind speed condition. Energ Procedia 105:1063–1069. https://doi.org/10.1016/j.egypro.2017.03.459

Intelligent Control-Based Effective Utilization of Renewable Energy Sources

G. Anandhakumar, M. Lavanya, G. B. Santhi, and Chidambaranathan Bibin

Abstract A rapid development is taking place in the field of renewable energy sources to increase the power generation because these sources are eco-friendly, non-polluting, freely available in nature sources like solar wind, biomass, hydro, and tidal. These renewable sources are mostly uncontrollable and all the same time different methods should be done to build a power plant to generate a continuous and constant power. The selection of the renewable energy source for the plant is one of the important roles for energy optimization. This is mainly focused toward the solar and wind power combination, whereas the solar system is the major renewable energy source for energy generation. In this work, a dynamic hardware model for an intelligent control-based effective utilization of hybrid renewable energy sources and Battery Management System. It also explains the implementation of fuzzy logic algorithm. The Battery Management System (BMS) is simulated in MATLAB software by using fuzzy logic controller (FLC). BMS explains the charging state and discharging state of battery. Then, it is implemented in hardware model for effective utilization of renewable energy sources. The identification of each subsystem has been made, and then, the proposed system is modeled and simulated using MATLAB—Simulink package. The proposed control strategy has been experimentally implanted, and practical results are compared to those obtained by simulation under the same metrological conditions, showing the effectiveness of the proposed system.

G. Anandhakumar (✉)
Energy and Environmental Engineering, Saveetha School of Engineering, Saveetha Institute of Medical and Technical Sciences, Saveetha University, Chennai 602105, India
e-mail: anandhresearch@gmail.com

M. Lavanya
Electrical and Electronics Engineering, Saveetha School of Engineering, Saveetha Institute of Medical and Technical Sciences, Saveetha University, Chennai 602105, India

G. B. Santhi
Computer Science and Engineering, New Prince Shri Bhavani College of Engineering and Technology, Chennai 600073, India

C. Bibin
Mechanical Engineering, RMK College of Engineering and Technology, Chennai 601206, India

1   Introduction

The renewable energy is a growing technology to meet the demands of energy consumption, solve the problems of fossil fuels, and at the same time reduce the pollution in the atmosphere. In the near future, the solution to the energy crisis will involve using all available technologies together in the most beneficial manner. Conventional energy sources using fossil fuels will become more efficient and clean. Hybrid system using renewable energy source will continue to grow in near future. Energy use and demand will be optimized through time-of-use management and efficient technologies. Today, the advent of modern renewable energy sources greatly improves our ability to collect or harvest energy, but not store them. Modern renewable energy sources intensify the search for robust, cost-effective means to store energy. Intermittent energy sources such as solar panels or wind turbines require energy storage capacity if they are to provide consistent, on-demand power to the user, and be able to replace traditional fossil fuel sources. Many advances in electrical energy storage technology and methods have been made in recent times. These advances have come in the areas of batteries, large-scale pumped hydroelectric storage plants, compressed air energy storage, flywheels, superconducting magnetic energy storage, and supercapacitors. Chemical energy storage, most commonly applied in batteries, is the world's most prolific form of energy storage. However, there are several drawbacks in batteries for large systems, including cost, short lifetime, and disposal concerns. Energy storage systems will emerge and evolve that would enable renewable energy source deployment and greatly reduce the wasted energy inherent in the current system. Excess energy produced by wind and solar generators is not usable without a means to store it.

2   Proposed Method

The Hybrid Solar PV and Wind Renewable Energy System is shown in Fig. 1. The energy from photovoltaic power system is given to DC–DC converter. DC–DC converter converts only DC voltage to constant 12 V DC. Output energy from the windmills fed into the converter. Rectifiers are used to convert AC to DC. Both the converter and the rectifier are connected to the battery through DC bus bar. The resultant energy can be effectively utilized through fuzzy logic controller.
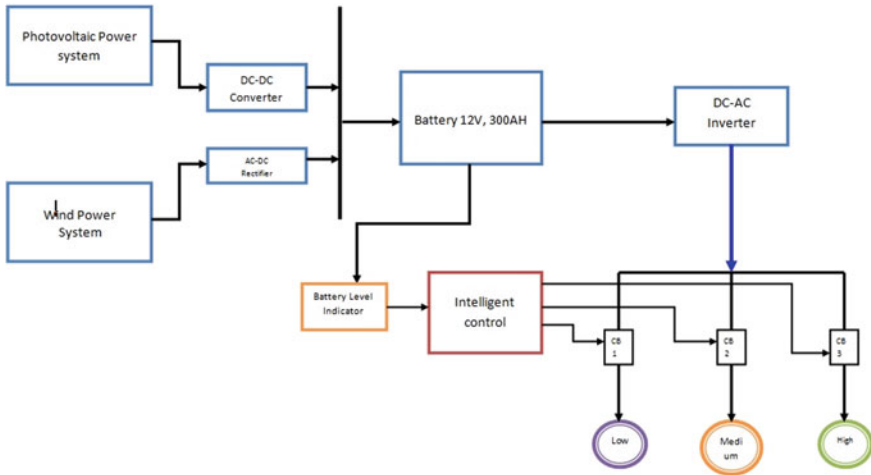
Fig. 1 Block diagram of proposed model

2.1 Simulation Model for Batter Management System (BMS)

Battery Management System (BMS) is simply battery monitoring, which keeps checking on the key operational parameters during charging and discharging such as voltages, currents, and temperatures (internal and ambient). The BMS normally provides inputs to protection devices which generate alarms or disconnect the battery from the load or charger when any of the parameters become out of limits. The major objectives of BMS are as follows:

(i)   To protect the cells or the battery from damage.
(ii)   To prolong the life of the battery.
(iii) To maintain the battery in a state in which it can fulfill the functional requirements of the application for which it is specified.

The MATLAB simulation model for Battery Management System (BMS) is shown in Fig. 2. The load is categorized like load 1, load 2, and load 3, and the voltage is distributed to loads through FLC. The loads can be controlled by circuit breaker through the controller. The output waveform of BMS simulation model is shown below.

If the fuzzy logic controller satisfies the condition $85\% \leq B_L \leq 100\%$, then the energy is distributed to all loads (load 1, load 2, and load 3). This is shown in Fig. 3. If the fuzzy logic controller satisfies the condition $75\% \leq B_L \leq 84\%$, then the energy is distributed to load 1 and load 2 as shown in Fig. 4. If the fuzzy logic controller satisfies the condition $60\% \leq B_L \leq 74\%$, then the energy is distributed to load 1 as shown in Fig. 5. If the fuzzy logic controller satisfies the battery voltage below 60%, then it switches off all the loads and connects the battery to charging mode. This is shown in Fig. 6.
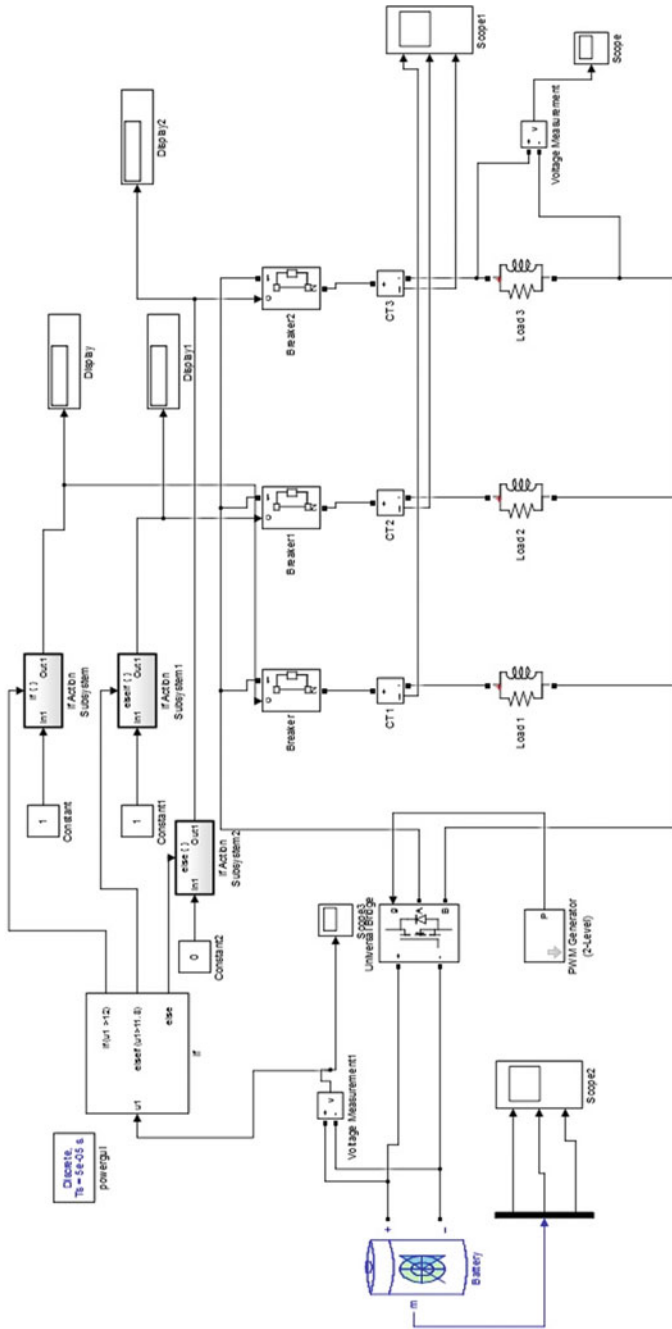
Fig. 2 MATLAB simulation model
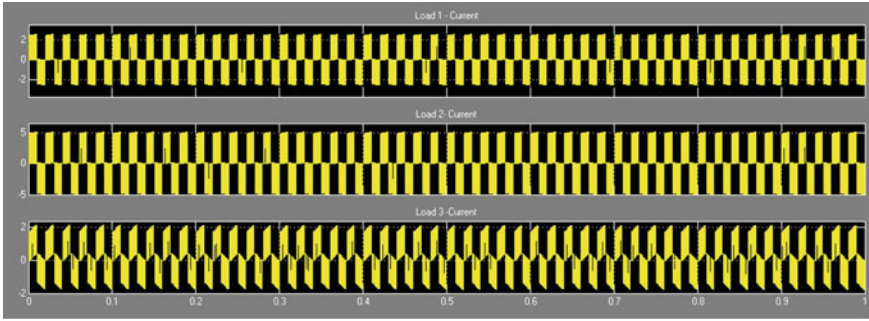
Fig. 3 Current waveform for all load
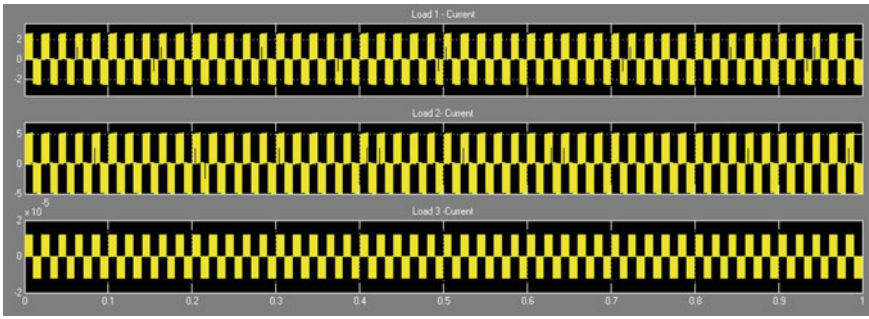
Fig. 4 Current waveform for load 1 and 2
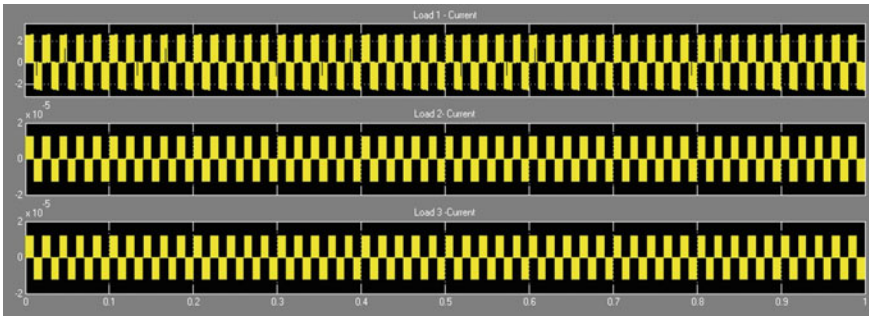
Fig. 5 Current waveform for load 1

2.2 Intelligent Control Hardware Model

An intelligent control hardware model is implemented for effective utilization of hybrid renewable energy sources. The fuzzy logic controller and fuzzy algorithm are used in the hardware model for proposed system. Loads are categorized for the
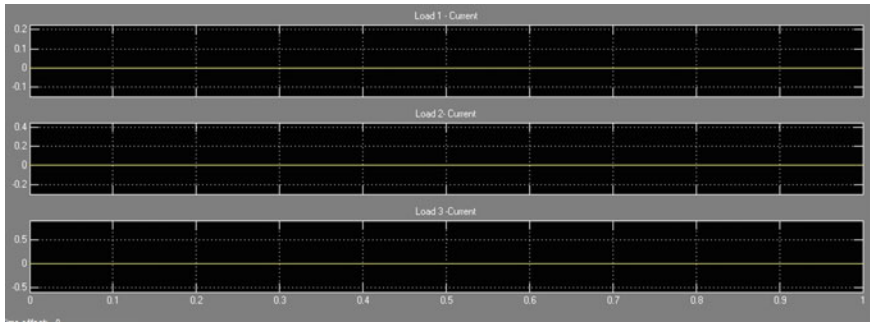
Fig. 6 Current waveform for no load

priority. The objective of this model is to utilize the optimized energy and energy management using fuzzy logic controller. In this model, the loads are connected based on priority.

2.2.1 Fuzzy Logic Algorithm

- Step1:- Start.
- Step2:- Read the Battery Capacity voltage and load the priority level.
- Step3:- Observe the Battery Capacity and load priority with the switch ON.
- Step4:- If the battery voltage is $85\% \leq B_L \leq 100\%$, then switch ON all the loads.
- Step5:- If the battery voltage is $75\% \leq B_L \leq 84\%$, then switch on P_{L1} and P_{L2} and switch OFF P_{L3}.
- Step6:- If the Battery voltage is $60\% \leq B_L \leq 74\%$, then switch ON P_{L1} and switch OFF P_{L2} and P_{L3}.
- Step7:- If the Battery voltage is below 60%, then switch OFF all the loads and connect to battery charging mode.
- Step8:- Repeat the step2 to step6 at every minute.
- Step9:- Stop.

Table 1 shows the fuzzy logic algorithm switching condition. The load priority can be selected based on the fuzzy logic condition. Load priority 1, 2, and 3 are

Table 1 Fuzzy logic algorithm switching condition

Condition	Load priority 1	Load priority 2	Load priority	Battery voltage in volts	Battery voltage in %
1	ON	ON	ON	13.3	95.4
2	ON	ON	OFF	11.7	83.7
3	ON	OFF	OFF	9.8	70.0
4	OFF	OFF	OFF	8.3	59.3
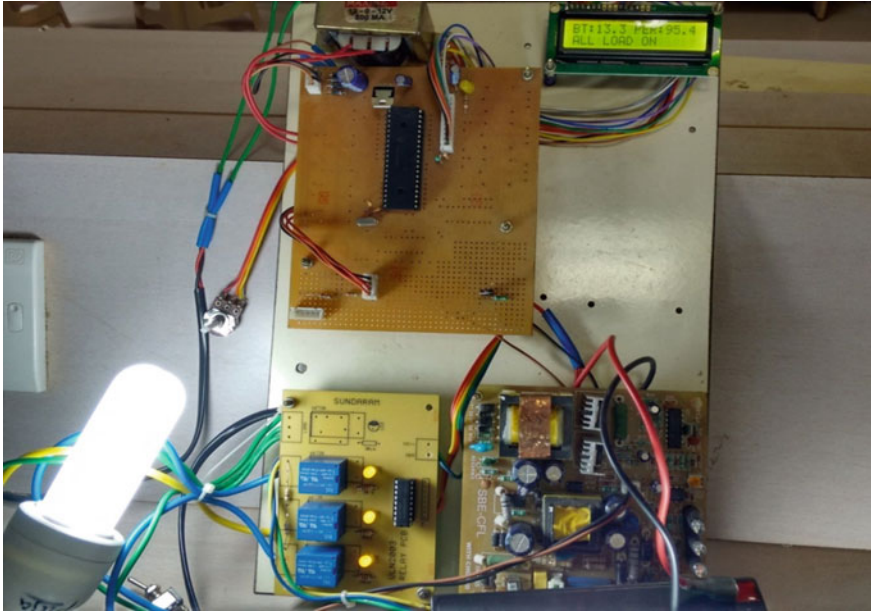
Fig. 7 Priority loads on

selected at condition 1, if it is satisfied where the battery voltage is 13.3 V and 95.4 in percentage. The load priority 1 and 2 are switched on and load priority 3 is switched off, if condition 2 is satisfied where the battery voltage is 11.7 V and 83.7 in percentage. Load priority 1 is switched on and load priority 2 and 3 are switched off, if condition 3 is satisfied where the battery voltage is 9.8 V and 70.0 in percentage. When condition 4 is satisfied, it shows that all the priority loads are switched off where the battery voltage is 8.3 V and 59.3 in percentage.

If the fuzzy logic controller satisfies the condition $85\% \leq B_L \leq 100\%$, then energy is distributed to all loads (load 1, load 2, and load 3) as shown in Fig. 7.

If the fuzzy logic controller satisfies the condition $75\% \leq B_L \leq 84\%$, then energy is distributed to load 1 and load 2. This is shown in Fig. 8.

If the fuzzy logic controller satisfies the condition $60\% \leq B_L \leq 74\%$, then energy is distributed to load 1. This is shown in Fig. 9.

If the fuzzy logic controller satisfies the battery voltage is below 60%, then it switches off all the loads and connects the battery to charging mode as shown in Fig. 10.
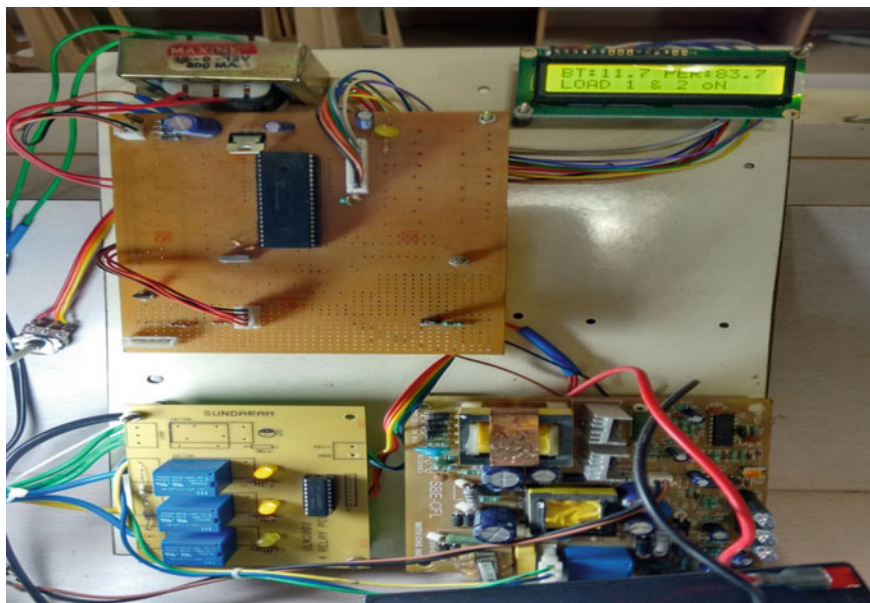
Fig. 8 Priority load 1 and priority load 2 are switched on
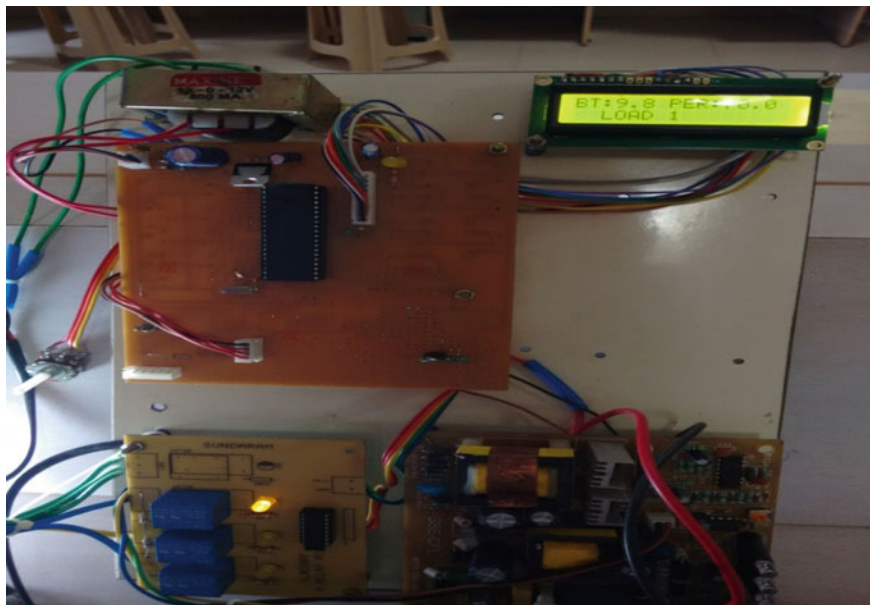
Fig. 9 Priority load 1 switched on
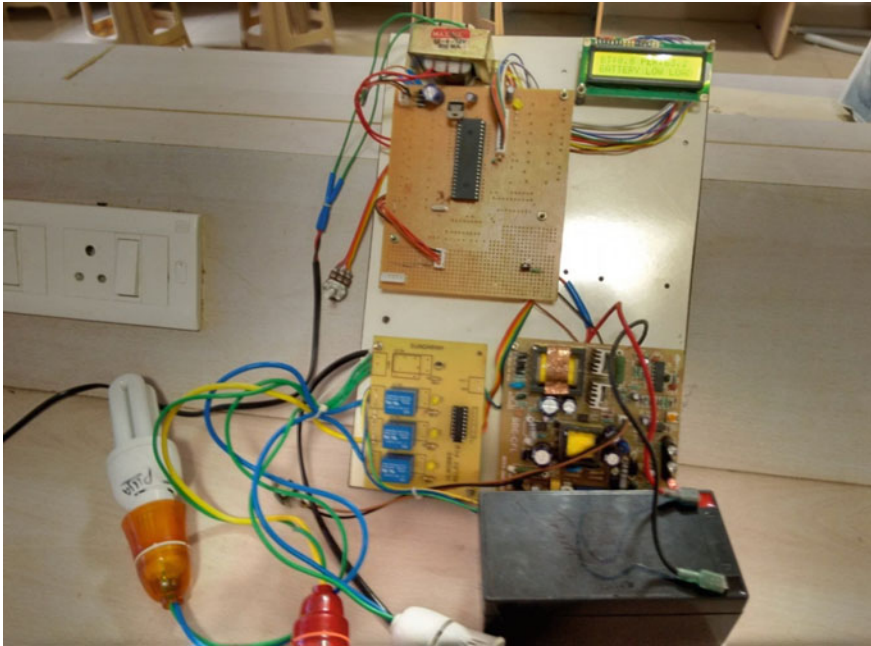
Fig. 10 No load and battery charging

3 Conclusion

An intelligent control hardware model is implemented for the effective utilization of hybrid renewable energy sources. The fuzzy logic controller and fuzzy algorithm are used in hardware model for proposed system. Thus, a Battery Management System for effective utilization of the renewable energy source has been achieved by effectively managing the charging time and draining time of the battery. The battery level indicator, which continuously monitors the status of the battery and indicates the battery voltage in terms of percentage, displays the connected loads. The priority of the load can be selected by fuzzy logic controller using fuzzy logic algorithms. Therefore, renewable energy can be utilized effectively.

References

1. Kiyokawa I, Niida K, Tsujikawa T, Motozu T (2000) Integrated VRLA-battery management system. In: 2000 Twenty-second international telecommunications energy conference INTELEC, pp 703–706. https://doi.org/10.1109/INTLEC.2000.88432
2. Anbuky AH, Hunter P, Johnson T, Lim D (2002) VRLA battery intelligent node. In: 2002 24th annual international telecommunications energy conference INTELEC, pp 169–175. https://doi.org/10.1109/INTLEC.2002.1048652

3. Lim D, Anbuky A (2004) Modeling and simulation of a distributed battery management system. In: IEEE international symposium on industrial electronics vol 1, pp 621–626. 4–7 May https://doi.org/10.1109/ISIE.2004.1571878

4. Wen J, Jiang J (2008) Battery management system for the charge mode of quickly exchanging battery package. In: IEEE 2008 Vehicle power and propulsion conference, VPPC '08, pp 1–4. https://doi.org/10.1109/VPPC.2008.467748.

5. Zhou J, Li H, Liu Z, Hu C, Xu D (2014) Control strategy of Li-Ion battery module in super UPS. In: 2014 International electronics and application conference and exposition (PEAC). 5–8 Nov, pp 1236–1241. https://doi.org/10.1109/PEAC.2014.7038039

6. Pattipati B, Sankavaram C, Pattipati KR (2011) System identification and estimation framework for pivotal automotive battery management system characteristics. IEEE Trans Syst Man Cybern Part C: Appl Rev 41(6):869–884. https://doi.org/10.1109/TSMCC.2010.2089979

7. Ma T, Serrano B, Mohammed O (2014) Fuzzy logic based power and thermal management system design for multi-cell lithium-ion battery bank protection and operation. In: 2014 Clemson university power systems conference (PSC). 11–14 March, pp 1–5. https://doi.org/10.1109/PSC.2014.6808111

8. Wey CL, Jui PC (2013) A unitized charging and discharging smart battery management system. In 2013 International conference on connected vehicles and expo (ICCVE). 2–6 Dec, pp 903–909. https://doi.org/10.1109/ICCVE.2013.6799924

9. Ma T, Serrano B, Mohammed O (2014) Fuzzy logic based power and thermal management system design for multi-cell lithium-ion battery bank protection and operation. In: 2014 Clemson University power systems conference (PSC). 11–14 March, pp 1–5. https://doi.org/10.1109/PSC.2014.6808111

10. Mangunkusumo KG, Lian KL, Aditya P, Chang YR, Lee YD, Ho YH (2014) A battery management system for a small microgrid system. In: 2014 international conference on intelligent green building and smart grid (IGBSG), pp 1–6. https://doi.org/10.1109/IGBSG.2014.6835277

11. Rajkumar RK, Ramachandaramurthy VK, Yong BL, Chia DB (2011) Techno-economical optimization of hybrid pv/wind/battery system using Neuro-Fuzzy. Energy 36(8):5148–5153

12. Thounthong P, Sikkabut S, Sethakul P, Davat B (2010) Control algorithm of renewable energy power plant supplied by fuel cell/solar cell/supercapacitor power source. In: Proceedings of the international power electronic conference (IPEC). 21–24 June, pp 1155–62

13. Khanh LN, Seo JJ, Kim YS, Won DJ (2010) Powermanagement strategies for a grid connected PV-FC hybrid system. IEEE Trans Power Deliv 25:1874–82

14. Chen Y, Wu J (2008) Agent-based energy management and control of a gridconnected wind/solar hybrid power system. In: 2008 Proceedings of the IEEE international conference on electrical machines and systems (ICEMS). 17–20 October, pp 2362–65

15. Jie W (2009) Control technologies in distributed generation system based on renewable energy. In: Proceedings of the IEEE international conference on power electronics systems and applications (PESA), pp 1–14.

16. Babazadeh H, Gao W, Wang X (2011) Controller design for a hybrid energy storage system enabling longer battery life in wind turbine generators. In: 2011 Proceedings of the North American power symposium (NAPS), pp 1–7

17. Das D, Esmaili R, Longya Xu, Nichols D. An optimal design of a grid connected hybrid wind/photovoltaic/fuel cell system for distributed energy production. In: 2005 Proceedings of the IEEE transactions on industrial electronics society (IECON). 6–10 November, pp 6–10

18. Esmaili R, Xu L, Nichols DK (2005) A new control method of permanent magnet generator for maximum power tracking in wind turbine applications. In: Proceedings of the 2005 IEEE power engineering society general meeting. 12–16 June, pp 2090–95

19. Bo D, Li Y, Zheng Z (2010) Energy management of hybrid DC and AC bus linked microgrid. In: Proceedings of the IEEE international symposium on power electronics for distributed generation systems (PEDG). 16–18 June, pp 713–16

20. Nguyen TA, Qiu Xin, Gamage TT, Crow ML, McMillin BM, Elmore AC (2011) Microgrid application with computer models and power management integrated using PSCAD/EMTDC. In: 2011 Proceedings of the North American power symposium (NAPS). 4–6 August, 2011, pp. 1–7

21. Miao Z, Xu L, Disfani VR, Fan L (2014) An SOC-based battery management system for microgrids. IEEE Trans Smartgrid, pp 966–73
22. Yong BL, Chia DB, Rajkumar RK, Ramachandaramurthy VK, Pasupuleti J (2010) Operation and management of an islanded mode hybrid power system- a Malaysian perspective. In: Proceedings of international conference on advances in renewable energy technologies. Malaysia
23. Tian G, Ding X, Liu J (2011) Study of control strategy for hybrid energy storage in wind-photovoltaic hybrid streetlight system. In: Proceedings of the international workshop on open-source software for scientific computation (OSSC). 12–14 October, pp 77–81
24. Gaztanaga H, Etxeberria-Otadui I, Bacha S, Roye D. Real-time analysis of the control structure and management functions of a hybrid microgrid system. In: 2006 Proceedings of the IEEE 32nd annual conference on industrial electronics (IECON). 6–10 November, pp 5137–42
25. Rezkallah M, Chandra A, Singh B, Niwas R. Modified PQ control for power quality improvement of standalone hybrid wind diesel battery system. In: 2012 Proceedings of the IEEE fifth power India conference, 19–22 December, pp 1–6

Hybrid Renewable Power Production on Unfavorable Conditions—A Review

N. Aravindhan [ORCID]**, P. K. Devan, K. Santhosh, V. Sathish Kumar, R. Tamil Selvan, and S. Yogesh**

Abstract Wind energy an unimpeded and simply accessible renewable source. It is a more abundant source regardless of the time factor. Further, the capability of wind in producing energy as a green source makes it a favorite for renewable power generation. Wind energy can be exploited for producing power in a fresh environment. The number of unconventional power generation resources is steadily increasing. In this review, we looked at the efficiency of wind turbines in comparison with solar energy, as well as the possibility of combining the two as a hybrid power source. The literature expressed that the power production using renewable sources are being seasonally successful. So, we analyzed the performance of hybrid renewable power generation as a source for future development.

Keywords Wind energy · Renewable power generation · Solar · Hybrid · Future

1 Introduction

Natural resources have been depleted in recent years as a result of greenhouse gas emissions, resource scarcity, and a lack of energy supplies. The researchers are putting forth effort because they want to use renewable energies to the greatest extent possible. Wind turbines with vertical and horizontal axes were tested for performance [1]. Wind energy, according to Djamal Hissein Diane et al., is a readily available, cost-free, and long-term sustainable source. Even though it is in high demand, the supply will remain constant in the future. It is a source of non-polluting, clean energy. There is no waste or greenhouse gas production. It is a green fuel source that, unlike coal or natural gas-fired power plants, does not pollute the air [2].

This paper is organized as follows. In Sect. 1, wind turbines classification, Sect. 2 unconventional wind turbines, Sect. 3 solar power generation, Sect. 4 effects of hybrid power generation and concluded in Sect. 5.

N. Aravindhan (✉) · P. K. Devan · K. Santhosh · V. S. Kumar · R. T. Selvan · S. Yogesh
Department of Mechanical Engineering, RMK College of Engineering and Technology, Puduvoyal, Tiruvallur 601206, India
e-mail: aravindhn25389@gmail.com

2 Wind Turbines Classifications

Horizontally axis wind turbines are distinguished by the fact that their rotating axis is on the same layer as the ground, and they are best suited for large-scale applications. Since they can be mounted on rooftops, vertical-axis wind turbines are ideal for small-scale wind turbines. Horizontal axis setups are typically used for higher power requirements, but they perform poorly in highly turbulent environments [3].

2.1 Horizontal Axis Upwind Turbines

The blade of an upwind turbine is facing the wind. Upwind designs have the major benefit of avoiding the wind shadow behind the tower. This is the most famous wind turbine design. In the vicinity of the tower, there is almost a wind shadow, this implies that the wind bends away from the tower until it hits the tower itself, even though the tower is not in the shade. As a result, each time the rotor approaches the tower, the wind turbine's power decreases slightly. The rotor must be made reasonably rigid and ride at a safe distance from the tower, which is the key flaw. To hold the rotor facing the wind, and the upwind machine needs a yaw mechanism [4].

2.2 Horizontal Axis Downwind Turbines

The rotor of a downwind turbine is mounted on the tower's low side. If the rotor and nacelle are constructed in such a way that the nacelle follows the wind passively, they can be mounted without a yaw mechanism. However, this will not be more efficient for large wind turbines since cables are needed to transport the current away from the generator. Also, the rotor must be made more flexible, which is a major lead. A downwind can be made lighter than an upwind machine is a huge advantage. The key drawback to this method is the fluctuation of wind power generated by the rotor passing through the wind shadow of the tower. It would result in higher fatigue loads upon on turbine than that of an upwind design [5].

2.3 Vertical-Axis Wind Turbines

The vertical-axis wind turbine (VAWT) is a wind turbine with a vertically oriented main rotational axis. They have a rotational axis that is vertical or perpendicular to the ground. The ability to produce well in turbulent wind conditions is a key benefit of using a vertical-axis turbine. Wind turbines with a vertical axis can also rotate in any

direction. When the wind blows from top to bottom, it can also be powered. Vertical-axis wind turbines are thought to be ideal for installations where wind patterns are unreliable or where public ordinances prevent the turbine from being mounted high enough to benefit from steady wind [6].

2.4 Darrieus Vertical-Axis Wind Turbines

Darrieus wind turbines are a type of vertical-axis wind turbine (VAWT) that consists of a collection of curved aerofoil blades mounted on a rotating shaft or framework. The curvature of the blade allows it to be strained only at high rotational speeds. Several highly associated wind turbines use straight blade wind turbines. The blades of a Darrieus turbine can be twisted into a helix, such as three blades with a 60° helical twist [6].

2.5 Savonius Vertical Wind Turbine

The Savonius vertical-axis wind turbine (VAWT) transforms the wind's power into torque on a spinning shaft. On the ground or in air-borne designs, the turbine is made up of several airfoil sections straddling vertically on a revolving shaft. It is a two- or three-scoop drag scheme [7]. When moving toward the wind, the turbine experiences less drag than when moving with the wind due to the curvature. The Savonius turbine spins due to the differential drag. Savonius turbines are known for their drag-type turbines. Since wind speeds are lower at lower altitudes, much of the swept area of a Savonius rotor may be close to the ground if it has a small mount without an extended post, lowering overall energy extraction efficiency [8].

3 Unconventional Wind Turbines

3.1 Savonius Wind Turbine

The shrouded wind turbine is a novel design that encloses the turbine in a venturi-shaped shroud or duct (vent-duct), creating a low-pressure sub-atmosphere behind it. The Betz limit is bypassed by the variable area shrouded turbine, which represents the volume of air over the turbine and helps it to run at higher efficiencies than if it were just a turbine. According to the claims, a shrouded turbine generates 1.15–4 times the energy of a non-shrouded turbine [9]. In an open flow, the 59.3% Betz conversion efficiency cap for a turbine still applies, although it can be increased further in veiled

applications. A shrouded turbine's output is determined by the shroud design; not all shrouded turbines are created equal [10].

Shrouded turbines cannot operate at optimum efficiency unless the shroud intercepts the current flow at the correct angle, which may happen as currents eddy and swirl. As a result, operational efficiency suffers. At lower turbine efficiencies, the increased cost of the shroud can be balanced, while at higher efficiencies, the cost of the shroud has less of an effect on commercial returns. The cost of the shroud's supporting structure must also be balanced against its increased performance. Although yawing (pivoting) the shroud and turbine at the proper angle, so that it always faces upstream like a windsock, could boost turbine output [11].

3.2 Wind-Lens Turbine

The hybrid approach, in which the flow and acoustic fields are solved separately, was found to be an efficient technique for such a study's computational. Since the possibility of using a wind-lens turbine was discovered, a need to examine this hypothesis has grown steadily. Wind-lens design, fringe size, and average velocity are some of the effective parameters investigated to improve the turbine's performance [12]. When a bare wind turbine's noise is compared with the noise produced by various types of wind-lens turbines, it is clear that the wind lens generate more noise. The human ear perceives loudness in the 20 Hz–20 kHz natural hearing range [13]. The noise generated by wind lens is the focus. In comparison with existing wind turbine designs, the wind lens needs considerably more materials. The fabrics for the shrouds, as well as the mesh, take a lot of time and money to make. The wind pressure on the wind lens is higher, and the wind lens may be too difficult to sustain due to structural issues [14]. This may indicate that it has a lot of power it's not using or that the wind lens is more prone to breaking. The wind lens is being considered as a way to boost clean energy generation and other clean energy sources[15].

The wind lens can be used to replace current manufacturing energy from fossil fuels, which is detrimental to the environment, as well as the less efficient wind turbine since it is adaptable to more conditions and produces more energy [16].

3.3 INVELOX Turbine

INVELOX is a novel approach for increasing the velocity of the wind. It works by the speed of the wind. The wind is collected by a large intake, funneled down to a venturi section by tapered tubing, and finally released by a diffuser. The INVELOX venturi portion houses the turbines [17]. The turbine converts kinetic energy into mechanical rotation, and we use a generator to generate electricity. The INVELOX system's venturi impact component concentrates and accelerates wind. The pressure is raised, causing a significant amount of kinetic energy to be transmitted to the turbine. It

separates the turbine from the intake, just like a hydropower plant [18]. It is based on the hydropower principle. The duct in the shape of a diffuser is the primary contributor to the accelerated flow of air toward the turbine. The following components make up the INVELOX system: Wind is carried into the pipe and is accelerated. System of intake When a fluid flowing through a pipe is forced through a narrow segment, the venturi effect occurs, resulting in a decrease in pressure and a rise in velocity [19]. The accelerated wind is sent to the turbines/generators, which convert it to electricity. Wind is funneled into the system. Because of the omnidirectional intake area, wind can be collected from any direction. The wind is captured at the top of the funnel-shaped INVELOX structure[20].

4 Solar Power Generation

Dry-sensitized solar cells could be used instead of P–n junction photovoltaic systems. In p–v applications, the semiconductor often achieves light absorption and charge carrier, but the light in these cells is absorbed by a sensitizer. To separate charges at the interface, photo-induced electron injection is used. More light can be captured by a sensitizer with a large absorption band. Electric energy is converted from photons of wavelengths ranging from ultraviolet to near infrared. An efficiency of about 10% can be achieved using dry-sensitized solar cells. Traditional silicon cells have a lower efficiency, whereas DSC is temperature tolerant [21].

Photovoltaic modules have a lower electric yield since the sun's irradiance is mirrored. With a refractive index of 1.3, water serves as a good medium between glass and air. Coatings and structured surfaces have been proposed as ways to reduce reflection, but they are neither cost effective nor long lasting. It also reduces reflection by 2–3%, reduces cell temperature by up to 220 °C, and increases electrical yield by 10.3% [22].

Quantum dot solar cells produce higher photovoltage or photocurrent by using hot photo-generated carriers, increasing the overall thermodynamic conversion of the solar photon. The accumulation of a hot carrier in a QD array photoelectrode until it relaxes to the band edges due to phonon emission causes the photovoltage to increase. The use of a hot carrier in QD solar cells increases photocurrent by producing and collecting extra electron–hole pairs through the ionization process. Solar cells are quickly gaining traction as a viable source of energy. To reduce solar irradiance reflection, an anti-reflection technique was suggested. This involves using nano-imprint lithography to create a nanometer-scale dot pattern array on the surface of GaInP/Ga(In)As/Ge solar cells [23].

As visible light has a longer wavelength than this nano-pattern, the effective refractive index near the surface gradually increases. As a result, the refraction of light at the surface in the total spectral area is reduced. The refraction was reduced to around 5.3% at a wavelength of 400 nm. GaAs' overall conversion efficiency improved from 27.77 to 28.69% as a result. To make polycrystalline thin films of tin sulfide, spray pyrolysis is used. The film's resistivity was 30 Ω, and its optical

energy bandgap was 1.38 eV. Indium-doped cadmium sulfide was used as a window coating and as an absorber in heterojunction solar cells. Finally, their systems were characterized to look into the performance of solar cells. The machine had a solar conversion efficiency of 1.3% and a quantum efficiency of 70%. The efficiency was lower due to the very thin thickness of SnS used in solar cells. As the thickness is increased to 1.5 μm or more, VOC levels rise [15].

The counter electrode for dry-sensitized solar cells was made of graphene and polystyrene sulfonate composite films deposited on indium tin oxide [24]. With a high transmittance and an indium tin oxide coating, this thick composite film can be used as an electrocatalyst. This form of cell's energy consumption performance was comparable to that of cells with platinum as a counter electrode. At a 100 mW AM 1.5 white light irradiance, they had a thermal efficiency of 4.3%. Because of their high transmittance, they were also used in power-generating windows. The use of a hard carbon spherule as a counter electrode for dye-sensitized solar cells has been proposed [24].

The cell's overall conversion efficiency is about 5.7%, which is comparable to Gratzel-type solar cells with a platinum-sputtered fluorine-doped tin oxide counter electrode, which has a conversion efficiency of 6.5%. The surface areas of the carbon material had a major impact on photovoltaic efficiency. The disordered microporous hard carbon spherules showed high electrocatalytic activity in the iodide/triiodide redox reaction, making them suitable for counter electrode fabrication on dye-sensitized solar cells [25].

5 Effects of Wind and Solar Using Together as the Hybrid Source for Power Generation

Jenkins et al. evaluated the possibility of using solar and wind as together for generating the power. They validated the design using the hybrid optimization model for the production of renewable electricity. They performed simulation for capable of producing 250 kW as 100 kW using ten wind turbines and 150 kW of solar PV [26]. Bob Burkett et al. patented the solar-driven fan to push the wind inside the vent for power production. They modeled the system for heating or cooling the room with this setup also they can utilize the setup for the power production [27]. Ehsan et al. described that hybrid power development using both wind and solar as a source of power generation. They tried a new approach of storing both powers in the battery, whereas wind can be utilized as a major contributor and solar as a supporter [15].

6 Conclusion

Power generation using renewable energy sources has been developing a lot on day to day basis. But still, the focus is mainly on individual resources. As we have reviewed the performance and efforts taken for hybrid development only works are limited and mostly not came in real-time applications. The identified issues are mainly the storage and power transmission. We are looking to overcome these shortcomings and will develop more in the future.

References

1. Saad MM, Asmuin N, Óskarsdóttir MÓ (2014) A general description and comparison of horizontal axis wind turbines and vertical axis wind turbines. IOSR J Eng www.iosrjen.org ISSN 04:2250–3021
2. Didane DH, Ab Wahab A, Shamsudin SS, Rosly N (2016) Wind as a sustainable alternative energy source in Malaysia—a review. ARPN J Eng Appl Sci 11:6442–6449
3. Cheng Z, Madsen HA, Chai W, Gao Z, Moan T (2017) A comparison of extreme structural responses and fatigue damage of semi-submersible type floating horizontal and vertical axis wind turbines. Renew Energ 108:207–219. https://doi.org/10.1016/j.renene.2017.02.067
4. Eriksson S, Bernhoff H, Leijon M (2008) Evaluation of different turbine concepts for wind power. Renew Sustain Energ Rev 12:1419–1434. https://doi.org/10.1016/j.rser.2006.05.017
5. Wang Z, Tian W, Hu H (2018) A comparative study on the aeromechanic performances of upwind and downwind horizontal-axis wind turbines. Energ Convers Manag 163:100–110. https://doi.org/10.1016/j.enconman.2018.02.038
6. Aslam Bhutta MM, Hayat N, Farooq AU, Ali Z, Jamil SR, Hussain Z (2012) Vertical axis wind turbine—a review of various configurations and design techniques. Renew Sustain Energ Rev 16:1926–1939. https://doi.org/10.1016/j.rser.2011.12.004
7. Zemamou M, Aggour M, Toumi A (2017) Review of savonius wind turbine design and performance. Energy Procedia 141:383–388. https://doi.org/10.1016/j.egypro.2017.11.047
8. Modi VJ, Fernando MSUK (1989) On the performance of the savonius wind turbine. J Sol Energy Eng Trans ASME 111:71–81. https://doi.org/10.1115/1.3268289
9. Zabarjad Shiraz M, Dilimulati A, Paraschivoiu M (2020) Wind power potential assessment of roof mounted wind turbines in cities. Sustain Cities Soc 53:101905. https://doi.org/10.1016/j.scs.2019.101905
10. Kc A, Whale J, Urmee T (2019) Urban wind conditions and small wind turbines in the built environment: a review. Renew Energy 131:268–283. https://doi.org/10.1016/j.renene.2018.07.050
11. Ohya Y, Karasudani T, Sakurai A, Abe K, ichi, Inoue M, (2008) Development of a shrouded wind turbine with a flanged diffuser. J Wind Eng Ind Aerodyn 96:524–539. https://doi.org/10.1016/j.jweia.2008.01.006
12. Clements L, Chowdhury A (2019) Performance evaluation of wind lens in turbulent environment. Energ Procedia 160:777–782. https://doi.org/10.1016/j.egypro.2019.02.161
13. Dessoky A, Bangga G, Lutz T, Krämer E (2019) Aerodynamic and aeroacoustic performance assessment of H-rotor darrieus VAWT equipped with wind-lens technology. Energy 175:76–97. https://doi.org/10.1016/j.energy.2019.03.066
14. Jayasurya M, Kumar PH (2019) Design and fabrication of shrouded diffuser casing for turbines
15. Ehsan MM, Ovy EG, Chowdhury HA, Ferdous SM (2012) A proposal of implementation of ducted wind turbine integrated with solar system for reliable power generation in Bangladesh. Int J Renew Energy Res 2:397–403. https://doi.org/10.20508/ijrer.36008

16. Xia G, Zhou L, Freedman JM, Roy SB, Harris RA, Cervarich MC (2016) A case study of effects of atmospheric boundary layer turbulence, wind speed, and stability on wind farm induced temperature changes using observations from a field campaign. Clim Dyn 46:2179–2196. https://doi.org/10.1007/s00382-015-2696-9
17. Solanki AL, Kayasth BD, Bhatt H (2017) Design modification and analysis for venturi section of invelox system to maximize power using multiple wind turbine. Int J Innov Res Sci Technol 3:125–127
18. Allaei D, Andreopoulos Y (2014) INVELOX: description of a new concept in wind power and its performance evaluation. Energy 69:336–344. https://doi.org/10.1016/j.energy.2014.03.021
19. Khamlaj TA, Rumpfkeil MP (2018) Analysis and optimization of ducted wind turbines. Energy 162:1234–1252. https://doi.org/10.1016/j.energy.2018.08.106
20. Venters R, Helenbrook BT, Visser KD (2018) Ducted wind turbine optimization. J Sol Energy Eng Trans ASME 140. https://doi.org/10.1115/1.4037741
21. Khare V, Nema S, Baredar P (2013) Status of solar wind renewable energy in India. Renew Sustain Energ Rev 27:1–10. https://doi.org/10.1016/j.rser.2013.06.018
22. Littlewood J, Howlett RJ (2009) Sustainability in energy and buildings
23. Masukume P-M, Makaka G, Tinarwo D (2014) Technoeconomic analysis of ducted wind turbines and their slow acceptance on the market. J Renew Energy 2014:1–5. https://doi.org/10.1155/2014/951379
24. Aravindhan N, Chidambaranathan B, Rokesh D, Jagadesh D, Pravin S, Ramkumar N (2020) Performance of statistical control tools in identifying the defect on plunger-a review. IOP Conf Ser Mater Sci Eng 906. https://doi.org/10.1088/1757-899X/906/1/012012
25. Aravindhan VDN, Bibin MKC (2017) Agglomeration in fluidized bed combustion system RMK college of engineering and technology 5:103–107
26. Jenkins P, Elmnifi M, Younis A, Emhamed A (2019) Hybrid power generation by using solar and wind energy: case study. World J Mech 09:81–93. https://doi.org/10.4236/wjm.2019.94006
27. Power SE (2013) (12) United States Patent. 1

Advanced IC Engine Studies

Performance and Emission Studies of Waste Vegetable Oil as Blends with Diesel and Kerosene—An Economic Route for Valorizing Liquid Waste

Pritam Dey and **Srimanta Ray**

Abstract Rise and instability in fuel prices and growing environmental concerns have promoted the scope for alternate to diesel fuel. Vegetable oils or their transesterified forms are used in the diesel engine after blending with various petroleum fuels. Waste vegetable oil (WVO), a known problematic liquid waste, holds potential in this regard. However, WVO is associated with the problem of higher viscosity and lower calorific value. The present work proposes to overcome such limitations by blending with diesel and kerosene. Three blends with varying volumes of WVO in diesel as well as kerosene were prepared. Physical properties of the blends showed similarity with that of diesel fuel and conformed to diesel standards. The various WVO blends showed acceptable engine performance and emission. WVO-kerosene blends recorded lower BSFC and higher BTE than diesel-kerosene blends. WVO-kerosene blends resulted in lower CO and HC emissions than diesel. A rise in the NO_x emission with the addition of WVO in the fossil fuels was recorded. Blending WVO with fossil fuels reduced the overall fuel price. WVO-kerosene blends can cause 22–40% reduction in overall price as compared to similar WVO-diesel blends.

Keywords Waste vegetable oil · Fuel blends · Emissions · BFSC · BTE

1 Introduction

Diesel is the fuel of choice for agricultural, transportation, industrial, logistics, and power generation sectors because of the capability to produce more energy and cleaner emissions characteristics in diesel engines [1]. The increment in demand for diesel associated with the demerits of price instability, depleting reserve, and rising environmental concerns pressed an emphasis toward an alternative to diesel fuel [2]. Vegetable oils hold a great potential in this regard as they are linked with renewable

P. Dey · S. Ray (✉)

Chemical Engineering Department, National Institute of Technology Agartala, Jirania, Agartala, Tripura 799046, India

e-mail: rays.nita@gmail.com

origin, lower sulfur content, superior storage, handling, and transportation capabilities [3]. As alternative engine fuels, vegetable oils have been successfully demonstrated as an effective substitute in diesel engines [4]. But, owing to the growing food versus fuel dispute, it has become imperative to search for oils from other sources [5, 6]. Waste vegetable oil (WVO) or waste cooking oil holds great promise in this regard. WVO is a problematic liquid waste, which is generated in huge quantities throughout the globe [7, 8]. WVO is often linked with economic losses and environmental disposal issue [9, 10]. Hence, re-utilization of WVO is the need of the hour.

1.1 Various Utilization Routes of WVO

The utilization of WVO as alternate blends in CI engines usually requires their derivatization into methyl esters, more commonly known as biodiesel. This process of derivatization is known as transesterification. But, the derivatization of WVO into biodiesel forfeits the economic gain, which is linked with direct utilization of WVO [11]. The reason is higher cost of biodiesel production, which brings the overall cost of their blends close to diesel [8]. Several reports on the engine performance, combustion, and emission studies using WVO-biodiesel are available [10]. In general, it has been reported that with the increase in the biodiesel fraction in the blend, the brake specific fuel consumption (BSFC) increases, while the brake thermal efficiency (BTE) decreases with respect to diesel. In terms of emissions, carbon monoxide (CO) tends to decrease, while unburnt hydrocarbon (HC) shows increasing trend. However, the oxides of nitrogen (NO_x) emission were reported to behave differently. Only a handful of reports are available on utilization of WVO as diesel blends. But, in all these studies, WVO was used either after preheating or with additives [5]. The literature on direct utilization of WVO (with preheating or additives) as alternative blend fraction for diesel is summarized in Table 1.

The literature survey suggested that WVO has been used as diesel blend, either upon preheating or with an additive. Thus, it is pertinent to study the impact of the direct blending of WVO with diesel on fuel properties, engine performance, and emission characteristics. Also, kerosene has been reported to lower the density and viscosity of vegetable oil blends and assists in improving engine performance [18–20]. Thus, engine performance and emissions of WVO blends containing kerosene need to be looked into.

Table 1 Literature (2000 onward) on WVO utilization in CI engine as fraction in diesel blends

WVO blend type	Engine operating parameters	Changes in engine performance and emissions*	References
Neat sunflower WFO Neat palm WFO	33 kW, 3.11 L, 4-s, 1-cyl, direct injection at 210 bar IP, 23ºTDC IT, 17.5:1 CR, 1500 RPM	Sunflower WFO: 9.8% ↑ in BSEC, 3.2% ↓ in CO, 28.1% ↑ in NOx Palm WFO: 11.8% ↑ in BSEC, 6.5% ↓ in CO, 22.4% ↑ in NOx	[3]
0.50 fraction WCO-diesel blend	4.4 kW, 0.661 L, 4-s, 1-cyl, direct injection at 210 bar IP, 23ºTDC IT, 17.5:1 CR, 1500 RPM	5% ↑ in BSEC, 5% ↓ in BTE, 50% ↑ in CO, 41.2% ↑ in HC, 7.2% ↓ in NOx	[11]
0.50 fraction WVO-diesel blend	3.8 kW, 0.553 L, 4-s, 1-cyl, direct injection at 210 bar IP, 23ºTDC IT, 16.5:1 CR, 1500 RPM	4.2% ↑ in BSEC, 10.7% ↓ in BTE, 40% ↑ in CO, 18.2% ↑ in HC, 10.4% ↓ in NOx	[8]
0.50 fraction WCO-diesel blend	4.4 kW, 0.661 L, 4-s, 1-cyl, direct injection at 210 bar IP, 23ºTDC IT, 16.5:1 CR, 1500 RPM	7.1% ↑ in BSEC, 3.8% ↓ in BTE, 50% ↑ in CO, 41.2% ↑ in HC, 6.7% ↓ in NOx	[12]
Neat WCO	3.7 kW, 0.630 L, 4-s, 1-cyl, direct injection at 200 bar IP, 27ºTDC IT, 16:1 CR, 1500 RPM	14.1% ↓ in BTE, 60% ↑ in CO, 25% ↑ in HC, and 24.4% ↓ in NOx	[13]
0.05 fraction palm WCO-diesel blend and 0.05 fraction coconut WCO-diesel blend	53.6 kW, 2.4 L, 4-s, 4-cyl, indirect injection CI at 22.3:1 CR, 3000 RPM	Palm WCO-diesel blend: 1.2% ↓ in BP, 27.3% ↓ in HC, and 2.1% ↑ in NOx Coconut WCO-diesel blend: 0.7% ↓ in BP, 36.4% ↓ in HC, and 0.8% ↓ in NOx	[14]
0.50 and 0.75 fraction WCO-diesel blend	40 kW, 1.590 L, 4-s, 4-cyl, indirect injection at 190 bar IP, 27ºTDC IT, 23.5:1 CR, 1500 RPM	No change in CO, 13.6% ↑ in HC and 125% ↑ in NOx for 0.50 WCO blend 175% ↑ in CO, 36.4% ↑ in HC and 300% ↑ in NOx 0.75 WCO blend	[15]
WFO heated above 75 ºC	3.7 kW, 4-s, 1-cyl, direct injection at 190 bar IP, 27º bTDC IT, 1500 RPM	20% ↑ in BSEC, 10.7% ↓ in BTE, 163.6% ↑ in CO, and 19.6% ↑ in NOx	[16]
WCO heated above 55 ºC	4.0 kW, 4-s, 1-cyl, direct injection at 3600 RPM	4.5% ↑ in BSFC, 8.8% ↓ in BP, 2% ↓ in BTE, 8.7% ↑ in CO, and 13.5% ↑ in NOx	[17]

WCO—waste cooking oil; WFO—waste frying oil; l—liter; s—stroke; cyl—cylinder; CR—compression ignition; RPM—rotations per minute; IP—injection pressure; IT—injection timing; bTDC = before top dead center; EGR—exhaust gas recirculation; BSFC—brake specific fuel consumption; BSEC—brake specific energy consumption; BP—brake power; BTE—brake thermal efficiency; CO—carbon monoxide; HC—hydrocarbon; NO_x—oxides of nitrogen; NR—not reported; ↑—increase; ↓—decrease; *- relative to neat diesel fuel

Table 2 Properties of diesel, kerosene, and WVO

Fuel samples	Density at 15 °C (g/cc)	Viscosity at 40 °C (mm²/s)	Flash point (°C)	Cetane index	Higher heating value (MJ/kg)
Diesel	0.823	3.12	48	52.25	46.47
Kerosene	0.797	1.67	46	49.16	46.79
WVO	0.881	32.03	189	44.28	39.99
Diesel standard (IS 1460:2017)	0.810–0.845	2.0–4.5	35 (min.)	46 (min.)	–
Test method	ASTM D 1217	ASTM D2983	ASTM D93	ASTM D976	ASTM D240
Instruments	Pycnometer	Digital rotational viscometer	Pensky Martens Closed-cup apparatus	Atmospheric distillation apparatus	Digital bomb calorimeter

2 Materials and Methods

2.1 Formulation of D-WVO and K-WVO Fuels

The WVO, collected from local restaurants and hostels, was precisely blended with diesel and kerosene in fixed volumetric proportions. The WVO fraction was precisely maintained at 0 (only fossil fuel), 0.20 (20% WVO and 80% fossil fuel), 0.35 (35% WVO and 65% fossil fuel), and 0.50 (50% of both WVO and fossil). As it is known that a stationary research engine with a conventional fuel injection system would find it difficult to handle fuels with viscosities several times higher than diesel [1]. WVO fractions greater than 0.50 were not considered while preparing WVO blend fuels. The properties of the diesel, kerosene, and WVO were characterized as per ASTM standard protocol and are presented in Table 2. The viscosity of kerosene was found to be very lower than diesel, whereas WVO showed more than 10 times higher viscosity than diesel. Also, the higher heating value of WVO was very lower than both diesel and kerosene. Thus, blending kerosene with WVO would likely to lower the viscosity of the blended fuels.

2.2 Experimental Setup

The experimental engine setup comprised of a stationary 0.553 L, four-stroke, single-cylinder, compression ignition (CI) diesel engine (Make: Kirloskar; Model: AV-1) paired with a custom-built meter for measurement of volumetric fuel consumption
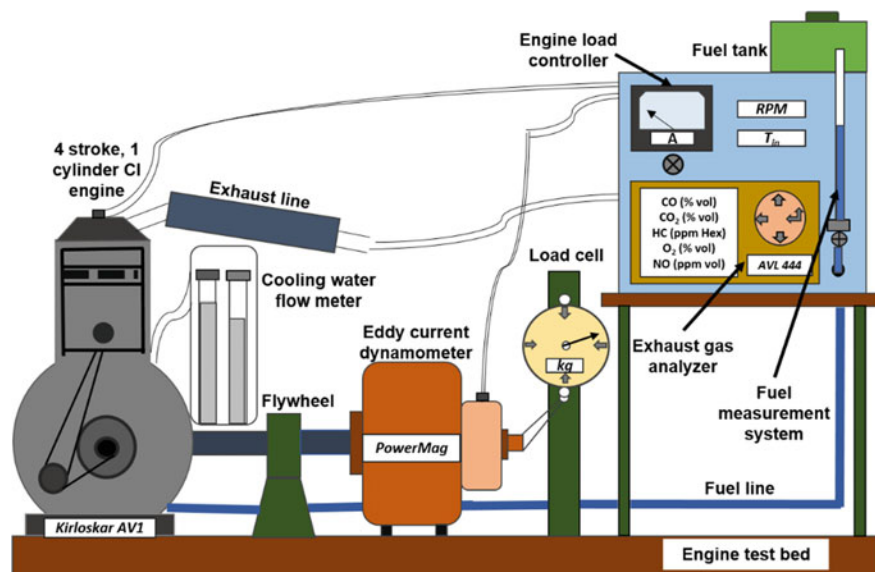
Fig. 1 Schematics of the experimental setup

rate, an eddy-current dynamometer, and a five-gas analyzer (Make: AVL; Model: Digas 444). The schematics of the experimental test setup is shown in Fig. 1. The engine was operated at 1500 RPM and at fixed operating conditions of 16.5:1 compression ratio, 210 bar injection pressure, and an injection timing of 23° before the top dead center. The engine load was varied from 0 to 60% of the full load, with increments of 20% at each step. Appropriate engine cool-off and lubrication were ensured for each experimental run with test fuels to maintain good engine health.

3   Results and Discussions

3.1   Properties of Various Fuels

The dissolution of WVO in both diesel and kerosene helped in preparing blends of the desired variations in WVO fractions. Various blends of WVO with diesel and kerosene were found to be quite stable with no phase separation occurring after 14 days. The six blends (3 D-WVO and 3 K-WVO) were analyzed for their fuel properties using ASTM standard test methods.

The density of the fuel determines the evaporation characteristics of fuel which affect its combustion and fuel economy. A denser fuel will cause higher mass flow for the same volume of fuel injected, thereby elevating the fuel consumption [19]. The denser WVO increased the densities of its blends with the increase in its fraction

in the blend (Fig. 1a). However, the lower densities of K-WVO blends than D-WVO blends were obtained. The various K-WVO blends conformed to the IS 1460:2017 standard (0.820–0.845 g/cc), whereas only D-WVO_0.20 and D-WVO_0.35 blends were within the standard limits. Thus, K-WVO blends were expected to show better fuel injection characteristics and lower fuel consumption than D-WVO blends. A minimum of 35 ºC flash point is required to be considered for fueling a CI engine, as per IS 1460:2017 standards. But, vegetable oil blends were known to have high flash points. Yet, they were reported to satisfactorily power a diesel engine [4]. Moreover, higher flash point is desired for safer handling and transportation of fuel. The flash points of the blended fuels increased with linearly with WVO addition (Fig. 2b). However, superior volatility of kerosene than diesel lowered the flash points of its blends than D-WVO blends.

Viscosity plays a pivotal role in the atomization and spray behaviors of a fuel. Higher viscosity minimizes jet penetration and causes poor atomization of fuel droplets, but also reduces fuel loss by enhancing lubricity [20]. The viscosity of diesel and kerosene blends was seen to increase with the addition of WVO fractions (Fig. 1b). The standard range for diesel, as per IS 1460:2017, is 2.0–4.5 mm^2/s at 40 ºC. Two K-WVO blends (K-WVO_0.20 and K-WVO_0.35) and only one diesel blend (D-WVO_0.20) conformed to the standard range. So, a better engine performance characteristics are expected of these particular blends. Calorific value is the measure of the energy obtainable form a fuel from its combustion and determines the thermal efficiency of an engine. A fuel should possess calorific value above 43.0 MJ/kg to be able to provide enough power to run an engine [5]. With the addition of WVO, the calorific value showed a steep decrease. However, the calorific values of all the WVO blends were above 43.0 kJ/kg (Fig. 2b). Thus, it can be confirmed that the blended fuels hold the ability to provide power to the CI engine similar, if not more, to neat diesel.

3.2 Engine Performance Analysis

The engine performance was evaluated at 60% engine load condition in terms of brake specific fuel consumption (BSFC) and brake thermal efficiency (BTE). BSFC is the rate of fuel consumption by an engine for producing a specific brake power. With a rise in the WVO fraction in blend, the BSFC of the various blends was found to increase, as presented in Fig. 3a. This trend is due to the higher density and viscosity of most of the blended fuels than diesel. Higher density of fuel affects the fuel atomization and fuel-jet penetration inside the cylinder. Conversely, the inherent lubricity of vegetable oils reduces fuel losses [21]. There exists a critical balance between the two phenomena and governs the rate of fuel consumption [8]. However, better fuel properties of K-WVO_0.20 blend resulted in 2.5% reduction in BSFC. As compared to the diesel blends, K-WVO blends caused only 3.3% increment in BSFC relative to diesel. Similar result is reported elsewhere [19].
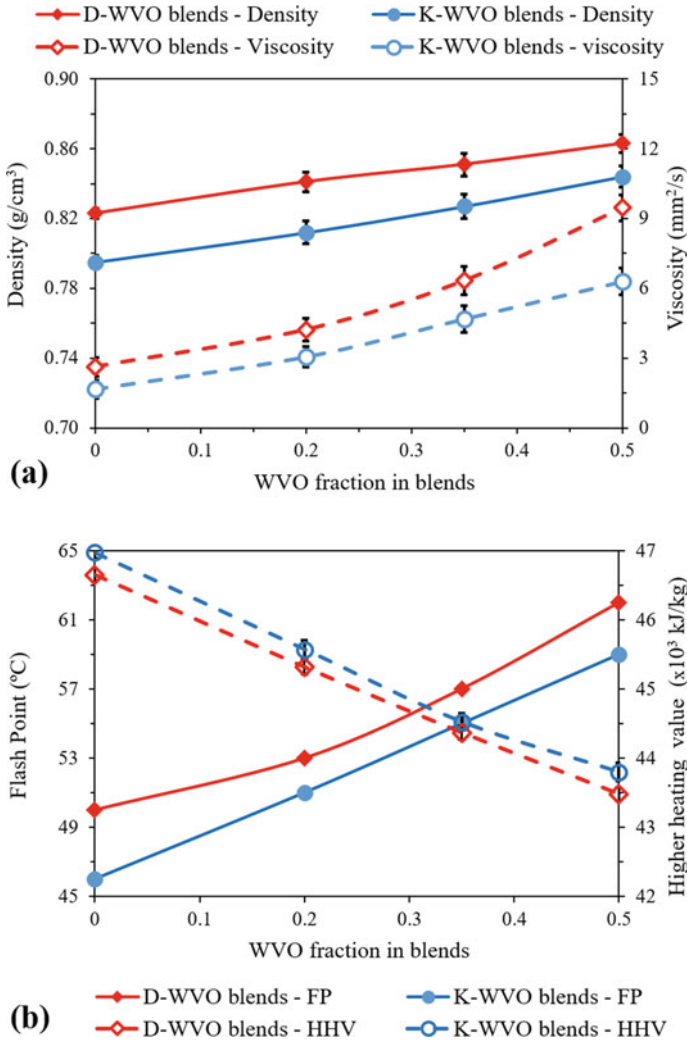
Fig. 2 Variations in different fuel properties for D-WVO and K-WVO blends

BTE is dependent on the rate of fuel consumption and the calorific value of the fuel [8]. The BTE of the blend fuel was found to drop with the rise in the WVO fraction. Lower calorific value and increased fuel consumption are the probable reasons. The K-WVO blends showed 3.3–4.8% higher BTE than neat diesel. Although the calorific values of theses blends were lower than diesel, their densities and viscosities were very much similar to diesel. Also, owing to the reduction in fuel loss [8] and superior volatility of kerosene caused faster air-fuel mixing, assisted the combustion process,

Fig. 3 Variations in engine performance—**a** BSFC and **b** BTE for D-WVO and K-WVO blends at the highest load condition
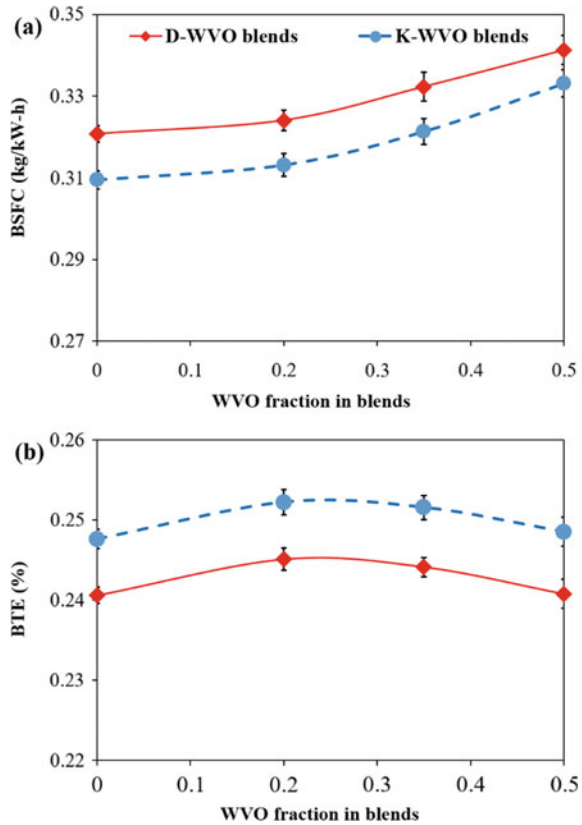
and increased the BTE [20]. The highest increase in BTE was recorded for the K-WV_0.20 blend. Thus, it can be inferred that K-WVO blends demonstrated superior engine performance over their diesel counterparts.

3.3 Engine Emission Analysis

Brake specific emissions were investigated for the various blended fuels in terms of carbon monoxide (CO), unburnt hydrocarbon (HC), and oxides of nitrogen (NO_x). The emission profile of various WVO blends at 60% engine load is presented and discussed in the subsequent paragraphs.

CO emission is the result of incomplete combustion of fuel inside the cylinder. CO emission decreases with an increase in engine load. This is because higher temperature inside the cylinder due to a rise in engine load improves the combustion efficiency of the engine [22]. It has been reported that CO emission reduces with the elevated oxygen content in the fuel. The reason is oxygenated fuel enhances combustion of

fuel and converts CO into CO_2 more efficiently [6]. Since WVO contains 10–12% oxygen, with the increment in the WVO fraction in the blended fuel, specific CO emission was found to decrease, as shown in Fig. 4a. In between the two types of blend fuels, the D-WVO blends recoded a slightly higher brake specific CO emission than their analogous kerosene blends. With respect to pure diesel, D-WVO blends caused 13.4–18.1% CO reduction, whereas for K-WVO blends, it reduced 26.7–30.7% relative to diesel.

HC is also produced due to incomplete combustion of fuel. Literature suggests that more HC emission occurs at lower loads due to low in-cylinder temperatures

Fig. 4 Variations in **a** CO, **b** HC, and **c** NO_x emissions for D-WVO and K-WVO blends at the highest load condition
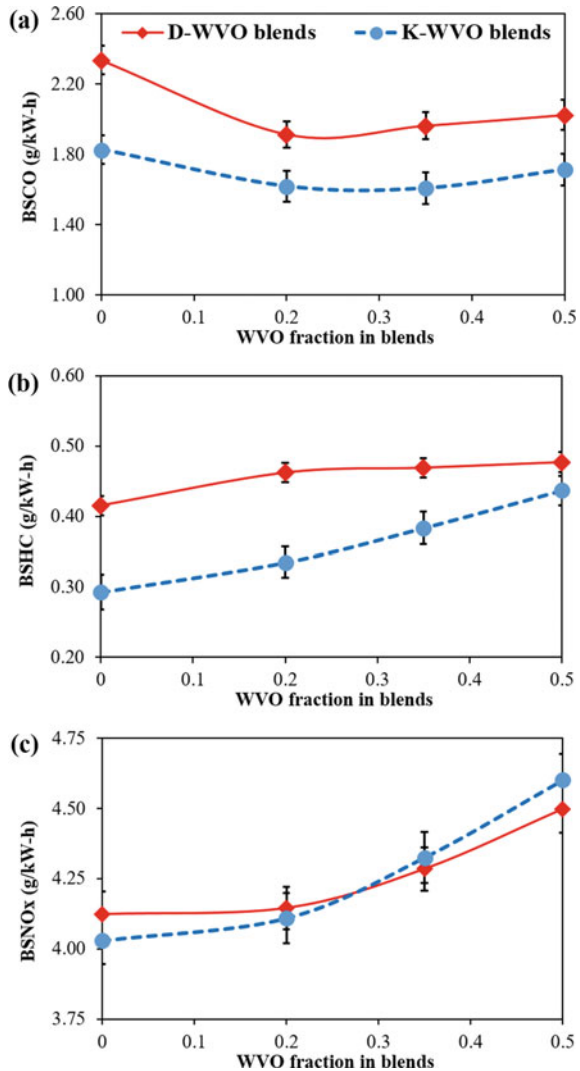
than at high loads [23]. The brake specific HC emissions for various WVO blends are shown in Fig. 4b. With the addition of WVO fraction in diesel, specific HC emission increased, but it remained somewhat steady (11–12% increase) for the varying WVO fractions in the blend. However, for the K-WVO blends, HC emission showed an increasing trend with the increment in WVO fraction. A probable reason would be higher volatility of kerosene and over-leaning effect at the power stroke which resulted in accumulation of fuel particles at the far corners of the engine cylinder. These fuel particles avoid complete combustion and are emitted as unburnt HC in the subsequent exhaust stroke [20]. However, an HC reduction of 5.3–19.3% was achieved with K-WVO blends when compared to diesel fuel. A reduction in the emissions for kerosene-biodiesel as opposed to diesel-biodiesel blend is reported in the literature [19].

Higher NO_x emission takes place at high engine load conditions. It is known that NO_x formation takes place at an elevated engine temperature and pressure, which occurs only at higher engine loads [18]. Figure 4c presents the brake specific NO_x emission at the highest engine load condition. It can be observed that for both D-WVO and K-WVO blends, the NO_x emission amplified with a rise in the portion of WVO. A significant increment in the fuel-bound oxygen is the probable reason behind this trend. At higher in-cylinder temperatures, enhanced oxidation of air-bound nitrogen takes place resulting in elevated NO_x emissions [7, 24]. As a result, higher WVO fractions caused more elevated NO_x emission. Only K-WVO_0.20 blend showed NO_x emission somewhat comparable to neat diesel. The D-WVO_0.50 and K-WVO_0.50 blends have caused 9.1–11.6% rise in NO_x emission relative to diesel. Similar trend was reported elsewhere [10, 18].

3.4 Economic Aspects of Utilizing WVO Blends

Since WVO is essentially a waste, its addition in fossil fuels should reduce the overall fuel cost [11]. A recent article has concluded that WVO-diesel blends are way cheaper than biodiesel-diesel blends [8]. A lower price of unmodified WVO makes it a promising alternative fuel fraction. Such an economic comparison between the diesel and kerosene blends of WVO should be an integral part of the study. The costs of various WVO blends were calculated from the fuel prices presented in the recent literature [10, 18]. The cost of different WVO blends is presented in Table 3. In order to identify the most economic WVO blend, such an economic analysis is pertinent. Blending 0.50 fraction of WVO with the fossil fuels, substantial reduction in the overall fuel cost can be achieved. Among the fossil fuels, a 61% reduction in overall fuel cost was recorded for K-WVO_0.50 blend, as opposed to 39% for D-WVO_0.50 blend. Lower cost of kerosene has made the K-WVO blends more economical than their respective diesel counterparts. The kerosene blends are recorded to lower the overall fuel cost by 22–40% when compared to the diesel blends containing similar fractions of WVO. Thus, WVO when blended in kerosene at equal proportions has the

Table 3 Economic comparison of various WVO blends against diesel

Fuel fraction in blend	Cost of diesel blends	Cost of kerosene blends	% reduction in cost for diesel blends	% reduction in cost for kerosene blends
WVO_0.00	$ 0.89	$ 0.49	–	–
WVO_0.20	$ 0.75	$ 0.44	10.77%	50.88%
WVO_0.35	$ 0.65	$ 0.39	27.23%	55.95%
WVO_0.50	$ 0.54	$ 0.35	38.94%	61.03%

Note Prices of various fuels were obtained from [10, 18]

potential to provide an economic equivalent of the diesel fuel with a great possibility in various industrial sectors.

4   Conclusions

A common and abundant liquid waste was valorized as alternate fuel fraction in this study. The effect of blending WVO with diesel and kerosene was investigated in this study. Three blends comprising of 0.20, 0.35, and 0.50 fraction WVO were separately formulated with diesel and kerosene. The fuel properties of such blends were determined and were found to be within the standards for diesel, except for the viscosity of D-WVO_0.50 blend. With replacement in diesel with kerosene, the WVO blends demonstrated fuel properties close to hose for diesel. K-WVO_0.20 blend showed better engine performance, with a reduced BSFC and elevated BTE relative to diesel. Lower density and viscosity and higher calorific value and superior volatility of kerosene should be the probable reason. K-WVO blends resulted in lower CO and HC emissions than diesel. However, with the addition of WVO in the blend, a rise in the NO_x emission was observed. Only K-WVO_0.20 blend recorded NO_x emission similar to diesel. Blending WVO with fossil fuels reduced the overall price. K-WVO blends can cause 22–40% reduction in overall fuel cost, relative to similar diesel counterparts.

References

1. Huang H, Teng W, Liu Q, Zhou C, Wang Q, Wang X (2016) Combustion, performance and emission characteristics of a diesel engine under low-temperature combustion of pine oil–diesel blends. Energ Conver Manag 128:317–326

2. Petroleum Planning and Analysis Cell (2018) Ministry of petroleum and natural gas, Government of India data. Accessed 20 August 2018. http://ppac.org.in/View_All_Reports.aspx.

3. D'Alessandro B, Bidini G, Zampilli M, Laranci P, Bartocci P, Fantozzi F (2016) Straight and waste vegetable oil in engines: review and experimental measurement of emissions, fuel consumption and injector fouling on a turbocharged commercial engine. Fuel 182:198–209

4. Dabi M, Saha UK (2019) Application potential of vegetable oils as alternative to diesel fuels in compression ignition engines: a review. J Energ Inst 92(6):1710–1726

5. Capuano D, Costa M, Di Fraia S, Massarotti N, Vanoli L (2017) Direct use of waste vegetable oil in internal combustion engines. Renew Sustain Energ Rev 69:759–770

6. Yesilyurt MK (2019) The effects of the fuel injection pressure on the performance and emission characteristics of a diesel engine fuelled with waste cooking oil biodiesel-diesel blends. Renew Energ 132:649–666

7. Dey P, Ray S, Newar A (2021) Defining a waste vegetable oil-biodiesel based diesel substitute blend fuel by response surface optimization of density and calorific value. Fuel 283:118978

8. Dey P, Ray S (2019) Valorization of waste vegetable oil (WVO) for utilization as diesel blends in CI engine–performance and emission studies. Energ Sources Part A Recov Util Environ Eff pp 1–14

9. Majhi S, Ray S (2016) A study on production of biodiesel using a novel solid oxide catalyst derived from waste. Environ Sc Pollut Res 23(10):9251–9259

10. Dey P, Ray S (2020) Comparative analysis of waste vegetable oil versus transesterified waste vegetable oil in diesel blend as alternative fuels for compression ignition engine. Clean Technol Environ Policy 22:1517–1530

11. Ravikumar J, Saravanan S (2017) Performance and emission analysis on blends of diesel, restaurant yellow grease and n-pentanol in direct-injection diesel engine. Environ Sci Pollut Res 24:5381–5390

12. Dhanasekaran R, Krishnamoorthy V, Rana D, Saravanan S, Nagendran A, Rajesh Kumar B (2017) A sustainable and eco-friendly fueling approach for direct-injection diesel engines using restaurant yellow grease and n-pentanol in blends with diesel fuel. Fuel 193:419–431

13. Senthil Kumar M, Jaikumar MA (2014) Comprehensive study on performance, emission and combustion behavior of a compression ignition engine fuelled with WCO (waste cooking oil) emulsion as fuel. J Energ Inst 87(3):263–271

14. Kalam MA, Masjuki HH, Jayed MH, Liaquat AM (2011) Emission and performance characteristics of an indirect ignition diesel engine fuelled with waste cooking oil. Energy 36(1):397–402

15. Hribernik A, Kegl B (2009) Performance and exhaust emissions of an indirect-injection (IDI) diesel engine when using waste cooking oil as fuel. Energ Fuels 23(3):1754–1758

16. Pugazhvadivu M, Jeyachandran K (2005) Investigations on the performance and exhaust emissions of a diesel engine using preheated waste frying oil as fuel. Renew Energ 30(14):2189–2202

17. Bari S, Yu CW, Lim TH (2002) Filter clogging and power loss issues while running a diesel engine with waste cooking oil. Proceed Inst Mech Eng Part D J Auto Eng 216(12):993–1001

18. Dey P, Ray S (2021) Comparative comprehensive assessment of sustainable low-cost waste vegetable-oil-based blend as a diesel substitute. Clean Technol Environ Policy

19. Aydin H, Bayindir H, İlkiliç C (2010) Emissions from an engine fueled with biodiesel-kerosene blends. Energ Sources Part A Recov Util Environ Eff 33:130–137

20. Bayindir H, Isık MZ, Aydın H (2017) Evaluation of combustion, performance and emission indicators of canola oil-kerosene blends in a power generator diesel engine. Appl Therm Eng 114:234–244

21. Dey P, Ray S (2020) Optimization of waste vegetable oil-diesel blends for engine performance: a response surface approach. Arabian J Sci Eng 45:7725–7739

22. Martin MLJ, Geo VE, Nagalingam B (2016) Effect of fuel inlet temperature on cottonseed oil-diesel mixture composition and performance in a DI diesel engine. J Energ Inst 90(4):563–573

23. Agarwal AK, Dhar A (2013) Experimental investigations of performance, emission and combustion characteristics and combustion characteristics of Karanja oil blends fueled DICI engine. Renew Energ 52:283–291
24. Prabu SS, Asokan MA, Roy R, Francis S, Sreelekh MK (2017) Performance, combustion and emission characteristics of diesel engine fueled with waste cooking oil bio-diesel or diesel blends with additives. Energy 122:638–648

Combustion, Performance and Emission Analysis of VCR Diesel Engine Using Water Emulsion in Flaxseed-Based Biodiesel Blend

S. Ganesan, J. Hemanandh, Sundarasetty Venkatesh, and Phani Kumar

Abstract Biodiesel are produced from plant derivatives and are highly potent in usage instead of diesel in diesel engines due to their low emissions which significantly reduce the environmental impacts and can use as fuel for diesel engines deprived of any alterations. The major drawback of biodiesel is associated with NO_x and smoke reduction. Emulsified fuels are known to have high potent in reducing harmful emissions into atmosphere. Nitrogen oxides (NO_x) and smoke are the major pollutants released through diesel combustion. Using water emulsions in biodiesel reduces the nitrogen oxide and smoke emissions. Span 80 is used as surfactant during emulsion to stabilise the whole blend. Nanoparticles increases the combustion rate and provides the combustion stability. Water is mixed with biodiesel in different proportions to study the emulsion stability, characteristics and performance. Water in biodiesel emulsion contains water range of about 5–15%. By literature survey and experimental analysis, we found that 5% water emulsion in biodiesel blend.

Keywords Water in biodiesel · Nitrogen oxides (NO_x) · Smoke · Nanoparticles · Surfactant

1 Introduction

Nowadays, pollution is becoming as major threat to the environment and life on the planet. This is due to release of materials and energy released into atmosphere which effects environment eventually leads to show a potent effect on human life, animal life, natural resources and eco-system [1–5]. Air pollution is recorded as major environmental threats for life. In developing countries like India more than 90% of children under 5 years age are exposed to toxic air [6, 7]. A World Health Organisation (WHO) study states that in 2016 over one lakh children in India are dead due to air pollution. Atmosphere is mainly composed of toxic gases and dust

S. Ganesan (✉) · J. Hemanandh · S. Venkatesh · P. Kumar
Department of Mechanical Engineering, Sathyabama Institute of Science and Technology, Chennai 600119, India
e-mail: gansuma@gmail.com

particles [8–11]. These are mainly produced due pollutants released by automobiles. Diesel is majorly used as a fuel for of automobiles. Diesel engines are necessary but their emissions and its impacts on environment drives us to search for an alternate fuel which can be used instead of diesel which facilitates the lower emissions and low environmental impacts [12–17].

Biodiesel is emerged as an alternate fuel for diesel due to its low emissions compared to diesel and can be manufactured easily. This reduces the urge for fossil fuels and stops the extinction of fossil fuels [18–23]. This provides fossil fuel conversation for future use. The main drawback of biodiesel is its inability to reduce the NOx and smoke. This drawback can be overcome by mixing a tiny amount of water in biodiesel. By using water emulsions in biodiesel, the peak temperature during the combustion process is reduced this is because a part of heat during combustion is utilised by water to vaporise [24–29]. This ultimately reduces the NO_x generation because the NO_x is generated at higher temperatures, addition of water decreases the peak temperature rise in cylinder. Generally, water and diesel are both immiscible liquids. Both the liquids get separated within no time. Hence, a surfactant named SPAN 80 is used for proper emulsion [30–34]. This surfactant makes the water molecules to get binded against the diesel molecules. This provides proper emulsion stability. We blended the surfactant and biodiesel blend using ultrasonic sonicator [35–38].

Here flaxseed oil extract is used for biodiesel preparation. Flaxseed oil is also known as linseed oil. Flaxseed oil consists of high amount of linoleic acid (40–60%). Various researchers have researched on reduction of exhaust emissions. When the emulsion ratio increases NO_x and smoke decreases [39]. Because the water content absorbs the heat and gets vaporised resulting in lower peak temperature in cylinder and provides enhanced mixing by micro-explosions [40–43]. Balanced water emulsified fuel creates lower BSFC compared with the non-water emulsified fuels. The best results for water emulsified fuels are found at 5% compared to all the remaining concentrations. Using nanoparticles like aluminium oxide nanoparticles are one of the most competent catalysts. When added these increases the combustion speed and combustion stability [44–48], this facilitates complete combustion. Thus, aluminium oxide nanoparticles helps in reducing the smoke emission rates.

2   Preparation of Biodiesel Blend

In this experiment, we extracted oil from flaxseed and the obtained flaxseed oil is converted into biodiesel in the presence of catalyst to form methyl esters. The obtained biofuel is mixed in diesel to form a biodiesel blend (B20) of composition 20% flaxseed biofuel + 80% diesel. This blend preparation is done in ultrasonic homogeniser. The resulting biodiesel blend properties are identified and are shown below.

Table 1 Properties of fuels

Properties	Diesel	Blend20 (B20)	5% water emulsion + B20	10% Water emulsion + B20	15% Water emulsion + B20	Method
Calorific value(MJ/kg)	42.5	39.7	38.78	37.89	37.1	ASTM D240
Density (kg/m^3)	810	842	852	869	884	ASTM D4052
Flash point (°C)	48	84	86	89	92	ASTM D93
Cetane index	46	36	47.5	48.58	44.03	ASTM D976

By comparing the biodiesel blend and diesel properties, we found that the properties of both the properties are almost similar and the flaxseed biodiesel can be used as an alternate fuel for diesel engines.

The resultant biodiesel blend water is added in different proportions with 3% surfactant (SPAN 80) to provide a homogeneous mixture. The water composition is varied from 5%, 10%, 15%, whereas the span 80 remains constant at 3% for all the three samples (Table 1). 25 ppm of aluminium oxide nanoparticles are added to each sample. The aluminium oxide acts as catalyst and provides combustion stability. NO_x and smoke emissions are scaled down by using water emulsions in fuels. After preparation of various samples, the properties of each sample are then identified.

3 Experimental Setup

The variable compression ratio (VCR) is a four-stroke diesel engine consists of single cylinder (Fig. 1). To this engine, an eddy current type dynamometer is connected to facilitate the electric start motion. We can change the compression ratio even without stopping the engine this is because of specially designed tilting chamber block arrangement. The engine specifications are listed in Table 2.

4 Results and Discussion

Various tests were conducted to evaluate the Engine characteristics at different flaxseed biodiesel blends. Fuel samples such as diesel and bio diesel were fuelled in different proportions in a VCR diesel engine. CO, CO_2, O_2, NO_X and HC emissions were measured as the loads varied. Samples of bio diesel were compared and analysed.

Fig. 1 VCR engine setup

Table 2 Engine specifications

Make	Kirloskar, 4 stroke
Rated power	3.5 kW with 1500 rpm
Bore diameter (D)	87.5 mm
Stroke (L)	110 mm
Compression ratio	17.5:1
Injection timing	17° BTDC

4.1 Specific Fuel Consumption

Figure 2 shows the comparison between the specific fuel consumption (SFC) and brake power (BP) of various blends of biodiesel and pure diesel. From the graph, we noticed that pure diesel has the low SFC compared to all the blends. The SFC for the for the flaxseed biodiesel blend (B20) is higher than diesel. SFC is of an engine is going on increase with increase in water content of the biodiesel blend. Flaxseed biodiesel blend with 15% water shows the highest SFC compared to all the blends [49–52].

4.2 Brake Thermal Efficiency

Figure 3 shows the graph comparison of brake thermal efficiency (BTHE) with BP. At beginning, the BTHE for all the sample blends remains similar as the load increases, the BTHE varies differently for different blends. Here pure diesel has the highest BTHE compared to all the blends. BTHE is reduced gradually upon the increase of
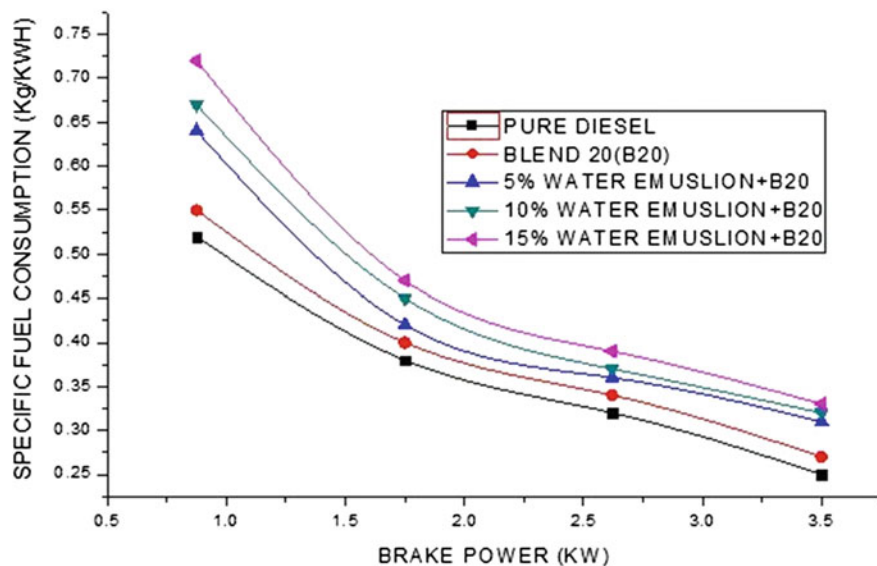
Fig. 2 BP versus SFC
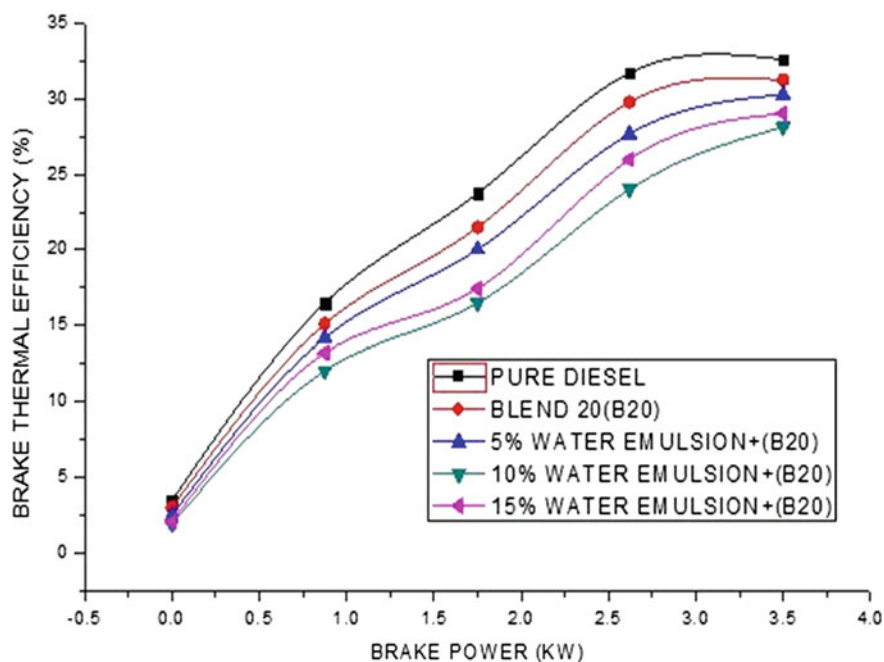
Fig. 3 BP versus BTHE

water content in biodiesel blend. 10% water emulsified biodiesel blend shows the least BTHE performance. This lowering of BTHE than pure diesel is because of heat utilisation of water content present in biodiesel blends. Due to water, a part of heat is lost for vaporisation. In general, brake thermal efficiency refers to the ratio of heat input to heat produced by the fuel during combustion [53–55]. Due to this loss of heat nearly 19% of heat is lower than pure diesel for 5% water emulsified biodiesel blend.

4.3 Nitrogen Oxide (NOx)

Figure 4 shows the comparison graphs for nitrogen oxide (NO_x) and BP for all the different concentrations of water emulsions in flaxseed biodiesel blend, flaxseed biodiesel blend (B20), pure diesel. From the above graph, it is absorbed that the NO_x emission is reduced as the water content in the blend gets increases. The flaxseed biodiesel blend (B20) shows an increase in NO_x production than the pure diesel while adding water to the same flaxseed biodiesel blend (B20) shows a drastic difference in reducing the NO_x production. Here 15% water emulsified biodiesel B20 shows least NO_x production compared to all the blends shown above. There is an effective reduction of 27% NO_x (ppm) with 15% water emulsified biodiesel blend than
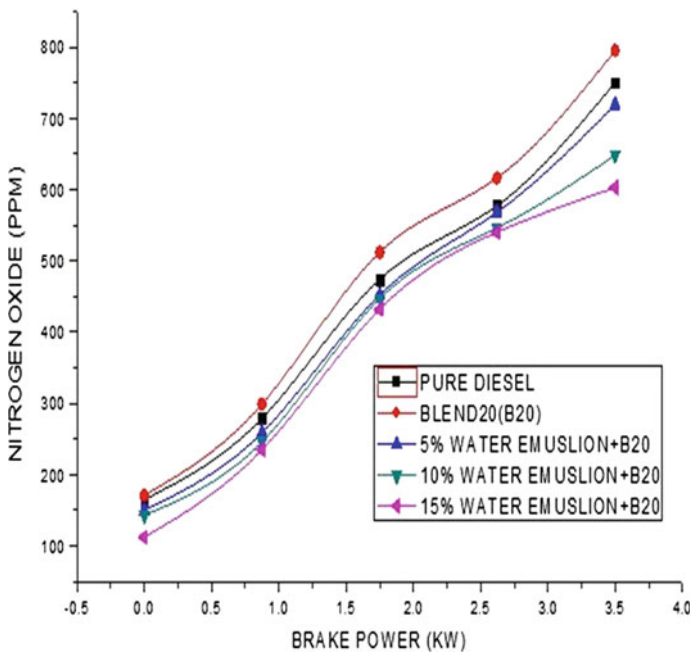
Fig. 4 BP with NO_x emission

pure diesel [56, 57]. This effective reduction is because of water content present in biodiesel blend and aluminium oxide nanoparticles because water content helps in reducing the peak temperature rise and aluminium nanoparticles acts as catalyst and facilitates smooth and fine combustion.

4.4 Hydrocarbon

Figure 5 shows a graphical comparison between hydrocarbon (HC) and BP with the blends of biodiesel. Here pure diesel has the least HC emission compared to all the blends. The blends other than diesel shows a drastic increase in HC emissions compared to pure diesel emissions [58–60]. The above graph clearly shows that with addition of water the HC emission percentage gets increased and has a maximum HC emission at 15% water emulsion + B20 in the above graph, 5% water emulsion in flaxseed biodiesel (B20) shows a minimum HC emission among all the biodiesel blends.
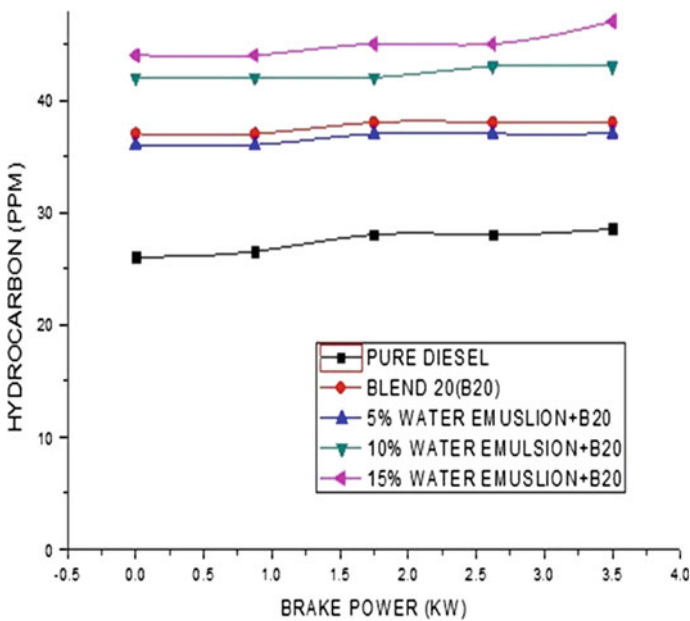
Fig. 5 BP with HC emission
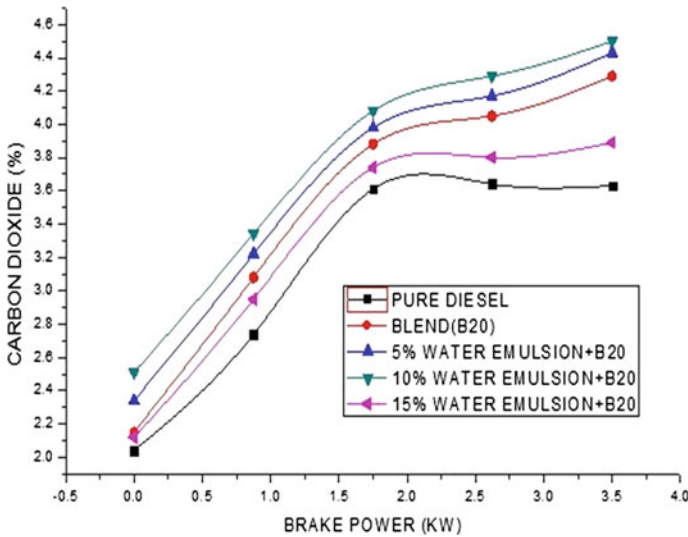
Fig. 6 BP with CO_2 emission

4.5 Carbon Dioxide

Figure 6 shows the graphical comparison with carbon dioxide (CO_2) emission and BP for various blends of biodiesel and pure diesel. From the above graph, it is clearly stated that with addition of water content the CO_2 emission is increased because of micro-explosion phenomenon of water molecules which facilitate the more homogeneous mixing of fuel and air and facilitate the smooth and complete combustion process. Nanoparticles also show major factor influencing the CO_2 emission because of its ability to perform smooth and faster combustion rates. Here 10% water emulsified flaxseed biodiesel blend shows a higher CO_2 emission compared to all the blends above while pure diesel shows a least CO_2 emission. This increase in CO_2 emission is nearly 30% higher than the pure diesel. But gets decreased upon addition of more water because of lowering the temperature during the combustion. So optimum usage of water should be used for increasing smooth combustion [61, 62].

4.6 Smoke Opacity

Water emulsified fuels show the continuous reduction in Fig. 7 and show the variation of brake power with smoke. Pure diesel emissions of smoke are less than blended biodiesel (B20). Increase the water micro-emulsion in blended biodiesel the smoke emission is decreased gradually. We can conclude that 5, 10, 20% composition water emulsion with biodiesel blend is lesser than the pure diesel and blend 20 (b20). But
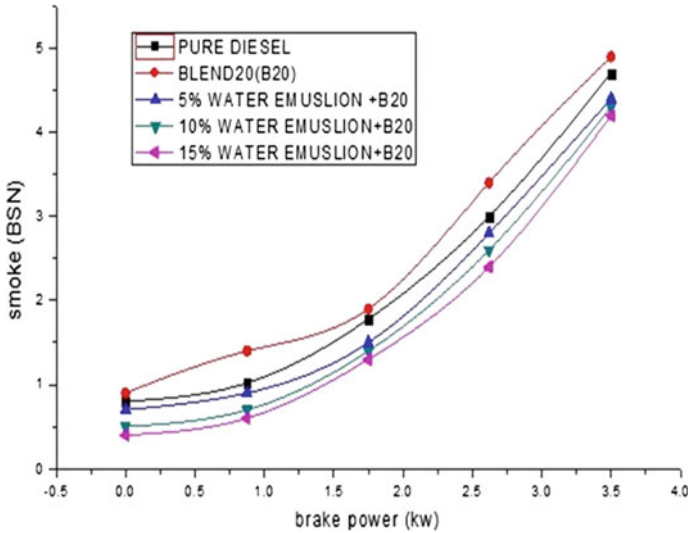
Fig. 7 BP versus smoke opacity

blend 20 is increase smoke emission then pure diesel. This reduction smoke is nearly 10, 13 and 15% by using 5, 10 and 15% water emulsions with blend (B20). The aluminium nanoparticles help in smooth and complete combustion of the resultant blend.

5   Combustion Analysis

5.1   Crank Angle Versus Pressure

Figure 8 describes various peak pressure rise of various samples with respect to crank angle. Here 5%, 10%, 15% water emulsified fuels are taken and are tested for their peak pressure rise. Here blend 20 shows a higher peak pressure than any other sample at full load. It shows nearly 15% pressure rise than any other sample. On the other hand, 15% water emulsified fuel shows a higher peak pressure than other samples it shows nearly 10% higher than other water emulsions with biodiesel blend. The pressure rise of diesel is higher than other samples.
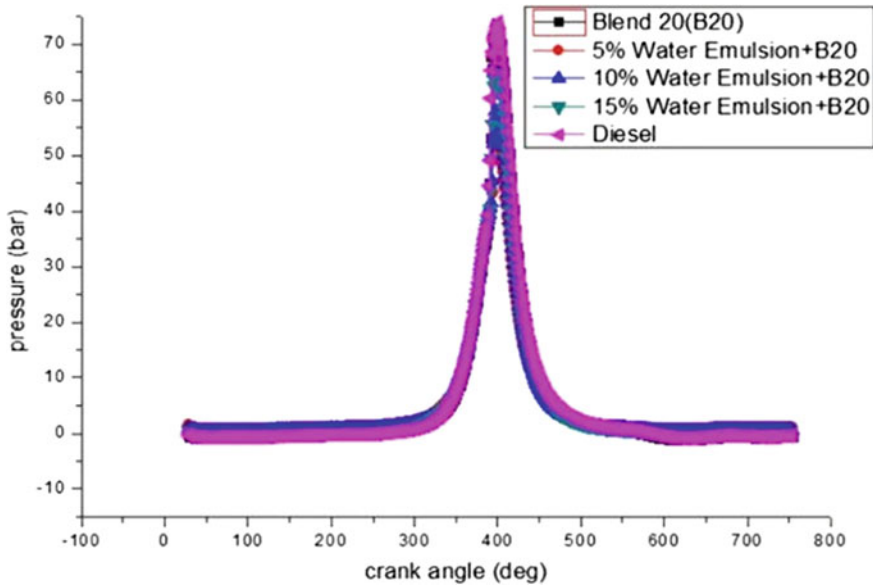
Fig. 8 Crank angle versus pressure

5.2 Net Heat Release

Figure 9 describes the net heat release of various samples with respect crank angle. Here various samples with different water emulsified biodiesel blends are taken and are tested for determining the net heat release of each sample. In above graph, blend 20 shows a maximum heat release than other samples. It is approximately 20% more heat is released than other samples at full load. This is because the heat released during the combustion process is utilised by water molecules for its vaporisation. This results in lower net heat release of water emulsified biodiesel blends. This lower net peak heat rise results in lowering the NO_x emissions because NO_x is generally produced at higher temperatures. So by using water emulsified fuels the NO_x production is reduced to a greater extent. Here the net heat release of blend 20 is higher than any samples, and it is nearly 50% more than the pure diesel.

6 Conclusion

By using water emulsions in flaxseed biodiesel, we obtained the emission and performance results through VCR single cylinder engine and AVL smoke meter for various compositions of water emulsions (5, 10 and 15%) in flaxseed-based biodiesel blend.
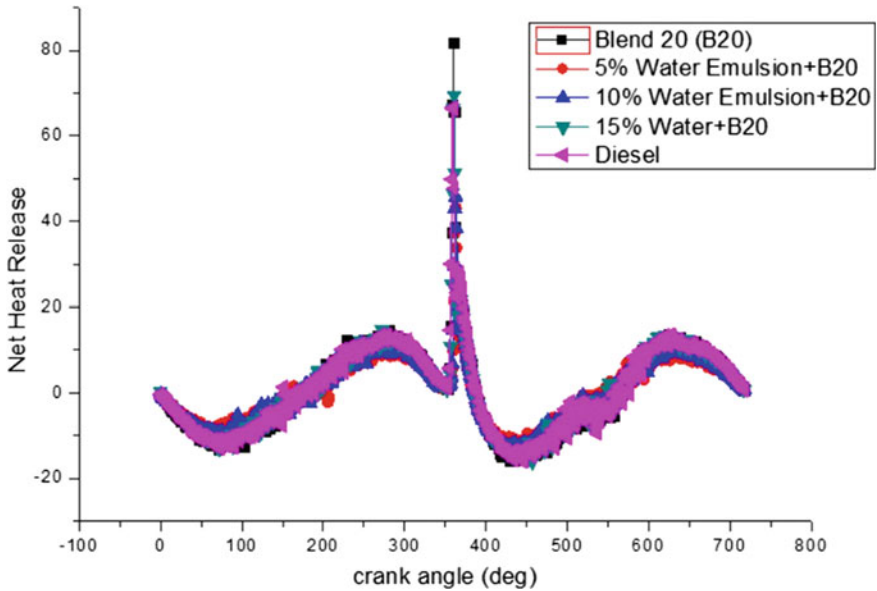
Fig. 9 Crank angle versus net heat release

1. Water emulsions cut down the peak temperature rise while combustion because, a part of heat is consumed by the water molecules for vaporisation. Generally, NO_x gases are produced at very higher temperatures. So, the NO_x generation is reduced.
2. Aluminium oxide nanoparticles are one of the most competent catalysts. When added these increases the combustion speed and combustion stability. This facilitates complete combustion. Thus, aluminium oxide helps in reducing the smoke emission rates.
3. From the results, we can say that 5% water emulsion in flaxseed biodiesel blend shows a better reduction in NO_x and smoke emissions.
4. Water emulsion in biodiesel results in reduction of smoke. This is because upon addition of water, during combustion micro-explosions takes place. Due to micro-explosions, the complete mixing of air fuel mixture takes place.

References

1. Eng. Dan, Dunarea de Jos of Galati Diesel-water emulsion, an alternative fuel to reduce diesel emissions. A review, Romania Machines, Technologies, ISSN 1313–0226. ISSUE 7/2013
2. Javier M (1996) Ballester, Norberto Fueyo and C6sar Dopazo combustion characteristics of heavy oil-water emulsions. Fuel 75(6):695–705

3. Rathinam S, Sajin JB, Subbiah G, Rajeev A, Prakash S, Christopherselvam D (2020) Assessment of the emission characteristics of the diesel engine with nano-particle in neem biodiesel 2019. Energ Sources Part A: Recovery Utilization Environ Eff 42(21):2623–2631

4. Sujesh G, Ganesan S, Ramesh S (2020) Effect of CeO2 nano powder as additive in WME-TPO blend to control toxic emissions from a light-duty diesel engine—an experimental study. Fuel 278:118177

5. Hemanandh J, Ganesan S, Devaraj R, Venkatesan SP, Ramprakash G (2020) Robust design approach for intake manifold of the 1 litre turbo charger intercooler diesel engines. Int J Ambient Energ 41(11):1214–1226

6. Padmanabhan S, Vinod Kumar T, Chandrasekaran M, Ganesan S (2020) Investigation of Sapindus seed biodiesel with nano additive on single cylinder diesel engine. Int J Ambient Energ 41(10):1106–1109

7. Rangabashiam D, Rathinam S, Subbiah G, Jb S, Sb S (2019) Emission behaviour studies on the cause of ZnO nanoparticle inclusion in neat biodiesel. Energ Sources Part A: Recovery Utilization Environ Effects 42(16):1989–1996

8. Devarajan Y, Munuswamy D, Nagappan B, Ganesan S (2020) Detailed study on the effect of different ignition enhancers in the binary blends of diesel/biodiesel as a possible substitute for unaltered compression ignition engine. Petroleum Sci 17(4):1151–1158

9. Sidheshware RK, Ganesan S, Bhojwani VK (2020) Experimental analysis of magnetic field effects on compressor energy saving cooling system. In: 2020 E3S web of conferences, p 170. https://doi.org/10.1051/conf/202017001020

10. Devarajan Y, Beemkumar N, Ganesan S, Arunkumar T (2020) An experimental study on the influence of an oxygenated additive in diesel engine fuelled with neat papaya seed biodiesel/diesel blends. Fuel 268

11. Rajasekar R, Ganesan S, Marynishanthi W (2020) Performance and emission characteristics of biodiesel derived from coconut acid oil 2018. Int J Ambient Energ 41(6):627–630

12. Venkatesan SP, Ganesan S, Devaraj R, Hemanandh J (2020) Design and analysis of exhaust manifold of the spark ignition engine for emission reduction. Int J Ambient Energy 41(6):659–664

13. Ganesan S, Padmanabhan S, Mahalingam S, Shanjeevi C (2020) Environmental impact of VCR diesel engine characteristics using blends of cottonseed oil with nano additives 2019. Energ Sources Part A: Recovery Utilization Environ Effects 42(6):761–772

14. Mahalingam S, Ganesan S (2020) Effect of nano-fuel additive on performance and emission characteristics of the diesel engine using biodiesel blends with diesel fuel. Int J Ambient Energ 41(3):316–321

15. Ganesan S, Mahalingam S, Raj RA, Rajesh S (2020) Effects of nano additives on performance and emission characteristics of Mentha longifolia biodiesel. Int J Ambient Energ 41(3):322–325

16. Ganesan S, Senthil Kumar J, Hemanandh J (2020) Optimisation of CI engine parameter using blends of biodiesel by the Taguchi method. Int J Ambient Energ 41(2):205–208

17. Ganesan S, Sridhar Raja KS, Senthil Kumar J (2020) Effects of MgO as an additive in canola oil–an experimental study. Int J Ambient Energ 41(1):1–4

18. Rajasekar R, Ganesan S, Logesh U, Prraveen NS, Javed M Effects of antioxidant additives on biodiesel/diesel performance and emission characteristics of ci engine. Indian J Environ Protect 40(3): 235–242

19. Rangabashiam D, Narayanaperumal KB, Subbiah G, Arumugam R (2020) Experimental study on utilizing peel oil, diesel and ignition-enhancer blends as fuel for diesel engine. Energy Sources Part A: Recovery Utilization Environ Effects. https://doi.org/10.1080/15567036.2020.1808743

20. Hemanandh J, Ganesan S, Puneeth C, Manikankata Tejesh G (2020) Vehicle emission analysis by using refined sunflower oil as alternate fuel and varying the injection timing in diesel engine. Int J Veh Struct Syst 12(1):65–69

21. Sidheshware RK, Ganesan S, Bhojwani V (2020) Enhancement of internal combustion engine efficiency by magnetizing fuel in flow line for better charge combustion. Heat Transf Res 21(5):419–431

22. Venkatesan SP, Ganesan S, Prabhahar JJ, Kaveti VR, Anoop A, Andrew A (2020) Performance and emission test on diesel engine using Prosopis juliflora seed oil. Int J Ambient Energ, pp 1–4. https://doi.org/10.1080/01430750.2020.1719887
23. Sujesh G, Ganesan S, Ramesh S (2020) Effect of compression ratio on the performance, combustion and emission of a single cylinder diesel engine using multi blended second generation biofuel. Int J Mech Prod Eng Res Dev 10(1):133–144
24. Hemanandh J, Ganesan S, Fiaz AS, Gunasekar P (2020) Investigation of Papaya seed methyl ester blended diesel for emission reduction in direct injection engines. Int J Vehicl Struct Syst 11(4):366–368
25. Devarajan Y, Munuswamy D, Nagappan B, Subbiah G (2019) Experimental assessment of performance and exhaust emission characters of a diesel engine fuelled with Punnai biodiesel/butanol fuel blends. Petrol Sci 16(6):1471–1478
26. Selvaraj M, Subbiah G (2019) The influence of injection parameters on the performance and emission characteristics of a DI diesel engine using biofuel-blended-pure diesel fuel. Int J Ambient Energ 40(8):800–803
27. Ganesan S, Rajasekar R (2019) Impact of dodecenyl succinic anhydride on performance and emission analysis of canola oil in direct injection variable compression ratio diesel engine. Indian J Environ Prot 39(11):985–988
28. Senthil Kumar J, Ganesan S, Sivasaravanan S (2019) Impact of nano additive on engine characteristics using blends of thyme oil with diesel. Int J Ambient Energ 40(7):768–774
29. Ganesan S, Hemanandh J, Sriharsh M, Anish M Experimental investigation on Di diesel engine with blends of black jamun seed oil using taguchi based optimization. In: AIP conference proceedings. vol 2161
30. Rangabashiam D, Logesh K, Yashvanth U, Ganesan S, Christopher Selvam D (2019) Detailed study on the effect of nano-particle size on emission characteristics of diesel engine. Petrol Sci Technol 37(18):2018–2024
31. Rathinam S, Sajin JB, Ganesan S, Yuvarajan D (2019) Performance and emission study on the effect of oxygenated additive in neat biodiesel fueled diesel engine. Energ Sources Part A: Recovery Utilization Environ Effects 41(16):2017–2027
32. Senthil Kumar J, Ramesh Bapu BR, Ganesan S, Krishnan L (2019) Evaluation of performance and emission behaviour of DI diesel engine powered by biofuel. Int J Ambient Energ 40(6):566–570
33. Rathinam S, Balan KN, Subbiah G, Sajin JB, Devarajan Y Emission study of a diesel engine fueled with higher alcohol-biodiesel blended fuels. Int J Green Energ 16(9):667–673
34. Sridhar Raja KS, Ganesan S, Senthil Kumar J (2019) Performance and emission characteristics of biodiesel from black pepper oil. Int J Ambient Energ 40(5):463–466
35. Senthil Kumar J, Ganesan S, Raja KSS (2019) Experimental analysis of the effects of cerium oxide nanoparticles on a single-cylinder diesel engine using biofuel blended with diesel as fuel. Int J Ambient Energ 40(5):490–493
36. Devarajan Y, Nagappan B, Subbiah G (2019) A comprehensive study on emission and performance characteristics of a diesel engine fueled with nanoparticle-blended biodiesel. Environ Sci Pollut Res 26(11):10662–10672
37. Mahalingam S, Ganesan S, Krishna GS, Perumalsamy V (2019) To study use of rubber seed oil blends diesel fuel at various injection pressures. Indian J Environ Prot 39(3):233–238
38. Rajasekar R, Ganesan S, Kumar MS (2019) Noise and emission characteristics of biodiesel used in multi-cylinder diesel engine. Indian J Environ Prot 39(10):924–927
39. Mathalai Sundaram C, Balam KN, Arunkumar T, Ganesan S, Rameshbabu A Emission study on the outcome of DMC on neem biodiesel ignited diesel engine. Part A: Recovery Utilization Environ Effects. https://doi.org/10.1080/15567036.2019.1691683
40. Rangabashiam D, Jayaprakash V, Ganesan S, Christopher D (2019) Investigation on the performance, emission and combustion pattern of research diesel engine fueled with higher alcohol and pongamia biodiesel blends. Energ Sources Part A: Recovery Utilization Environ Effects. https://doi.org/10.1080/15567036.2019.1670760

41. Rangabashiam D, Jayaprakash V, Ganesan S, Nagaraj M, Rameshbabu A (2019) Emission, performance, and combustion study on nanoparticle-biodiesel fueled diesel engine. Energy Sources Part A: Recovery Utilization Environ Effects. https://doi.org/10.1080/15567036.2019.1677

42. Ganesan S, Padmanabhan S, Hemanandh J, Venkatesan SP Influence of substrate temperature on coated engine piston head using multi-response optimization techniques. Int J Ambient Energ. https://doi.org/10.1080/01430750.2019.1653988

43. Sidheshware RK, Ganesan S, Bhojwani V Experimental investigation on the viscosity and specific volume of gasoline fuel under the magnetisation process. Int J Ambient Energ. https://doi.org/10.1080/01430750.2019.1653987

44. Rajasekar R, Ganesan S (2018) Experimental analysis of engine performance and emission characteristics using biodiesel obtained from winter green oil. Indian J Environ Protect 38(12):998–1003

45. Mahalingam S, Ganesan S, Krishna GS, Perumalsamy V (2018) Comparative analysis of performance and emission characteristics of thermal barrier coated diesel engine using biodiesel fueled with diesel fuel. Indian J Environ Prot 38(10):848–852

46. Padmanabhan S, Pradeep B (2018) Influence of cerium oxide additive and aloe vera biodiesel on a CI engine. Int J Ambient Energ 39(5):516–520

47. Ganesan S, Karthikayan S, Krishna GS, Reddy GVR (2018) Investigation on performance and emission characteristics of diesel engine with the blends of rosemary oil with magnesium oxide. ARPN J Eng Appl Sci 13(1):386–390

48. Padmanabhan S, Rajasekar S, Ganesan S, Saravanan S, Chandrasekaran M (2017) Performance and emission analysis on ci engine using soapnut oil as biofuel. ARPN J Eng Appl Sci 12(8):2491–2495

49. Padmanabhan S, Chandrasekaran M, Ganesan S, Khan Patan MN, Navakanth P (2017) Optimal solution for an engineering applications using modified artificial immune system, iop conference series: materials science and engineering. 183(1)

50. Karthikayan S, Ganesan S, Vasanthakumar P, Sankaranarayanan G, Dinakar M (2017) Innovative research trends in the application of thermal barrier metal coating in internal combustion engines. Mater Today: Proc 4(8):9004–9012

51. Senthil Kumar J, Ganesan S, Sivasaravanan S, Padmanabhan S, Krishnan L, Aniruthan VC (2017) Effects of nano additives in engine emission characteristics using blends of lemon balm oil with diesel. In: IOP conference series: materials science and engineering 197(1)

52. Ganesan S, Padmanabhan S, Senthil Kumar J, Polina N, Kumar SK (2017) Influence of MgO on performance and emissions of di engine using blends of castor oil. In: 2017 IOP conference series: materials science and engineering 197(1)

53. Padmanabhan S, Ganesan S, Jeswin Arputhabalan J, Chithrala V, Ganesh Bairavan P (2017) Performance test on compression ignition engine by blending ethanol and waste plastic pyrolysis oil with cetane additive. In: IOP conference series: materials science and engineering 197(1)

54. Sundararajan K, Ganesan S, Gomathinayakam S (2016) Emission estimation of neat paradise tree oil combustion assisted with superheated hydrogen in a 4-stroke natural aspirated DICI engine. Thermal Sci 20:S1137–S1144

55. Ganesan S, Elango A (2015) Analysis of emission characteristics on direct injection engine using biodiesel with MgO. Int J Appl Eng Res 10(9):13704–13713

56. Ganesan S, Elango A, Krishna EV, Balaji A (2013) Influence of nano catalyst on emission characteristics of di diesel engine with blends of lemon grass oil using taguchi approach. Int J Appl Eng Res 9(21):9941–9949

57. Ganesa S, Elango A (2013) Influence of nano catalyst in the performance of direct injection CI engine using blends of castor oil, ICANMEET, pp 723–725

58. Padmanabhan S, Ganesan S, Chandrasekaran M, Srinivasa Raman V (2010) Gear pair design optimization by genetic algorithm and FEA. In: Proceedings of the international conference on frontiers in automobile and mechanical engineering, pp 301–307

59. Ganesan S, Padmanabhan S, Vihaari V, Krishna Kumar S, Yamini P (2017) Influence of MgO on emissions of DI engine using blends of biodiesel. ARPN J Eng Appl Sci 12(6):1792–1795
60. Mangesh VL, Padmanabhan S, Ganesan S, Prabhudevrahul D, Kumar Reddy TD (2017) Prospects of pyrolysis oil from plastic waste as fuel for diesel engines: a review. In IOP conference series: materials science and engineering 197(1)
61. Dhanasekaran R, Ganesan S, Rajesh Kumar B, Saravanan S (2019) Utilization of waste cooking oil in a light-duty DI diesel engine for cleaner emissions using bio-derived propanol. Fuel 235:832–837
62. Badran O, Emeish S, Abu-Zaid M, Abu-Rahma T, Al-Hasan M, Al-Ragheb M (2011) Impact of emulsified water/diesel mixture on engine performance and environment. Int J Thermal Environ Eng 3(1):1–7

Analysis of Cyclic Variations and Combustion Behavior of Liquid Phase Hydrocarbons Under Uniform Axial and Radial Magnetic Fields

Libin P. Oommen and G. N. Kumar

Abstract The present study experimentally investigates the combustion characteristics of a multi-cylinder MPFI spark ignition engine fuelled by gasoline under uniform magnetic fields. Permanent magnets made of N38 grade NdFeB are used to magnetize the liquid phase hydrocarbons and the impact produced on combustion characteristics like in-cylinder pressure and net heat release rate are studied under different speeds and load conditions of the engine operation. Three different magnetic intensities (3200 G, 4800 G, and 6400 G) are employed in two different magnetization patterns (axial and radial) at an inbuilt ignition timing of 5 deg bTDC. Magnetic field assisted combustion is observed to enhance the performance characteristics of the engine, while simultaneously reducing the exhaust emissions to a significant level. A statistical analysis of cyclic fluctuations in magnetic field-assisted combustion is also made which shows a reduction in fluctuations (COV) with the application of each stage of ionization. The increase observed in peak pressures and heat release rates along throughout the combustion cycles with reduction in cyclic variations indicate that magnetic field-assisted combustion exhibits better combustion characteristics as compared to normal gasoline combustion.

Keywords Combustion · Cyclic variation · Magnetic field · Peak pressure · Heat release rate · Coefficient of variation

L. P. Oommen (✉)
Department of Mechanical Engineering, Providence College of Engineering, Chengannur, India
e-mail: libinpanavelil@gmail.com

G. N. Kumar
Department of Mechanical Engineering, National Institute of Technology Karnataka, Surathkal, India

Nomenclature

COV	Coefficient of Variation
G	Gauss
IMEP	Indicated Mean Effective Pressure
NHRR	Net Heat Release rate
P	Pressure ($N.m^{-2}$)

Greek Letters

θ	Crank angle location
μ	Mean of data population (Pa.s)
σ	Standard deviation of data population

Subscripts

Max	Maximum

1   Introduction

The accelerated depletion rate of conventional energy sources and the stringent regulations in exhaust emissions have made the researchers around the globe to focus on methods to enhance the combustion efficiency of the fuels. These methods include physical and chemical treatment of fuels, engine coatings, exhaust gas recirculation, catalytic reduction etc. Magnetic field-assisted combustion is an under-investigated technology of physical treatment of the fuel just before the injection into the cylinder.

Any hydrocarbon fuel is a molecule-by-molecule compound. These molecules are made up of atoms, which are made up of nuclei and electrons. These molecules form a cluster within themselves and will not actively interlock with oxygen molecules during combustion [1]. On the application of an external polarizing field, electrons are excited into states with a higher principal quantum number, resulting in the generation of a magnetic moment [2]. The induced magnetic moment alters the nuclear spin orientation and converts normal paramagnetic hydrogen molecules into the more reactive and unstable ortho state, resulting in the debilitating of Vandervaal's bonds and thus the de-clustering of the clusters formed due to intermolecular forces of attraction [2]. Subsequently, the penetration of oxidant to hydrocarbon structure is enhanced which will result in the active interlocking between fuel and oxygen molecules, ensuring complete combustion [3].

In the thermodynamic perception, fuel consumption of an engine is directly dependent on the values of combustion enthalpy. This combustion enthalpy is quantified using the bonding energy of reactants and products [4]. The polarizing field is found to alter the bonding energies of fuel molecules, thereby effecting the combustion enthalpies and subsequently reducing the consumption of fuel [5]. The applicability of magnetic polarization in increasing the energy efficiency of fishing vessels was examined by Gabina et al. [6]. Their experiments on three compression ignition engines yielded that the fuel consumption was found to decline at higher loads in-situ conditions. The impact of magnetic fields on hydrocarbon-based R600 refrigerant and non-hydrocarbon-based R134A for a vapor compression system was experimentally analyzed by Khedawan and Gaikwad [7]. Fuel economy improved and exhaust concentration decremented for hydrocarbon-based refrigerant upon polarization [8].

Gad [9, 10] experimentally studied the impact of exposure of polarizing magnetic fields on a single cylinder, four-stroke Kirloskar CI engine at full load and no load conditions. The fuel economy improved by 3 to 8.5% from no load till full load conditions. The emission of Carbon monoxide showed a reduction of 10% and 4.5% whereas oxides of nitrogen declined by 13% and 24% respectively. The influence on the combustion and emissions of a generator fuelled by diesel when a magnetic tube is incorporated in the fuel intake was examined by Chen et al. [11]. Kurji and Imran [12] installed permanent magnetic assembly before the injection pump in a single cylinder four stroke CI engine and observed a reduction of 15.71% in the consumption of fuel induced due to reduced surface tension due to applied fields.

The operating parameters of spark ignition engines are limited by cyclic variations. The flame propagation in SI engines is dependent on condition of the mixture and airflow in the region of sparking at the time of spark which directly influences cyclic variations. Aydin [13] concluded that average laminar flame velocity, intensity of turbulence, and velocity are the elements that influence cyclic fluctuations in combustion. Ceviz et al. [14] studied the impact of AFR on cyclic variations in a lean combustion system. Their results prove that an increase in air–fuel ratio will result in increased cyclic variations. Studies have proven that a surge in power harvest for the same amount of fuel consumed can reduce cyclic variations in combustion [15, 16]. From early days, combustion in an engine is studied in terms of cylinder pressure. The magnitude (P_{max}) and location of maximum pressure (θ_{pmax}) are the most commonly utilized parameters for analyzing combustion. The major downfall in the case of parameters derived directly from pressure is the insufficient knowledge of on-going cylinder processes [17]. Coefficient of Variation of IMEP is an effective parameter that indicates engine behavior because it visualizes the torque fluctuations [18]. Experimental studies on the combustion and emission characteristics of an MPFI engine fuelled by liquid phase and gas phase fuels proved that magnetic polarization is beneficial in enhancing the performance characteristics [19–23]

2   Description of Experimental Rig and Instrumentation

The experimental setup and instrumentation consists of a multi-cylinder four stroke engine of Maruthi Zen as depicted in Fig. 1. The required load to the engine is applied by an eddy current dynamometer and imperative instruments for sensing combustion pressures and corresponding crank angles are provided. The signals obtained from these instruments are interfaced to the PC using NI-based USB-6210 data acquisition system. IC Engine Soft V15.0, commercially available combustion analysis software, is employed for online combustion evaluation.

High-grade NdFeB magnets are installed on the fuel line using special fixtures to produce the required magnetization pattern. The losses in magnetic intensity during the operation are prevented through the administration of a stainless steel covering to the magnetic assembly. The cyclic variations in combustion are studied under axial and radial patterns of magnetization.

The magnetic intensity of permanent magnets is measured using a gauss meter which is named after the great scientist Carl Friederich Gauss. The modern Gauss meter is an advanced version of Gauss' magnometer. It consists of a gauss probe, the meter, and a cable for connection and works on the principle of Hall effect. To measure the magnetic intensity, the instrument is switched on and the probe which is available on the end is placed on the magnet to be measured. When the magnet is slid over the sensor, the highest rating picked up on the meter is noted which corresponds to the Gauss value of that particular magnet. Both the intensity and direction of magnetic fields can be measured using this instrument.

The instruments are calibrated before they are used in the experimental data collection. The dynamometer, load cell, exhaust gas analyzer, and the pressure transducer are calibrated by their respective suppliers. The repeatability of data is ensured when the experiment is conducted. Prior to the data acquisition, the engine is operated for some time to reach steady state operation. Experimental error is minimized by taking average value of three readings at each test points. Periodic leak checks are done for LPG fuel line and injectors to ensure safety. Fire extinguishers are provided near to
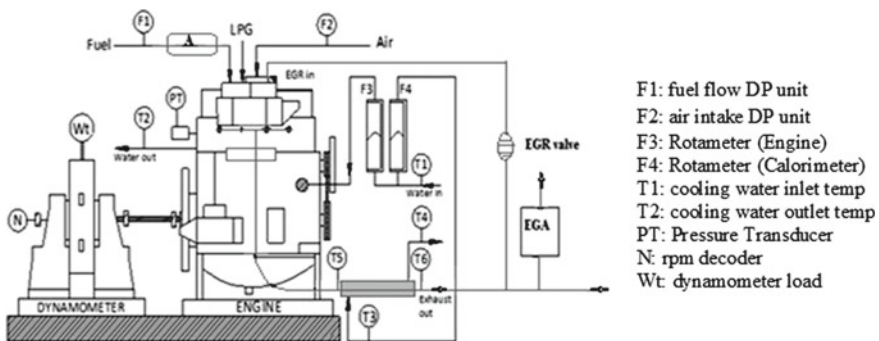
Fig. 1   Schematic representation of engine test rig and associated parts

the rig in case of any occurrence of fire. Storage devices like HDD are kept away at a safe distance from the strong magnetic field. A warning board is also hung to keep away people with pacemakers from the impact of magnetic fields.

3   Analysis of Combustion Parameters and Combustion Stability

The heat release analysis is effectuated on the basis of first law of thermodynamics with the intake and exhaust valves closed making the engine a closed system. The cylinder contents are considered to be a single zone of which the thermodynamic properties are uniform and constituted by mean values. The first law of thermodynamics as applicable to this case can be expressed as

$$\frac{dQ}{dt} - p\frac{dV}{dt} + \sum_i m_i h_i = \frac{dU}{dt}$$

where Q is the heat transferred (J), p is the pressure (Pa), V is the volume (cubic meter), mi is the mass of injected fuel, hi is the enthalpy (J/kg), and U is the internal energy (J). The only mass which is crossing the system boundary is the injected fuel and hence the mass-enthalpy term in the expression can be reframed to mass of fuel enthalpy. Using a simplified assumption that the net heat release is the difference in energy released from combustion and the energy lost to the walls through heat transfer, the above equation can be reframed to

$$\frac{dQ}{dt} = p\frac{dV}{dt} + \frac{dU}{dt}$$

If a further assumption can be made that the contents of the cylinder can be modeled as ideal gas

$$\frac{dQ}{dt} = p\frac{dV}{dt} + mc_v\frac{dT}{dt}$$

In which c_v corresponds to the specific heat at constant volume. The temperature term in this expression can be eliminated by differentiating the ideal gas law because temperature term is mostly unavailable in pressure analysis.

$$\frac{dQ_{net}}{dt} = \frac{\gamma}{\gamma - 1}p\frac{dV}{dt} + \frac{1}{\gamma - 1}V\frac{dp}{d\theta}$$

In this equation, γ corresponds to the ratio of specific heats and Q_{net} is the net heat release rate in J/deg. In a spark ignition engine the value of γ is obtained by matching single zone model analysis to a two zone model analysis for various fuels.

Heat transfer in the combustion chamber occurs by both convection and radiation in between the burning gases, cylinder walls, cylinder head, intake, and exhaust valves and piston during the working cycle. Among the two modes, convection comprises the major part. Considering the impact of heat transfer to the walls of combustion chamber, the gross heat release is expressed as

$$\frac{\mathrm{d}Q_{\mathrm{Gross}}}{\mathrm{d}\theta} = \frac{\mathrm{d}Q_{\mathrm{Net}}}{\mathrm{d}\theta} + \frac{\mathrm{d}Q_{\mathrm{ht}}}{\mathrm{d}\theta}$$

4 Results and Discussion

The combustion characteristics of an engine are best represented using in-cylinder pressure variation and net heat release rate with respect to the crank angle locations. Here, the cyclic variations in combustion are analyzed at four different speeds of the engine (3500 rpm, 3000 rpm, 2500 rpm, and 2000 rpm) and full load condition. Figures 2, 3, 4, and 5 show the average cylinder pressures in 100 consecutive cycles at four engine speeds and four stages of axial magnetization (no magnetization, 3200 G, 4800 G, and 6400 G).
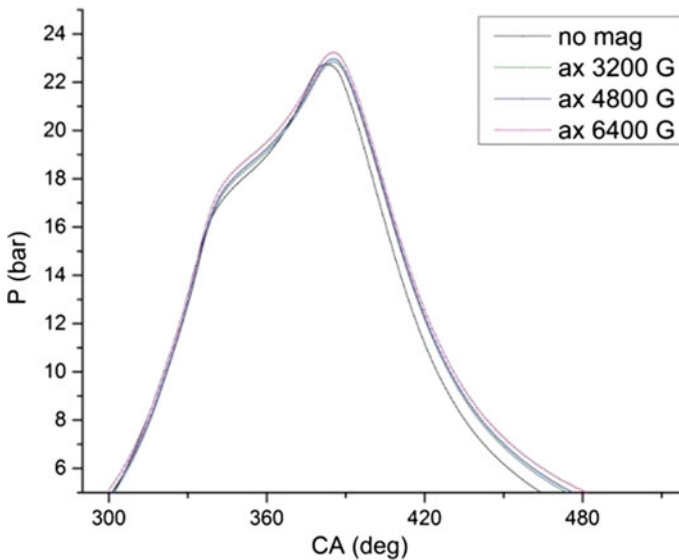
Fig. 2 In-cylinder pressure at 3500 rpm
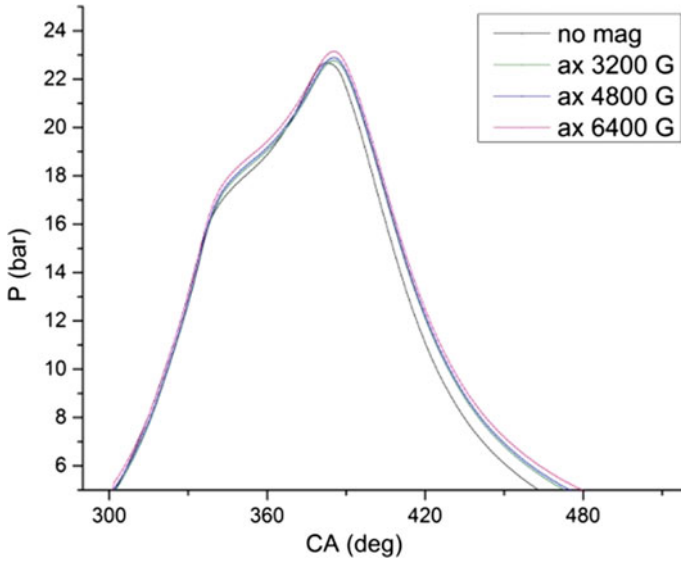
Fig. 3 In-cylinder pressure at 3000 rpm
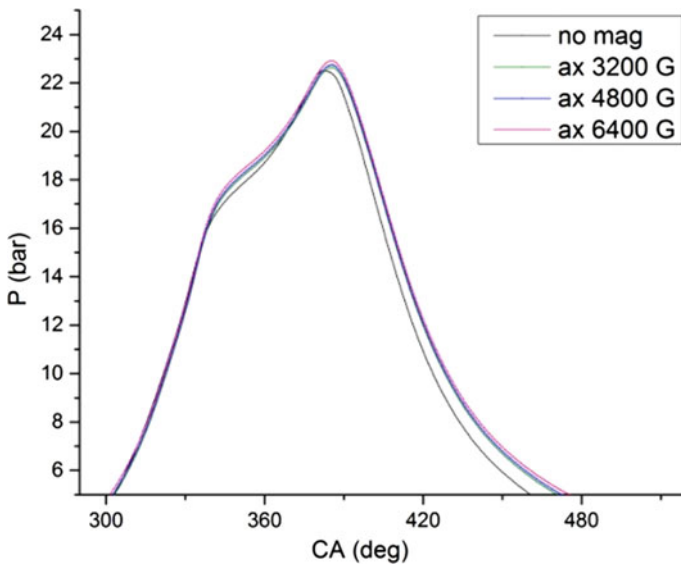
Fig. 4 In-cylinder pressure at 2500 rpm
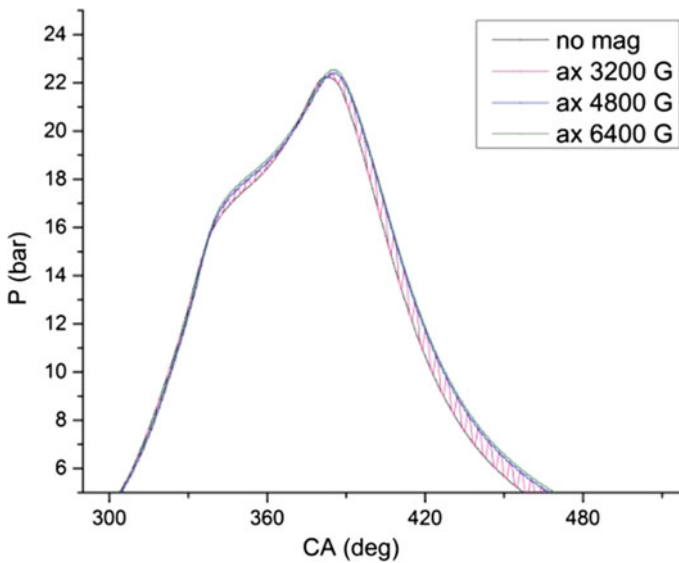
Fig. 5 In-cylinder pressure at 2000 rpm

4.1 Combustion Characteristics Under Axial Magnetization Pattern

It can be observed that there is a small variation in pressures between the magnetized and non-magnetized conditions even though the engine is operated under the same fuel and at the same speed. The peak pressure is found to increase with each stage of magnetization and is maximum at 6400 G for all the speeds. The highest value of cylinder pressure observed (P_{max}) is 23.23 bar at 3500 rpm and at 6400 G magnetic intensity, which is 2.75% higher than the case of same engine speed without magnetization. The increase in peak pressure indicates the enhancement of combustion properties with higher intensities of magnetization.

The stability of combustion is one of the most important parameters to be analyzed whenever a modification in fuel or operating parameters is experimented on an engine. The extent of lean burning and tolerance of EGR are all subjected to the stability of combustion. Although the stability of combustion could be deduced from the engine performance and emission data, a substantial and conclusive evidence of it can be made through a statistical analysis of coefficient of variation (COV) of indicated mean effective pressures and peak pressures during the working cycle (Figs. 6 and 7).

The NHRR characteristics for experimented speeds of the engine at full load operation and all the tested intensities of axial fields are shown in Figs. 8, 9, 10, and 11. The net heat release rate is an effective means to analyze the combustion phenomena critically. This parameter has the advantage of identifying combustion

Fig. 6 COV of P_{max} in axial magnetization

Fig. 7 COV of IMEP in axial magnetization

Fig. 8 NHRR at 3500 rpm in axial magnetization

Fig. 9 NHRR at 3000 rpm in axial magnetization

Fig. 10 NHRR at 2500 rpm in axial magnetization
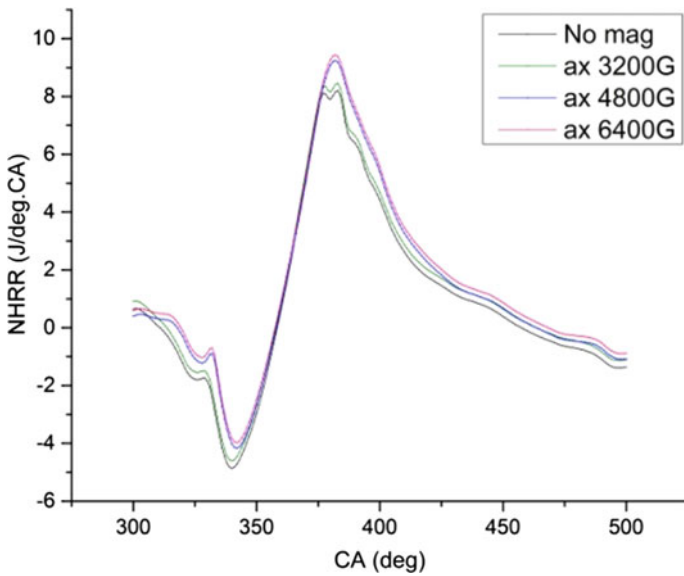
Fig. 11 NHRR at 2000 rpm in axial magnetization

indicators like ignition delay, duration of combustion, rate of heat release, and its crank angle locations.

As seen in the figures, the rate of heat release increases with increasing intensity of magnetization. Though the duration of heat release has not varied, the locations of maximum heat release vary with higher intensity of magnetization. This may be due to the fact that hydrocarbons have realigned themselves on subjected to magnetic fields, breaking the normally occurring clustered structure, thus making the combustion more efficient.

4.2 Combustion Characteristics Under Radial Magnetization Pattern

In the second stage of experimentation, the cyclic variations in combustion are analyzed under radial magnetization pattern. The engine is operated under the same load and speed conditions as in the case of axial magnetization. Figures 12, 13, 14, and 15 represent the variation in in-cylinder pressures in 100 consecutive cycles under four stages of radial magnetization.

As observed in the case of axial magnetization, the cylinder pressure increased with the increase in intensity of applied magnetic field and is maximum in the case of 6400 G. The highest magnitude of cylinder pressure observed (P_{max}) is 23.91 bars at 3500 rpm and at 6400 G magnetic intensity, which is 4.89% higher than the case
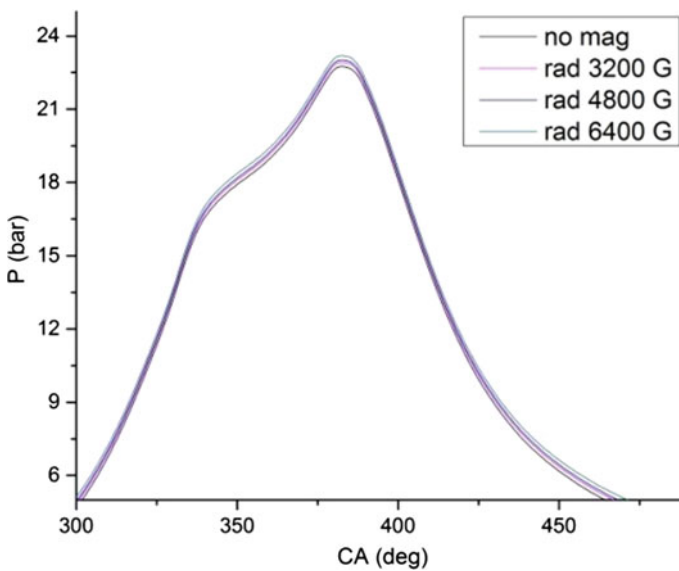
Fig. 12 In-cylinder pressures at 3500 rpm in radial magnetization
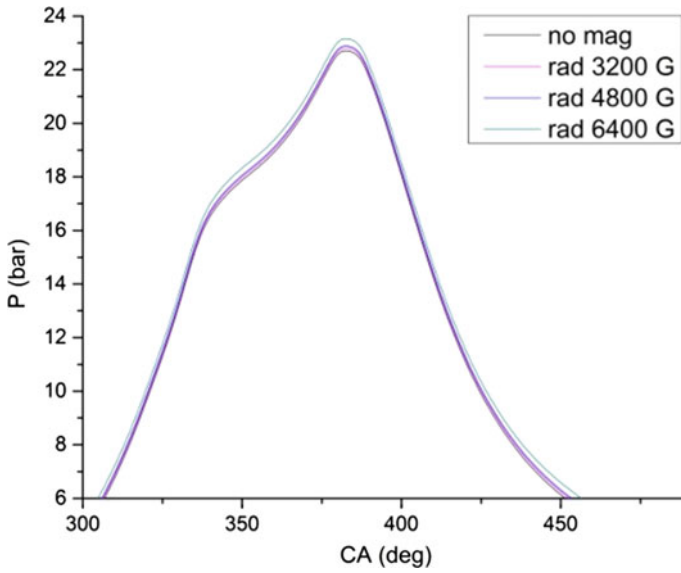
Fig. 13 In-cylinder pressures at 3000 rpm in radial magnetization
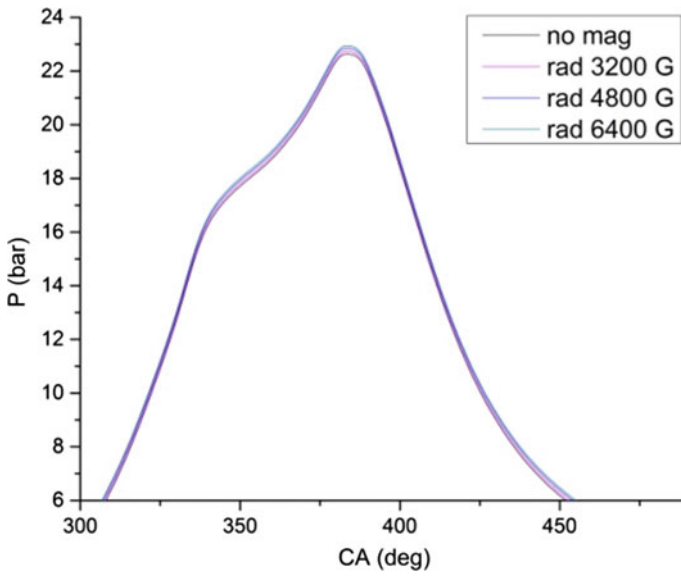
Fig. 14 In-cylinder pressures at 2500 rpm in radial magnetization
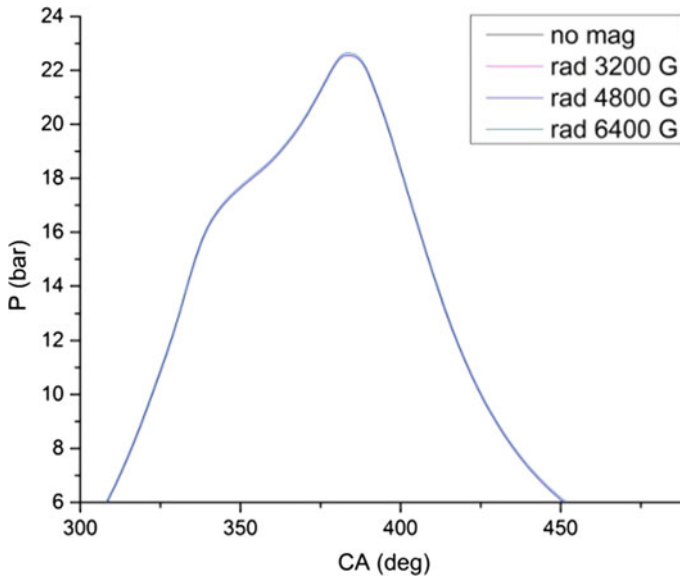
Fig. 15 In-cylinder pressures at 2000 rpm in radial magnetization

of same engine speed without magnetization. When both the magnetization patterns are compared, the peak pressure in the case of radial magnetization is 2.14% higher than that in the case of axial magnetization. This may be due to the fact that the radial magnetization pattern is shown to produce more underling torque and torque ripple than an axial field of similar intensity [24] (Figs. 16 and 17).

The statistical investigation of fluctuations of P_{max} and IMEP throughout the combustion cycles shows analogous results as in the case of axial magnetization. The damping of fluctuations in maximum pressure and mean effective pressures is due to the enhancement in combustion and yielding of more output power for the same amount of fuel burnt.

The analysis of NHRR also provides similar information on combustion character in radial pattern. The peak location of heat release regularly increased with each stage of magnetization and is maximum in the case of 6400 G. This increase in combustion efficiency due to magnetization reflects in the operational characteristics and thermal efficiency of the engine as well. The NHRR characteristics under radial magnetization are shown in Figs. 18, 19, 20, and 21.

The heat release pattern and the duration of heat release are found to be similar in both cases of magnetization. The higher rate of heat release may also be attributed to the increased penetration of oxygen molecules into the interior carbon atoms in the hydrocarbon chain [20, 25]. However, the ability of radial magnetization to decluster and re-align the hydrocarbon molecules is higher when compared to axial pattern and this results in efficient combustion.
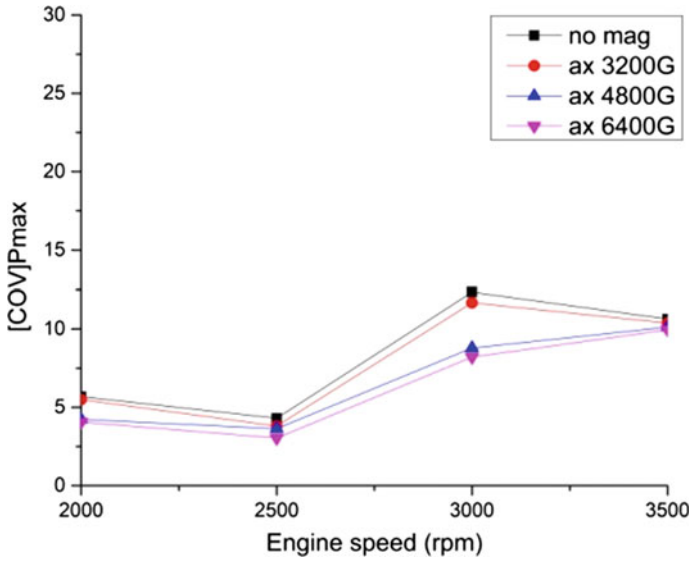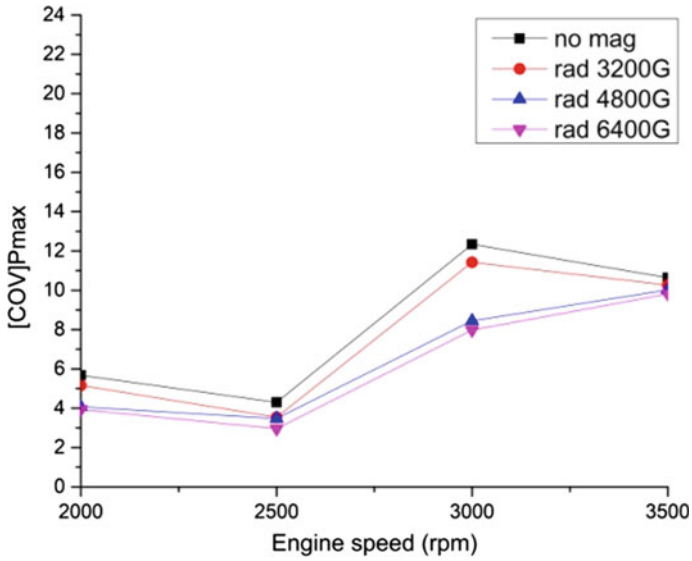
Fig. 16 COV of P_{max} in radial magnetization
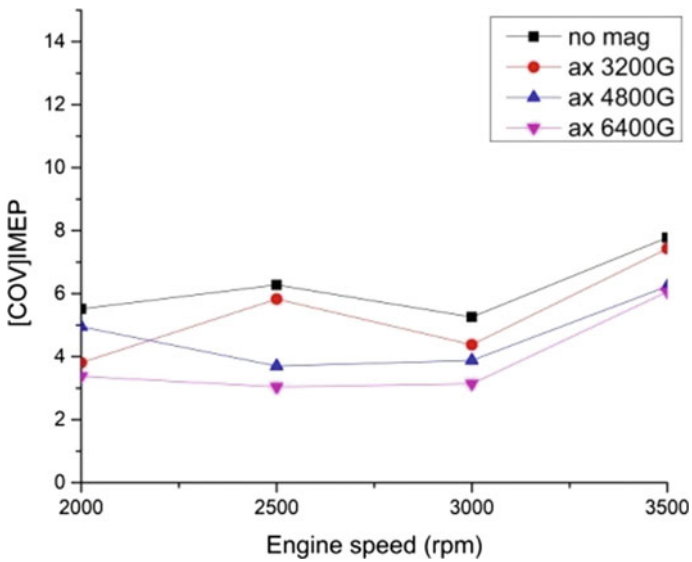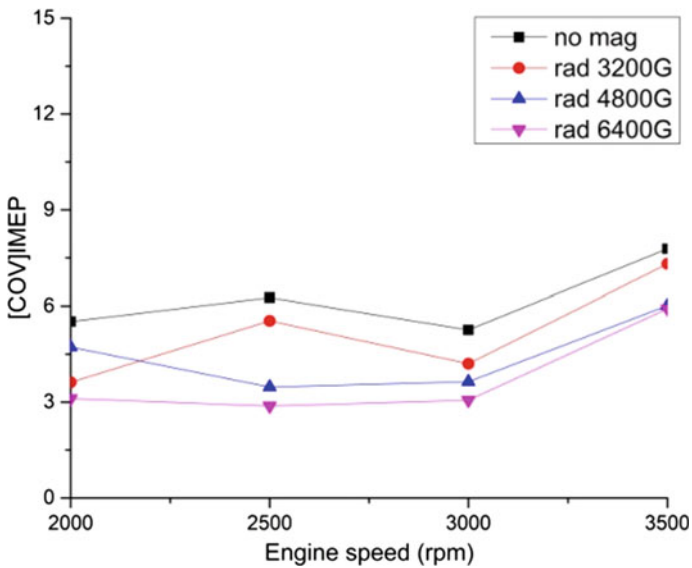

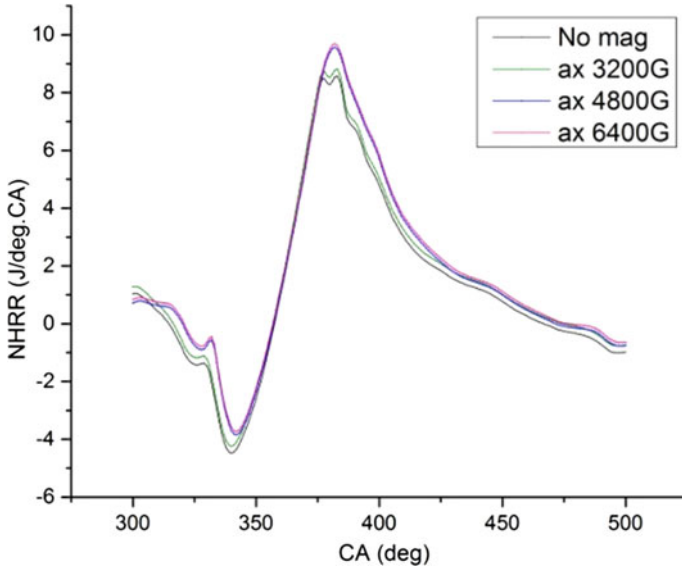**Fig. 17** COV of IMEP in radial magnetization
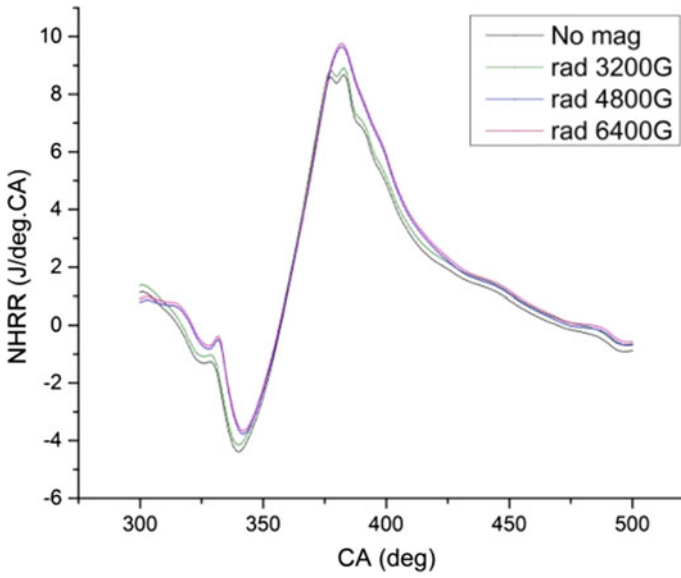
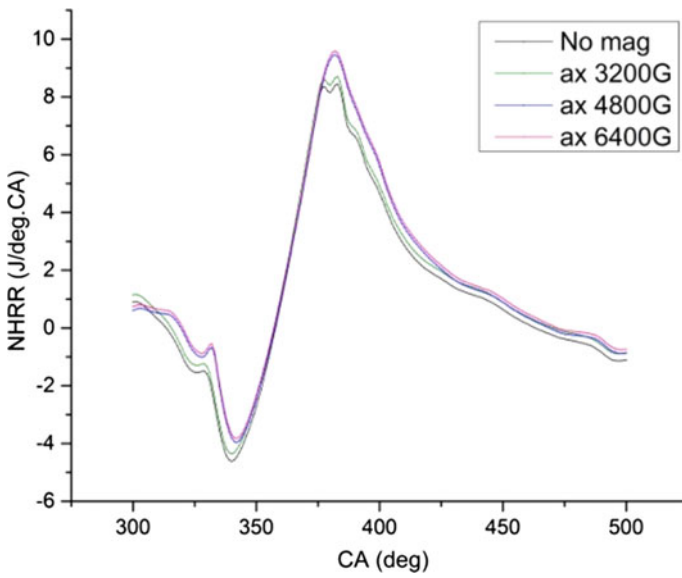**Fig. 18** NHRR at 3500 rpm in radial magnetization
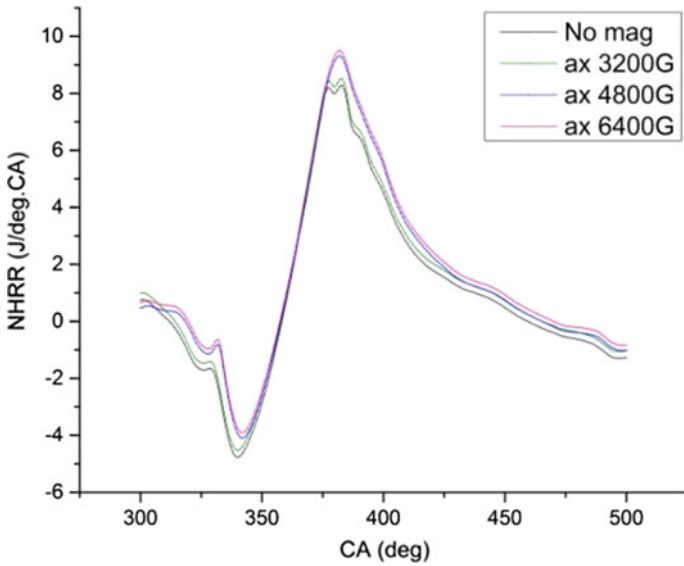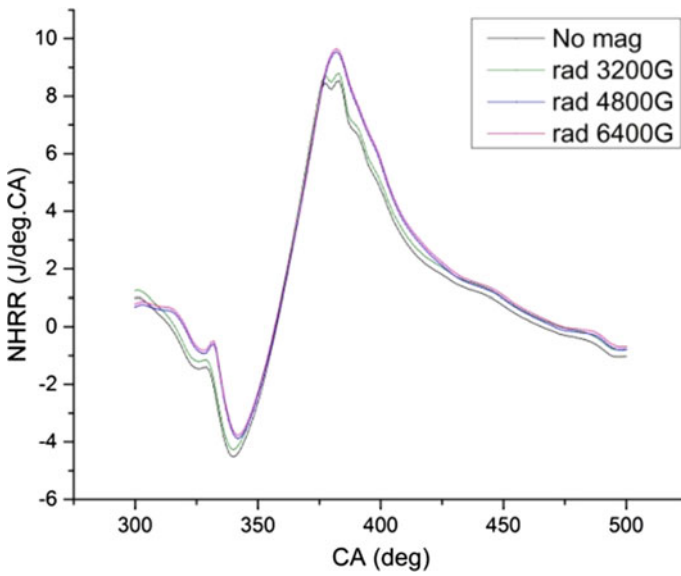

Fig. 19 NHRR at 3000 rpm in radial magnetization
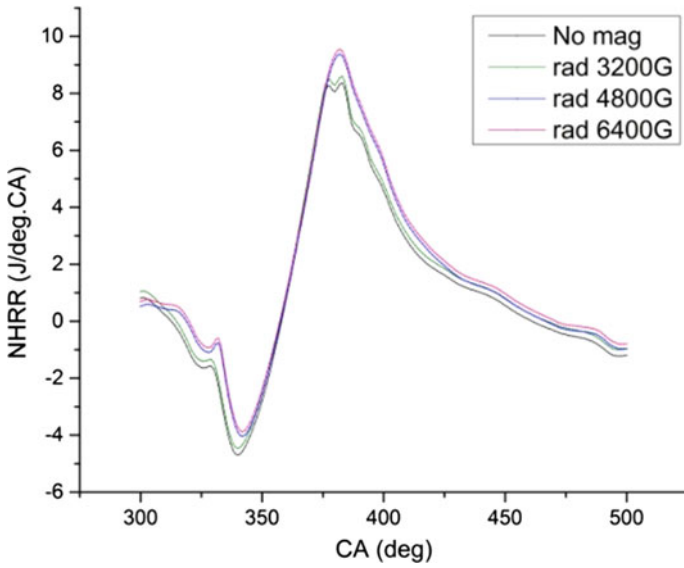
Fig. 20 NHRR at 2500 rpm in radial magnetization
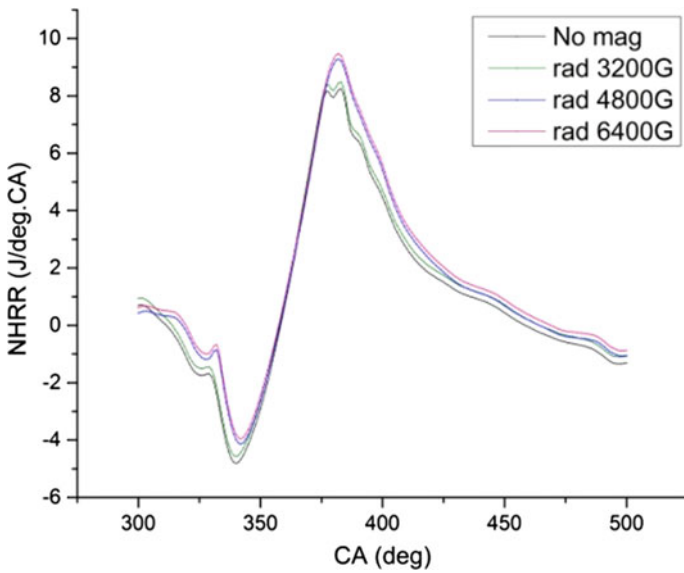
Fig. 21 NHRR at 2000 rpm in radial magnetization

5   Conclusions

An experimental study was conducted on a multi-cylinder MPFI engine to analyze the combustion characteristics of gasoline under four stages of intensities and two patterns of magnetization. The major findings of the experimental study can be summarized as:

- Increase in intensity of magnetization results in higher in-cylinder pressures and P_{max} values in both patterns of magnetization.
- The rate of heat release increased with increased strength of the applied magnetic field. However, the heat release pattern and the duration of combustion remained similar.
- Radial magnetization pattern is found to increase the peak pressure value by 4.89% whereas axial magnetization is found to enhance the same by 2.75%. The net heat release rate under radial magnetization is also found to be higher than that of axial magnetization.
- The statistical investigation of fluctuations of P_{max} and IMEP throughout the combustion cycles shows that the fluctuations and cyclic variations in combustion reduce with increase in intensity of the applied magnetic field and also with a change in magnetization pattern to radial fields.

References

1. Faris AS et al (2012) Effects of magnetic field on fuel consumption and exhaust emissions in two-stroke engine. Energy Procedia 18:327–338
2. Fatih FA El, Gad M (2010) Effect of fuel magnetism on engine performance and emissions. Aust J Basic Appl Sci 4:6354–8
3. Kumar PV et al (2014) Experimental study of a novel magnetic fuel ionization method in four stroke diesel engines. Int J Mech Eng Rob Res 3:151–159
4. Oommen LP, Kumar GN (2019) A study on the effect of magnetic field on the properties and combustion of hydrocarbon fuels. Int J Mech Prod Eng Res Dev 9:89–98
5. Govindasamy P, Dhandapani S (2007) Performance and emissions achievements by magnetic energizer with a single cylinder two stroke catalytic coated spark ignition engine. J Sci Ind Res 66:457–463
6. Gabiña G et al (2015) Energy efficiency in fishing: are magnetic devices useful for use in fishing vessels ? Appl Therm Eng 94:670–678
7. Khedvan AVG (2015) Review on effect of magnetic field on hydrocarbon refrigerant in vapor compression cycle. Int J Sci Eng Technol 4:1374–8
8. Patil S, et al (2017) Effect of magnetic field on hydrocarbon refrigerant, pp 1443–9
9. Gad MS et al (2016) Effect of fuel magnetism on industrial oil burner performance burning waste cooking oil. Int J Eng Technol 16:25–37

10. El-Baz FK et al (2017) Comparative study of performance and exhaust emissions of a diesel engine fueled with algal, used cooked and Jatropha oils biodiesel mixtures. Int J Mech Mechatron Eng 17:90–100
11. Chen CY et al (2017) Impact of magnetic tube on pollutant emissions from the diesel engine. Aerosol Air Qual Res 17:1097–1104
12. Kurji HJ, Imran MS (2018) Magnetic field effect on compression ignition engine performance. ARPN J Eng Appl Sci 13:3943–3949
13. Aydin K (2011) Effect of engine parameters on cyclic variations in spark ignition engines, proceedings of 6th international advanced technology symposium, vol 16. Elazığ, Turkey, pp 57–63
14. Ceviz MA et al (2011) Analysis of the thermal efficiency and cyclic variations in a SI engine under lean combustion conditions. J Therm Sci Technol 31:121–127
15. Litak G et al (2007) Cycle-to-cycle oscillations of heat release in a spark ignition engine. Meccanica 42:423–433
16. Litak G et al (2009) Combustion process in a spark ignition engine: Analysis of cyclic peak pressure and peak pressure angle oscillations. Meccanica 44:1–11
17. Johansson B (1996) Cycle to cycle variations in SI engines—the effects of fluid flow and gas composition in the vicinity of the spark plug on early combustion, SAE technical paper. https://doi.org/10.4271/962084
18. Nayak V et al (2015) Combustion characteristics and cyclic variation of a LPG fuelled MPFI four cylinder gasoline engine. Energy Procedia 90:470–480
19. Oommen LP, Kumar GN. Influence of magneto combustion on regulated emissions of an automotive engine under variable speed operation. Int J Veh Struct Syst 11. https://doi.org/10.4273/ijvss.12.1.25
20. Oommen LP, Kumar GN (2020) Experimental studies on the impact of part-cooled high-pressure loop EGR on the combustion and emission characteristics of liquefied petroleum gas. J Therm Anal Calorim 141:2265–2275. https://doi.org/10.1007/s10973-020-09762-0
21. Oommen LP, Kumar GN (2020) Experimental studies on the influence of axial and radial fields of sintered neo-delta magnets in reforming the energy utilization combustion and emission properties of a hydrocarbon fuel. Energy sources, part A: recovery, utilization, and environmental effects. https://doi.org/10.1080/15567036.2020.1767729
22. Oommen LP, Narayanappa KG, Vijayalakshmi SK (2020) Experimental analysis of synergetic effect of part-cooled exhaust gas recirculation on magnetic field-assisted combustion of liquefied petroleum gas. Arab J Sci Eng 45:9187–9196. https://doi.org/10.1007/s13369-020-04696-z
23. Oommen LP, Narayanappa KG (2021) Assimilative capacity approach for air pollution control in automotive engines through magnetic field-assisted combustion of hydrocarbons. Environ Sci Pollut Res. https://doi.org/10.1007/s11356-020-11923-5
24. Morcos AC, et al (2002) Nd-Fe-B magnets for electric power steering, EPS Intermag, pp 3–5
25. Oommen LP, Kumar GN (2022) Experimental analysis of conjoint effect of semi-cooled exhaust recirculation in magnetic field assisted combustion of liquid phase hydrocarbons. Arab J Sci Eng. https://doi.org/10.1007/s13369-022-06842-1

Combustion, Noise and Vibrational Analysis of Linseed Biodiesel Fuelled Engine

A. Venkata Swami, Ravi Kumar Naradasu, and A. Swarna Kumari

Abstract With the rising population day-to-day there is surge in number of automobiles in the world. The huge increase in quantity of vehicles on track more demand for fuel. The widespread use of petrol and diesel leads to unadorned environmental problems like global warming, emissions of greenhouse gases, and reduction in their levels. Due to more demand and usage of fuels, stringent emission norms there is a need for development of renewable fuel. Engine vibration is higher in diesel engines, resulting in a shorter engine life cycle. Using a single cylinder compression ignition engine, an experimental study was conducted to measure combustion, noise, and vibration properties, as well as their similarities. The tests were conducted without maximum charge, using Linseed biodiesel, 10% and 20% (v/v) Linseed mix and baseline-mineral diesel. Samples of engine combustion noise were used with a microphone. In 3 direction measurements of motor acceleration, a triaxial accelerometer is utilized: vertical, lateral, and longitudinal. NI LabVIEW is used to collect data and perform research. Within the range of 0–100 Hz and three ways, higher peak amplitudes are observed for both diesel and linseed biodiesel at the frequency of 25 Hz. The highest level of combustion noise was observed with a 20% biodiesel mix, related to a longer delay in ignition and an increased rate of heat release. These findings were supported by other observations concerning combustion noise, ignition delay, and heat release rates.

Keywords Linseed biodiesel · Combustion · Noise · Engine · Vibration

A. V. Swami (✉)
Department of Mechanical Engineering, JNTU University, Kakinada, India
e-mail: venkata170@gmail.com

R. K. Naradasu
Department of Mechanical Engineering, MVGR College of Engineering(A), Vizianagaram, India
e-mail: naradasuravi@mvgrce.edu.in

A. S. Kumari
Department of Mechanical Engineering, JNT University, Kakinada, India

Nomenclature

B0   100% Diesel fuel
B10   10% Linseed oil and 90% of diesel
B20   20% Linseed oil and 80% of diesel
B100   100% Of linseed oil
BP   Brake Power
Bsfc   Brake specific fuel consumption
BTE   Brake Thermal Efficiency
CO   Carbon monoxide
HC   Hydrocarbon
NOx   Oxides of Nitrogen

1   Introduction

Because of their high efficiency, diesel engines have long been a popular option for heavy-duty applications, such as trucks. However, they have disadvantages such as excessive noise, weight, and vibrations. The world is heading toward a more sustainable energy age with an emphasis on renewable energy and energy conservation. Concerns over diesel's long-term availability and environmental impact have prompted a hunt for a clean diesel replacement. Alternative fuels have grown in popularity in recent decades as a result of environmental issues and country-specific pollution laws. One of the most appealing features of biodiesel is that it can be used in existing generators, cars, and facilities with little or no modification. The pumping, storage, and burning of biodiesel can be done in the same way as the diesel petrol fuel and can be used either alone or to a certain extent with petrol diesel.

Oleic acid, linoleic acid, and linoleic acid are the principal composition of linseed oils. Oils of linseed are of 26–30 mm^2/s at 40 °C kinematic viscosity. They have a high viscosity due to their greater molecular weight and chemical composition. The molecular weights of vegetable oils are 600–900, three to four times that of petrol. Linseed oil has a very high flash point (around 222 °C). The temperature of auto-ignition is around 343°C. It is 931 kg/m^3 in density and 0.93 in particular. The heat value is about 40 MJ/kg, lower than diesel fuels (approximately 45 MJ/kg).

Balamurugan et al. [1] An experimental test of a CI engine showed how alcohol mixing affects heat breaking performance, CO, HC, and NOx emissions, and that alcohol mixed biodiesel increases the thermal braking efficiency while CO, HC, and NOx emissions are decreased. Ashok Kumar et al. [2] Explained that the performance and emission characters of the VCR-tested esterified pinnai oil were found to be marginally higher than that of standard part load diesel for all compression ratios the frequency strength of the biodiesel. Ramkumar et al. [3] Diesel engine output and emission characteristics were investigated. Fueled by neem oil, the brake heat efficiency decreased when blends increased with an increase, and increased with

an increase in compression ratio, as the compression ratio increased from 15 to 18 Ravi Kumar et al. [4]. The experiment was performed on a VCR diesel engine with soybean meat ester (SOME) in combustion and vibration analysis as a fuel in a compressive variable engine, at different loads, and compression ratios. Combustion and vibration analysis of diesel engine was investigated under different engine loads and compression ratios. The emission characteristics at compression ratio 15, 16, 17, and 18 were plotted and the variations observed. Vibration data was measured using Lab view vibration tool kit. During combustion, the performance parameters are investigated such as individual fuel consumption, thermal brake efficiency, and burn characteristics, including heat release rates, burned mass fractions, and cylinder pressure. The particular fuel consumption at CR 15 and maximum at CR 16 was also observed and remained identical to the higher compression ratio of 17. Parikh et al. [5] Analyzes of effectiveness and emission of 4-stroke, ethanol-based biodiesel engines combined with diesel fuel, and it was found that using ethanol/diesel mixtures raises the ignition lag time due to ethanol's low cetane amount.

Knothe et al. [2010] find Methanol is an alcoholic-based fuel additive with about 30% more oxygen in basis than mineral gasoline, allowing diesel engines to reach higher full combustion. Because of the extra oxygen in the liquid, complete combustion is possible. Furthermore, the use of alcohol additives reduces PM, HC, and CO levels in exhaust greatly. Rakopoulos et al. [6] A turbocharged diesel engine's transient output and emissions were investigated. Biodiesel blends have the greatest impact on combustion activity and reliability, while the n-butanol blend had the least. Low speed proved to have the greatest effect on the production of combustion noise and its absolute values. Sanjid et al. [7] analyzed the experimental findings of a study that looked at the brake-specific fuel intake, Characteristics of a palm–jatropha blend's exhaust and noise emissions because of their lubricity and damping characteristics, the sound level emitted by biofuel blends was lower as compared to diesel fuel.

2   Methodology

Before being used in IC Engines, raw vegetable oils must undergo some changes to their properties such as viscosity and density. Transesterification is a method of lowering the viscosity and density of crude. An alcoholic-reacting triglyceride responds to a mixture of fatty acid alkyl ester and glycerol in the presence of either an acid or a base catalytic in vegetable oils. Linseed oil in the presence of a basic catalyst is generated to react with methanol (NaOH). Table 1 shows the chemical properties of linseed oil biodiesel.

Experimental Setup

The experimental design consists of an oil checked vertical four-stroke, one-cylinder, water-cooled, direct injection engine; Table 2 lists the specifications for the engine. The figure of the experimental arrangement is shown in Fig. 1. The air flow was

Table 1 Properties of linseed biodiesel and its blends

Properties	Diesel	Linseed oil	B10	B20
Density (kg/m^3)	846	899	885.2	868.4
Kinematic viscosity (centistokes)	4.75	4	5.41	5.07
Flash point (˚C)	62	64	66	78
Fire point (˚C)	76	72	76	98
Calorific value(kJ/kg)	42,500	38,000	42,050	41,600

Table 2 Engine specifications

Features	Specifications
Make	Kirloskar oil engine
Type	Four stroke, water cooled diesel
No of cylinders	One
Combustion principle	Compression ignition
Max speed	1500 rpm
Connecting rod length	234 mm
Cylinder diameter	87.5 mm
Stroke length	110 mm
Compression ratio	Variable
Capacity	661 cc

determined by the technique of the air box, which involved the pressure drop by a manometer through the sharp edge opening of the air surge chamber. The amount of diesel flow was calculated by recording the time it took to consume 5 cc of fuel. A digital tachometer was used to determine the engine's speed. For loading the turbine, an electric current dynamometer is used. The HC, CO, CO_2, NOx, and O_2 exhaust gas constituents are tested using an AVL DiGas 444 gas analyzer, and an AVL 437C smoke meter was used to assess smoke opacity. Engine vibration and noise were measured using NI Labview coding and sensors.

3 Results and Discussion

This section compares the power, combustion, emission, friction, and noise characteristics of a high-speed diesel engine running on linseed biodiesel at various loads, from no load to full load.

The difference of brake thermal efficiency with engine load is visualized in Fig. 2. The BTE increases significantly with load irrespective of the fuel type. The maximum BTE was observed for pure linseed oil and next to it was B20 (20% linseed oil and
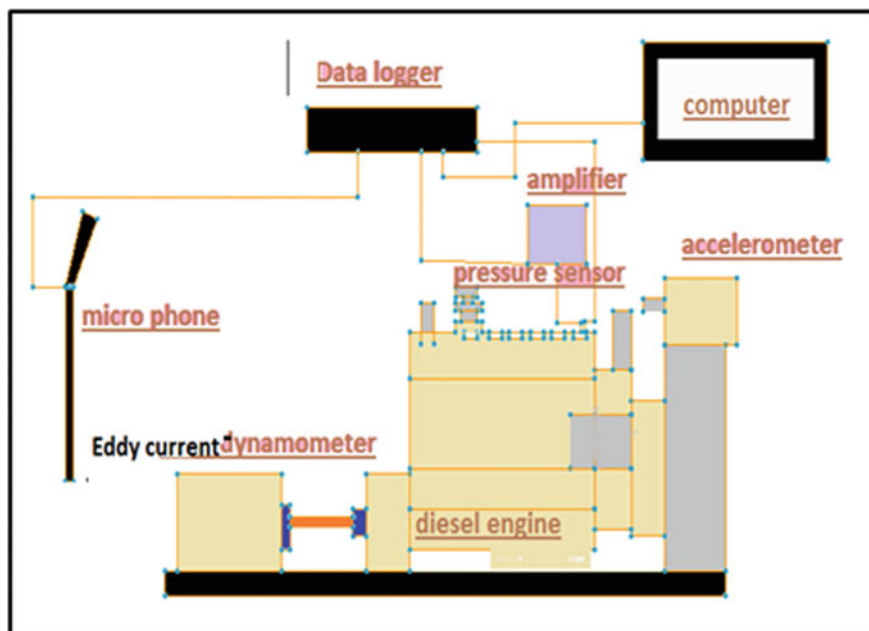
Fig. 1 Experimental setup of computerized diesel engine with exhaust gas analyzer, smoke meter, vibration, and noise sensors

80% diesel). At maximum load the BTE of pure linseed oil was 6.865% greater than pure diesel and BTE of B20 was 4.26% greater than pure diesel.

Figure 3 illustrates how bsfc changes with engine load; for all fuel blends, bsfc decreases as load increases. When the engine's load or power output is increased, the turbulence and in-cylinder temperature increases which results better combustion efficiency of the fuel and decrease in fuel consumption.

Figures 4 and 5 demonstrate the change in cylinder pressures at no load, maximum load at constant speeds of 1500 RPM for different test blends. The peak pressure was obtained for B-10 blend with a value of 43.856 bar at no-load and at full load it is 62.26 bar for Diesel. It was discovered that as the load within the cylinder increased, the peak pressure inside the cylinder increased for all fuel blends.

The change in NOx and HC emissions for Diesel engines operating on Diesel and Linseed biodiesel blends as seen in Figs. 6 and 7. Since linseed biofuel blends have lower calorific values than pure diesel, the pressure and temperature inside the combustion chamber are lower, resulting in lower NOx pollution. The peak NOx concentration for diesel is 128 PPM which is 25.78, 26.56, and 41.41% greater than the peak NOx concentrations for B-10, B-20, and pure linseed oil. However, from the graph it can be inferred that the peak NOx value is obtained at slightly lean mixture for all blends. Since the flame temperature is already very high and oxygen can be excessive and react to various oxides by nitrogen, the situation has been dangerous.
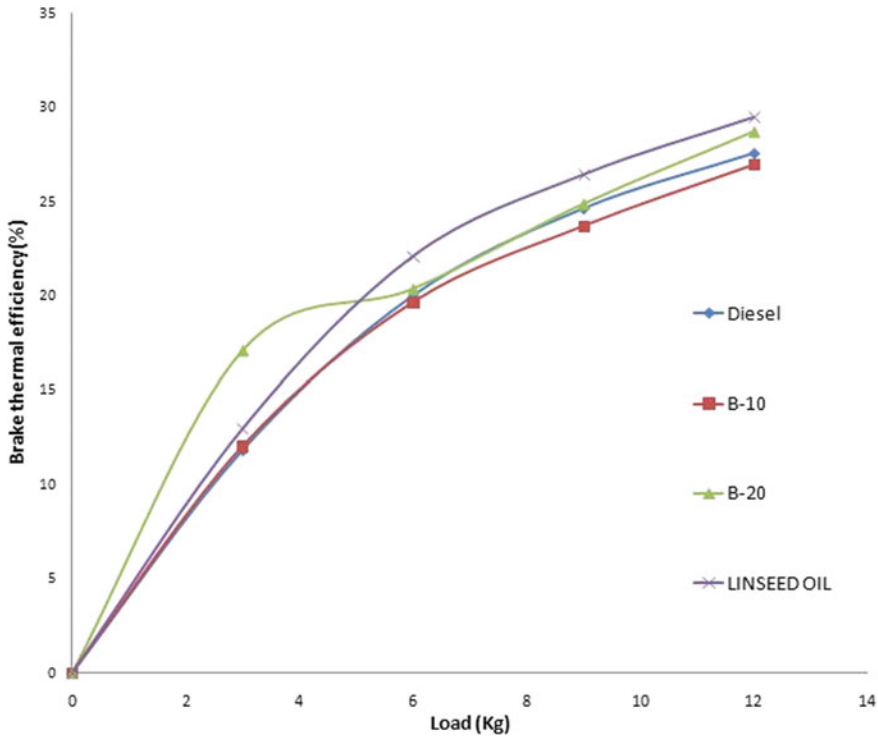
Fig. 2 Variation of brake thermal efficiency with load

Similarly, the biodiesels are oxygenated fuels and contain excess oxygen. This allows proper combustion in the engine cylinder to minimize HC emissions in biodiesel mixtures as opposed to gasoline.

The majority of the smoke is made up of elemental carbon from incomplete fuel combustion and traces of engine lubricant. The smoke concentration from the test engine is depicted in Fig. 8 represented as a bar graph with various blends. The bar graph shows that as more linseed oil was substituted for diesel fuel, the smoke concentration increased. Highest smoke concentration was observed at peak loads, due to the abundance of fuel and non-availability of enough oxygen. The reasons for increasing emissions at higher fractions of linseed oil may be the strong fuel viscosity resulting in reduced Reynolds, higher mean fuel drop sizes and lower fuel air mixture.

The changes in the speed and vibration amplitude of the diesel motor with diesels and various biodiesel blends at full load conditions are presented in Figs. 9 and 10. The time domain vibration signals were calculated using an accelerometer at no load and a sampling frequency of 25.6 kHz for all fuel blends. Out of all fuel blends B-10 is showing the highest vibration amplitude at no load whose values range from 259.04 to 302.944 m/s^2, which is 4.74% greater than that of pure diesel. The peak
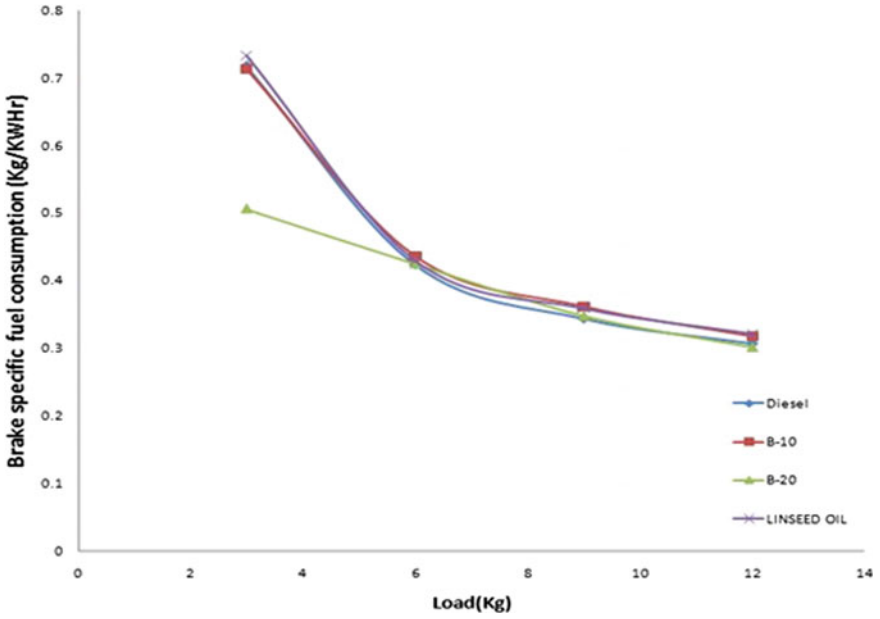
Fig. 3 Variations of bsfc with load
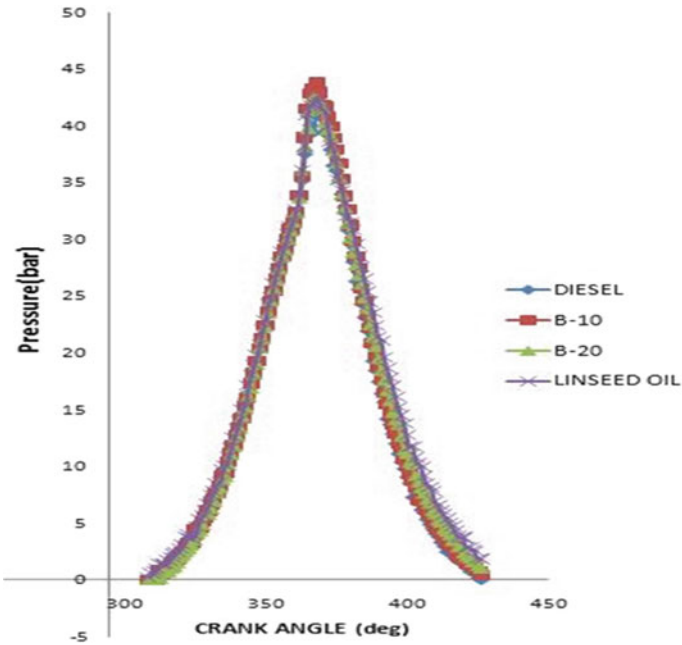
Fig. 4 P-θ diagram for diesel engine running with different fuel blends at no load
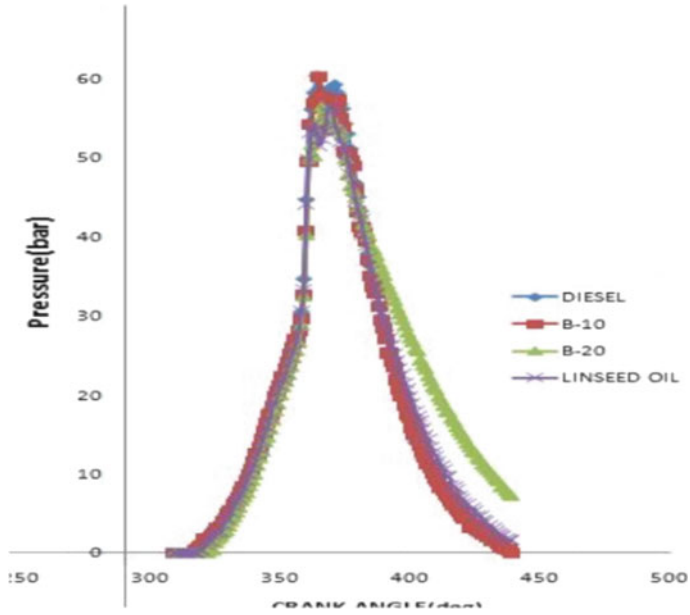
Fig. 5 P-θ diagram for diesel engine running with different fuel blends at full load
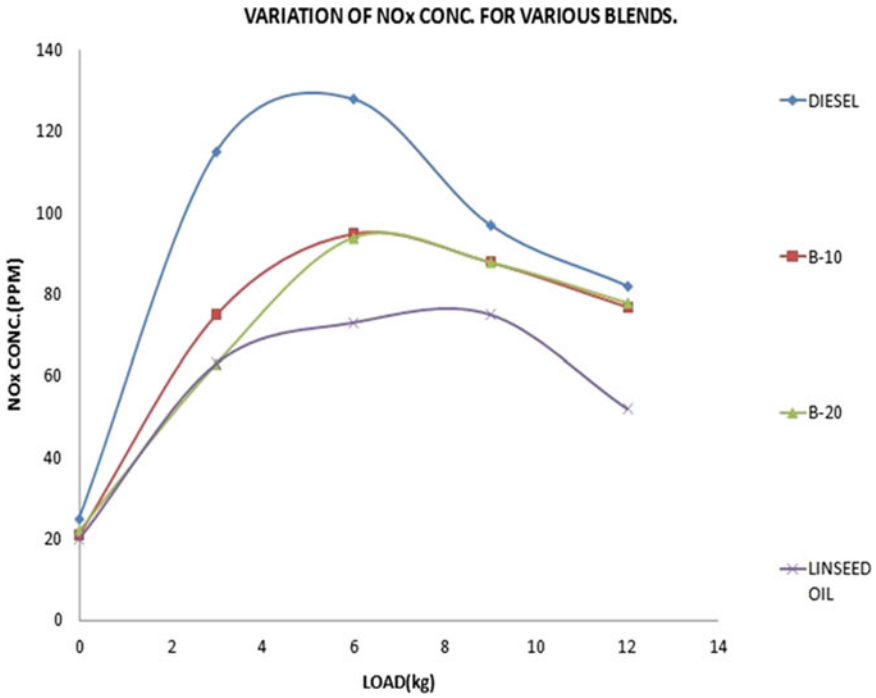
Fig. 6 Variation of NOx with load for different fuel blends
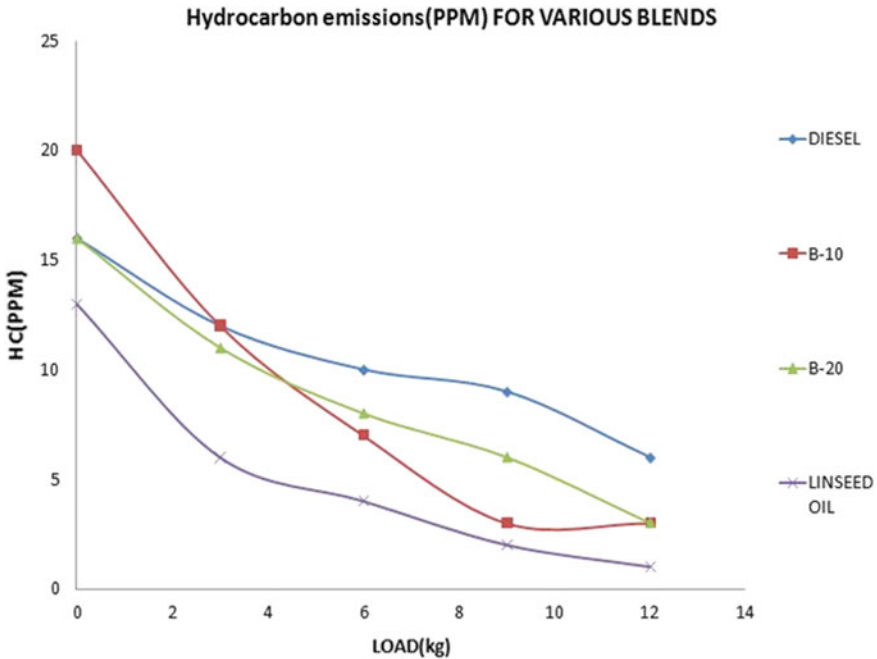
Fig. 7 Variation of HC emissions with load

amplitude (RMS) values for diesel, B-10, B-20, and linseed oil are 4.71, 4.586, 4.437, 4.43 m/s^2 respectively at full load condition.

The above Fig. 11 represents the change in noise level of Diesel engine running with linseed oil at no load condition. The running speed and the cylinder pressure produced within the cylinder have a significant impact on combustion noise. The rate at which cylinder pressure rises during the engine cycle determines combustion noise. At no load as the ignition delay is maximum it leads to lower combustion temperatures and lower peak pressure values as it can be observed from the P-Θ diagram. At no load the noise level for biodiesel blends is significantly identical but higher than pure diesel. For pure linseed oil the noise levels vary with time with amplitudes ranging from 89 to 96 db. At peak loads as the combustion process is steady and efficient therefore the combustion noise is stable and doesn't vary much from the part loads.

4 Conclusions

In order to investigate various engine characteristics, the biodiesel linseed and its diesel blends were produced and tested on a diesel engine.
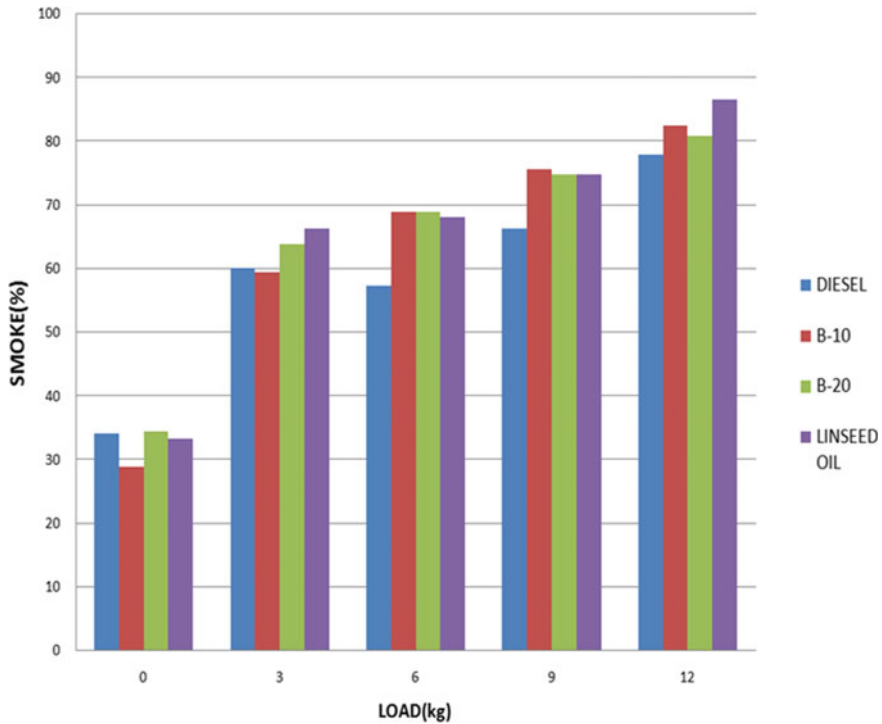
Fig. 8 Variation of smoke with load for different fuel blends

The maximum BTE was observed for pure linseed oil and B20. At maximum load the BTE of pure linseed oil was 6.865% greater than pure diesel and BTE of B20 was 4.26% greater than pure diesel.

Higher combustion and flame temperature influence the formation of NO_X. For biofuels, the emissions of NOx are relatively lower. The peak NOx concentration for Diesel is 128 PPM which is 25.78, 26.56, and 41.41% greater than the peak NOx concentrations for B-10, B-20l and pure linseed oil.

The peak amplitudes for Diesel, B-10, B-20, and linseed oil are 1.8148, 1.7162, 1.4731, and 1.510 m/s2 respectively. The peak amplitudes of biofuel blends are clearly smaller than those of pure Diesel. The engine noise levels of diesel and biodiesel mixtures vary between 85 and 96db.
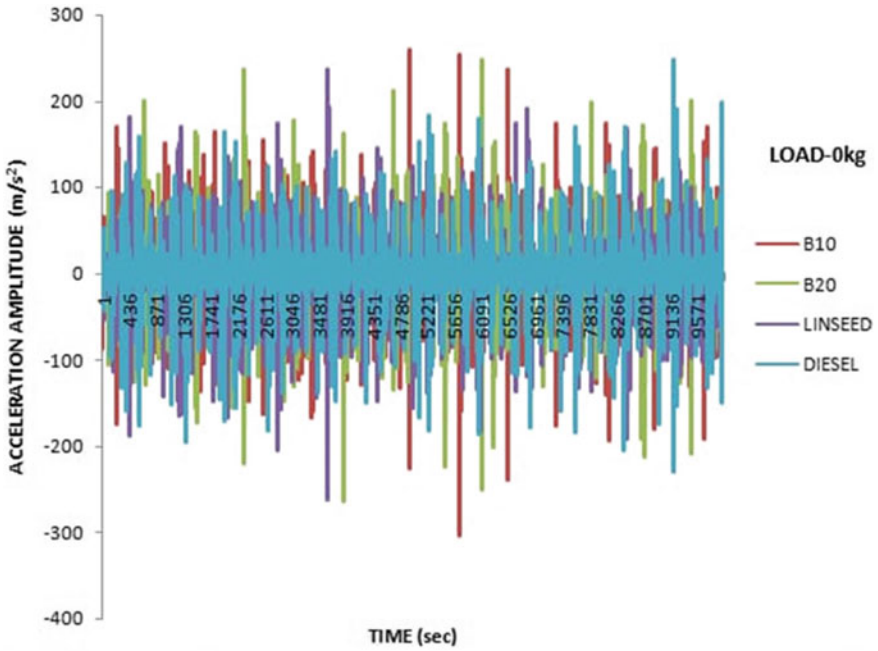
Fig. 9 Change in acceleration of engine at no load
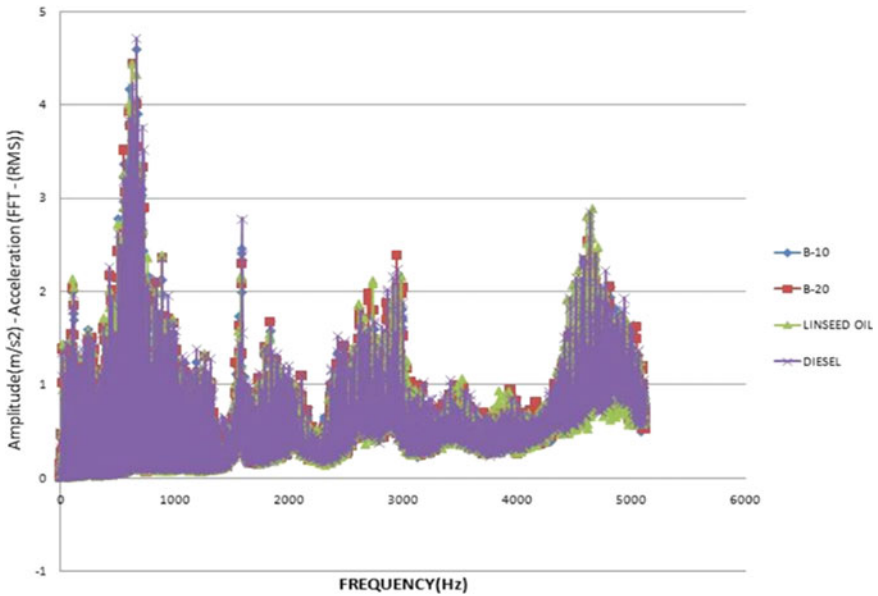
Fig. 10 Change in Vibration amplitude (RMS) for all full blends at full load

Fig. 11 Variation of noise
level in Diesel engine at no
load running with linseed
biodiesel
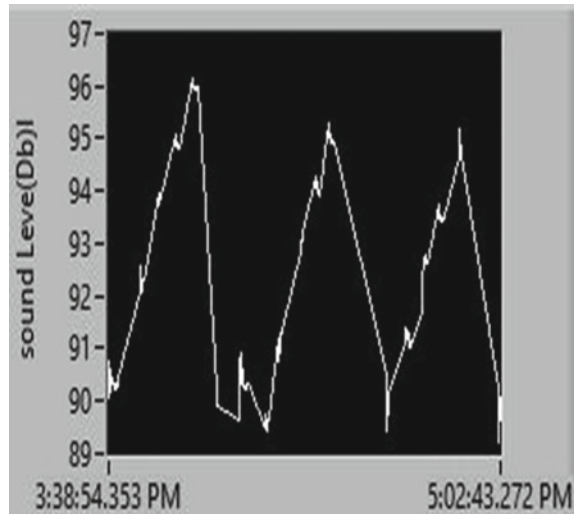
References

1. Balamurugan T, Nalini R (2014) Effect of blending alcohol with diesel on performance, combustion and emission characteristics of 4 stroke diesel engine—an experimental study. Int J Chem Tech Res CODEN (USA) 6(1):750–762
2. Ashok Kumar T, Chandramouli R, Mohan Raj T (2015) A study on the performance and emission characteristics of esterified Pinnai oil tested in VCR engine. Ecotoxicol Environ Saf
3. Ramkumar S, Chinnasaamy C, Yoga Raja J, Karthik B (2015) Performance and emission characteristics studies of diesel engine fuelled with neem oil. Int J Mech Eng Res 5(1)
4. Ravi Kumar N, Prashanthi G, Madhav Varma B (2014) Combustion and vibration analysis of VCR diesel engine running with soybean methyl ester. Research gate, ICEE conference
5. Parikh HB, Prajapathi VM, Thakkar KH (2013) Performance evaluation and emission analysis of 4-stroke IC engine using ethanol biodiesel blended with diesel fuel. IJRET: Int J Res Eng Technol
6. Rakopoulos CD, Dimaratos AM, Giakoumis EG, Rakopoulos DC (2011) Study of turbocharged diesel engine operation, pollutant emissions and combustion noise radiation during starting with bio-diesel or n-butanol diesel fuel blends. Appl Energ 3905–3916
7. Sanjid A, Masjuki HH, Kalam MA, Ashrafur Rahman SM, Abedin MJ, Palash SM (2014) Production of palm and Jatropha based biodiesel and investigation of palm-jatropha combined blend properties, performance, exhaust emission and noise in an unmodified diesel engine. J Cleaner Prod 295–303

Experimental Investigation on Performance and Emissions of HCCI Engine Using Kusum Oil Biodiesel Blends

N. V. Mahesh Babu Talupula, P. Srinivasa Rao, and B. Sudheer Prem Kumar

Abstract In recent times, with more thermal efficiency, low NO_x and particulate matter, Homogeneous Charge Compression Engines (HCCI Engines) emerged for renewed interest. However, knocking and misfiring were considered as classic problems in HCCI engines. To compensate the impact of depletion of petroleum reserves also to lessen the deleterious effects of most regularly used fossil fuels, alternate fuels emerged into the scenario. Researchers studied that Compression ignition engines faced difficulties due to the inherent nature of high viscosity, when vegetable oils were consumed. In the present research, the impact of Kusum oil biodiesel blends on performance and emission characteristics were examined using experimental investigation. Conventional diesel engine has been converted into HCCI engine to operate in homogeneous mode. The blends B20, B50 and pure biodiesel were taken, by varying the input air temperature and port fuel injection pressure, the variation of performance and emission characteristics were analyzed. To implement HCCI mode operation, Homogenous mixture of air and fuel is made by port fuel injection technique which is the basic requirement. Using an external device, the mixture formation and fuel vaporization was done. Varying the temperature of the blends at different port fuel injection pressures, the performance parameter brakes thermal efficiency, NO_x, CO, CO_2, HC emissions and smoke density were analyzed in the HCCI mode. Also optimal parameters were found by using the experimental investigations.

Keywords Kusum oil biodiesel · Alternative fuel · HCCI engine · Engine emission · Port fuel injection pressure · Air inlet temperature

N. V. M. B. Talupula (✉)
Department of Mechanical Engineering, JNT University, Hyderabad, India
e-mail: tnvmaheshbabu@gmail.com

P. S. Rao · B. S. P. Kumar
Department of Mechanical Engineering, Institute of Aeronautical Engineering, Dundigal, Hyderabad, India

155

Abbreviations

BTE   Brake Thermal Efficiency
B20   Blend of 20% biodiesel and 80% petroleum diesel
BTDC   Before Top Dead Center position
CO   Carbon Monoxide emissions (% volume)
CKO   Crude Kusum Oil
ECU   Engine Control Unit
FFA   Free Fatty Acid content
HC   Hydrocarbon emissions (ppm)
HCCI   Homogeneous Charge Compression Ignition
HSU   Hartridge Smoke Units
KME   Kusum oil Methyl Ester (Kusum oil biodiesel)
NOx   Nitrogen Oxides
Ppm   Parts per million
RKO   Refined alkaloid-free Kusum Oil
RPM   Revolutions Per Minute
TEO   Transesterified oil

1 Introduction

Due to the increase in cities and industries over the decades, pollution of the vehicles increased manifold. The quantity of petroleum-based resources was decreasing gradually and the entire globe is facing severe problem due to the lack. The hazardous exhaust gases emitted by vehicles into the environment make the environment contamination and became severe health problems to human beings as well as other living beings. Hence governments across the globe were tagging stringent action for the reduction of emissions to a great extent and trying to mitigate the problems. Also the depletion of fuel resources and reserves became a severe problem, due to which the prices of fuels are increasing manifold, which impart burden to the users. Hence, a need has arrived at for Alternate fuels [1] which emit lower emissions. Fuels based on alcohol and biodiesel were used by researcher in diesel engine. [2, 3] The fuel consumption, durability, maintenance, fuel cost are advantageous for CI engines compared to SI engines and hence the former are more used [4]. Sindhu et al. [5] studied the effects of exhaust gas recirculation (EGR), variation of fuel injection timing and split injection, to reduce NO_x and soot emissions. It was observed that injections with split performed well and controlled NO_x emissions compared to retardation timing and EGR. Wang et al. [6], done experiments to study the variation of NO_x and smoke emissions using diesel/butanol blends. They had identified that usage of diesel/butanol blend improvised ignition delay, decreased combustion phasing as well as premixed combustion ratio were improvised. Owing to this blend, the smoke opacity was decreased but has no effect on NO_x. Rahman et al. [7] inducted fine

quantity of Hydrogen into biodiesel which reduced Carbon monoxide, smoke emissions and Hydrocarbons, also thermal efficiency of the engine was improvised. Still induction of 10% EGR reduced NO_x at low temperatures but at more load the effect has been reversed on η_t, bsfc, CO_2, CO and opacity of smoke.

Algayyim et al. [8] conducted experiments and concluded that the best options for conventional fuels were biodiesel with no modification of the engine design. Oxygen present in the biodiesel has an advantage to decrease emissions of CO and HC. Also comparing the properties of biodiesel and diesel, they have similarities and blending them both is easily done [8]. Warkhade et al. experimentally evaluated the effect of higher blend biodiesel/diesel on the Variable Compression Ratio (VCR) performance. They identified that without affecting the engine performance characteristics, 30% biodiesel can be used. But, due to the proportions of blend exhaust emissions such as CO, CO_2, HC, NOx, soot increased.

HCCI technology existed since long ago but renewed attention and enthusiasm is paid recently. It is a clean and highly efficient technology of engines that can be scaled to any size with no limitations whether they are for stationary applications or transportation. HCCI engines benefit through lean/dilute operation efficiently. Compared to conventional spark ignition gasoline engine, HCCI technology gives better fuel efficiency as well as good emissions control.

Owing to more number of advantages in electronic controls, HCCI concept was brought into reality and further refinements are very essential to bring an edge to convert into every day utility in automobiles. Agawal et al. [9] done experiments to find the effect of intake air temperature, air–fuel ratio on combustion parameters, ringing intensity, combustion efficiency, thermal efficiency, and HCCI engine emissions were analyzed. Sanli et al. [10] done experiments on the biodiesels fuel quality generated from waste frying oil using methanol and ethanol, tested and measured the emissions. The impact of compression ratio on HCCI combustion, performance and emissions were parametrically investigated by Calam et al. [11]. Optimizing process parameters of Kusum Oil biodiesel for utilization in HCCI engine were done and explained by Maheshbabu et al. [12].

Das et al. [13] operated diesel engine by dual-injection technique and converted into HCCI mode that reduced NOx and smoke emissions to a major extent. During their experimentation, at the time of suction stroke, pilot injections were made, and at the end of the compression stroke at top dead center (TDC). Experiments were performed under constant speed and 0–67% engine load conditions, experimentation was made. With premixed ratio 0 to 80%, the effect of EGR rate 15 to 30% was studied for 80 percent. On improvising the mass of the pilot fuel, the PRR, HRR and start of combustion were advanced. The impact of ethanol and methanol blend on parameters of combustion and emissions with gasoline direct injection HCCI engine was studied experimentally by Turcan et al. [14]. For this study, Gasoline fuel, and its blends E10, E20, M10 and M20 were taken for the study. Injection timing at first was fixed at 120° after the TDC and varying from 30° to 15° CA bTDC second injection was done. At 120° aTDC 80% of the overall fuel was made injected and remaining fuel was injected during the second injection timing, also got conclusion that the decrement of second injection timing made delay of SOC, cylinder pressure

decreased and also HRR. Compared the soot and NOx emissions, there is no effect of second injection time, on HC and CO emissions.

On port-injected Ricardo hydra test engine Uyumaz [15] done experiments to find the effect of pure, n-heptane and n-butanol blends (B40, B30, B20) and blend of n-heptane and isopropanol fuels (P40, P30, P20). Conclusion of the above experiment includes for knocking to happen, the n-heptane and blend B20 were the reason and except these, the remaining fuels decreased the emissions of NOx to a large extent.

The effective method of controlling HCCI combustion is fuel blending and also injection of two variety of fuels at various locations control combustion in HCCI mode (port and in-cylinder). A few examples depicting the above statement were explained as under.

Experiments were conducted taking methanol and diesel fuel in HCCI mode engine and the impact of methanol at three various locations was studied by Jia, and Danbtratt [16]. During three different timings, Methanol fuel was injected; at $-350\,°C$ TDC port fuel injection was made, direct injection, direct injection (DI_E) at $-358\,°C$ aTDC direct injection and a direct injection at compression stroke at (DI_L) $-100\,°C$ aTDC. Results shown by comparing DI_L strategy shown poor performance in comparison to port injection and DI_injection. Also DI_E strategy has shown NO_x and soot in lesser content in comparison with other two strategies. Lalwani et al. [17] did experiments and applied Numerical analysis; in their experiment, for port injection gasoline was used and for direct injection diesel was used. Concluding the above, after 40% of the engine load HCCI mode possibly would not persist, the engine converted into to diesel mode. In HCCI mode, NO_x, CO_2 and η_t were improved by 80%, 30% and 15% respectively. But at part load conditions, emissions HC and CO greatly increased compared to conventional diesel engine. To find the impact of methanol contribution, intake temperature, EGR, injection timing on soot emission in diesel/methanol dual fuel engine, experiments were conducted by Dou et al. [18]. Into the intake manifold, Methanol was injected and diesel was injected in the combustion chamber. At constant speed, i.e. at 1600 rpm and at 50% of the engine load, experiment was conducted. Results shown that on improving ethanol percentage and retardation of injection timing of diesel were the reason for less soot and particulate matter (PM) emissions in comparison with early injection of diesel.

The challenges of HCCI engines that are same as dual fuel mode HCCI engine were overcome, reactivity controlled compression ignition (RCCI) technique was used. RCCI example combustion was as follows.

Experiments were conducted to determine the effect of various parameters like EGR rate, intake pressure, diesel injection timing, gasoline proportion etc. on RCCI engine by Wang et al. [19]. In this experiment, at the time of suction gasoline was supplied and after the compression of homogeneous mixture, diesel was injected. They had identified that the operation made using gasoline/diesel RCCI engine operates good with moderate to heavy load conditions with very low NO_x, soot emissions and also improved thermal efficiency (η_t), but under low load conditions, single-shot

fuel injection performed better. Also, for RCCI combustion with high load condition, high EGR rate, early injection timing and high gasoline fraction were agreeable; conversely, very high rate of EGR or more advanced fuel injection enabled the combustion uncontrolled.

Same type of experimentation work was done by Park, and Yoon [20] on RCCI engine. In port fuel injection, gasoline and biogas were used and for direct injection diesel was used. Variation of port fuel injection was made from 0.2 to 0.8 and at 40° bTDC, diesel with direct injection was made. As the mass of the fuel used in port fuel injection increased, caused more ID, also the period of ID was more for diesel–biogas dual fuel mode in comparison with gasoline–diesel dual fuel mode of combustion. Apart from this, NO_x and soot emission decreased to a great extent but emissions of CO and HC improvised in dual fuel mode operation.

In order to master challenges with HCCI engines, numerous researchers operated dual fuel or RCCI mode operations for part-load or particular load conditions. Some researchers varied load conditions and studied their nature. In the present work, variation in port fuel injection pressures and intake air temperatures were made, the variation of performance and emission parameters were studied and analyzed and also what are the optimal parameters are investigated.

2 Biodiesel Production

2.1 *Kusum Oil Extraction*

Schleichera oleosa, other name as Kusum, belongs to Sapindaceae family is almost evergreen tree or deciduous with medium size upto 40 m height, available in South and South East Asia (native). The other names of the trees are macassar oil tree, honey tree, lac tree, Ceylon oak tree. Almost all parts of the plant seeds, fruits and new leaves of the plant are edible and utilized in medical field and for the purpose of die as explained by Kant et al. [21]. The content of oil in Kusum seeds varies from 51 to 62% but in village oil mills, the yields are 25 to 27% and in oil expellers, the yield is approximately 36% as concluded by Acharya et al. [22]. The Iodine value of the oil was 215–220 and has total fatty acid content 91.6%. The potential of Kusum oil is approximately 66,000 tonnes per year in India, in that 4000 to 5000 tonnes are collected. The flowers are appeared from February to April and fruits are yielded in the months of June–July. Kusum seeds are collected from tribal people of Raipur of Chattisgarh were crushed in a mechanical expeller in the laboratory to extract Kusum oil (Schleicheraoleosa) for present study (Figs. 1 and 2).

Considering the report of Council of Scientific & Industrial Research et al. 1985, FFA composition of kusum oil consists of 16 components such as Linoleic acid, Arachidic acid, Capric acid, Palmitic acid, Heneicosanoic acid, Oleic acid, Stearic acid, Lauric acid, Myristic acid, Behenic acid, Docosahexaenoic acid, Cis Linoleic acid, Eicosenonic acid, Erucic acid, Palmitoleic acid and alpha-Linolenic acid. Since

Fig. 1 Kusum oil tree and seeds

Fig. 2 Oil blends prepared from Kusum oil biodiesel and fossil diesel

the FFA of Kusum oil seeds are high, by alkaline-catalyzed esterification process biodiesel could not be produced. Esterification process in two steps is developed to make biodiesel from Kusum, which is a high FFA (5% to 11%) non-edible vegetable oil. It also consists of 215–220 iodine value and 91.6% total fatty acid content. The oil can be utilized alternate to diesel but the major difference between Kusum oil and diesel oil is variation of viscosity. Owing to the viscosity of Kusum oil being very high, complete combustion does not take place, thus reduces the engine life.

For making the biodiesel from Kusum oil, esterification process in two steps was followed, wherein the first step acid catalyzed pre-treatment is done, which reduces the FFA content of the crude oil from high to about 2%. Second step consists of transesterification of oil wherein the oil is added with alkaline catalyst. Fatty acid composition was known by GC/MS after methylation. The viscosity and density of Kusum oil biodiesel are found to be nearer to those of diesel but compared to diesel, flash point is more. When the esters concentration in biodiesel is less, then the performance of biodiesel can be improved (Fig. 3).

Pecci GC et al. Bailey et al. [23, 24] revealed that in the last decade ethanol and biodiesel were considered to be the best known liquid biofuels and a number of studies reveal different chemical structures as possible biofuels and elevated their pros and cons. As per University of Idaho et al. [25, 26] 1996, nature of Biodiesel is non-toxic, have nil aromatics, compared to fossil diesel, less pollutant to water

Fig. 3 Transesterification process and preparation of Kusum oil biodiesel

and soil, higher biodegradability and have no Sulphur content. In neat form, utilizing biodiesel is safe, shows less oral and dermal toxicity, mutagenic and carcinogenic compounds. According to Howell et al. [27], it is the most environment friendly and sensitive in nature and also certain areas where environmental concerns and protection of worker attain high standards (underground mines, quarries). Important advantage of KME biodiesel is raw material availability independent for production.

As per Greek Government Gazette et al. [28], 1999, KME added to traditional marine diesel fuel. As per Neeft et al. [29]. PM emissions improve which encompass a severe disadvantage of the diesel engine, majorly in polluted areas similar to Mediterranean Sea. However low temperature operability of KME in absolute mode is still imperative. The parameters affecting the production of biodiesel from Kusum oil were optimized by using grey relational analysis in Taguchi method by Mahesh Babu et al. [12].

2.2 Preparation of KME

2.2.1 Removing Gums and Alkaloids

Using REMI Model-24 centrifuge machine, the crude Kusum oil was centrifuged at 950 rpm and collected the supernatant oil from heavy contaminates, with 100 ml crude oil 25 ml methanolic H_3PO_4 solution (12% v/v) was made homogenized and made it stand throughout the overnight. The next day, oil was taken separated from methanol and the filtration was done under suction to filter precipitated compounds through silica gel (960–120 mesh). On the next day oil was separated from methanol layer and the precipitated compounds were filtered through silica gel (60–120 mesh) under suction. For degumming the Kusum oil, Methanol and phosphoric acid filtrate could be recycled three times which makes the process more viable. The oil was stored with 0.1 aqueous NaOH solution throughout the night, after degumming.

Next day, the aqueous part was removed two times and washing was done two times utilizing water for removing the residual alkali. To remove the content of moisture from the oil, it is heated on boiling water for about an hour and then passed through wormed anhydrous Na_2SO_3 (in an oven at 105 °C before use). Oil obtained thus, stored as refined alkaloid-free Kusum oil (RKO). Thus in the whole process, 98% of the crude Kusum oil (CKO) was converted into RKO.

Transesterification in Two Steps

In esterification process, the degummed and alkali-free oil (RKO) was added to Sulphuric acid and methanol mixture in the ratio 50:10:1 (oil: $CH_3OH:H_2SO_4$, v/v/v) proportion and using magnetic stirrer it was stirred (5 lit capacity) at 900 RPM at 65 °C for three hours. After the completion of esterification, separation of the two layers was made within 30 min.

The lower layer was removed and then neutralization was done with methanoic caustic soda solution and from the oil, methanol was removed. The neutral oil is further mixed with NaOH and Methanol in the ratio 50:10:0.2 (oil:methanol:alkali) and mechanically stirred well at 900 rpm for 4 h at 55 °C. After the transesterification, the oil was separated by using separating funnel from the lower layer and washed with hot water 3 to 5 times for removing impurities and resultant transesterified oil (TEO) was stored for further analysis. This two-step transesterification resulted in conversion of 92% RKO into TEO.

2.2.2   Properties of Kusum Oil and Its Blends

Properties of kusum oil were obtained from Anacon Labs from the test samples, listed below in Table 1.

Table 1 Properties of Kusum oil, KME and its blends with diesel blends of KME

Blends of KME	Density @40 °C (Kg/m^3)	Calorific value (KJ/kg)	Kinematic viscosity @40 °C (cSt)	Flash point (°C)	Fire point (°C)
B10	804	42,150	3.15	78	81
B20	809	41,930	3.33	80	84
B30	818	41,890	6	84	87
B40	820	41,860	8.0	85	89
B50	827	41,820	9.01	87	90
B100	850	41,650	14.2	150	157
Raw oil	860	38,140	40.33	225	231
Diesel	840	42,490	3.05	85	78

Reference: Anacon Lab

3   Experimental Setup

The experimental set up, fuel measurement, fuel injection systems, engine modifications, dynamometers etc. were detailed. Fuel injection system consisted of port fuel injector; in-cylinder injector and ECU unit are discussed as follows.

3.1   Test Engine

The engine test setup consists of computerized single cylinder, 4 stroke, Diesel engine, Kirloskar make, Model TV1, water cooled, develops 5.2 kW power at 1500 rpm, stroke 110 mm, bore 87.5 mm. 661 cc, CR 17.5. Test engine is along with an eddy current dynamometer is used for load measurement and is water cooled. The engine load percentage was controlled manually. The propeller shaft is connected with universal joints. The engine consisted of an air box consisting of MS fabricated with orifice meter and manometer. The capacity of fuel tank is 15 L fuel metering column made of glass. Pipe in pipe Caloriemeter, 5000 psi piezo sensor range, with low noise cable are used. Crank angle sensor resolution is 1 degree, speed 5500 RPM with TDC pulse. The engine is connected to data acquisition system, 16 bit, 250 kS/s. The software used is "Enginesoft" which is Engine performance analysis software. Flow rate of fuel is measured by gravimetric basis and air flow rate is measured by volumetric basis. Fuel consumption is measured by using a burette for a particular specified time interval. During the time interval, the quantity of fuel consumed is measured by using stop watch. The engine is fitted with an air box M S fabricated with the orifice meter and manometer. Capacity of fuel tank is 15 lit with glass fuel metering column. Calorimeter used is pipe in pipe type. NI USB-6210, 16-bit, 250kS/s is used as Data acquisition device. AX-409 Piezo powering unit Model is used. Temperature measurement sensors are Type RTD, PT100 and Thermocouple, Type K. Load sensor used is Load cell, type strain gauge, range 0–50 kg. Fuel flow transmitter is DP transmitter, Range 0–500 mm WC. Air flow transmitter is Pressure transmitter, Range (−) 250 mm WC. Rotameter Engine cooling 40–400 LPH; Calorimeter 25–250 LP. Pump Type is Monoblock (Fig. 4).

3.2   Air Heater

To convert diesel mode into HCCI mode, the inlet air is heated by air heater of 800 W placed in the inlet manifold. The HCCI combustion process is controlled by the heated air to convert the fuel into vapor. To make homogeneous mixture, air heater is an important component and governs the starting of the ignition point. Air heater consists of heating element, ceramic pipe and heater cover. The maximum temperature of air that can be achieved by the present arrangement is 160 °C. The
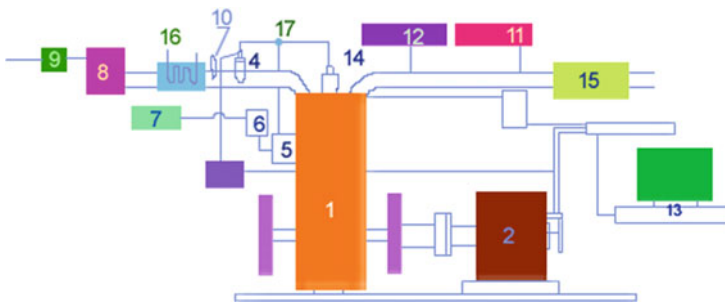
1. Kirloskar TV1 engine 2.Eddy current dynamometer 3.Direct injector 4.Port fuel injector 5.Fuel pump 6.Fuel filter 7.Fuel tank 8.Air stabilizing tank 9.Air filter 10.Temperature sensor 11.AVL smoke meter 12. AVL Di-gas analyzer 13.Combustion setup 14.Pressure transducer 15.Exhaust silencer 16.Air heater 17.Control valve

Fig. 4 Engine test rig setup block diagram
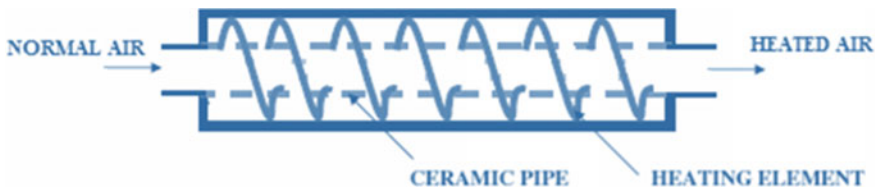
Fig. 5 Line diagram of electrical air heater

present investigation involves the inlet air temperature to be controlled in between the range of 40 °C and 100 °C (Fig. 5).

3.3 Fuel Injection System

Two injection systems are existing for HCCI mode of operation such as port fuel and direct injection systems. In HCCI mode, the fuel injection is fully automated and completely controlled by electronic control unit. Fuel injection system consisted of fuel tank, fuel filter, fuel pump, fuel injector and ECU.

3.4 In-Cylinder Injector

In this study, in-cylinder, direct injected multi-holes injector was used. Initially the engine was started by direct injector in diesel mode and then it was switched to

HCCI mode. Fuel injection timing was fixed as 5–10 deg bTDC and the injection duration was controlled by mechanical governor based on the speed of the engine. The switching between direct injection and port fuel injection were controlled by the mechanical governor. To start the port fuel injection, the direct injection is completely stopped as the fuel should be shared equally for both the injection systems. For maintaining the engine's rated speed the quantity of fuel from one injection system should be equally shared from both injection systems, which was achieved efficiently by mechanical governor. Thus the engine is converted as a HCCI engine and tests were carried out.

3.5 Port Fuel Injector

To prepare premixed air/fuel charge, port fuel injector was used. The premixed charge absorbs the heat from the inlet air and the homogeneous mixture of air–fuel was prepared. Port fuel injector was fixed at a distance of 6 cm from the inlet valve [30]. If the injector is placed far from the inlet valve, fuel gets deposited over the suction pipe. Hence, port fuel injector is placed near the inlet valve. To avoid the fuel accumulation in the suction pipe and making better mixing, port fuel injector is placed at an angle of 45° to the suction pipe (Ahmet 2015). The HCCI mode engine was run using premixed fuels and readings were taken upto 75% load condition. Under full load condition the operation of the engine was made both by direct and port fuel injected fuel, due to the difficulty observed in controlling the combustion.

The electronic controlled port fuel injector was controlled by ECU model. Fuel injection timing was fixed at 25 deg after top dead center (aTDC) during the suction stroke. Port fuel injection consists of fuel tank, electronic controlled fuel pump and injector. Fuel injection duration, injection quantity and injection pressure are controlled manually (Fig. 6).

Electronic control unit controls the fuel injection system efficiently, which consists of position sensor, speed sensor, fuel pump and control board. ECU monitors engine

Fig. 6 Schematic diagram of port fuel injection ECU unit
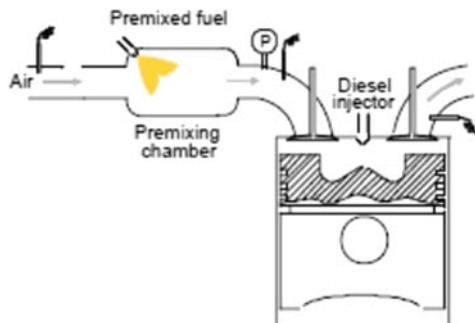
speed, if the engine speed is reduced due to load, it increases the fuel injection quantity from port fuel injector and maintains constant engine speed of 1800 rpm.

3.6 Measurement of Load and Speed

To eddy current dynamometer the engine shaft was connected. The engine was made to run at constant speed of 1800 rpm. Using dial gauge reading load of the engine was obtained. A photo sensor along with the digital speed indicator monitors the speed of the engine.

3.7 Fuel Supply Measurement

Using the diesel tank placed in the panel board, fuel was supplied to the engine. Also burette was attached in the same panel board. During the close of the fuel cock, fuel flow from the burette, not from the fuel tank. Fuel flow rate measurement was made by taking time taken for 20 cc of the fuel consumption.

3.8 Measurement of Temperature

Inlet air and exhaust gas temperatures were measured with chromel–alumel thermocouple (K-type). Cooling outlet temperature was measured using resistance temperature detector.

3.9 Experimental Procedure

In the present research work, experimental investigations were made on both conventional and HCCI mode engine operated by diesel, methyl ester fuels and blends. First the operation was done by conventional mode by diesel and biodiesels (Mustard, Kusum and chicken waste oil) and diesel–biodiesel blends of B20, B50 and B100. Performance parameters such as Brake thermal efficiency etc., emissions such as NOx, CO, HC, and smoke density were measured.

Later, the engine was operated using HCCI mode using diesel, three methyl esters and their blends. The performance and emission parameters were measured at different loads such as 25%, 50%, 75% and 100% respectively.

The fuel injection timing and duration of injection were measured by the position of the rocker arm in the combustion chamber. In HCCI operation, the air is preheated

Fig. 7 Test engine setup

and when the fuel is injected, absorbs heat from the vaporized air, homogeneous air–fuel mixture is prepared before the combustion process starts.

The research was carried out at different port fuel injection pressures and different inlet air temperatures. The purpose of the investigation is to find the optimal inlet air pressure and fuel injection pressure for different blends of fuel operated HCCI engine. The optimal blend, temperature and port fuel injection pressure were found and based on the combustion, performance and emission values (Figs. 7 and 8).

4   Results and Discussion

4.1   Effect of Air Temperature and Injection Pressure on Brake Thermal Efficiency

Figure 9 shows the graph between Brake Power (kW) and Brake Thermal Efficiency (%). The graphs show the effect of brake thermal efficiency on KME (Kusum Oil Methyl Ester) B20 blend at various port fuel injection pressures and temperatures. The port fuel injection pressure varied as 6 bar, 7 bar, 10 bar and 11 bar. The inlet air temperatures varied as 90 °C, 100 °C, 110 °C to make it in HCCI mode. Also the B20 biodiesel of KME was operated by CI mode. From the graphs it is inferred that as the inlet air temperature is increased, the brake thermal efficiency is increased which is shown by comparing B20 with HCCI mode 110 °C has shown more Brake Thermal Efficiency than B20 with HCCI mode 90 °C. Also as the injection pressure is increased with HCCI mode, the brake thermal efficiency
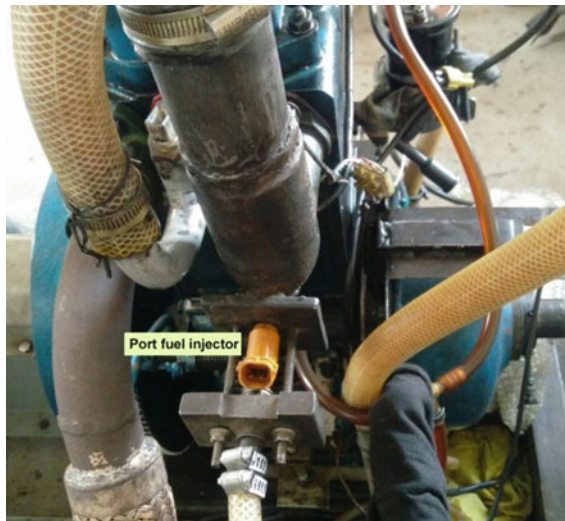
Fig. 8 Port fuel injector in the test engine

Fig. 9 Variation of brake thermal efficiency at 6 bar, 7 bar, 10 bar, 11 bar injection pressure at different inlet air temperatures for KME B20 blend

also increased as the atomization of the fuel is increased due to increase in injection as well as increase in temperatures. Due to atomization homogeneous charge was prepared which improved the combustion rate and combustion temperature. Also increase in inlet air temperature may shorten the combustion process and liberates high heat energy. The high combustion temperature vaporized more fuel and well premixed homogeneous charge was prepared and hence the brake thermal efficiency increased.

Fig. 10 Variation of brake thermal efficiency at 6 bar, 7 bar, 10 bar and 11 bar injection pressures at different inlet air temperatures for KME B50 blend

At 10 bar and 11 bar pressures, as the inlet air temperatures increased, the brake thermal efficiency decreased due to the fact that increase in inlet air temperature and injection more than certain limit resulted in advanced start of combustion and combustion duration is reduced.

The similar properties of changes are also observed in KME (Kusum Oil Methyl Ester) B50 blend. The port fuel injection pressure was varied as 6 bar, 7 bar, 10 bar and 11 bar. The inlet air temperatures are varied as 90 °C, 100 °C, 110 °C. As the injection pressure increased and inlet air temperatures increased, the brake thermal efficiency initially increased and then decreased as the port fuel injection pressure increased and inlet air temperature further increased. The same effect was also observed in the Fig. 10.

4.2 Effect of Air Temperature and Injection Pressure on NOx Emission

When biodiesel and biodiesel blends were used as fuels in conventional diesel engine, they emitted high NOx compared to diesel fuelled engine due to cetane number high and oxygen molecules of methyl ester. But, HCCI engine emits less NOx emission, even operated using neat biodiesel (B100) and blend fuels (B20 and B50) fuels. The NOx emissions were observed when the engine fuelled by biodiesel blends in HCCI mode at various injection pressures and inlet air temperatures. The graphs in Figs. 11 and 12 show the NOx emissions at port fuel injection pressures 6 bar, 7 bar, 10 bar and 11 bar and the inlet air temperatures varied as 90 °C, 100 °C, 110 °C and also conventional CI mode. The blends of fuel used were B20 and B50 by varying inlet pressures and temperatures observed that B20 and B50 fuelled HCCI mode engine

Fig. 11 Variation of NOx at 6 bar, 7 bar, 10 bar and 11 bar injection pressures at different inlet air temperatures for KME B20 blend
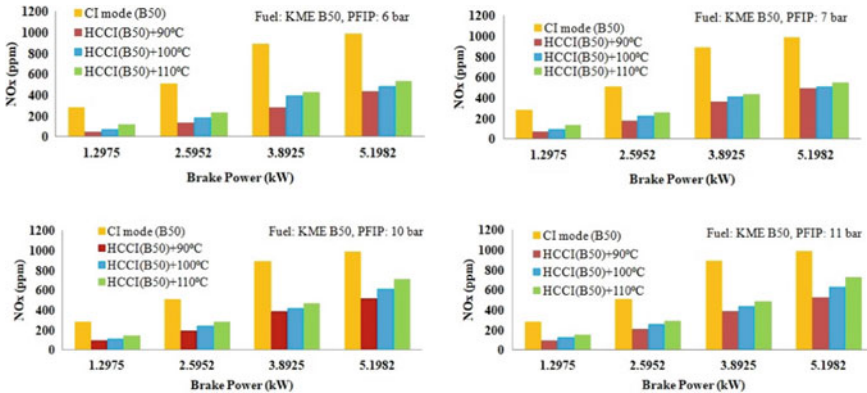
Fig. 12 Variation of NOx at 6 bar, 7 bar, 10 bar and 11 bar injection pressures at different inlet air temperatures for KME B50 blend

emitted low NOx emissions compared to conventional mode engine. HCCI mode engine reduced NOx emissions upto 40–50%, at low load operations and increased the emissions with load.

The same was observed in both B20 as well as B50 blends.

4.3 Effect of Air Temperature and Injection Pressure on Smoke Density

One of the advantages of HCCI mode engine is low smoke density even when operated by fuel blends KME (B20) and KME (B50). This is due to the fact that HCCI engine mode operates using premixed lean air–fuel charge and by self-ignition of charge combustion starts. This premixed fuel induction eliminates rich fuel region and high temperature regions in HCCI combustion, and the combustion takes place at multiple points in the combustion chamber, which eliminates flame front that occurs in conventional mode engine. These are the factors that make HCCI mode engine low smoke emission engine. Further increase in injection pressure and inlet air temperature may shoot up smoke emission due to misfire and incomplete combustion in the charge.

The results of the HCCI combustion also proved the low smoke emission compared to conventional mode engine, the diesel blended fuels B20 and B50 of Kusum oil Methyl Ester fuelled HCCI mode gave low smoke emissions compared to CI mode. The same decrease in smoke emission is seen in graphs for port fuel injection pressures 6 bar, 7 bar, 10 bar and 11 bar. From the Figs. 13 and 14 it is also observed that the smoke emissions have increased, when the HCCI mode engine operated with more than 9 bar injection pressure. The smoke emission further increased with increase in inlet air temperature. At 110 °C operated HCCI mode engine registered high amount of smoke values, which are almost nearer to the conventional mode engine.

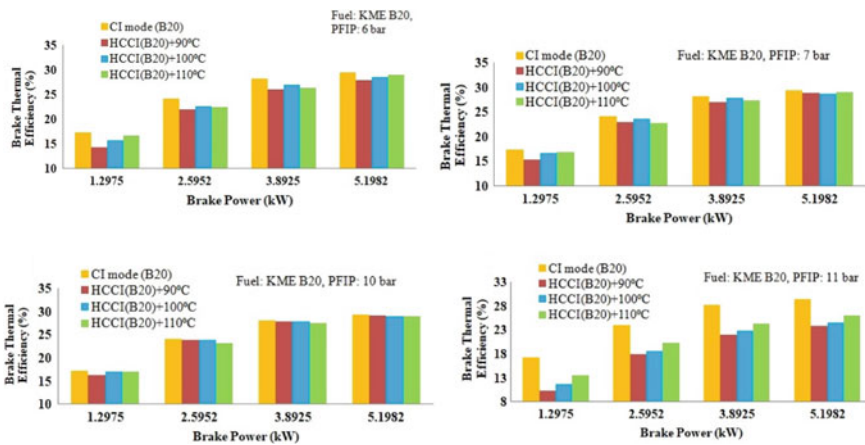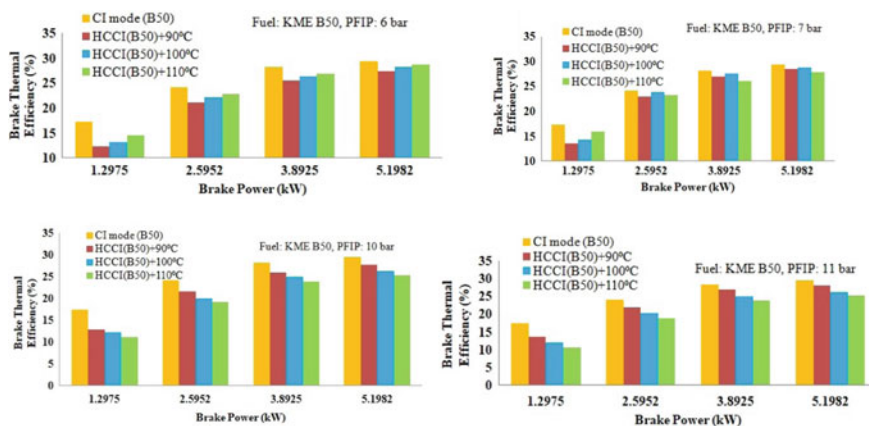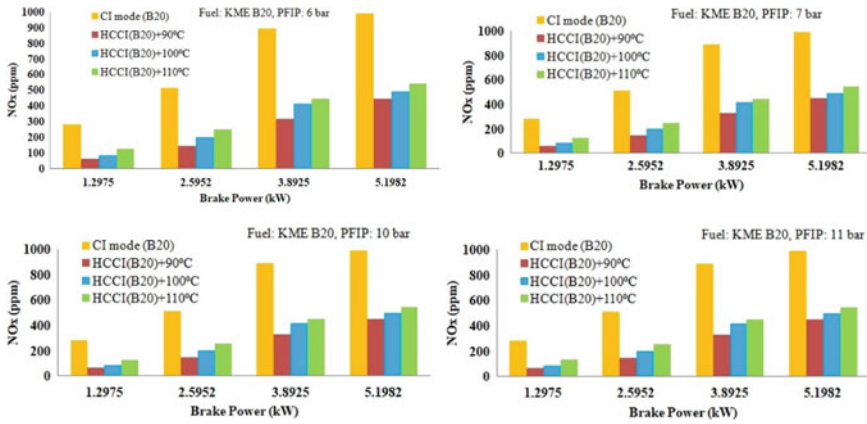**Fig. 13** Variation of smoke density at 6 bar, 7 bar, 10 bar, 11 bar injection pressures at different inlet air temperatures for KME B20 blend

Fig. 14 Variation of smoke density at 6 bar, 7 bar, 10 bar and 11 bar injection pressure at different inlet air temperatures for KME B50 blend

4.4 Effect of Air Inlet Temperature and Injection Pressure on CO Emission

In the study, KME (B20) and KME (B50) fuelled HCCI mode engine registered low CO emissions compared to diesel fuelled engine. This is due to the lack of oxygen in combustion chamber. Biodiesels have nearly 11% more oxygen molecules than petroleum diesel. Hence accelerates the combustion process and converts the CO molecule into CO_2.

The variation of emission of CO with different BP for injection pressures 6 bar, 7 bar, 10 bar, 11 bar and 90 °C, 100 °C,110 °C air temperatures operated KME blends B20 and B50 fuelled HCCI mode were shown in figures. Compared to conventional mode engine, CO emissions were high, and the value of CO is decreased with increasing the fuel injection pressure and inlet air temperature. Initially, the CO emissions decreased upto 10 bar injection pressures at all temperatures, but at 11 bar injection pressure it increased at all temperatures. This is due to the fact that by increasing the air temperature, mixture quality was improved and combustion process accelerated. When the charge gets complete combustion, all the CO molecules get oxidized and converted into CO_2.

But at 11 bar pressure, the CO emissions shoot up with increase in injection pressure during the low load conditions. Formation of CO further increased with increase in temperature. The reason is at high injection pressure, accumulation of fuel in the piston crevice takes place and exhausted without combustion. The high fuel injection causes liner wetting and oil dilution, which leads to CO emission high. Another reason is the inlet air temperature; the higher the inlet air temperature advances the start of combustion and reduces the combustion duration. Due to the low combustion duration, the combustion process shortened and combustion will complete before the piston reaches the TDC position. Due to the short combustion process, the time available is less for combustion, which caused high CO emission. This was evident in the figures clearly (Figs. 15 and 16).

Fig. 15 Variation of CO emission at 6 bar, 7 bar, 10 bar and 11 bar injection pressures at different inlet air temperatures for KME B20 blend
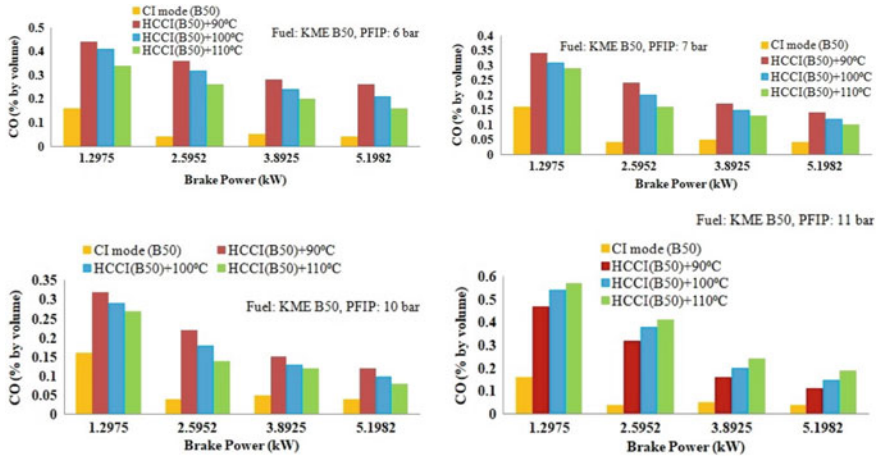
Fig. 16 Variation of CO emission at 6 bar, 7 bar, 10 bar and 11 bar injection pressures at different inlet air temperatures for KME B50 blend

4.5 Effect of Air Temperature and Injection Pressure on HC Emission

Figures indicate the variation of hydrocarbon emission with BP for 6 bar, 7 bar, 10 bar and 11 bar injection pressures and 90 °C, 100 °C and 110 °C inlet air temperatures. It is observed that the HCCI mode engine emitted high HC emissions operating with various injection pressures and temperatures. The levels of HC emissions from HCCI mode were nearly twice higher than the conventional mode engine. This is due to the fact that HCCI mode engine utilizes lean premixed charge, that leads to partial burn

or no combustion at certain locations. From the figures, it is observed that increasing fuel injection pressure and inlet air temperature reduces the HC emission due to high combustion temperature. Beyond that, HCCI mode engine turns to operate with high HC emission due to short combustion duration and misfiring of the charge.

Figures 17 and 18 show the level of formation of HC decreased with increase in the engine load. This is due to the fact that increase in engine load raises the combustion temperature, which favors in reducing the HC emission.
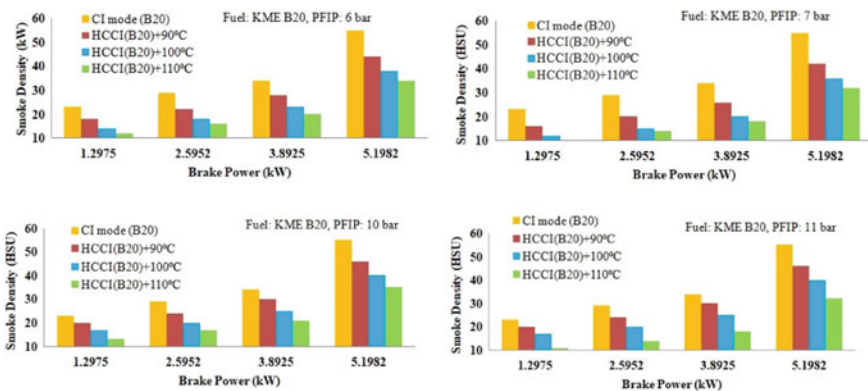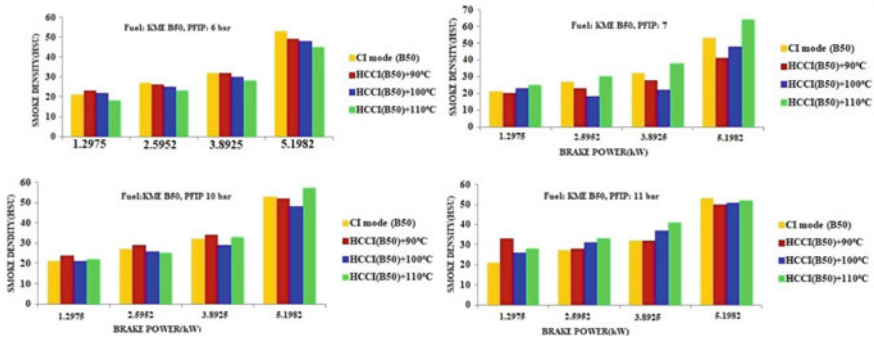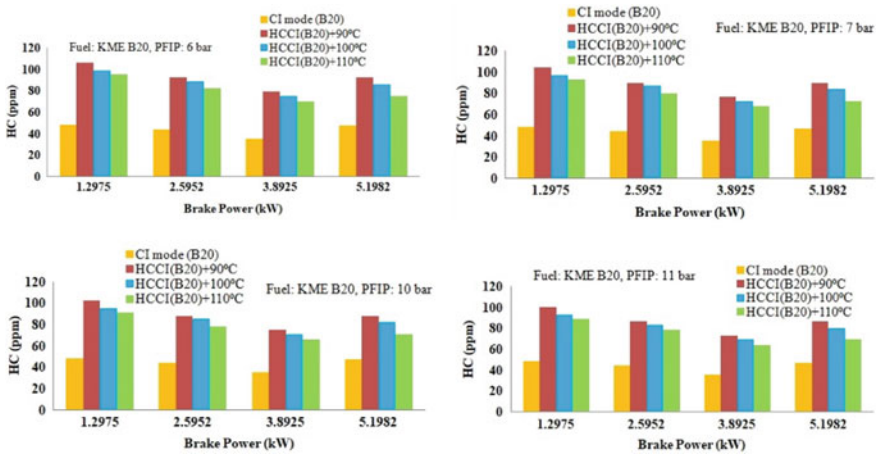

Fig. 17 Variation of smoke density at 6 bar, 7 bar, 10 bar and 11 bar injection pressures at different inlet air temperatures for KME B20 blend
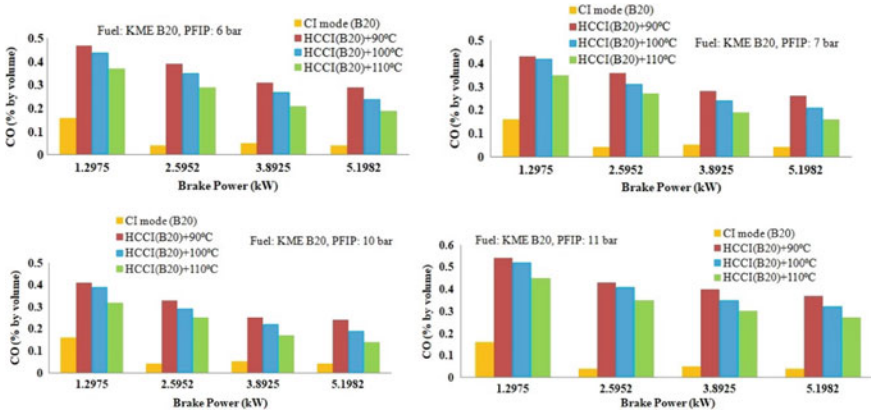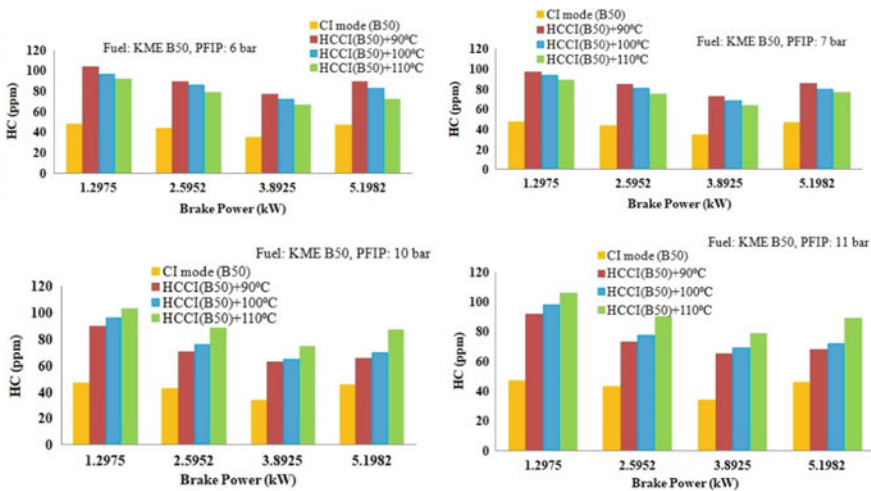

Fig. 18 Variation of HC Emissions at 6 bar, 7 bar, 10 bar and 11 bar injection pressures at different inlet air temperatures for KME B50 blend

5 Conclusion

- When the inlet air temperature is increased, the brake thermal efficiency is also increased. Also as the injection pressure increased with HCCI mode, the brake thermal efficiency also increased.
- At 10 bar and 11 bar pressures, as the inlet air temperatures increased, the brake thermal efficiency decreased owing to the fact that inlet air temperature increases and injection more than certain limit resulted in advanced start of combustion and also combustion duration is reduced.
- With biodiesel and biodiesel blends used as fuels in conventional diesel engine, they emitted high NO_x in comparison with diesel fuelled engine owing to high Cetane number and oxygen molecules of methyl ester.
- B20 and B50 fuelled HCCI mode engine emitted low NO_x emissions compared to conventional mode engine.
- HCCI mode engine emits with low smoke density even when operated by fuel blends KME (B20) and KME (B50). This is due to the fact that HCCI engine mode operates using premixed lean air–fuel charge and by self-ignition of charge combustion starts.
- The smoke emission increased as the inlet air temperature increased.
- Compared to conventional mode engine, emissions of CO were high, and the CO emission is decreased with increasing the fuel injection pressure and inlet air temperature.
- The CO emissions increased more with injection pressure increase during the low load conditions.
- As the fuel injection pressure and inlet air temperature increases, reduced the HC emission owing to high combustion temperature. Beyond that, HCCI mode engine turns to operate with high HC emission due to short combustion duration and misfiring of the charge.

References

1. Talupula NVMB, Rao PS, Kumar BSP, Praveen C (April 2017) Alternative fuels for internal combustion engines: overview of current research. SSRG Int J Mech Eng (SSRGIJME) 4(4)
2. Çelebi Y, Aydın H (2019) An overview on the light alcohol fuels in diesel engines. Fuel 236:890–911. https://doi.org/10.1016/j.fuel.2018.08.138

3. Agarwal AK (2007) Biofuels (alcohols and biodiesel) applications as fuels for internal combustion engines. Prog Energy Combust Sci 33:233–271. https://doi.org/10.1016/j.pecs.2006.08.003

4. Heywood JB (1988) Internal combustion engines fundamentals. McGraw-Hill, New York (USA)

5. Sindhu R, Rao GAP, Murthy KM (2018) Effective reduction of NOx emissions from diesel engine using split injections. Alexandria Eng J 57:1379–1392. https://doi.org/10.1016/j.aej.2017.06.009

6. Wang Q, Sun W, Guo L, Fan L, Cheng P, Zhang H, et al (2019) Effects of EGR and combustion phasing on the combustion and emission characteristic of direct-injection CI engine fueled with n-butanol/diesel blends. Energy Proc 160:364–71. https://doi.org/10.1016/j.egypro.2019.02.169

7. Rahman A, Ruhul AM, Aziz MA, Ahmed R (2016) Experimental exploration of hydrogen enrichment in a dual fuel CI engine with exhaust gas recirculation. Int J Hydrogen Energy 1–10. https://doi.org/10.1016/j.ijhydene.2016.11.109

8. Algayyim SJM, Wandel AP, Yusaf T (2019) Butanol–acetone mixture blended with cottonseed biodiesel: spray characteristics evolution, combustion characteristics, engine performance and emission. Proc Combust Inst 37:4729–39. https://doi.org/10.1016/j.proci.2018.08.035

9. Agarwal AK, Dhar A, Gupta JG, Kim WI, Choi K, Lee CS (2015) Effect of fuel injection pressure and injection timing of Karanja biodiesel blends on fuel spray, engine performance, emissions and combustion characteristics. Energy Convers Manag

10. Sanli H, Alptekin E, Canakci M (2019) Production of fuel quality ethyl ester biodiesel: 1. Laboratory-scale optimization of waste frying oil ethanolysis, 2. Pilot-scale production with the optimal reaction conditions. Waste Biomass Valor 10:1889–1898. https://doi.org/10.1007/s12649-018-0195-z

11. Calam A, Solmaz H, Yılmaz E, Içingür Y (2019) Investigation of effect of compression ratio on combustion and exhaust emissions in A HCCI engine. Energy, Elsevier, 168(C):1208–1216

12. Talupula NVMB, Rao PS, Kumar BSP, Multi-objective optimization of kusum oil biodiesel production using grey relational analysis in taguchi method

13. Das P, Subbarao PMV, Subrahmanyam JP (2015) Control of combustion process in an HCCI-DI combustion engine using dual injection strategy with EGR. Fuel 159:580–589. https://doi.org/10.1016/j.fuel.2015.07.009

14. Turkcan A, Ozsezen AN, Canakci M (2013) Effects of second injection timing on combustion characteristics of a two stage direct injection gasoline—alcohol HCCI engine. Fuel 111:30–39. https://doi.org/10.1016/j.fuel.2013.04.029

15. Uyumaz A (2015) An experimental investigation into combustion and performance characteristics of an HCCI gasoline engine fueled with n-heptane, isopropanol and n-butanol fuel blends at different inlet air temperatures. Energy Convers Manag 98:199–207. https://doi.org/10.1016/j.enconman.2015.03.043

16. Jia Z, Denbratt I (2018) Experimental investigation into the combustion characteristics of a methanol-diesel heavy duty engine operated in RCCI mode. Fuel 226:745–753. https://doi.org/10.1016/j.fuel.2018.03.088

17. Lalwani A, Awate S, Chowdhury A, Sreedhara S (2019) Conversion of a single-cylinder internal combustion engine to dual—mode homogeneous charge compression ignition engine. Clean Technol Environ Policy 21:23–37. https://doi.org/10.1007/s10098-018-1613-4

18. Dou Z, Yao C, Wei H, Wang B, Liu M, Chen C et al (2017) Experimental study of the effect of engine parameters on ultrafine particle in diesel/methanol dual fuel engine. Fuel 192:45–52. https://doi.org/10.1016/j.fuel.2016.12.006

19. Wang Y, Yao M, Li T, Zhang W, Zheng Z (2016) A parametric study for enabling reactivity controlled compression ignition (RCCI) operation in diesel engines at various engine loads. Appl Energy 175:389–402. https://doi.org/10.1016/j.apenergy.2016.04.095

20. Park SH, Yoon SH (2016) Effect of dual-fuel combustion strategies on combustion and emission characteristics in reactivity controlled compression ignition (RCCI) engine. Fuel 181:310–318. https://doi.org/10.1016/j.fuel.2016.04.118

21. Kant P, Shuirong W, Chaliha S, et al (2011) Going beyond Jatropha: can an expanded land and feedstock base help India meet its ambitious biodiesel target institute of green economy, IGREC working paper IGREC-22
22. Acharya SK, Mishra AK, Rath M (2011) Performance analysis of karanja and kusum oils as alternative bio-diesel fuel in diesel engine. Int J Agric Biol Eng 4(2):23–28
23. Pecci GC, Clerici MG, Giavazzi F, Ancillotti F, Marchionna M, Patrini R (1991) Oxygenated diesel fuels, part 1—structure and properties correlation. Proceedings of the ninth international symposium on alcohol fuels (ISAF), Firenze, pp 321–6
24. Bailey B, Eberhardt J, Goguen S, Erwin J (1997) Diethyl ether (DEE) as a renewable diesel fuel. SAE Paper No. 972978, SAE, Warrendale, PA
25. University of Idaho (Department of Biological and Agricultural Engineering) (1996) Acute toxicity of biodiesel to fresh water and marine organisms. Development of rapeseed biodiesel for use in high-speed diesel engines, Progress Report, pp 117–31
26. University of Idaho (Department of Biological and Agricultural Engineering) (1996) Biodegradability of biodiesel in the aquatic environment. Development of rapeseed biodiesel for use in high-speed diesel engines, Progress Report, pp 96–116
27. Howell S, Weber AJ (May 1997) Biodiesel use in underground metal and non-metal mines. MARC-IV, LLC, Consulting. http://www.dieselnet.com/papers/9705howell.html
28. Greek Government Gazette (1999) Marine fuel requirements and test methods 133(B):2103–4
29. Neeft J, Makkeem P, Moulijn J (1996) Diesel particulate emission control, review article. Fuel Process Technol 47(1):1–69
30. Fang Q, Fang J, Zhuang J, Huang Z (2012) Influences of pilot injection and exhaust gas recirculation (EGR) on combustion and emissions in a HCCI-DI combustion engine. Appl Therm Eng 48:97–104

Advancement in Electrical Control Systems

Load Frequency Control in Three-Area Interconnected Power System Using PID Tuning Based on Artificial Bee Colony Optimization

Nashwa Shaik and Benjamin Shimray

Abstract This work discusses the load frequency control of a three-area interconnected power system regulated employing a PID controller whose gain parameters are tuned using one of the optimization algorithms instigated and inspired by smart foraging or searching deportment of honey bees. The three-area power system depicted is assembled in such a way that the area-1 consists of a non-reheated turbine, area-2 consists of a reheated turbine while the third area consists of a combination of both non-reheated and reheated turbine units as the power consumed is profoundly generated by thermal power plants across the world and they exist to a greater degree. All the existing areas are equipped with PID controllers, and the objective function taken into account is Integral Time Absolute Error (ITAE). To subdue all the fluctuations attributed to the perturbations in the system and reacquire the frequency to the nominal quantity swiftly is primary intent of this work. The performance of the controller is simulated in the MATLAB/ SIMULINK version. The results depicted the swift settling down of the frequency deviations with minimum steady state error.

Keywords Load frequency control (LFC) · Artificial bee colony (ABC) · Area control error (ACE) · PID controller

1 Introduction

Generation, transmission, and distribution of electricity to various loads are what a power system network is meant for. It has been developed exceptionally over the last few decades by [1]. Various components connected in the network of power system are usually subtle to the flair of the electrical power attributes such as voltage and frequency and their continuity. The load on the power system varies continually from time to time while the frequency is related inversely with the variation in load and the frequency of the system is influenced by the variation in real power.

N. Shaik · B. Shimray (✉)
Department of Electrical Engineering, National Institute of Technology Manipur, Imphal 795004, India
e-mail: benjaminshimray@gmail.com

181

Frequency in fact is cresting on real power, and voltage veritably is contingent on the reactive power [2]. Regulation of power flow among various areas while maintaining the frequency constant is regarded as Load Frequency Control (LFC). The primary intentions of LFC in multiple area interconnected power system (PS) are to match the entire power system load, to manage the error in system electrical frequency to zero. To distribute the generation among the control areas for that there would be a matching between tie-line power flows and schedules of power flow by [2].

A power system in general comprises multiple areas of generating units which are interconnected together so that the power could be exchanged between the utilities. The electric energy attributes such as frequency, tie-line power flows, and voltage in interconnected systems have to be preserved within the prescribed limits of the nominal values.

LFC in interconnected power system can be obtained by several methods. To curtail the Area Control Error (ACE), the first proposed control methodology is Integral Control Action, but the activity of the system is restricted by its integral gain. PID type controller is considerably employed for the resolution of LFC problem irrespective of the potential of present control techniques with different structures due to their simplicity, reliability, faster operation, and efficiency.

The traditional methods such as trial and error method and Cohen-Coon are not able to provide fine robust performance. Also, the controllers in use conventionally have some other problems such as objectionable overshoot in speed and sluggish response owing to sudden load disturbance. The impediments in LFC are in devising a controller that is robust and in obtaining the optimal solution by optimizing its parameters effectively. To accomplish this, many optimization techniques are applied and accessible in literature such as Genetic Algorithm (GA), Differential Evolution Algorithm (DEA), Particle Swarm Optimization (PSO) technique, Bacterial Foraging Optimization (BFO) [3], Fuzzy Logic Control, and other intelligent techniques.

This work discusses the LFC for a three-area interconnected PS constituting of non-reheated thermal power turbine units and area comprising the combination of reheated and non-reheated thermal turbine power units. To display the effectiveness of the ABC technique, it is assimilated with Trial and Error method.

2   Modeling of Power System

A matter of contention to a power system operator is Automatic Generation Control (AGC). The robust frequency controller design for a multiple area has been an immense challenge in stability and control of PS. The modeling of a power system can be depicted as shown in Fig. 1.

The thermal power plant can be modeled where it contains speed governor, turbine, and generator.

Fig. 1 Control loops in a synchronous generator
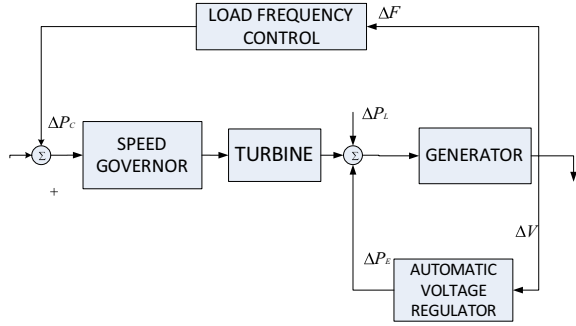
2.1 Modeling of Speed Governing System

The following order of events out turn by the command signals (ΔPC): the upward movement of the pilot valve, the movement of piston downwards when the oil with high pressure rushes on the upper portion of the piston, thereby opening the valve corresponding the steam suitably, the turbine speed spurs resulting in the frequency to mount.

2.2 Turbine Model

Changes in the opening of the steam valve (ΔYE) affect the response of the steam turbine with respect to the power output. The range of the time constant is 0.2 to 2.5 s.

2.3 Load-Generator Model

The frequency and the change or augmentation in the input power to the generator-load can be related as:

$$\Delta F(S) = \left(\frac{KPS}{1 + TPS} \right) * [\Delta PG(S) - \Delta PD(S)] \tag{1}$$

The isolated power system composing turbine, generator, governor, load, and a thermal power plant with a non-reheat turbine is illustrated in the Fig. 2.

Owing to the presence of various stages because of high and low steam pressure, the reheat turbine block can be modeled as a second order unit. The reheat turbine's transfer function can be denoted as:
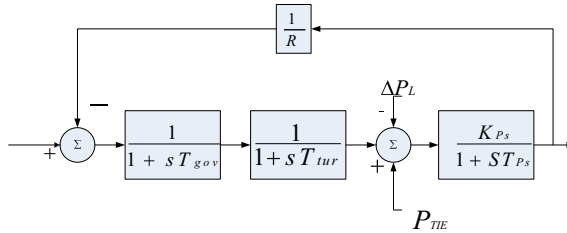
Fig. 2 Non-reheat turbine in a power system
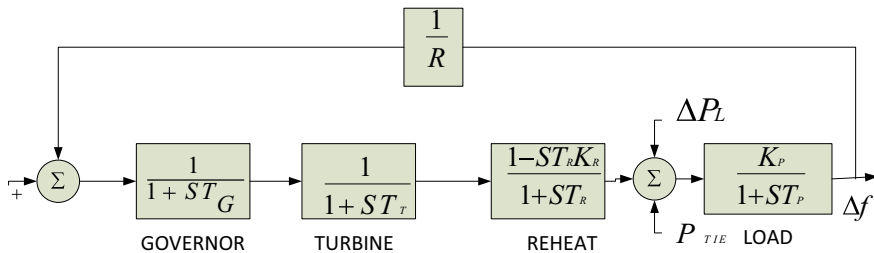
Fig. 3 Power system with a reheat turbine

$$GR(S) = \frac{1 + KrTrs}{1 + Trs} \tag{2}$$

where K_r denotes reheat time during the low pressure and Tr denotes reheat time during the high pressure. The block diagram of a thermal power plant with reheat turbine can be represented as in Fig. 3.

An interconnected PS in general is a category of control areas connected by tie lines. The motion of the valve because of the disturbances in three areas is given by [4].

$$\Delta xE1(S) = \left[\frac{1}{1 + STG1}\right]\left[\Delta PC1 - \frac{1}{R1}\Delta F1(S)\right] \tag{3}$$

$$\Delta xE2(S) = \left[\frac{1}{1 + STG2}\right]\left[\Delta PC2 - \frac{1}{R2}\Delta F2(S)\right] \tag{4}$$

$$\Delta xE3(S) = \left[\frac{1}{1 + STG3}\right]\left[\Delta PC3 - \frac{1}{R3}\Delta F3(S)\right] \tag{5}$$

The changes in power turbine are given by:

$$\Delta PC1 = \left[\frac{1}{1 + STt1}\right][\Delta E1(S)] \tag{6}$$

$$\Delta PC2 = \left[\frac{1}{1 + STt2}\right][\Delta E2(S)] \tag{7}$$

$$\Delta PC3 = \left[\frac{1}{1 + STt3}\right][\Delta E3(S)] \tag{8}$$

The frequency deviation in the three area is given by:

$$\Delta F1(S) = [\Delta PG1(S) - \Delta PD1(S) - \Delta PTIE1(S)]\left[\frac{KPS1}{1 + STPS1}\right] \tag{9}$$

$$\Delta F2(S) = [\Delta PG2(S) - \Delta PD2(S) - \Delta PTIE2(S)]\left[\frac{KPS2}{1 + STPS2}\right] \tag{10}$$

$$\Delta F3(S) = [\Delta PG3(S) - \Delta PD3(S) - \Delta PTIE3(S)]\left[\frac{KPS3}{1 + STPS3}\right] \tag{11}$$

The tie-line power deviation of three area:

$$\Delta PTIE1(S) = \frac{K12}{S}[\Delta F1(S) - \Delta F2(S)] + \frac{K13}{S}[\Delta F1(S) - \Delta F3(S)] \tag{12}$$

$$\Delta PTIE2(S) = \frac{K23}{S}[\Delta F2(S) - \Delta F3(S)] + \frac{K13}{S}[\Delta F2(S) - \Delta F1(S)] \tag{13}$$

$$\Delta PTIE3(S) = \frac{K31}{S}[\Delta F3(S) - \Delta F1(S)] + \frac{K32}{S}[\Delta F3(S) - \Delta F2(S)] \tag{14}$$

Area control error for three area is given by:

$$ACE1 = \Delta PTIE1 + B1\Delta F1(S) \tag{15}$$

$$ACE2 = \Delta PTIE2 + B2\Delta F2(S) \tag{16}$$

$$ACE3 = \Delta PTIE3 + B3\Delta F3(S) \tag{17}$$

2.4 Objective Function

A classical LFC is characterized by tie-line power flow control, and every area has a tendency to decline its ACE to zero. In each of the area, the control error comprises an incorporation of frequency and tie-line error. The individual area control errors (ACE) are the error input to the controllers which is given by:

$$ACE_i = \Delta P_{TIE,i} + Bi\Delta F \qquad (18)$$

Where number of areas is represented by i. PID controllers along with the area control errors

$$UI = KP, IACEI + \int ACEIdt + KD, I\frac{d(ACEI)}{dt} \qquad (19)$$

Here, the ITAE is used as an objective function for the LFC.

3 Artificial Bee Colony

Honeybees come in the group of insects that are most closely analyzed due to their foraging behavior, learning and memorizing, and characteristics of information sharing igniting interest in swarm intelligence research areas.

Karaboga and Bastruk, Akay and Karaboga [5] have proposed ABC algorithm for the optimization problems which is in accordance with the smart searching or foraging deportment of honeybees. The brilliant foraging deportment of honeybees warms is simulated by the algorithm. Being simple and robust, it has gained popularity and is basically having a random probability distribution. As it organizes and carries out global search and local search in every iteration, the likelihood of detecting the optimal gain specifications has notably been supplemented thus avoiding local optimum to a greater degree.

ABC constitutes of three categories of bees: employed bees, onlookers and scouts. A bee which goes to the food source which it has already been inspected by it previously is the employee bee. A bee which remains on the dance arena to select the food source is termed as the onlooker bee. A bee which carries out random investigation is a scout bee. By enacting the waggle dance, the bees communicate the flair of the food sources among themselves.

In ABC algorithm, the employed bees are identical in number to the onlooker bees and food or nectar sources surrounding the hive. The employee bee of which the food sources have been whipped by the rest of the bees of its kind becomes a scout.

The steps carried out in the ABC algorithm are as given by Akay and Karaboga [5]:

- Initialization
- Repeat
- Allocating a certain position of the nectar sources present in the memory to the employed bees
- Allocating a certain position of the food sources present in the memory to the onlookers.

- Dispatching scout bees to the investigating zone for the inspection of fresh food sources.
- UNTIL (meeting the requirements).

In ABC algorithm, every sequence of the foraging comprises three operations: To dispatch the employed bees to the fresh nectar sources and analyze the nectar contents, selection of the respective nectar sources by the onlooker bees after obtaining the details from employed bees and determining the quantity of nectar in the food sources, to dispatch the scout bees to the possible food sources.

Fig. 5 depicts the flowchart of ABC algorithm. At the stage of initialization, a random selection of a group of nectar sources is done by the bees and the nectar contents have been analyzed. After approaching the hive, the bees part the details on the nectar content with the onlookers remaining on the dance zone in the hive.

Next, each employed bee proceeds to the nectar source area which is sought by it during the last sequence according to the position existing in its memory, and selects a fresh food source with the aid of perceptible details that exists in the nearby arena of the current zone.

Now, an onlooker bee tends to choose a nectar source in accordance with the details on nectar content that is dispersed by the employed bees in the dancing zone. As the nectar quantity of a source is high, the possibility of choosing that nectar source by the onlooker is also higher. After reaching the chosen sector, it opts a fresh nectar source in the proximity of the existing one in the further is dependent on the contrast of the nectar source locations. While the nectar source is exploited by the bees, a scout bee determines a fresh nectar source randomly and replaces the exploited one by it.

At every sequence, not more than a single scout goes out to search a fresh nectar source while the employed bees remain equal in number with the onlookers.

In ABC algorithm, the nectar source location concerns a feasible resolution to the minimization problem while the quantity of nectar in a nectar source concerns the flair or fitness of the corresponding solution.

An employed or onlooker bee possibly generates a change in solution in its memory to find a fresh nectar source and determines the quantity of nectar or fitness value of the fresh nectar source or new solution.

The details perceived from the employed bees are evaluated and chosen with corresponding probability related to the quantity of the nectar by the onlooker bees. The employed bee generates a change in the location or solution in its memory and examines the quantity of nectar of the corresponding source only if the nectar quantity is more than the last one, the fresh location is memorized by the bee, forfeiting the last one.

The nectar source is selected by the onlooker bee based upon the probability value corresponding to the source which is evaluated by the expression Akay and Karaboga [5]:

$$PI = \frac{fiti}{\sum\limits_{n=1}^{SN} fitn} \tag{20}$$

Here, fiti is fitness or flair of the solution 'i' which is assessed by the employed bee and is proportionate to the nectar quantity of the nectar source in the location to generate a food location from the older one; the initial population is distributed randomly of SN solutions or the nectar source locations. ABC uses the following expression by Akay and Karaboga [5]:

$$Vij = Xij + \phi ij(Xij - Xkj) \tag{21}$$

Here, $k \in \{1, 2, ., BN\}, j \in \{1, 2, \ldots, D\}$ are indices picked, k is obtained randomly and it is varied from i which is any casual value lying in the range $[-1, 1]$. It regulates the generation of a nearby food source location engulfing x_{ij}, and the change corresponds to the neighborhood food positions by the bee visually. As the variation between x_{ij} and x_{kj} declines, the concernment on the location x_{ij} declines too. Hence, as foraging reaches the optimum solution in the search volume, the stride length is accordingly declined. If a quantity generated by it outdoes beyond its predecided limit, the quantity is set to a permissible value. The parameter value surpassing its limit must be fixed to its limit.

In algorithm, a random production of a position and replacement of the abandoned source with it simulates it. If a location cannot revamp further using a predecided number of sequences called 'limit' then that nectar source is considered to be deserted.

Subsequent to the production of every candidate food source location 'v_{ij}', the bee evaluates the performance and is compared. Thus, the three parameters of control used in the basic ABC are: Population, limit, and Maximum Cycle Number (MCN).

In the ABC algorithm, the onlooker bees and employed bees conduct the operation of exploitation while the scout bees control the exploitation process.

3.1   ABC-Based PID Type of LFC

Though there have been significant developments in control technology, PID controllers are employed in most of the industries and in power system sectors as well due to their wide class performance, resilient performance for a wider range of operation [2, 3]. The operation of the PS is dependent on the tuning of the PID controllers' gain parameters with respect to the frequency deviations as the load changes.

The block diagram of ABC-tuned PID controller to resolve the LFC problem for every area of control is shown in the Fig. 4.
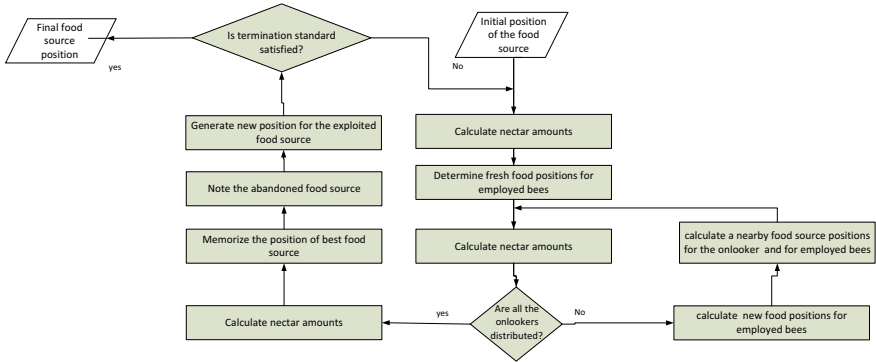
Fig. 4 Flowchart diagram for ABC algorithm
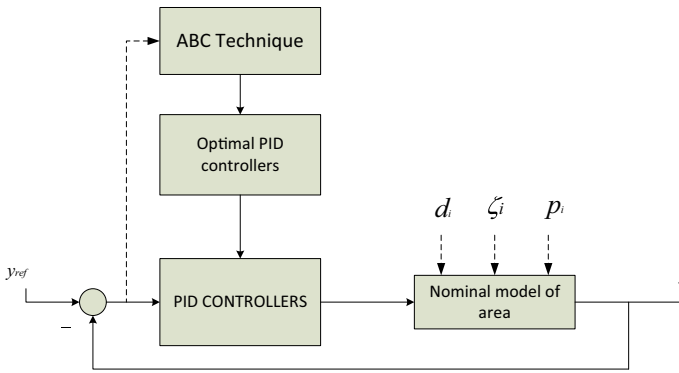
Fig. 5 ABC-based PID controller

The control vector in each control area for PID controller by considering *ACEi* as the system output is given by:

$$ui = kpiACEi + kli \int ACEidt + kdi\frac{d}{dt}ACEi \tag{22}$$

The gain parameters are modeled using ABC and then the PID controller produces a control signal that is applied to the set point of governor in all the areas. Integral Time Absolute Error is the objective function considered here. In order to calculate objective function, the time domain simulation is carried out for a certain simulation period. For improving the response of the system with reference to time of settling and peak overshoots, the objective function is minimized. The parameter bounds of PID controller to formulate the gain parameters can be composed as:

$$k_{Pi}^{\min} \leq k_{Pi} \leq k_{Pi}^{\max}$$
$$k_{Ii}^{\min} \leq k_{Ii} \leq k_{Ii}^{\max} \qquad (23)$$
$$k_{Di}^{\min} \leq k_{Di} \leq k_{Di}^{\max}$$

Usual scale of the parameters optimized is [0.01–20].

4 Results of Simulation

A three-area PS interconnected is taken for the analysis of LFC. Area-1 comprises thermal plant with a reheated turbine, area-2 comprises thermal plant with a non-reheated turbine, and area-3 consists of a combined reheated and non-reheated thermal unit. Fig. 6 shows the proposed simulation model with ABC-PID controller. The MATLAB code using ABC algorithm has been run in MATLAB software.

ABC parameters considered for optimization are as follows: Population size = 100, Maximum number of iterations = 70, lower and upper limits are 0 and 10, and simulation time = 10 s. Simulation is done with 0.1pu step load perturbation in area-(1), area-(2), and area-(3), respectively. The optimized controller parameters, frequency deviations, are as shown (Figs. 7, 8, 9,10, 11, 12, 13, 14, 15, and 16. Tables 1, 2, and 3).

It can be perceived from the above results that the deviation in frequency when subjected a sudden disturbance settle down quickly with a minimum steady state error as desired contrasted with the trial and error values.
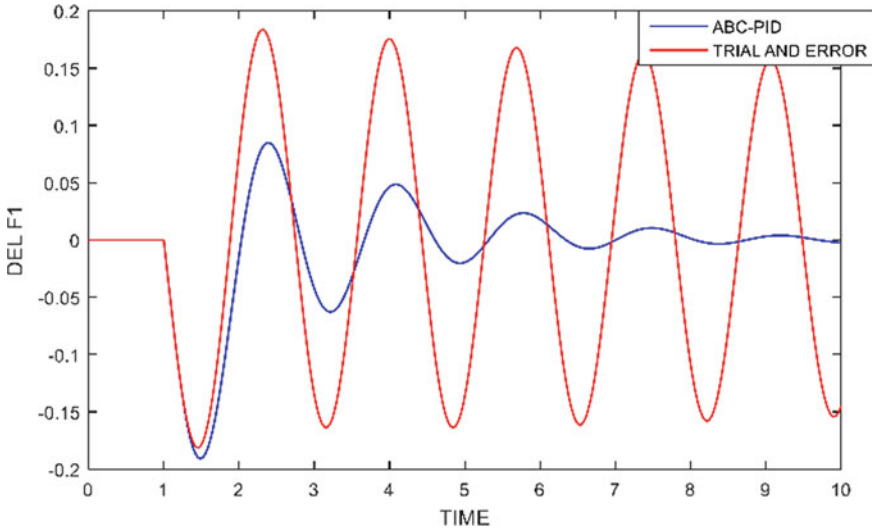
Fig. 7 Frequency fluctuation in area-1 due to 0.1pu step change in area-1
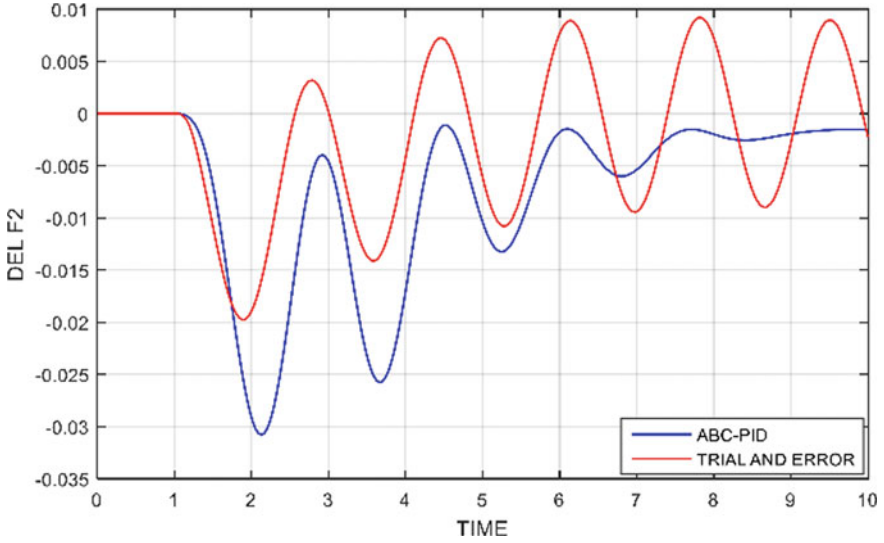
Fig. 8 Frequency fluctuation in area-2 due to 0.1pu step change in area-1
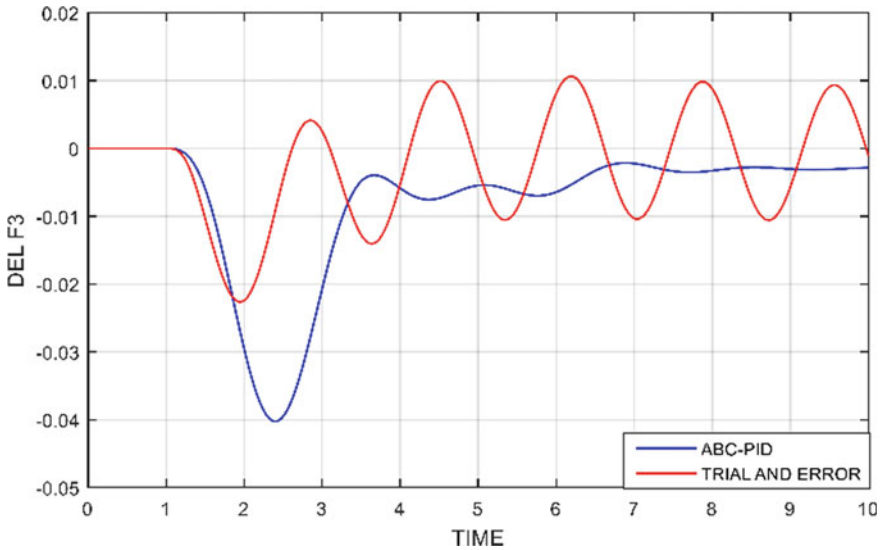
Fig. 9 Frequency fluctuation in area-3 due to 0.1pu step change in area-1

5   Conclusion

This work discusses the use of ABC-tuned PID controller in a three-area inter-connected PS using dissimilar types of turbine in thermal power generating units
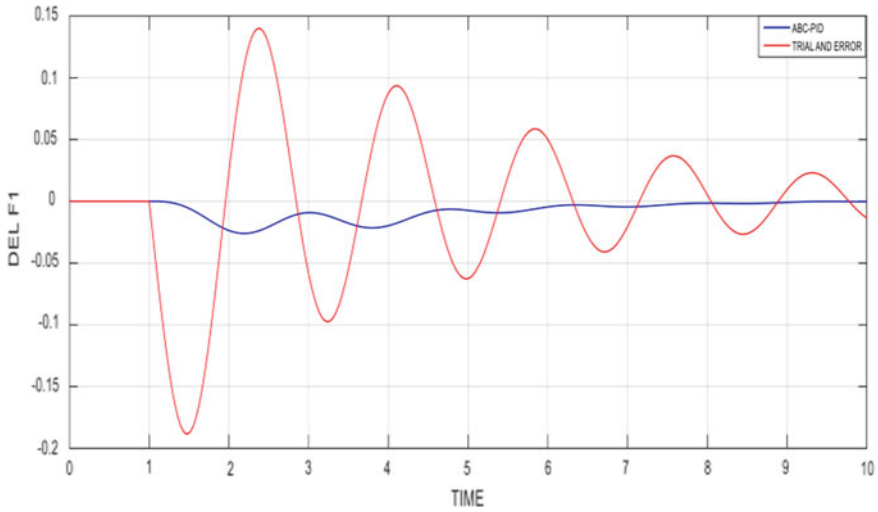
Fig. 10 Frequency fluctuation in area-1 due to 0.1pu step change in area-2
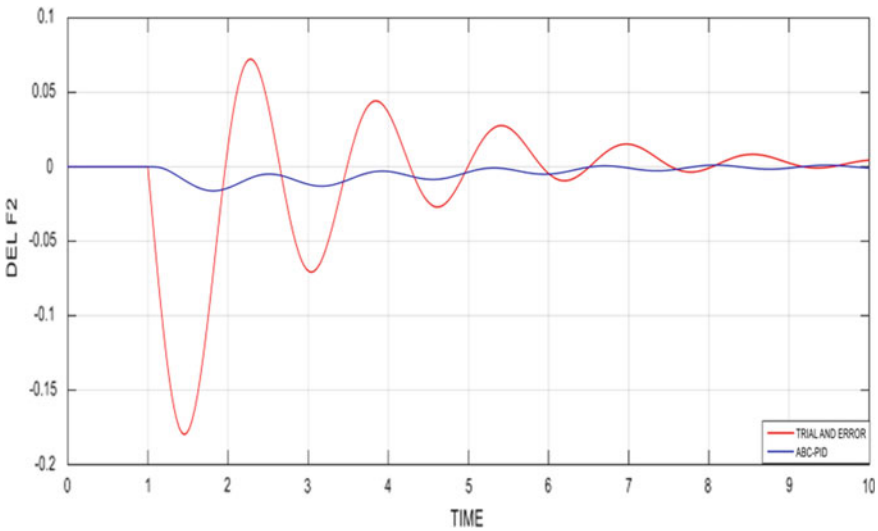
Fig. 11 Frequency fluctuation in area-2 due to 0.1pu step change in area-2

employing ITAE as the objective function due to its effectiveness. As most of the already existing systems are thermal based in India, it is particularly pressing to manage the existing systems in a productive way by handling the deviations in frequency and power through a nature-inspired algorithm.
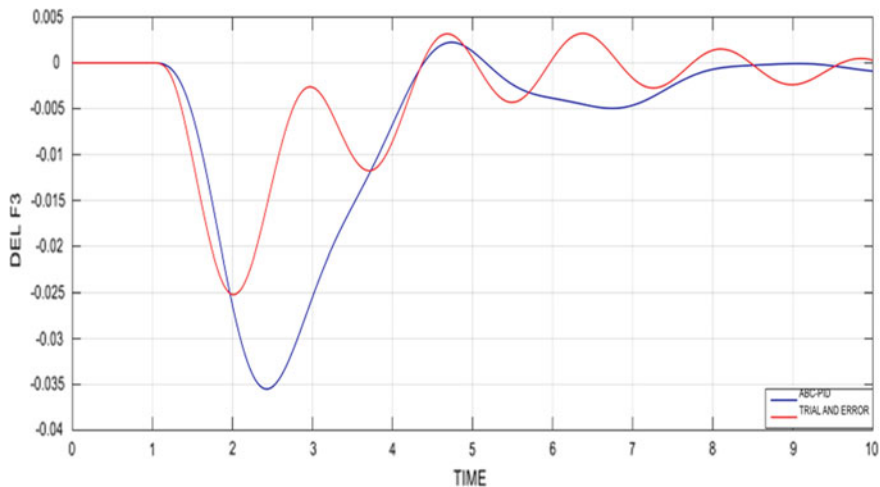
Fig. 12 Frequency fluctuation in area-3 due to 0.1pu step change in area-2
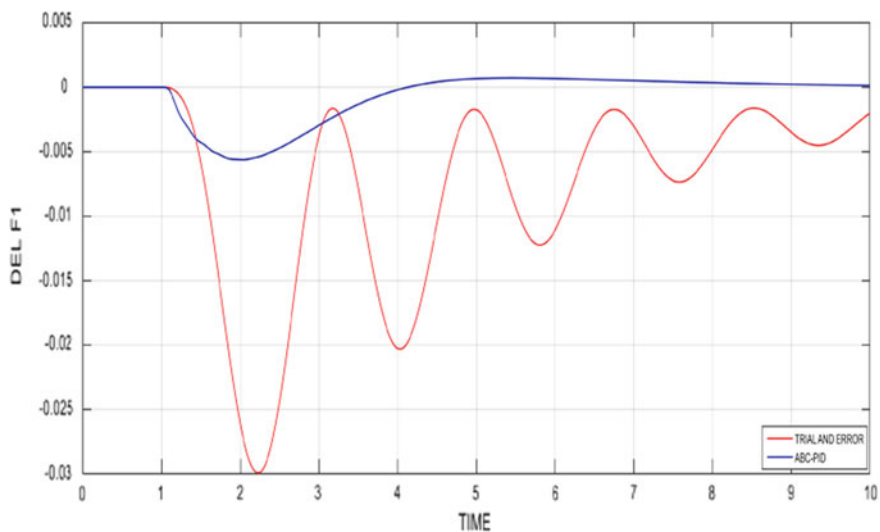
Fig. 13 Frequency fluctuation in area-1 due to 0.1pu step change in area-3
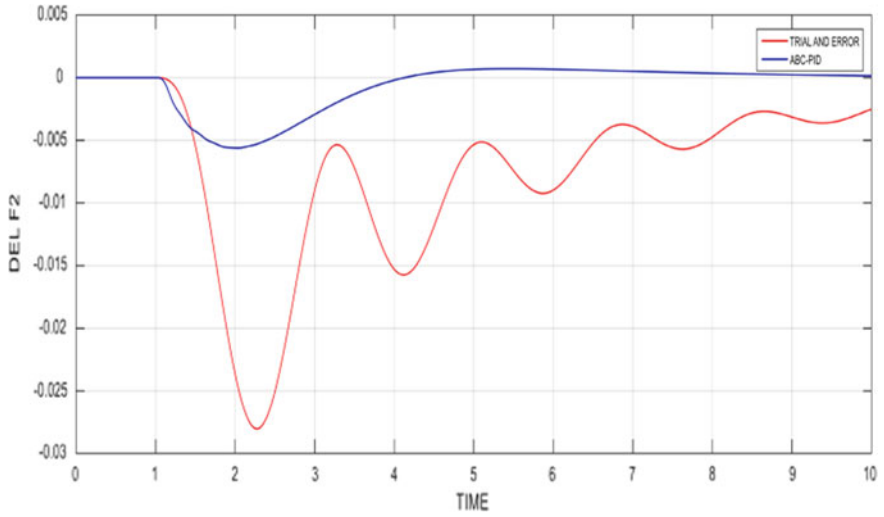
Fig. 14 Frequency fluctuation in area-2 due to 0.1pu step change in area-3
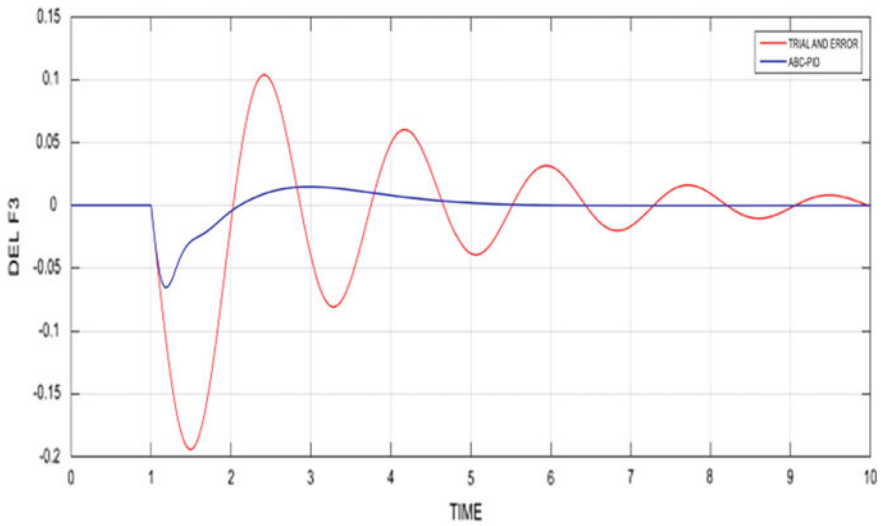
Fig. 15 Frequency fluctuation in area-3 due to 0.1pu step change in area-3
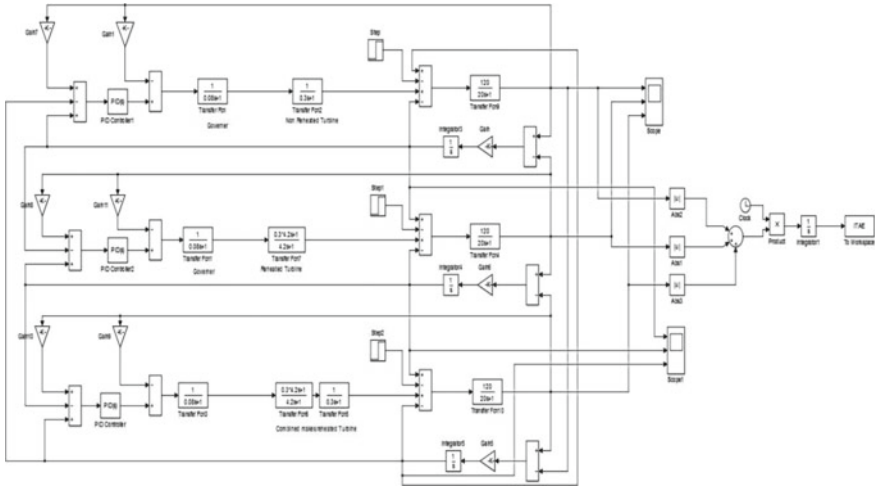
Fig. 16 Simulation diagram for three-area interconnected system

Table 1 Optimized values of gain parameters for PID controller for step disturbance in area-1

Trial and error	kp	ki	kd
1	1.4393	2.7177	1.468
2	1.8727	0.6127	0.5673
3	0.6995	1.1978	0.3485
ABC-PID			
1	1.2482	1.1228	0.0387
2	0.0384	0.5795	0.0344
3	1.2278	0.4532	0.3087

Table 2 Optimized values of gain parameters for PID controller for step disturbance in area-2

Trial and error	kp	ki	kd
1	1.4393	2.7177	1.468
2	1.8727	0.6127	0.5673
3	0.6995	1.1978	0.3485
ABC-PID			
1	0.3248	1.1239	0.0267
2	1.2356	0.4986	0.0325
3	1.2098	0.4329	0.2984

Table 3 Optimized values of gain parameters for PID controller for step perturbation in area-3

Trial and error	kp	ki	kd
1	1.4393	2.7177	1.468
2	1.8727	0.6127	0.5673
3	0.6995	1.1978	0.3485
ABC-PID			
1	0.3248	1.1239	0.0267
2	1.2356	0.4986	0.0325
3	1.2098	0.4329	0.2984

References

1. Kouba NEY, Menaa M, Hasni M, Boudour M (2015) Optimal load frequency control based on artificial bee colony optimization applied to single, two and multi-area interconnected power systems. In: 3rd International conference on control, engineering and information technology, CEIT 2015. Institute of Electrical and Electronics Engineers Inc
2. Nour El Yakine K, Menaa M, Hasni M, Boudour M (2014) Application of artificial neural networks to load frequency control in multi-area power system, Request PDF. In: International conference on information processing and electrical engineering. pp 357–362
3. RV-IJ of SC (2012) Undefined intelligent bacterial foraging optimization technique to economic dispatch problem
4. Ahsan Zamee M, Mitra D, Yusuf Tahhan S (2013) Load frequency control of interconnected hydro-thermal power system using conventional PI and fuzzy logic controller. Int J Energy Power Eng 2:191–196. https://doi.org/10.11648/j.ijepe.20130205.12
5. Akay B, Karaboga D (2012) Artificial bee colony algorithm for large-scale problems and engineering design optimization. Springer 23:1001–1014. https://doi.org/10.1007/s10845-010-0393-4

A High-Gain Non-Isolated DC–DC Boost Converter with Two-Level Output Voltage for PV Applications

N. Sivasankar and K. R. Devabalaji

Abstract A high-gain non-isolated DC–DC PWM boost converter of two-level output voltage is discussed. In traditional step-up converter like, transformerless converters using switched capacitor, switched inductor, etc., maximum voltage gain is not satisfied our expectations because of maximum duty cycle (i.e. duty cycle closely one). Switches are facing severe problem in reverse recovery, high on-state losses, high electromagnetic interference (EMI), etc., when they are operating at extreme duty cycle. Generally, grids are interconnected with AC supply from various power stations. But increase in solar energy demands the use of grid for DC supply. Nowadays, DC micro-grid is having higher attention due to rise in load requirement in DC and betterment in power quality. Based on power rating, these DC loads need various output voltages. In DC micro-grid, photovoltaic source (PV) is the best source of energy. The purpose of non-isolated converters is low cost and high reliability. A high-gain converter with PWM control is an essential for DC micro-grid due to very minimum voltage from photovoltaic. To achieve this, a boost DC–DC PWM converter configuration is discussed that exhibits a maximum voltage gain behaviour and the switches are controlled by a single control signal, which simplifies the operation. The new converter functions in uninterrupted output current mode.

Keywords Non-isolated converters · Boost converter · Multi-level output · PWM control

1 Introduction

Energy consumption in the world tends to grow endlessly, the requirement for electric power satisfied in opposite to the history of the reduction of traditional fossil

N. Sivasankar (✉) · K. R. Devabalaji
Department of EEE, Hindustan Institute of Technology and Science, Padur, Chennai 603103, India
e-mail: sivasankarnallusamy@gmail.com

K. R. Devabalaji
e-mail: krdevab@hindustanuniv.ac.in

resources. To reduce greenhouse gas emissions and for establishing a sustainable energy supply the experimenters approaches on-site generation (OSG) that helps sustainable source of energy to generate electric power. Direct current power generated directly from solar energy [1]. Lithium-ion battery and super capacitors are best example to store energy, and it supplies direct current power. So nowadays, DC micro-grid used to supply lossless power to clients and manage adequate power to load in the on-site generation [1, 2].

One more vital view is taken lighting and 'electronics apparatus' for example. In global electricity consumption, 20% of energy used for lighting purpose and 14.5% of household energy consumed by electronic gadgets (a report from the International Energy Agency-IEA)—i.e. computers, its accessories and domestic electronics. As a suitable choice, LEDs are emerging for low losses in lighting, and they operate on DC supply. Thus, many apparatus function on DC power. Electricity consumed by global increased by direct current apparatus. Nowadays LT and HT consumers are fed from Alternating Current supply through numerous separate transformers [3]. As a result, high-gain DC/DC converters are an essential component of solar energy systems. In the making of high-gain DC/DC choppers, creators face difficulties such as minimum cost and maximum reliability. PV generation system is the foremost renewable source in distributed generation system. It is unable to connect PV panel in series due to issues in reliability and it has low voltage in single cell. To eliminate this problems, a boost converter is used to connect with output terminals of photovoltaic panel, and this converter is connected with DC bus (Fig. 1).

In traditional step-up converter, transformerless DC–DC converter (switched inductors of converter, switched capacitor converter), cascaded boost converter, etc. facing severe problem in reverse recovery, high on-state losses, high electromagnetic interference (EMI) at the time of maximum duty ratio, to reach maximum voltage gain. The above issues are avoided with isolated converters, which provide an electrical barrier between the input and output of the DC–DC converter where high voltage gain has been overcome by varying the ratio of transformer turns [3]. However, the method used to control the power device of these converters, affect from transient voltage and low efficient power because of inductance leakage of

Fig. 1 Block diagram of DC/DC converter for PV applications
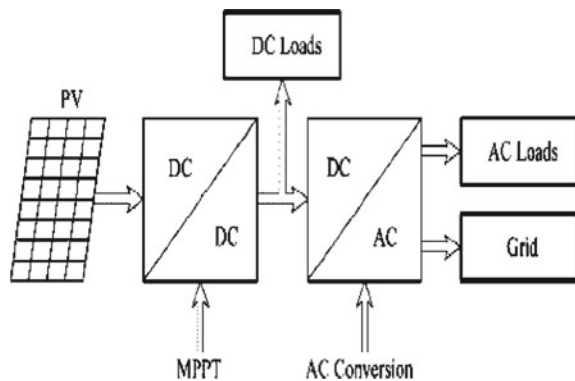
Table 1 Gain equations

S. No.	Types of converter	Gain equation
1	Traditional step-up converter	$1/(1 - \alpha)$
2	Multilevel step-up converter	$N/(1 - \alpha)$
3	Switched inductor step-up converter	$(1 + \alpha)/(1 - \alpha)$
4	Multi-level step-up converter using switched inductor	$N(1 + \alpha)/(1 - \alpha)$

the transformers [4]. Voltage lift techniques can help to avoid the drawbacks which has numerous energy storage elements like inductors and capacitors to increase the voltage. Here, two various level voltages across the capacitors achieved (Table 1).

2 Regular Configurations of High Voltage Gain DC–DC Converter

Though inventors concentrated specially on high-gain DC–DC converter topologies, the dynamic modelling and voltage variation of those converters are not been explained clearly in the literature surveyed. But, designing procedures of DC–DC converters with higher order is indicated in the research article which possesses new designing techniques for high-gain DC–DC converter. Isolated converters are provided with transformer which increases the cost, weight and size of circuit configuration. But, non-isolated converter used for low cost and high reliability purposes [5, 6]. Figure 2 shows the high-gain converter and its losses associated with switching process also less. Figure 3 shows converter operates under zero voltage switching and zero current switching. Figure 4 shows boost converter operates with high efficiency. But all of these configurations of converters possessing only single-level output voltage.
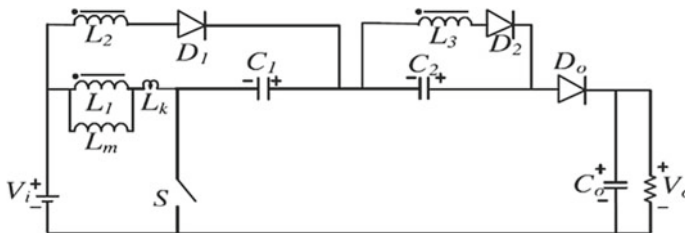
Fig. 2 Converter with high-gain and low switch loss
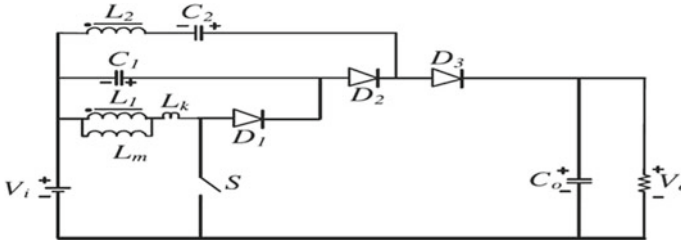
Fig. 3 ZVS and ZCS converter
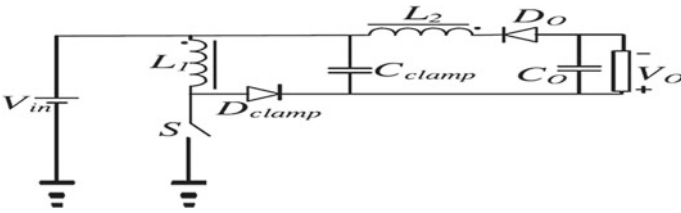
Fig. 4 Boost converter with max. efficiency

3   NEW Configuration

A high-gain boost DC–DC converter is discussed in this article. It avoids the aforesaid problems. It is easy to have two levels of DC voltage for load 2 (high power DC bus) and load 1 (for low power DC bus), that ensures it more relevant for DC micro-grid usage as given in Fig. 1. In transformerless boost converters, high voltage capacitors are used in high numbers to achieve high voltage gain [7, 8]. Whereas in the novel converter (Fig. 5), it helps to minimize the high voltage condensers. So, the size of the system reduced. As we proposed high voltage gain, low duty cycle is used to reach high voltage. The switches used in the new converter controlled by single control signal. So, circuit complication is minimized. Single control signal controls the gain of the voltage at two buses and also helps to continue the voltage within the
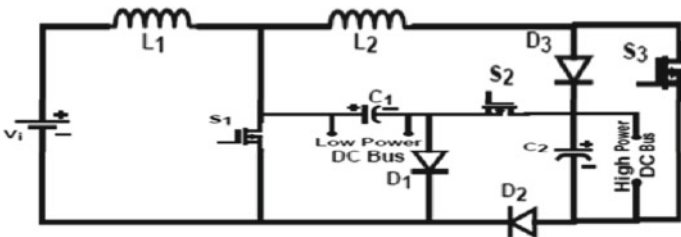
Fig. 5 Proposed converter

desired level. Various modes of operation of new converter explained in Sect. 3. In Sect. 5, simulation results discussed. Conclusion is given in Sect. 7.

4 Novel High-Gain Boost Converter

The new DC–DC boost converter has been constructed to obtain two various level of voltages: one for higher power DC bus and another for low power DC bus. In the novel DC–DC boost converter, L_1, L_2 are inductors. C_1 is the capacitor connected across low power DC bus. C_2 is the capacitor connected across high power DC bus. D_1, D_2, D_3 are diodes conducting when forward biased. Three MOSFETS (S_1, S_2, and S_3) are used as switches. As MOSFET being voltage controlled device, it requires V_{GS} to turn on device. Turn on process of MOSFET depending on duty cycle. But in this converter (Fig. 6), all the switches are controlled using single control signal. So, sensing device and control circuits are reduced.

The working modes of the novel converter are discussed. In this circuit, we consider resistive loads instead of DC bus. Voltage across load 1 and load 2 is same across the capacitors C_1 and C_2 as they are connected in parallel.

Let,

V_i	Input voltage form PV panel
V_{L1}	Voltage of inductor L_1
V_{L2}	Voltage of inductor L_2
V_{C1}	Voltage of capacitor C_1
V_{C2}	Voltage of capacitor C_2
T_s	Switching time period of switches
T_{on}	Turn on period of S_1, S_2, S_3
D	Duty cycle of controlled switches (ratio between T_{on} to T)

I. **During Turned off of S_1, S_2, S_3**

All the three diodes are in conducting state as they are in forward biased conditions. Supply current from V_i passing through inductors L_1 and L_2 and satisfies the load requirements using C_1 and C_2. By applying Kirchhoff's law (Fig. 7),
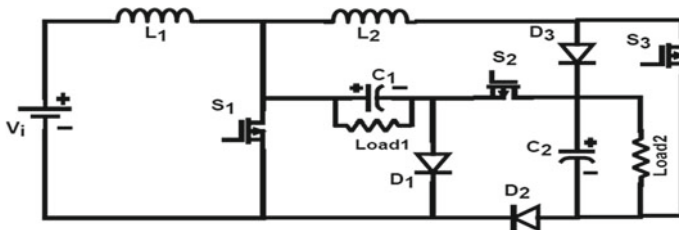
Fig. 6 Proposed high-gain converter with resistive load 1 and 2
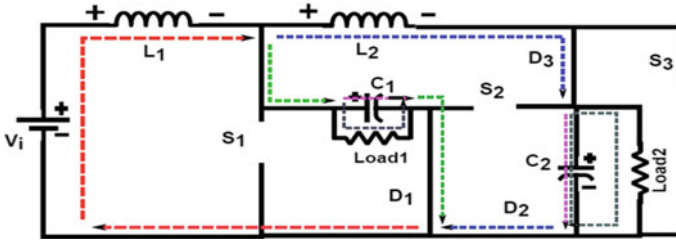
Fig. 7 When S_1, S_2 and S_3 are turned off

$$V_i - V_{C1} = V_{L1} \tag{1}$$

$$V_{C1} - V_{C2} = V_{L2} \tag{2}$$

II. **During Turned on of S_1, S_2, S_3**

All the diodes (D_1, D_2, and D_3) are in reversed biased condition and are in off state. All the three switches are in conducting state. Voltage across capacitors C_1 and C_2 are not only satisfying the load requirements also energizing inductors L_1 and L_2 with input voltage V_i. By applying Kirchhoff's voltage law, inductor voltages can be written,

$$V_i = V_{L1} \tag{3}$$

$$V_{C1} + V_{C2} = V_{L2} \tag{4}$$

From Eqs. 1 and 2

$$(V_i - V_{c1})(1 - D)T_s + V_i \, D \, T_s = 0 \tag{5}$$

$$V_{c1} = V_i(1 - D) \tag{6}$$

By applying volt-time balance across inductor L_2, from Eqs. (2) and (4),

$$V_{c1} - V_{c2}(1 - D)T_s + (V_{c1} + V_{c2})DT_s = 0 \tag{7}$$

$$V_{c2} = V_{c1}(1 - 2D) \tag{8}$$

from the value of V_{C1} from Eq. (6),

$$V_{c2} = V_i(1 - D)(1 - 2D) \tag{9}$$
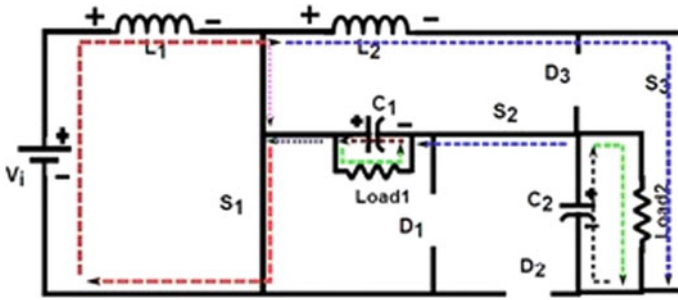
Fig. 8 During turned on condition of $S1$, $S2$, and $S3$

Equation 9 shows that capacitor $C2$ has high voltage gain. Also, it is clear that small duty ratio α is needed to get higher step-up voltage. Equation 5 shows that the voltage can be stepped up for low power DC bus also using duty ratio α. In Load 1, the voltage gain is lesser than the voltage gain of load 2, when we apply same duty ratio α. The control signal for switches $S1$, $S2$, and $S3$ is produced using the pulse width modulation technique (Fig. 8).

III. **Pulse Width Modulation Control**

In PWM technique, we can change either T_{on} or T_{off} without changing its total time period. When there is no change in total time, there is no change in switching frequency. That is constant frequency. The comparator is used to compare both carrier and reference signals.

The following advantages are considered from this technique.

I.   On period is changed to vary the output voltage.
II. Design of filter circuit not difficult as the chopper functioning at constant frequency.

a. **Types of pulse width modulation technique**

   I.   Single PWM
   II.   Multiple PWM
   III. Sinusoidal PWM

In the above PWM techniques, we use single PWM for generating control signal. The comparator receives saw tooth wave as carrier signal and square wave as reference signal.

b. **Generation of control signal**

Amplifier receives voltage signal of both desired and actual. The resultant is that signal is applied to comparator as carrier signal. The comparator also receives reference signal. Finally, it compares both and gives control signal (Figs. 9 and 10).
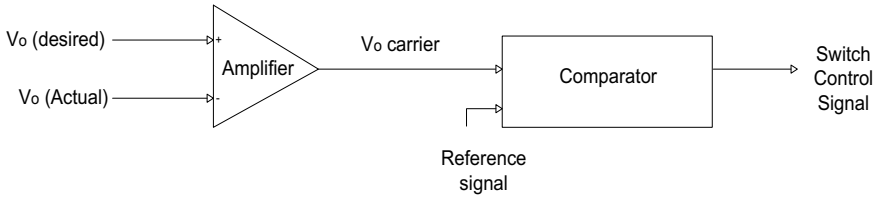
Fig. 11 Simulation diagram

(iii) ***Duty cycle = 0.7***

Output of the simulation diagram (Fig. 11) now verified for duty cycle 0.7 where converter acts as boost converter. Applied voltage 12 V is boosted into two levels. In the first level, output voltage is 11 V, and it is useful for low power loads. In the second level, output voltage is 20 V, and it is useful for high power loads (Fig. 12).

$$\text{Input Voltage}(V_s) = 12\,\text{V}, V_{\text{load1}} = 11\,\text{V}, V_{\text{load2}} = 20\,\text{V}$$
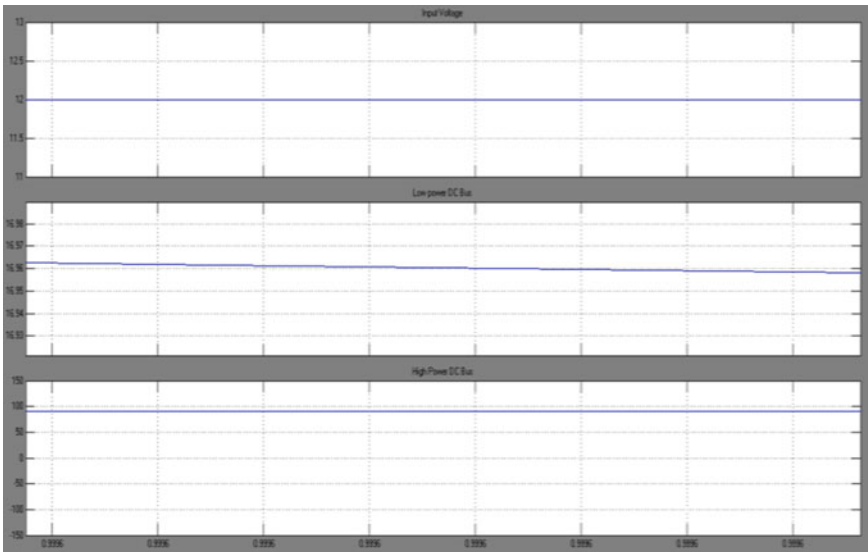
Fig. 12 Voltage waveforms when $\alpha = 0.8$

Scale: Time axis (Horizontal) 1 cm = 1 ms, voltage axis (vertical) 1 cm = 1 V (Fig.12).

It can be observed from the above plot that duty cycle is not less than 0.5.

$S3$, $D3$ are having higher voltage ratings as load 2 for high power DC bus.
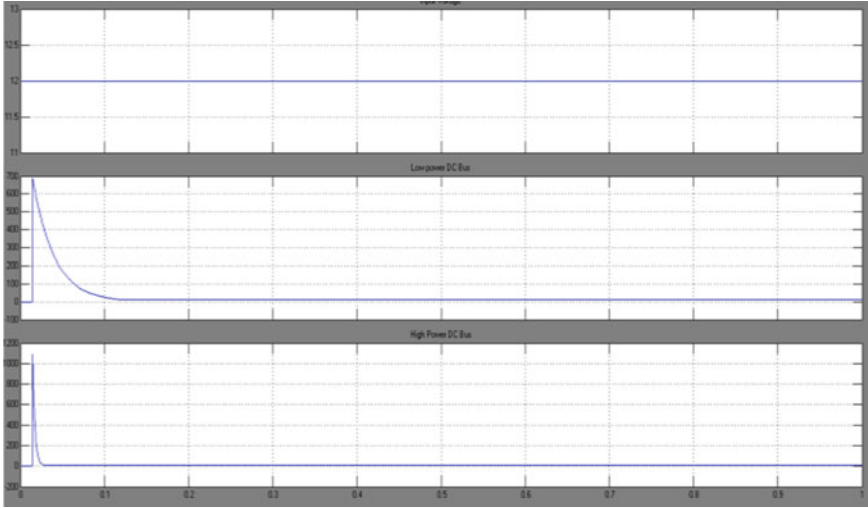
Fig. 13 Voltage waveforms when $\alpha = 0.7$

Fig. 14 Hardware module
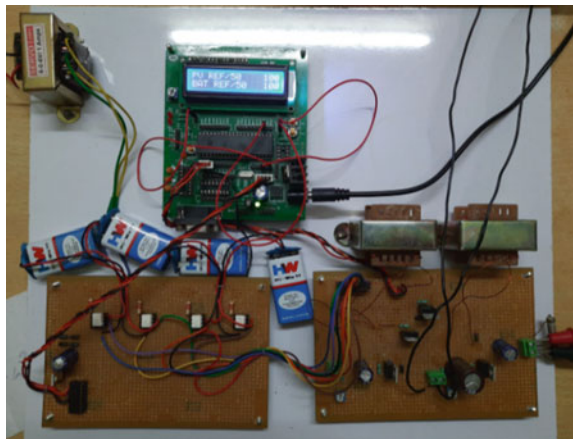
6 Hardware Module

Hardware module shown in Fig. 14 is provided with power circuit and control circuit. We used PIC controller, ULN2003 for driver circuit, IRF 540 MOSFETS, voltage regulators 7812, opto isolators MCT 2E.

Inductors voltage and current have been measured in our hardware module. As inductors are playing major roles in the boost operation of the converter output, voltage and current of the inductors $L1$ and $L2$ have been measured separately.

Voltage of inductor $L1$ is 50 V as shown in Fig. 15, and $L1$ is used to get boost voltage of load 1 or level 1 in which low power load is connected.

Current of inductor $L1$ is 5 A as shown in Fig. 16, and $L1$ current confirms that input is continuous current.

Voltage of inductor $L2$ is 500 V as shown in Fig. 17, and $L2$ is used to get boost voltage of load 2 or level 2 in which high power load is connected.

Current of inductor $L2$ is 3 A as shown in Fig. 18, and $L2$ current confirms that ripples content is minimized. So, voltage across capacitor $C2$ maximizes that helps to boost up the voltage.
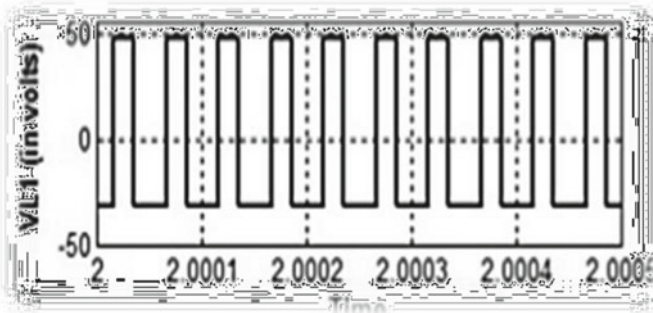
Fig. 15 Inductors voltage $L1$ (V)
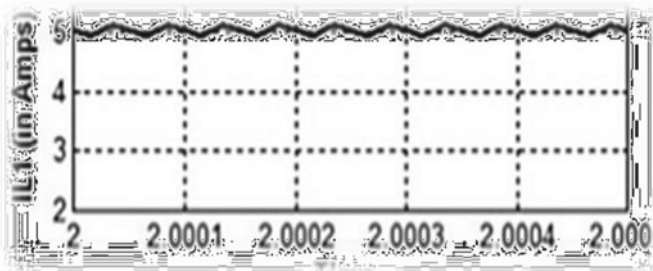
Fig. 16 Inductor current $L1$ (in A)
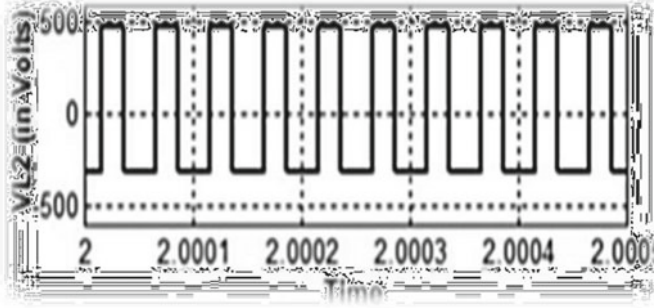
Fig. 17 Inductor voltage $L2$ (V)
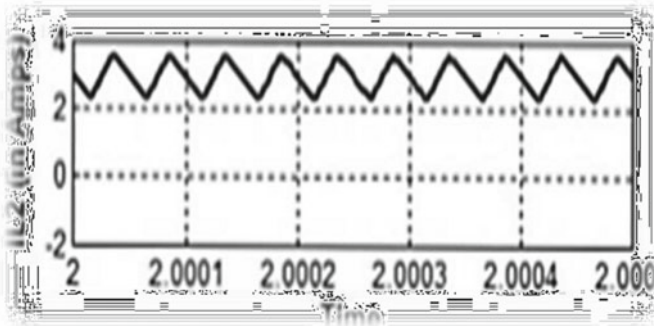
Fig. 18 Inductor current $L2$ (in A)

7 Conclusion

The importance of isolated and non-isolated converters is differed based on its place where it is used. In this PV application, non-isolated converters are very useful to achieve our objectives. To reach different voltage level, that is one for high power DC bus and the other for low power DC bus, single control signal is used. A novel high-gain non-isolated boost converter is designed to satisfy two different output voltages for two different loads. It eliminates the drawbacks of reverse recovery issues. At the same time, it has all the advantages of normal boost converter and transformerless DC–DC converters. Normally, low power bus is said for DC loads and high power bus is said for AC loads. Both loads are needed high voltage gain, which can be obtained from the same duty cycle but greater than 0.7 in this simulation work. Single pulse width modulation technique is suitable for this type of converter. The working modes are discussed and experimented by simulation work using MATLAB/Simulink. In future, the same converter can be designed for closed-loop control by using suitable controller.

References

1. Bragard M, Soltau N, Thomas S, De Doncker RW (2010) The balance of renewable sources and user demands in grids: Power electronics for modular battery energy storage systems. IEEE Trans Power Electron 25(12):3049–3056
2. Wang B, Sechilariu M, Locment F (2012) Intelligent DC microgrid with smart grid communications: control strategy consideration and design. IEEE Trans Smart Grid 3(4):2148–2156
3. Braun M, Stetz T, Bründlinger R, Mayr C, Ogimoto K, Hatta H, Kobayashi H, Kroposki B, Mather B, Coddington M, Lynn K, Graditi G, Woyte A, MacGill I (2012) Is the distribution grid ready to accept large-scale photovoltaic deployment? State of the art, progress, and future prospects. In: Progress in photovoltaics research and applications
4. Ardi H, Reza Ahrabi R, Najafi S (2014) Non isolated bidirectional DC–DC converter analysis and implementation. IET Power Electron 5(12):3033–3044
5. Chien LJ, Chen CC, Chen JF, Hsieh YP (2014) Novel three-port converter with high-voltage gain. IEEE Trans Power Electron 29(9):4693–4703
6. Tseng K-C, Huang C-C (2014) High step-up high-efficiency interleaved converter with voltage multiplier module for renewable energy system. IEEE Trans Ind Electron 61(3):1311–1319
7. Huber LH, Jovanoiv MM (1999) Forward flyback converter with current doubler rectifier: analysis design and evaluation results. IEEE Trans Power Electron 14(1):184–192
8. Ghosh A, Saran SS (2018) High gain DC–DC step-up converter with multilevel output voltage. In: 2018 international symposium on devices, circuits and systems (ISDCS)

Automatic Generation Control of Hydro-Thermal Power System Using 2DOF Fractional Order PID Controller Optimized with Crow Search Algorithm

Appala Naidu Karanam and Binod Shaw

Abstract The unceasing efforts to design an optimal controller in automatic generation control (AGC) of electrical power system motivate the design of a Two-Degree-of-Freedom Fractional Order PID (2DOF-FOPID) controller. Two-area interconnected reheat thermal and hydro including boiler dynamics and dead zone nonlinearity in each area is tested using the designed controller. The performance of the proposed controller is studied with the conventional PID controller and classical Two-Degree-of-Freedom PID (2DOF-PID) controller. The elemental intension of designing supplementary controllers aims to diminish the area control error (ACE). A new crow search algorithm (CSA) is chosen to evaluate the suitable values of controller gain parameters in order to curtail the figure of demerit (ITAE). The transient response of the system is investigated pertaining to 0.01 p.u. load disturbance in area-1. Investigations reveal that the transient response is superior using the 2DOF-FOPID concerning the stability indices, viz. overshoot (O_{sh}), undershoot (U_{sh}) and settling time response of the power system.

1 Introduction

The intent of automatic generation control in an interlinked power system is to supervise the real power from the output of generator in return to the aberration in frequency and alteration in tie-line power. The progress in electrical power consumption had made the power system networks complex and necessitates the development of more intelligent controllers. In AGC, the elementary control to mitigate frequency error due to a load disturbance is accomplished by the speed governor characteristics of the power system. However, an ancillary control is essential to modulate the aberration in frequency and alteration of power deviations in tie-line due to the disturbances

A. N. Karanam (✉) · B. Shaw
Department of Electrical Engineering, National Institute of Technology, Raipur, India
e-mail: karanam2010@gmail.com

in any one areas of the interlinked power system [1]. Automatic generation control must be capable of regulating the frequency at a preset value there by preserving the power exchange among the control areas at their programmed values by altering the real power output of the generators [2]. The direct merging of error in frequency and deviation in tie-line power is the actuating quantity and is called the area control error (ACE). The ACE is ceased to null it implies that both the errors in tie-line power and frequency are forbaded.

Numerous classical control techniques like PID, PIDF, PI-PD, 2DOF-PID, PD-PID, IDD, FOPID and 3DOF-PID are purposed by to improve AGC performance [3–11]. The selection of suitable optimization technique is equally important to controller design to extract the most ideal value of gains. Numerous computation practices were utilized to optimize the suitable gain parameters in various controllers and ratified in this area. BFOA, FPA, BA and DE [3–6] optimization algorithms are fruitfully studied in AGC and optimize the gain parameters of the controllers. Hybrid and adaptive techniques were proposed by many authors to improve the stability and overcome the weaknesses of traditional optimization algorithms. Hybrid DE and PSO [12] and LUS-TLBO [13] are proposed for various controllers and were executed in AGC.

In this work, the novel 2DOF-FOPID controller is validated with the conventional PID and classical 2DOF-PID controllers of interlinked thermal-hydro-power system with governor dead band and dead zone nonlinearities. The gain parameters and scaling factors of the controllers are enhanced by using crow search algorithm (CSA) for optimal system performance. The fundamental objectives of this paper are:

(a) To compare the execution of CSA optimization algorithm with elephant herding optimization (EHO) and Ziegler–Nichols (ZN) algorithms for optimizing the gains of classical PID controller

(b) To develop the (2DOF-FOPID) controller optimized by CSA optimization technique and compare its performance with classical PID controller and existing 2DOF-PID controller.

(c) To investigate the dynamic performance of 2DOF-FOPID controller under a 1%SLP in area-1(thermal) considering nonlinear constraints.

Investigations reveal that the transient response is superior using the 2DOF-FOPID concerning the peak overshoot (O_{sh}), undershoot (U_{sh}) and settling time (T_s) of the deviations in frequency and tie-line power in the proposed thermal-hydel two-area power system. Integral of time multiplied absolute error (ITAE) is opted as the objective or fitness function of the system to be minimized.

2 Description of the System Model

The dynamic load frequency control behavior of two-area thermal-hydel power plants that are interlinked through tie-lines is studied. The plants have distinctive sources and dissimilar principle of operation. The overall system is portrayed in Fig. 1 using
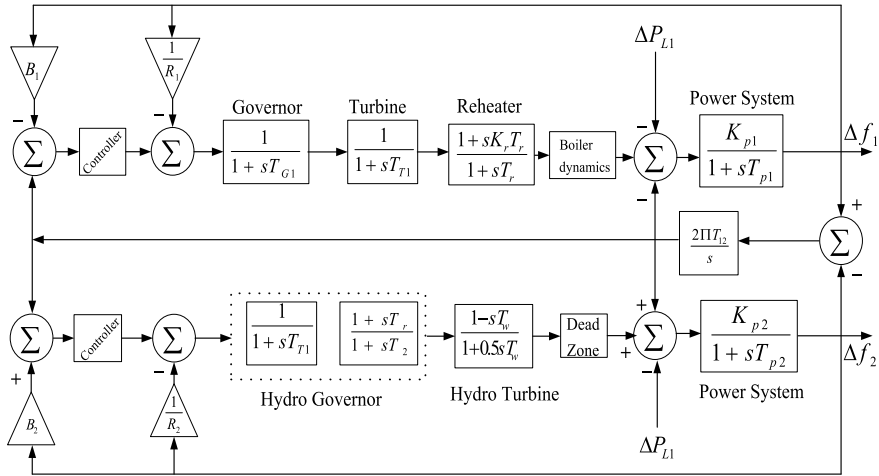
Fig. 1 Power system model

transfer functions of each component. The comparative study of the proposed model is executed with the nominal system parameters [11]. In the proposed system, R_1 and R_2 denote the speed governor regulation constants. B_1 and B_2 are bias factors of frequency. T_{sg} is time constant of hydro-speed governor. T_t is steam turbine time constant. T_r is time constant of reheater unit. K_r is controller gain of reheater. K_{ps}, T_{ps} are power systems gain and time constant, respectively. T_w is water flow time constant of hydro-turbine.

K_D, K_P, K_I are respectively the gains of controller, Δf_1 and Δf_2 are area-1 and area-2 frequency respectively, ΔP_{tie} is the tie-line power deviation and ΔP_D is the cumulative change in system loading condition. The linear aggregation of frequency error and tie-line power is the actuating quantity and is called as the area control error (ACE). The ACE is nullified; it implies that both the errors in frequency and tie-line power are nullified. ACEs concerning deviations of frequency and tie-line power that are to be nullified are shown in Eqs. (1) and (2) which serves as the inputs to the PID controller. These errors are processed by their respective PID controllers to give the control signals to the plant.

$$\text{ACE}_1 = B_1 \Delta f_1 + \Delta P_{tie} \tag{1}$$

$$\text{ACE}_2 = B_2 \Delta f_2 + \Delta P_{tie} \tag{2}$$

The frequency mismatch from their nominal value at area-1 is Δf_1 and at area-2 is Δf_2. The deviation of tie-line power is ΔP_{tie} and is shown in Eq. (3).

$$\Delta P_{tie} = \frac{2\pi T_{12}}{s}(\Delta f_1 - \Delta f_2) \tag{3}$$

A load demand shift of 1% (0.01) in area-1 is applied to study the dynamic response of the proposed system. The proposed controllers are executed in each area to investigate the controller potential to achieve predominant performance of system. Intelligent 2DOF-FOPID controller is determined to be the predominant controller over conventional PID and 2DOF-PID controllers. The deviations prone to be more sensitive with time. The deviations toward the settling end are more sensitive to the load shift than the large deviations in the initial transients. The fitness function ITAE (Eq. 4) is chosen to be the fitness function for error deviations (Δf_1, Δf_2 and ΔP_{tie}). ITAE is chosen objective function can be modified to make it more competitive for optimization process, but it may lead to misleading results when proper weighting factors are not chosen.

$$\text{ITAE} = \int_o^T (|\Delta f_1| + |\Delta f_2| + |\Delta P_{\text{tie}}|).t.\text{d}t \qquad (4)$$

where T is final simulation time. The controller parameters are subjected to the bounds $0.001 \leq Ki \leq 2$ for $i = 1, 2, 3, \ldots, n$, where n is the designed variables. The values of the controller gains must be small enough to avoid generator disturbances during small offsets.

3 Two-Degree-of-Freedom FOPID Controller

The performance of system principally lies upon the design of controller. So, learning about the suitable gain parameters is additionally a vital factor. 2DOF-PID controller is superior over classical PID controller furnishing better damping to the oscillations in system over an extensively varying load disturbances and system indices.

Fractional calculus suggests the peculiar fractional order PID controller is a neoteric approach. The non-integral (less than unity) values of orders of the decimal integration and decimal differentiation (λ and μ) enables profound solutions to the errors. The FOPID controller is represented in transfer function by the equation

$$G_C(s) = K_P + \frac{K_I}{s^\lambda} + s^\mu K_D$$

The system stability is preserved by virtue of fractional (non-integral) order, and it gives superior control than classical PID controller. PID controller is shown in Fig. 2a and FOPID controller structures are portrayed in 2(b). The application of FOPID in AGC minimizes the frequency deviations due to its additional flexibility in design of controller. The additional tuning of the gains provided by fractional values λ and μ supplemented by the CSA optimization technique for interconnected power system provides better dynamic performance over the conventional controllers. The addition of two degrees of freedom provides quality control in tracking the set point and noise
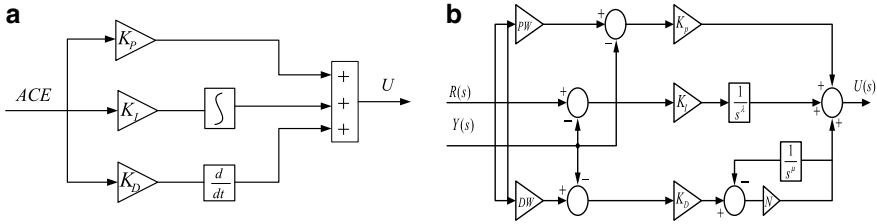
Fig. 2 **a** PID controller structure. **b** 2DOF-FOPID controller structure

rejection. The additional series filter with derivative term suppresses the disturbances and enhance the system stability.

4 Crow Search Algorithm-Based Optimization Technique

Crows are considered the savviest creatures. There are ample evidences to prove their shrewdness. In mirror tests, they have shown awareness and have the capability to create instruments. Crows can gather faces and be cautious when one methodology is threatening. They can also use instruments, communicate in advanced ways and examine the hiding place of their food a short time later.

CSA is developed based on the principle that crows live in groups and they memorize their food hiding places and protect them from other crows by awareness probability (AP) [14]. For a d-dimensional space (boundary) with total N crows, the vector $X_{i,j}$ gives the position of ith crow in the seek area at jth redundancy:

$$x_{i,j} = \left[x_1^{i,j}, x_2^{i,j}, x_3^{i,j}, \ldots, x_d^{i,j} \right] \text{ for } (i = 1, 2, 3 \ldots, N; j = 1, 2, 3, 4, \ldots, j_{\max})$$

$j_{\max}$ represents the maximal iterations or cycles. The crow veiling place is memorized at $m_{i,j}$. Each crow features a memory within which it memorizes the position. For jth iteration, the hiding place of crow i is memorized at $m_{k,j}$. This can be the most effective position that crow i had acquired and then they move for higher places. Suppose, at a iteration j, crow k need to go to its hiding place, $m_{k,j}$. At this iteration, crow i choses to pursue crow j to attend the veiling spot of the crow j.

$$x^{i,j+1} = \begin{cases} x^{i,j} + r_k \times fl^{i,j} \times \left(m^{k,j} - x^{i,j} \right) & r_k \geq \mathrm{AP}^{i,j} \\ a \quad \text{random position} \ldots \text{Otherwise} \end{cases}$$

where r_k indicates an evenly distributed random number in the range 0–1, and for a jth iteration to crow k, the awareness probability is given by $\mathrm{AP}_{i,j}$ Metaheuristic methods ought to give a decent harmony among expansion and convergence by considering

AP value. A low value of AP increases convergence in lo local region while a large value estimates the good solution in global search space.

Algorithm for Optimization Using CSA

This section provides steps for the application of CSA.

Step 1   Compute the number of crows (N), maximal count of redundancies ($j_{\max}$), flight length (f_1) and awareness probability (AP).

Step 2   In d-dimensional search domain with N crows, adopt a random position to each location as decision variables memory location of each crow.

Step 3   Calculate fitness (objective) function.

Step 4   Develop a new position: suppose crow i want to generate a new position. It follows crow j and discover its memory at ($m\,j$).

$$m^{i,j+1} = \begin{cases} m^{i,j}, \ f\left(x^{i,\text{iter}+1}\right) \text{ is better than } f\left(m^{i,j}\right) \\ m^{i,j}, \quad \text{Otherwise} \end{cases}$$

Step 5   The usefulness of new solutions is analyzed and update current position when the calculated fitness value is improved than fitness value of memorized location.

The above steps are repeated for J times, and best memory position is reported.

5   Result and Analysis

CSA algorithm is borrowed to enhance the gain parameters of PID controller of thermal-hydro-power system [15, 16]. CSA algorithm optimized PID controller is investigated with ZN PID [15] and EHO PID [16]. The CSA optimized PID controller gain parameters are $K_{P1} = 2.9614$, $K_{I1} = 3.0000$, $K_{D1} = 1.4963$, $K_{P2} = 0.5199$, $K_{I2} = 0.0010$, $K_{D2} = 2.5889$. The deviations of frequency and power are depicted in Figs. 3, 4 and 5. The numerical values performance parameters such as peak overshoot (O_{sh}), undershoot (U_{sh}) and settling time (T_{s}) of the deviations are tabulated in Table 1. From Figs. 3, 4 and 5 and Table 1, CSA optimized PID controller is substantiated over ZN-based PID [15] and EHO-based PID [16].

CSA algorithm is chosen and executed simultaneously to attain optimum parameters for the proposed PID, 2DOF-PID and 2DOF-FOPID controllers. 100 iterations with 50 populations of crows are executed for each controller. Primary objective of selecting the CSA algorithm is to minimize the Integral Time Absolute Error (ITAE) as cited in Eq. (4). CSA optimized gains parameters of the controllers for the given system are tabulated in Table 2.

Dynamic response characteristics limiting the settling time, undershoot and peak overshoot in the transient response of the frequency deviation and interline power deviations are showing in Table 3. A clear insight of the table values gives a better performance rank to the proposed CSA optimized FOPID controller. 2DOF-FOPID
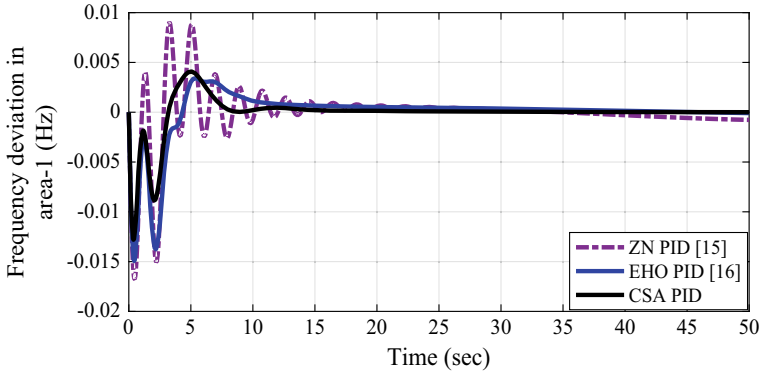
Fig. 3 Frequency deviation in area-1 (Hz)
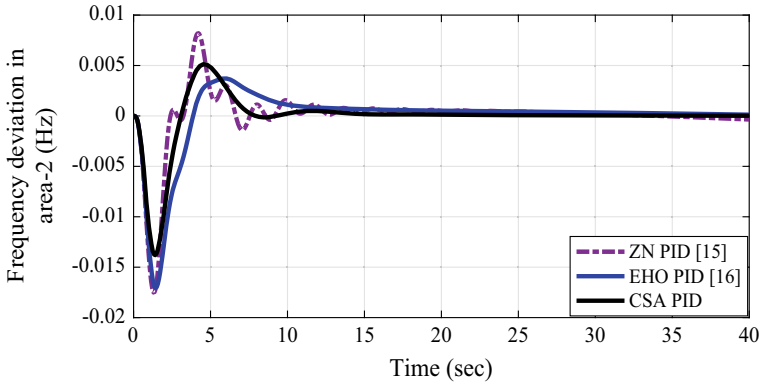
Fig. 4 Frequency deviation in area-2 (Hz)
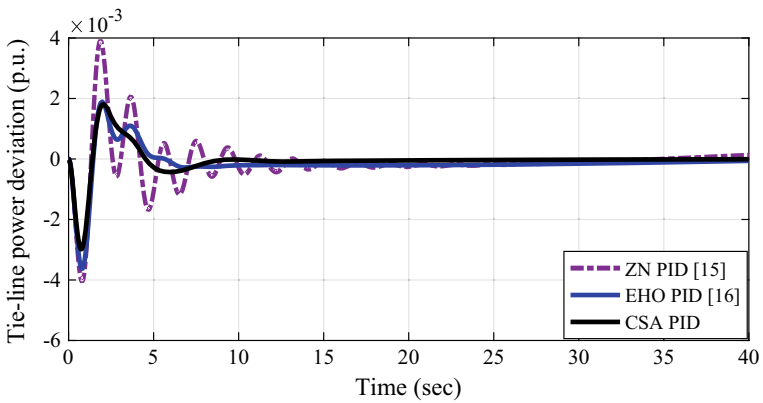
Fig. 5 Tie-line power deviation (p.u.)

Table 1 Performance responses of the system with PID controllers optimized by CSA

Controllers		ΔF_1	ΔF_2	ΔP_{tie}
CSA PID	U_{sh}	− 12.7215	− 13.6542	− 2.9841
	O_{sh}	4.0954	5.1324	1.7845
	T_{s}	17.98	17.85	16.14
EHO PID [16]	U_{sh}	− 16.5945	− 21.0125	− 3.3250
	O_{sh}	3.4152	3.7148	1.8932
	T_{s}	22.564	18.98	22.98
ZN PID [15]	U_{sh}	− 17.1025	− 18.9589	− 3.6012
	O_{sh}	8.8427	8.2164	3.9175
	T_{s}	46.53	46.29	42.54

Table 2 CSA optimized controller parameters

Controllers		K_P	K_I	K_D	N	PW	DW	μ	λ
2DOF-FOPID	Area-1	1.5434	1.8719	1.5738	181.5887	4.8785	3.8002	1.0000	0.9999
	Area-2	0.0016	2.4015	0.4605	90.9575	1.0812	0.4680	0.7541	0.0083
2DOF-PID	Area-1	2.0000	2.0000	1.6869	10.0000	5.0000	0.0010		
	Area-2	1.2931	0.0010	1.5273	300.0000	0.3004	0.6895		
PID	Area-1	2.0000	2.0000	1.8591					
	Area-2	0.0010	0.0010	0.8610					

Table 3 Performance responses of the system with different controllers optimized by CSA

Controllers		ΔF_1	ΔF_2	ΔP_{tie}
2DOF-FOPID	U_{sh}	− 4.9065	− 5.2351	− 0.8614
	O_{sh}	1.1092	1.1375	0.6434
	T_{s}	11.16	11.16	8.17
2DOF-PID	U_{sh}	− 9.6847	− 5.2059	− 1.4826
	O_{sh}	2.7954	0.8729	0.7876
	T_{s}	14.59	14.59	8.55
PID	U_{sh}	− 12.7358	− 16.7852	− 3.1681
	O_{sh}	5.6732	6.5324	1.4930
	T_{s}	20.96	21.56	14.36

controller gives minimum values of peak overshoot, undershoot and settling time. The fluctuations in frequency and tie-line power are displayed in Fig. 6, 7 and 8. A tolerance of 0.05% is considered for evaluating the settling time of response characteristics. Performance index ITAE value of the system with PID, 2DOF-PID and 2DOF-FOPID controllers is 0.5323, 0.1057 and 0.0745 respectively.
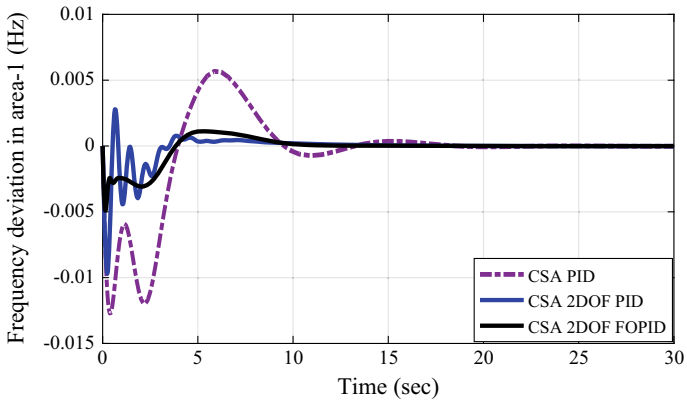
Fig. 6 Frequency deviation in area-1 (Hz)
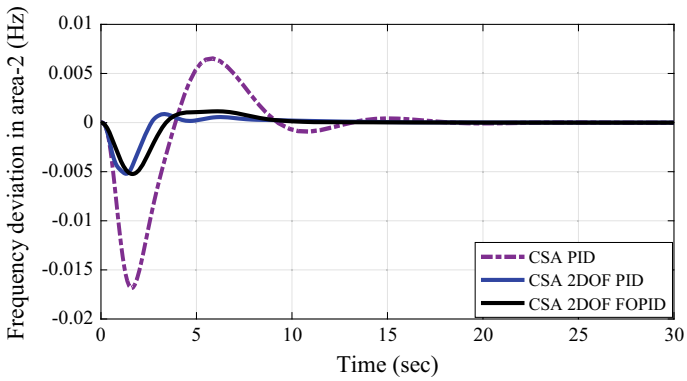
Fig. 7 Frequency deviation in area-2 (Hz)
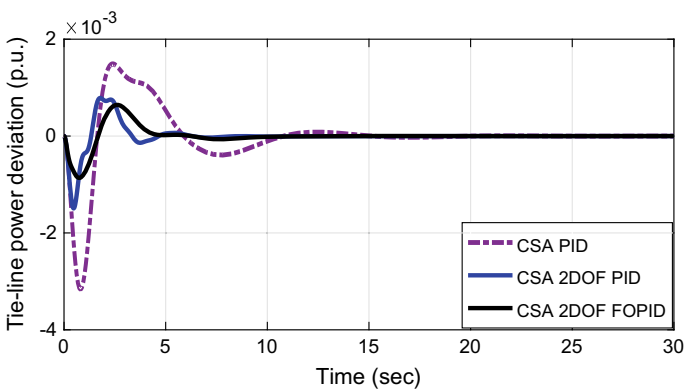
Fig. 8 Tie-line power deviation (p.u.)

Figures 6, 7 and 8 and Table 3 precisely represent the supremacy of the 2DOF-FOPID controller. 2DOF-FOPID controller enhances the dynamic response (undershoot, overshoot and settling time) of the system.

6   Conclusion

In this paper, the fulfillment of AGC is enhanced by enforcing CSA in a two-area inter-linked thermal-hydro-power system. The design of controller and choice of appropriate algorithms to adjust the controller's parameters are the essential requisites to achieve AGC superior performance. A unique 2DOF-FOPID controller is implemented for AGC system and its predominance among the distinct controllers viz. PID, 2DOF-PID and 2DOF-FOPID are used to validate the superiority of 2DOF-FOPID controller. CSA algorithm is executed to enhance the controller gain, scaling parameters and filter constants. From the comparative investigation of results, it is realized that CSA optimized 2DOF-FOPID controller reinforce the system dynamic response illustrating merest peak overshoot, undershoot and settling time of frequency and tie-line power deviations with 1% load disruptions in area-1. CSA optimized 2DOF-FOPID is effective in handling sudden load variations, and parametric deviations are illustrated using simulation results and mathematical examination.

Appendix 1

$T_{G1} = 0.08$ s, $T_{T1} = 0.4$ s, $K_{P1} = K_{P2} = 120$ Hz/p.u. MW, $T_{P1} = T_{P2} = 20$ s, $R_1 = R_2 = 2.4$ Hz/p.u. MW, $B_1 = B_2 = 0.425$ p.u. MW/Hz, $T_{12} = 0.0707$, $T_w = 1$ s, T_r 10 s $K_r = 0.33$ $T_1 = 48.7$ s, $T_2 = 0.513$ s.

References

1. Kundur P (1994) Power system stability and control. McGraw-Hill
2. Ibrahim PK, Kothari DP (2005) Recent philosophies of AGC strategies in power system. IEEE Trans Power Syst 20(1):346–357
3. Ali ES, Abd-Elazim SM (2013) BFOA based design of PID controller for two area Load frequency control with nonlinearities. Int J Electr Power Energy Syst 51:224–231. https://doi.org/10.1016/j.ijepes.2013.02.03
4. Dash P, Saikia LC, Sinha N (2016) Flower pollination algorithm optimized PI-PD cascade controller in automatic generation control of a multi-area power system. Int J Electr Power Energy Syst 82:19–28
5. Dash P, Saikia LC, Sinha N (2015) Automatic generation control of multi area thermal system using bat algorithm optimized PD-PID cascade controller. Int J Electr Power Energy Syst 68:364–372

6. Sahu RK, Panda S, Rout UK (2013) DE optimized parallel 2-DOF PID controller for load frequency control of power system with governor dead-band nonlinearity. Int J Electr Power Energy Syst 49(1):19–33
7. Gorripotu TS, Sahu RK, Panda S (2016) DE optimized PID controller with derivative filter for AGC of interconnected restructured power system. Comput Intell Data Min 1:395–403
8. Sondhi S, Hote YV (2014) Fractional order PID controller for load frequency control. Energy Convers Manage 85:343–353
9. Singh R, Sen I (2004) Tuning of PID controller based AGC system using genetic algorithms. TENCON 3:531–534
10. Chandra L, Nanda J, Mishra S (2011) Electrical power and energy systems performance comparison of several classical controllers in AGC for multi-area interconnected thermal system. Int J Electr Power Energy Syst 33(3):394–401
11. Rahman A, Saikia LC, Sinha N (2016) Automatic generation control of an unequal four-area thermal system using biogeography-based optimized 3DOF-PID controller. IET Gener Transmis Distrib 10:4118–4129
12. Pati S, Sahu BK, Panda S (2014) Hybrid differential evolution particle swarm optimisation optimized fuzzy proportional-integral derivative controller for automatic generation control of interconnected power system. IET Gener Transm Distrib 8(11):1789–1800
13. Sahu BK, Pati TK, Nayak JR, Panda S, Kar SK (2016) A novel hybrid LUS-TLBO optimized fuzzy-PID controller for load frequency control of multi-source power system. Int J Electr Power Energy Syst 74:58–69
14. Askarzadeh A (2016) A novel metaheuristic method for solving constrained engineering optimization problems: crow search algorithm. Comput Struct 169:1–12
15. Verma R, Pal S (2013) Intelligent automatic generation control of two-area hydrothermal power system using ANN and fuzzy logic. In: 2013 international conference on communication systems and network technologies. IEEE, pp 552–556
16. Sambariya DK, Fagana R (2017) Load frequency control of multi-area hydro thermal power system using elephant herding optimization technique. J Autom Control 5(1):25–36

Design of Quasi-Oppositional-Based CSA Optimized Cascade Pi-Fractional Order PID Controller for Interconnected Power System

Jyoti Ranjan Nayak and Binod Shaw

Abstract In this work, an adequate approach is depicted to endorse the superiority of cascade PI-fractional order PID (PI-FOPID) controller over PID and FOPID controllers and also to validate the quasi-oppositional-based crow search algorithm (QOCSA) to elect the peerless gains of the controllers over CSA algorithm. PI-FOPID controller is implemented in an interconnected reheat-thermal power system to amend system performances. The system is designed with nonlinearity such as generation rate constraint (GRC) and ITAE as fitness function. The fundamental intention of this system is to diminish the divergence of frequency and power. For this purpose, a hybrid QOCSA and CSA algorithms are implemented to determine the significant parameters of controllers by which the divergence reducing competence of controller can be improved. This analysis to substantiate the proposed PI-FOPID controller and QOCSA algorithm is accomplished with a step load of 0.01 p.u. injected in area-1. Finally, QOCSA is substantiated over CSA algorithm, and PI-FOPID controller is confirmed as an excel controller over FOPID and PID controllers.

Keywords Automatic generation control (LFC) · PID · Fractional order PID (FOPID) controller · Cascade controller · Crow search algorithm (CSA)

1 Introduction

In recent power system, divergence of frequency and power exceedingly influences the stability and security of the entire interconnected system. The primary causes of the frequency instability are precipitous load fluctuation, fault, etc. The load

J. R. Nayak (✉)
Department of Electrical and Electronics Engineering, Vignan's Institute of Information Technology, Visakhapatnam, India
e-mail: bapi.jyoti.2@gmail.com

B. Shaw
Department of Electrical Engineering, National Institute of Technology, Raipur, Chhattisgarh, India

fluctuation is very frequent and cannot be regulated. The interconnected system is eminently influenced by this fluctuation of load, and the divergence of frequency raised by this fluctuation may be circulated throughout the interconnected system. Primary control scheme (droop) is a fast response control scheme, but it is incapable to restore the system frequency. Secondary control schemes such as automatic generation control (AGC) are highly effective to maintain the steady-state frequency response of the system. AGC is an admirable control scheme to contribute reliable, stable, and economic power to consumer [1, 2]. The central objective of AGC is to counterbalance the load demand and generation by coordinating the valve position of generators.

Different structures of PID controllers such as PID, PI-PD, PD-PID, 2DOF PID, IDD, FOPID, 3DOF PID, and 3DOF FOPID controllers have enforced to achieve the surpass performance of frequency divergence [3–12]. Some researchers have blended FLC with PID controller to accomplish better performance of nonlinear power system [13–19].

Computational/optimization techniques are absolutely significant tools to achieve admirable improvement of frequency response by plucking pertinent pairs of controller gains. The pertinent parameters of controllers are highly responsible for the responses of the power system. Different optimization algorithms with capability to figure out the optimal point of the search space are eminently obligatory. In AGC, some optimization algorithms such as DE, BBO, and CSA algorithms are enforced prosperously to achieve optimal controllers [6, 11, 16]. Single optimization algorithm may not competent enough to boost the performance admirably. For this purpose, some researchers have designed hybrid or adaptive optimization algorithms which are realized in this field. DEPSO [20], LUS-TLBO [17], ASOS [21], and MGHS [22] are some modified/hybrid algorithms enforced fruitfully in this field.

In this work, cascade PI-FOPID controller is proposed by blending PI and FOPID controllers. This proposed controller is enforced in interconnected power system which is substantiated over FOPID and PID controllers. The optimal PI-FOPID controller is achieved by using crow search algorithm (CSA) proposed by Askarzadeh [23]. CSA algorithm is modified by some researchers with better competence to solve complex problems such as PGCSA and DECSA [24, 25]. Quasi-oppositional-based CSA (QOCSA) is proposed to boost the power system responses over CSA.

2 Power System Modeling

The interconnected power system considered for this analysis is a reheat-thermal power system. This power system is proposed with generation rate constraint (GRC) as shown in Fig. 1. Each area of the power system has capability to generate 2000 MW. The nonlinearity (GRC) is considered to design a more realistic power system. The responses of power system are eminently manipulated by GRC. Generally, GRC with 3%/min ($\pm$ 0.0005) is preferred for thermal power plant. Appendix 1 consists the gain and time constants of power system. An immediate load variation of 1% in area-1
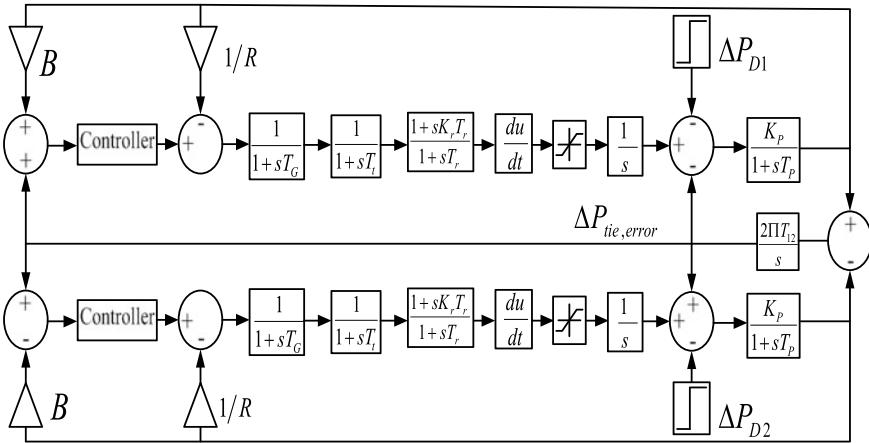
Fig. 1 Power system model

is applied to realize the system responses with proposed controller and optimization algorithm. The errors appear in areas (area control error-ACE) are characterized in Eqs. 1 and 2.

$$ACE_1 = B_1 \Delta f_1 + \Delta P_{\text{tie,error}} \tag{1}$$

$$ACE_2 = B_2 \Delta f_2 + \Delta P_{\text{tie,error}} \tag{2}$$

where, B_1 and B_2 are frequency bias factors.

Integral time absolute error (ITAE) is adopted as fitness function of the system to minimize the divergence of both frequency and tie-line power. The expression of the fitness function is described in Eq. (3).

$$ITAE = \int_0^T t(\Delta f_1 + \Delta f_2 + \Delta P_{\text{tie,error}}) \tag{3}$$

3 Purposed Cascade PI-FOPID Controller

The purposed PI-FOPID controller has two closed loops such as inner and outer loops. These two loops are constructed in such a way that the output of each loop behaves as input of other loop. The structure of proposed controller is illustrated in Fig. 2 [5]. As FOPID controller is flexible and competence enough to handle supply
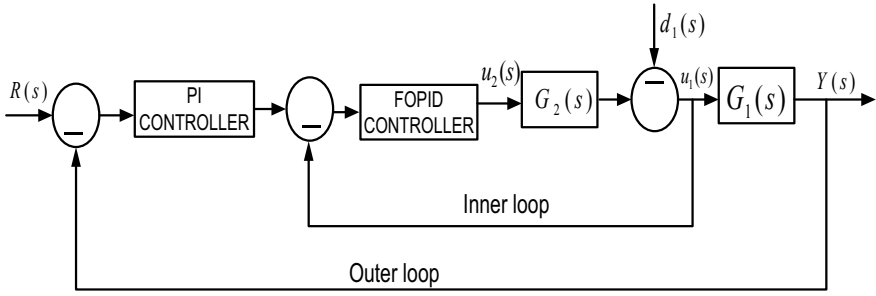
Fig. 2 Cascade controller structure

disorder by which the reliability of outer loop is enhanced. The PI controller is used as outer loop measure to administer the output quality of the system. The noise reduce capability of the controller is the advantage.

3.1 Outer Loop

The mathematical expression of the outer loop process is characterized as below. This loop is characterized by concerning process output $Y(s)$, process of outer $G_1(s)$ and load distortion $d_1(s)$ as

$$Y(s) = G_1(s)U_1(s) + d_1(s)$$

$Y(s)$ Output of the process.
$G_1(s)$ Outer process.
$d_1(s)$ Load disturbance.
$U_1(s)$ Input of the process.

The referral error is eliminated by the outer loop.

3.2 Inner Loop

The expression of inner loop is expressed as

$$y_2(s) = G_2(s)U_2(s)$$

The inner loop output is delivered as input to the outer loop, i.e., $y_2(s) = U_1(s)$. The error in the inner loop is regulated by inner loop. The rapidity of inner measure (FOPID controller) highly affects the response of the controller. The expression of the proposed controller is

Fig. 3 Fractional order PID
controller structure
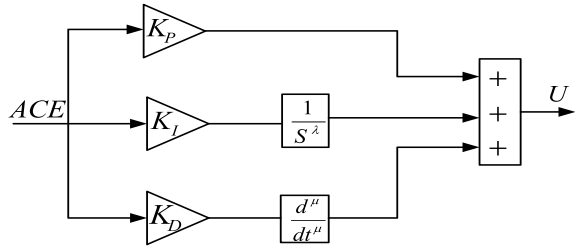
$$Y(s) = \left[\frac{G_1(s)G_2(s)C_1(s)C_2(s)}{1 + G_2(s)C_2(s) + G_1(s)G_2(s)C_1(s)C_2(s)} \right] R(s)$$
$$+ \left[\frac{G_1(s)}{1 + G_2(s)C_2(s) + G_1(s)G_2(s)C_1(s)C_2(s)} \right] d_1(s)$$

In this work, PI and FOPID controllers are considered as outer loop and inner loop respectively and the structure of fractional order PID controller is illustrated in Fig. 3.

4 Quasi-Oppositional-Based Crow Search Algorithm (QOCSA)

Crows are opted as the preeminent smart bird. Compared to their environmental structure, they have enormous brain. Crows cover up their overabundance food in undoubted location and the crow redeems the food when necessary. Crows attain foods by doing a great team work always. Hiding foods for future is not simple for them because some challenger crows can also come after to follow the food. At that moment, the crow endeavors to cheat by altering the direction in the colony. The position in the colony is acknowledged as food position. Crows divert the hiding nourishment of other crows by tracking them, and at the same time, the crows take some auxiliary avoidance like altering the concealing places to stay away from becoming an upcoming easy target. By conceding these, clever action CSA algorithm has established [23].

The oppositional-based learning (OBL) was introduced by Tizhoosh [26]. The prime object of this approach is to increase the skill of the result and to stimulate the diversity factor toward the optimal solution by concerning the opposite point of the particle.

The steps followed for QOCSA algorithm are described as

1. Initialize the flock of crows of size $X_{[NP \times D]}$ within the restraint 0.001–2.
2. Initialize the memory of crows of size $M_{[NP \times D]}$.
3. Determine the opposite position of the initial matrix as below

$$MO_j = \frac{para^{min} + para^{max}}{2}$$

M_j is the middle of the search space. The opposite position of initial matrix (X) is described as

$$OX = para^{min} + para^{max} - X$$

where $para^{min}$ and $para^{max}$ are the minimal and maximal of the search space.

The quasi-oppositional position may be defined as

$$QOX = M + rand \times (M - X)$$

4. The best NP crows among QOX are preferred as better crows and the worst crows are eliminated.
5. The positions of the crows are updated by using equation described below.

$$X_{new}^i = \begin{cases} X_{old}^i + r \times fl^i \times (M^j - X_{old}^i) & r_1 \geq AP \\ LB + rand \times (UB - LB) & \text{Otherwise} \end{cases}$$

where r and $r1$ are two distinct random numbers [0, 1]. AP is the awareness probability.
6. The memory of the crows is updated with fitter crow as depicted as

$$M_{new}^i = \begin{cases} X_{new}^i & \text{if } f(X_{new}^i) \geq f(M_{old}^i) \\ M_{old}^i & \text{Otherwise} \end{cases}$$

7. Steps from 4 to 10 are repeated until maximum generation reached.

5   Results and Discussion

CSA and QOCSA algorithms are endorsed to construct optimum PID, FOPID and cascade PI-FOPID controllers for two-area reheat-thermal power system with GRC. Both CSA and QOCSA algorithms are accomplished separately with 50 populations and 100 iterations for different controllers. The prime aim of CSA and QOCSA algorithms is to minimize ITAE as referred in Eq. (3). The optimal parameters of different controllers plucked by applying both CSA and QOCSA algorithms are portrayed in Table 1. The performance of CSA algorithm is enhanced by implementing oppositional-based technique. The deviations of frequency and tie-line power are illustrated in Figs. 4, 5 and 6. The system responses (settling time, under-shoot and overshoot) of frequency and tie-line power divergence are portrayed in Table 2. Settling time is determined with tolerance band of 0.05%. ITAE value of

Table 1 Optimal gain parameters of different controllers optimized by CSA and QOCSA algorithms

Controllers		K_1	K_2	K_3	K_4	K_5	λ	μ
QOCSA PI-FOPID	Area-1	0.3608	0.4577	0.7563	0.0010	1.0482	0.8421	0.5666
	Area-2	0.3742	0.0769	1.1976	1.4419	0.3286	0.0970	0.3279
CSA PI-FOPID	Area-1	0.3900	0.4481	1.6216	0.0261	1.0534	0.5082	0.5680
	Area-2	0.3987	0.0686	0.9593	0.5175	0.3957	0.2358	0.2267
CSA FOPID	Area-1	1.1436	1.4284	1.5882			0.9854	0.8561
	Area-2	0.0010	0.2130	1.7503			0.9518	0.0010
CSA PID	Area-1	0.9549	0.7511	1.2417				
	Area-2	1.1655	0.9343	0.7388				
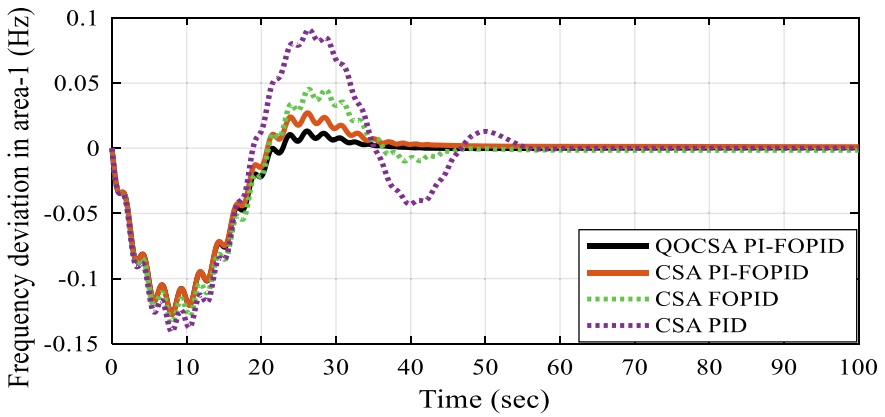
Fig. 4 Frequency deviation in area-1
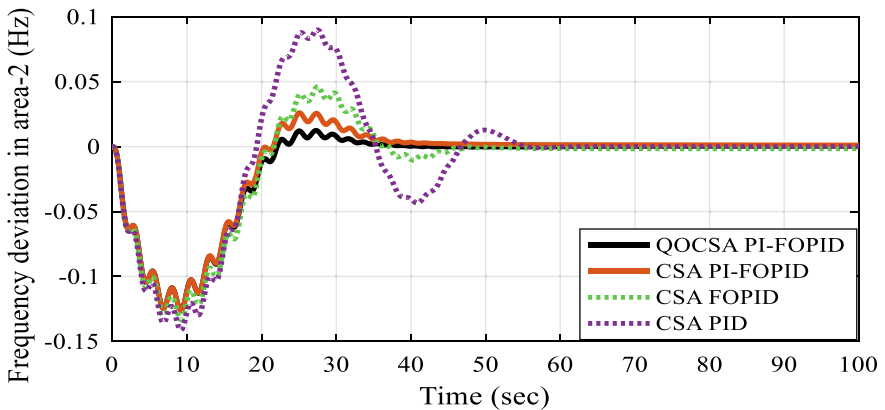
Fig. 5 Frequency deviation in area-2
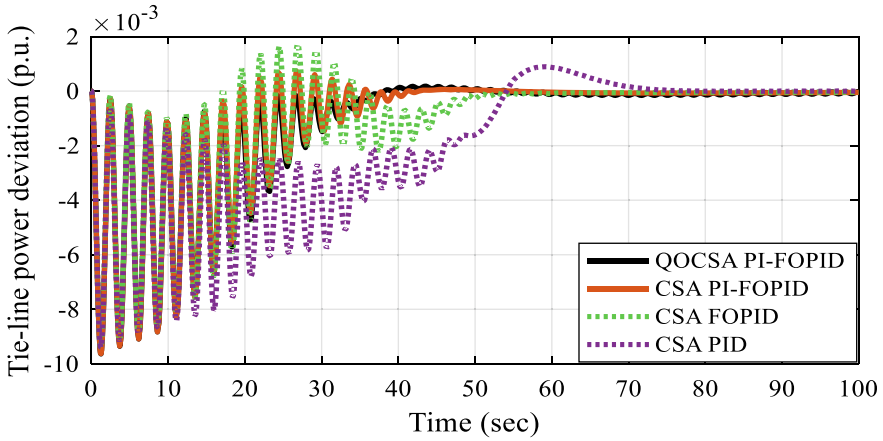
Fig. 6 Tie-line power deviation

Table 2 Performance responses of the system with different controllers optimized by QOCSA and CSA

Controllers		ΔF_1	ΔF_2	ΔP_{tie}
QOCSA PI-FOPID	$U_{sh} \times 10^{-3}$	-140.8512	-126.0215	-9.6351
	$O_{sh} \times 10^{-3}$	13.2410	12.0859	0
	$T_s \times 10^{-3}$	39.82	38.51	46.04
CSA PI-FOPID	$U_{sh} \times 10^{-3}$	-134.1248	-126.1453	-9.6229
	$O_{sh} \times 10^{-3}$	27.1385	26.0321	0.7271
	$T_s \times 10^{-3}$	42.49	43.06	54.58
CSA FOPID	$U_{sh} \times 10^{-3}$	-127.6541	-133.4574	-9.4052
	$O_{sh} \times 10^{-3}$	45.3923	46.1386	1.7224
	$T_s \times 10^{-3}$	47.12	45.61	60.33
CSA FOPID	$U_{sh} \times 10^{-3}$	-127.5218	-141.3258	-9.3921
	$O_{sh} \times 10^{-3}$	90.9874	89.9915	0.8822
	$T_s \times 10^{-3}$	55.34	54.29	73.63

the system with PID, FOPID and cascade PI-FOPID controllers optimized by CSA algorithm is 53.2453, 31.4785 and 20.0788, respectively. ITAE value of system with QOCSA algorithm optimized cascade PI-FOPID controller is 15.1248.

Figures 4, 5 and 6 and Table 2 precisely describe the suprimacy of the cascade PI-FOPID controller. Cascade PI-FOPID controller lessen the transiency (undershoot-U_{sh}, overshoot-O_{sh} and settling time T_s) and ITAE of the system.

6 Conclusion

The purpose of this paper is to validate the cascade PI-FOPID controller optimized by CSA and QOCSA algorithms as a supreme AGC for the reheat-thermal power system with GRC. For this purpose, PID and FOPID controllers are enforced separately in each area as AGC. With 1% load disturbance in area-1, cascade PI-FOPID controller optimized by CSA algorithm is validated. CSA optimized intelligent FOPID and PID controllers are validated as enhanced controllers. Further, the efficacy of the CSA algorithm is boosted by implementing quasi-oppositional technique. Finally, QOCSA algorithm optimized cascade PI-FOPID controller is substantiated with supreme performance of the system.

Appendix 1: Power System Parameters

$K_p = 120$ Hz/p.u. MW, $T_P = 20$ s, $B = 0.4249$; $R = 2.4$ Hz/p.u. MW; $T_g = 0.08$ s; $T_t = 0.3$ s;

References

1. Kundur P (1994) Power system stability and control. McGraw-Hill
2. Ibrahim PK, Kothari DP (2005) Recent philosophies of AGC strategies in power system. IEEE Trans Power Syst 20(1):346–57
3. Ali ES, Abd-Elazim SM (2013) BFOA based design of PID controller for two area load frequency control with nonlinearities. Int J Electr Power Energy Syst 51:224–231. https://doi.org/10.1016/j.ijepes.2013.02.03
4. Dash P, Saikia LC, Sinha N (2015) Automatic generation control of multi area thermal system using bat algorithm optimized PD-PID cascade controller. Int J Electr Power Energy Syst 68:364–372. https://doi.org/10.1016/j.ijepes.2014.12.063
5. Sahu RK, Panda S, Rout UK (2013) DE optimized parallel 2-DOF PID controller for load frequency control of power system with governor dead-band nonlinearity. Int J Electr Power Energy Syst 49(1):19–33. https://doi.org/10.1016/j.ijepes.2012.12.009
6. Gorripotu TS, Sahu RK, Panda S (2016) DE optimized PID controller with derivative filter for AGC of interconnected restructured power system. Comput Intell Data Min 1:395–403. https://doi.org/10.1007/978-81-322-2731-1
7. Sondhi S, Hote YV (2014) Fractional order PID controller for load frequency control. Energy Convers Manage 85:343–353
8. Singh R, Sen I (2004) Tuning of PID controller based AGC system using genetic algorithms. TENCON 3:531–534
9. Dash P, Saikia LC, Sinha N (2016) Flower pollination algorithm optimized PI-PD cascade controller in automatic generation control of a multi-area power system. Int J Electr Power Energy Syst 82:19–28
10. Chandra L, Nanda J, Mishra S (2011) Performance comparison of several classical controllers in AGC for multi-area interconnected thermal system. Int J Electr Power Energy Syst 33(3):394–401

11. Rahman A, Saikia LC, Sinha N (2016) Automatic generation control of an unequal four-area thermal system using biogeography-based optimised 3DOF-PID controller. IET Gener Transmis Distrib 10:4118–4129

12. Nayak JR, Shaw B, Sahu BK (2020) Implementation of hybrid SSA–SA based three-degree-of-freedom fractional-order PID controller for AGC of a two-area power system integrated with small hydro plants. IET Gener Transmis Distrib 14(13):2430–2440

13. Indulkar CS, Raj B (1995) Application of fuzzy controller to AGC. Electr Mach Power Syst 23:209–220

14. Nayak JR, Shaw B, Sahu BK (2020) Hybrid Alopex based DECRPSO algorithm optimized fuzzy-PID controller for AGC. J Eng Res 8(1)

15. Pati TK, Nayak JR, Sahu BK, Kar SK (2015) Automatic generation control of multi-area thermal power system using TLBO algorithm optimized fuzzy-PID controller. In: 2015 international conference on circuits, power and computing technologies [ICCPCT-2015]. IEEE, pp 1–6

16. Guha D, Roy PK, Banerjee S (2021) Performance evolution of different controllers for frequency regulation of a hybrid energy power system employing chaotic crow search algorithm. ISA Trans

17. Sahu BK, Pati TK, Nayak JR, Panda S, Kar SK (2016) A novel hybrid LUS-TLBO optimized fuzzy-PID controller for load frequency control of multi-source power system. Int J Electr Power Energy Syst 74:58–69

18. Nayak JR, Pati TK, Sahu BK, Kar SK (2015)F uzzy-PID controller optimized TLBO algorithm on automatic generation control of a two-area interconnected power system. In: IEEE international conference on circuit, power and computing technologies, ICCPCT 2015, pp 4–7

19. Pati TK, Nayak JR, Sahu BK (2015) Application of TLBO algorithm to study the performance of automatic generation control of a two-area multi-units interconnected power system, In: IEEE international conference on signal processing, informatics, communication and energy systems (SPICES)

20. Pati S, Sahu BK, Panda S (2014) Hybrid differential evolution particle swarm optimisation optimised fuzzy proportional-integral derivative controller for automatic generation control of interconnected power system. IET Gener Transmis Distrib 8(11):1789–1800

21. Nayak JR, Shaw B, Sahu BK (2018) Application of adaptive-SOS (ASOS) algorithm based interval type-2 fuzzy-PID controller with derivative filter for automatic generation control of an interconnected power system. Eng Sci Technol Int J 21(3):465–485

22. Nayak JR, Shaw B, Das S, Sahu BK (2018) Design of MI fuzzy PID controller optimized by modified group hunting search algorithm for interconnected power system. Microsyst Technol 24(9):3615–3621

23. Askarzadeh A (2016) A novel metaheuristic method for solving constrained engineering optimization problems: crow search algorithm. Comput Struct 169:1–12

24. Das S, Sahu TP, Janghel RR (2020) PSO-based group-oriented crow search algorithm (PGCSA). Eng Comput 38(2):545–571. https://doi.org/10.1108/EC-07-2019-0305

25. Nayak JR, Shaw B, Dewangan NK (2020) Generation control of isolated small hydro power plant by using DECSA optimized FPI controller. World J Eng 18(2):280–292. https://doi.org/10.1108/WJE-07-2020-0244

26. Tizhoosh HR (2005) Opposition-based learning: a new scheme for machine intelligence. In: International conference on computational intelligence for modelling, control and automation and international conference on intelligent agents, web technologies and internet commerce (CIMCA-IAWTIC'06), vol 1. IEEE, pp 695–701

Optimization of the Controller Parameter to Improve the Frequency Response in the Hybrid System

Umer Farooq Tak, A. K. Vamsi Krishna Reddy, and Javed Dhillon

Abstract Since from the last decade, there is increase in the operation of renewable-based hybrid power system for the power generation purpose, which may cause frequency-related problem due to the use of small capacity synchronous and induction generator, which offers lesser inertia. To deal with these problems, a linearized model of wind and small hydrosystem with frequency controller loop has been developed for an isolated system. The controller used in the system, not only improves the transient response of the generation but also deals with the load uncertainty. The controller parameter has been optimized by particle swarm optimization (PSO) technique to provide the proper coordination between the wind and small hydrosystems to improve the output frequency response.

Keywords Small hydropower system · Wind system · Particle swarm optimization (PSO) · Frequency

1 Introduction

Renewable and sustainable power sources and their framework are for the most part used to diminish the pollution from ordinary electric force sources, as the sources of hybrid power plant have moderate to small greatest up to 10 MW which are associated with the appropriation distribution voltage level. Wind power plants work at most extreme operating to achieve increasingly monetary advantages. Because of adaptable element of wind power, the turbine can be controlled to deliver crucial dynamic force for the improvement of recurrence for a small hydropower (SHP) plant. In this paper, an attempt has been made to improving the frequency response of the SHP plant by considering the speed droop and inertial control of wind turbine. In this study, proportional-integral (PI) and proportional-derivative (PD) have been used to represent the speed and inertial control, respectively, for the wind turbine.

U. F. Tak (✉) · A. K. Vamsi Krishna Reddy · J. Dhillon
School of Electronics and Electrical Engineering, Lovely Professional University, Phagwara, Punjab 144411, India
e-mail: junaidfarooq194@gmail.com

PI and PD controller are tuned by using the exploratory prowess of particle swarm optimization (PSO)—the classical optimization paradigm, to reduce the frequency error through the perfect balancing of the power generation and load demand. In this paper, doubly fed induction generator (DFIG) has been adopted for frequency regulation.

A design method for the load frequency control with PID has been proposed by many authors [1–7] that established various advanced control theories. Because of effortlessness, wide scope of uses and simple execution on any stage, regular controller, for example, P PI and PD are as yet utilized in the power industry. In this paper, it is recommended that the limit augmentation of current framework has created the need of coordinating wind energy conversion system (WECS) with the power grid. With the increase of wind generation, the influence on frequency control of system takes place. Due to the vulnerability in wind power production, the issue to control the frequency and voltage become another exploration zone in the field of generation control. WECS utilizes variable speed wind turbine (VSWT) is outfitted with pitch edge angle control that engages its speed to stay coordinated with the network frequency. Whenever there are disturbances in network frequency, VSWTs coupled with DFIG are used to control the output frequency in a wide range with the help of stored mechanical energy in wind turbine which further enable the short-term real power support. With the increase in DFIG-based WECS, there is decrease in the natural inertial response capability of the system as the decoupling of natural dynamics of $\Delta P \sim \Delta f$ in power electronic converters occurs, due to which the conventional generators stop them from responding to change in system frequency. An additional control mechanism in DFIG has been introduced to overcome above mentioned issue to restore the inertial capability of the WECS. In order to achieve the better frequency regulation, a controller has been introduced in WECS to provide the additional pseudo-hidden inertia without effecting the performance of AGC controller Optimization algorithm pays increased attention in the past few years by industry and research community. It is a numerical algorithm or method to determine the minima or maxima of a function operating with certain constraints. A technique based on swarm optimization is referred as particle swarm optimization (PSO) technique. The 'swarm' is referred with particle of random solutions. In swarm optimization techniques, each particle corresponds a various possible set of the unknown parameters to be optimized. The controller boundaries are appropriately tuned to alter inertial control method to halfway utilize the stored kinetic energy put away of WECS. Additionally, reaction in WECS is connected to the ordinary units (SHP) so as to lessen frequency deviation and to deal with the imbalances in the load.

2   Single Area AGC Model for Small Hydrosystem

In modelling of hydropower plant, it consists of governor, turbine and generator. The schematic block diagram representation of small hydropower plant is depicted in Fig. 1.
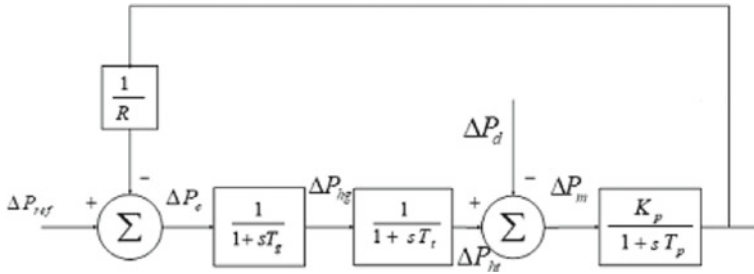
Fig. 1 Single area controller for small hydrosystem

From the block diagram representation, speed governor transfer function is given as;

$$G_g(s) = \frac{\Delta P_{\text{hg}}(s)}{\Delta P_e(s)} = \frac{1}{1 + sT_g} \tag{1}$$

Hydrogovernor transfer function is given below as;

$$G_t(s) = \frac{\Delta P_{\text{ht}}(s)}{\Delta P_{\text{hg}}(s)} = \frac{1}{1 + sT_t} \tag{2}$$

The transfer function of generator which is connected to the power system is given as;

$$G(S) = \frac{\Delta F(S)}{\Delta P_m(s)} = \frac{K_P}{1 + K_P T_P} \tag{3}$$

2.1 Single Area AGC Model with WECS

The linearized system model for the load frequency control (LFC) of single region associated power framework having little hydroframework with penetration of wind power is represented in Fig. 2. As delineated in Fig. 3, the DFIG goes about as generator for wind capacity to real power through both rotor and stator of the induction generator. To make interconnection between two converters capacitor is placed in between them. Two cases arise for the proper function of the converters in DFIG. At the typical conditions to accomplish the course of action of the maximum power point tracking (MPPT), converters permit the variable speed wind turbine (VSWT) to catch wind vitality over a wide range of wind speeds. Presently during unpredictable state of wind or having any disturbance in network, the controllers for the both the converters in that condition achieve a quick control of reactive and active
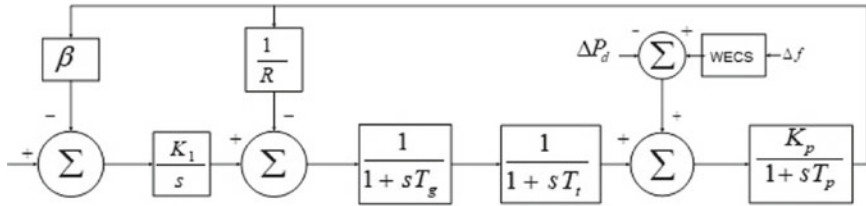
Fig. 2 Single area interconnected power system with WECS
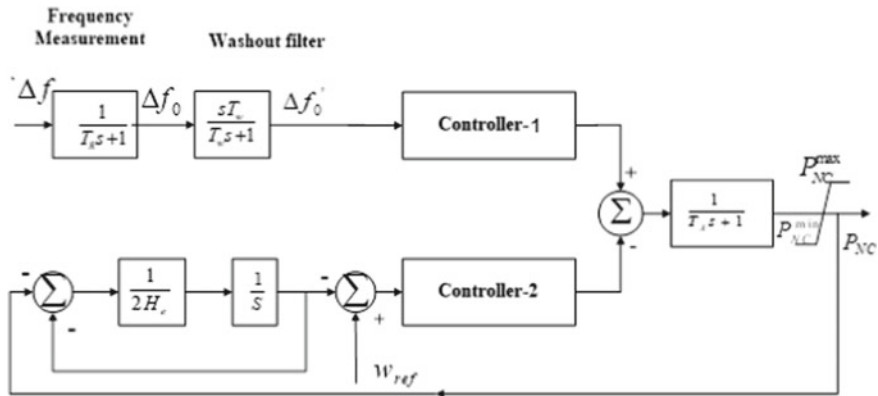
Fig. 3 DFIG-based WECS

power yield by resulting in a proper control techniques (Kellog et al. [8], Hughes et al. [9], Anaya-Lara et al. [10], Almeida and Lopes [11], Mauricio et al. [12], and Bhatt et al. [13]).

Due to real power, control capability of DFIG frequency regulation is maintained in the system. In wind turbines, substantial quantity of kinetic energy is stored in the rotating mass of the blades. When there occurs sudden step change in the load DPL, having penetration of wind level (LP), impact of the inertia from the wind farm could be appropriately improved due to the improved power step away from the steady state power setting.

In hydrowind system, values of regulation droop (R) system inertia (H) change with a variation in Lp.

Two types of controllers have been used to control system frequency in wind integrated hydropower system.

2.2 Controller-1 (Inertia Controller)

The controller-1 is an inertial controller (PD controller). The function of the controller in VSWT, is to control the active power injection in the integrated system for providing the frequency support. Equation 4 defines the additional power supplied by the inertial controller to the reference power which is been followed by the equivalent controller of the small hydromachine.

$$p_f = -K_{dd}\frac{d\Delta f_0}{dt} - K_{pd}\Delta f_0 \qquad (4)$$

where K_{pd} and K_{dd} are the tuning parameters for the PD controller which provides the frequency support to the integrated system. The frequency deviation (Δf) is applied through a high pass filter, and whenever the Δf violating the filter limits, it triggers the PD controller to set the new power demand by adding the signal to the Eq. 4. As the power demand increases, it reduces the Δf to provide the frequency support to the system. The value of the inertia (H) into a system can be established arbitrarily by varying K_{dd}. When value of K_{dd} is positive, original damping term is increased to reduce the frequency oscillation across the output. The main advantage of the inertial controller is that inertia is increased into the system, but there is no direct frequency support.

2.3 Controller-2 (Frequency Controller)

Controller-2 comprises of PI controller. Crafted by the PI controller's work is to retain the ideal speed of the ordinary generators, after the transient time frame is finished. The quick speed recuperation in littler time of transient speed variety is allowed due to the design constants (K_{wp}, K_{wi}) of the PI controller. The machine may maybe go in the period of deferral (phase of delay), if the speed is admissible to diminish for expanded length by the effect in frequency regulation. The new steady state has been achieved for the system frequency which is to some extent less than the required value this deviation is controlled by the speed droop effects of SHP.

The DFIG-based WECS has been shown in Fig. 3, which consists of washout filter (high pass filter). The work of the washout filter is to regulate the frequency for a longer duration. Permanent system frequency in case of non-conventional generators is not possible due to the stored kinetic energy and can only act in a transient period, hence cannot afford deviation in permanent system frequency.

3 Methodology for Optimization

3.1 Problem Formulation

In the study, three types of controller have been used, controller-1 (PD) for DFIG, controller-2 (PI) for wind turbine rotor and integral controller for the hydrosystem. PSO-based optimization technique has been used to tune these parameters (K_i, K_{pd}, K_{dd}, and K_{wp}, K_{wi}) to improve the output response of hybrid system. The key objective of the optimization problem is to minimize the square of the error signal and maximum overshoot of error signal as given in Eq. 5 Parameters are subjected to various inequality constraints which have been defined in Eq. 6

$$J = \sum_{i=0}^{t}(|\Delta f_i|)^2 + \max(|\Delta f_i|) \tag{5}$$

Subjected to

$$K_{i_{\min}} \leq K_i \leq K_{i_{\max}}$$
$$K_{pd_{\min}} \leq K_{pd} \leq K_{pd_{\max}}$$
$$K_{dd_{\min}} \leq K_{dd} \leq K_{dd_{\max}}$$
$$K_{wp_{\min}} \leq K_{wp} \leq K_{wp_{\max}}$$
$$K_{wi_{\min}} \leq K_{wi} \leq K_{wi_{\max}} \tag{6}$$

3.2 Particle Swarm Optimization (PSO)

It is a swarm/population-based meta-heuristics optimization technique, developed by Kennedy [14] and Kennedy and Eberhart [15]. Particle swarm optimization (PSO) is a population-based stochastic algorithm which draws its inspiration form the natural behaviour of birds or fishes to find the food sources that also known as swarm intelligence. This computer-based algorithm modelled on the swarm intelligence to find an optimal solution to an optimization-based problem in order to satisfy the objective function, subjected to various linear and nonlinear constraints. The algorithm initialized with a population of random variable known as particles denoted by x_{id}, and velocity vector vid is used to update the particle position by the following local and global best solution denoted by p_{id} and p_{gd}, respectively. Each particle is updated its position as per the following equation.

$$v_{id}(n+1) = wv_{id}(n) + c_1 r_1\big(p_{id}(n) - x_{id}(n)\big) + c_2 r_2\big(p_{gd}(n) - x_{id}(n)\big) \tag{7}$$

$$x_{id}(n + 1) = x_{id}(n) + v_{id}(n + 1) \tag{8}$$

where w stands for the initial weight, $c1$ and $c2$ are the velocity constants used for the global and local exploitation and $r1$ and $r2$ are the random variable which varies their values between [0, 1]. The detailed process of optimization of the PSO algorithm for the given problem has been shown in Fig. 4.

Fig. 4 Flowchart of the PSO algorithm
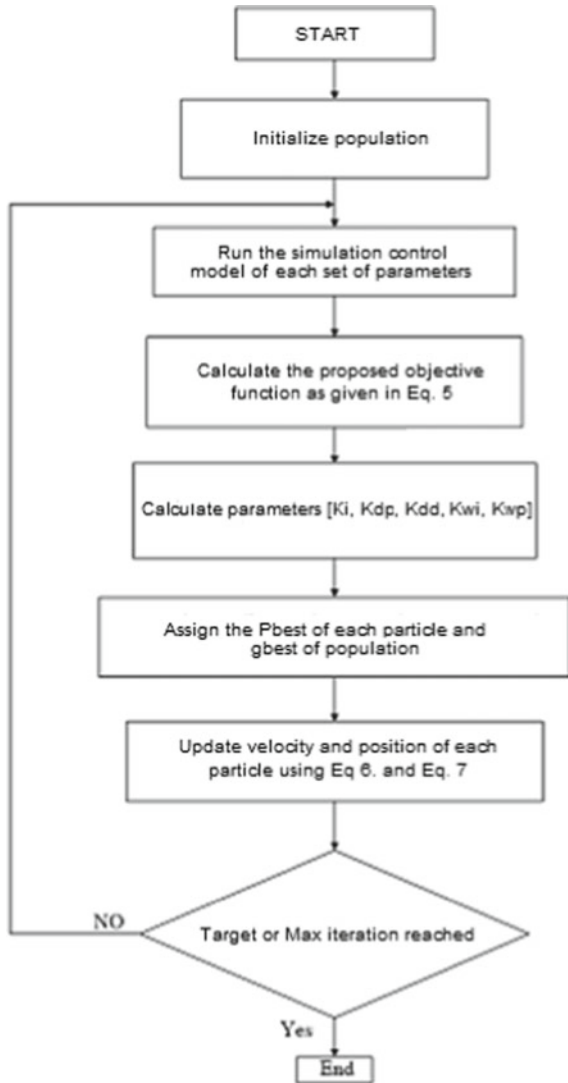
4 Results and Discussion

The control areas system has been considered in the paper subjected to the 2% load variation, whereas the input to the wind and small hydrosystem assume to be constant. Due to the effect of change in load, the frequency deviation across the system for the single area with and without the WECS system has been depicted in Figs. 5 and 6, respectively.

The proposed method has been used to optimize the controller parameters through metaheuristic optimization for both single and two area system using MATLAB/Simulink. The parameter of the controller has been tuned with the help of the PSO to reduce the frequency deviations and the real power imbalance. Table 1 shows the results of controller parameters for single area and two area system, respectively, optimized by the PSO to minimize the objective function while satisfying the various bounding constraints.
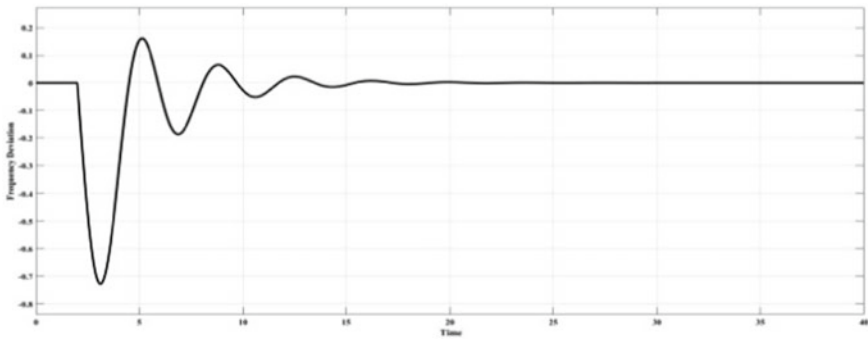
Fig. 5   Frequency response of small hydrosystem
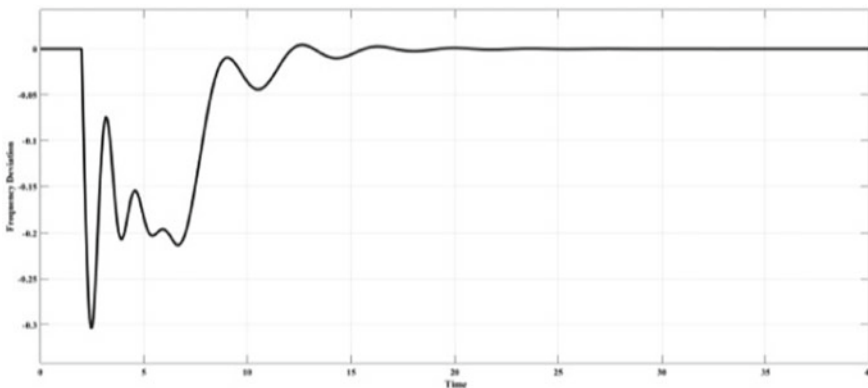
Fig. 6   Frequency response of single area hybrid system (small hydro and WECS)

Table 1 Optimized controller parameter

PID parameter	K_i	K_{dp}	K_{dd}	K_{wi}	K_{wp}
Single area	0.16	3.97	0.028	1.191	0.5
Two area	0.08	1	0.196	0.002	1

The effect of the optimized parameter on the single and two areas system has been shown in Figs. 7 and 8, respectively. It has been seen that the maximum frequency deviation of two areas system is reduced to nearly half compared to single areas system, which will further be reduced in the largely interconnected power system, where stored energy of wind power is efficiently utilized to reduce the effect of power and frequency imbalance.
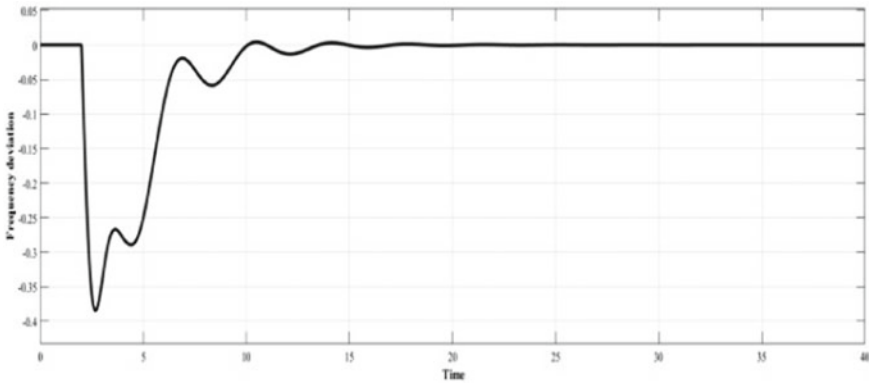
Fig. 7 Frequency response of single area hybrid system with optimized controller parameter (small hydro and WECS)
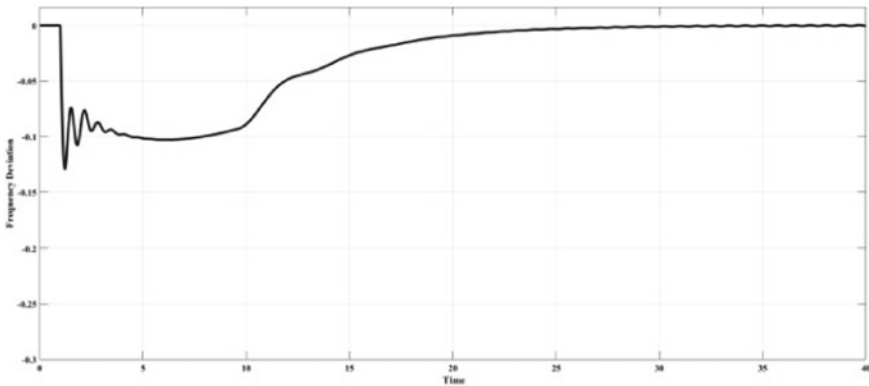
Fig. 8 Frequency response of two area hybrid system with optimized controller parameter (small hydro and WECS)

5   Conclusion

Load frequency control gets important, when wind power production is presented in huge sum. In this paper, load frequency control with huge immersion of sustainable has been inspected in the presence of hydro and wind framework with PID controller. It is seen that frequency deviation is low when wind system is introduced into the actual hydrosystem and is within the acceptable limits for fixed variations in load. The parameters of PID controller are optimally tuned based on the particle swarm optimization algorithm, and controller coefficients are optimized. Optimal purpose of the controller by particle swarm optimization algorithm shows that this algorithm is quite successful in tuning of the parameters of PID controller and is more promising compared with the outcomes of other optimization methods. In comparison to other methods, PID controller with new structure gives well performance. In this paper, PI controller is optimized by using particle swarm optimization algorithm to regulate frequency during the load variations or uncertainties occurring in the system. Also, a hybrid power system has been designed in an isolated mode with a wind energy conversion system and hydropower plant. The wind turbine implemented for hybrid system is variable and is considered to function in a medium wind speed range. To tune PI controller by dominant computational techniques, PSO is executed to improve the frequency response for the hydropower plant. From the simulation results, it shows that PI controller utilized for hydropower plant alongside creating edge of wind energy transformation framework effectively controls the variation in frequency within the changes in load change and deviation in wind speed.

References

1. Bevrani H, Daneshmand PR (2012) Fuzzy logic-based load-frequency control concerning high penetration of wind turbines. IEEE Syst J:173–180
2. Bevrani H, Mitani Y, Tsuji K (2004) Robust decentralized load-frequency control using an iterative linear matrix inequalities algorithm. Proc Inst Electr Eng Gener Transm Distrib 151:3
3. Datta M, Senjyu T, Yona A, Funabashi T (2011) Fuzzy control of MW-class PV generation to reduce frequency and tie-line power fluctuations in three control area power system. In: 2011 IEEE international conference on fuzzy systems, Taipei, pp 2440–2447
4. Majhi S, Padhan DS (2013) A new control scheme for PID load frequency controller of single-area and multi-area power systems. ISA Trans:242–251
5. Naik S, Chandra Sekhar K, Vaisakh K (2005) Adaptive PSO based optimal fuzzy controller design for AGC equipped with SMES. J Theor Appl Inf Technol:8–17
6. Liu XJ, Zhang JW (2009) CPS compliant fuzzy neural network load frequency control. In: American control conference, St. Louis, pp 2755–2760
7. Zhang S, Mishra Y, Shahidehpour M (2016) Fuzzy-logic based frequency controller for wind farms augmented with energy storage systems. IEEE Trans Power Syst 31(2):1595–1603
8. Kellogg WD et al (1998) Generation unit sizing and cost analysis for stand-alone wind, photovoltaic and hybrid wind/PV systems. IEEE Trans Energy Convers 13(1):70–75
9. Hughes FM, Anaya-Lara O, Jenkins N, Strbac G (2005) Control of DFIG-based wind generation for power network support. IEEE Trans Power Syst 209(4):1958–1966

10. Anaya-Lara O, Hughes FM, Jenkins N, Strbac G (2006) Contribution of DFIG-based wind farms to power system short-term frequency regulation. Proc Inst Elect Eng Gen TransmDistrib 153(2):164–170
11. Almeida RG, Lopes RG (2007) Participation of doubly fed induction wind generation in system frequency regulation. IEEE Trans Power Syst 22(3):944–950
12. Mauricio JM, Marano A, Gomez-Exposito A, Martinez RJL (2009) Frequency regulation contribution through variable-speed wind energy conversion systems. IEEE Trans Power Syst 24(1):173–180
13. Bhatt P, Roy R, Ghosbal SP (2011) Dynamic participation of doubly fed induction generator in automatic control. Sci Direct Renew Energy 36:1203–1213
14. Kennedy J (1997) The particle swarm: social adaptation of knowledge. In: Proceedings of IEEE international conference on evolutionary computation, Indianapolis, pp 303–308
15. Kennedy J, Eberhart RC (1995) Particle swarm optimization. In: Proceedings of IEEE international conference on neural networks, Piscataway, NJ, pp 1942–1948

Automatic Generation Control of Multi-Area Power System

Teresa Devarapalli and M. S. Krishnarayalu

Abstract In a power system, the load differs continuously. As a result, frequency also differs continually. Automatic generation control (AGC) has a crucial role in the entire power system network, which is used to control the changes in scheduled tie-line powers by maintaining rated frequency within tolerable limits. Basic load frequency control (LFC) with only primary controllers like governors may or may not satisfy the power system constraints due to steady-state errors and sluggish response. Unsatisfactory secondary controllers also may result in power blackouts. To get good transient and steady-state responses, different secondary controllers like proportional, integral, and derivative (PID), active disturbance rejection controller (ADRC), and PI-PD controllers are used for the real three area power system (IEEE paper) with reheat and non-reheat thermal plants. Here the method of particle swarm optimization is used for tuning the PID and PI-PD controllers. The resulting power systems are simulated and analyzed using MATLAB/Simulink software to present a better secondary controller.

Keywords Active disturbance rejection controller · Automatic generation control · Frequency deviation · Multi-area power system · Particle swarm optimization · Deviation of tie-line power · PID and PI-PD controllers

Nomenclature

$\triangle P_L$	: Change in load of an area.
$\triangle F_i$	: Deviation of frequency in ith area.
$\triangle P_{\text{Tiei}}$	: Deviation of tie-line power in ith area subscripts.
t	: Turbine.
g	: Governor.

T. Devarapalli (✉) · M. S. Krishnarayalu
Department of Electrical and Electronics Engineering, VR Siddhartha Engineering College, Kanuru, India
e-mail: teresadevarapalli@gmail.com

r   : Reheat.
p   : Plant.
P   : Proportional.
I   : Integral.
D   : Derivative.

1 Introduction

The primary responsibility of the load frequency control of a power system is to balance the load demand and generation of power for maintaining the nominal frequency and tie-line powers within the tolerable limits. Automatic generation control is essential in a power system for quality power and reliability of the system Hadi Saadat [1], Wood [2]. The tie lines in the power system help to get connected to the various areas. AGC can also be used to achieve maximum economy by dividing the loads among system stations and generators and adjusting the tie-line powers at the same time attaining a reasonable uniform frequency.

To make the interconnected power system more reliable, economic, and effective, secondary controllers such as PID, PI-PD, and ADRC are used for automatic generation control. Few tuning techniques of PID and PI-PD controllers are Ziegler–Nichols (ZN), trial and error, particle swarm optimization (PSO) by Zwe-Lee Gaing [3], Charitha Reddy [4–8], fuzzy logic (FL), artificial neural network (ANN), and genetic algorithm (GA) methods. PID controller is used in many appliances because of its simplicity and stability. PID controllers improve transient and steady-state responses. And the cascaded PI-PD controller is a combination of two processes where the output of the inner process supplies to the outer process. Reduction of disturbance effect on the outer process is the main objective of this controller. The improved system performance is obtained with the cascaded PI-PD controller by Reddy [4]. The main task is to maintain the steady-state deviations at zero with good transient response. To overcome the variations in frequency, voltage, and tie-line powers, secondary controllers like active disturbance rejection control (ADRC) have been developed to minimize these variations in the power system. Automatic generation control is simulated with different secondary controllers like PID tuned by the PSO algorithm, ADRC controllers by Nagarjuna [3, 9–11], and fuzzy controller by Yousef [12]. Automatic voltage regulator (AVR) with ADRC by Nagarjuna [9], PSO-PID controller by Zwe-Lee Gaing [3] simulated. Load frequency control (two area system) with the ADRC controller implemented in Krishnarayalu [10, 11].

J. Han proposed the active disturbance rejection control which estimates and rejects the uncertainties both internally and externally in real-time Jing-Qing Han [13]. This controller mainly deals with the extended state observer and a state feedback controller. Extended state observer (ESO) is expected the unknown fractions (nonlinearities, uncertainties, and external disturbances) are taken as a total disturbance. Reduction of uncertainties and robustness of the controller are the main

features of ADRC controller. To detect the disturbance and rejection of that disturbance in the real time is the capability of ADRC. This paper aim is to establish good secondary controller for AGC of a multi-area power system. ADRC, PID, and PI-PD controllers are tested for this purpose.

2   Automatic Generation Control

AGC is useful for the operation of interconnected power system. The important aspect of the system's operation and control is to supply quality power. AGC always tries to maintain the frequency and tie-line powers to scheduled values by controlling the generation automatically to meet the load demand. The area control error (ACE) is minimized to zero for maintenance of deviations in the frequency and tie-line powers within tolerable limits. Secondary controllers are constructed to regulate the ACE to zero.

2.1   AGC of a Multi-Area Power System

Consider the two area power system represented by equivalent generating units interconnected by a lossless tie line with reactance Xtie as shown in Fig. 1.

The mathematical representation of the multi-area power system is shown.

AGC is more on the tie-line bias control, and each area tends to minimize the area control error to zero. ACE is function of frequency and tie-line power deviations in each area.

Fig. 1 Two area power system equivalent network
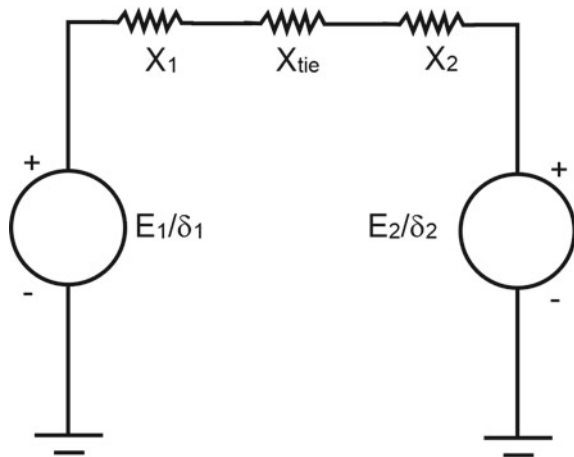
$$ACE_i = \sum_{\substack{j=1 \\ \neq i}}^{n} \Delta P_{ij} + K_i \Delta \omega_i \tag{1}$$

K_i represents the amount of interaction for the neighboring areas during the disturbance. For the satisfactory performance, K_i will be equal to the frequency bias factor B_i.

$$ACE_i = \sum_{\substack{j=1 \\ \neq i}}^{n} \Delta P_{ij} + B_i \Delta \omega_i \tag{2}$$

Block diagram of AGC of a two area power system is shown in Fig. 2.
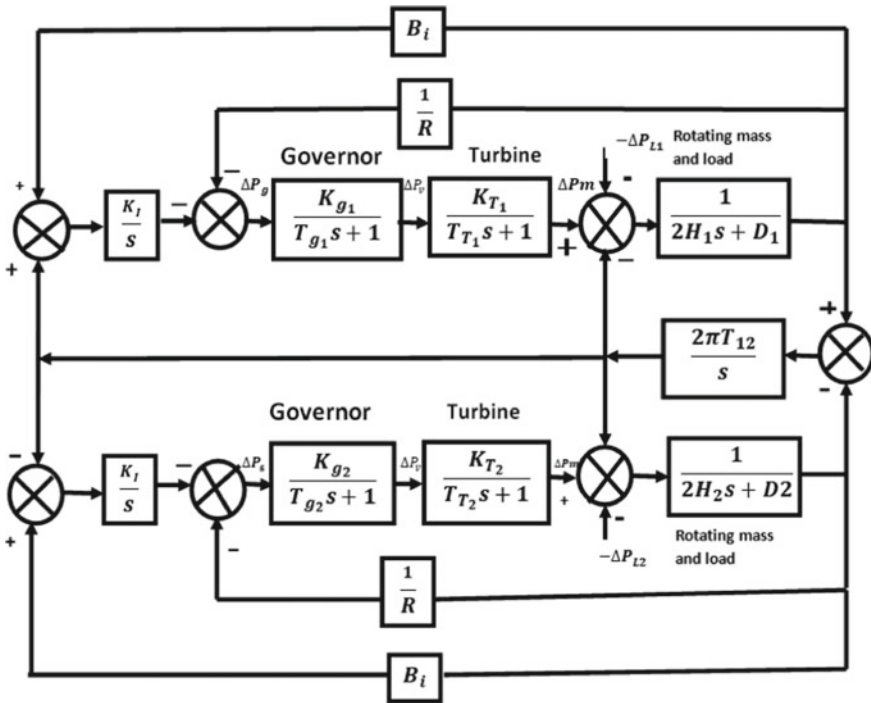
Fig. 2 AGC block diagram of a two area power system

3 Active Disturbance Rejection Control

Active disturbance rejection control (ADRC) was proposed by Jing-Qing Han [13]. In the process of designing, the observer plays a major role in knowing the actual disturbances and different uncertainties. It has extended state observer and a state feedback controller. Extended state observer of $(n + 1)$th order estimates the states of nth-order system with both the internal and external disturbances. For regulating the tracking error between the real output and reference signal, state feedback controller is used for the plant or system Nagarjuna [10], Gang Tian [9], Gao [3]. Successful application of ADRC will mainly depend upon the reformulating the problem by putting different known and unknown quantities which have an effect on system performance into total disturbance. The complex problem is transformed into simple by this fundamental step. The basic diagram of power system with primary loop is in Fig. 3.

3.1 Design of ADRC Controller [14]

There are three steps included in the ADRC design for nth-order system. They are:

1. Plant simplification
2. Observer gains calculation
3. Controller gains computation.

The general physical model form of transfer function including primary loop is represented by

$$G_p(s) = \frac{Y(s)}{U(s)} = \frac{b_{m+1}s^m + b_m s^{m-1} + \cdots + b_2 s + b_1}{a_{n+1}s^n + a_n s^{n-1} + \cdots + a_2 s + a_1}, n \geq m \qquad (3)$$

where $U(s)$ and $Y(s)$ are input and output plants. ai and bj are transfer function coefficients. By long hand division principle, the plant is remodeled and represented as

Fig. 3 Basic figure of power system with primary loop
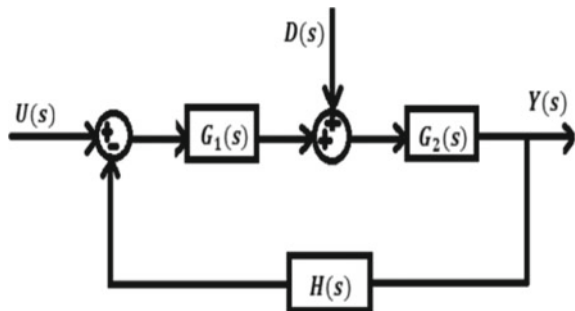
$$s^{n-m}Y(s) = b_0 u(s) + D(s) \tag{4}$$

where

$$b_0 = \frac{b_{m+1}}{a_{n+1}} \tag{5}$$

D(s) involves the internal and external disturbance, b_o is the high-frequency gain and plant is of the order $n - m$. ESO is the one which estimates the disturbance, and by the disturbance rejection process, these effects will be removed. The process of evaluating the observer and controller gains is discussed in Sai teja (2015).

Observer gains with the bandwidth of ω_o,

$$l_i = \binom{n-m+1}{i} \omega_0^i, \quad i = 1, 2, ...n - m + 1 \tag{6}$$

Controller gains with the bandwidth of ω_c,

$$K_i = \binom{n-m}{n-m-i+1} \omega_c^{n-m-i+1}, \quad i = 1, 2, ...\, n - m. \tag{7}$$

The model of ESO may be represented as

$$\begin{pmatrix} \dot{\hat{x}}_1 \\ \dot{\hat{x}}_2 \\ \dot{\hat{x}}_3 \\ \dot{\hat{x}}_4 \end{pmatrix} = \begin{pmatrix} -l1100 \\ -l2010 \\ -l3001 \\ -l4000 \end{pmatrix} \begin{pmatrix} \hat{x}_1 \\ \hat{x}_2 \\ \hat{x}_3 \\ \hat{x}_4 \end{pmatrix} + \begin{pmatrix} 0 \\ 0 \\ b0 \\ 0 \end{pmatrix} u(t) + \begin{pmatrix} l1 \\ l2 \\ l3 \\ l4 \end{pmatrix} y(t)$$

The basic topology of the ADRC is shown in Fig. 4.

Design of ADRC for Reheat Thermal Plant 1: (**Area1**).

The overall transfer function of primary loop of reheat thermal plant is obtained as

$$G_p(s) = \frac{Y(s)}{U(s)} = \frac{0.3s + 1}{16.7s^4 + 200.424s^3 + 350.988s^2 + 175.004s + 25.4}$$

From the plant transfer function $n = 4$, $m = 1$, $a_5 = 16.7$, $b_2 = 0.3$.

$$b_o = \frac{0.3}{16.7} = 0.017964.$$

Model of ESO is obtained as
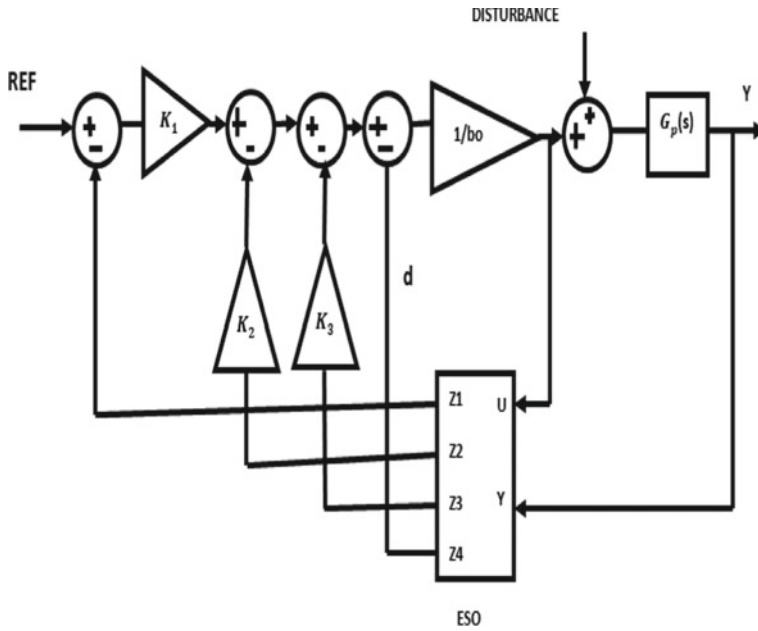
Fig. 4 Basic topology of the ADRC

$$
\begin{pmatrix} \dot{x}_1 \\ \dot{x}_2 \\ \dot{x}_3 \\ \dot{x}_4 \end{pmatrix} = \underbrace{\begin{pmatrix} 0 & 1 & 0 & 0 \\ 0 & 0 & 1 & 0 \\ 0 & 0 & 0 & 1 \\ 0 & 0 & 0 & 0 \end{pmatrix}}_{A} \begin{pmatrix} x_1 \\ x_2 \\ x_3 \\ x_4 \end{pmatrix} + \underbrace{\begin{pmatrix} 0 \\ 0 \\ 0.017964 \\ 0 \end{pmatrix}}_{B} u + \underbrace{\begin{pmatrix} 0 \\ 0 \\ 0 \\ 1 \end{pmatrix}}_{E} \dot{d}
$$

Observer bandwidth $\omega_o = 20 \text{rad/s}$
ESO may be written in terms of observer gains as

$$
\begin{pmatrix} \dot{\hat{x}}_1 \\ \dot{\hat{x}}_2 \\ \dot{\hat{x}}_3 \\ \dot{\hat{x}}_4 \end{pmatrix} = () \begin{pmatrix} \hat{x}_1 \\ \hat{x}_2 \\ \hat{x}_3 \\ \hat{x}_4 \end{pmatrix} + \begin{pmatrix} 0 \\ 0 \\ 0.017964 \\ 0 \end{pmatrix} u(t) + \begin{pmatrix} 80 \\ 2400 \\ 32000 \\ 160000 \end{pmatrix} (y - \hat{y})
$$

$$
= \underbrace{\begin{pmatrix} -80 & 1 & 0 & 0 \\ -2400 & 0 & 1 & 0 \\ -32000 & 0 & 0 & 1 \\ -160000 & 0 & 0 & 0 \end{pmatrix}}_{A-LC} \begin{pmatrix} \hat{x}_1 \\ \hat{x}_2 \\ \hat{x}_3 \\ \hat{x}_4 \end{pmatrix} + \underbrace{\begin{pmatrix} 0 \\ 0 \\ 0.017964 \\ 0 \end{pmatrix}}_{B} u(t) + \underbrace{\begin{pmatrix} 80 \\ 2400 \\ 32000 \\ 160000 \end{pmatrix}}_{L}
$$

Controller gains: for $\omega_c = 20 \text{rad/s}$

$K_1 = 1000, K_2 = 300, K_3 = 30$.

Design of ADRC for Reheat Thermal Plant 2: (**Area2**).

The overall transfer function of primary loop of reheat thermal plant is obtained as

$$G_p(s) = \frac{Y(s)}{U(s)} = \frac{0.3s + 1}{8.95s^4 + 107.411s^3 + 188.082s^2 + 97.231s + 25.11}$$

From the plant transfer function $n = 4$, $m = 1$, $b_2 = 0.3$, $a_5 = 8.95$.

$$b_o = \frac{0.3}{8.95} = 0.033519$$

Observer gains: $l_1 = 80$; $l_2 = 2400$; $l_3 = 32{,}000$; $l_4 = 160{,}000$.

Controller gains: $K_1 = 1000$; $K_2 = 300$; $K_3 = 30$.

Design of ADRC for Non-Reheat Thermal Plant: (**Area3**).

The transfer function of the plant is

$$G_p(s) = \frac{Y(s)}{U(s)} = \frac{1}{0.93s^3 + 11.6268s^2 + 23.273s + 25.046}$$

From the plant transfer function $n = 3$, $m = 0$, $a_4 = 0.93$, $b_1 = 1$.

$$b_o = \frac{1}{0.93} = 1.07526$$

Observer gains: $l_1 = 80$; $l_2 = 2400$; $l_3 = 32{,}000$; $l_4 = 160{,}000$.

Controller gains: $K_1 = 1000$; $K_2 = 300$; $K_3 = 30$.

4   Tuning of PID and PI-PD Controllers

4.1   PID Controller

Proportional–integral–derivative (PID) controller is a control device employed in the industries. The difference between the set point which is desired controlled variable, and measured process variable is the error $e(t)$. PID controller converts this error signal into a manipulated variable $u(t)$ which will be applied to plant. PID controller is error activated with simple structure and easy to understand the functionality and applicability. The mathematical representation of PID controller is

$$G_{PID}(s) = K_P + \frac{K_I}{s} + K_D s \tag{8}$$

Fig. 5 Feedback control system with PID controller
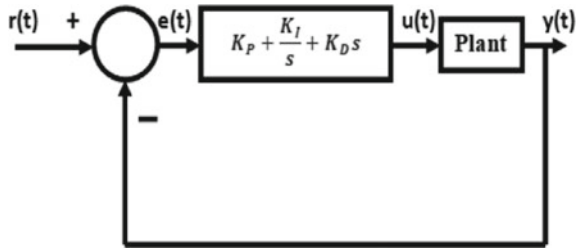
where K_P, K_I, K_D are the proportional, integral, and derivative gains, respectively. Basic diagram of the PID controller is shown in Fig. 5.

There are different tuning techniques for these controllers. Some of them are Ziegler–Nichols (ZN) method, genetic algorithm technique, trial and error method, particle swarm optimization method (PSO). In this paper, PID and PI-PD controllers are tuned using the PSO technique.

4.2 Cascaded PI-PD Controller

The name itself indicates that it is a combination of two processes where the output of the inner process supplies to the outer process. This controller mainly deals with the outer process disturbance reduction effect. Because of its cascaded effect, we can observe the improved performance of the system Chittimuru [4]. The mathematical representation of PI-PD controller is

$$G_{PI-PD}(s) = (K_P + \frac{K_I}{s})(K_I + K_D s) \qquad (9)$$

K_P, K_I, K_D are the proportional, integral, and derivative gains. The basic block diagram of the PI-PD controller is shown in Fig. 6.
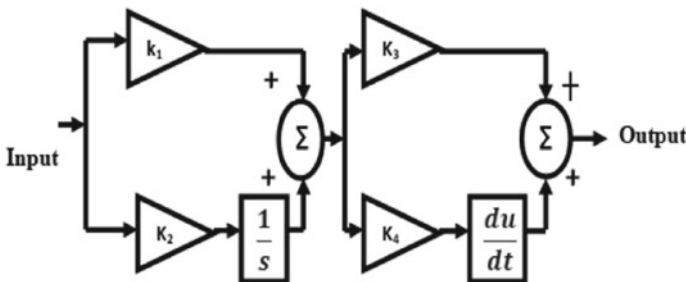
Fig. 6 Basic block diagram of PI-PD controller

4.3   *Particle Swarm Optimization (PSO)*

Kennedy and Eberhant introduced the particle swarm optimization (PSO) method by the year 1995. It is one of the techniques of optimization. This method is developed from swarm research such as bird flocking and fish schooling. All the particles in PSO fly passing in the search space with velocities which are individually adjusted based on own flying experience and neighbors' experience. In the problem space, each particle sets track its coordinates which are connected with evaluating value achieved before. This value is nothing but the Pbest value. Other best value is obtained by the particle swarm optimizer is the overall best value. This value is called Gbest value. Changing the each particle velocity toward the Pbest, Gbest values at each time step is the basic concept of PSO Gaing [15]. The velocity and each particle's position are calculated by using the following equations.

$$v_i(t+1) = v_i(t)w + [c_1 r_1 (p_i^{\text{best}} - x_i(t))] + [c_2 r_2 (g_i^{\text{best}} - x_i(t))] \qquad (10)$$

$$x_i(t+1) = x_i(t) + v_i(t+1) \qquad (11)$$

where $v_i(t)$ is the ith particle velocity at time t; $x_i(t)$ is the ith particle position at time t; c_1 and c_2 are the learning factors, and r_1 and r_2 are the random factors within the range of 0–1. The algorithm involves the following three basic steps and continues until the maximum iterations are reached. They are

1.   Calculation of best fitness value Pbest for each particle.
2.   Evaluating Gbest for the whole particle.
3.   Updating velocity and position of the particle [7, 8].

Objective Function

For the design of PID and PI-PD controllers, using PSO algorithm is having four commonly used indices to describe the performance of the system. They are integral square error (ISE), integral absolute error (IAE), integral time square error (ITSE), and integral time absolute error (ITAE). Compared to other performance indices, ITAE is better. The equations of these performance indices are represented as

$$\text{IAE} = \int_0^T |e(t)| \, \mathrm{d}t, \ \text{ISE} = \int_0^T e^2(t) \, \mathrm{d}t, \ \text{ITSE} = \int_0^T t e^2(t) \, \mathrm{d}t, \ \text{ITAE}$$

$$= \int_0^T |t e(t)| \, \mathrm{d}t ISE = \int_0^T e^2(t) dt, \qquad (12)$$

5 Results and Discussions

The block diagram of IEEE three area power system is shown in Fig. 7, and the data is given in Table 1. AGC simulation diagrams of this system for ADRC and PID and PI-PD controllers are shown in Figs. 8 and 9. PSO algorithm is used for tuning the PID and PI-PD controllers.

For the three area power system, ADRC, and PID and PI-PD controllers are employed as secondary controllers. Choosing a good secondary controller is very important. As we can observe the different performances of these controllers are shown in Figs. 10, 11, 12, 13, 14, and 15. From these figures and Tables 2 and 3, it is observed that

Fig. 7 Block diagram of IEEE three area power system
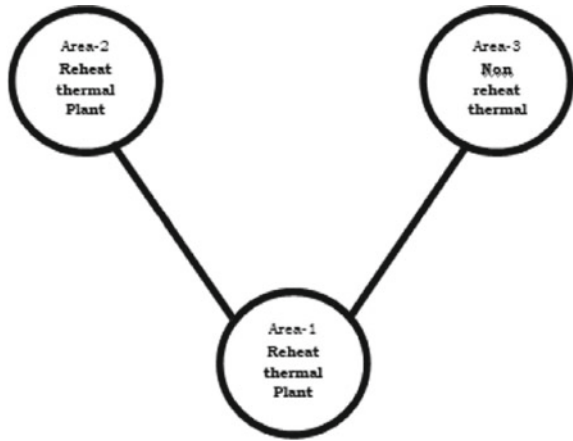
Table 1 System parameters

Parameter	Area-1	Area-2	Area-3
$D(pu)$	0.24	0.11	0.046
K_r	0.3	0.3	
$2H(s)$	167	89.5	23.25
$R(pu)$	0.04	0.04	0.04
$T_{t1}(s)$	0.4	0.4	0.1
$T_{g1}(s)$	0.1	0.1	0.4
$T_{t2}(s)$	1.0	1.0	
$T_{g2}(s)$	0.1	0.1	
$T_{ri}(s)$	1.0	1.0	
$T_{12} = T_{21}$	8.4	8.4	
$T_{13} = T_{31}$	2.3		2.3
$\triangle P_L(pu)$	0.3	0.1	0.01
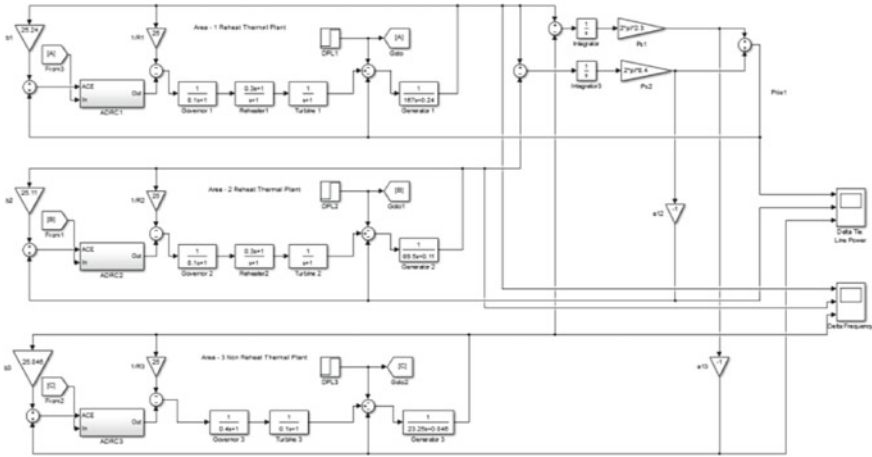
Fig. 8 Simulation of three area power system AGC using ADRC
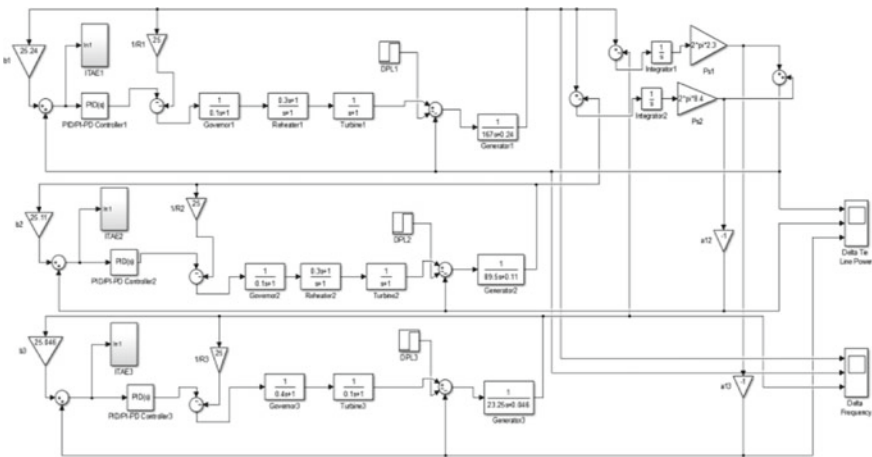
Fig. 9 Simulation of three area power system AGC using PID/PI-PD controllers

1. All the controllers provided good steady-state responses and results in the frequency in steady state and deviations of tie-line power to zero.
2. PI-PD controller gives lesser settling times compared to the ADRC and PID controllers denoting good transient response.
3. PI-PD controller results in minimum ISE of frequency deviations of three areas.

Hence, it concluded that PI-PD controller is better than ADRC and PID controllers with minimum ISE and settling times. Furthermore, it is observed that the results of PI-PD controller are superior to that of PID and ADRC.
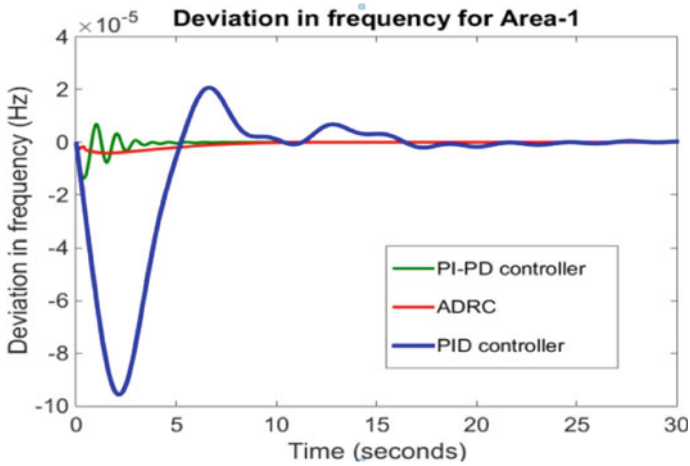
Fig. 10 Frequency deviation (Area-1)
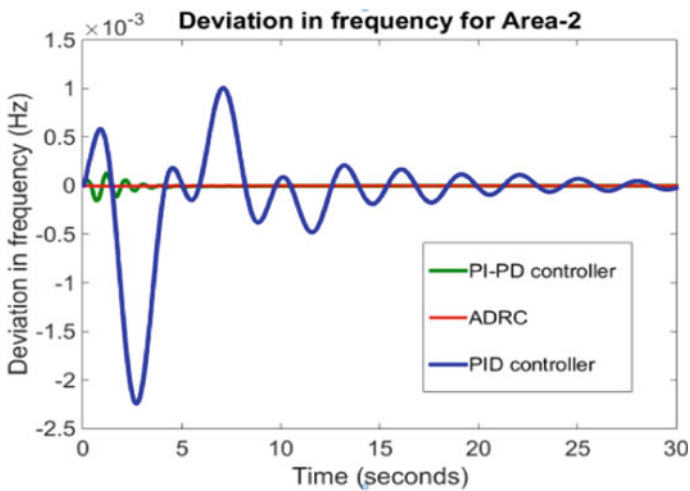
Fig. 11 Frequency deviation (Area-2)

6 Conclusion

It is well known that automatic generation control plays a vital role in the power system to maintain the frequency and tie-line powers to the reference value by using secondary controllers. Hence, the selection of proper secondary controller is crucial. A three area power system of IEEE paper by Yousef [12] is studied with ADRC, PID, and PI-PD secondary controllers. From the above discussion, it is observed that
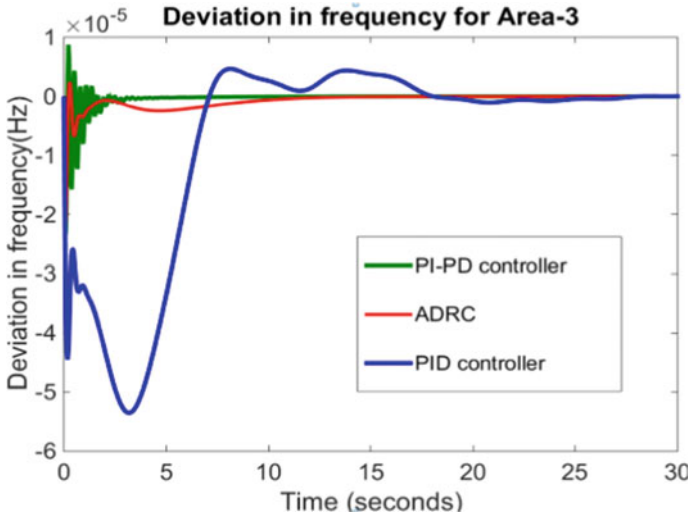
Fig. 12 Frequency deviation (Area-3)
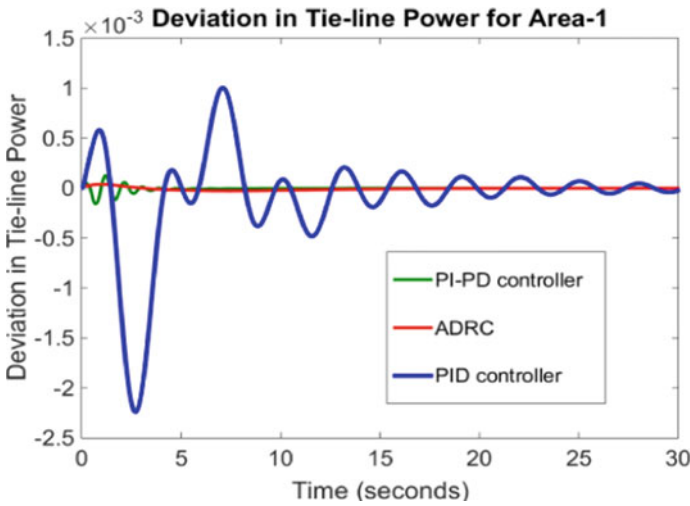
Fig. 13 Tie-line power deviation (Area-1)

PI-PD controller gives the best performance with zero steady-state error, less settling times, and ISE.
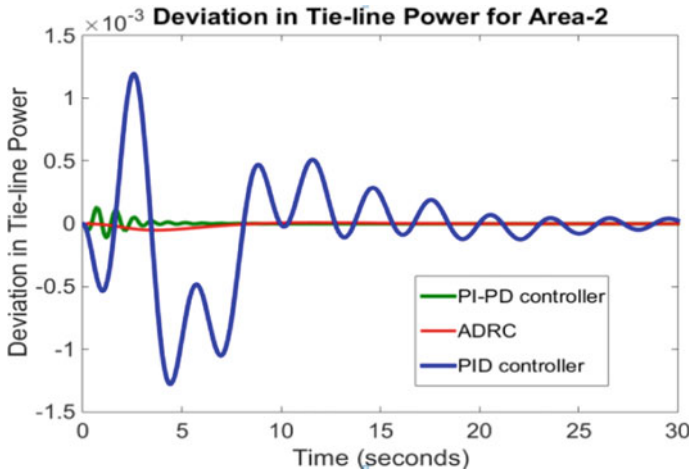
Fig. 14 Tie-line power deviation (Area-2)
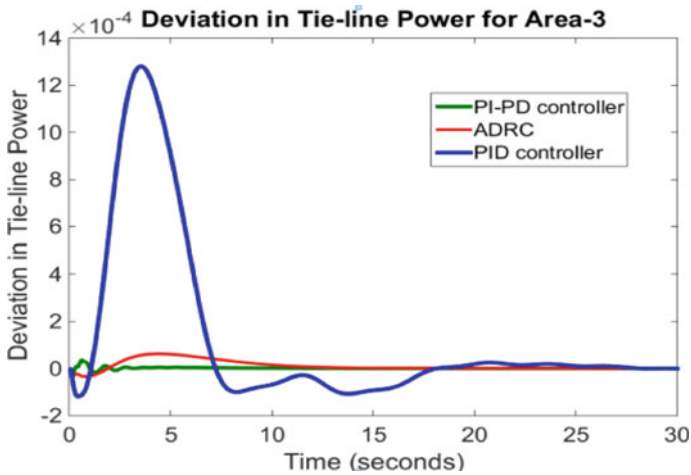
Fig. 15 Tie-line power deviation (Area-3)

		PID controller	PI-PD controller	ADRC
Table 2 Settling times, in seconds, of frequency and tie-line power deviations of three areas for different controllers	$\triangle F_1$	25	8	11
	$\triangle F_2$	32	7.5	2
	$\triangle F_3$	28	9	16
	$\triangle P_{Tie1}$	30	12	20.5
	$\triangle P_{Tie2}$	32	6	14
	$\triangle P_{Tie3}$	25	7	15

Table 3 Integral square errors of frequency deviations of three areas for different controllers

Controller	Area-1	Area-2	Area-3
PID	$3.436e^{-06}$	$4.044e^{-06}$	$1.613e^{-06}$
ADRC	$1.593e^{-08}$	$1.484e^{-08}$	$1.157e^{-08}$
PI-PD	$3.171e^{-08}$	$1.32e^{-08}$	$1.291e^{-09}$

References

1. Saadat H (2002) Power system analysis, Tata McGraw-Hill edition, New Delhi
2. Wood AJ, Wollenberg BF A textbook on power generation, operation and control, 2nd edn, Wiley Student Edition
3. Gao Z, Zhang Y, Dong L (2009) Load Frequency control for multiple-area power systems. In: American control conference Hyatt regency riverfront, St. Louis, MO, June 10–12
4. Reddy Chittimuru S, Sarvesh B (2017) A new optimized PD-PI controller using NSGA-II for automatic generation control. Int J Adv Res Electric Electron Instrum Eng (IJAREEIE) 6(7)
5. Charitha Reddy YVL, Krishnarayalu MS (2017) Automatic generation control of multi-area power system using active disturbance rejection control. Int J Eng Trends Technol (IJETT) V43(4):212–221. ISSN: 2231-5381
6. Charitha Reddy YVL, Krishnarayalu MS (2017) AGC of Multi source multi area power system using ADRC. Int J Adv Res Electric Electron Instrum (IJAREEIE) 6(7)
7. Charitha Reddy YVL, Krishnarayalu MS (2018) AGC of multi source multi area deregulated power system using PID controller. J Electric Eng (JEE), Article 18.1.40, www.jee.ro
8. Sharma D, Kumar B (2015) PSO optimized PID controller for load frequency control. Eur J Adv Eng Technol 2(11):43–48
9. Tian G, Gao Z (2007) Frequency response analysis of active disturbance rejection based control system. In: 16th IEEE international conference on control applications part of IEEE Multi-conference on systems and control Singapore, 1–3 October
10. Nagarjuna K, Krishnarayalu MS (2014) ADRC for two area LFC. Int J Eng Res Technol (IJERT) 3(11)
11. Nagarjuna K, Krishnarayalu MS (2014) AVR with ADRC. Int Electric Eng J (IEEJ) 5(8):1513–1518
12. Yousef HA, AL-Kharusi K, Albadi MH, Hosseinzadeh N (2014) Load frequency control of a multi-area power system: an adaptive fuzzy logic approach. IEEE Trans Power Syst 29(4)
13. Han J (2009) From PID to active disturbance rejection control. IEEE Trans Ind Electron 56(3)
14. Saiteja K, Krishnarayalu MS (2015) Load frequency control of two-area smart grid. Int J Comput Appl (0975–8887) 117(14)
15. Gaing Z-L (2004) Particle swarm optimization approach for optimum design of PID controller in AVR system. IEEE Trans Energy Conv 19(2)

Numerical Studies for Smart Systems

Numerical Simulation of Reacting Flow Field in a Solid-Propellant Ducted Rocket

Nitin Sharma, Yash Pal, and Vivek Warade

Abstract The scope of the current study is to estimate the flow fields in reacting and non-reacting flow regimes of a solid-propellant ducted rocket combustor (SDRC) at different ram duct angles. The 2D simulation and combustion modelling of the reacting and non-reacting flow were carried out using OpenFOAM. The flow fields and the mass fraction distribution were computationally modelled and qualitatively compared. The predicted axial and vertical flow velocities were compared with the experimental and analytical results from the literature to validate the current study at different ram duct angles. The performance in terms of flow velocity and mass fraction was found out to be the highest in the 45° configuration.

1 Introduction

A solid-propellant ducted rocket is an integrated ram rocket propulsion system, together with a solid-propellant rocket motor and a ram duct. The SDRC motor assembly carries a stable solid propellant containing low-oxidizer levels, which upon burning releases a fuel-rich combustion gaseous stream as described in the work done by Chen et al. [1]. Within the combustor, the fuel-rich combustion products are further burnt with the air introduced through a ram duct. The combustion products are further accelerated through the exhaust nozzle to produce useful propulsive power.

SDRs are moderately efficient in comparison with solid and liquid rockets as extra payload can be carried instead of an oxidizer, which is utilised from the environment. The flow is driven due to the change of pressure inside the combustor. The thrust

N. Sharma (✉) · Y. Pal
School of Aeronautical Sciences, Hindustan Institute of Technology and Science, Chennai, India
e-mail: nitinofficialsharma@gmail.com

V. Warade
Zeus Numerix Private Limited, Pune, India
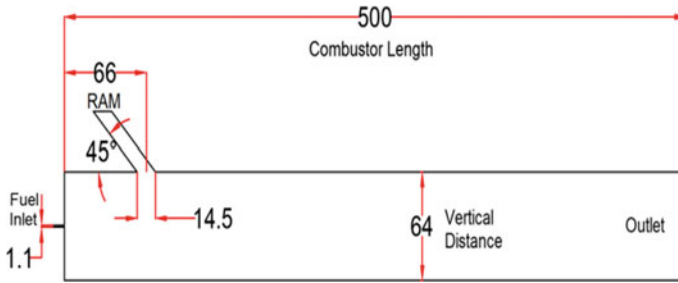
Fig. 1 Computational domain of SDR

is produced through the ignition of a hydrocarbon fuel with air brought from the atmosphere. The approaching air is compressed by means of a shock wave. The configuration of an SDR propulsion system used in this study is shown in Fig. 1 that consists of a fuel inlet, the main combustion chamber, and a ram inlet. The velocity is crucial and decides the flow field inside the combustor. The reacting flow is thus formed when the two streams meet. A huge amount of energy is released when the reacting flow is achieved. The flow is then passed through the exit nozzle in which due to expansion, the flow is expelled out with high velocities which was studied by Cherng et al. [2].

The studies of the past on the same research area of SDR were surveyed to work out the approach of the current study. The information acquired from Hsieh et al. [3] and Chao et al. [4] investigation is supportive in understanding the blending procedures and stream structures in the combustor. The works [6–10] also highlight the need to investigate the flow field further as it is dependent on the factors like dome height, momentum ratios of the flow and ram duct angles. This work comprises the inclusion of mass fraction as an important parameter to study the flow and combustion characteristics at different angles of the ram inlet.

2 Numerical Scheme

The numerical simulation was carried out using OpenFOAM for both the cases: non-reacting as well as the reacting flow field. The solver used for the non-reacting flow field was Rho Simple Foam which is a steady-state SIMPLE solver for laminar or turbulent RANS of compressible flows. Whereas, for the reacting flow field case, the solver used was ReactingFoam which is a solver for combustion with chemical reactions. In this study, the following assumptions were considered:

- Fuel is considered as a single C3H8 stream
- The flow is 2-dimensional
- The geometry is symmetric about x-axis
- The ram flow is free of impurities

- Radiation effects are not considered.

The numerical simulations for all the design configurations were performed on unstructured meshes. The models used for the simulations are described as follows.

2.1 Turbulence Model

The k-epsilon variant is adopted for both the non-reacting and reacting flow cases since it stands out amongst the most typical turbulent models. It incorporates two or more transport conditions to express the turbulent background of the flow. This allows a two condition adaptation to represent results. The variables decide the extent of the turbulence. The k-epsilon model has been appeared to be valuable for noting shear layer streams with very little pressure inclinations. So also, for inward streams, the model offers reliability.

2.2 Combustion Model

The eddy dissipation concept (EDC) model was used in the reacting flow case which is an augmentation of the swirl dispersal model to incorporate detailed chemical mechanisms in high-turbulent streams. The EDC demonstrates endeavours to fuse the centrality of fine structures in a turbulent responding stream where the burning is dynamic. EDC has been proficiently demonstrated without the requirement for changing the constants and has premixed and dissemination controlled ignition issues, both where the substance energy is quicker than the general fine structure blending just as in situations where the compound energy has a commanding impact.

2.3 Type of Reaction

The reaction type used for the simulation is an irreversible Arrhenius reaction. Arrhenius reaction delivers better results for real chambers as described in Ristori and Dufour [5]. The reaction model functions admirably, over moderate temperature ranges, to show the temperature difference. A 2 step reaction was used, which involves two independent equations from Cherng et al. [2].

$$C_3H_8 + 3.5(O_2 + nN_2) \rightarrow 3CO + 4H_2 0 + 3.5nN_2 \qquad (1)$$

$$3CO + 1.5(O_2 + nN_2) \rightarrow 3CO_2 + 1.5nN_2 \qquad (2)$$

Table 1 Non-reacting flow conditions

Properties	Ram	Inlet	Wall	Outlet
Velocity (m/s)	Ux = 122 Uy = 103	313	No slip	
Pressure (atm)	1.24	1.7	Zero gradient	
Temperature (K)	273	245		

Table 2 Reacting flow conditions

Properties	Ram	Inlet	Wall	Outlet
Velocity (m/s)	Ux = Uy = 65.5	569	No slip	Zero gradient
Pressure (atm)	5.84	7	Zero gradient	5.97
Temperature (K)	535	1021		Zero gradient
C_3H_8	Zero gradient	0.294		
H_2O		Zero gradient		
CO_2		0.174		
CO		Zero gradient		
N_2	0.767			
O_2	0.233			

Different chemical elements constitute to form different species that are used to model the reacting flow inside the SDR combustor. The species are solely required which determines the extent of combustion and thus the performance of the combustor. The species namely Propane, Oxygen, Nitrogen, Carbon Monoxide, Water, and Carbon Dioxide were studied in flow field out of which oxygen and nitrogen were injected into the combustor through the ram duct whereas; propane and carbon dioxide were injected through the fuel inlet and the remaining species were the by-products. The boundary conditions for non-reacting and reacting flow cases are presented in Table 1 and Table 2 respectively.

3 Results and Discussion

The analysis of the SDRC was carried out in two cases, first the non-reacting case and then the reacting case. The validation was done for both the cases using the earlier experimental and analytical data Hsieh et al. [3].

3.1 Non-reacting Flow Field

For simulating the non-reacting flow field, the conditions of cold gases were considered in both fuel and ram inlet. The incoming flow from the ram inlet was slightly at a higher temperature than the flow incoming from the fuel inlet. The non-reacting flow field was numerically simulated using the Rho Simple Foam solver in OpenFOAM.

The non-reacting flow field as shown in Fig. 2 is a surface LIC generated using ParaView. The flow field depicts the formation of three recirculation zones. Two of them are upstream of the ram duct and one was downstream. The biggest recirculation zone is the one that is downstream of the ram duct. The recirculation zones near the inlet are less turbulent when compared with the downstream zone. However, these two zones completely define the direction and behaviour of the stream coming out of the fuel inlet. The flow field was validated with the flow field reported in the experimental and other numerical work of Cherng et al. [2] and Hsieh et al. [3].

The flow field of an SDRC is complex due to the violent turbulent regions. The flow field is dynamic and the turbulence modelling for a numerical simulation can capture the flow properties as developed in real-time. In this study, the K-epsilon turbulence model was used, and results were compared with the experimental data and analytical data. The data used for validation were obtained at different inlet parameters and compared with the current data to understand the variation in profiles and outlines a general trend. This evaluation was done by comparing the axial and vertical velocities at different axial locations which are represented on x-axis in Figs. 3, 4, 5, 6, 7, 8, 9, 10, 11, and 12.

Figure 3 shows that the trend followed by the computational data validates with the experimental data. The negative velocity indicates a region of recirculation zone just downstream of the fuel inlet. The computational data trace perfectly the analytical data till 0.05 m nearing the combustor walls thereafter large deviation in the data was observed on the track, however, the velocities calculated in this study match with that of the analytical.

Figure 4 represents the vertical velocity variation with vertical distance. It validates the trace in the region of the incoming flow from the fuel inlet. The computational data trace perfectly matched with the analytical data from 0 to 0.035 m and then again from 0.05 till the end of the combustor walls.
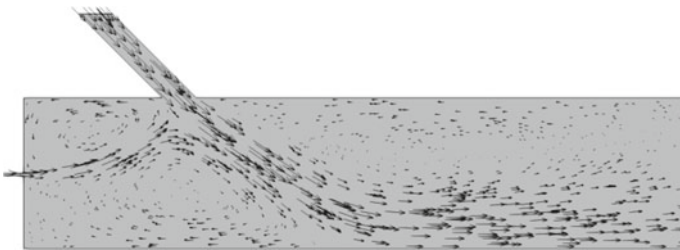
Fig. 2 Non-reacting flow field

Fig. 3 Axial velocity versus
vertical distance at x = 0.03
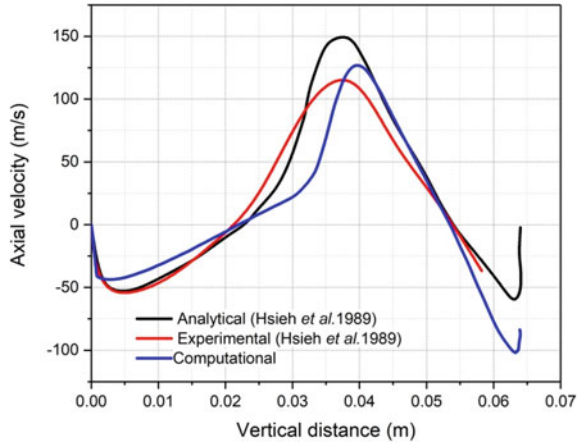
Fig. 4 Vertical velocity
versus vertical distance at x
= 0.03
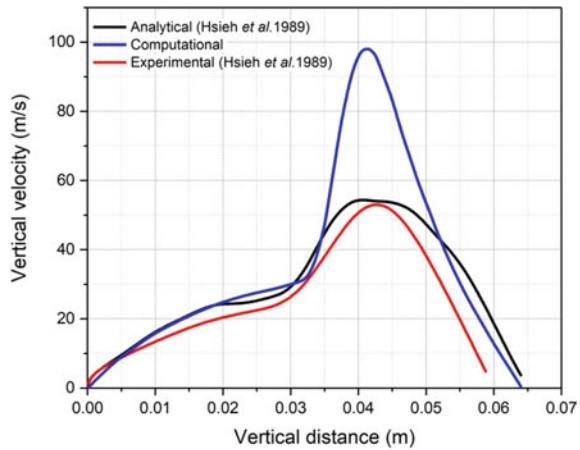
In Fig. 5, at x = 0.045 m, the computational data trace both the experimental as
well as the analytical till 0.02 m. However, ends at the same point describing 0 m/s.
The computational data does not trace the axial velocity of the other two cases and
were off-limits indicating the dependence of the initial conditions on the flow field
of this combustor. The trend with different magnitude was seen and besides this case
shows the axial velocity tends to zero at the combustor walls. A large variation in
computational data was observed at a higher vertical distance compared to the other
two cases.

Figure 6 shows the computational data does not match with the experimental and
analytical data until 0.06 m nearing the wall ends. The nature of the curves matches
the experimental data, however, the magnitude of the velocities is higher by a factor
of almost two at a vertical distance of 0.05 m.

Fig. 5 Axial velocity versus vertical distance at x = 0.045
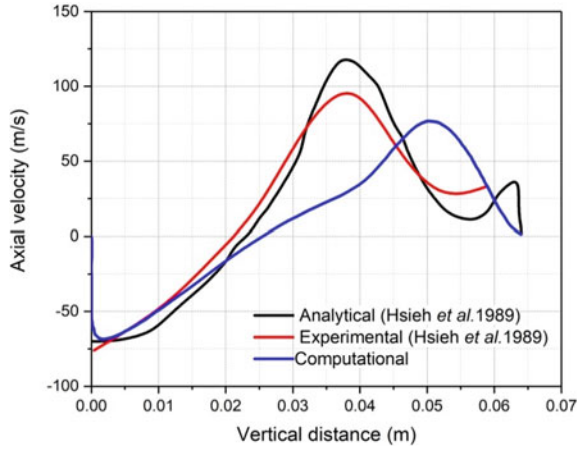
Fig. 6 Vertical velocity versus vertical distance at x = 0.045
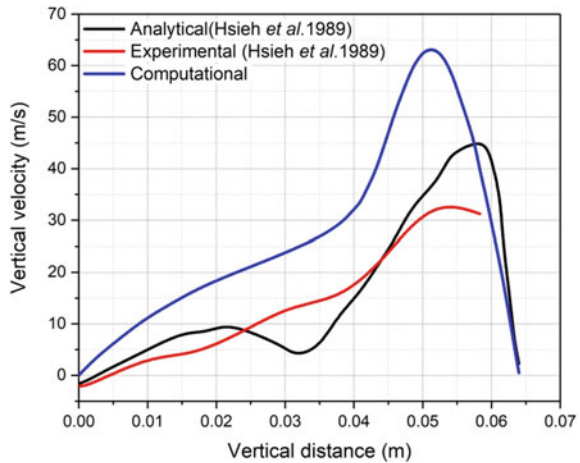
At an axial distance of x = 0.06 m, the flow from the ram duct entered in the combustor. In Fig. 7, the computational data trace the analytical and experimental data only at the extremes of the combustor height. The computational data depict almost a linear increasing trend. As in the case of x= 0.045 m, the velocity trend was offset and occurring at a higher vertical distance.

In Fig. 8, it was observed that the vertical velocity variation reported in the computational analysis was higher compared to experimental and analytical. The nature of the curve matched the profile, however, it was offset and the significant drop and slight increase were observed at 0.06 m instead of 0.03 m.

In Fig. 9, at a vertical distance of x = 0.09 m, the computational data completely match the experimental data from halfway of the combustor height to the upper wall, and eventually, the axial velocity dips negative to reach 0 m/s at the wall. The trend

Fig. 7 Axial velocity versus vertical distance at x = 0.06
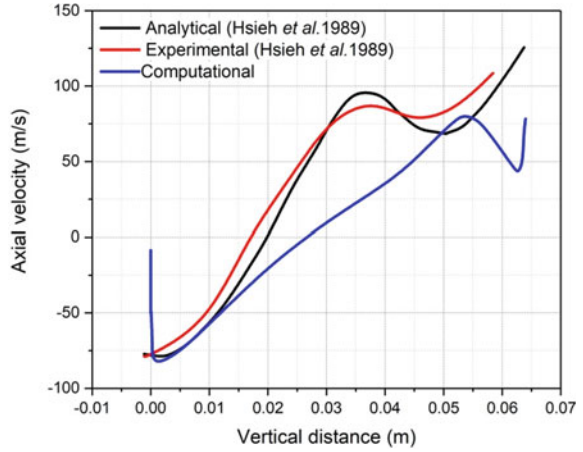
Fig. 8 Vertical velocity versus vertical distance at x = 0.06
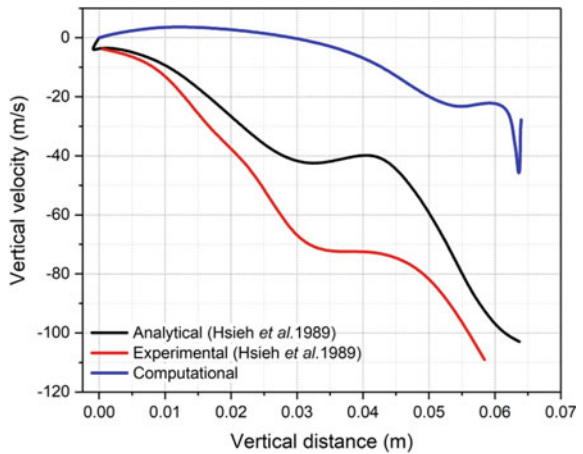
Fig. 9 Axial velocity versus vertical distance at x = 0.09
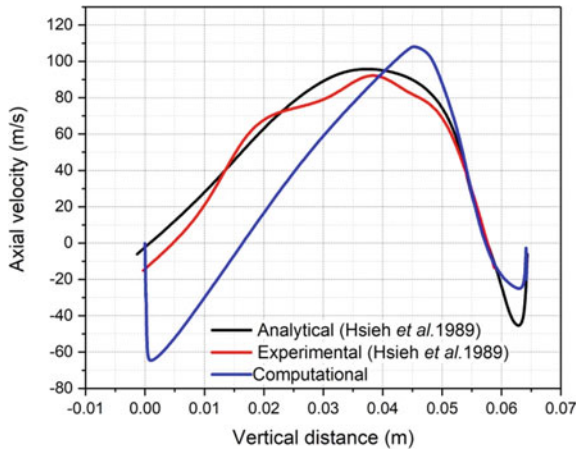
of rising from the negative values to the positive for axial velocity versus the vertical distance describes the presence of the turbulent zone in that region. After a vertical distance of 0.05 m, all the three data curves almost coincide with each other which means at an axial distance of 0.09, the flow field acts similarly. The magnitude of the velocity dropped to approximately -50 m/s instead of -25 m/s.

In Fig. 10, the vertical velocity again traces the trend at extremities deviating from experimental values at an axial distance of x $=0.025$ m then again matched at 0.057 m. The deviation in velocity is offset by almost 0.01 m vertical distance.

For x $= 0.3$, Figs. 11 and 12 depict the velocity trend being the same, however, the magnitudes are different for axial velocity. The vertical velocity does not match due to the presence of recirculating zone which is stronger and is spread in a larger area when compared to the other cases.

Fig. 10 Vertical velocity versus vertical distance at x $= 0.09$
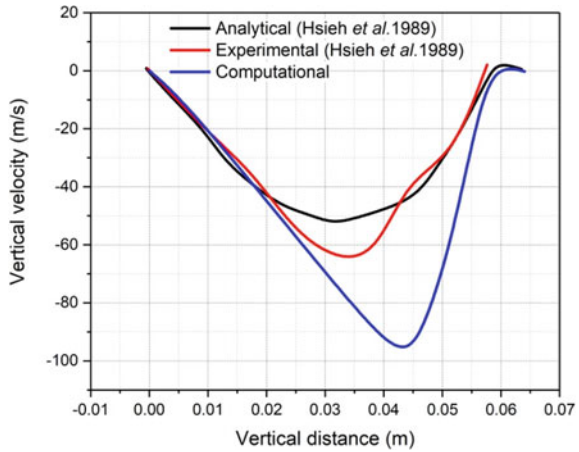
Fig. 11 Axial velocity versus vertical distance at x $= 0.3$
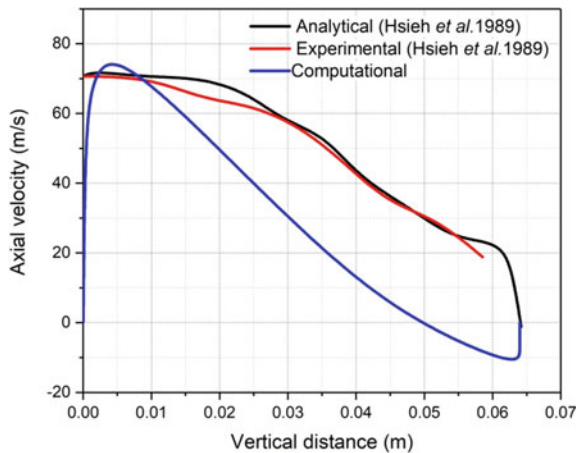
Fig. 12 Vertical velocity
versus vertical distance at x
= 0.3
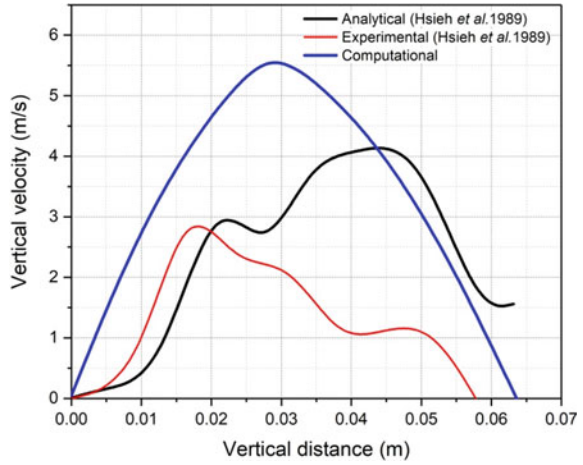
3.2 Reacting Flow Field

The reacting flow field was numerically simulated using the ReactingFoam solver of
OpenFOAM. The reacting flow field as shown in Fig. 13 is a vector representation
generated using ParaView. It clearly shows the flow behaviour. The flow field depicts
the formation of four recirculation zones. Two of them are upstream of the ram duct
and one is downstream. The biggest recirculation zone is observed downstream of
the ram duct. The other three are less turbulent when compared with the downstream
one. However, these two zones completely define the direction and behaviour of the
stream coming out of the fuel inlet. This flow field validates the flow field reported
in the experimental and other numerical work done by Cherng et al. [2] as shown in
Fig. 13.

Figure 14 depicts a surface plot of pressure for the reacting case. The pressure
was the maximum at the fuel inlet validating the boundary conditions, and the trend
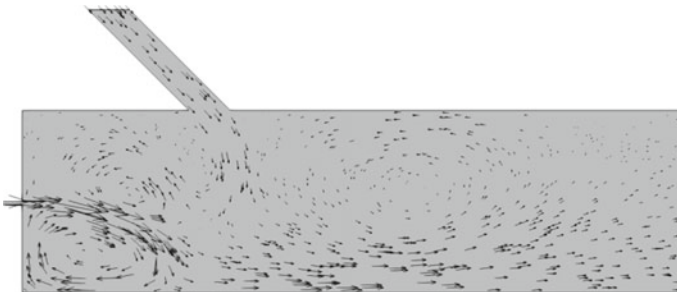
Fig. 13 Reacting flow field
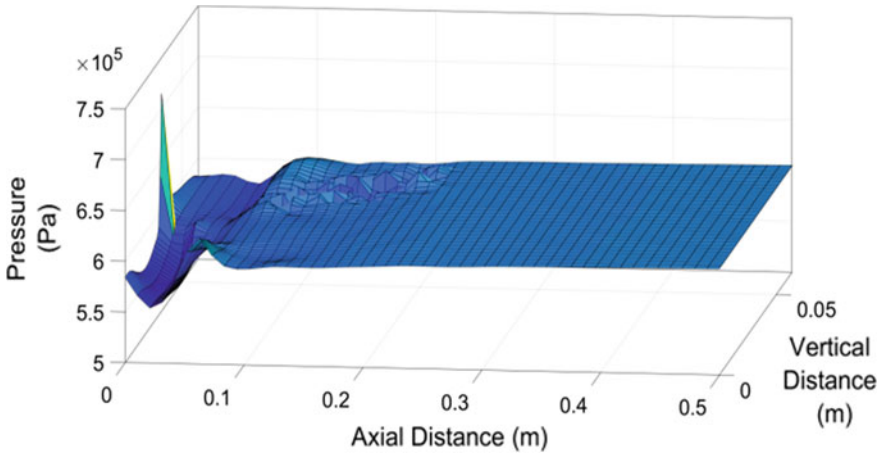
Fig. 14 Surface plot of pressure

matches with the work done by Chao et al. [4]. The pressure almost becomes constant nearing 0.1 m.

3.3 Variation in Ram Duct Angles

This section focuses on the changes in the reacting flow properties subjecting to the changes in the ram duct angles. The changes in the angle of the ram duct lead to variation in combustion which was evaluated using the mass fraction of gases.

The geometry was redesigned to change the angles and study the variation for 6 configurations that were 15°, 30°, 45°, 60°, 75°, and 90°. The flow characteristics changes in each case purely due to the duct configurations and the boundary conditions for each model were same as used in the reacting flow field simulation as mentioned in Table 2. Figures 15, 16, 17, 18, 19, and 20 depict the changes in mass fraction against vertical distance that is the height of the combustor viz. 0.064 m. The data were plotted at an axial distance of 0.03 m to determine the behaviour of the flamelet which is dependent on the flow field and changes with the angle variation of the duct. Performance of the combustor shall be greater if the fuel stream remains to be curling down so that much fuel is transported downstream and mixes with ambient air rather than being trapped in the recirculation zones.

Figure 15 depicts the variation of mass fraction of the gases with change in vertical distance. The axial distance for this measurement was fixed at x = 0.033 m. All gases except O_2 follow the same trend but with different magnitudes.

Figure 16 depicts the mass fraction versus the vertical distance variation of reacting gases at x = 0.033 m for the 30° case. With the increase in the vertical distance, the
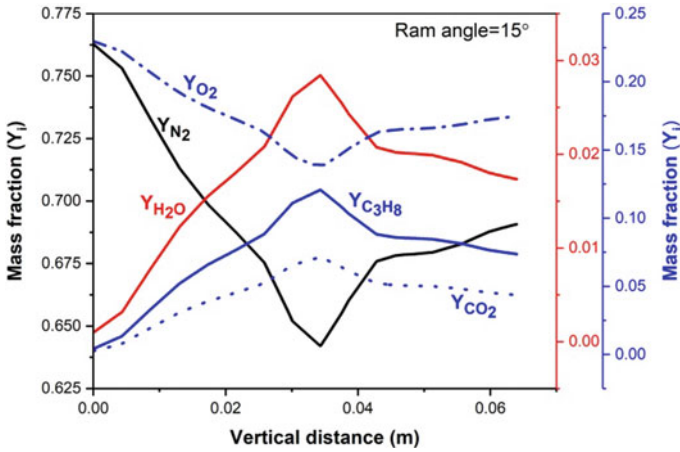
Fig. 15 Gases mass fraction at 15°
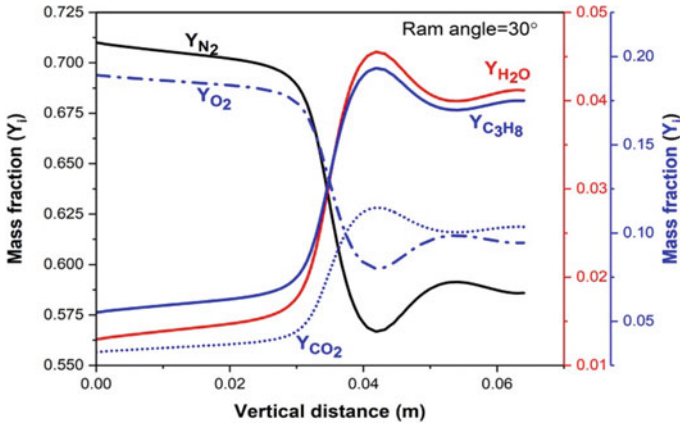
Fig. 16 Gases mass fraction at 30°

mass fraction of C_3H_8, H_2O, and CO_2 increases from a vertical distance of 0.03 m. The C3H8 levels increase and create a bump nearing 0.042 m.

Figure 17 the variation of gases mass fraction and vertical distance is plotted to depict the consumption of C_3H_8 as it reaches the halfway height of the combustor and drops down tending to 0. CO_2 and H_20 follow a similar trend and O_2 gets used up initially, but then, the mass fraction increases nearing the wall defining the abundance of O_2 at the walls. All the gases are almost in parallel to the x axis at approximately 0.055 m.

Figure 18 depicts the mass fraction versus the vertical distance variation of reacting gases at x = 0.033 m for the 75° case. With the increase in the vertical distance, the
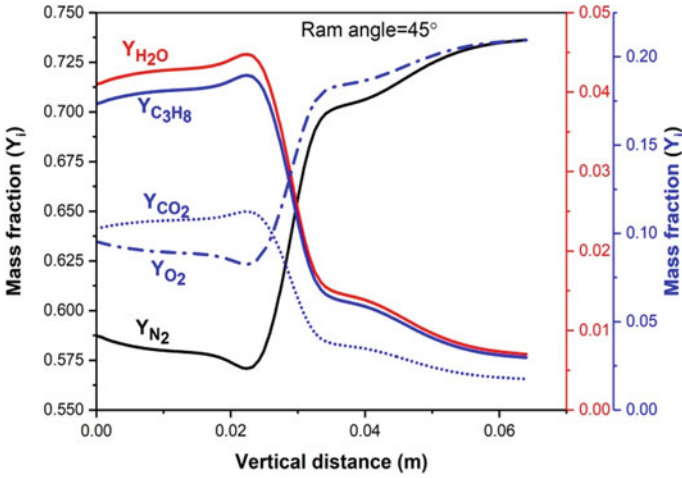
Fig. 17 Gases mass fraction at 45°
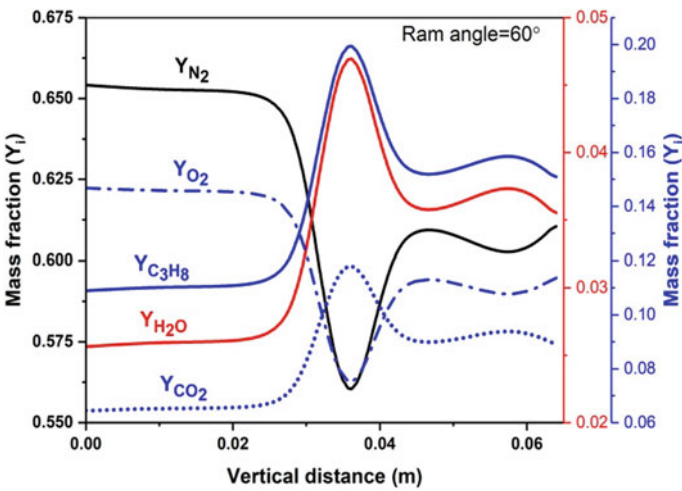
Fig. 18 Gases mass fraction at 60°

mass fraction of C_3H_8, remains almost constant from 0 m vertical distance. The C_3H_8 levels increase to 0.038 m and then start to decrease.

Figure 19 depicts the mass fraction versus the vertical distance variation of reacting gases at x = 0.033 m for the 75° case. With the increase in the vertical distance, the mass fraction of C3H8 remains almost constant from 0 m vertical distance till 0.025 m.
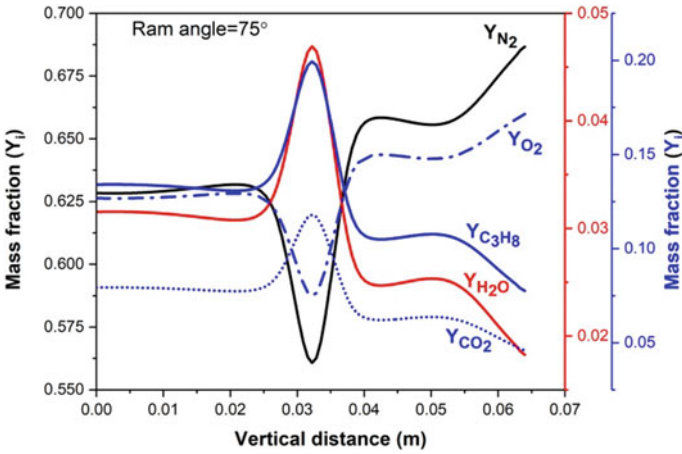
Fig. 19 Gases mass fraction at 75°

Figure 20 depicts the mass fraction versus the vertical distance variation of reacting gases at x = 0.033 m for the 90° case. With the increase in the vertical distance, the mass fraction of C_3H_8, H_2O, and CO_2 drops to almost zero. The C_3H_8 levels increase to 0.03 m and then drop till 0.064 m.
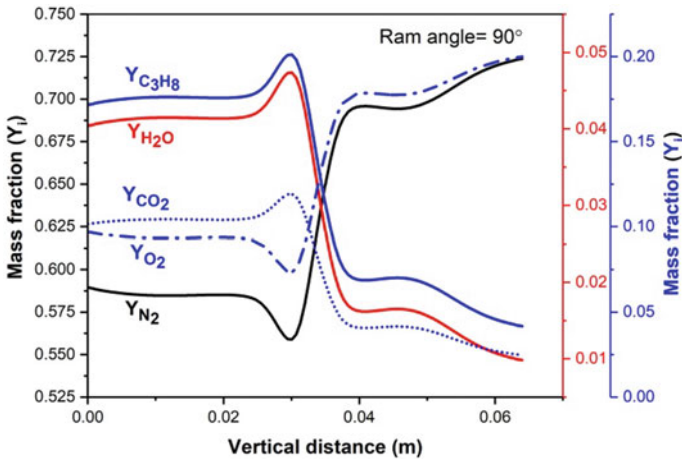
Fig. 20 Gases mass fraction at 90°

4 Conclusion

In this study, numerical simulation was carried out to study an exceptionally perplexing reacting flow problem. The methodology taken was to build up computational capability of solving a SDR case, fundamentally centred on the portrayal of the stream properties and correlation with burning test information for the pattern case. The non-reacting flow field was the case study for the reacting flow field case which was simulated considering cold gases. The flow regime is highly turbulent and was dependent on the momentum and temperature properties of the flow. The computational study validates the pressure variation over the combustor, and the comparative study of the computational and experimental velocity data suggests that the SDR flow field is highly dependent upon the momentum of the streams. The data suggest variation in the magnitude of velocities whilst not much variation was found in the trend as some features were witnessed at a higher vertical distance. The reacting flow field involved injection of C_3H_8 as a fuel from the fuel inlet and the computational data validates the experimental data tracing the mass fraction distribution of gases. With a change in the inlet flow angle of the air duct, the flow field behaviour changes and thus the performance. The SDR combustion requires obtaining complete combustion providing sufficient thrust at different operating conditions. The comparative study shows that reaction of C_3H_8 increases with the duct angle. Interestingly, the C_3H_8 reaction trend was almost comparable in $45°$ and $90°$ configuration though the magnitudes of the mass fraction were different initially eventually; the mass fraction of the fuel tends to zero. This study suggests that the dependency of the ram duct angle for the fixed conditions is important as it changes the momentum, and thus, the flow field which in turn changes the combustion characteristics. The complete combustion was only achieved in the above two configurations. The optimal configuration based upon the study of velocity and the mass fraction is the $45°$ ram duct configuration.

References

1. Chen L, Tao C (1989) Study on the side-inlet dump combustor of solid ducted rocket with reacting flow. In: 20th joint propulsion conference. Presented at the 20th joint propulsion conference, American Institute of Aeronautics and Astronautics, Cincinnati (1984)
2. Cherng DL, Yang V, Kuo K (1989) Numerical study of turbulent reacting flows in solid-propellant ducted rocket combustors. J Propuls Power 5:678–685
3. Hsieh W, Settles G, Kuo K (1989) Study of flow field structure in a simulated solid-propellant ducted rocket. In: 27th aerospace sciences meeting. Presented at the 27th aerospace sciences meeting, American Institute of aeronautics and astronautics, Reno

4. Chao Y-C, Chou W-F, Liu S-S (1995) Computation of turbulent reacting flow in a solid-propellant ducted rocket. J Propuls Power 11:473–482

5. Ristori A, Dufour E (2001) Numerical simulation of a ducted rocket motor. In: 37th joint propulsion conference and exhibit. Presented at the 37th joint propulsion conference and exhibit, American Institute of Aeronautics and Astronautics, Salt Lake City

6. Liou TM, Chen L, Wu YY (1993) Effects of momentum ratio on turbulent nonreacting and reacting flows in a ducted rocket combustor. Int J Heat Mass Transf 36:2589–2599

7. Montazel X, Samaniego J, Lacas F, Poinsot T, Candel S (1992) Turbulent combustion modelling in a side dump ramjet combustor. In: 28th joint propulsion conference and exhibit. Presented at the 28th joint propulsion conference and exhibit, American Institute of Aeronautics and Astronautics, Nashville

8. Pein R, Krishnan S (1996) Performance calculations for solid propellant ramrockets. In: 32nd joint propulsion conference and exhibit. Presented at the 32nd joint propulsion conference and exhibit, American Institute of Aeronautics and Astronautics, Lake Buena Vista

9. Stowe R, DeChamplain A, Mayer A, Niemeijer S (1998) Modelling and flow visualization of mixing in a ducted rocket combustor. In: 34th AIAA/ASME/SAE/ASEE joint propulsion conference and exhibit. Presented at the 34th AIAA/ASME/SAE/ASEE joint propulsion conference and exhibit, American Institute of Aeronautics and Astronautics, Cleveland

10. Stowe RA, Dubois C, Harris PG, Mayer AEHJ, DeChamplain A, Ringuette S (2004) Performance prediction of a ducted rocket combustor using a simulated solid fuel. J Propuls Power 20:936–944

Computational Study of Safe Separation of Sabot from Penetrator in APFSDS

Himanshu Patanwala, C. Suresh, and Vighnesh Pawar

Abstract The paper addresses the computational fluid dynamics solution for safe separation of sabot from the penetrator in armour piercing fin stabilised discarding sabot. The design and functional characteristics of sabot are modelled to achieve a safe trajectory. Driving bands are important components of APFSDS which adds the sabot together to efficiently transfer the gas forces on penetrator. Sabot, penetrator, fins, and driving bands are modelled separately which further assembled together using solid works CAD software. All tri-element is used to generate the unstructured surface mesh of the model using ICEM software. The aerodynamic coefficients of lift, drag, and moment acting on the penetrator and sabot discard process are evaluated by using in house developed finite volume-based implicit solver. The discarding process of sabot generates shocks at supersonic speed which can affect the trajectory of the penetrator during flight. The timely breaking of bands, after muzzle exit, the APFSDS is an important phenomenon to simulate and govern safe separation of sabots. Based on finite element method software, the breaking of bands was simulated to find the stress and deformation under pressure force exerted on sabot cups. The pressure exerted on sabot cups and separation of sabot due to aerodynamic forces were simulated using in house developed finite volume-based implicit CFD solver. The Cl, Cd, and pitch moment are plotted against the angle of sabot with penetrator which clearly indicates the uniform separation of the sabot.

Keywords CAD · APFSDS · Cl · Cd · CFD · Lift · Drag · Moment · Muzzle · Sabot · Penetrator

H. Patanwala (✉) · C. Suresh
School of Aeronautical Sciences, Hindustan Institute of Technology and Science, Chennai 603103, India
e-mail: himanshupatanwala09@gmail.com

V. Pawar
Zeus Numerix Pvt. Ltd., Pune 41057, India

Nomenclature

P   Pressure (N/m^2)
L   Length (M)
b   Breadth (M)
d   Thickness (M)
g   Acceleration (m/s$^{2)}$)
A   Area (m^2)
F   Force (N)
v   Velocity (m/s)
AOA   Angle of attack (degree)
Alpha   Discard angle (degree)
g   gravity (m/s^2)

1   Introduction

The evolution of ammunition from sling-shot type ammunition to rifling ammunition, an attempt for development of weapons became more refined and more requirement for more specialised ammunition increased. Modern and latest ammunition are more precise and accurate towards target and possess greater ability to penetrate through the thick armour. The invention of armour piercing fin stabilised discarding sabot was to ensure penetration through the thick armour covering long range with supersonic speed and designed such that maximising the damage inflicted by a single round (Fig. 1).

Gopalapillai et al. [7] presented computational fluid dynamics (CFD) approach as well adapted to simulate the unsteady aerodynamics of a projectile launched from a ballistic range in the near field aerodynamics of a projectile. The multi- domain technique was used to investigate the unsteady flow with the boundary layer. Ghosh et al. [3] presented the study of computational techniques to precise kinetic energy projectile accuracy and lethality in techniques to improve precision of kinetic energy projectile through motion study. The study over the projectile is done about the supersonic speed of Mach 5–6. The discard of the sabot from the projectile is considered

Fig. 1 APFSDS illustration
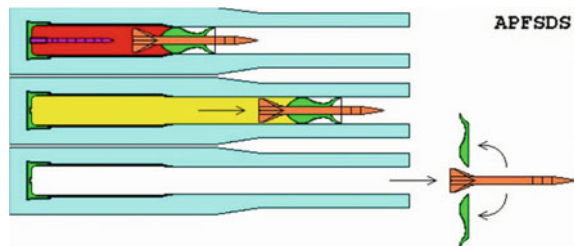
as major criteria. He compared and conclude that MK-code predicts better base pressure than AVCO code and predicts that pressure increase at the tail and sabot and perturbation is moderate. Schmidt et al. (1978) the publication refers to experimental study to investigate trajectory disturbance developed due to the discard of sabot components from a gun-launched fin stabilised projectile. The projectile and sabot components are studied near the muzzle of a 60 mm gun using an orthogonal array of flash X-rays. The study also shows the yawing motion of the projectile with the axisymmetric one sabot discard. Narayanamurthy et al. [10] the study shows the ballistic impact of a steel projectile on armour plate using 3D finite element code. He examined 3D explicit finite element code ANSYS LS-DYNA and attempted to capture large strain using simple strain rate dependent plasticity model. Simulations are attempted to capture large strains, strain rate hardening, and fracture encountered at high-speed velocity impact. Balos et al. (2010) the publication discusses the problems and perspectives of jacketed long rod penetrators. The study shows the influence of jacket material on the free flight of the penetrator. In which the effect of the jacketed projectile on different targets such as vertical, oblique, and spaced one was shown. Zhen-gui et al. (2014) presented the sabot discard process of fin stabilised armour piercing discard process and its stability. The muzzle velocity is taken Mach 4, and angle of attack is considered as 0. The author uses unstructured tetrahedral mesh with commercial solver fluent 12.0 to perform computational fluid dynamics. The trajectories and numerical simulations are also of 6DOF using CFD are studied. Nusca [13] presented CFD analysis using Navier–stokes equations to study sabot discard aerodynamics of an armour piercing projectile. He studied complex aerodynamic interference between discarding sabot and projectile using numerically simulation. He used three symmetrical sabot components at various positions at Mach 4.5. Plostins [14] performed experimental programme to study the nature and magnitude of the launch perturbations of the projectile motion during sabot discard. He also gave an explanation of the discard dynamics of the projectile and sabot components and also isolates the date from the sources and quantify the launch perturbations. Eches et al. presented about the efficiency of large calibre armour piercing fin stabilised discarding sabot projectile and their ballistic performance and also about the accuracy in parameters like yaw at the impact is studied. The paper describes about the balloting of the projectile in which the survivability of the projectile during the launch phase. The computational fluid dynamics was performed to find the early moments of the firing. Ferry et al. [7] researched about the computational fluid dynamics calculations and chimaera composite type of grid to perform numerical simulations for various orientations of the sabot component and projectile. All the numerical simulations were performed at Mach 4 and 0, 5, 10, 15, 25 degrees of angle of attack to study the flow field and shocks generated. Cayzac et al. [4] used FRIEN code which is basically developed to compute 3D ballistics computational fluid dynamics problems. The paper focussed about the investigation of unsteady, intermediate, and exterior ballistics for a weapon environment and used Euler equation to numerically simulate for two different immiscible gases. Huang et al. [9] investigated about the launch of the projectile at Mach 4 and to study the separation of asymmetric sabot discard using computational fluid dynamics approach

and six degrees of freedom. The study shows the aerodynamic forces on the projectile at a different angle of attack and their coefficients are also discussed. Acharya et al. [1] the study presents the dynamical motion of APFSDS penetrator due to the force exerted by muzzle blast and forces generated on the penetrator due to the shock wave.

Penetrator is a high-density projectile which is used to penetrate thick armour of tanks. The projectile works on high-kinetic energy. The penetrator designed in such a manner such that the target can be achieved in a single round. Penetrator can work over a range of supersonic velocities. The high density of penetrator helps to achieve high-impact velocity and toughness to penetrate thick metals. Penetrator strikes the metal armour with the minimum area, thus increasing impact velocity.

The common materials used in penetrator are steel and tungsten alloys. Sabot is mass components used to stabilise the projectile. The sabot petals are termed as parasitic mass. When the projectile leaves the barrel with the muzzle velocity, the aerodynamic forces act on the sabot cups which further separate from the projectile. Sabots are designed to provide a tight fit with the barrel and also support the driving bands and prevent any pressure loss form the muzzle. Aluminium alloys are used in designing the sabot components. Driving bands are thin, tough, and deformable seal needed to trap propellant gasses behind the projectile and keep the projectile centred in the barrel. Driving bands are used to seal the projectiles in the barrel. Driving bands are made from the material that can deform when stress applied and help uniform discard of the sabot from the projectile. Nylon material basically used to make the driving bands.

Fins are the tail part of the armour piercing fin stabilised discarding sabot. Fins provide the aerodynamic stability to the projectile and help to achieve the target with supersonic speed. A total number of fins on the projectile depends on the range of velocity projectile operates. The firing of the armour piercing fin stabilised discarding sabot is shown in Fig. 2. Initially, the projectile is fixed inside the barrel which then further fired after getting muzzle velocity from muzzle blast. In the third case, when

Fig. 2 Basic components of APFSDS and sabot discard illustration
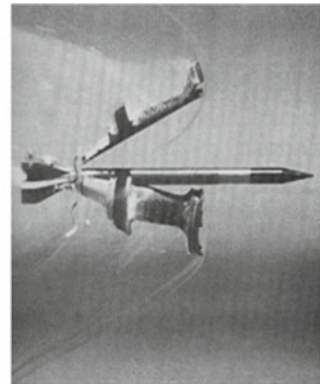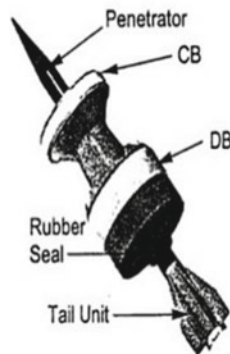
the projectile escapes the barrel, the sabot which is attached with the penetrator discards and provides reduction in mass to the projectile.

2 Model Description

The sabot of 30 mm diameter is considered for the current study. The conventional parabolic domain is selected, with their characteristics and applications of fluids to be modelled or the details of any solid edges or flow inlets/outlets. The simulation is then ready to be run and when a converged solution is found, it must be carefully analysed to establish whether the mesh is appropriately modelling the flow conditions. Generally, some form of mesh refinement will be necessary to put in further detail around the areas of interest. Parabolic computational domain of the armour piercing fin stabilised discarding sabot. The domain is created using spline line option in ICEM CFD. The points were marked at distance in axial and vertical direction using spline technique, curves are drawn. After finishing with the curves, surface was created using create surface option. The top view and rear view of parabolic domain are shown in Fig. 3. The rear part of the computational domain is a semi-circle draw by using create arc from 3 points.

The CAD model for the computational fluid dynamics analysis of safe separation of sabot from penetrator involves major three components. There are total of five components in the 3D geometry, which are sabot, penetrator, driving bands, and fins. The different views of the 3D geometry are presented in Fig. 4.

The sabot discard angle considered for the present study is 0, 10, 25, and 50 degree and is shown in Fig. 5. The sabot components are assembled using the solid works and ICEM CFD software.

3D geometry of the penetrator assembly with the fins is shown in Fig. 5. The total 6 fins attached at the tail of the penetrator to stabilise at supersonic speed. Figure 6 represents side view of the penetrator and fins. The sabot finally separates from the penetrator, and the total aerodynamic forces act on the penetrator and fins. The aerodynamic coefficients for the penetrator and fins will be calculated at different angle of attack.
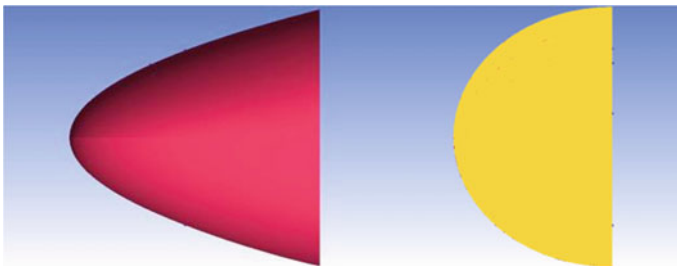
Fig. 3 Computational domain
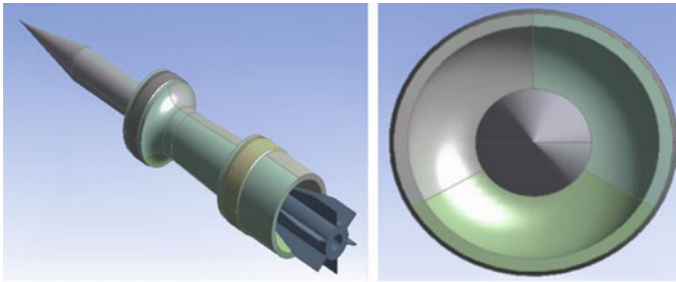
Fig. 4 Isometric and front view illustration of APFSDS
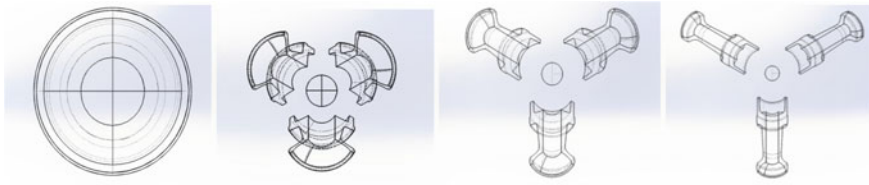
Fig. 5 Sabot and penetrator at different discard angle

Fig. 6 Penetrator and fin assembly

The element size of the density box is created as 0.05 in. The total elements and total number of nodes present for discard angle 0°, 10°, 25°, and 25° are 1,006,767 and 174,894, 4,511,625 and 766,783, 3,116,798 and 529,372, 5,345,018 and 910,316, 4,095,192 and 694,944, respectively. The total elements and total number of nodes for penetrator and fin assembly are 4,095,192 and 694,944, respectively.

3 Numerical Scheme

Finite volume-based implicit solver is a in house solver developed bt Zeus Numerix Pvt Ltd to perform computational fluid dynamics. Simulations for all the cases were performed using finite volume-based implicit solver. Figure 7 shown represents the computational scheme used to analyse aerodynamic forces at different discard angle.

Fig. 7 Sabot discard process
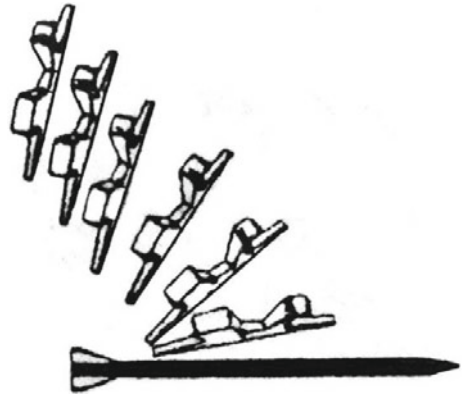
3.1 Continuity Equation

Continuity equation is a very essential equation to analyse any type of system and is based on the conservation laws. The continuity equation always gives better results when analysed on the conserved quantity.

$$\frac{D\rho}{Dt} + \rho\Delta.\vec{v} = 0 \tag{1}$$

$$\frac{D\rho}{Dt} + \rho\left(\Delta.\vec{v}\right) = 0 \tag{2}$$

3.2 Momentum Equation

The momentum equation also tells that in any system if no external force is applied to the system, then the moment of the element inside the system remains conserved. The general form of momentum equation as follows.

$$\rho\frac{Du}{Dt} = \frac{\partial p}{\partial x} + \rho f x \tag{3}$$

$$\rho\frac{Dv}{Dt} = \frac{\partial p}{\partial y} + \rho f y \tag{4}$$

$$\rho\frac{Dw}{Dt} = \frac{\partial p}{\partial z} + \rho f z \tag{5}$$

3.3 Energy Equation

The energy equation used in computational fluid dynamics is based on the basis principle of energy equation which say that energy can neither be created nor be destroyed.

$$\rho \frac{D}{Dt}\left(e + \frac{e^2}{2}\right) = pq - \frac{\partial(up)}{\partial x} - \frac{\partial(vp)}{\partial y} - \frac{\partial(wp)}{\partial z} - \rho \overrightarrow{f}.\overrightarrow{V} \tag{6}$$

The boundary conditions are set for inlet, outlet, sabot, and penetrator of the geometry. All the simulations are done in ambient condition. Simulation for sabot discard and penetrator at different angle of attack is performed to get the aerodynamics force acting on the sabot component in sabot penetrator assembly and pressure force on penetrator at a different angle of attack. A finite volume-based implicit solver is a powerful computational fluid dynamics solver developed by Zeus Numerix Pvt Ltd. The solver is based on the Spalart–Allmaras model. Spalart–Allmaras is a one-equation model that solves a modelled transport equation for the kinematic eddy turbulent viscosity. The Spalart–Allmaras model was designed specifically for aerospace applications involving wall-bounded flows and has been shown to give good results for boundary layers subjected to adverse pressure gradients. The simulations performed are solved using inviscid conditions. The aim is to find the coefficient of lift, the coefficient of drag, and coefficient of the moment for sabot during different angle of separation from penetrator after it is fired. The operating conditions were set as follows (Table 1).

4   Results and Discussion

The pressure contours for the safe separation of the sabots are illustrated in Figs. 8, 9, 10, and 11 for different discard angle. The computational fluid dynamics analysis is done for two different phases of the launch of armour piercing fin stabilised discarding sabot. The events occurred after the projectile is fired are the discard process of sabot and effect of angle of attack on the penetrator.

The launch of the projectile at Mach 4 imposed a very high pressure on the face of the sabot cups. The pressure is much high that it breaks the driving bands. The sabot

Table 1 Operating conditions

Parameters	Values
Density	1.225 kg/m^3
Inlet velocity	1372 m/s
Pressure	101,325 Pa
Temperature	300 K

Fig. 8 Pressure contour illustration before separation
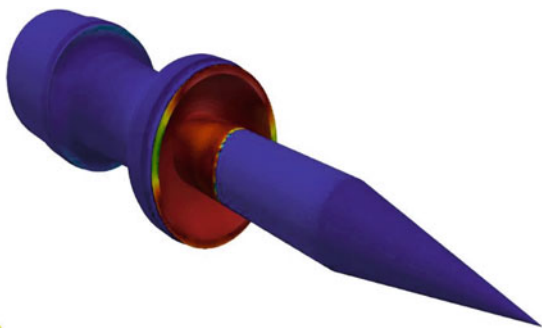
Fig. 9 Pressure contour illustration at 10° sabot separation
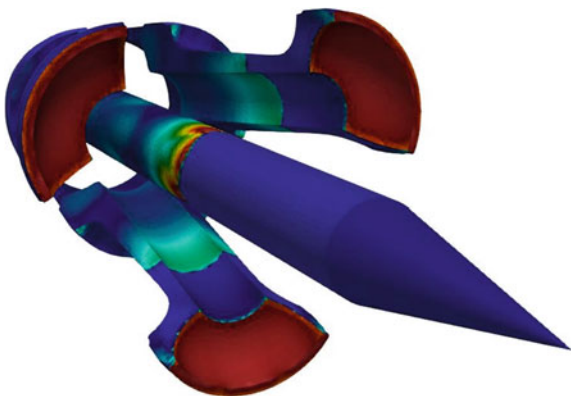
Fig. 10 Pressure contour illustration at 25° sabot separation
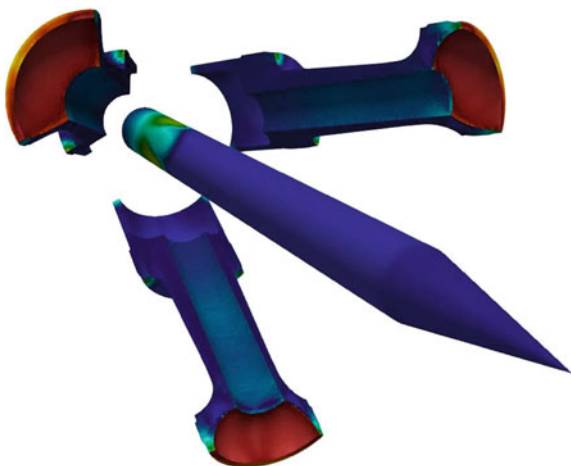
Fig. 11 Pressure contour illustration at 50° sabot separation
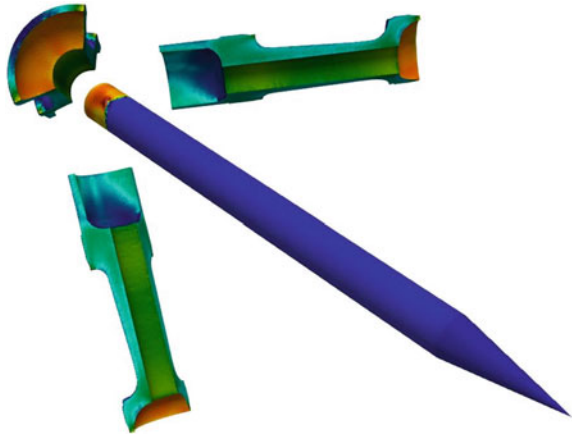
components started separating with the shock formed on the surface of the projectile and sabot face. The red colour in the figure indicates the presence of the shock over the surface and sabot cup. The sabot discard process was analysed at 10° and the change in the position of the bow shock positioned downstream when compared with the position of bow shock before separation of sabot from penetrator. The shocks formed interact with each sabot and provide required aerodynamic forces and moment to the sabot for the discard process. The other angles which are considered as discard angle are 25° and 50°. The position of the bow shock is continuously shifted towards the downstream of the projectile and is illustrated in the pressure contours of respective discard angles. The sabot discard process occurred because the mass flow coming at Mach 4 hits the sabot cup but the mass flow does not get outlet path to escape. Thus, the sabot started forming a converging channel between sabot and penetrator and a series of expansion waves accelerates the flow inside it. The high-pressure region is formed until the sabot completely discarded and chocked flow disappeared.

The bow shock formed provides axial as well as radial forces to the sabot components. The sabot components also associated with the pitch moment. The high-pressure zone and low-pressure zones are easily identified, and the formation of bow shock varies in different sabot discard phase. The bow shock illustration is shown for 0, 10, 25, and 50 sabot discard angles in Fig. 12, respectively.
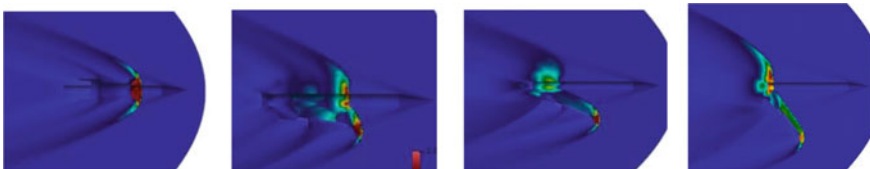
Fig. 12 Bow shock illustration of different sabot discard angle

Fig. 13 Pressure illustration on penetrator and fin assembly at 0° AOA
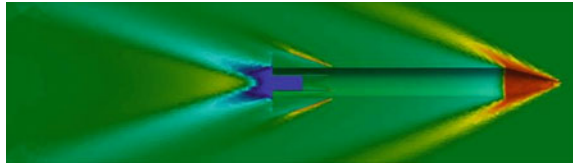
Fig. 14 Pressure illustration on penetrator and fin assembly at 2° AOA
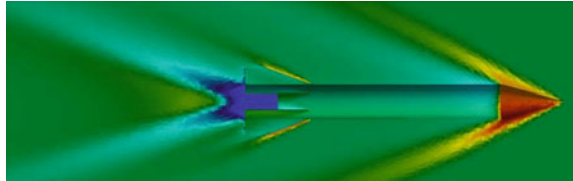
Fig. 15 Pressure illustration on penetrator and fin assembly at 4° AOA
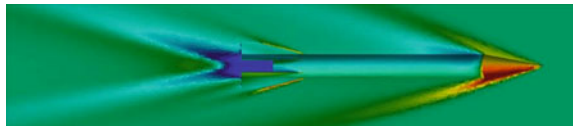
Fig. 16 Pressure illustration on penetrator and fin assembly at 6° AOA
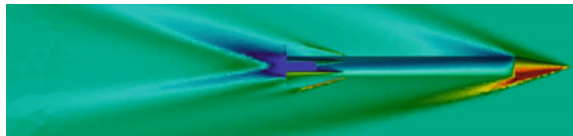
The penetrator was assembled with the fin, which provides the stability during flight at supersonic Mach number. The penetrator and fin assembly were analysed at different angle of attack to understand the forces and moment on the penetrator. The pressure contour of penetrator and fan assembly at different angle of attack. The present study deals with 0, 2, 4, and 6 of angle of attack are shown in Figs. 13, 14, 15, and 16, respectively. The increasing angle of attack decreases the pressure over one face of the penetrator and increases over another.

4.1 Aerodynamic and Moment Coefficient

The aerodynamic forces acting on the sabot during discard process must be uniform for the safe separation of sabot. The aerodynamic coefficient of drag and lift for different sabot discard angle were found out. The coefficient of lift and coefficient of drag plotted against different sabot discard angles and is shown is Figs. 17 and 18.

The lift coefficient follows nearly linear pattern for all discard angles. The Cl value is zero at discard angle zero and maximum at discard angle 50. The coefficient
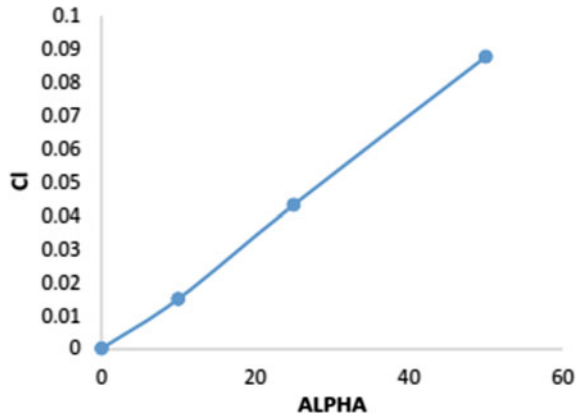
of lift for axisymmetric bodies is nearly zero. The pattern followed by coefficient of drag against the discard angle is linear from angle 0–10 and from angle 25–50. The sabot interaction increases with the increase in discard angle results in increase in drag force acting on it. The value of slope between the discard angle 10–25 shows non-linear relation. The pitch moment calculated at centre of gravity was also found out for the sabot at different discard angle. The pitch moment coefficient for different discard angle is shown in Fig. 19.

Graph plotted for the coefficient of lift and drag against angle of attack is shown in Figs. 20 and 21. The graph shows non-linear increasing trend for the various values of angle of attack. The slope for the drag coefficient of penetrator between angle of attack 0–2 degree shows less value of slope, but slope for the values between angle of attack 2–6 degrees tends to increase this drag drag coefficient. The plot for the drag coefficient of the penetrator shows different trend when compared with the lift coefficient of the penetrator at different angle of attack. The value of drag coefficient

Fig. 19 Coefficient of pitch moment of sabot versus alpha
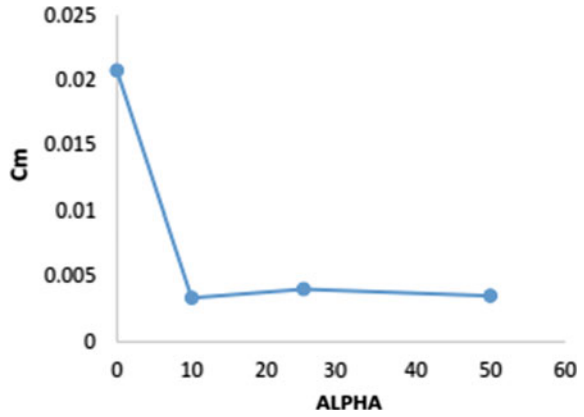
Fig. 20 Coefficient of lift of penetrator versus angle of attack
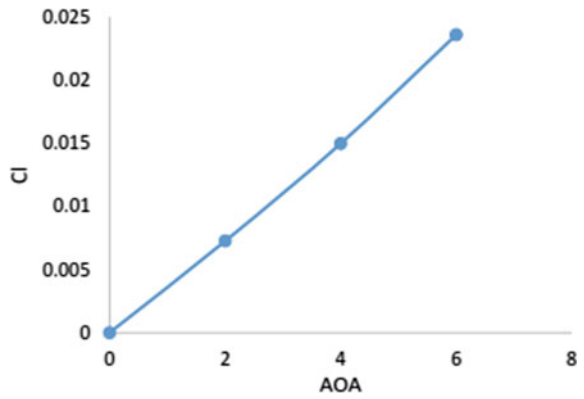
Fig. 21 Coefficient of drag of penetrator versus angle of attack
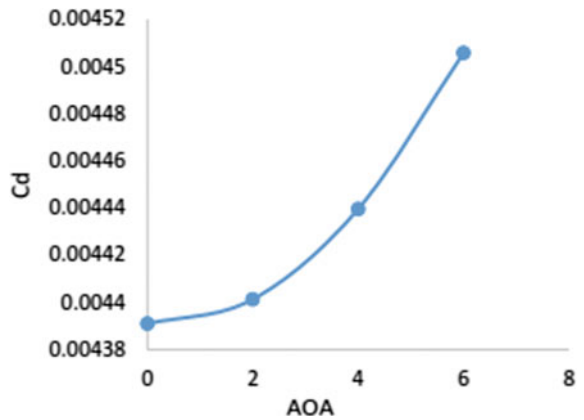
Fig. 22 Coefficient of pitch
moment of penetrator v/s
angle of attack for sabot
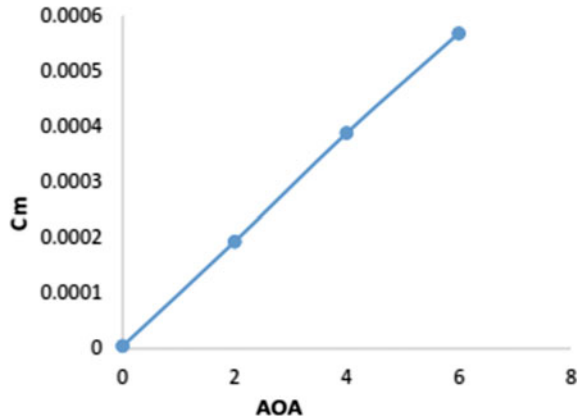
for zero degree angle of attack is 0.002195. The drag coefficient for angle of attack
2, 4, and 6 is 0.002201, 0.00222, and 0.002253, respectively.

The trend for the drag coefficient also indicated that the variation of drag coeffi-
cient with the angle of attack is not linear. Graph plotted for the coefficient of pitch
moment against angle of attack is shown in Fig. 22. The graph follows linear pattern
for all the values of angle of attack. The slope variation for the pitch moment of the
penetrator at various angle of attack seems nearly uniform. The peak value for the
coefficient of pitch moment comes for angle of attack 6 degree which is 0.000567917,
and the minimum value for the pitch moment came for 0-degree angle of attack which
is 4.6868E−06. The trend for the graph is comparable from the graph plotted for
coefficient of lift against angle of attack which was also a linear trend.

Finite element analysis is also done to check the breakdown of the driving bands.
The pressure generated on the sabot cup before sabot separation is used to check the
breakdown of driving bands. The peak pressure generated at the sabot cups was used
to check the finite element analysis for the breakdown on the driving bands. The
material used to manufacture the driving band is Nylon. The peak pressure applied
on the sabot cups is 1.9 Mpa. The maximum equivalent stress acting on the face of
sabot cup is 522.73 MPa. The maximum equivalent stress is denoted by red colour in
the Fig. 23a. The total deformation in the driving belt is also shown in the Fig. 23b.
The material chosen for the driving belt is Nylon 6. The density of the nylon 6 is
1.12 g/cc, and the poisons ratio of nylon-6 is considered between 2 and 4.

5 Conclusions

The study concludes the aerodynamic forces acting on the sabot during discard
process. The aerodynamic forces such as lift, drag, pitch moment, and the coef-
ficients related with them were found out. The muzzle velocity of the given to the
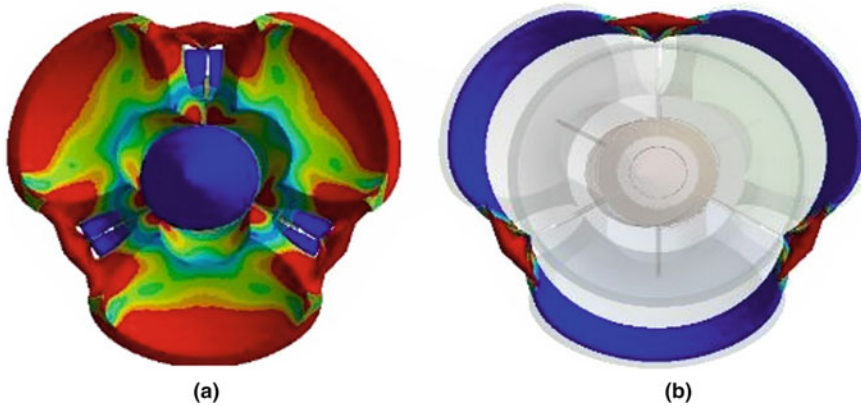
Fig. 23 Driving bands deformation

projectile is Mach 4 which operate at the atmospheric condition. To analyse the aero-dynamic forces for sabot and penetrator, various cases were considered to proceed compute computational fluid dynamics over armour piercing fin stabilised discarding sabot. Simulations were performed on sabot kept at various angles such as 0, 10, 25, and 50 degree with respect to the penetrator. The effect of angle of attack on the penetrator is also studied, and aerodynamic forces were calculated. The angle of attack considered for the study of flow around the penetrator of armour piercing fin stabilised discard sabot is 0, 2, 4, and 6 degrees. The data collected from the simulations for sabot and penetrator were further used to generate the plots against angle of attack and angle between sabot and penetrator. The plots generated using aerodynamic coefficients show increasing trends with respect to the increase in angle between sabot and penetrator of sabot and various angles of attack for penetrator and fins. When sabot and penetrator were in contact and no separation is initialised, the presence of high pressure found at the sabot cups and this peak pressure is found to be 1.9 MPa. Using this peak pressure presents on the sabot cups before sabot is discarded, the structural analysis for the breakdown of the driving band is done. The structural analysis of the driving band is to study the deformation due to the peak pressure generated from the CFD analysis.

References

1. Acharya RS, Naik SD (2007) Modelling of shockwave force and its effect during sabot discard process. Def Sci J 57:677–690
2. Baloš S, Nika M, Risti P, Ši L Jacketed long-rod penetrators: problems and perspectives 6
3. Bhange N, Sen A, Ghosh A (2009) Technique to improve precision of kinetic energy projec-tiles through motion study. In: AIAA atmospheric flight mechanics conference. Presented at the AIAA atmospheric flight mechanics conference, American Institute of Aeronautics and Astronautics, Chicago, Illinois

4. Cayzac R, Carette E Computational fluid dynamics and experimental validations of the direct coupling between interior. Intermed Exterior Ballistics Euler Eqs 19

5. Engineering design handbook. SABOT Technology Engineering, n.d. 295

6. Ferry E, Sahu J, Heavey K Navier-Stokes computations of sabot discard using chimera scheme 34

7. Gopalapillai R, Kim H-D, Setoguchi T, Matsuo S (2007) On the near-field aerodynamics of a projectile launched from a ballistic range. J Mech Sci Technol 21:1129–1138

8. Huang Z, Wessam ME, Chen Z (2014) Numerical investigation of the three-dimensional dynamic process of sabot discard. J Mech Sci Technol 28:2637–2649

9. Huang Z, Xia C, Cao Y, Chen Z, Zhang H (2019) Numerical investigations on the sabots discard process of an APFSDS at different angles of attack. J Eng 2019:373–378

10. Narayanamurthy V, Rao C, Rao B (2014) Numerical simulation of ballistic impact on armour plate with a simple plasticity model. Defence Sci J 64:55–61. https://doi.org/10.14429/dsj.64.4521

11. Nusca M (1991a) Numerical simulation of sabot discard aerodynamics. In: 9th applied aerodynamics conference. Presented at the 9th applied aerodynamics conference, American Institute of Aeronautics and Astronautics, Baltimore, MD

12. Nusca M (1991b) Numerical simulation of sabot discard aerodynamics. In: 9th applied aerodynamics conference. Presented at the 9th applied aerodynamics conference, American Institute of Aeronautics and Astronautics, Baltimore, MD

13. Nusca, M., 1990a. Computational fluid dynamics application to the aerodynamics of symmetric sabot discard, in: Flight Simulation Technologies Conference and Exhibit. Presented at the Flight Simulation Technologies Conference and Exhibit, American Institute of Aeronautics and Astronautics, Dayton, OH

14. Plostins P (n.d.) Launch dynamics of APFSDS Ammunition 55

15. Schmidt EM (1982) Disturbance to the launch of fin-stabilized projectiles. J Spacecr Rocket 19:30–35

16. Schmidt EM (n.d.) Measurement of sabot discard and analysis of associated launch disturbances 33

17. Schmidt EM, Shear D (1978) Aerodynamic interference during sabot discard. J Spacecr Rocket 15:162–167

18. Sorensen BR (n.d.) Design and analysis of kinetic energy projectiles using finite element optimization 37

19. Xiangping L, Lu J, Feng J (2018) Simulation of sabot discard for electromagnetic launch integrated projectile. IEEE Trans Plasma Sci 46:2636–2641

Analysis of Bidding Strategies in Virtual Power Plant

Poushali Pal, A. K. Parvathy, K. R. Devabalaji, P. DeivaSundari, S. Joseph Antony, and S. E. Ocheme

Abstract Penetration of renewable energy sources has become an important matter due to rapid diminishing of conventional sources. Environmental pollution is also one of the main reasons in many countries. Virtual power plant (VPP) is a new technology which can manage the uncertainties caused by the renewable sources in demand side. VPP will aggregate the capacities of distributed energy resources (DERs) to create a single operating profile. Each DER will get visibility and controllability in the electricity market with this technique. In this paper, virtual power plant concept is demonstrated and the bidding strategies of energy among VPP and grid are developed for four different scenarios. A model is considered for the analysis of the system which consists of two solar power generation units and one wind power generation unit with energy storage system (ESS).

Keywords Virtual power plant · Energy storage system · Distributed generation

1 Introduction

The continuing growth of environmental pollution and energy consumption due to conventional energy source, penetration of DG increases rapidly in the market. But to manage all the DGs together is a serious problem which can affect the system security

P. Pal (✉)
TPLC, Government Engineering College, Barton Hill, Kunnukuzhy, Thiruvananthapuram 695035, India
e-mail: poushali.nits@gmail.com

P. DeivaSundari
Department of Electrical and Electronics Engineering, KCG College of Technology, Karappakam, Chennai 600097, India

S. Joseph Antony · S. E. Ocheme
School of Chemical and Process Engineering, University of Leeds, Leeds LS2 9JT, UK

A. K. Parvathy · K. R. Devabalaji
Department of Electrical and Electronics Engineering, Hindustan Institute of Technology and Science, Padur, Chennai 603103, India

[1]. So, VPP provides an efficient solution by aggregating all the DGs, interruptible loads (ILs), ESS, and EV. VPP will act as a single operating profile, and with this concept, every DER can take part to the electricity market alone. Controllability and visibility of each DER will increase with VPP.

Modeling and simulation of VPP were introduced with different operating modes of VPP. Amount of power purchased and sold to the grid is tabulated for three operating modes as no power exchange mode, grid import, and export mode [2]. Improved model predictive control (MPC) strategy developed which can reduce prediction error by compensation. Predicted value and real value differences for stochastic generation measured with this technique [3]. Combination of deterministic and interval optimization together is used to solve optimal dispatch strategy of VPP [4]. This combined strategy can be used to manage VPP uncertainties within limited computational time. Optimization of bidding strategy done using stochastic bidding model for balancing market and day-ahead market [5] addressing maximum profit, optimal capacity of battery energy storage system (BESS). Stochastic optimization model is converted to deterministic optimization model using sample average approximation (SAA) [6]. Congestion management for distribution network is also highlighted. An improved VPP regulation strategy is developed for reducing the load and fluctuation effect of intermittent power on regulation performance [7]. Mixed-integer linear programming (MILP) is formulated to minimize the total operation cost of integrated energy systems (IES) with combined cooling, heating, and power [8]. A combination of PSO, binary PSO, and improved particle swarm optimization (IMPSO) formulated with MATLAB program for multi-objective optimization such as reduction of pollution treatment cost, total power generation cost, unit startup, and shut-down cost [9]. Optimal dispatch strategy developed for VPP for unified electricity market considering DER constraint, security constraint, and power balance constraint [10].

2 VPP Concept

VPP is an aggregation of renewable energy sources, controllable loads, and energy storage system which can take part as a single power plant in the electricity market. An aggregator will make contracts with each DG owner and thus can supply the power to the consumers with improved power quality. VPP will create a flexible portfolio for all the consumers by operating as a single power plant. One important part of VPP is energy management system (EMS) which mainly aims at trading electrical energy with the main grid and electricity market. VPP will dispatch energy to grid and among its elements as a core energy management system. EMS will act as centralized controller which collects all the generation and demand data from VPP and also the grid requirement.

3   Formulation of Objective Function

The objective function can be formulated as minimization of the cost of power purchased from grid

$$y = a * (P_D - \sum P_{Gi}) + b * P_{Gi} \tag{1}$$

where P_D is total demand, y is the cost of power purchased from grid, a is power purchased rate from the grid, b is price rating for grid, and P_{Gi} is the total generation.

4   Results Analysis

The test system used for evaluation of optimal dispatch strategy has been introduced in this section. VPP network configuration is shown in Fig. 1. The VPP contains three DGs (S1, S2, and S3) of capacity 4000, 3000, and 5090 W. The DGs contain intermittent generation like solar generator and wind generator. It does not contain any dispatchable generator. In this research, let us consider the microgeneration has its own battery management system. The solar/wind power will generate the power and store in the dedicated battery management system. Hence, each microplant has capable of delivering constant power to the VPP. In case any one of the microgeneration got internal failure, then the power cannot be sell to VPP.

Different conditions of power purchased and sold to the grid are shown below.

A.   When generation is equal to demand

When production is equal to the demand then VPP will sell the power to the load.

B.   When generation is more than demand

When electricity production by VPP is more than demand, VPP will sell electricity to grid and load. VPP can charge battery for use during the peak demand.

C.   When generation is less than demand

Fig. 1   VPP single line diagram
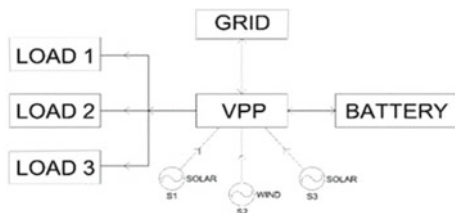
When electricity production is less than the demand, then VPP will purchase electricity from the grid for supplying the load or it will discharge the battery.

So, from these cases, it can be told that VPP will purchase the power when production is less and VPP will sell power to the grid when production is high or else it can charge/discharge the battery.

Let us consider the constitution of loads as given in Tables 1, 2, 3, 4, and 5.

Four scenarios can be broadly explained with these examples:

Scenario 1

Considering three generators in 'OFF' condition for first 1–7 h and 18–24 h and 'ON' condition for 8–17 h. In this case, no generator is working for 1–7 h, in that time, the power is purchased from grid to meet the demand of 10,075 W. From 8–17 h, two solar systems are working, and wind generator is not considered. So, for 1–7 h

Table 1 Load 1 data

S. No.	Name of the load	Quantity	Individual power consumed (W)	Subtotal power consumed (W)
1	Bulb	1	60	60
2	Bulb	4	40	160
3	Air conditioner	1	1500	1500
4	Small air conditioner	2	500	1000
				Total 2720

Table 2 Load 2 data

S. No.	Name of the load	Quantity	Individual power consumed (W)	Subtotal power consumed (W)
1	Air conditioner	1	1075	1075
2	Heater	2	200	400
3	Computer	1	620	620
4	Washing machine	1	2000	2000
				Total 4095

Table 3 Load 3 data

S. No.	Name of the load	Quantity	Individual power consumed (W)	Subtotal power consumed (W)
1	Dryer	1	560	560
2	Tube light	2	40	80
3	Computer	1	620	620
4	Washing machine	1	2000	2000
				Total 3260

Table 4 The day-ahead market scenario

Time (h)	Price/kWh
1	4
2	5
3	5
4	6
5	6
6	8
7	8
8	8
9	10
10	13
11	13
12	10
13	13
14	13
15	13
16	12
17	10
18	10
19	10
20	10
21	5
22	5
23	5
24	5

Table 5 Price rate of power production from different generator

S. No,	Type	Minimum capacity (W)	Maximum capacity (W)	Rate/kWh
1	PV	0	4000	6
2	Wind	0	3000	6
3	PV	0	5090	6

10.075 kW power is purchased from grid, for 8–17 h 0.985 kW power is purchased from grid, and from 18 to 24 h VPP generation is considered as zero, so the power purchased from the grid is 10.075 kW.

Scenario 2

Considering one solar generator 'ON' for 6 h and 'OFF' condition for 6 h, in this case, one PV generator is working. The generator is considered in 'OFF' condition

for 1–7 h and 18–24 h. Generator is in 'ON' condition for 8–17 h. The amount of power purchasing from grid is 10.075 kW, and VPP generation is 4 kW.

Scenario 3

In this case, VPP generation is not considered, and 10.075 kW power is purchased from the grid for supplying the load.

Scenario 4

In this case, all generators of VPP are working. Total generation from VPP is 12.090 kW power is purchased from grid. The generation status of all the four scenarios is shown in Table 6.

The cost and amount of power transaction with grid and the cost of VPP generation for all the four scenarios are shown in Table 7 and Table 8, respectively.

The amount of power transaction with the grid is shown in the Figs. 2, 3, 4, and 5 for the four scenarios.

5 Overall Analysis

VPP with four different scenarios has been considered in this paper. Amount of power purchasing from grid and selling to grid is tabulated with plotting considering different scenarios for 24 h. For each scenario, the cost of power purchase from grid and the cost of power selling to grid are calculated. From this paper, it is analyzed that the cost of power purchase from grid is lowest with VPP generation, and the cost is highest without VPP generation.

6 Conclusion

VPP is a new concept for participating small generating units in electricity market, and distributed generation is used for this concept which will reduce the power losses and increase both the power quality and reliability of power supply. To investigate the performance of the proposed method, four different scenarios have been introduced, and the simulation results in each scenario have been tabulated. From this paper, researcher will get an idea of the bidding strategies of VPP with the grid.

Table 6 Explanation of the scenarios

Time	Scenario 1			Scenario 2			Scenario 3		Scenario 4	
	Gen 1	Gen 2	Gen3	Gen 1	Gen 2	Gen 3	Generator 1, 2, 3	power from grid	Generator 1, 2, 3	Grid
1	Off	Off	Off	Off	Off	Off	Off	✓	On	•
2	Off	Off	Off	Off	Off	Off	Off	✓	On	•
3	Off	Off	Off	Off	Off	Off	Off	✓	On	•
4	Off	Off	Off	Off	Off	Off	Off	✓	On	•
5	Off	Off	Off	Off	Off	Off	Off	✓	On	•
6	Off	Off	Off	Off	Off	Off	Off	✓	On	•
7	Off	Off	Off	Off	Off	Off	Off	✓	On	•
8	On	Off	On	On	Off	Off	Off	✓	On	•
9	On	Off	On	On	Off	Off	Off	✓	On	•
10	On	Off	On	On	Off	Off	Off	✓	On	•
11	On	Off	On	On	Off	Off	Off	✓	On	•
12	On	Off	On	On	Off	Off	Off	✓	On	•
13	On	Off	On	On	Off	Off	Off	✓	On	•
14	On	Off	On	On	Off	Off	Off	✓	On	•
15	On	Off	On	On	Off	Off	Off	✓	On	•
16	On	Off	On	On	Off	Off	Off	✓	On	•
17	On	Off	On	On	Off	Off	Off	✓	On	•
18	Off	Off	Off	Off	Off	Off	Off	✓	On	•
19	Off	Off	Off	Off	Off	Off	Off	✓	On	•
20	Off	Off	Off	Off	Off	Off	Off	✓	On	•

(continued)

Table 6 (continued)

Time	Scenario 1			Scenario 2			Scenario 3		Scenario 4	
	Gen 1	Gen 2	Gen3	Gen 1	Gen 2	Gen 3	Generator 1, 2, 3	power from grid	Generator 1, 2, 3	Grid
21	Off	Off	Off	Off	Off	Off	Off	✓	On	•
22	Off	Off	Off	Off	Off	Off	Off	✓	On	•
23	Off	Off	Off	Off	Off	Off	Off	✓	On	•
24	Off	Off	Off	Off	Off	Off	Off	✓	On	•

Table 7 Cost of the power transaction of VPP and grid

Time (h)	Case I		Case II		Case III	Case IV	
	Cost of power purchased from the grid (Rs.)	Cost of power generation from VPP (Rs.)	Cost of power purchased from the grid (Rs.)	Cost of power generation from VPP (Rs.)	Cost of power purchased from the grid (Rs.)	Cost of power purchased from the grid (Rs.)	Cost of power sold to the grid (Rs.)
1	40.3	0	40.3	0	50.375	40.3	0
2	50.375	0	50.375	0	50.375	50.375	0
3	50.375	0	50.375	0	50.375	50.375	0
4	60.45	0	60.45	0	55.4125	60.45	0
5	60.45	0	60.45	0	60.45	60.45	0
6	80.6	0	80.6	0	80.6	80.6	0
7	80.6	0	80.6	0	80.6	80.6	0
8	7.88	54.54	48.6	24	80.6	0	16.12
9	9.85	54.54	60.75	24	100.75	0	20.15
10	12.805	54.54	78.975	24	130.975	0	26.195
11	12.805	54.54	78.975	24	130.975	0	26.195
12	9.85	54.54	60.75	24	130.975	0	20.15
13	12.805	54.54	78.975	24	100.75	0	26.195
14	12.805	54.54	78.975	24	130.975	0	26.195
15	12.805	54.54	78.975	24	130.975	0	26.195
16	11.82	54.54	72.9	24	120.9	0	24.18
17	9.85	54.54	60.75	24	100.75	0	20.15
18	100.75	0	100.75	0	100.75	100.75	0
19	100.75	0	100.75	0	100.75	100.75	0
20	100.75	0	100.75	0	100.75	100.75	0
21	50.375	0	50.375	0	50.375	50.375	0
22	50.375	0	50.375	0	50.375	50.375	0
23	50.375	0	50.375	0	50.375	50.375	0
24	50.375	0	50.375	0	50.375	50.375	0
Total Price	1040.18	545.4	1625.53	240	2090.563	926.9	231.725
Total Price	1585.575		1865.525		2090.563	231.725(gain)	

Table 8 Amount of power transaction of VPP and grid

Time (h)	Case I		Case II		Case III	Case IV	
	Power purchased from grid	Power from VPP	Power purchased from grid	Power from VPP	Power purchased from grid	Power purchased from grid	Power sold to the grid
1	4	0	10.075	0	10.075	10.075	0
2	5.5	0	10.075	0	10.075	10.075	0
3	5	0	10.075	0	10.075	10.075	0
4	6	0	10.075	0	10.075	10.075	0
5	6	0	10.075	0	10.075	10.075	0
6	8	0	10.075	0	10.075	10.075	0
7	8	0	10.075	0	10.075	10.075	0
8	8	9.09	6.075	4	10.075	0	16.12
9	10	9.09	6.075	4	10.075	0	20.15
10	13	9.09	6.075	4	10.075	0	26.195
11	13	9.09	6.075	4	10.075	0	26.195
12	10	9.09	6.075	4	10.075	0	20.15
13	13	9.09	6.075	4	10.075	0	26.195
14	13	9.09	6.075	4	10.075	0	26.195
15	13	9.09	6.075	4	10.075	0	26.195
16	12	9.09	6.075	4	10.075	0	24.18
17	10	9.09	6.075	4	10.075	0	20.15
18	10	0	10.075	0	10.075	10.075	0
19	10	0	10.075	0	10.075	10.075	0
20	10	0	10.075	0	10.075	10.075	0
21	5	0	50.375	0	10.075	10.075	0
22	5	0	50.375	0	10.075	10.075	0
23	5	0	50.375	0	10.075	10.075	0
24	5	0	50.375	0	10.075	10.075	0
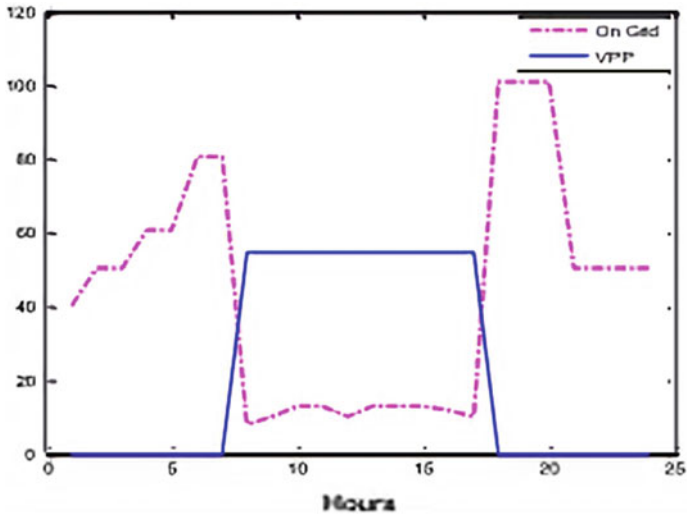
Fig. 2 Shows the amount of power purchased from grid and VPP for scenario 1
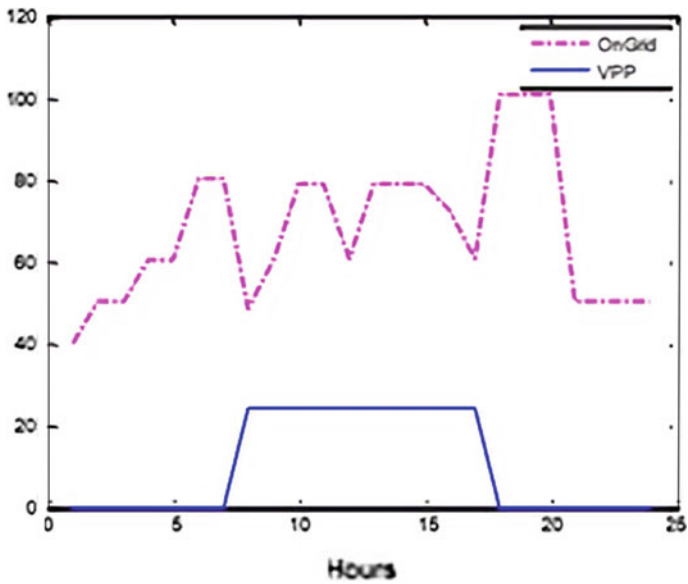
Fig. 3 Shows the amount of power purchased from grid and VPP for scenario 2
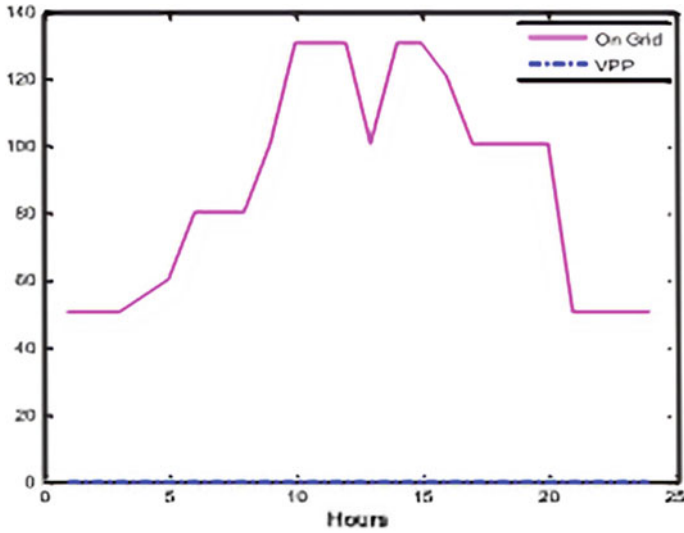
Fig. 4 Shows the amount of power purchased from grid and VPP for scenario 3
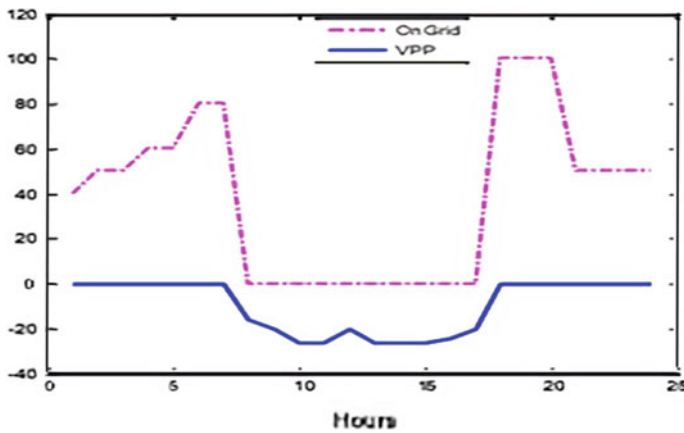
Fig. 5 Shows the amount of power purchased from grid and VPP for scenario 4

References

1. Petersen M, Bendtsen J, Stoustrup J (2012) Optimal dispatch strategy for the agile virtual power plant. In: American control conference Fairmont Queen Elizabeth, Montréal, June 27–29, pp 288–294
2. Naina PM, Rajamani H-S, Swarup KS (2017) Modelling and simulation of virtual power plant in energy management system applications. In: 7th international conference on power systems (ICPS), College of Engineering Pune, Dec 21–23, pp 392–396
3. Zhang Z, Zhang J, Peng WDR, Xu C (2018) Research on economic optimal dispatching strategy

of microgrid based on model predictive control. In: MATEC web of conferences, vol 232, pp 1–5

4. Liua Y, Lia M, Liana H, Tanga X, Liua C, Jiangb C (2018) Optimal dispatch of virtual power plant using interval and deterministic combined optimization. Electric Power Energy Syst 102:235–244

5. Kang Y, Lo K (2016) Optimal control and bidding strategy of virtual power plant with renewable generation. World J Eng Technol 4:27–34

6. Yu J, Feng Q, Li Y, Cao J (2015) Stochastic optimal dispatch of virtual power plant considering correlation of distributed generations. Math Prob Eng 1–8

7. Yang J, Huang Y, Wang H, Ji H, Li J, Gao C (2017) A regulation strategy for virtual power plant. In: The 4th international conference on systems and informatics (ICSAI), pp 375–379

8. Li G, Zhang R, Jiang T, Chen H, Bai L, Cui H, Li X (2017) Optimal dispatch strategy for integrated energy systems with CCHP and wind power. Appl Energy 192:408–419

9. Cheng H, Gao Y, Zhang J, Li R, Liang H (2014) The power system multi-objective optimization dispatching containing virtual power plant. In: International conference on power system technology (POWERCON 2014), Chengdu, 20–22 Oct. 2014, pp 1–6

10. Bai H, Mao S, Ran X, Ye C (2015) Optimal dispatch strategy of a virtual power plant containing battery switch stations in a unified electricity market. Energies 8:2268–2289

DSMC Simulation of Rocket Plume Interactions with Extra-Terrestrial Regolith

Isha Mohan Sharma, Vishnu Kiran Kadiyala, and G. Malaikannan

Abstract Soft landings on extra-terrestrial surfaces are vital for any sample return missions. Moreover, during landing on such bodies, dust impingement on the lander module and Extra-Vehicular Activity (EVA) systems can cause serious complications. To prevent system failures due to scoured regolith, and also minimize contamination of surface regolith for sample collection, the rocket can be used to decelerate the spacecraft to a vertical descent velocity from which it can freefall. A Direct Simulation Monte Carlo (DSMC) technique is developed to investigate the interaction of rocket plume with surface regolith of an airless extra-terrestrial body. Continuum breaks down as the exhaust exits the engine nozzle, and the gases expand rapidly into the vacuum. Near the nozzle exit, the process enters a rarefied flow regime and an open-source DSMC code is developed to model the movement and collision stages of rarefied plume gas and dust particles. In this simulation, the collision occurs between gas particles of the rocket plume as it impinges on such an extra-terrestrial surface. The solver used for carried out this simulation is dsmcFOAM solver, a part of OpenFOAM. The surface properties such as pressure coefficient and heat flux are computed and analysed to observe the impact of plume impingement on extra-terrestrial regolith.

Nomenclature

A_e	Area of the exit of nozzle (m^2)
A_t	Area of the throat of nozzle (m^2)
c	Soil cohesion (Pa)
c_r	Relative speed of two colliding molecules (m/s)

I. M. Sharma (✉) · V. K. Kadiyala · G. Malaikannan
Department of Aerospace Engineering, Faculty of Engineering & Technology, SRM Institute of Science & Technology, Tamil Nadu, Kattankulathur, Kancheepuram District 603203, India
e-mail: isha_man@srmuniv.edu.in

d	Diameter of the molecule (m)
D_e	Diameter of the exit of nozzle (m)
F	Thrust of rocket engine (N)
F_{num}	Number of simulated molecules representing a finite number of real molecules
g_o	Acceleration due to gravity (m/s^2)
I_{sp}	Specific impulse of the rocket (s)
K_b	Boltzmann constant (m^{2}kg/s^{2}K)
Kn	Knudsen Number
L	Characteristic length (m)
m	Mass of the molecule (kg)
$\dot{m}$	Propellant mass flow rate (kg/s)
Ma	Mach Number
n	Number density of molecules
P	Static pressure (Pa)
P_o	Stagnation pressure (Pa)
T	Static temperature (K)
T_o	Stagnation temperature (K)
Δt	Time step (s)
V	Velocity (m/s)
V_e	Exhaust velocity of the rocket (m/s)
Δx	Size of each cell (m)
λ	Mean free path (m)
Ω	Solid collision angle
θ	Internal Friction angle
σ'	Normal Stress to Failure Plane (Pa)
σ_T	Molecular cross-section (m)
Φ	Angle along the cylinder surface from stagnation point
ρ	Mass density (kg/m^3)
τ	Mean collision time (s)
τ_s	Shear Stress of Lunar soil (Pa)
υ_{th}	Average thermal speed (m/s)

1 Introduction

1.1 Motivation

When a rocket lands on extra-terrestrial bodies, its exhaust plume consists of a high-speed, high-density gas which expands rapidly into the vacuum after exiting the nozzle. When this plume impinges on the extra-terrestrial surface, the solid particles of dust disseminate at high velocities. Dust impingement caused by this plume

on the lander module as well as other extra-vehicular systems can cause serious complications during landing.

This work draws motivation from the Apollo landings that occurred between 1969 and 1972, which landed manned crews (Apollo 11, 12, 14, 15, 16, and 17) on the lunar surface. Mission documents from six Apollo missions were studied in-depth to catalogue the consequences of dust erosion on Extra-Vehicular Systems [1]. The effects were found to be of the following types: vision obscuration, loss of traction, clogging of systems, seal malfunctions, false instrument readings, thermal control problems, and inhalation and irritation. Some problems, like loss of traction, were overcome by simple dust mitigation measures, but these measures rendered useless for problems of much dire nature (i.e. abrasion, clogging, diminished heat rejection).

The ground tests performed before Apollo missions could never estimate how truly severe the effect of dust impingement would be, which was indicative of a greater necessity for the design and development of improved simulation facilities and trials in order to overcome this problem.

The world's vision for Space exploration entails an expanding human presence in the solar system. Before human spaceflight is possible on other extra-terrestrial bodies, it is important to understand the interaction of the propulsion system of lander modules with the surface of that body. This is achieved by carrying out sample return missions to acquire and return with a sample, after a scientific characterization of the landing site as well as the surface. Such missions include the "Phobos Sample Return (PhSR)", a candidate mission of ESA's "Mars Robotic Exploration Preparation (MREP-2)" [2]. Soft landings are imperative for the success of such missions to ensure that the plume ejected from the lander's propulsion system has not contaminated the soil or has caused an undesirable degree of wear-off to the surface, which can potentially endanger the mission.

The aim of this work is to investigate the interaction of rocket plume with the surface regolith which is an integral part of figuring out the solutions to concerns regarding dust impingement. The existence of computational methods for modelling such conditions and flows has great potential in future exploration missions.

1.2 Knudsen Number and Flow Regimes

The Knudsen Number (Kn) is a dimensionless quantity, which can be described as the ratio of the molecular mean free path to a characteristic length. It is used to quantify the degree of rarefaction and is given by:

$$Kn = \frac{\lambda}{L} \qquad (1)$$

where λ = Mean Free Path
    L = Characteristic Length.

Table 1 Different flow regimes classified based on Knudsen Number

Flow regime	Kn	Governing equations
Inviscid flow	$Kn \to 0$	Euler fluid equations
Continuum regime	$Kn \leq 0.001$	Navier–Stokes-Fourier fluid equations
Slip regime	$0.001 \leq Kn \leq 0.1$	Navier–Stokes-Fourier fluid equations with velocity slip and temperature jump boundary conditions
Transition regime	$0.1 \leq Kn \leq 10$	Boltzmann Equation or particle methods like DSMC
Free-molecular regime	$Kn \geq 10$	Collision-less Boltzmann equation or particle methods like DSMC

Adapted from [3]

When the Knudsen number tends to zero, inter-molecular collisions are dominant and the gas is in thermodynamic equilibrium. With the increase in Knudsen Number, the frequency of molecular collisions decreases until the free-molecular limit is reached, where inter-molecular collisions become highly improbable. The non-equilibrium effects begin to dominate with increasing Knudsen Number. This can be explained by the fact that it is inter-molecular collisions and gas surface interactions that drive a system towards thermodynamic equilibrium [3].

The different flow regimes are explained below (Table 1).

1.3 Rocket Plume Interaction with Extra-Terrestrial Regolith

Inside the rocket nozzle, the gas flow is excessively hot, compressible, and largely inviscid. As soon as the plume exits the nozzle, it expands into vacuum resulting in a rapid decrease in temperature, pressure, and density. The continuum breaks down in free space as the plume gas transitions towards a free-molecular flow regime, becoming more and more rarefied. The flow field corresponding to rocket impingement on extra-terrestrial regolith is depicted in Fig. 1.

1.4 Direct Simulation Monte Carlo Solver: dsmcFOAM (OpenFOAM)

The Direct Simulation Monte Carlo (DSMC) technique is a stochastic particle-based method for simulating and solving rarefied gas flow models. G. A. Bird popularized this method in the 1960s, and since then it has been extensively used for studying gas flows in the non-equilibrium regime. It is a probabilistic method, which does not necessarily provide a solution to the Boltzmann Equation but instead, provides
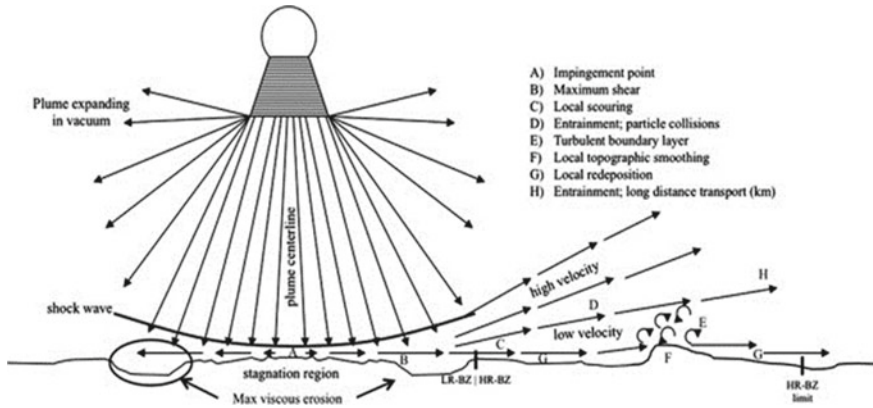
Fig. 1 A schematic visualization of rocket Plume Impingement on ET soil. Adapted from [4]

a process for modelling a real gas flow by adding a certain number of simulated molecules. This number of simulated molecules can vary from the order of hundreds to millions, depending upon the computing power of the machine. The numerical tool used in the completion of this work is dsmcFOAM. This DSMC code is inscribed in C++ within the framework of the open-source CFD software package Open-FOAM. Its capabilities include, but not limited to, modelling 2-D/3-D geometries, carrying out unlimited parallel processing and perform steady and transient solutions. Analyses have shown dsmcFOAM results bear good agreement with data collected through theoretical solutions as well as other present-day codes like DAC, MONACO, and SPARTA.

2 Methodology

The principle of the Direct Simulation Monte Carlo (DSMC) method is that it employs the probabilistic (Monte Carlo) simulation to solve the Boltzmann equation. It is a technique applied for modelling a real gas flow of finite Knudsen number to be simulated by DSMC molecules which range in order of hundreds. However, the DSMC method does not exactly provide a solution to the Boltzmann Equation. The DSMC method requires the user to input simulated molecules of precise molecular size. The technique embodies a fixed number of real gas molecules as one simulated molecule. As the collision of the molecules is simulated in physical space with the appropriate boundary interactions, the spatial coordinates, velocity components, and internal physical states of simulated molecules are constantly stored and modified with time. The conservation of mass, momentum, and energy are imposed within to roundoff error of the compiler [5].

The elementary approximation of the DSMC technique is to decouple the deterministically modelled molecular motions and probabilistically modelled intermolecular collisions over small-time intervals. These small-time intervals are further subdivided into smaller discrete subintervals over which the molecular motions and collisions are decoupled. The decisive computational approximations associated with the DSMC simulation are the number of simulated molecules representing a finite number of the real molecule (Fnum), the time step and the cell sizes in the computational space.

It is crucial to select the time step such that it is less than the mean collision time. If the formulated time step is too large, the molecules will not be able to collide with each other and as a result, have a high probability of moving too far away. This will cause to produce unrealistic solutions.

The cell size where the DSMC particles are inserted in the computational domain must be within the close approximation to the order of the mean free path of the variable hardsphere model. If the cell size exceeds the mean free path, it allows a nonphysical transfer of energy, mass and momentum. This corresponds to the dilute gas assumption.

The DSMC simulation advances from an array of prescribed initial conditions. Different parameters are written by the user that define the particle positions boundary conditions, particle velocities and collision cross-sections which dictate the ensuing evolution of the process. The properties of the molecules entering the computational domain are stated by the boundary conditions. The DSMC method develops the flow with time from its initial state in a realistic manner rather than by an initial approximation to the flow. In this technique, molecules constantly enter and leave the computational domain [5].

3   Numerical Validation

3.1   Overview

OpenFOAM is an open-source software package used to develop or customize the numerical solvers and run simulations that need to be validated to ensure reliability before foregoing with the actual simulation.

Hence, a comparison was made between the results of dsmcFoam in Open-FOAM to a previous DSMC simulation by Lofthouse on the "study of the effects of continuum breakdown on hypersonic aerothermodynamics". The author simulated the flow in different hypersonic regimes was simulated using Computational Fluid Dynamics (CFD) as well as Direct Simulation Monte Carlo (DSMC) by Lofthouse, Boyd and Wright [6]. A hybrid simulation technique was employed where the CFD method is incorporated for the flow field until continuum regime breakdowns (primarily due to superior numerical performance). As the continuum begins to break down, the DSMC method is employed. The author used MONACO code (a

contemporary DSMC code which can be applied hypersonic and rarefied flows) to provide the DSMC results.

The investigation considered a "…Mach 10 hypersonic flow of argon over a two-dimensional, 30.48 cm diameter cylinder with a fixed surface temperature of 500 K, and free stream temperature 200 K".

The author varied the density of the free stream such that regimes from continuum regime through a transitional/slip flow regime to rarefied regime were captured [6]. To validate dsmcFOAM results at Knudsen Number = 0.01 from the above investigation were considered.

3.2 Geometry and Initial Conditions

The blockMesh utility of OpenFOAM was used to generate the geometry (Fig. 2) and the meshing of the domain.

The initial conditions considered for the case were:

- Inlet Temperature = 200 K
- Outlet Temperature = 200 K
- Surface Temperature of Cylinder = 500 K
- Inlet Velocity = (2634.1, 0, 0) m/s
- Number density of Argon = 4.247 e20
- Number of cells in X & Y = (250, 250).
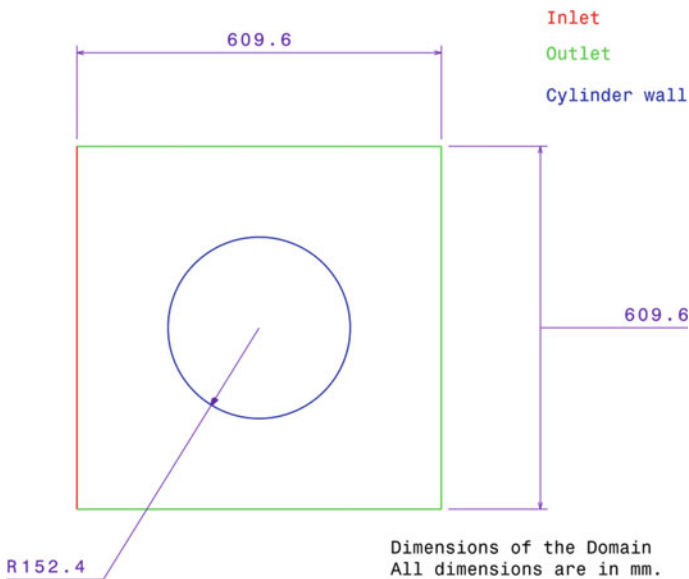
Fig. 2 Computational domain of flow over cylinder case

3.3 Results

The hypersonic flow of the Knudsen number $= 0.01$ regime is considered to be at the near limit of the continuum regime. Hence, continuum breakdown is evident near this Knudsen number. dsmcFOAM is able to predict the bow shock significantly which eventually resulted in change in temperature as well as velocity across the shock.

To validate dsmcFOAM, the plots of temperature along the stagnation line, velocity magnitude along a line normal to the surface at $\Phi = 90°$ and surface pressure coefficient across the surface of the cylinder is compared with MONACO solver used by Lofthouse, Boyd and Wright [6].

It can be observed from the graph shown in Fig. 3 that the surface pressure coefficient accurately matches with results yielded from MONACO. dsmcFoam, first, overpredicts the temperature at a distance $= 0.15$ m from the cylinder, however, afterwards was able to accurately simulate the temperature as shown in Fig. 4. At further distances, dsmcFOAM overpredicted the velocity magnitude, however, the velocity near the surface is in accordance with results by MONACO as shown in Fig. 5. Therefore, the results yielded from dsmcFOAM solver are in good agreement with MONACO solver used by Lofthouse, Boyd and Wright. ***Hence, it can be concluded that the DSMC code in openFOAM is capable of simulating rarefied gas dynamics***.
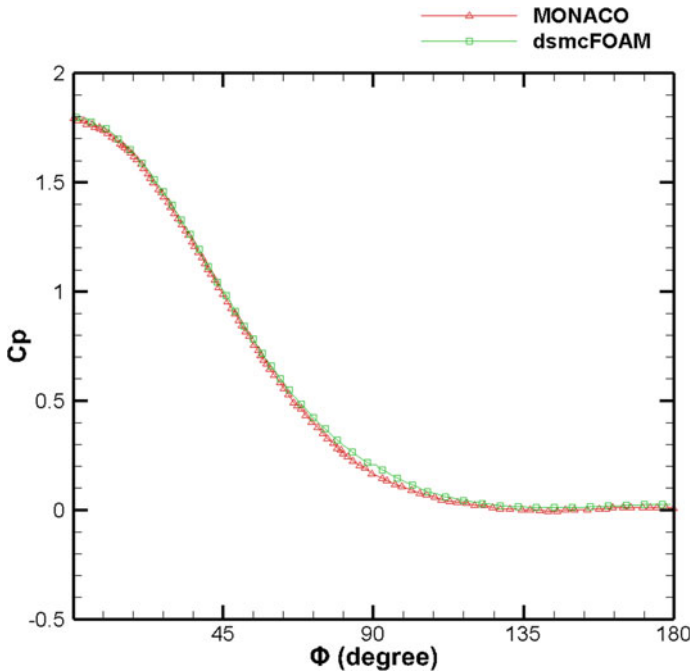
Fig. 3 Surface pressure coefficient across the surface of the cylinder
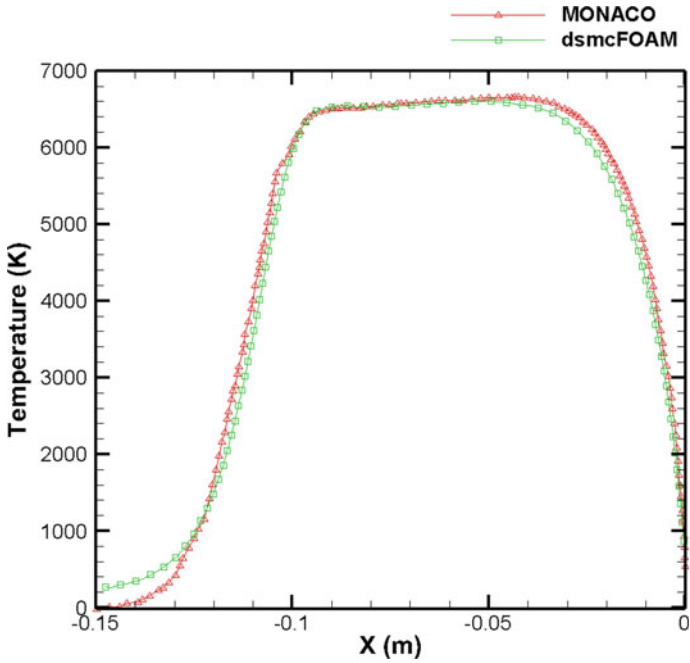
Fig. 4 Variation of temperature along the stagnation line
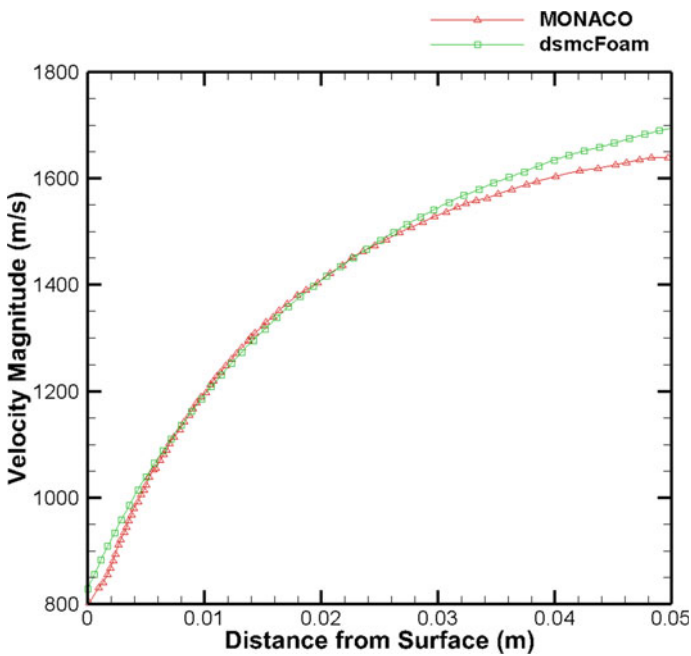
Fig. 5 Velocity magnitude along a line normal to the body surface

4   Rocket Plume Interaction Model

In this work, the rocket exhaust plume of the Lunar Module Descent Engine (LMDE) is modelled to interact with the lunar surface regolith at a thrust of 13.34 kN. Hence, at the nozzle throat, the mean flow properties are obtained to use as boundary conditions. The specific impulse (I_{sp}) of a rocket is used to quantify the fuel efficiency of the rocket. The approximate values of the propellant mass flow rate (m)˙ and exhaust speed (V_e) were obtained using the specific impulse and rocket thrust (F) via [7]:

$$I_{sp} = \frac{F}{g_o \dot{m}} = \frac{V_e}{g_o} \tag{2}$$

Considering a calorically perfect gas and isentropic expansion inside the nozzle, the throat properties are computed. The inflow boundary condition is obtained from the results of these calculations and is summarized in Table 2.

The computational domain along with the corresponding boundary conditions are shown schematically in Fig. 6.

The rocket plume within the nozzle, impingement and interaction simulation is handled entirely within the DSMC solver, i.e. (dsmcFOAM of OpenFOAM package). This dsmcFOAM solver was chosen solely because it was an open-source solver. The solver is written for a load-balanced processor distribution for parallel simulation in order to achieve computational efficiency.

Table 2 Estimated exit plane and throat properties of LMDE [7]

	Ma	ρ [kg/m^3]	P [Pa]	T [K]	V [m/s]	Re, D	T_o [K]	P_o [kPa]
Throat	1.00	1.27×10^{-1}	144,630	2458	1214	297,000	2730	261.4
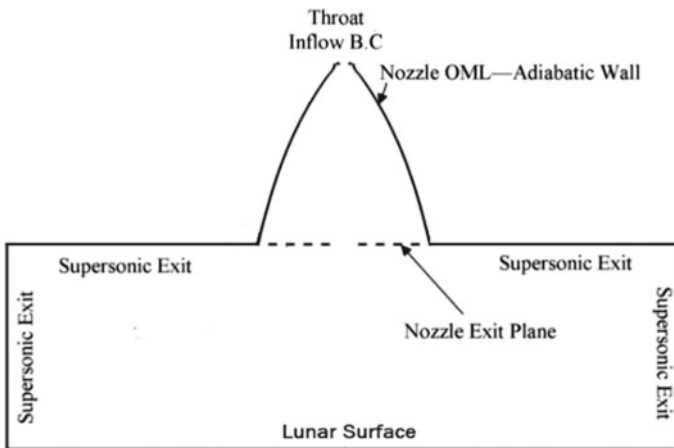
Fig. 6   Outline of the computational domain along with the boundary conditions

4.1 Initial Conditions

The propellant used for LMDE is Aerozine-50. Thus, after combustion in the nozzle, the exhaust gases released mainly consists of NH_3 and H_2O [7, 8]. However, for the sake of simplicity, the rocket exhaust gas is assumed to be "Argon" gas, since it is monoatomic and non-reacting in nature. The following boundary conditions were input:

- Throat Inlet Temperature = 2458 K
- Lunar Surface Temperature = 400 K
- Velocity at throat inlet = (0, −1214, 0) m/s
- Number of molecules represented by simulated molecule = 4.1 e13
- Mass of Argon molecule = 66.3e−27 kg
- Diameter of Argon molecule = 4.17e−10 m
- Number Density = 4.247 e20 molecules.

4.2 Flow Field Within the Nozzle

It can be observed from the velocity contour that the velocity imparted to the gases near the throat is maximum as shown in Fig. 7. Near the walls of the nozzle, i.e. outside
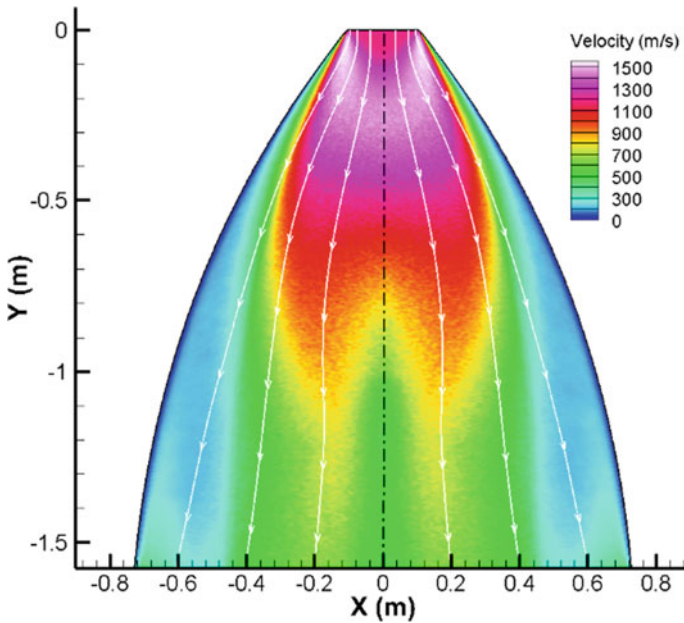
Fig. 7 Velocity contours of plume from nozzle throat to nozzle exit
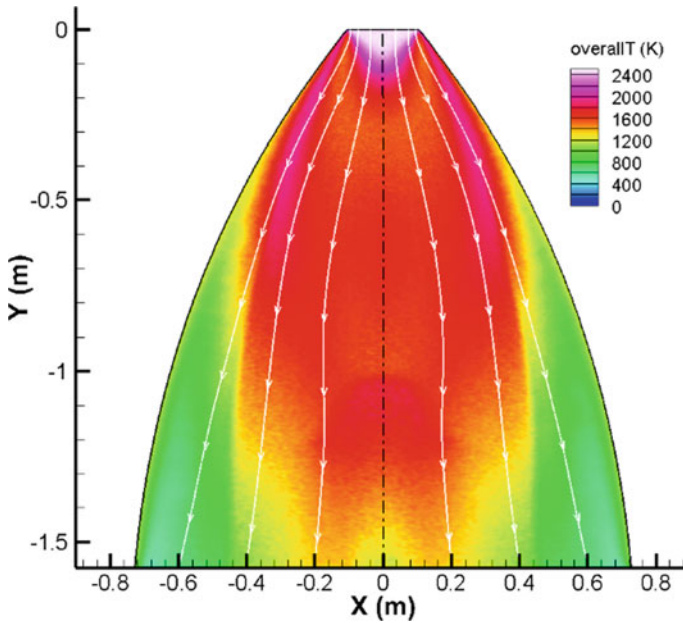
Fig. 8 Temperature contours of plume from nozzle throat to nozzle exit

the viscous boundary layer, the velocity is significantly constant indicating the nozzle is well designed. Hot gases enter the throat of the nozzle at 2500 K and cool down gradually as the gas expands through the nozzle with relatively higher temperatures near the centreline exhaust when compared to the nozzle walls as observed in Fig. 8.

At the throat of the nozzle, the maximum pressure is attained due to an expansion wave; it can be observed in Fig. 9. The pressure decreases steeply across the expansion wave after which it more or less remains constant in the nozzle chamber before expanding into vacuum.

4.3   Rocket Plume Interaction with Lunar Surface Regolith

The impingement of plume gas on the lunar surface is modelled at two different altitudes (i.e. 1.5-*D* and 2-*D* where $D = 1.57$ m).

It is observed from the pressure contours (Figs. 10 and 11) when the plume strikes the surface regolith, a detached bow shock is formed which runs almost parallel to the surface dispersing the flow outwards. The detached bow shockwave becomes thicker and is more prominently visible at lower altitude, i.e. 1.5-*D* as shown in Fig. 11.

The hot exhaust gases from the nozzle expand rapidly into vacuum. These gases impinge onto the lunar surface after interacting through the detached bow shock. Across the bow shock, the temperature of the gases decreases steeply and again
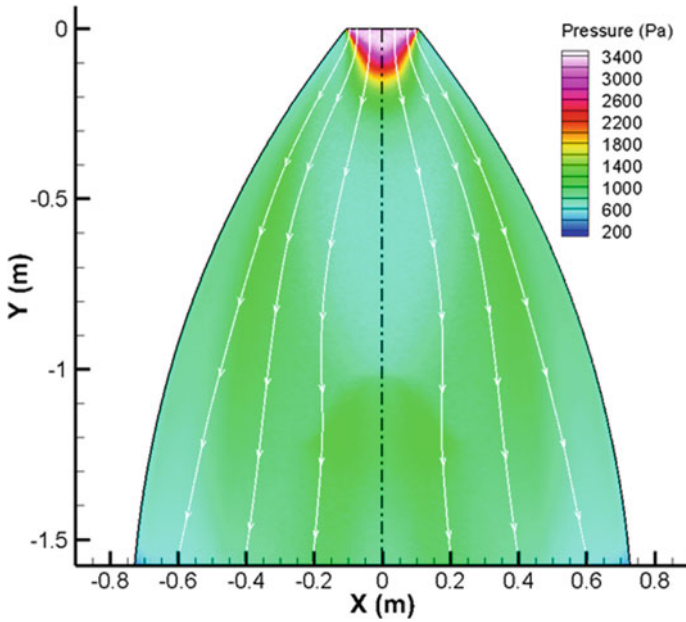
Fig. 9 Pressure contours of plume from nozzle throat to nozzle exit
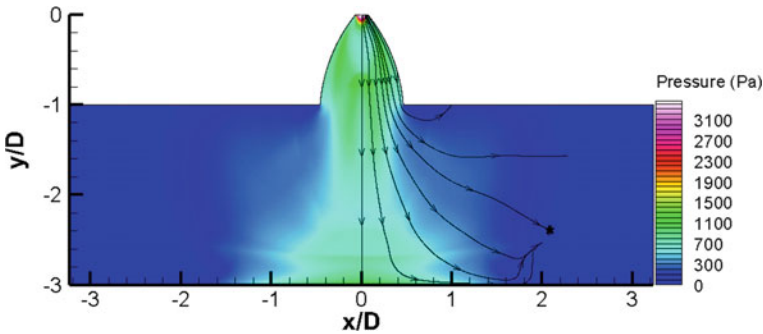
Fig.10 Pressure contour of plume impingement at an altitude of 2-*D*

increases gradually at the impingement surface. Due to the stronger bow shock formation at 1.5-*D*, as shown in Fig. 13, much of the plume gas is turned outwards. It can also be observed that at this altitude, hot gases spread to a greater distance near the surface as compared to plume distribution at 2-*D* (shown in Fig. 12).

The velocity contour visualizes the bow shock prominently and apprehends the flow direction of the exhaust gases expanding into vacuum. The velocity of the flow decreases rapidly across the bow shock running nearly parallel to the surface. A stronger bow shock is formed at 1.5-*D* height that is capable to turn the high velocity
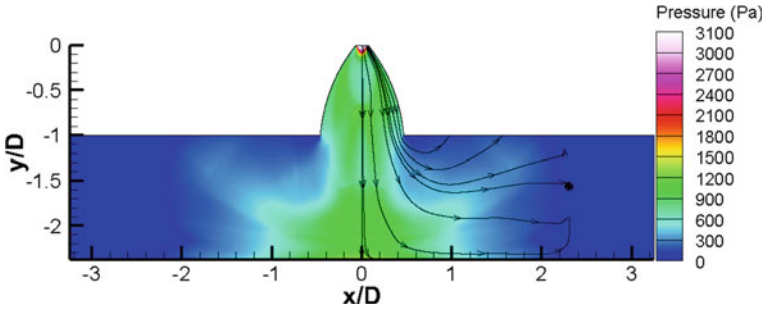
Fig. 11 Pressure contour of plume impingement at an altitude of 1.5-*D*
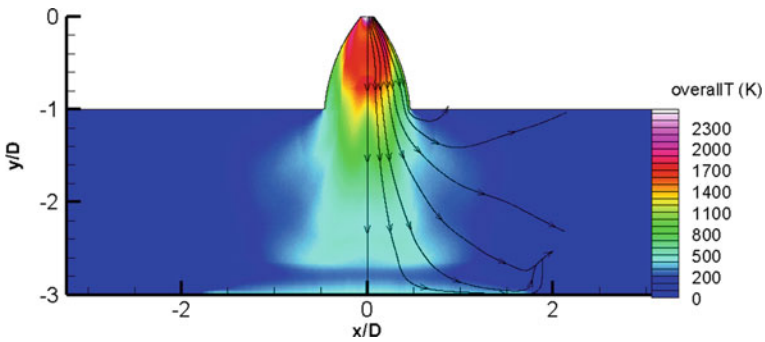
Fig.12 Temperature contour of plume impingement at an altitude of 2-*D*
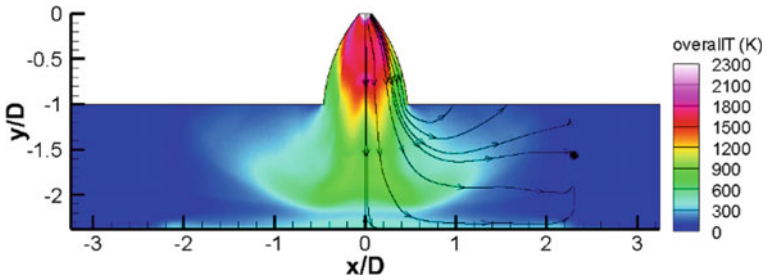
Fig.13 Temperature contour of plume impingement at an altitude of 1.5-*D*

of the exhaust gas cone outwards as shown in Fig. 15. When the exhaust plume impinges on the surface, the momentum of the gas is imparted on the loose surface regolith and the dust is dispersed further away from the normal impingement line. The velocity contour at 2-*D* depicted in Fig. 14 shows a weaker bow shock and reduced dispersion of lunar dust .
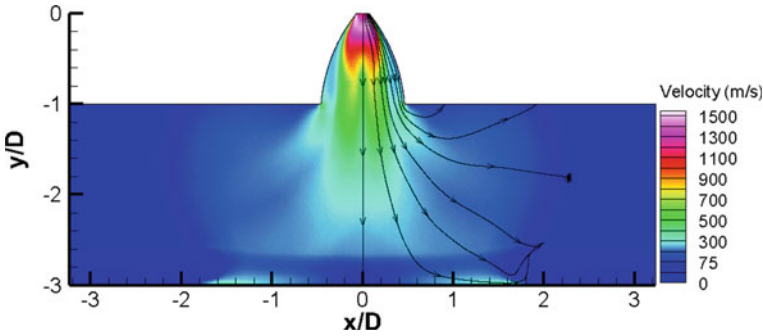
Fig.14 Velocity contour of plume impingement at an altitude of 2-*D*
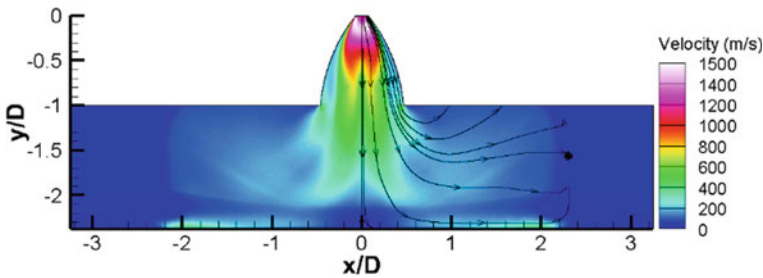
Fig.15 Velocity contour of plume impingement at an altitude of 1.5-*D*

5 Results and Discussion

The LMDE nozzle is a bell-shaped nozzle. Having a large expansion section near the throat, expansion shock waves are generally formed right after the throat. These expansion shock waves further increase the velocity of the gas which is accurately predicted by the solver as shown in Fig. 16. However, the reversal of the slope of nozzle geometry to bring the nozzle exit to near-zero degree causes compression shock waves. These shock waves thus effectively decrease the flow velocity before the gases expand further into vacuum. The flow after exiting the nozzle interacts with detached bow shock, where the velocity decreases before impinging onto the lunar surface.

It can be observed from the graph shown in Fig. 17 that the temperature of the exhaust gases gradually decreases after exiting the nozzle but its trend changes as it encounters the bow shock. When the flow interacts with the detached bow shock, a sudden increment in temperature is observed, which is more outstanding at 1.5-*D*. This is because the number of gas molecules scattered into vacuum before interacting with the bow shock is less when compared to 2-*D* case. This increases the probability of collision between gas molecules, therefore, imparting kinetic energy to each other which in turn affects the temperature. At 2-*D* altitude, the temperature continues to
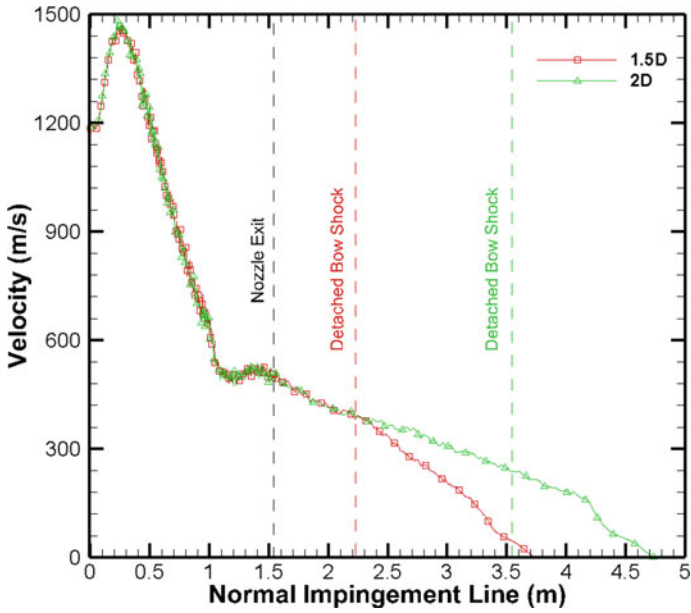
Fig.16 Variation of velocity along the normal impingement line
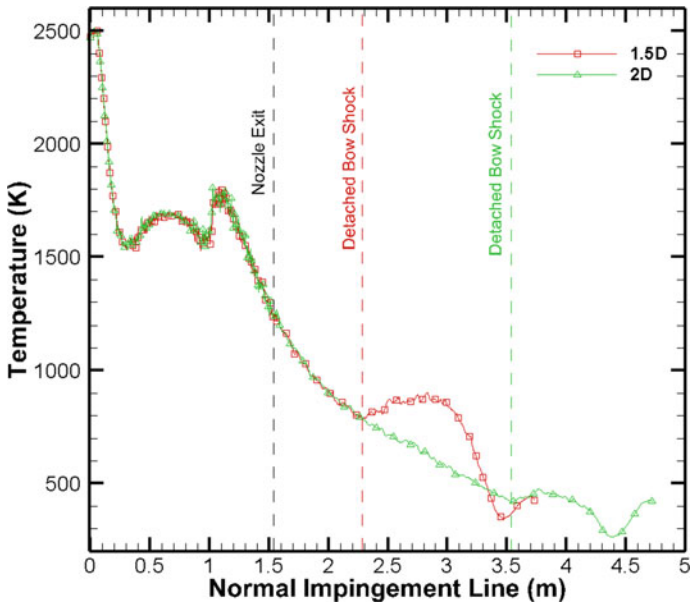
Fig.17 Variation of temperature along the normal impingement line
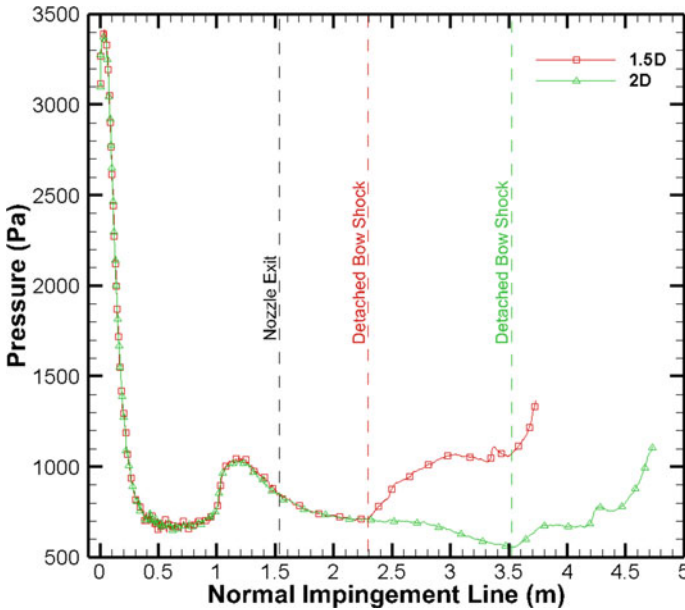
Fig.18 Variation of pressure along the normal impingement line

decrease at a steady rate before interacting with the detached bow shock, after which an increment in temperature is clearly visible.

Figure 18 shows the trend line of pressure variation along the normal impingement line at different altitudes. Due to the bell shape of the nozzle, an expansion wave formed near the throat of the nozzle increases the pressure which has been accurately predicted by the solver. The pressure steeply decreases afterwards before the exhaust gases expand into the vacuum. But, as soon as the flow encounters a bow shock, the pressure increases suddenly. The increase in temperature and pressure along with a decrease in velocity, downstream the shock is in agreement with the typical behaviour of these properties on an encounter with a bow shockwave.

J. K. Mitchell and W. N. Houston found in their study of **"Mechanical properties of Lunar Soil: Density, porosity, cohesion and angle of internal friction"** that the mechanical properties of lunar soil closely align with the mechanical properties of terrestrial soils (like silty fine sand) even though, the two soils are compositionally dissimilar. From the available data, it indicated that the density of lunar soil varied locally along with the depth. It was found that density on the lunar surface is as low as 1 g/cm^3. However, at depths of few centimetres, the density of lunar soil almost doubles [9].

Although the granular interaction between the lunar regolith and rocket exhaust plume is not calculated here, the surface erosion can be predicted by either of the two ways:

Method A: Comparing the surface shear stress to the intermediate cohesive van der Waals forces of the surface regolith.

Method B: Comparing the stagnation pressure with the bearing capacity of the lunar soil to check for mechanical compression on the surface [2].

Since the breakdown of the continuum regime involves the breakdown of the constitutive equations that correlate shear stress, it poses a challenge to determine the shear stress acting along the surface. Usually, the prediction of surface shear stress involves complexity as the parameter itself is modelled from a complex equation namely, the Boltzmann Equation.

Mathematically, predicting the shear strength of the lunar soil presents another challenge. Conventionally, the shear strength of the soil can be predicted by a mathematical model known as Mohr–Coulomb's theory. It can be determined by the following equation:

$$\tau_s = c + \sigma' \tan \theta \tag{3}$$

where

τ_s is the shear stress of lunar soil

c is the soil cohesion

σ' is the normal stress to the failure plane

θ is the internal friction angle.

However, the following observation was made by Carrier, W. D., III, J. K. Mitchell, and A. Mahmood (1973) in their study of **"…the nature of lunar soil"** [10], that the cohesion and internal friction angle was greatly underestimated when compared with previous ground testing of lunar soil. This proves that Mohr–Coulomb' theory underpredicts the shear strength of lunar soil and therefore, is not suitable for application in this case.

Hence, in this work *Method B* was adopted to predict surface erosion.

The bearing capacity of soil is the capability of the soil to withstand external load before undergoing shear failure. In his experimental study of "Bearing Strength of Lunar Soil", L. D. Jaffe measured the bearing strength, experimentally, with a sample of 1.3 g of lunar soil brought from the surveyor 3 soil sample mission. Using a 2 mm diameter circular indenter, lunar soil was penetrated to measure the bearing capacity from a range of bulk densities varying from 1.15 to 1.9 g cm^{-3} [11].

From the experimental data, a graph between bulk density and logarithm of the bearing capacity was plotted using the least square fit method indicating a roughly linear nature as shown in Fig. 19. Therefore, L. D. Jaffe concluded that the bearing capacity of lunar soil varied from 0.02 to 0.04 N cm^{-2} at a bulk density of 1.15 g cm^{-3} to 30–100 N cm^{-2} at 1.9 g cm^{-3}.

From the combination of data from the mechanical properties data of Lunar regolith by (Carrier, 1973), different lunar regolith properties such as bulk density values, are tabulated at different depths in Table 3.

In this work, lunar soil erosion is predicted only at the surface. Hence, from Table 3, bulk density at the lunar surface (up to a depth of 15 cm) is 1.50 g cm^{-3}. Also,
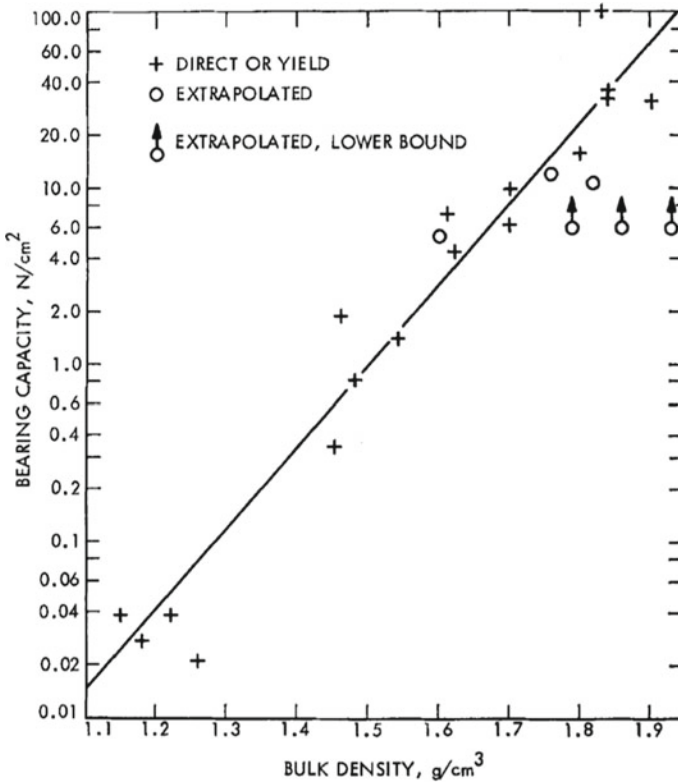
Fig.19 Bearing capacity versus bulk density. The line indicates a least-squares fit. Bearing capacity was taken at a penetration equal to indenter diameter. Adapted from [11]

Table 3 Engineering properties of lunar regolith

Depth range (cm)	Void ratio (±0.07)	Average bulk density (±0.05) (g cm^{-3})	Relative density (±3%)	Average cohesion (kPa)	Average friction angle
0–15	1.07	1.50	63	0.52	42

Adapted from [10]

from the graph plotted between bearing capacity and bulk density of lunar soil by Jaffe [11] in Fig. 19, it can be inferred that the bearing capacity of lunar soil at a bulk density of 1.5 g cm^{-3} is somewhere between 0.9 and 1 N/cm^2.

The stagnation pressure was calculated using dsmcFOAM and a graph is plotted between the calculated stagnation pressure acting along the lunar surface at both altitude, i.e. 1.5-*D* and 2-*D* as shown in Fig. 20. It is compared with the bearing capacity of the soil.
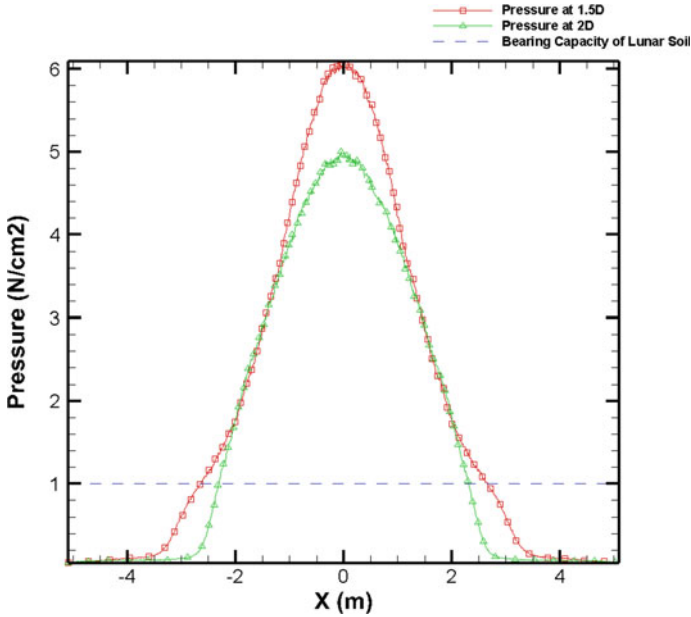
Fig. 20 Variation of pressure (N/cm^2) along the lunar surface

It can be inferred from the graph that the maximum stagnation pressure is acting at the normal impingement line of the rocket exhaust plume where maximum surface erosion can be predicted. However, gradually moving away from the normal impinge-ment line, the stagnation pressure decreases sharply. At approximately 2.6 m away from the normal impingement line, for an altitude of 1.5-*D*, the value of stagnation pressure becomes equal to the bearing capacity and continues to decrease along the surface.

Similarly, for nozzle at an altitude of 2-*D*, the maximum stagnation pressure acts at the nozzle impingement line and declines sharply, becoming equal to the bearing capacity of lunar soil at 2.3 m from the normal impingement line.

Therefore, for nozzle at the altitude of 1.5-*D*, the shear failure of lunar soil effec-tively causing cratering due to rocket exhaust plume is observable up to 2.6 m from the normal impingement line and for nozzle at the altitude of 2-*D*, the cratering would be visible up to 2.3 m from the normal impingement line. The mechanical compression of lunar soil causing cratering would thus lead to a finite amount of lunar surface regolith erosion.

6 Future Scope

This field of work holds tremendous promise and scope for future development. Further studies can explore the following:

- Modelling chemically-reacting gas species as plume exhaust to impinge on lunar and Martian soil.
- Modelling two-phase flow interactions such as:
  - Solid–gas
  - Solid–solid
  - Gas–gas.
- Adding an adsorption/desorption boundary condition on the extra-terrestrial surface can bring the simulation closer to the real cases.

In addition to studying the interaction of plume gas with dust particles in a simulated space environment, attention can be given to analysing different methods to curb this erosion in order to safeguard the lander module, minimize the degree of contamination of the regolith. Construction of in situ landing pads, implementation of a Plume Deflection fence and fabric mat are all innovative ideas that need to be studied, simulated and improvised even further, to ensure safe and smooth landings on any extra-terrestrial body in the future.

References

1. Metzger P, Li X, Immer CD, Lane JE (2009) ISRU implications for lunar and martian plume effects. In: 47th AIAA aerospace sciences meeting, Orlando, Florida
2. White C, Scanlon TJ, Merrifield JA, Kontis K, Langener T, Alves J (2016) Numerical and experimental capabilities for studying rocket plume-regolith interactions. In: 30th International symposium on rarefied gas dynamics AIP Conference. https://doi.org/10.1063/1.4967667
3. White C, Borg MK, Scanlon TJ, Longshaw SM, John B, Emerson DR, Resse JM (2017) dsmcFOAM+: An OpenFOAM based direct simulation Monte Carlo solver. Comput Phys Commun
4. Clegg RN, Jolliff BL, Robinson MS, Hapke BW, Plescia JB (2013) Effects of rocket exhaust on lunar reflectance properties. Icarus 227
5. Prasanth PS, Kakkassery JK (2006) Direct simulation Monte Carlo (DSMC): a numerical method for transition-regime flows–a review. J Indian Inst Sci
6. Lofthouse AJ, Boyd ID, Wright MJ (2007) Effect of continuum breakdown on hypersonic aerothermodynamics. AIP Publishing
7. Morris AB (2012) Simulation of rocket plume impingement and dust dispersal on the lunar surface.; Astronomy Department, The University of Texas at Austin
8. Morris AB, Goldstein DB, Varghese PL, Trafton LM, Modeling the interaction between a rocket plume, scoured regolith and a plume deflection fence. Astronomy Dept, The University of Texas at Austin
9. Mitchell JK, Houston WN, Scott RF, Costes NC, Carrier III WD, Bromwell LG (1972) Mechanical properties of lunar soil: Density, porosity, cohesion and angle of internal friction. In: Proceedings of the third lunar science conference
10. Carrier WD III, Mitchell JK, Mahmood A (1973) The nature of lunar soil. J Soil Mech Found Div. American Society of Civil Engineers
11. Jaffe LD (1971) Bearing strength of lunar soil; earth, moon, and planets. Int J Solar Syst Sci

Shock Tube Performance Studies with Argon and Carbon Dioxide Using Unsteady Numerical Simulation

J. P. Ananthu and N. Asok Kumar

Abstract The aim of this study is to evaluate the performance of the shock tube with argon and carbon dioxide as working fluid using unsteady numerical simulations. A two-dimensional axisymmetric model of a shock tube is taken for the study. Simulations were carried out for different diaphragm ratios to study the dependency on temperature behind the incident shock wave, shock Mach number and temperature behind the reflected shock wave. Time-dependent flow is necessary to understand the properties of gas behind the shock. Effects of viscosity are neglected to reduce the computation times for highly non-uniform processes. For an inviscid flow, Navier–Stokes equation is reduced to the Euler equation. Adaptive mesh refinement (AMR) technique was used to correctly resolve and capture shock waves and contact surface. Different gas combinations of argon and carbon dioxide were taken in driver/driven regions for the simulation. The different driver/driven gas model shows an advantage in shock Mach number of 4.7% at lower diaphragm pressure ratios and significant changes in temperature of shocked gas and temperature behind reflected shocks wave are also.

Keywords Shock tube · Reflected wave · Pressure ratio

Nomenclature

M_s Shock Mach number*
P   Pressure (Pa)
T   Temperature (K)
ρ Density (Kg/m^3)

J. P. Ananthu (✉) · N. A. Kumar
Department of Mechanical Engineering, College of Engineering Trivandrum,
Thiruvananthapuram, Kerala 695015, India
e-mail: ananthujp@cet.ac.in

Superscripts

*   Dimensionless

1   Introduction

Shock tubes are the devices used for creating high energy flows for the ground
testing of supersonic flow fields in which the flow is initiated by a sudden rupture
of the diaphragm separating low-pressure and high-pressure gases. A shock tube
basically consists of a uniform area duct, divided into driver and driven sections
by a metallic diaphragm. Initial driver section is filled with a high-pressure gas
and driven section with a low-pressure gas, respectively. Pressure ratio across the
diaphragm is increased till an abrupt rupture occurs. This will result in a plane
propagating shock wave moving towards the wall in the driven section. Incident
shock wave increases the temperature and pressure of the gases in driven section
when it moves. Rupture of diaphragm also creates an expansion fan, which travels in
the driven section producing a cooling effect for the driver gases. The discontinuities
get reflected by the end walls of the cylindrical structure. Aim of this study is to
analyse various driver–driven gas combinations and identify the gas combinations
for specific purposes (Fig. 1).

Figure shows the shock patterns in a shock tube flow. The section containing
low-pressure test gas is shown in right side of the diaphragm (stage 1) and the
high-pressure driver gas (stage 4) on the left of diaphragm. Rupture of diaphragm
is assumed to be occurred when time is equal to zero, leads to the propagation
of the rapidly steepening compression wave in the driver side. Region behind the
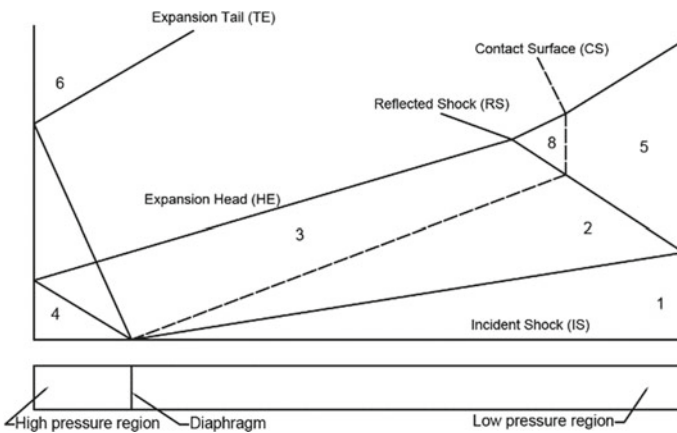
Fig. 1   Ideal shock tube flow

compression wave experiences a sudden rise in pressure and temperature (stage 2). Simultaneously, a gradual fall in temperature and pressure is observed in the driver side when expansion or rarefaction wave travels towards the left wall (stage 3). The interface separating the driver and driven gases is known as contact surface. Contact surface moves in the same direction as that of the incident shock wave, but with a lesser speed. Expansion fan and shock wave get reflected by the end wall. The region behind the reflected shock wave will undergo additional heating (stage 5). Moreover, region behind the reflected shock wave is represented by stage 6.

Most of the previous researchers failed to capture nonlinear physical phenomenon on the flow field of shock tube flow as they assumed one-dimensional flow, in which, unsteady multi-dimensional models produce better results compared to one-dimensional model. Mouna Lamnaouer [1] numerically studied about a shock tube with and without considering viscous effects. Ananthu [2] numerically simulated the propagation and reflection of the shock wave in a shock tube. Argrow [3] used a TVD predictor–corrector scheme with a reflective end wall boundary condition to simulate the growth of the wave field of a Van der Waals gas. Reddy [4] had explained about a micro shock tube capable of producing Mach 2 waves. Luan [5] conducted numerical study about the shock tube with small exit nozzle using order ROE scheme. Al-Falahi [6] conducted a numerical study for the hypersonic test facility, in which, author used a new two-dimensional accurate Euler solver. This solver uses second-order accurate fvd scheme and fourth-order accurate Runge–Kutta integration over time. Mohammed [7] discusses about advection upstream splitting method for shock capturing.

The literature survey gave an idea about the flow field and non-ideal phenomenon in a shock tube. Multi-dimensional models produce better results to modelling nonlinear and unsteady process compared to one-dimensional model.

The aim of this research is to find the relative advantage of using different gases in driver–driven sections over the same gases. This study may help to find the suitable gas combination for various specific applications. Propagation and reflection of shock waves are simulated with an unsteady two-dimensional model. Since viscous effects are not significant in high speed flows, viscosity is neglected. Computational time can be saved with inviscid flows and Navier–Stokes equation reduces into Euler equations. Adaptive mesh refinement technique is used for accurate resolution of incident shock and other associated discontinuities. Geometry is modelled using ICEM CFD and simulated with Ansys FLUENT. The new model is validated against analytical as well as experimental results. Argon–argon, argon–CO_2 and CO_2–CO_2 gas combinations are simulated with this numerical model.

2   Numerical Modelling

2.1   Governing Equations

Since viscosity does not plays a significant role in supersonic regimes, viscous effects
are neglected. Navier–Stokes equation reduces to Euler equations for an inviscid flow.
Avoiding viscous effects will save the computational times also. Euler equation in
Cartesian coordinates is given:

$$\frac{\partial U}{\partial t} + \frac{\partial E}{\partial x} + \frac{\partial F}{\partial y} = 0 \tag{1}$$

where E, F and U vectors are defined as:

$$U = \begin{bmatrix} \rho \\ \rho u \\ \rho v \\ \varepsilon \end{bmatrix}; E = \begin{bmatrix} \rho u \\ \rho u^2 + p \\ \rho u v \\ u(\varepsilon + p) \end{bmatrix}; F = \begin{bmatrix} \rho v \\ \rho u v \\ \rho v^2 + p \\ v(\varepsilon + p) \end{bmatrix} \tag{2}$$

Pressure:

$$p = (\gamma - 1)\left(\varepsilon - \frac{1}{2}\rho\left(u^2 + v^2\right) \right) \tag{3}$$

Specific energy is given by:

$$\varepsilon = \frac{1}{\gamma - 1}\frac{p}{\rho} + \frac{1}{2}\left(u^2 + v^2\right) \tag{4}$$

where the overall fluxes in x and y directions are represented by E and F, and U is
the conserved variable. And u, v and ρ are the velocity per unit mass of the fluid in
x and y directions and density, respectively.

2.2   Flow Domain

Cylindrical shock tube domain is assumed as a rectangle while doing simulation.
Dimensions of the geometry consist of 650 cm in width and 29 cm in height.
Diaphragm is located at 50 cm from the left end of the geometry. Length of the
driver and driven sections is considered as 50 cm and 600 cm, respectively. Same
and different gas combinations of argon and CO_2 are taken in the driver and driven
sections for the simulations. Geometry is modelled in ICEM CFD and simulated
using commercial code Ansys FLUENT. The geometry is shown in Fig. 2.
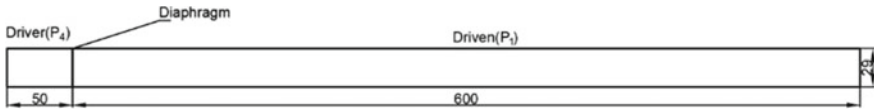
Fig. 2   Flow domain
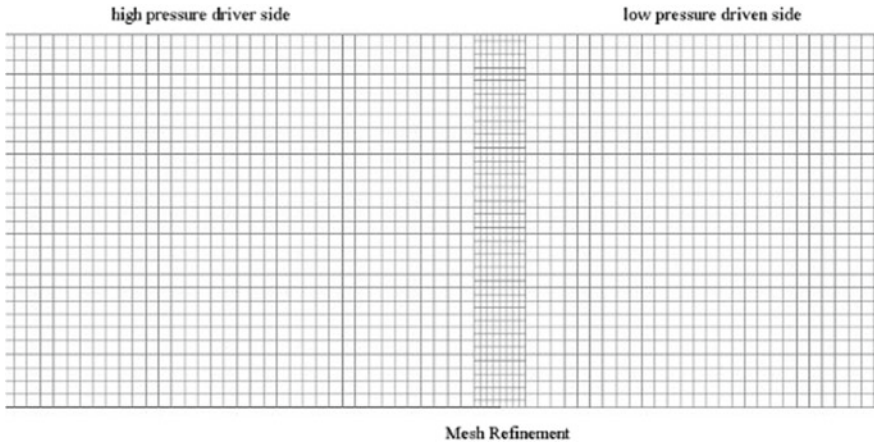
Fig. 3   Initial grid around diaphragm section

2.3   Meshing

A uniform structured grid consists of uniform quadrilateral elements which are considered for the mesh. Adaptive mesh refinement technique is used for better resolution of shock with less computational times. Initial coarse mesh is containing 20,000 elements. AMR refines the regions of steepest density gradient with a greater number of finer sub grids. This ensures a cluster of fine mesh elements around the fast-moving shock wave. More number of mesh elements are added to the mesh when solution proceeds. Initial coarse grid with cluster of fine mesh elements around the diaphragm region is shown in Fig. 3. Shock can be captured accurately with less computational time in AMR.

2.4   Initial and Boundary Conditions

Flow variables at driver and driven sections are defined before starting the simulation. Pressure for the driver section (P_4) is made fixed at 6 atm and on the driven section (P_1), and it is varied from 1 to 0.2 atm. The pressure ratios obtained across the diaphragm will be 6–30. Temperature for both driver and driven sections is assumed as 302 K pressure values considered, and corresponding density values are shown

Table 1 Initial pressure values are corresponding density values for driver and driven sections

P_1 (atm)	Argon		CO_2		Argon–CO_2	
	$\rho_{4 \text{ (kg/m}^3)}$	$\rho_{1 \text{ (kg/m}^3)}$	$\rho_{4 \text{ (kg/m}^3)}$	$\rho_{1 \text{ (kg/m}^3)}$	$\rho_{4 \text{ (kg/m}^3)}$	$\rho_{1 \text{ (kg/m}^3)}$
1	9.69	1.61	10.653	1.775	9.69	1.775
0.8	9.69	1.29	10.653	1.420	9.69	1.420
0.6	9.69	0.97	10.653	1.065	9.69	1.065
0.4	9.69	0.65	10.653	0.710	9.69	0.710
0.3	9.69	0.48	10.653	0.532	9.69	0.532
0.2	9.69	0.32	10.653	0.355	9.69	0.355

in Table 1. Since shock tube domain has two closed ends, left and right boundaries are defined as end walls. This will make the end surfaces to reflect shock wave and prevent mass flow rate in the momentum equation to penetrate through the walls.

3 Validation

The new numerical model is validated against analytical solution of one-dimensional shock theory as well as experimental results. Analytical solution is based on Rankine–Huguenot relations. Experimental studies are conducted over a piston-driven shock tube in high enthalpy testing facility of College of Engineering, Trivandrum. Air is considered as the medium for both driver and driven sections. Incident shock wave Mach number for various diaphragm ratios is plotted for both ideal shock theory solution and two-dimensional inviscid model as shown in Fig. 4. Temperature behind the reflected shock on shock Mach number is compared in Fig. 5. Validation plots show that the inviscid model is in perfect agreement with ideal shock theory as
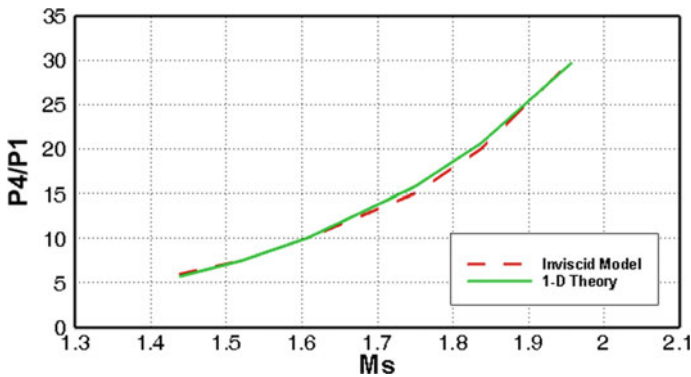
Fig. 4 Shock Mach number (Ms) versus diaphragm pressure ratio
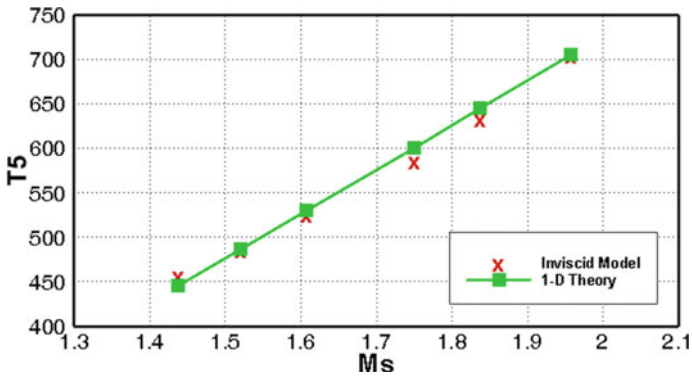
Fig. 5 Incident shock Mach number required to generate temperature behind reflected shock

expected. This model can be used to conduct future simulations with other gases in the flow domain.

4 Result

Parametric study is conducted on the shock tube for DPR from 6 to 30. Three models were considered for simulations. Argon gas is taken in both driven and driven section for the first model. Similarly, CO_2 is taken in second model. In the different gas model, argon in taken in the driver section and CO_2 is taken in the driven section. Parameters considered for the studies are shock Mach number, temperature behind the incident shock and reflected shocks. Dependency of diaphragm pressure ratio on the parameters is studied.

Pressure contours for a different gas model at a diaphragm pressure ratio of 6 are shown in Fig. 6, in which (a) represents the contour before rupture of the diaphragm and (b) represents 110 micro seconds after the rupture of diaphragm. Temperature contours are shown in Fig. 7, where (a) represents the contours after the rupture of diaphragm and (b) represents the contour after the reflection of shock wave.
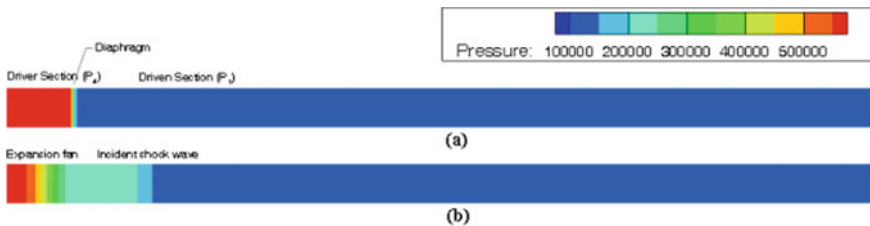
Fig.6 Pressure contours for a DPR of 6 for a different gas model
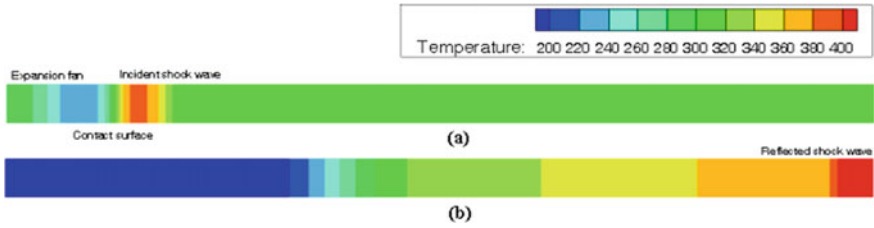
Fig.7 Temperature contours for a DPR of 6 for a different gas model

Dependency of DPR on shock Mach number for all the three models are shown in Fig. 8. Shock Mach number is in direct relation with that of the diaphragm pressure ratio for all models. There is no significant advantage is obtained for any particular model. However, at higher diaphragm pressure ratios, a significant hike of 0.69% is shown by carbon dioxide model. Least values of shock number are obtained for argon same gas model. Shock Mach number for the different gas model is found in between same gas models.

Dependency of temperature behind incident shock wave on DPR is shown in Fig. 9. Temperature behind the incident shock increases for all three models when DPR changes from 6 to 30. Highest values are shown by argon–carbon dioxide different gas models and the least values are shown by carbon dioxide same gas models. Different gas model shows a total hike of 43 K when the pressure ratio changes from 6 to 30. A significant advantage of 62 K is obtained for different gas model compared to carbon dioxide same gas model at higher DPRs.

Dependency of diaphragm pressure ratio on the temperature behind reflected shock for all the three models is shown in Fig. 10. Temperature behind reflected shock wave is in direct relation with that of the diaphragm pressure ratio for all models. There is significant advantage of 80 K is obtained for different gas model
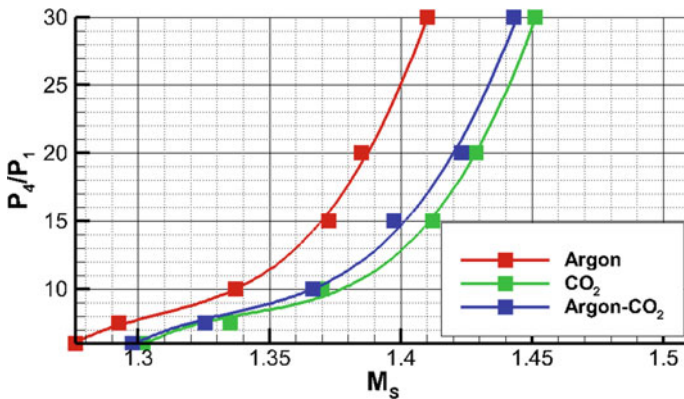
Fig. 8 Diaphragm pressure ratios versus incident shock Mach numbers for argon–argon, CO_2–CO_2 and argon–CO_2 models
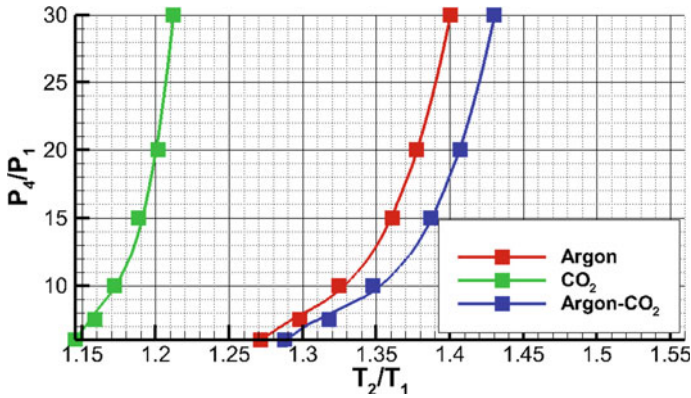
Fig. 9 DPR versus temperature of shocked gas
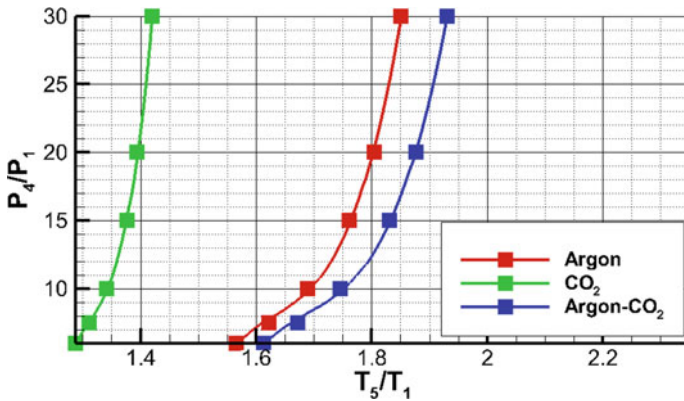
Fig. 10 DPR versus temperature behind reflected gas

at lower diaphragm pressure ratio. Here, the different gas model shows the highest value of temperature behind reflected shock. Total hike in temperature for the argon–carbon dioxide different gas model is 106 K and 86 K and 57 K for argon, carbon dioxide same gas models, respectively. Carbon dioxide shows the least values for the temperature. Argon–carbon dioxide different gas model shows a significant advantage of 80–129 K compared to the same gas models as the pressure ratio changes from 6 to 30.

5   Conclusion

A two-dimensional inviscid sock tube model is developed and validated against analytical and experimental results. The validated model is used to conduct numerical simulations for different combinations of argon and carbon dioxide gas. Dependency of diaphragm pressure ratio on various parameters such as shock Mach number, temperature of shocked gas and reflected shock waves is studied. All parameters considered are found to be directly dependent on the diaphragm pressure ratio. Carbon dioxide same gas model shows an advantage of 4.75 at lower diaphragm pressure ratios and it increases up to 5.7% at higher diaphragm pressure ratios. There is a significant advantage of 80 and 129 K for temperature behind incident, and reflected shock wave is obtained for different gas models.

References

1. Argrow BM (1996) Computational analysis of dense gas shock tube flow. Shock Waves 6:241–248. Springer
2. Lamnaouer M (2004) Numerical modeling of the shock tube flow fields before andduring ignition delay time experiments at practical conditions. Ph.D. Thesis
3. Ananthu JP (2018) Shocktube performance studies with different driver and driven gases. In: Proceedings of the seventh Asian joint workshop on thermophysics and fluid science (AJWTF7), Trivandrum, India
4. Reddy KPJ, Fomin NA (2013) Manually operated piston driven shock tube. Curr Sci 104(2)
5. Chang KS, Kim JK (1995) Numerical investigation of inviscid shock wave dynamics in an expansion tube. Shock Waves 5:33–45
6. Al-Falahi A, Yusoff MZ, Yusaf T (2008) Numerical simulation of inviscid transient flows in shock tube and its validations. Int J Phys Math Sci 2
7. Luan Y, Olzmann M, Magagnato F (2018) Simulation of a shock tube with a small exit nozzle. J Therm Sci 27(1):34–38

Simulation of Continuous Hot Air Multistage Fluidized Bed Dryer for Exergy Analysis Using Aspen Plus Simulator

D. Yogendrasasidhar and Y. Pydi Setty

Abstract Modeling and simulation helps in acquiring successful results of any process. Energy assessment is one of the important studies of process equipment. To intensify the process results multistage design was implemented in continuous medium dryer. In this study, simulations were carried with multistage fluidized bed dryer using Aspen Plus Simulator by changing the values of air temperature from 40 to 80 °C and flow rate of air from 40 to 80 kg/h(Rate of solids flow -10 kg/h and feed moisture percentage -10%). The final moisture content, exergy efficiency and exergy loss of multistage fluidized dryer model were analyzed. From simulation results, the exergy efficiency obtained is in the range 0.07–0.73 for the multistage dryer. Comparison with single stage dryer is reported. The experiments were conducted on multistage fluidized bed dryer to validate the simulation results. The simulation results have shown good agreement with experimental results.

Keywords Multistage fluidized bed dryer · Exergy loss · Exergy efficiency · Aspen plus simulation

Nomenclature

c_p	Specific heat capacitance of air (kJ/kg.K)
m_a	Air flow rate (kg dry air/s)
η_{mEx}	Multistage dryer's energy efficiency
Ex	Rate of exergy (kJ/s)
Ex_{msL}	Multistage dryer's energy loss (kJ/s)
Ex_{msi}	Multistage dryer's energy inflow (kJ/s)
Ex_{mso}	Multistage dryer's energy out flow (kJ/s)
IMC	Initial moisture content of solids (kg water/ kg dry solid)
MFB	Multistage fluidized bed dryer

D. Yogendrasasidhar · Y. P. Setty (✉)
Department of Chemical Engineering, National Institute of Technology Warangal, Warangal 506004, India
e-mail: psetty@nitw.ac.in

S_F Solids flow rate (kg/h)
T   Air temperature (°C)
T_{in} Temperature of the inlet air (°C)
T_∞ Ambient temperature (°C)
T_o Temperature of the air leaving the outlet (°C)

Subscripts

1   Stage one
2   Stage two
3   Stage three
4   Stage four
a   Air
Ex   Exergy
F   Flow rate
i   Inlet
ms   Multistage fluidized bed
o   Outlet

1   Introduction

The fluidized bed dryers are frequently used in several industries for removing particulate moisture. Fluidized bed dryers (FBD) are adapted in various industries like pharmaceutical, agriculture, chemical, food, ceramic and polymer, for drying of granular and particulate solids. With the presence of better gas to solid contact ratio, high heat and mass transfer rates are achieved in fluidized bed dryers compared to other conventional types of dryers. Particle-particle interactions and wall-particle interactions inside the bed help in maintaining the temperature and moisture distribution uniformly. In general, fluidized bed dryers are designed to send the hot gas stream at the bottom of the column through a distributor plate toward the drying zone.

Various modifications were implemented to batch fluidized bed dryer like vibratory, agitation, ultra-sound, microwave and solar, etc., to improve the product quality with lower energy utilities [1–5]. The continuous dryers are handled continuous with inlet feeds to process large quantity of product. Multistage effect is another approach for improving product quality in continuous medium to reduce the drying time. It enhances the heat transfer between particles and gas in fluidized beds. Gomez-garcia et al. (2017) have developed an analytical model of a multistage fluidized bed heat exchanger for particle-based solar power plants and reported parametric analysis for heat exchanger [6]. Hasatani et al. (1985) have investigated on multistage inclined

fluidized dryer with experimentation and developed a mathematical model [7]. Srini-vasakannan and Balasubramanian (1998) examined the drying behavior of ragi and poppy seeds using internally staged multistage fluidized bed dryer [8]. Choi et al. (2002) conducted studies on continuous multistage fluidized bed dryer staged internally, reported drying characteristics of millet and developed mathematical model [9].

Energy is an important parameter of study for any process equipment and thermodynamic approach can be used to analyze the energy assessment of any process. The second law of thermodynamics makes it easier to determine the maximum amount of work that can be done in a given system using various energy sources. Exergy is the amount of energy available for conversion from a source of energy with a reference environmental condition.[10]. Various investigators conducted exergy and energy studies in modified dryers and analyzed the performance of dryers. Yahya et al. (2017) have examined the exergy and energy performance of solar assisted fluidized bed drying system using biomass as bed material [11]. Azadbakht et al. (2017) have investigated on energy and exergy examination of bed of cubical potato feed in batch fluidized bed dryer [12]. Darvishi et al. (2018) have analyzed exergetic performance of mushrooms in fluidized bed dryer with effect of air flow ratio [13]. Ergun et al. (2017) have conducted the exergy and energy study on solar assisted fluidized bed dryer using various plant species as bed material [14]. Yahya et al. (2018) have implemented exergetic performances and economic analysis using heat pump fluidized bed dryer with solar assistance in rice drying [15]. Motevali and Amiri chayjan (2017) have conducted exergy analysis with different drying beds, i.e., Fixed bed, Semi fluidized bed and Fluidized beds in dryers [16].

In general, the successful design for any research equipment takes more process time and cost. Before designing any process equipment, work on modeling and simulation process helps in achieving better design. Various simulators which are based on the computer aided design are available for simulating the process.

Modeling is defined as the process of translating physical laws to mathematical equations used to design or analyze the process. Simulator is computer software which consists of mathematical models and graphic interface for predicting the performance of system or process. To analyze the economic production, product quality and energy quality, designing is a technique for rating and sizing a process [17]. Drying characteristics of particles in dryers are time-variant, the phenomenon is dynamic and nonlinear. Modeling the drying process is critical for simulating and optimizing the process, as well as controlling moisture levels.

Presently, modeling and simulation studies have increased in drying fields with different modified designs and various bed materials. Various researchers have investigated on modeling of drying process and conducted simulation studies using different mathematical equations and modeling and simulation software (like MATLAB, ANSYS, ASPEN, DryDSim, etc.). Badaoui et al. (2019) have developed new drying models using tomato pomace waste drying in a new solar greenhouse [18]. Khanli et al. (2018) have worked on mathematical modeling for plug flow fluidized bed dryer and analyzed the change of different parameters on drying for shelled corn [19]. Tarigan (2018) has conducted studies on mathematical and CFD modeling on

solar agriculture dryer and temperature distribution in drying chamber [20]. Azmir et al. (2018) have developed CFD-DEM model of food particles in fluidized bed dryer and analyzed moisture profiles and temperature profiles [21]. Malekjani et al. (2018) have reported the review on recent approaches for food drying by computation fluid dynamics (CFD) [22]. Neba and Nono (2017) have developed novel solar-biomass hybrid dryer model using dryer design software (DryDSim) [23]. Stange et al. (2018) have conducted studies on hot air chamber design in continuous flow grain dryer using CFD and studied the flow distribution, temperature distribution of dryer [24]. Norbert et al. (2018) have performed simulation and experimental investigation on four stage spray dryer and reported humidity and temperature profiles [25].

Very few studies were observed in literature on simulation of exergy for dryers. Aghbashlo et al. (2016) have conducted theoretical approach to analyze the exergy using heat and mass transfer model for combined infrared-convective drying process [26]. Ranjbaran and Zare (2013) have studied the energetic and exergetic performance of drying soybeans in microwave-assisted fluidized bed. Mathematical modeling and simulation was executed in the study [27]. Lucatero et al. (2015) have conducted investigations on exergetic and energetic performance of solar dryer using COMSOL [28]. The process simulator is software that allows modeling and simulation for different processes. Process simulator suits better, for studying the performance of any industrial process. Dogbe et al. (2018) have investigated the exergetic performance of a typical sugar mill using Aspen Plus simulator and the exergy analysis of dryer was studied [29]. Based on literature survey, no work has been reported on simulation studies of multistage fluidized bed dryer using Aspen Plus simulator. In this study, simulations of multistage fluidized bed dryer are executed and exergy performance is analyzed using Aspen Plus simulator. Simulations results were validated with experimental results.

2 Materials and Methods

2.1 Simulation Model

A model for continuous multistage fluidized bed dryer is designed using Aspen Plus simulator (Aspen Corp V 8.4). The model consists of four stages of fluidized bed dryers (Fig. 1). Simulations have been carried out in step wise process, (i) the components were specified as water, air and sand (silica) from Aspen database (ii) the dimensions of continuous multistage fluidized bed dryer model were given with, height as 0.4 m and area as 0.0078 m^2 for each stage. Here in this study, solids and air were used as two major streams. Size of particles was given as 0.6 mm in particle size distribution section. The solid and water were given in mixed inlet stream to obtain the moisture content of solids. The simulation was carried out with 100 iterations for each run with minimum error of 0.0001. Simulations were executed with changing condition of air flow rates, air temperatures, solids flow rates and initial moisture

SOIN → : Solids inlet stream, AIRIN → : Air inlet stream, SOLOU → : Solids outlet stream
AIROUT → : Air outlet stream
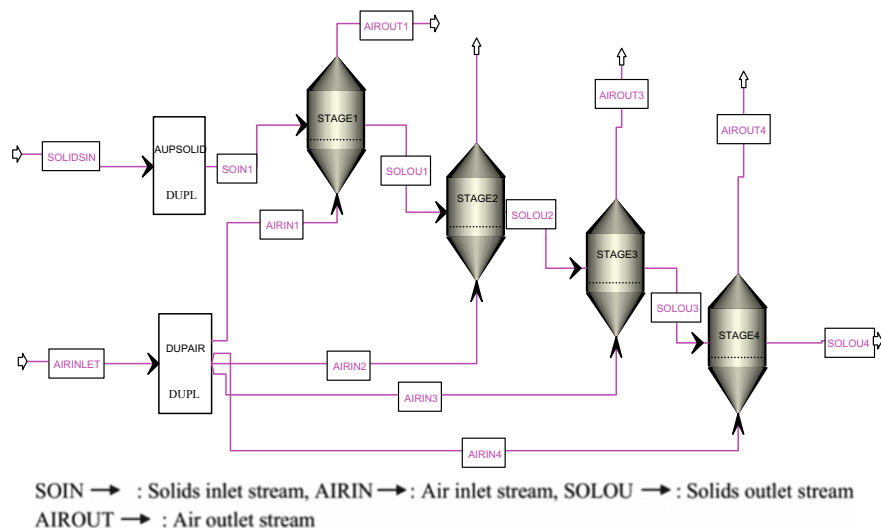
Fig.1 Multistage fluidized bed dryer model in Aspen Plus

Table 1 Simulation model specifications for multistage fluidized bed dryer model

Parameter	Range
Inlet temperature	40–80 °C
Inlet air flow rate	40–80 kg/h
Inlet moisture percentage	10%
Solid flow rate	10 kg/h
Diameter of particle	0.6 mm

contents. Inlet parameters were varied using sensitivity analysis and outputs of the dryers were examined. The simulation of multistage fluidized bed drying is done for steady state operation and the values of moisture content of solids obtained indicate the moisture content at equilibrium. Hence, the output of the simulation of the continuous dryer are solids outlet moisture content (the final moisture content of solids), solids temperature, exergy efficiency and exergy loss. The input parameters were specified in Table 1.

2.2 Experimental Studies

In experimental approach, continuous multistage fluidized dryer (Fig. 2) consists of four stages with 0.4 m height and 0.1 m diameter for each column. The distributor plates having 40% opening area with 2 mm orifice size were used in each stage. The air temperature was maintained through temperature controllers and air heater.

(1. Vibratory solids feeder, 2. Inlet hopper for solids, 3. Humidity and temperature sensors at air outlet, 4. Data scanner (for air), 5. Solids outlet temperature, 6. Data logger (for solids), 7. Air compressor, 8. By pass valve, 9. Air heater, 10. Humidity and temperature sensor at air inlet, 11. Rotameter and 12. Solids outlet)
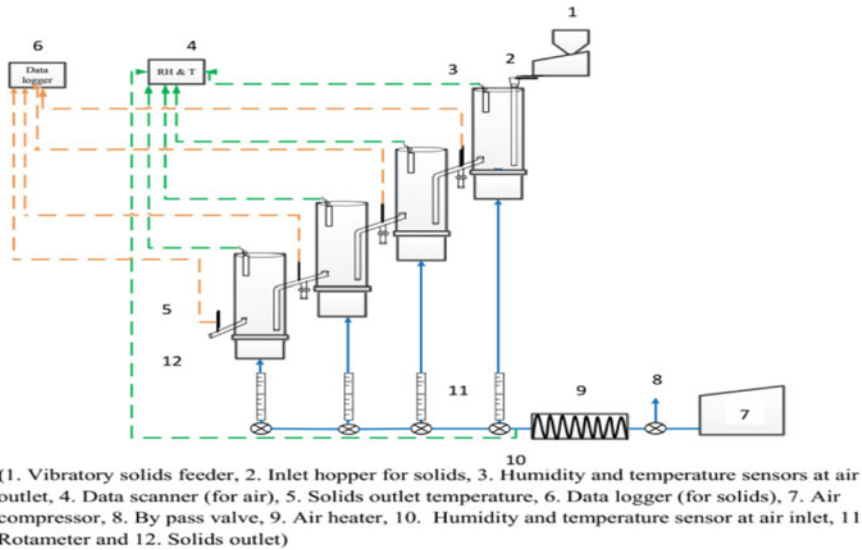
Fig. 2 Continuous hot air multistage fluidized bed dryer setup

The hot air was passed through rotameter and flow rate was maintained by operating bypass valve. Air leakages and temperature losses are avoided by using gaskets and glass wool sealing. Temperature and humidity sensors are placed at inlet and outlets of each stage and data was recorded using USB interface data scanner (8 Channel universal scanner logger-CT708U). Solids outlet temperatures were measured using temperature sensors and data logger. In the present study, sand particles were used as bed solids having density of 2600 kg/m³ with 0.6 mm uniform particle size. The solids were discharged through solid hopper into stage 1 and then passed through remaining stages. Experimentation was done to determine the moisture, temperature profiles, exergy loss and exergy efficiency of continuous multistage fluidized bed dryer by changing the operating conditions.

2.3 Exergy Analysis

According to the thermodynamics second law, the exergy can explain the quantity and quality of energy flow of system [30, 31]. At steady state flow condition, the exergy equation general form can be in the following form as given by Eq. 1.

$$\text{Exergy} = \text{Internal energy} - \text{entropy} + \text{gravity} + \text{work} + \text{chemical energy} \tag{1}$$

Or it can be represented as Eq. 2.

$$\text{Exergy} = (u - u_\infty) - T_\infty.(s - s_\infty) + (\text{Po}/J).(v - v_\infty) + (V^2/2gJ)$$
$$+ (z - z_\infty).(g/g_c J) + \sum (\mu_c - \mu_\infty).N_c \tag{2}$$

The momentum and gravitational terms are neglected in addition to the pressure change, i.e., $v = v_\infty$. The chemical exergy is neglected because there is no chemical reaction in the present drying process [32]. After simplification, the equation takes the following form (Eq. 3) and specific heat capacity of air calculated is from Nazghelichi et al. [33].

$$\text{Ex} = m_a c_{\text{pa}}[(T - T_\infty) - T_\infty \ln(T/T_\infty)] \tag{3}$$

The exergy inlet of stage1 can be calculated using Eq. 4.

$$\text{Ex}_{i1} = m_a c_{\text{pa}}[(T_{i1} - T_\infty) - T_\infty \ln(T_{i1}/T_\infty)] \tag{4}$$

Similarly, the exergy inlets of remaining stage Ex_{i2}, Ex_{i3}, Ex_{i4} were calculated. The exergy outlet of stage1 can be calculated using Eq. 5.

$$\text{Ex}_{o1} = m_a c_{\text{pa}}[(T_{o1} - T_\infty) - T_\infty \ln(T_{o1}/T_\infty)] \tag{5}$$

Similarly, the exergy outlets of remaining stage Ex_{o2}, Ex_{o3}, Ex_{o4} were calculated. The exergy inflow and outflow for a multistage fluidized bed dryer can be written as follows: Eqs. 6 and 7.

$$\text{Ex}_{\text{msi}} = \text{Ex}_{i1} + \text{Ex}_{i2} + \text{Ex}_{i3} + \text{Ex}_{i4} \tag{6}$$

$$\text{Ex}_{\text{mso}} = \text{Ex}_{o1} + \text{Ex}_{o2} + \text{Ex}_{o3} + \text{Ex}_{o4} \tag{7}$$

From the Eq. 8, Exergy loss for multistage fluidized bed dryer was obtained.

$$\text{Ex}_{\text{msL}} = Ex_{msi} - Ex_{mso} \tag{8}$$

Exergy efficiency can be determined using the Eq. 9 for multistage fluidized bed dryer.

$$\eta_{m\text{Ex}} = (\text{Ex}_{\text{msi}} - \text{Ex}_{\text{msL}})/\text{Ex}_{\text{msi}} \tag{9}$$

Fig. 3 Solids outlet moisture with change of inlet air temperatures
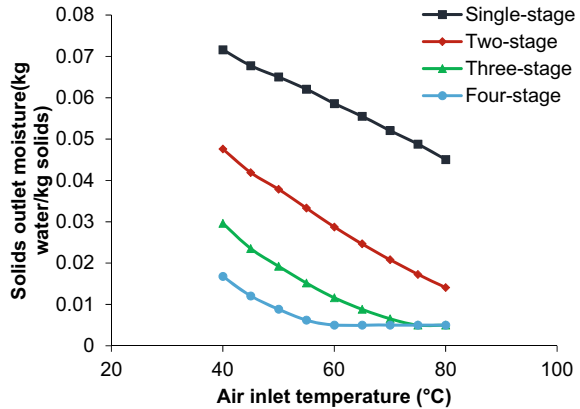
3 Results and Discussion

3.1 Influence of Air Temperature on Solids Outlet Moisture

Simulations were conducted using continuous multistage fluidized bed model by varying air temperature ranging from 40 to 80 °C with an increment of 5 °C at constant flow rate of air as 50 kg/h, and flow rate of solids as 10 kg/h with initial moisture content of material as 10%. It can be observed from the Fig. 3 that the solids outlet moisture content showed decreasing trend while increasing air inlet temperature and it can be observed that by increase in stages of the dryer, the solids outlet moisture content is decreasing. In stage 3, it can be observed that 0.5% (i.e., 0.005) solid moisture content is reached at 70 °C and further increment in air temperature does not show any affect. Similarly at stage 4, the solids outlet moisture of 0.5% was observed at 60 °C. The increase in stages in dryer helps to reach equilibrium moisture content quickly at lower temperatures. Figure 4 reveals that as the air inlet temperature rises, so does the solids outlet temperature, which rises with the number of stages in dryer.

3.2 Exergy Efficiency and Exergy Losses for MFB with Air Temperature

Simulation studies were conducted to examine the air temperature influence on exergy loss and efficiency of continuous multistage fluidized bed model by varying air temperature from 40 to 80°C with an increment of 5 °C at constant flow rate of air as 50 kg/h and solids flow rate as 10 kg/h with initial moisture content of the material as 10%. The exergy loss has risen with an increase in air temperature in multistage fluidized dryer, as can be seen in Fig. 5. The increasing air inlet temperature increases the exergy loss of multistage dryer because the higher air temperatures

Fig. 4 Solids outlet temperature with change of inlet air temperatures
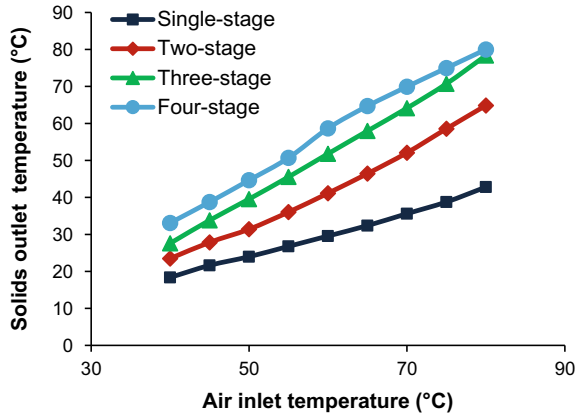
Fig. 5 Exergy loss and exergy efficiency with change of air inlet temperatures
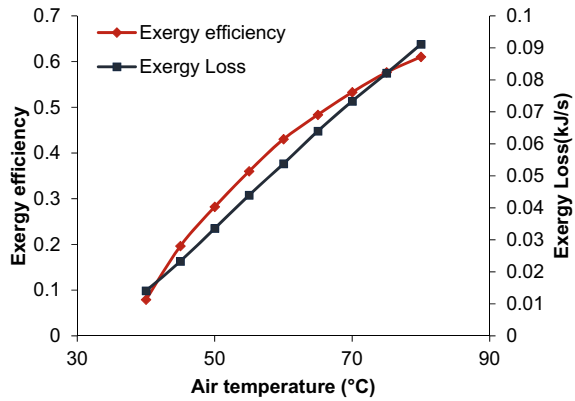
results in higher exergy inflow and exergy utilization also increases for the evaporation of solids moisture in multistage dryer. It can be perceived from Fig. 5 that the exergy efficiency showed increment while increasing air inlet temperature of multistage fluidized dryers.

3.3 Exergy Losses and Exergy Efficiency for MFB with Air Flow Rate

Simulations studies were conducted to investigate the impact of air flow rate on exergy loss in a continuous multistage fluidized bed model by varying mass flow rate of air from 40 to 80 kg/h with an increment of 10 kg/h and keeping air temperature as 50°C, feed moisture at 10% and using solids flow rate of 10 kg/h. Figure 6 shows that as the mass flow rate of air in a multistage fluidized bed dryer increases, the exergy

Fig. 6 Exergy loss and
exergy efficiency
with change of air inlet flow
rates
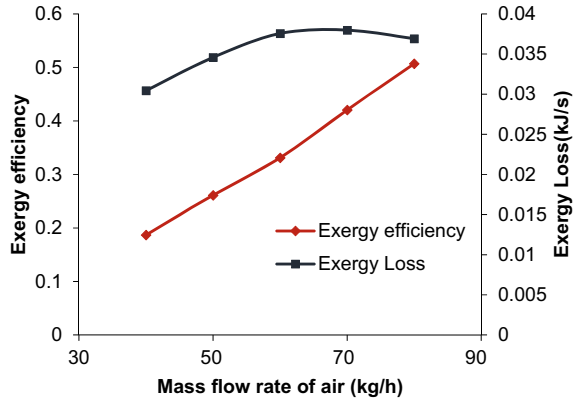
loss increases. Also can be seen in Fig. 6, the exergy efficiency of a multistage
fluidized bed dryer increased as the mass flow rate of air increased.

3.4 Comparison with Single Stage Fluidized Bed Dryer

Simulations were carried out with single stage fluidized bed dryer for comparison
with multistage dryer varying air flow rate from 40 to 80 kg/h with an increment
of 10 kg/h and keeping air temperature as 80 °C, feed moisture at 10% and using
solids flow rate of 10 kg/h. From Fig. 7, it can be observed that the exergy losses
are high in multistage dryer than single stage dryer. From the results, In comparison
to a single stage fluidized bed dryer, the exergy loss of a multistage dryer does not
vary significantly as the air flow rate increases. From Fig. 8, it can be noticed that
the exergy efficiency of multistage dryer is higher than single stage.

Fig. 7 Comparison of MFB
exergy loss profiles with
single stage at different air
flow rates
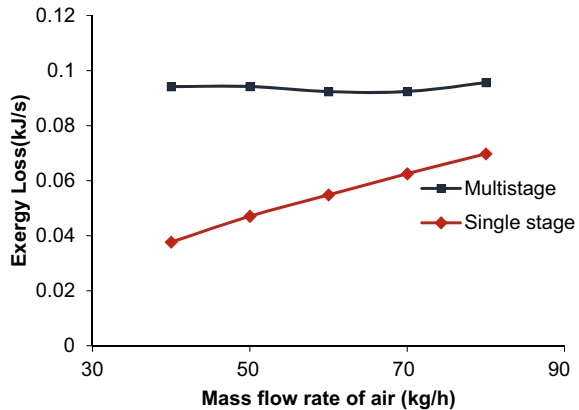
Fig. 8 Comparison of MFB exergy efficiency profiles with single stage at different air flow rates
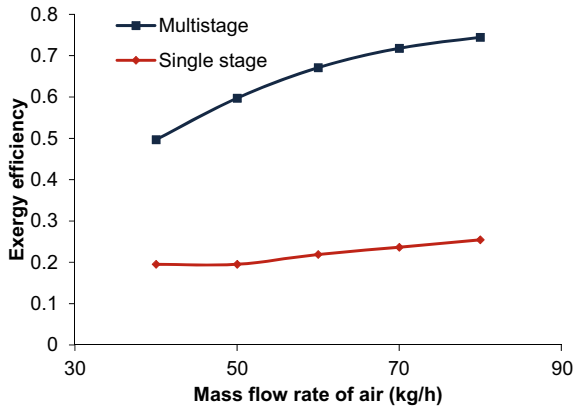
3.5 Comparison with Experimental Results

Experiments were conducted in continuous multistage fluidized bed dryer by changing air temperature from 40 to 80 °C. The experimental results (Fig. 9) represent, drying characteristics of solids in multistage fluidized bed dryers. From Fig. 9, the drying rate of solids is increased with increasing air temperature and the equilibrium moisture content of solids decreased with increasing air temperature. The experimental results have shown similar trend with simulation results. Figure 10 shows variation of equilibrium moisture content of solids with air temperature which shows similar trends for both simulation and experimental studies. In the experimental study it is noticed that the influence of air temperature at higher values of temperature (60 to 80 °C) on moisture content is less compared to that at lower temperatures (40 to 60 °C). Similar trend is noticed in the simulation study also, where it is found that increase in air temperature at higher temperatures (60 to 80 °C) does not alter the moisture content. From Figs. 11 and 12, it can be noticed that the exergy loss and exergy efficiency profiles show similar trends with simulation results.

Fig. 9 Drying characteristics of solids in MFB dryer
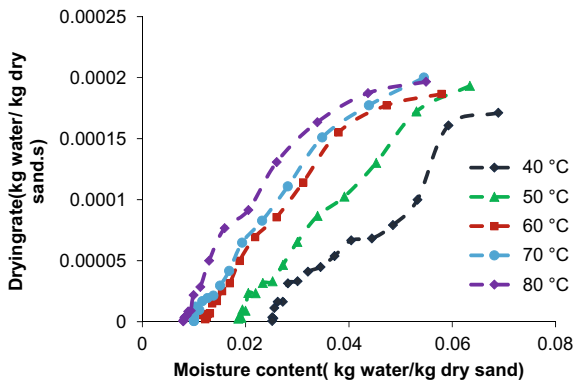
Fig. 10 Comparison of
MFB with experimental
solids outlet moisture
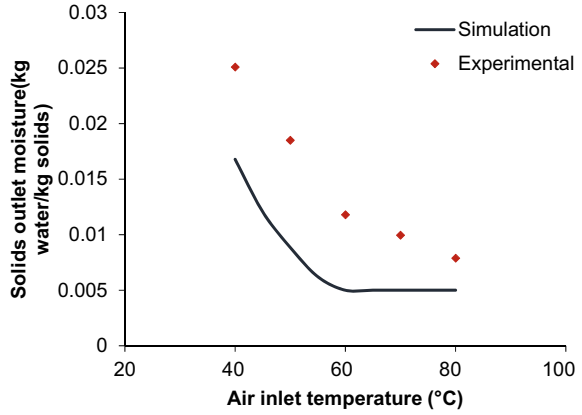
Fig. 11 Comparison of
MFB with experimental
exergy loss
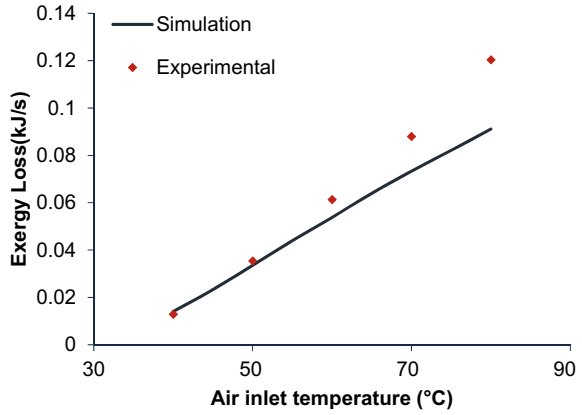
Fig. 12 Comparison of
MFB with experimental
exergy efficiency
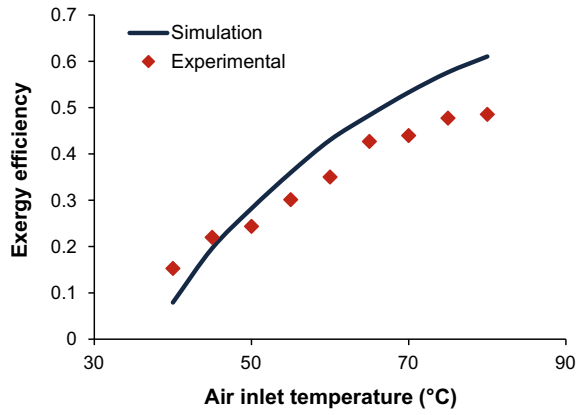
4 Conclusions

The simulation results of multistage fluidized bed dryer using Aspen Plus simulator were reported. From simulation study the following findings were noticed:

1. Final moisture content of solids showed decrement while increasing stages in multistage dryer.
2. As compared to single stage fluidized bed dryers with lower air inlet temperatures and air flow rates, multistage fluidized bed dryers had lower moisture content of solids.
3. Final moisture content of solids showed decrement while increase in air inlet temperature and flow rate of air in multistage fluidized bed dryer.
4. Exergy loss of multistage fluidized bed dryer showed increment while increasing temperature of air inlet and flow rate of air.
5. Exergy efficiency of multistage fluidized bed dryer showed increment while increasing temperature of air inlet and flow rate of air.
6. The lowest exergy loss has been found to be 0.014 kJ/s at air inlet temperature of 40 °C (air flow rate-50 kg/h, solids flow rate 10 kg/h and IMC-10%) of multistage fluidized dryer, whereas highest exergy loss has been found to be 0.096 kJ/s (air inlet temperature- 80 °C, air flow rate-80 kg/h, solids flow rate 10 kg/h and IMC-10%) of multistage fluidized dryer.
7. The lowest exergy efficiency has been found 0.07 at air inlet temperature of 40 °C (air flow rate-50 kg/h, flow rate of solids 10 kg/h and IMC-10%) of multistage fluidized dryer. The higher exergy efficiency has been found 0.73 (air inlet temperature- 80 °C, air flow rate-80 kg/h, solids flow rate 10 kg/h and IMC-10%) of multistage fluidized dryer.
8. The exergy loss and exergy efficiency of multistage fluidized dryer are higher than single stage fluidized dryer.
9. The simulation results have shown similar trends with experimental results of multistage fluidized bed dryer.

References

1. Zhao P, Zhong L, Zhu R, Zhao Y, Luo Z, Yang X (2016) Drying characteristics and kinetics of Shengli lignite using different drying methods. Energy Convers Manage 120:330–337
2. Moreno RM, Antolin G, Reyes AE (2016) Heat transfer during forest biomass particles drying in an agitated fluidised bed. Biosystem Eng 151:65–71
3. Jafari A, Zare D (2017) Ultrasound-assisted fluidized bed drying of paddy: energy consumption and rice quality aspects. Drying Technol 35:893–902

4. Tahmasebi A, Yu J, Han Y (2014) A kinetic study of microwave and fluidized-bed drying of a chinese lignite. Chem Eng Res Des 92:54–65

5. Hu X, Kurian J, Gariepy Y, Raghavan V (2017) Optimization of microwave-assisted fluidized-bed drying of carrot slices. Drying Technol 35:1234–1248

6. Gomez-garcia F, Gauthier D, Flamant G (2017) Design and performance of a multistage fluidised bed heat exchanger for particle-receiver solar power plants with storage. Appl Energy 190:510–523

7. Hasatani M, Arai N, Hori K (1985) Drying of granular particles in a multistage inclined fluidized bed with mechanical vibration. Drying Technol 3:39–62

8. Srinivasakannan C, Bala subramanian N (1998) Some drying aspects of multistage fluidized beds. Chem Eng Technol 21:961–966

9. Choi KB, Park SI, Park YS, Sung SW, Lee DH (2002) Drying characteristics of millet in a continuous multistage fluidized bed. Korean J Chem Eng 19:1106–1111

10. Nazghelichi T, Aghbashlo M, Kianmehr MH, Omid M (2011) Prediction of energy and exergy of carrot cubes in a fluidized bed dryer by artificial neural networks. Drying Technol 29:295–307

11. Yahya M, Fudholi A, Sopian K (2017) Energy and exergy analyses of solar-assisted fluidized bed drying integrated with biomass furnace. Renew Energy 105:22–29

12. Azadbakht M, Aghili H, Ziaratban A, Torshizi MV (2017) Application of artificial neural network method to exergy and energy analyses of fluidized bed dryer for potato cubes. Energy 120:947–958

13. Darvishi H, Azadbakht M, Noralahi B (2018) Experimental performance of mushroom fluidized-bed drying: Effect of osmotic pretreatment and air recirculation. Renew Energy 120:201–208

14. Ergün A, Ceylan İ, Acar B, Erkaymaz H (2017) Energy–exergy–ANN analyses of solar-assisted fluidized bed dryer. Drying Technol 35:1711–1720

15. Yahya M, Fahmi H, Fudholi A, Sopian K (2018) Performance and economic analyses on solar-assisted heat pump fluidised bed dryer integrated with biomass furnace for rice drying. Sol Energy 174:1058–1067

16. Motevali A, Amiri CR (2017) Effect of various drying bed on thermodynamic characteristics. Case Stud Therm Eng 10:399–406

17. Mujumdar AS (2014) Handbook of industrial drying. Marcel Dekker, New York

18. Badaoui O, Hanini S, Djebli A, Brahim H, Benhamou A (2019) Experimental and modeling study of tomato pomace waste drying in a new solar greenhouse: evaluation of new drying. Renew Energy 133:144–155

19. Khanali M, Giglou AK, Ra S (2018) Model development for shelled corn drying in a plug flow fluidized bed dryer. Eng Agric Environ Food 11:1–8

20. Tarigan E (2018) Mathematical modeling and simulation of a solar agricultural dryer with back-up biomass burner and thermal storage. Case Stud Therm Eng 12:149–165

21. Azmir J, Hou Q, Yu A (2018) Discrete particle simulation of food grain drying in a fluidised bed. Powder Technol 323:238–249

22. Malekjani N, Jafari SM (2018) Simulation of food drying processes by Computational Fluid Dynamics (CFD); recent advances and approaches. Trends Food Sci Technol 78:206–223

23. Neba FA, Nono YJ (2017) Modeling and simulated design: a novel hybrid dryer and dryer design software. Comput Chem Eng 104:128–140

24. Strange L, Poulsen M, Sørensen K, Condra T (2018) Modelling of hot air chamber designs of a continuous flow grain dryer. Eng Sci Technol Int J 21:1047–1055

25. Norbert L, Kjølstad N, Henrik H, Utzen C, Bagterp J (2017) An experimentally validated simulation model for a four-stage spray dryer. J Process Control 57:50–65

26. Aghbashlo M (2016) Exergetic simulation of a combined infrared-convective drying process. Heat Mass Transf 52:829–844

27. Ranjbaran M, Zare D (2013) Simulation of energetic- and exergetic performance of microwave-assisted fluidized bed drying of soybeans. Energy 59:484–493

28. Lucatero H, Ruiz E, Mayorga M (2015) Solar dryer exergetic and energetic efficiency analysis. In: Proceedings of COMSOL conference Boston

29. Dogbe ES, Mandegari MA, Gorgens JF (2018) Exergetic diagnosis and performance analysis of a typical sugar mill based on Aspen Plus simulation of the process. Energy 145:614–625
30. Karthikeyan AK, Murugavelh S (2018) Thin layer drying kinetics and exergy analysis of turmeric (Curcuma longa) in a mixed mode forced convection solar tunnel dryer. Renew Energy 128:305–312
31. Sarker MSH, Ibrahim MN, Abdul Aziz N, Punan MS (2015) Energy and exergy analysis of industrial fluidized bed drying of paddy. Energy 84:131–138
32. Dincer I, Zamfirescu C (2016) Drying phenomena—theory and applications. Wiley, United Kingdom
33. Nazghelichi T, Kianmehr MH, Aghbashlo M (2010) Thermodynamic analysis of fluidized bed drying of carrot cubes. Energy 35:4679–4684

Computational Fluid Dynamic Analysis of Exhaust Gas Calorimeter

Bibin Chidambaranathan, S. Senthil Kumar, S. Gopinath, S. Madhu, and Raghavan Sheeja

Abstract This study employs a four-stroke gasoline engine with water cooling. Trials are being conducted to determine if the exhaust gas calorimeter model can be used to measure heat losses incurred by exhaust gas. The model took into account calorimeter system elements such as the water reservoir, inlet and outlet tubing, as well as cold and hot fluids. If the engine speed increases, the throttle can open wider, allowing more air to enter the cylinder during combustion. As a result, the fuel mass will increase, influencing the exhaust gas temperature. Investigate the rate of heat losses from exhaust gas using an exhaust gas calorimeter. A heat exchanger is a piece of equipment that is intended to efficiently transfer heat from one medium to another. Computational fluid dynamics (CFD) is a simulation methodology that employs powerful computers and applied mathematics to simulate fluid flow situations in order to estimate heat, mass, and momentum transfer and to optimise architecture.

Keywords Exhaust gas · Calorimeter · Computational fluid dynamics · Simulation

1 Introduction

1.1 Computational Fluid Dynamics

Computational fluid dynamics (CFD) is a modelling technique used to simulate heat, mass and momentums transmission and optimise the configuration in manufacturing processes by powerful computers, and the application of mathematical

B. Chidambaranathan (✉) · S. S. Kumar · S. Gopinath
RMK College of Engineering and Technology, Chennai, India
e-mail: drcbibin@gmail.com

S. Madhu
Saveetha School of Engineering, Saveetha Institute of Medical and Technical Sciences, Chennai, India

R. Sheeja
Easwari Engineering College, Chennai, Tamil Nadu, India

tools [1]. CFD approaches address the solution of fluid motion equations and fluid-rigid body interactions [2]. The governing equations (Navier–Stokes's equations) are the motion equations of a non-viscous fluid (Euler equations) and a viscous fluid. Computational fluid dynamics is a fluid mechanic branch that uses computational processes and algorithm to solve and analyse fluid flow problems [3]. The computer uses specialised tools to complete special tasks, which requires a complex estimation of the expected flow operation simulation [4]. A computer model of a machine or unit that we want to analyse may be developed by CFD. For us, CFD–FLUENT is a programme which resolves a series of mathematical equations numerically to model fluid flow, thermal and mass transfers, chemical reactions, and other phenomena [5]. Experimental analytics of new designs, systematic product creation, troubleshooting, and overhaul may be added to findings of CFD analysis. As a consequence, we will use CFD FLUENT to provide a "visual version" of the device or machine we intend to analyse and to then add to the model real-world dynamics and chemicals [6].

1.2 Exhaust Gas Calorimeter

The comparison in this analysis is a 4-h gasoline engine with a water coolant. Testing is conducted to assess the exhaust gas calorimeter model's applicability for the quantification of thermal losses due to exhaust gas [7]. The model took into consideration the elements of the calorimeter system, such as a water pump, a water pipe in and out, and a heat fluid pipe [8]. With the engine rpm, the throttle opens to allow the cylinders to receive more air as combustion occurs. The mass of petrol thereby increases and affects the exhaust gas's temperature. Explore the heat loss rate from exhaust gas using an exhaust gas calorimeter [9]. A heat exchanger is an instrument that can transfer heat efficiently from medium to medium. The media may be isolated or kept in close proximity by a concrete wall, to avoid mixing [10].

2 Literature Review

There is a high demand for sensors that can calculate the various gas components in vehicle exhaust. For future progress in engine control systems and on-board diagnostics for the determination of emissions from tailpipes, the development of these instruments is crucial. Sensors based on the principle of differential calorimetry have been listed as one of the best short-term automotive applicants for hydrocarbons and other types of fuel [11]. This calorimetric devices consist of two sensing components, each with a catalytic layer [12]. The temperature of the catalytically coated part increases compared to the other, providing a measurement of the exhaust concentration for fuel released by the fuel product oxidation [13]. Under laboratory and dynamometer conditions a number of prototype calorimetric instruments have to date been tested. The sensitivity of the instruments being tested was historically less

than that theoretically achievable by the temperature rise per fuel concentration [14]. This essay examines how the concept of calorimeter influences the maximum sensitivity that can be achieved. To understand why sensitivities of the sensors measured so far have been significantly lower than theoretical thresholds, simply physical concern is used. The results of a calorimeter concept analysis model and a basic experiment validating key features of the model are examined.

The OSU device and cone calorimeter are two typically used tools for the calculation of the HRR in combustion-forced flammable material and components [15]. All are calibrated in the same way, but obey a different philosophy. The findings of the HRR are not necessarily acceptable, however. In the current analysis the OSU was updated to measure oxygen use and sensible enthalpy (temperature increase) in the appliance during the test, in addition to the normal sensitive enthalpy of exhalation gases [16]. After calibration, comparable findings have been achieved for thin samples in the OSU with overall sensitive heat (exhaust emissions + equipment) and oxygen intake methods. The OSU findings for thin samples did not, however, comply with the cone calorimeter (ASTM 1354/ISO1556) results until the HRR-background of the cone was adjusted for smear caused by air dilution, the exhaust duct and scrubber of the combustion gases, as well as by oxygen analyser reaction time [17].

A new type of corrugated Plate Heat Exchanger (PHE) was developed. The flow resistance of the working fluid in this modern corrugated PHE was reduced by more than 50% as compared to the standard chevron-type one, and the resulting heat transfer efficiency was reduced by around 25%, according to the results of both computational simulations and experiments. The flow field of the working fluid in the corrugated PHE was transformed, resulting in an output difference in flow resistance and heat transfer [18]. A new plate with longitudinal and transverse corrugations can essentially remove flow path blockage, allowing PHEs to be used in cases with unclean working fluids.

Modern gasoline engines are so strong that they warm up at low temperatures and are very cold [19]. In mail deliveries, in which the average speed is poor and driving time requires a great deal of idling, the issue is especially severe. The problem is normally fixed by installing an auxiliary motor heater that is used to preheat the engine when the coolant temperature drops below thermostat during the drive cycle and by additional heater [20]. Nevertheless, this extra radiator will increase considerably the overall fuel consumption and exhaust emissions of the engine. In this analysis, a combination of an exhaust gas heat recovery system and a latent heat accumulator for thermal energy storage was added to the additional heater [21].

3   Scope and Objective

3.1   Objectives of This Study

1.   To calculate the heat generation from exhaust of the engine
2.   To use CFD to analyse fluid flow situations in order to forecast heat, mass, and momentum transfer in optimal configuration.

3.2   Scopes of the Study

This 4-stroke single cylinder gasoline engine model is used to calculate the engine's heat losses through the exhaust gas. The heat losses are measured using the temperature reading from the exhaust gas calorimeter. The simulation is run at various engine speeds. The heat to be measured would be applied to a flowing stream of water. The weight of water passing through the calorimeter during the period that a known amount of combustible is absorbed in the turbine, as well as the temperature of the water, provide the information needed to quantify the heat imparted to the water. However, there is a heat leakage by the calorimeter, the extent of which would be ignored in this treatise. Inlet and outlet thermometers are used to determine the temperature of the water entering and exiting the calorimeter. In order for the thermometer to reflect the true mean temperature of the effluent stream, a large body of water must be provided in the bottom of the calorimeter to thoroughly mix the water until it enters the outlet thermometer cup. The rate of flow of water, and thus the rate of temperature increase, is regulated by appropriate valves in the supply line. The prime mover is a gasoline engine, which drives an alternator to generate electrical energy. The gas engine draws an air–fuel mixture into the cylinder and compresses it to a high ratio. Following this compression, a spark plug is used to generate the spark needed for the power stroke.

4   Computational Fluid Dynamics

4.1   CFD

CFD is a mathematical modelling process based on computer which resolves basic fluid flow equations, the Navier Stokes equations, and other related equations. CFD includes both a solution of heats, mass, and other transportation and field equations dependent on turbulence experimentation. CFD offers Computers are used to conduct these activities, carried out by using specialist software that allows the simulation of the expected flow operation to be completed in complicated calculations. There are three phases to CFD:

- Pre-processing or geometry construction, normally performed in a CAD tool;
- mesh development of a suitable computational domain to solve the flow equations on;
- post-processing or simulation of a CFD code's predictions.

In the early 1980s commercial CFD codes were first introduced to the open market. Large companies worldwide have started to use industrial CFD implementations instead of trying to build CFD codes in-house. Commercial CFD programme is thus built on a variety of extremely complicated nonlinear mathematical words, defining the 16 basic equations of fluid flow, heat transfer and transport of liquid [22]. In order to resolve these equations iteratively, complex computer algorithms implemented in CFD implementations are used. Thus, as long as the object structure is understood, physics and chemistry are defined and the initial flow conditions are specified, a user can computerise any flow area [23]. The outputs of a CFD programme can be graphically expressed as velocity vector colour plots, pressurised contours, continuous flow field lines or as "hard" numerical data and X–Y plots.

CFD is now recognised as a CAE technique, and its approach to fluid flow dynamics modelling enables system makers and science researchers to track the simulated wind tunnel on their desktop computer [24]. CFD technology has advanced well past what Navier, Stokes, or Da Vinci might have predicted. CFD has been a critical component of the aerodynamic and hydrodynamic modelling processes for aeroplanes, boats, trucks, missiles, ships, and submarines, as well as any Moving craft or manufacturing device conceived by mankind.

4.2 Advantages of CFD

CFD modelling software is also commonly used in a variety of industries around the world. CFD is used to model a diverse range of technologies, including the aerospace, nuclear, and automotive industries, as well as the manufacturing, chemical, and process sectors, pharmaceuticals, biomedical, and electronics industries [25].

The advantages using this software:

1. Using this programme, we can make changes to the study at any time during the initialisation, solution, or post-processing processes. This saves time and helps us to more easily optimise our projects. The user-friendly interface facilitates understanding. Only the modelling methods that are applicable to the current issue configuration are shown in smart panels. Geometries from computer-aided design (CAD) can be conveniently imported and modified for CFD solutions.
2. Any new version of our programme includes solver improvements and computational algorithms that reduce the time to solution. Our advanced, stable, and scalable parallel processing capability allows us to tackle larger challenges faster and has been demonstrated on the industry's broadest range of platforms.

3. FLUENT's post production offers many layers of reporting, allowing us to meet the demands and interests of all audiences. Quantitative data processing will be as thorough as we need it to be. High-resolution photographs and animations allow us to communicate our findings effectively. There are several data export opportunities for use in structural analysis and other computer-aided engineering (CAE) software programmes.

4.3 Geometry Design and Meshing

In order to create an acceptable model to run in FLUENT applications, pre-design geometry must be created to meet the needs of FLUENT.

5 Experimental Setup and Analysis

Computational fluid dynamics is a branch of fluid mechanics that solves and analyses fluid flow problems using computational methods and algorithms.

5.1 Experimental Setup

See Fig. 1.

5.2 Meshing

Ansys workbench is used for meshing. Tetrahedral mesh is usually a more automated way of measuring volume and can also be used to increase precision in vulnerable areas with mesh controls. On the other hand, a hexahedral mesh is more accurate but harder to construct. An individual route system for meshing was used with a top-down methodology (creates volume mesh and extracts surface mesh from boundaries). The patch-independent technique uses only geometry to harmonise mesh frontiers with areas of concern, eliminating holes, overlaps and other issues affecting other meshing instruments [26]. The advanced size feature is the industry norm for fluid applications and it is designed to capture geometry correctly whilst preserving a smooth growth rate between curvature and proximity regions (Fig. 2).

Fig. 1 Experimental setup

5.3 Temperature Distribution

The commercial CFD code ANSYS Fluent was used for the numerical simulation. The code uses a flow-based solver with simple method for fluid analysis (Fig. 3).

6 Result and Conclusion

The exhaust from the engine is routed into long pipes that are encased in a water jacket, allowing the water to flow continuously. The exhaust pipe becomes hot due to the transit of exhaust from the engine, causing water to flow in the opposite direction and carry heat from the exhaust pipe.

The temperature of the heat carried water rises, allowing us to calculate the total heat produced using the counter flow LMTD process. The amount of heat produced will vary depending on the load applied.

The study of EGC using CFD deals with temperature transfer and reveals how heat is dissipated in EGC. Using this analysis, we can consider heat transformation by convection from one component and heating another fluid by convection.

Fig. 2 Mesh analysis
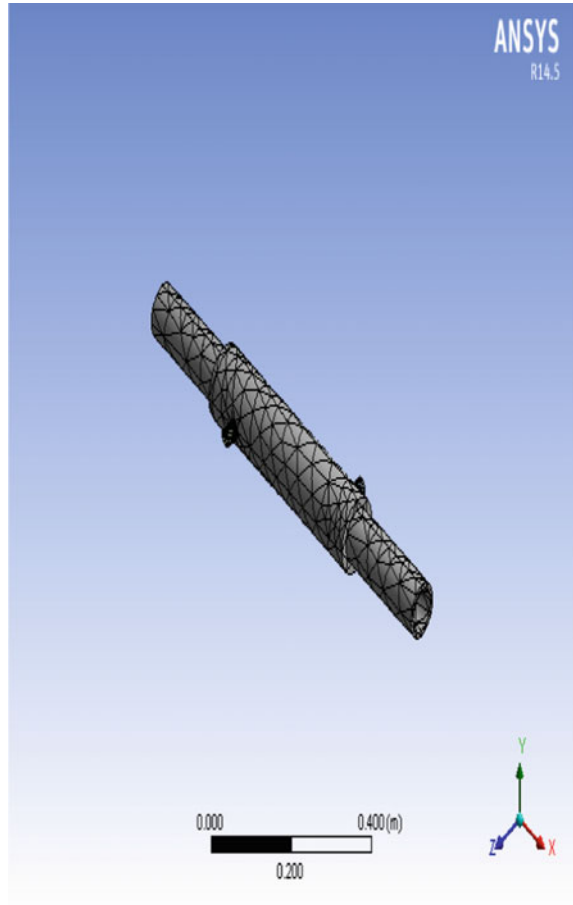
It is critical to locate a heat balance sheet in the case of an I.C engine. How much heat is lost in braking, how much heat is lost in exhaust gas, and how much heat is lost in cooling water. There was also an attempt made to use cooling media as a bath.

It is difficult to determine how much exact heat goes into the exhaust gas using an existing spiral tube style heat exchanger as an exhaust gas calorimeter; but, by using CFD flow analysis, we can see the temperature distribution in EGR and it displays the temperature distribution in temperature contours, which mean heat distribution. We can have a wide range of applications for heat produced by doing an exact heat transformation analysis.

In factories, the exhaust is massive, so we can produce massive amounts of heat from it, which we can also use for small applications such as preheating.
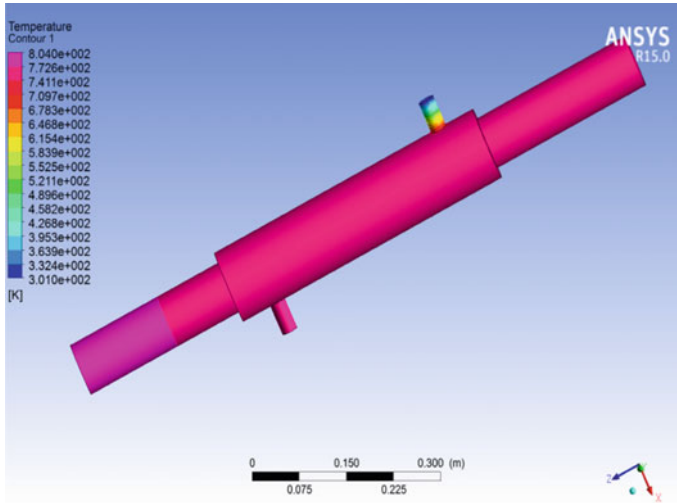
Fig. 3 Temperature distribution

References

1. Haloua F, Ponsard J, Lartigue G, Hay B, Villermaux C, Foulon E, Zaréa M (2012) Thermal behaviour modelling of a reference calorimeter for natural gas. Int J Therm Sci 55:40–47. https://doi.org/10.1016/j.ijthermalsci.2011.12.014
2. Huang Q, Lu S, Liu X, Zheng K, Xu D (2021) Experimental thermal hazard investigation on carbonate electrolytes using a cone calorimeter. Case Stud Therm Eng 25:100912. https://doi.org/10.1016/j.csite.2021.100912
3. Terrei L, Acem Z, Lardet P, Boulet P, Parent G (2021) In-depth wood temperature measurement using embedded thin wire thermocouples in cone calorimeter tests. Int J Therm Sci 162:1–11. https://doi.org/10.1016/j.ijthermalsci.2020.106686
4. Narode A, Ducoste JJ, Barlaz MA (2021) Measurement of heat release during hydration and carbonation of ash disposed in landfills using an isothermal calorimeter. Waste Manag 124:348–355. https://doi.org/10.1016/j.wasman.2021.02.030
5. Terrei L, Acem Z, Lardet P, Boulet P, Parent G (2021) Study of wood self-extinguishment with a double sliding cone calorimeter. Fire Saf J 122:103316. https://doi.org/10.1016/j.firesaf.2021.103316
6. Purcell SA, Johnson-stoklossa C, Rayane J, Tibaes B, Frankish A, Elliott SA, Padwal R, Prado CM (2020) Clinical nutrition ESPEN accuracy and reliability of a portable indirect calorimeter compared to whole-body indirect calorimetry for measuring resting energy expenditure. Clin Nutr ESPEN 39:67–73. https://doi.org/10.1016/j.clnesp.2020.07.017
7. Nishiyama E, Tsukushi I, Fujimura J, Yokota M (2020) Construction of a top-loading adiabatic calorimeter equipped with a refrigerator. Thermochim Acta 692:178751. https://doi.org/10.1016/j.tca.2020.178751
8. Sato K, Lee JW, Banno S, Campbell M, Comfort J, Furukawa T, Iwai E (2020) CsI calorimeter for the J-PARC KOTO experiment. Nucl Inst Phys Res A 982:1–16. https://doi.org/10.1016/j.nima.2020.164527
9. Longo S, Roney JM, Cecchi C, Cunliffe S, Ferber T, Hayashii H, Hearty C (2020) CsI (Tl) pulse shape discrimination with the Belle II electromagnetic calorimeter as a novel method to

improve particle identification at electron–positron colliders. Nucl Inst Methods Phys Res A 982:164562. https://doi.org/10.1016/j.nima.2020.164562

10. Kim J, Nam SM, Jang H, Chung J, Kim JS, Kim B, Jin K, Lee W (2020) Development and application of chip calorimeter as an X-ray detector. Curr Appl Phys 20:337–343. https://doi.org/10.1016/j.cap.2019.11.020

11. Ramadhan ML, Zarate S, Carrascal J, Osorio AF, Hidalgo JP (2020) Effect of fuel bed size and moisture on the flammability of Eucalyptus saligna leaves in cone calorimeter testing. Fire Saf J 103016. https://doi.org/10.1016/j.firesaf.2020.103016

12. Cao J, Ju X, Peng Y, Zhou X, Hu Y, Li L, Wang D, Cao B (2020) Experimental study on fire hazard of $LiCoO_2$-based lithium-ion batteries with gel electrolyte using a cone calorimeter. J Energy Storage 32:101884. https://doi.org/10.1016/j.est.2020.101884

13. Sereda VV, Sednev-lugovets AL, Malyshkin DA, Tsvetkov DS, Zuev AY (2020) High-temperature heat-flux inverse drop calorimeter. Thermochim Acta 694:178802. https://doi.org/10.1016/j.tca.2020.178802

14. Oshima T, Delsoglio M, Dupertuis YM, Singer P, De Waele E, Veraar C, Heidegger C, Wernermann J, Wischmeyer PE, Berger MM, Pichard C (2020) The clinical evaluation of the new indirect calorimeter developed by the ICALIC project. Clin Nutr 39:3105–3111. https://doi.org/10.1016/j.clnu.2020.01.017

15. Collaboration TC, Chefdeville M, Repond J, Schlereth J, Smith JR (2019) Analysis of testbeam data of the highly granular RPC-steel CALICE digital hadron calorimeter and validation of Geant4 Monte Carlo models. Nucl Inst Methods Phys Res A 939:89–105. https://doi.org/10.1016/j.nima.2019.05.013

16. Ma S, Zheng J, Tang D, Lv X, Li Q, Yang M (2019) Experimental investigation on the decomposition characteristics of natural gas hydrates in South China Sea sediments by a micro-differential scanning calorimeter. Appl Energy 254:113653. https://doi.org/10.1016/j.apenergy.2019.113653

17. Hilgert C, Howar F, Röger M (2019) Flow through calorimeter to measure fluid heat capacity in CSP applications. Sol Energy 194:804–814. https://doi.org/10.1016/j.solener.2019.11.029

18. Perez-sanz FJ, Sarge SM, Van Der Veen A, Culleton L, Beaumont O, Haloua F (2019) First experimental comparison of calorific value measurements of real biogas with reference and field calorimeters subjected to different standard methods. Int J Therm Sci 135:72–82. https://doi.org/10.1016/j.ijthermalsci.2018.06.034

19. Tanaka T, Kato M, Saito N, Owada S, Tono K (2018) Absolute laser-intensity measurement and online monitor calibration using a calorimeter at a soft X-ray free-electron laser beamline in SACLA. Nucl Inst Methods Phys Res A 894:107–110. https://doi.org/10.1016/j.nima.2018.03.045

20. Sut A, Metzsch-Zilligen E, Großhauser M, Pfaendner R, Schartel B (2018) Rapid mass calorimeter as a high-throughput screening method for the development of flame-retarded TPU. Polym Degrad Stab 156:43–58. https://doi.org/10.1016/j.polymdegradstab.2018.08.004

21. Marc Y, Oshima T, Ragusa M, Heidegger C, Pichard C (2017) Clinical Nutrition ESPEN Methods to validate the accuracy of an indirect calorimeter in the in-vitro setting. Clin Nutr ESPEN 22:71–75. https://doi.org/10.1016/j.clnesp.2017.08.009

22. Walters RN, Safronava N, Lyon RE (2015) A microscale combustion calorimeter study of gas phase combustion of polymers. Combust Flame 162:855–863. https://doi.org/10.1016/j.combustflame.2014.08.008

23. Lee Y, Kim Y, Lee J, Lee H, Seo Y (2015) CH_4 recovery and CO_2 sequestration using flue gas in natural gas hydrates as revealed by a micro-differential scanning calorimeter. Appl Energy 150:120–127. https://doi.org/10.1016/j.apenergy.2015.04.012

24. Abrams R, Ankenbrandt C, Flanagan G, Hauptman J, Kahn S, Lee S, Notani M (2012) A gas-filled calorimeter for high intensity beam environments. Phys Procedia 37:364–371. https://doi.org/10.1016/j.phpro.2012.02.387. In: TIPP 2011—technology and instrumentation in particle physics 2011

25. Sergey P (2009) Liquid noble gas calorimeters at Budker INP. Nucl Inst Methods Phys Res A 598:248–252. https://doi.org/10.1016/j.nima.2008.08.086

26. Matsumura T, Asano Y, Chiba R, Hashimoto T, Miura A, Shimizu H (2007) A sharp gas-bremsstrahlung beam capable of testing electromagnetic calorimeters. Nucl Inst Methods Phys Res A 582:489–496. https://doi.org/10.1016/j.nima.2007.09.006

Analysis of Internal Flow and Velocity Characteristics of Threaded Convergent Nozzle Using CFD for Abrasive Jet Application

S. Madhu, M. Balasubramanian, and V. Benaline Sheeba

Abstract Abrasive jet machining process is finding great importance in engineering applications. It is a machining process, where removal of material happens due to erosion effect by passing a high velocity stream of abrasive particles along with a gas medium. A nozzle is used to supply the jet of abrasive particles with air at a very high velocity. The conventional nozzle presently used for the process gives low velocity and results in lower material removal rate (MRR). In this work, three different types of convergent nozzles, (i) Geometry type-I (25 mm length), (ii) Geometry type-II (50 mm length), and (iii) Geometry type-III (newly designed nozzle), have been designed and analyzed using CFD. Multistart thread is employed in all the three types of the nozzle for improving the velocity and flow rate of the mixture of air and abrasive particle. Ansys Fluent 16.0 tool is used for computational fluid dynamics analysis. The velocity of the mixture from nozzles with thread was analyzed. Velocity, pressure, and angular velocity of mixture inside the nozzle were compared. The results showed improvement in newly designed nozzle, and the velocity was 42.84 m/s. The rate of flow obtained through the newly designed nozzle is high compared with other conventional types of nozzles.

Keywords Computational fluid dynamics · Swirl flow · Convergent nozzle · Swirl velocity

S. Madhu (✉)
Saveetha School of Engineering, Saveetha Institute of Medical and Technical Sciences, Chennai 602105, India
e-mail: mathumarine@gmail.com

M. Balasubramanian
R.M.K College of Engineering and Technology, Puduvoyal, Thiruvallur 601206, India

V. Benaline Sheeba
Infant Jesus College of Arts and Science for Women, Mulagumoodu, Tamilnadu, India

Nomenclature

A	Nozzle area
CFD	Computational Fluid Dynamics
ρ	Density
V	Velocity
P	Pressure
F	Frequency (Hz)
T	Time (s)
H	Height of water in tank (m)
D	Diameter of the circular tank (m)
L	Length of the rectangular tank
G	Acceleration due to gravity (m/s^2)
Ω	Angular velocity(rad/s)
F	Sinusoidal force applied
M	Viscosity (kg/m-s)
$\emptyset$	Interface
ρ	Fluid density (kg/m^3)

1 Introduction

In AJM, abrasive particles are made to intrude the base material at high velocity. The abrasive particles are mixed with a carrier gas or air. Hence, high velocity stream is generated by correcting the pressure energy. High velocity stream removes the material by micro level cutting action accompanied by the brittle fracture of the work material. Convergent nozzles are widely used in abrasive jet machines to get uniform flow rate. These nozzles are termed as based on their geometrical parameter. Convergent nozzle has gradually decreased the diameter toward the tip of the nozzle, whereas divergent nozzle has increased the diameter. Hence, there is a decrease also in the velocity of fluid. However, convergent divergent nozzle has throat section which is increasing in their performance.

The shape of the machined surface was investigated using semi-empirical equation in abrasive jet machine. From this work, it was noticed that the shape of the machined surface is like a reverse bell with an edge radius at the entry side of the target surface [1]. Investigations was carried out on glass, ceramic, and EDM die material using aluminum oxide and silicon carbide as abrasive particles and tungsten carbide or sapphire as nozzle materials justified the importance of process parameters like standoff distance, spray angle, and pressure [2]. Systematic study was carried out on abrasive jet deburring on AISI-304 stainless steel and plaster of paris work piece. The thickness of the work piece was 4 and 10 mm. The experiments carried out using HCHCr hardened steel nozzle. The nozzle tip distance was 5, 15 mm. The effects of various input parameters on the response parameters were investigated in detail

[3]. Cross-drilled hole on was made on plaster of paris work piece using abrasive jet deburring machine. The effects of process parameters to maximize the material removal rate were discussed in detail [4].

The effect of inlet pressure on skin friction coefficient and jet exits kinetic energy. The analysis also reveals a significant decrease in the skin friction coefficient and jet kinetic energy as resulting from an increase in volume fraction of abrasive concentration in water [5]. The erosion model provided a method for determining the material removal or erosion rate density. Ansys CFX 11.0 was used for the computational fluid dynamics (CFD) simulation, where investigation was done on the water jet air and abrasive velocity. The author has eroded the focusing tube by varying the mass flow rate of the abrasive and the abrasive particle form factor [6].

Several researchers performed numerical nozzle simulation to determine the strain, velocity, and mass flow rate. Supersonic nozzle with minimal length has been designed, and uniform flow at the nozzle exit at both converging and diverging nozzle section was measured. It is rational to assume the flow holds the consistency in the converging section and, thereby, an arbitrary shape is assumed for the converging section of the converging–diverging nozzle. The design considerations are concentrated at the diverging section [7]. The erosion wear behavior of the (W,Ti)C/SiC gradient nozzle was investigated and compared with a conventional ceramic nozzle. Gradient ceramic nozzles resisted erosion wear over the conventional nozzles. This was due to the stress from the tensile at the entry region of the nozzle being greatly reduced. This effect may lead to an increase in resistance to fracture and thus increase the erosion wear resistance of the gradient nozzle. The effectiveness of gradient structures in ceramic nozzles is indicated for improving the erosion wear resistance of conventional ceramic nozzles [8]. The effect of collisions between incoming and rebounding abrasive particles was found using computer simulation. The goal was calculated by a grid of cubic cells representing the surface, each of which was assigned a damage parameter based on the number of particles that were impacted [9]. For the erosion in micro-hole drilling and channel cutting, holes and channels were rendered on 5 mm thick soda lime glass using abrasive jet machine and predictive mathematical model. An experimental investigation covering a number of specific process parameters, which were evaluated, and capability of the models were also ascertained [10].

Dynamic characteristics of abrasive particle distribution and particle to particle collision were studied using discrete element analysis. The process parameters include pressure 0.43 and 0.69 MPa, nozzle diameter 0.36 and 0.46 mm, and nozzle length 7 mm. The result showed that the increase in the aerodynamic drag resulted in higher particle velocities that allow the abrasive particles to remain more centrally along the centerline of the jet axis [11]. Numerical model developed earlier was used for predicting the steady state roughness. Maximum pressure reduced the surface roughness [12]. One-dimensional isentropic flow model was developed to calculate the particle exit velocity of each abrasive particle in the airflow for cylindrical and line shaped laval type nozzle. The work revealed that for cylindrical nozzle the air velocity is limited due to its converging section. The laval nozzle achieved

the maximum particle velocity. Particle image velocimetry was employed for verifying the simulation results [13]. The erosion of the target material caused by the high pressure waterjet was developed under waterjet impingement using nonlinear finite element model A combination of Eulerian–Lagrangian elements is used, and the results obtained from this numerical simulation were in agreement with the experimental results.

Even though many studies on this process have been conducted, still there is scope for research and development. To improve the design of the nozzle, an understanding of the hydrodynamic characteristics (e.g., velocity and pressure distributions) of an abrasive jet is required. But the abrasive particle interaction in the mixing chamber is extremely intricate while the ultrahigh velocity and small nozzle make the investigation difficult. Nevertheless, some important investigations have been reported [14] on the understanding of the dynamic characteristics for relatively low velocity and for particular jet cutting status through theoretical and experimental studies as well as CFD simulation. However, research on ultrahigh abrasive jets to arrive at a comprehensive understanding of the jet properties has received little attention [15].

Studies have been made on swirling of abrasives by imparting internal threads in the nozzle. Swirl effect of abrasive particles produced using abrasive fluidized bed machining revealed a better surface roughness and material removal rate [16]. The nozzle with open loop feed system was introduced to minimize the taper angle while machining a quartz glass of 2 mm thickness. Al_2O_3 of 320 grit size abrasive particles was used through a 0.896 mm nozzle. The hole diameter machined was reduced by 29% at the entry side and taper angle by 58% approximately, when the nozzle tip was 2 mm away from the work piece [17]. A shadow mask eliminated the cost and mask fabrication time further, thus increasing nozzle standoff distance and mask thickness which produced a good surface finish [18]. Significant process parameters affecting the abrasive jet process were identified. The effect of abrasive jet process parameters on the material removal rate and the quality of drilling was also studied [19].

In this work, three-start thread profile has introduced inside the surface of the convergent nozzle for achieving a swirl flow of abrasive particles. The flow of the fluid gets swirling motion through introduction of the threaded profile. Swirl flow is a rotational motion of fluid mass within the cylinder. It enhances the mixing of air and abrasive particle to give a homogeneous mixture within a short time. Owing to the swirl motion convergent nozzle with thread delivers fluid flow of high velocity at the tip of the nozzle compared with other nozzles, which increase the materials removal rate.

In this work, numerical simulation was conducted on three different geometry types of convergent nozzles: (i) geometry type-I (25 mm length), (ii) geometry type-II (50 mm length), and (iii) geometry type-III (newly designed nozzle). Ansys fluent software was used for the computational fluid dynamics (CFD) simulation, where investigation was done on the Abrasive jet velocity, pressure, and the swirl flow of the mixture of air and abrasive particle in the nozzle.

2   Numerical Scheme

The pressure and velocity of the air and abrasive particles of the nozzle are determined using two equations: (a) One-dimensional continuity equation and (b) gas characteristic equation (thermodynamic approach). One- and two-dimensional compressible flows have already been seen in earlier sections. This section deals with the quasi-one-dimensional flows. The flow was considered to be one dimensional for Rayleigh and Fanno flows [20].

2.1   Calculation of Abrasive Jet Velocity

The principal explanation for this statement is the constancy in the direction of flow of the cross-sectional area of the pipe. Unless the area varies in flow direction, the flow should be viewed as a three-dimensional flow. When such a variation is incremental, however, the changes taking place in cross-stream directions can be overlooked. Such flows are called quasi-one-dimensional flows. The mathematical model of the problem includes one-dimensional and a quasi-one-dimensional flow given in Eq. (1).

$$\rho_1 \mu_1 A_1 = \rho_2 \mu_2 A_2 \tag{1}$$

Here, flow is considered as one-dimensional as other direction values are small. Assume density is constant which means flow is incompressible [21]. The input boundary conditions are already known. For the newly designed convergent nozzle, A1-Area inlet of the nozzle (0.09 m), A2-Area outlet of the nozzle (0.03 m), P1-6 bar and V1—4.5 m/s. The input values applied in the continuity Eq. (2)

$$\rho_1 \mu_1 A_1 = \rho_2 \mu_2 A_2 \tag{2}$$

Density is constant (for Incompressible Flow)

$$V_1 A_1 = V_2 A_2,\ V_2 A_2 = V_2 A_2,\ V_2 = {V_1 A_1}/{A_2} = V_2 = 42 \text{ m/s}$$

The analytical result showed that the newly designed internal thread nozzle delivered 42 m/s velocity for the given inlet pressure.

2.2   Abrasive Jet Pressure Calculation

The solution is obtained using through thermodynamic approach gas characteristic Eq. (3)

$$PV = mRT \tag{3}$$

where P—pressure, V—volume, M—mass, R—gas constant, and T—temperature. Equation (3) is re-written as in Eq. (4).

$$P = (m/V)RT \tag{4}$$

Here, density is constant. The above equation is modified as

$$\frac{P_1}{R_1 T_1} = \frac{P_2}{R_2 T_2}$$

The boundary conditions are $P_1 = 6$ bar, $T_1 = 288$, $T_2 = 430$, and $P_2 = 9$ bar, the final result.

3   Experimental Parameters

For the CFD simulation, a three-dimensional model of three different nozzles was designed in CATIA V5R17 and Ansys fluent tool was used for meshing. All the necessary boundary conditions were applied in Ansys CFX 11.0. Table 1 shows the geometry type and nozzle parameter, and Table 2 shows the boundary conditions for the CFD analysis. In the symmetrical model, the computation was made in less time as the total number of mesh decreased compared to the full model [22].

3.1   Geometry Type I

With information from the previous literature, the authors have designed a convergent nozzle with the length of 25 mm. The inlet and outlet diameters are 18 mm and 3 mm, respectively. Figure 1a shows the details of internal threads of the convergent nozzle with 25 mm. The length of the nozzle is short when compared to the other existing nozzle. A model of 3D convergent nozzle was made symmetrical with increase in its respective axis. In the existing convergent nozzle, the authors introduced three-start thread inside the surface area of the nozzles with the purpose of increasing the fluid flow. Figure 1b shows the cross section of the convergent nozzle with 25 mm length with three-start thread. The presence of new profile causes increase in the swirl motion of the fluid. The velocity also increases in the meanwhile.

Table 1 Geometry type and nozzle parameter

Geometry/boundary condition	Parameters
Geometry type 1 Convergent nozzle with 25 mm length	Inlet diameter—18 mm
	Nozzle tip diameter—3.01 mm
	Length—25 mm
	Thread profile length—8 mm
	Thread pitch diameter—2 mm
Geometry type 2 Convergent nozzle with 50 mm length	Inlet diameter—18 mm
	Nozzle tip diameter—3 mm
	Length—50 mm
	Thread profile length—23.96 mm
	Thread pitch diameter—2 mm
Geometry type 3 Newly designed nozzle	Inlet diameter—18 mm
	Nozzle tip diameter—3 mm
	Length—25 mm
	Thread profile length—25 mm
	Thread pitch diameter—2 mm

Table 2 Boundary condition

S. No.	Boundary condition	Values
1	Air density	1.225 kg/m^3
	Air pressure	6 bar
2	Abrasive particle young's modulus	410 GPa
3	Abrasive particle poisons ratio	0.14

3.2 Geometry Type II

In this design, the length of the convergent nozzle was increased to 50 mm. Figure 2a the two-dimensional details of the threaded nozzle. Increasing the length of the convergent nozzle will result in higher velocity ratio when compared to convergent nozzle short length. So the distance between the inlet and outlet of the nozzle is higher than short length nozzle. Owing to increasing length of the nozzle, the length of the thread profile increases. The length of the thread profile for this nozzle is 24 mm as shown in Fig. 2b. Hence, swirl motion of the fluid will be higher than the short length nozzle.
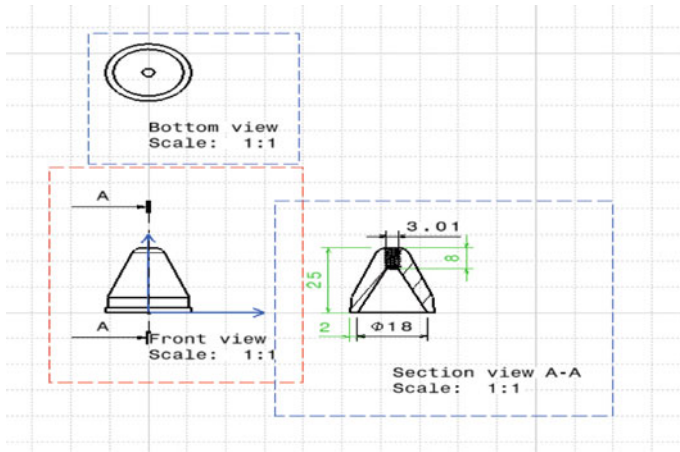
(a)
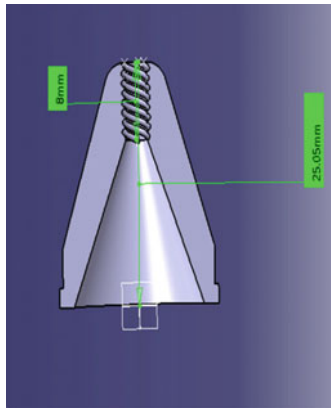
(b)

Fig. 1 **a** Details of the internal threads of convergent nozzle with 25 mm length. **b** Cross section of the convergent nozzle

3.3 Newly Designed Nozzle

Based on the existing design calculations, some design modifications were made on the convergent nozzle with 50 mm length. We have taken for our experiment; let us increase the length of the nozzle through some extended surface from the outlet of the nozzle. The whole structure of the nozzle is look like in the shape of a Funnel. Figure 3a shows the two-dimensional view of the threaded modified convergent nozzle. Owing to the presence of thread profile, the swirl motion as well as velocity of the fluid will be high. When compared to existing nozzle by the combination of both convergent performance and thread profile performance, the velocity rate of
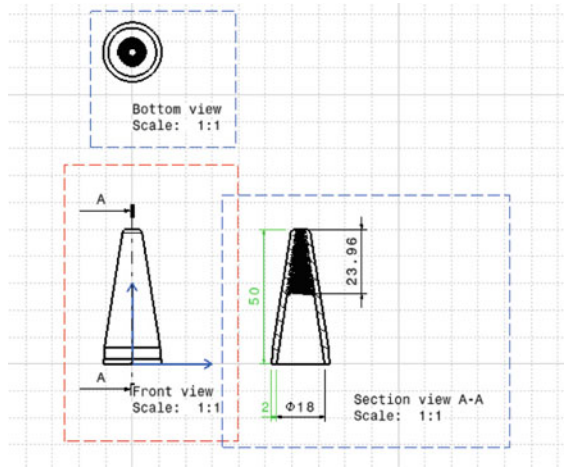
(a)
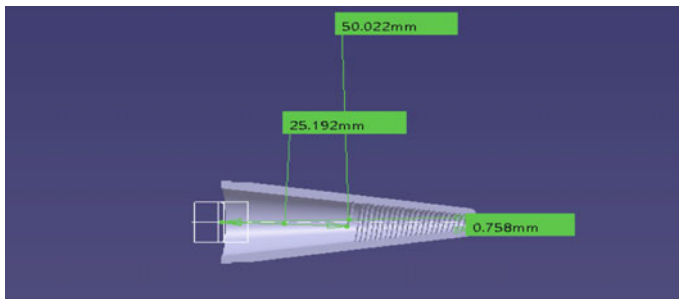
(b)

Fig. 2 **a** Details of the internal threads of convergent nozzle (Geometry Type II). **b** Cross-sectional view of geometry type-II

fluid flow is enormously high. Figure 3b shows the cross-sectional view of three-start threaded newly designs nozzle.

3.4 *Mesh Details and Boundary Conditions*

The entire process, a nonlinear FE model (using ANSYS 16.0) developed, simulated the air and abrasive flow inside the nozzle. A combination of tetrahedron elements was used for all three types of the nozzle for handling their interaction. The mesh method was adopted to simulate and solve the abrasive jet muzzle problem. Advanced meshing was used to mesh the entire system of the nozzle, and the target material.

The main aim is to develop a fine mesh near the wall of the nozzles for gaining better accuracy in velocity profile and pressure contour. In addition, the mesh at the
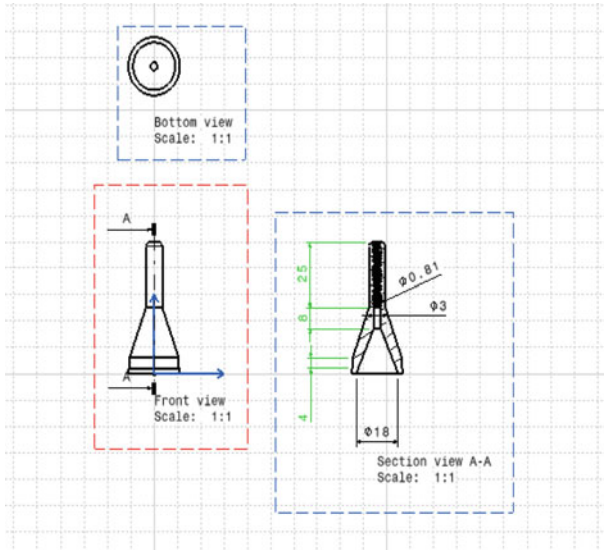
(a)
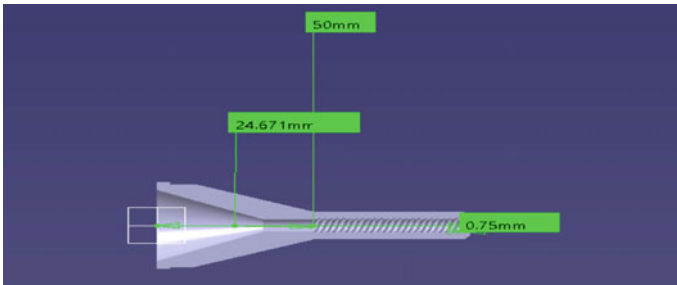
(b)

Fig. 3 **a** Details of the internal threads of newly designed nozzle. **b** Cross-sectional view of newly designed internal threaded nozzle

surface of the target was intended to enable very fine computation of the erosion stages. The type of element used was 8-node brick and the abrasive jet nozzle data are identical. Table 3 shows the meshing condition used for this simulation, and it shows details of nodes and elements used in all three types of nozzles. Figure 4a–c shows the meshing condition for all the three different nozzles for simulation.

Table 3 Meshing condition

S. No.	Geometry section	Tetrahedron mesh	
		Mesh elements	Number of nodes
1	Convergent nozzle 25 mm length	203,413	40,412
2	Convergent nozzle 50 mm length	4,476,525	826,144
3	Modified convergent Nozzle	944,946	181,663

4 Results and Discussions

The input pressure for all these types of nozzle was is 6 bar, and the nozzle diameter was 3 mm. This was important for calculating the velocity profile of the abrasive jet at the exit of the nozzle, considering a uniform entry velocity. In this work, velocity profile was analyzed for all three types of nozzles in without internal threads and with internal thread conditions [23].

4.1 Velocity Profile

Table 4 shows the velocity profile in three different nozzles. Figure 5a shows the velocity of the convergent nozzle without thread. The velocity of this nozzle obtained from the analysis was 33.016348 m/s. Figure 5b shows that the velocity of the convergent nozzle of 25 mm length with thread was 34.049961 m/s.

The velocity contour value of the convergent nozzle of 50 mm length without internal thread was shown in Fig. 6a. The simulation value obtained was 32.972918 m/s. The velocity of the air and abrasive particle mixture inside the nozzle with internal thread was 39.242693 m/s as shown in Fig. 6b. The swirl flow rate of the fluid was high when compared to the convergent nozzle length as the thread length of the nozzle was increased [24]. A better removal rate is achieved using this nozzle in abrasive jet machine when compared to the convergent nozzle with 25 mm length.

Figure 7a shows the velocity profile of air and abrasive particles without internal thread inside the newly designed nozzle. The velocity of this nozzle obtained from the analysis was 33.463763 m/s. Figure 7b shows that the velocity of the newly designed nozzle with internal thread was 42.841246 m/s.

From Fig. 8, it can be noticed that the newly designed internal threaded nozzle delivers more velocity compared with other two nozzles [25].

4.2 Swirl Flow

From the CFD Analysis of three different nozzles, the modified convergent nozzle with three-start thread gives more velocity at the nozzle tip. To find the swirl flow
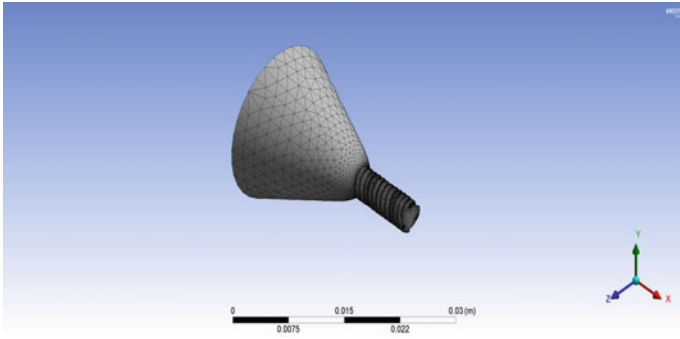
(a)
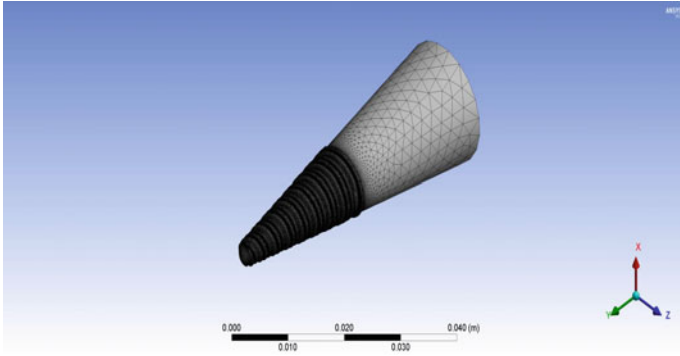
(b)
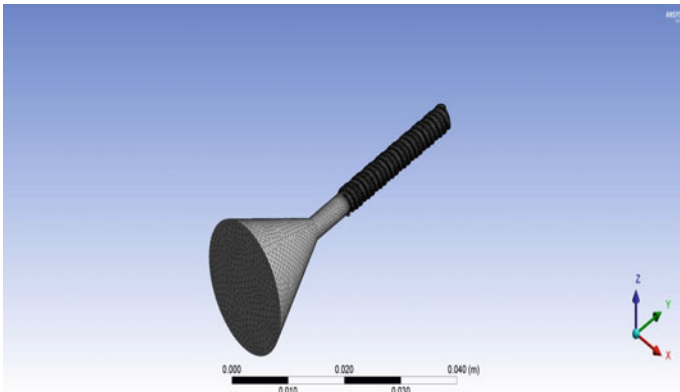
(c)

Fig. 4 **a** Geometry type-I. **b** Geometry type–II. **c** Geometry type-III

Table 4 Velocity profile in three different nozzles

Nozzle type	Velocity (m/s)	
	Without internal threads	With internal threads
Geometry Type I	33.016348	34.049961
Geometry Type II	32.972918	39.242693
Geometry Type II	33.463763	42.841246
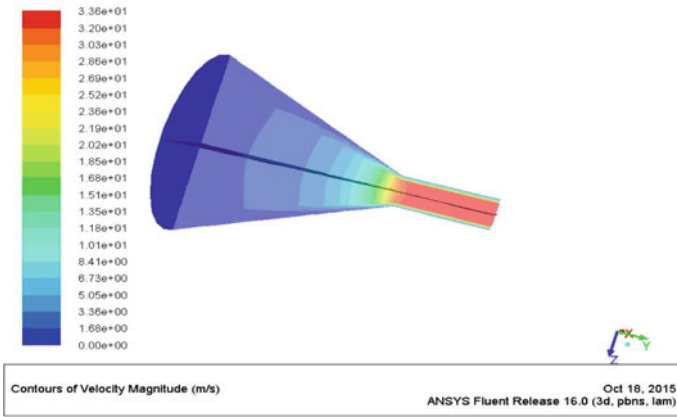
(a)
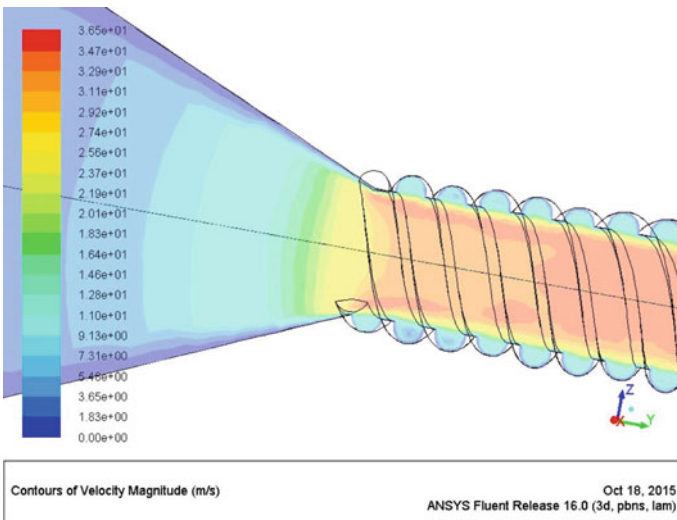
(b)

Fig. 5 **a** velocity of the convergent nozzle without thread—Geometry Type I. **b** velocity of the convergent nozzle with internal thread—Geometry Type I
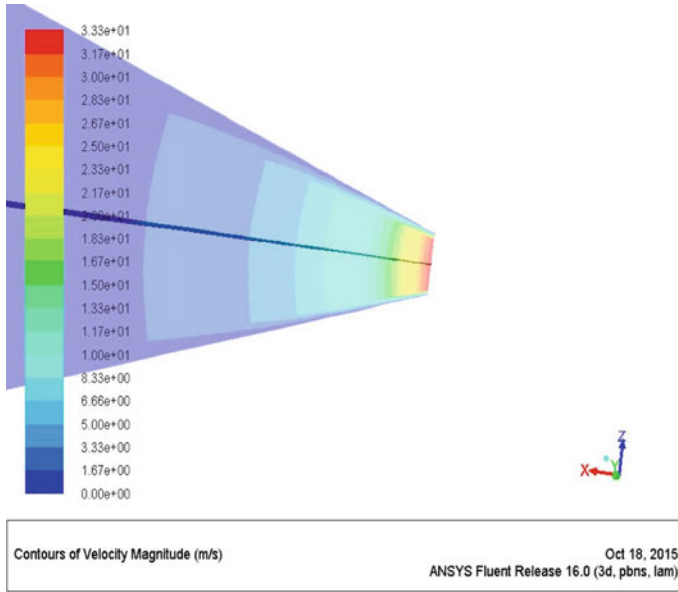
(a)
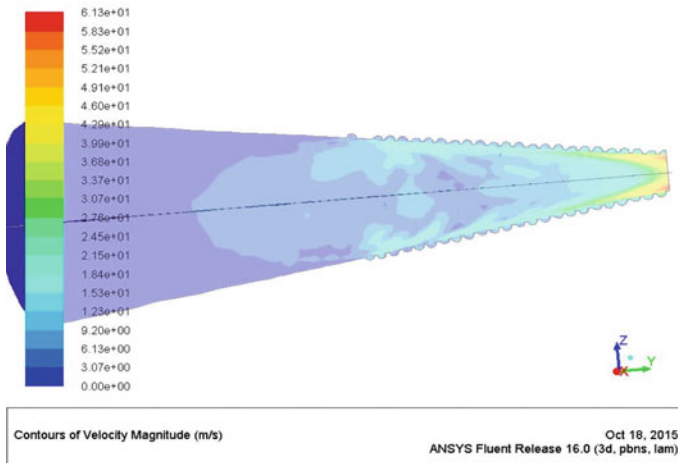
(b)

Fig. 6 **a** velocity of the convergent nozzle without thread—Geometry Type II. **b** velocity of the convergent nozzle with thread—Geometry Type II
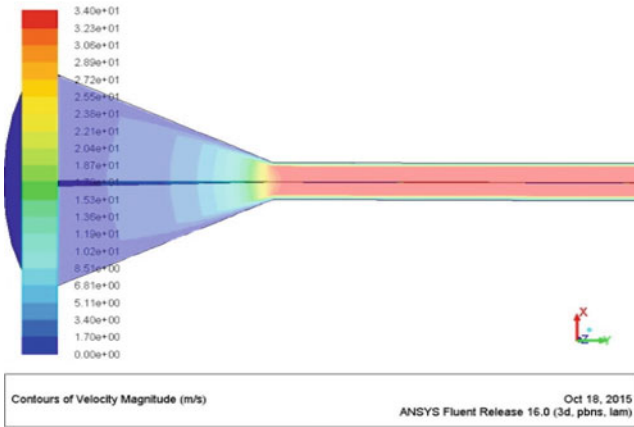
(a)
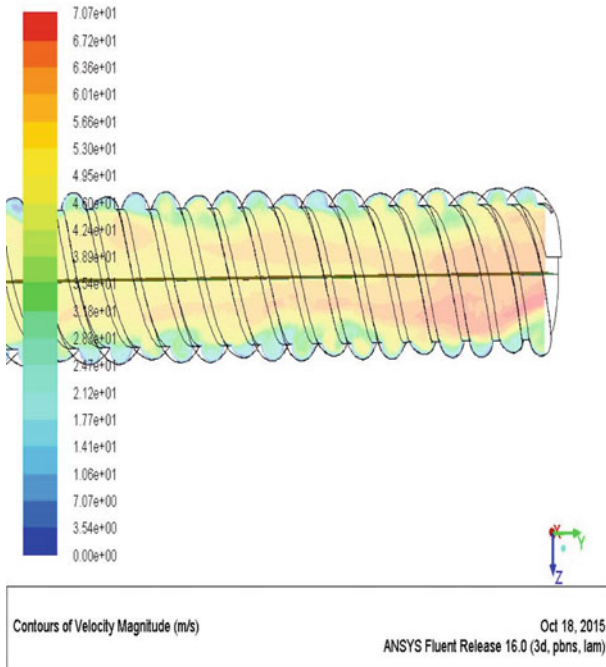
(b)

Fig. 7 a velocity of the convergent nozzle without thread—Geometry Type III. **b** velocity of the convergent nozzle with thread—Geometry Type III
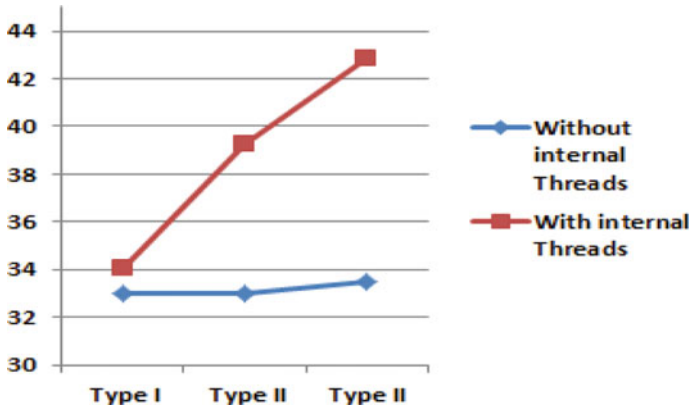
Fig. 8 Comparison of velocity profile

Table 5 Swirl flow of abrasive particles in modified convergent nozzle

Position (from nozzle tip)	X Velocity (m/s)	Y Velocity (m/s)	Z Velocity (m/s)
25 mm	0.487334	31.72748	1.120646
20 mm	0.487334	31.72748	1.120646
15 mm	0.487334	34.53738	1.120646
10 mm	0.487334	34.53738	1.120646
5 mm	0.487334	37.34728	1.120646
1 mm	3.540689	37.34728	4.1797619

motion of air and abrasive particles, dynamic analysis has been conducted inside the nozzle at various distances (1, 5, 10, 15, 20, 25 mm from the nozzle tip). Same boundary and mesh conditions were applied as in the earlier analysis. Table 5 shows the swirl flow values of abrasive and air mixture inside the modified convergent nozzle [16].

The swirl flow rate of the fluid is high when compared to both convergent nozzle (25 mm L) and convergent nozzle (50 mm L), because the thread length of the nozzle has increased and also a long narrow region with threaded position produces high swirl flow rate. By using this nozzle in abrasive jet machine, a better material removal rate can be achieved when compared to the existing nozzles. Threaded modified convergent nozzle shows that its performance has considerably increased the velocity in the specially designed nozzle [26]. From the figure, it was seen swirl flow of air and abrasive mixture in modified convergent nozzle at X- and Z-axis. It was noticed the overall velocity distribution of air and abrasive particles inside the three types of threaded nozzles along the nozzle length.

5 Conclusion

From the above arguments based on the simulation and observations, the velocity of the modified convergent nozzle with thread is relatively high in the order of 42.84 m/s. The magnitude of the velocity of the cone funnel nozzle is the highest when compared with all the three types of nozzle. By machining three-start thread inside the modified convergent nozzle, high swirl flow was obtained. Hence using this modified convergent nozzle, the material removal rate will be increased. The simulation model has provided lot of results to the user, and it proves to be useful in studying the overall nozzle velocity.

References

1. Balasubramaniam R (2002) A study on the shape of surface generated by abrasive jet machining. J Mater Process Technol 121:102–106
2. Venkatesh VC (1989) An empherical study of process parameters in abrasive jet machining. Int J Tools Manuf 29(4):471–479
3. Balasubramaniam R (2000) An empirical study on the generation of an edge radius in abrasive jet external deburring (AJED). J Mater Process Technol 99:49–53
4. Balasubramaniam R, Krishnan J, Ramakrishnan N (1999) An experimental study on the abrasive jet deburring of cross-drilled holes. J Mater Process Technol 91:178–182
5. Deepak D, Anjaiah D, Vasudeva Karanth K, Yagnesh Sharma N (2012) CFD simulation of flow in an abrasive water suspension jet: the effect of inlet operating pressure and volume fraction on skin friction and exit kinetic energy. Adv Mech Eng 186430:8
6. Mostofa G, Kil KY, Hwan AJ (2010) Computational fluid analysis of abrasive waterjet cutting head. J Mech Sci Technol 24:249–252
7. Ali H, Mashud M, Al Bari A, Misbah-Ul Islam M (2012) Numerical solution for the design of minimum length supersonic nozzle. ARPN J Eng Appl Sci 7:5
8. Jianxin D, Fengfang W, Jinlong Z (2007) Wear mechanisms of gradient ceramic nozzles in abrasive air-jet machining. Int J Mach Tools Manuf 47:2031–2039
9. Shafiei N, Getu H, Sadeghian A, Papini M (2009) Computer simulation of developing abrasive jet machined profiles including particle interference. J Mater Process Technol 4366–4378
10. Fan JM, Wanga CY, Wang J (2009) Modeling the erosion rate in micro abrasive air jet machining of glasses. Wear 266:968–974
11. Li H, Lee A, Fan J, Yeoh GH, Wang J (2014) On DEM–CFD study of the dynamic characteristics of high speed micro-abrasive air jet. Powder Technol 267:161–179
12. Haj Mohammad Jafar R, Nouraeia H, Emamifara M, Papini M, Spelt JK (2015) Erosion modeling in abrasive slurry jet micro-machining of brittle materials. J Manuf Process 17:127–140
13. Achtsnick M, Geelhoed PF, Hoogstrate AM, Karpuschewski B (2005) Modeling and evaluation of the micro abrasive blasting process. Wear 259:84–94
14. Li HZ, Wang J, Fan JM (2009) Analysis and modeling of particle velocities in micro-abrasive air jet. Int J Mach Tools Manuf 49:850–858
15. Behera U, Paula PJ, Kasthurirengan S, Karunanithi R, Ram SN, Dinesh K, Jacob S (2005) CFD analysis and experimental investigations towards optimizing the parameters of Ranque-Hilsch vortex tube. Int J Heat Mass Transfer 48:10
16. Francis NK, Viswanadhan KG, Paulose MM (2015) Swirling abrasive fluidized bed machining: effect of process parameters on machining performance. Mater Manuf Process 30(7):852–857

17. Kumar A, Hiremath SS (2016) Improvement of geometrical accuracy of micro holes machined through micro abrasive jet machining. Proc CIRP 46:47–50
18. Nouhi A, Sookhak Lari MR, Spelt JK, Papini M (2015) Implementation of a shadow mask for direct writing in abrasive jetmicro-machining. J Mater Process Technol 223:232–239
19. Madhu S, Balasubramanian M (2015) A review on abrasive jet machining process parameters. Appl Mech Mater 766–767:629–634
20. Maniadaki K, Kestis T, Bilalis N, Antoniadis A (2007) A finite element-based model for pure waterjet process simulation. Int J Adv Manuf Technol 31:933–940
21. Liu H, Wang J, Kelson N, Brown RJ (2004) A study of abrasive water jet characteristics by CFD simulation. J Mater Process Technol 153–154:488–493
22. Mostofa MdG, Kil KY, Hwan AJ (2010) Computational fluid analysis of abrasive waterjet cutting head. J Mech Sci Technol 24:249–252
23. Prisco U, D'Onofrio MC (2008) Three-dimensional CFD simulation of two-phase flow inside the abrasive water jet cutting head. Int J Comput Methods Eng Sci Mech 9:300–319
24. Sheng M, Huang Z-W, Tian S-C, Zhang Y, Gao S-W, Jia Y-P (2020) CFD analysis and field observation of tool erosion caused by abrasive water jet fracturing. Petrol Sci 17:701–711
25. Kotousov LS (2005) Measurement of the water jet velocity at the outlet of nozzles with different profiles. Tech Phys 50(9):1112–1118
26. Madhu S, Balasubramanian M (2018) Effect of swirling abrasives induced by a novel threaded nozzle in machining of CFRP composites. Int J Adv Manuf Technol 95:4175–4189

CFD Simulation of 1.5 MW HAWT with Vortex Generator

Ramesh Chinnappan, Mohanraj Chandran, G. Hari Prasanth, S. Navaneethan, and M. Harshankumar

Abstract Over the years, many developments have been encountered in both offshore and onshore wind turbine blade design. In this study, the aerodynamic effect of vortex generators in WindPACT 1.5 MW wind turbine blade is made by NREL. The turbine contains three types of airfoils, i.e., S818+, S825+, and S826+ which are developed by NREL. Vortex generator (VG) is attached with the wind turbine along throughout length of blade. Geometry was created in solid works software and meshed using a fluent watertight meshing workflow for better accuracy, the full-scale wind turbine CFD (computational fluid dynamics) analysis was done with ANSYS fluent solver, and series of computation was done to validate. The flow in the wind turbine with and without vortex indicator has been visualized. The aerodynamic structural effects and pressure distribution along the surface of the blade and their impact on the strength of the blade were studied. The results indicate that the vortex generators along the length of the blade reduce the flow separation over the blade surface and also maintain the pressure difference that causes the deformation of the blade.

Keywords Vortex generator · Flow separation · CFD

Abbreviations

CFD	Computational Fluid dynamics
HAWT	Horizontal axis wind turbine
NREL	National Renewable energy laboratory
SEM	Scanning Electron Microscope
VG	Vortex Generator

R. Chinnappan (✉) · M. Chandran · G. Hari Prasanth · S. Navaneethan · M. Harshankumar
Department of Mechanical Engineering, M.Kumarasamy College of Engineering, Karur, Tamilnadu 639113, India
e-mail: mkceceramesh@gmail.com

1 Introduction

Life without energy has become unimaginable in this digital era. At the same time, the depletion of the non-renewable resources is increasing now and then. Hence, it is too urge to shift toward renewable resources. Wind is the alternate source of energy that produces the electricity from renewable wind power. The wind energy can be harvested in both the onshore and offshore regions. The onshore wind turbines are less expensive and are more efficient when compared to the offshore turbines, because the offshore turbine requires more landscapes for the installation. The wind energy in India began even from 1952. Since it is much essential to improve the efficiency of wind power, the NREL has been working with this and has made different models of airfoil shapes. Thus, we have utilized these shapes and analyzed by implementing the vortex generator into those models. The vortex generators are incorporated into each model along the length of the turbine blades with the help of solid works software and have done meshing in the ANSYS fluent software. Computational fluid dynamic analysis has been done for investigating the flow through the turbine in both the cases of with vortex generators and without vortex generators. We have analyzed the pressure, and the velocity impacts the turbine structure for the deformation. The NREL S809 aerofoil was analyzed, and it has been identified that the torque and thrust increase with the vortex generators. The vortex generator is capable of reducing the drag co-efficient at the certain particular angle of attacks, and they have also found that at the higher angle of attacks the lift co-efficients are further improved. Their work also revealed that the double vortex generators are capable of further reducing the thickness of the airfoils. Finally, the overall experiment revealed to us, in the airfoil S809, the better performance in the control of the flow separation along with the boundary layer offered by the double vortex generator [1]. The wind turbine aeroelastic analysis was carried out in the basic areas and cutting edge trends. They have identified that in the handling of the realistic models it is mandatory to model the system with various requirements such as wind shear and in the inflow of the wind at the complex areas, offshore applications with the hydrodynamic effects, the methods of manufacturing and the distribution of the materials, larger deflection which lead to the nonlinearity. The multidisciplinary framework system will be much useful to identify the configurations of the system and various possible control, structural, and various aerodynamic characteristics [2]. A thick wind turbine airfoil was analyzed with the application of vortex generators and validated the turbine sensitivity. The study reveals that with the increasing angle of attacks it reported that performance was improved with vortex generator. For the prediction of the aerodynamic performances, it is demonstrated that it is a step ahead to use the scale resolving simulations with respect to the promising tool and the RANS [3].

The wind turbine airfoil analyzed undergoing pitch oscillations and unsteady aerodynamics, and it is concluded that utilization of the passive vortex generators on the blades are highly promising. It was also identified that to more careful assess the performance characteristics of the vane height and the position along chordwise to get the overall better design of the air flows both in the case of the steady and

the unsteady flows [4]. The composite structured wind turbine blade model was analyzed in multiple failure modes using general FEA modeling and found to be structure of blade influences more in failure of blades [5]. The impact of vortex generator on wind turbine blade profile was investigated and reported the installed VG upon the surface of the vortex generators where the expanding and contracting flow passages occur periodically. And the surface pressure at the reduced angles of attack is being changed only locally by the vortex generators but at the large angles of attack the vortex generators change the surface pressure along the entire airfoil [5]. The experimental investigation on the clay composite for wind turbine blades was carried out. And, it was identified that the optimum hardness and the higher tensile stress are obtained with the 1% montmorillonite composite and it is much suitable for the turbine blade applications. It has been made evident through the SEM and ANSYS analysis through images [6]. The material degradation in the composite turbine blades is analyzed for reliability, and it revealed that the reliability and the structural strength of the structure of the blade can be improved by using the composite materials. The sensitivity tests done in this work have revealed that the reliability of the blades should be identified only based upon the influence of the time [4]. Among those investigations, no work is found in the analysis of incorporating the vortex generator with NREL S818+, S825+, and S826 blade profiles.

The objective of this work is to analyze the effect of addition of vortex generator throughout the blade span in order to determine the intensity of flow separation, pressure and velocity distribution around the blade profiles by using the Ansys Fluent software. The results from inclusion vortex generator, such as flow profiles, pressure, and velocity distribution, were compared with the blade without vortex generator.

2 Materials and Methods

After comparing various wind turbine large scales, the NREL wind pact 1.5 MW wind turbine blade is selected for this study. The blade rotor is based on the 1.5 MW, and geometry was created based on reference Table 1. An old model three-bladed upwind HAWT with variable-speed variable pitch control. The details of the WindPACT 1.5 MW wind turbine are summarized in Table 1 and are referenced from WindPACT model Wind Turbines [7]. This blade has two shear webs and three types of airfoils, i.e., S818+, S825+, and S826+. The wind turbine blade 3D geometry was modeled using solid works and shown in Fig. 1. One-third wind turbine was modeled in order to decrease complexity and computational time.

Figure 1 shows the whole blade with airfoil placement along the span. According to Table 1, the blade is created three different airfoils. The hub is created using circular profile, and then, it is drafted to NREL S818 airfoil up to 16.15 m. Further, the NREL S825 airfoil is used to build the blade form 16.15 m to 29.45 m. Also, the blade tip was created by S826 airfoil. The lift and drag co-efficient changes of three airfoils based on different angle of attack are provided in Fig. 2. The S818 airfoil was set aerotwst angle about 11.1° which creates better lift and it was reduced gradually

Table 1 Wind turbine geometry definition

Distributed blade aerodynamic properties for the WindPACT 1.5-MW model

Node (−)	RNodes (m)	AeroTwst (°)	Chord (m)	Airfoil (−)
1	2.85833	11.1	1.949	Circular Foil 0.5
2	5.075	11.1	2.269	s818
3	7.29167	11.1	2.589	s818
4	9.50833	10.41	2.743	s818
5	11.725	8.38	2.578	s818
6	13.94167	6.35	2.412	s818
7	16.15833	4.33	2.247	s818
8	18.375	2.85	2.082	s825
9	20.59167	2.22	1.916	s825
10	22.80833	1.58	1.751	s825
11	25.025	0.95	1.585	s825
12	27.24167	0.53	1.427	s825
13	29.45833	0.38	1.278	s825
14	31.675	0.23	1.129	s826
15	33.89167	0.08	0.98	s826

4.3°. Also, S825 was created and set from 2.85° to 0.38°. The tip was modeled 0.23° and 0.08°.

For considering the incompressible flow, the Navier stokes equation is simplified into

$$\frac{\partial p}{\partial t} + \frac{\partial}{\partial x_i}(\rho u_i) = 0 \tag{1}$$

$$\frac{\partial}{\partial t}(\rho u_i) + \frac{\partial}{\partial x_j}(\rho u_i u_j) = \frac{\partial}{\partial x_j}(\sigma_{ij}) - \frac{\partial p}{\partial x_i} - \frac{\partial \tau_{ij}}{\partial x_j} \tag{2}$$

The stress tensor is a function of viscosity and defined by

$$\sigma_{ij} \equiv \left[\mu\left(\frac{\partial u_i}{\partial x_j} + \frac{\partial u_j}{\partial x_i}\right)\right] - \frac{2}{3}\mu\frac{\partial u_l}{\partial x_l}\delta_{ij} \tag{3}$$

$$\tau_{ij} \equiv \rho u_i u_j(\text{avg}) - \rho u_i u_j(\text{ind}) \tag{4}$$

Using the Boussinesq technique, the sub-grid turbulent stresses are given as

$$\tau_{ij} - \frac{1}{3}\tau_{kk}\delta_{ij} = 2\mu_t S_{ij} \tag{5}$$
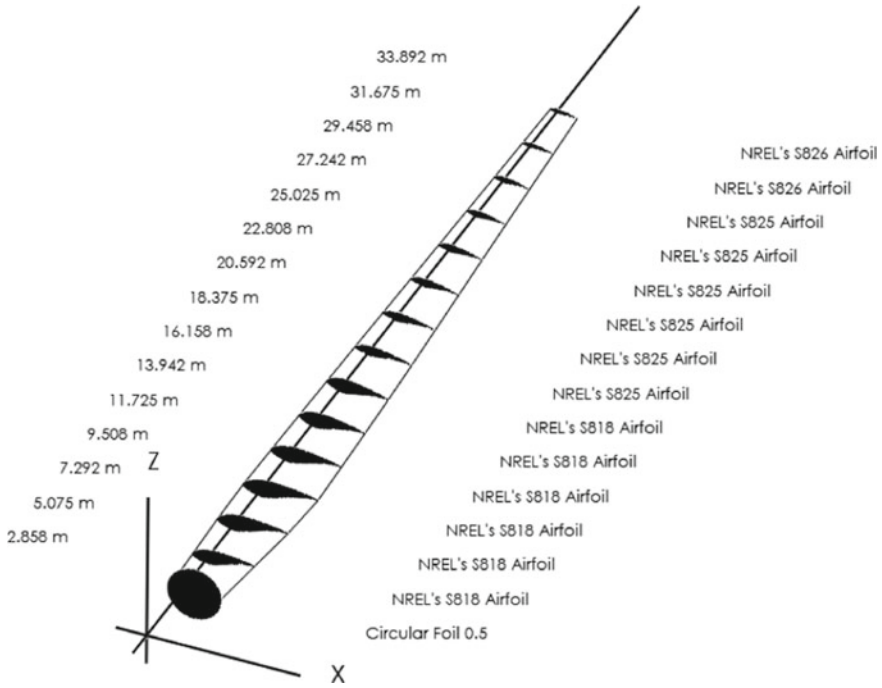
Fig. 1 Airfoil distribution along the span of blade

Here, μ_t turbulent viscosity in sub-grid scale.

The S_{ij} is a rate of strain tensor

$$S_{ij} \equiv \frac{1}{2}\left(\frac{\partial u_i}{\partial x_j} + \frac{\partial u_j}{\partial x_i}\right) \tag{6}$$

Among various sub-scale models such as smagorinsky-lilly, dynamic smagorinsky-lilly, WALE (wall adapting local eddy viscosity), and kinematic viscosity model, the turbulent kinematic energy and dissipation rate model was modeled to find accurate stresses.

Turbulence Kinetic Energy

$$\frac{\partial k}{\partial t} + U_j\frac{\partial k}{\partial x_j} = P_k - \beta^* k\omega + \frac{\partial}{\partial x_j}\left[(v + \sigma_k v_T)\frac{\partial k}{\partial x_j}\right] \tag{7}$$

Specific Dissipation Rate

$$\frac{\partial \omega}{\partial t} + U_j\frac{\partial \omega}{\partial x_j} = aS^2 - \beta\omega^2\frac{\partial}{\partial x_j}\left[(v + \sigma_\omega v_T)\frac{\partial \omega}{\partial x_j}\right] + 2(1 - F_1)\sigma\omega^2\frac{1}{\omega}\frac{\partial k}{\partial x_i}\frac{\partial \omega}{\partial x_j} \tag{8}$$
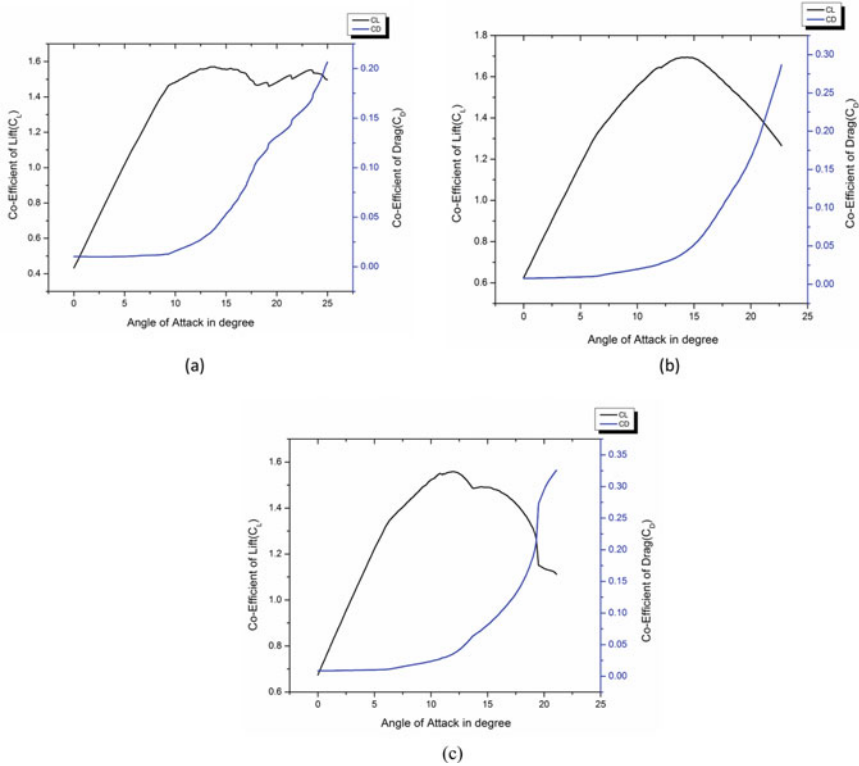
Fig. 2 Co-efficient of lift and drag Vs angle of attack: **a** S818, **b** S825, and **c** S826

Kinematic Eddy Viscosity

$$v_T = \frac{a_1 k}{\max(a_1 \omega, \, SF_2)} \tag{9}$$

2.1 Vortex Generator Configuration

Vortex generator configuration is designed and created based on Wang et al. [8] are shown in the following Equations:

The angle of the VG $(\beta) = 18°$.

The height of the VG $(Hvg) = \left(\frac{1}{100}\right) \times$ chordlength in m.

The length of the vortex generator $(Lvg) = 2 \times Hvg$ in m.

The distance between the trailing edges within a pair $(Svg) = 3 \times Hvg$ in m.

The distance between pairs $(Zvg) = 6 \times Hvg$ in m.
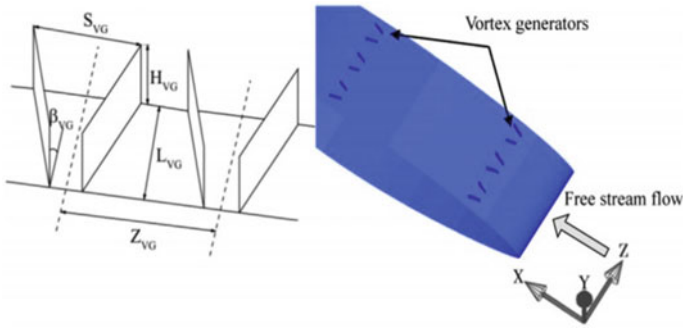
Fig. 3 Vortex generator configuration
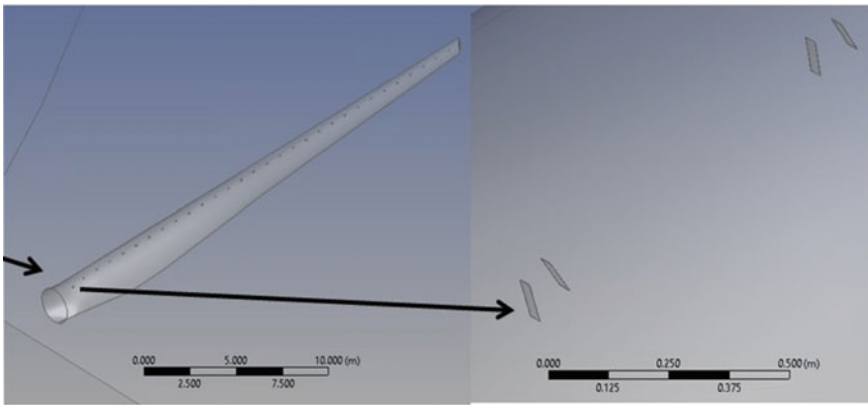
Fig. 4 Vortex generator placement along the blade length

Vortex generators are placed along the length of the Wind PACT blade. The horizontal length and vertical length of vortex generator are 27.43 mm and 54.86 mm, and angle from horizontal axis is 18°. Distance between two vanes is 82.29 mm, and distance between two vortex generator array configurations is 164.58 m (Figs. 3 and 4).

2.2 Mesh Generation and Boundary Conditions

The mesh for the wind turbine CFD analysis is generated using ANSYS watertight machine workflow for better accuracy in CFD analysis shown in Fig. 5. The Blade face sizing and inflation layers applied to have better resolution of boundary layer flow over the blade. Match control 120** rotation was applied for flow domain rotational periodicity. Mesh sensitivity study, i.e., +0.4 m, +0.2 m, +0.1 m, and +
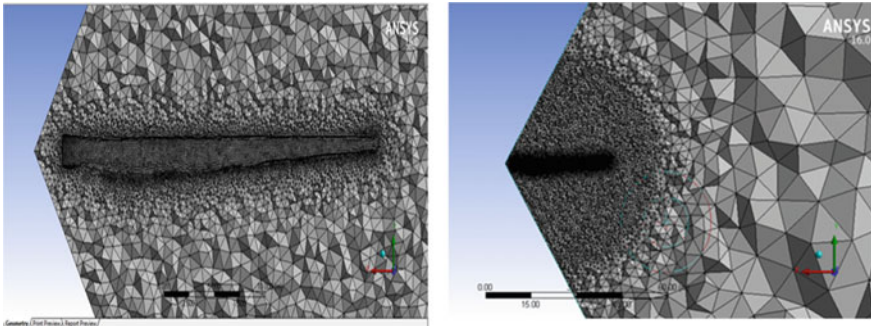
Fig. 5 Mesh generation
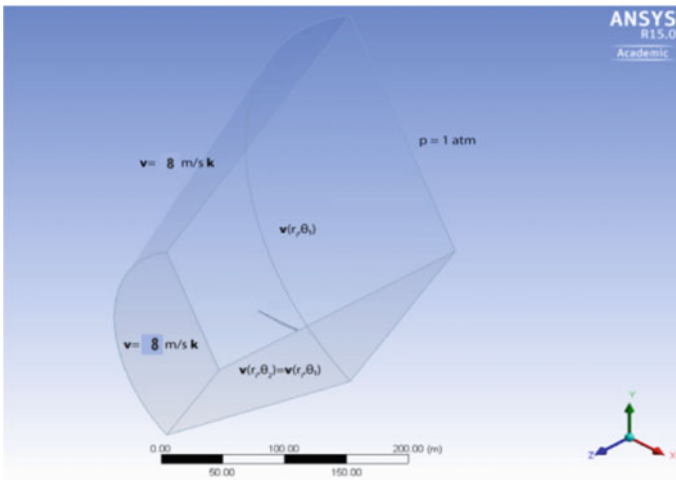
Fig. 6 Boundary conditions

0.05 m blade face sizing, is carried to find appropriate mesh face size at wind turbine blade surfaces. The boundary condition wind turbine CFD analysis is the wind speed 8.0 m/s, rotor rotational speed 15.0 rpm, and pitch angle 02.6° wind turbine blade.

The boundary conditions for this study are mentioned in Fig. 6, the velocity was given as 8 m/s normal to the domain face, and other faces are considered as pressure far fields.

2.3 Solution Method

In our work, $k - \omega$ Shear-Stress-Transport model is opted for turbulence modeling which will be more appropriate for the stimulation of far-field flows and modeling the

boundary layer. This is a subsonic region problem of Mach number below 0.3 Mach, so incompressible 1.225 kg/m^2 constant density for air and constant viscosity 1.7894 × 10^{-5} kg/ms^{-1}. The incompressible RANS which is nothing but the Reynolds-Averaged Navier–Stokes equations are solved with the help of the coupled algorithm which is based on the pressure, which solves the pressure and as well as the momentum-based continuity equations in the form of closely coupled manner which significantly improves the rate of convergence (Ansys Fluent–16.0).

2.4 Convergence Criteria

To verify analysis of the CFD solution, imbalances of the residual values and net mass are examined. The solution is converged when these residual values are below than 10^{-4}, which is the common value used for residual convergence. The verification of the net mass imbalances confirms the convergence. The convergence of the net mass imbalance of an analysis is less than 0.1%.

3 Results and Discussions

Various advantages of wind turbines because of wind turbine vortex generators are discussed below.

3.1 Pressure Distributions

The pressure distributions on various airfoil sections of the wind turbine with and without vortex generators are shown Fig. 7. The low negative pressure is resulted in the rear blade surface due to the large negative pressure on the leading edges of the blade and the large positive pressure next to the leading edge of blade which causes stagnation points shifted to the suction surface because of reduced air velocity. Pressure sign reversed by pitching action and also results in faster moving airflow over the lower side of the blade lead to low suction on the pressure surface.

3.2 Velocity Contour

The velocity contour on various airfoil sections of the wind turbine with and without vortex generator are shown Fig. 8. The flow separation on airfoil sections without vortex generators can be visualized on the velocity contour. There is flow separation on one-third of the chord of the airfoil of the wind turbine. Because of vortex generator
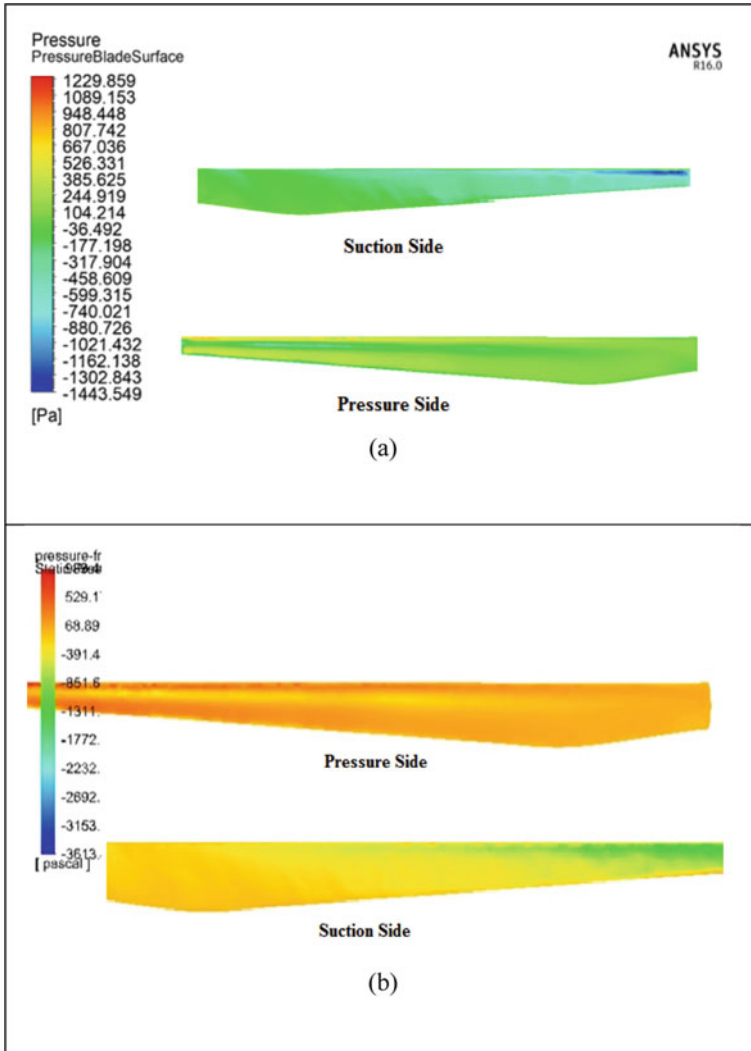
Fig. 7 Pressure distribution along blade **a** without VF **b** with VF

application on airfoils of turbine blade, there is stall delay and also stabilizes the flow over the blade surface. The above-discussed effects will result in an increase in performance of the wind turbine.

Velocity Contour at X= 5.075m NREL'S S818 Airfoil	Velocity Contour at X= 5.075m NREL'S S818 Airfoil with VG
Velocity Contour at X= 11.72m NREL'S S818 Airfoil	Velocity Contour at X= 11.72m NREL'S S818 Airfoil with VG
Velocity Contour at X= 20.59m NREL'S S825 Airfoil	Velocity Contour at X=20.59m NREL'S S825 Airfoil with VG
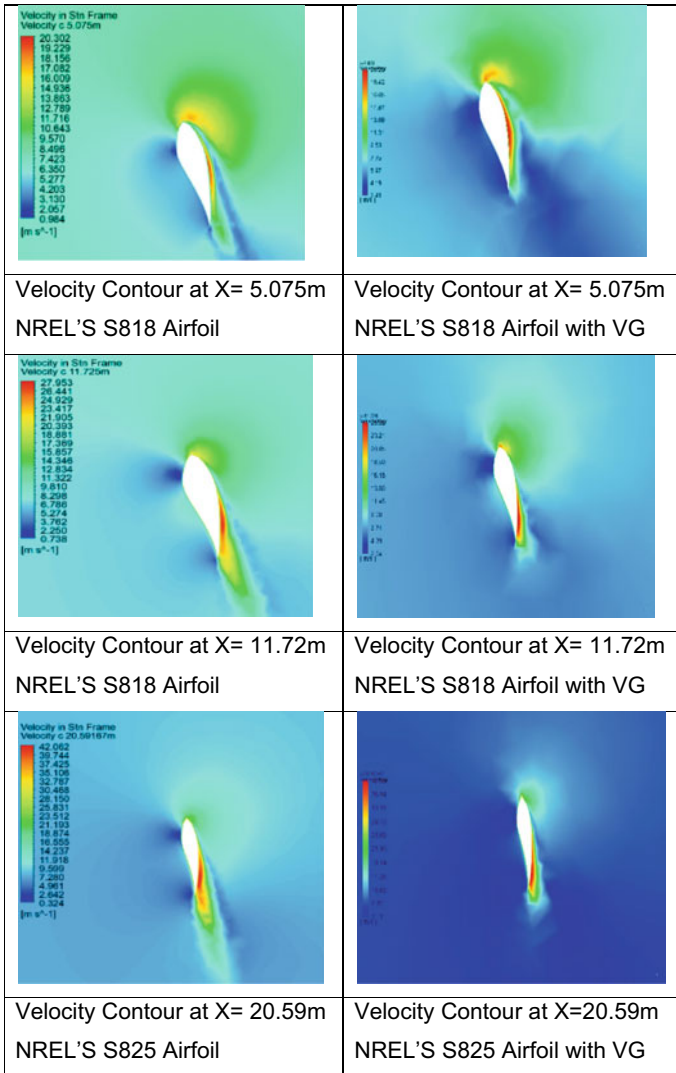
Fig. 8 Velocity distribution around airfoil cross section with and without VG

3.3 Velocity Vector

From the velocity vector, there is an increase in velocity found when the blade with VG along the span of blade. The variation of velocity along the blade was in accordance with the one-dimensional mathematical calculation of the wind turbine. Velocity vector is shown in Fig. 9.
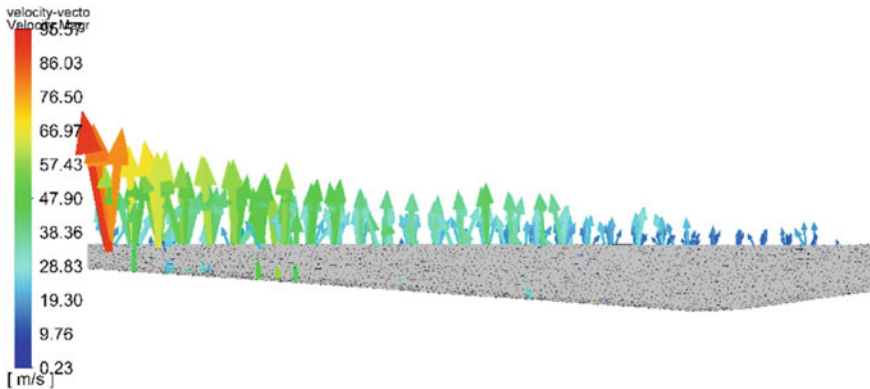
Fig. 9 Velocity vector on blade surface with vortex generator

4   Conclusion

In this study, the aerodynamic effects of the vortex generator in the wind turbine blade are visualized by using computational approach. The WindPACT 1.5-megawatt turbine is taken as a reference and has S818+, S825+, and S826+ airfoils, and vortex generators are placed along the length of blade. The CFD analysis is done for the wind speed 08 m/s, rotor rotational speed 015 rpm, and pitch angle 02.6°. For turbulence modeling, the $k - \omega$ SST model is used and various analyses were done to ensure mesh independency. The local airfoil's pressure and velocity are compared and discussed about the wind turbine blades in two different cases which consist of vortex generators and which does not have vortex generators. This study shows the results in flow stability and decrease in flow separation and stall of the wind turbine blade in which the vortex generators are placed along the length of the turbine. Because of this aerodynamic effect of vortex generator, the performance of turbine was increased.

References

1. Abbot IH, Von Doenhoff AE, Stivers LS (1945) Summary of airfoil data
2. Baker JP, Mayda EA, van Dam CP (2006) Experimental analysis of thick blunt trailing-edge wind turbine airfoils. J Sol Energy Eng 128:422. https://doi.org/10.1115/1.2346701
3. Barlow JB, Rae WH, Pope A (1999) Low-speed wind tunnel testing, 3rd edn. Wiley, New York
4. Griffin DA (1996) Investigation of vortex generators for augmentation of wind turbine power performance. National Renewable Energy Lab., Golden, CO
5. Johnson SJ, Berg DE (2008) Active load control techniques for wind turbines. Sandia National Laboratories
6. Khoshvaght-Aliabadi M, Sartipzadeh O, Alizadeh A (2015) An experimental study on vortex-generator insert with different arrangements of delta-winglets. Energy 82(C):629–639

7. Dykes KL, Rinker J (2018) WindPACT reference wind turbines. United States: N. p., 2018. Web. https://doi.org/10.2172/1432194
8. IRENA (2019) Renewable capacity statistics (2019) Report. International Renewable Energy Agency (IRENA)

Design, Development, and Validation of an Intake System for an FSAE Racecar

Saliq Shamim Shah, Kshitij Singh, Leenus Jesu Martin, and M. Jerome Stanley

Abstract The aim of this paper is to design the intake system for an engine to optimize the performance of restricted KTM 390-supported powertrains of a Formula Society of Automotive Engineers (FSAE) combustion car of team Camber Racing. Keeping in a view the safety of students, power produced by the engine is restricted by inclusion of a 20 mm air restrictor. It is made mandatory for all the student teams to participate in the racing event. With a goal of exploring and understanding various parameters involved in modeling a 20 mm air restrictor which is to be incorporated in the intake of 390 cc KTM single-cylinder engine, the required engine performance need to be attained. Analysis is done with the help of the CFD software ANSYS Fluent. With the incorporation of air restrictor upstream the intake system, pressure loss is observed. This in turn reduces the volumetric efficiency of the engine significantly. The goal of the intake system was to reduce the pressure loss caused due to restriction and to provide a reservoir to act as an infinitely large reservoir of air, to improve the breathing characteristics of engine (Hadjkacem et al., Arab J Sci Eng 2018). The constraint was engine response delay. The volumetric efficiency could have been further improved but would have been detrimental to engine response time (Mattarelli and Rinaldini in SAE Technical Paper 01-0833:2012, 2012 [1]).

Keywords FSAE · Intake · Plenum · IC engine · KTM 390

S. S. Shah · K. Singh
Department of Mechanical Engineering, College of Engineering and Technology, SRM Institute of Science and Technology, Tamil Nadu, Kattankulathur, Kanchipuram 603203, India

L. J. Martin · M. Jerome Stanley (✉)
College of Engineering and Technology, SRM Institute of Science and Technology, SRM Nagar, Kattankulathur, Kanchipuram, Chennai, Tamil Nadu 603203, India
e-mail: stanleystallion07@gmail.com

1   Introduction

Volumetric efficiency is a parameter that defines the performance of an internal combustion engine [2]. Going by the rule of thumb, higher the volumetric efficiency higher the power. That being the reason of the rule incorporated by the Formula Society of Automotive Engineers hereafter referred as FSAE. Keeping in view the safety of students and to challenge the engineering caliber of students, the air restrictor of 20 mm was made a necessity for an FSAE car to restrict the power that IC engine can produce. According to the rules, the intake setup for a naturally aspirated FSAE car should be as shown in Fig. 1 and that in turbocharged car is shown in Fig. 2.

Taking in the consideration of the team goals of FSAE combustion team Camber Racing of building a "Light Weight Agile Car," the design decision of using a naturally aspirated system was done. According to the rules, the design had to be throttle body followed by a restrictor, a plenum, a runner, and finally the engine. Accordingly, the design was started.
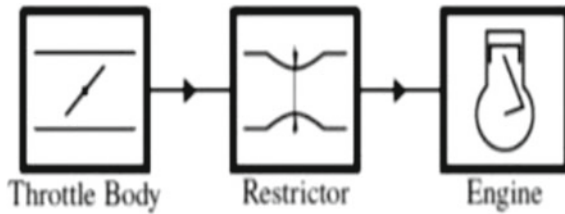
Fig. 1   FSAE rules for naturally aspirated engine
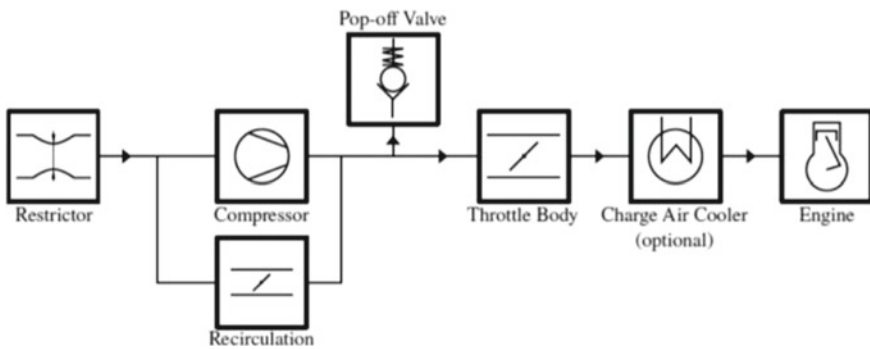
Fig. 2   FSAE rules for turbocharged engine

2 Restrictor

While designing a restrictor, there were two ways to do it. First one being the Orifice plate and other being the Converging Diverging Nozzle [3]. The aim of the design was to maximize the pressure recovery between the restriction and the restrictor outlet. There was a significant drop in pressure of air since it flows through the restriction. The goal was to gradually bring the air back to as high a pressure as possible near the engine inlet so as to maximize volumetric efficiency of the engine.

Orifice Plate

This is a plate with a circular hole in the middle. In this scenario, "*vena contracta*" is observed. This is the decrease in cross section area of the flow at the orifice. This effect brings two issues. Firstly, since the cross section for flow is decreased the flow gets choked much more "quickly" than otherwise. Secondly since the flow through the restriction effectively increases, the pressure becomes lower than before. As a result, greater pressure recovery would be needed. It had a coefficient of discharge of 0.6.

Converging Diverging Nozzle

In the case of a convergent divergent nozzle, the flow is gradually accelerated as it is sent to the restriction and then the flow gradually regains the pressure as it exits out through the diverging section. The downside of CD nozzle was that it induced higher amounts of drag when compared to the orifice plate. This is because it has more surface area in contact with the flow. It had coefficient of discharge of 0.99 which is way higher than orifice plate.

Comparison of orifice plate to the CD nozzle was done; it was evident that the CD nozzle recovers pressure more effectively than the orifice plate. The CD nozzle has a higher coefficient of discharge than the orifice plate. Hence, we decided to make our restrictor in the form of a Convergent Divergent nozzle. After the decision was done, ANSYS fluent model was created to understand and quantify the pressure losses. Diverging angles of 6°, 9°, 12°, and 15° were studied (Figs. 3 and 4), and the results were tabulated in Table 1.

Hence, a diverging angle of 6° was selected for the restrictor. When the downstream pressure in the orifice is decreased and the mass flow rate of fluid keeps increasing until it reaches the velocity of air reaches mac 1 at the throat. On further decreasing the pressure downstream, the mass flow rate stagnates and that point is said to be choke point. Using the compressible flow equation shown below, we can calculate the mass flow rate at choking point for a 20 mm restriction

$$\dot{m} = \frac{A P_t}{\sqrt{T_t}} \times \sqrt{\frac{\gamma}{R}} M \left(1 + \frac{\gamma - 1}{2} M^2\right)^{-\frac{\gamma+1}{2(\gamma-1)}}$$

Here, the values were taken as follows:
$P_t = 101325 \ Pa$ $T_t = 300 \ K$ $\gamma = 1.4$
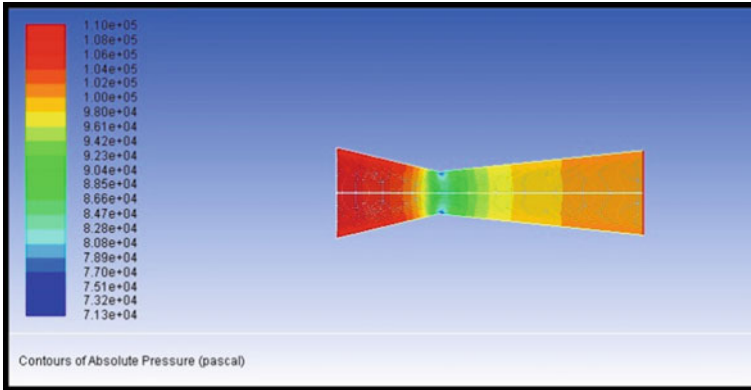
Fig. 3 Pressure contour for 6°
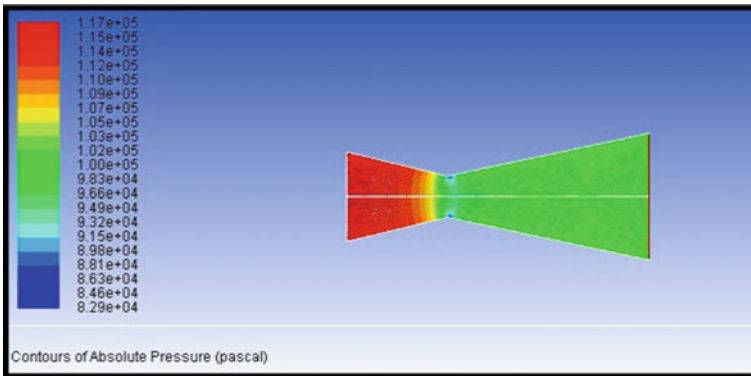
Fig. 4 Pressure contour for 12°

Table 1 Diverging angles

S. No.	Diverging angles (°)	Pressure loss (Pa)
1	6	298.845
2	9	381.921
3	12	487.63
4	15	568.378

R (air) $= 0.287$ kJ/Kg-K

$A = \pi r^2 = 0.000314$ m^2 [Here $r = 20$ mm].

$M = 1$

From the calculations, the mass flow rate was found to be 0.074 kg/s.

For KTM 390 engine, RPM at the Choke Point

RPM $= x$

CPM = $x/2$

CPS = Intake Strokes/s = $(x/2)/60 = x/120$

ρ = Density = 1.2 kg/m^3

$\dot{m}$ = 0.074 kg/s

Volume of air/sec= $(x/120)(373.2/1000)$ L

$(0.074/0.00012) = (x/120)(373.2/1000)$

$x = 19{,}870$ RPM

RPM: Rotation per minute

CPM: Cycle per minute

CPS: Cycle per second

From the calculations, the choke point RPM was found to be 19,870 RPM.

3 Plenum

To decrease the impact of the restrictor on airflow, it is important to limit the most fast moving air particles. An approach to achieve this goal is to put a plenum between the restrictor and the prime mover. The plenum permits to limit the pulsating flow through the restrictor. As a result, the pressure loss at the restrictor diminishes and the mass flow rate to the prime mover ascents, thus increasing the volumetric efficiency of the IC engine. Higher the volume of plenum, higher the power produced by the engine. Then again, with increase in volume of plenum the engine response time increases and thus the concept of throttle lag. If put in those exact words, power requested by the driver is supplied after a time lag, thus detrimental to the driveabiltiy. A similar issue happens during decelerations when the brake torque helps reduce vehicle speed. The restrictor on the intake system affects single-cylinder engines more than multi-cylinder engines, due to their great pulsating mass flow. To determine the plenum volume, an iterative experimental setup is manufactured and implemented on team Camber Racing's FSAE racecar. A PVC model of intake is manufactured, and the volume is reduced in increments. A data logger AIM EVO 4 of the team is used to monitor manifold absolute pressure (MAP) (Fig. 6), throttle position (TP). The MAP sensor is placed on the runner as near to the flange of engine as possible considering packaging constraints. A compromise is done between MAP and the engine response time by monitoring throttle position and RPM (Fig. 7), thus fulfilling the initial goals of the plenum (Fig. 5).

The plenum was decided to be 2.8 L. The shape of the plenum aids in having a better flow in the intake system improving the volumetric efficiency. Two designs of plenum were investigated, one was a rectangular-shaped plenum while the other was Bezier curve-based plenum. The volume and length of the two designs were kept same, and CFD analysis was done along with the restrictor portion. A bell mouth was used at the inlet end of runner in the plenum. This was done in order to decrease vena contracta effect [4, 5]. From the analysis, the outlet velocity of the Bezier curve plenum was greater than the rectangular one [6] (Figs. 8, 9, 10, and 11).

Fig. 5 PVC Intake iterative setup

Fig. 6 RPM VS Manifold absolute pressure table
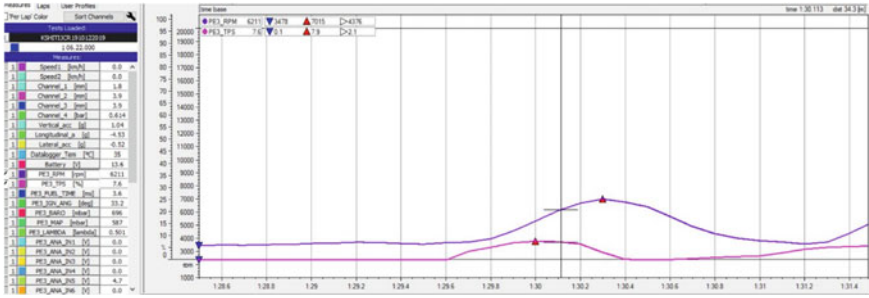
Fig. 7 Throttle position versus RPM plot
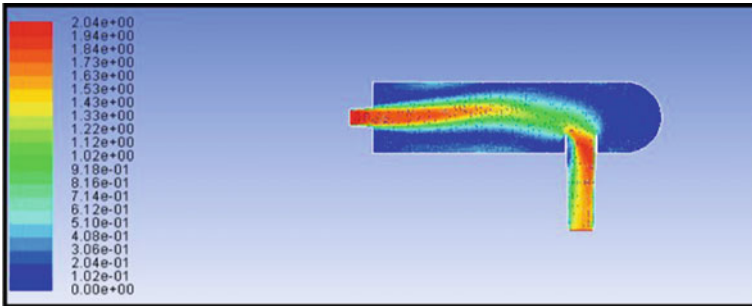
Fig. 8 Velocity contour for rectangular plenum without bell mouth
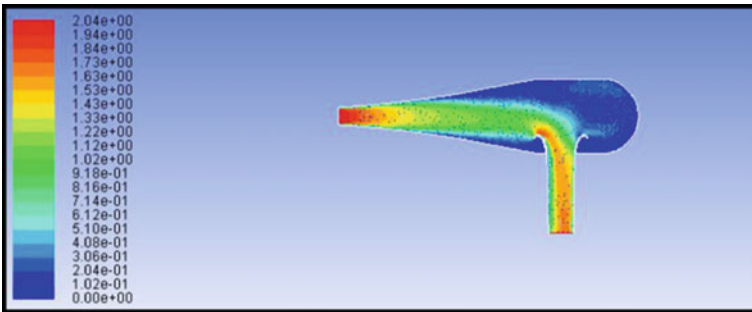
Fig. 9 Velocity contour Bezier curved plenum with bell mouth

Structural Design

An accelerometer was placed on the end of the plenum, and the car was run. Maximum acceleration was found to be 3G's. A structural simulation was run to study stress, strain, and FOS on the plenum (Figs. 12 and 13).

Various materials and manufacturing techniques were taken into consideration (Table 2). The manufacturing of the plenum was done through SLS process using
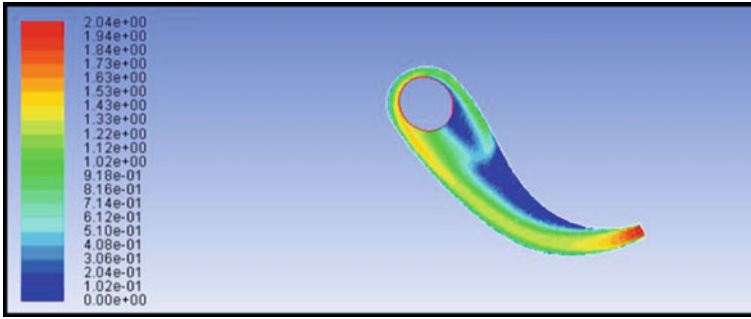
Fig. 10 Velocity contour Bezier curved plenum with bell mouth and a bend
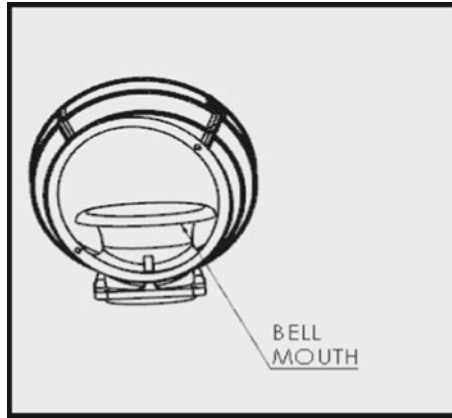
Fig. 11 Bell Mouth
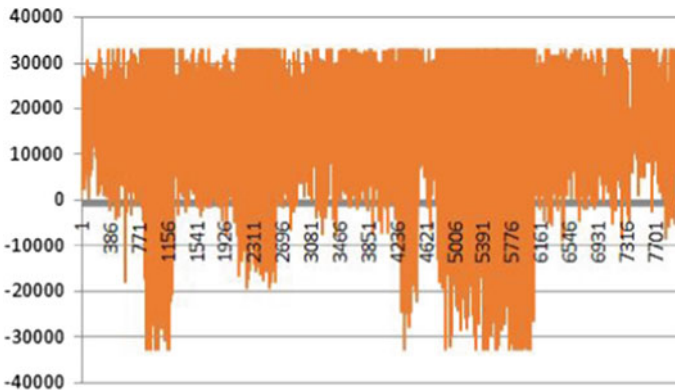
Fig. 12 Accelerometer plot
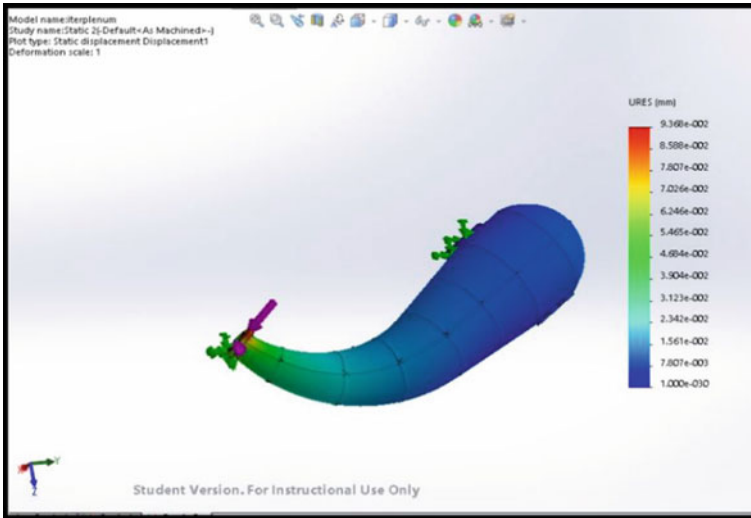
Fig. 13 Finite element analysis of the plenum

Table 2 Material decision matrix

Process	Nylon 12 (SLS)	PC (FDM)	PC-ABS (FDM)	ULTEM 9085 (FDM)
Tensile strength (MPa)	48	68	41	**72**
Flexural strength (MPa)	47	104	68	**115**
Heat deflection temperature	95	138	96	**153**
Tensile modulus (MPa)	1650	2280	Na	na
Flexural modulus (MPa)	1500	2234	1931	**2507**
Fatigue resistance	High number of cycles	very low	Average	Average
Cost and availability	Average/common	Average/common	Average/abundant	High/rare

Nylon12 material. This was chosen over other methods like FDM because of the superior finish and quality of the product. Conventional techniques were not used due to the complex geometry and its high weight.

4 Runner

Runner is essentially a connection between plenum and engine. The Helmholtz frequency is the frequency at which the "Ram effect" happens in the intake runner, subsequently giving a more prominent mass of air into the chamber; thus, the volumetric efficiency and subsequently other performance parameters like power torque curve get enhanced. The relationship is such that the frequency of Helmholtz is double the RPM of the engine; the Ram impact builds the volumetric efficiency. The thought was to decide the Helmholtz frequency for a particular runner length for a particular RPM band for which this length offers the highest volumetric efficiency. For drivetrain targets of the team Camber Racing, the operating RPM band was selected to be 8000 RPM. The valve-timing diagram of the KTM 390 engine was studied. The time for closing of intake valve at 8000 RPM is studied. Speed of acoustic was found using a data book at ambient temperatures. Thus, the wavelength of wave is found. It was found to be 1.88 m. This was fundamentally impossible to package in the template of car. Considering the packaging, 8th harmonic of the said wave was used. It was calculated to be 0.235 m, and this could be effectively packaged. Hence, 0.235 m of runner length was selected. The stock runner was reverse engineered, and the injector angle was found. It was found to be 36.5° with respect to the runner axis. A MAP sensor was placed as close to the engine flange as possible so as to get the precise pressure data (Fig. 14).

The runner was a crucial part of the intake in which spontaneous fires could occur; hence, a fire- and fuel-resistant material ULTEM 9085 was considered but due to the high cost and lack of availability an aluminum runner was made. The aluminum portion of runner length was 107 mm because of the port on the engine had a length of 79 mm and bell mouth of 41 mm length was integrated with the plenum.

Fig. 14 KTM 390 Valve timing diagram
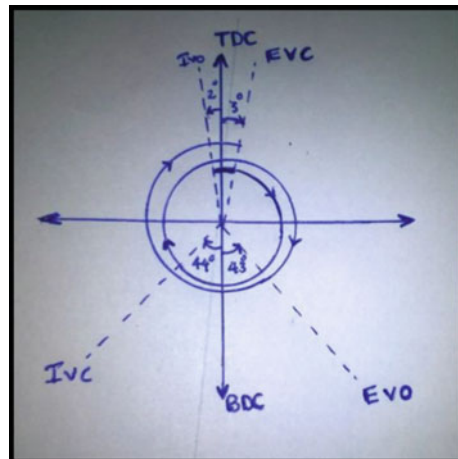
Table 3 Comparison

Parameter	KTM 390 stock	Camber racing's racecar
Peak power	42.9 BHP @ 9000 rpm	47.5 BHP@ 9500RPM
Peak torque	37 Nm@ 7000RPM	34.1 Nm @ 9500RPM

Fig. 15 Commercial eddy current dynamometer

5 Validation

To validate the intake system and powertrain as a whole, Camber Racing's racecar was taken to a chassis eddy current dynamometer, and multiple runs were done on part load and full load conditions. The comparative data of stock KTM 390 and Camber Racing's powertrain design has been tabulated in Table 3. On observing the power and torque data of stock KTM 390 and customized KTM 390 powertrain, it was observed that even after running restricted intake setup as mandated by the FSAE rules, higher power figures were achieved. That was possible only if higher volumetric efficiency is achieved and hence the intake system was validated [5] (Figs. 15 and 16).

6 Conclusion

Formula society of automotive engineers imposes a rule of incorporation of 20 mm restrictor into the intake system downstream the throttle valve, which is detrimental not only to pressure downstream the restrictor but also the volumetric efficiency of the engine. This poses an engineering challenge to recover the pressure effectively while maintaining the engine response. This paper undertakes the challenge to
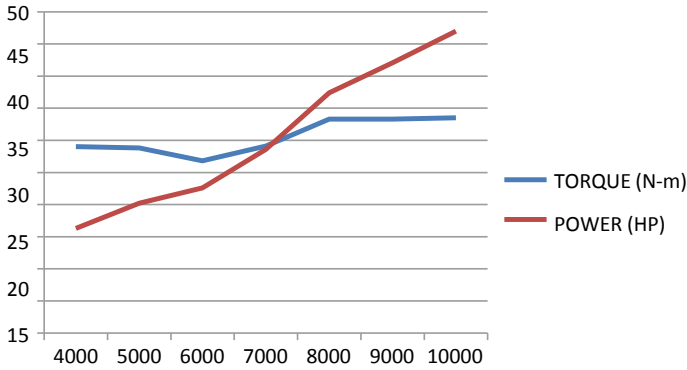
Fig. 16 Power torque graph of camber racing customized powertrain

design, develop, and validate an intake system to model the restrictor in a way that could maximize the pressure recovery after the restrictor and improve the volumetric efficiency of the engine while maintaining the engine response. In this paper, work was to make a best possible compromise between the maximum power and engine response time. On analyzing the data, it was found that the engine response time was found to be 0.02 s (Figs. 17 and 18).

Fig. 17 CAD model of Intake system
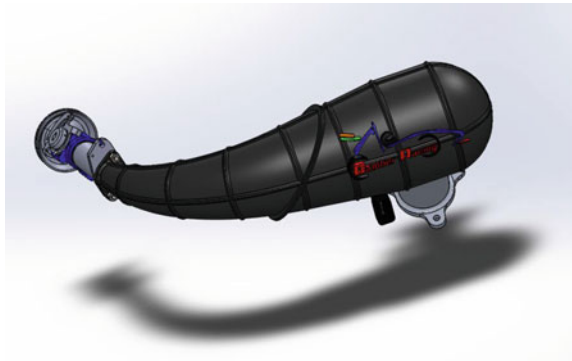
Fig. 18 Real Intake system

References

1. Hadjkacem S, Ali M, Mohamed J, Abid S (2018) Volumetric efficiency optimization of manifold with variable geometry using acoustic vibration for intake manifold with variable geometry in case of LPG-enriched hydrogen engine. Arab J Sci Eng
2. Biancolini M (2007) Engine/vehicle matching for a FSAE race car. SAE Technical Paper 2007: 01-3541
3. Mattarelli E, Rinaldini C (2012) Development of a high performance engine for a formula SAE Racer. SAE Technical Paper 2012: 01-0833
4. Hamilton L, Lee J (2009) The effects of intake plenum volume on the performance of a small normally aspirated restricted engine. SAE Int J Engines 1:1312–1318
5. Cauchi J, Farrugia M, Balzan N (2006) Engine simulation of a restricted FSAE engine, focusing on restrictor modelling. SAE Technical Paper 2006: 01-3651
6. Yan F, Wang J (2012) Pressure-based transient intake manifold temperature reconstruction in diesel engines. Control Eng Pract 20:531–538

An Efficient Lattice Boltzmann Model for 3D Transient Flows

Raoudha Chaabane, Abdelmajid Jemni, and Fethi Aloui

Abstract In this paper, we report on the development and the implementation of the mesoscopic approach based on the Lattice Boltzmann method (LBM) in order to simulate three-dimensional coupled modes of thermal and fluid flows. First the lattice Boltzmann method (LBM) has been used to solve transient heat conduction problems in 3D Cartesian geometries. To study the suitability of the LBM, the problem has also been extended to deal with a coupled conduction-radiation heat transfer problem in a three-dimensional cavity containing an absorbing, emitting, and scattering medium. In this case, the radiative information is obtained by solving the radiative transfer equation (RTE) using the control volume finite element method (CVFEM). Second, a 3D incompressible thermal lattice Boltzmann model is proposed to solve 3D incompressible thermal flow problems. A D3Q19 particle velocity model is incorporated in our thermal model where the density, velocity, and temperature fields are calculated using the two double population lattice Boltzmann equation (LBE). It is indicated that the present thermal model is simple and easy for implementation. It is validated by its application to simulate the 3D natural convection of fluid in a cubical enclosure, which is heated differentially at two vertical side walls. In order to test the efficiency of the developed method, comparisons are made for the effect of Rayleigh number on the temperature and velocity distributions in the medium. Validation and the analysis of numerical results of flow and thermal fields in the cubic cavity are at Rayleigh numbers of 10^3–10^6. In all studied cases, it is found that the numerical results agree well with the results reported in previous studies. The 3D LBGK algorithm presented here can also be extended for a convective radiative problem in a three-dimensional grey participating medium in the presence of computers with sufficient memory and computational power to perform well-resolved calculations of the hybrid 3D-proposed model.

R. Chaabane · A. Jemni
National Engineering School of Monastir (ENIM), LESTE Laboratory, University of Monastir, Avenue Ibn El Jazzar, 5019 Monastir, Tunisia

F. Aloui (✉)
Université Polytechnique Hauts-de-France (UPHF), LAMIH, CNRS UMR 8201, INSA Hauts-de-France, 59313 Valenciennes, France
e-mail: fethi.aloui@uphf.fr

Keywords LBM · Conduction · Convection · Radiation

1 Introduction

Numerical modelling of the coupled steady conduction or convection and radiation heat transfer problem has been an area of great interest because of its broad applications in engineering. It has numerous applications in the area of fire protection, glass processing, industrial furnaces, Fuel cell, and optical textile fibre processing [1].

Nowadays, solutions of multidimensional transient conductive and radiative transfer are an active research subject because of their practical and interesting engineering applications. Several works are available dealing with combined conduction and radiation heat transfer in 1D and 2D geometries [2–6]. Interaction of transient conduction radiation was found to be interesting, and ignoring one of these modes could result considerable deviation from real situation. The LBM-CVFEM [6] shows very successful results from the viewpoint of accuracy, grid, and CPU time compatibility. It is proved to be a reliable future numerical tool for combined heat transfer problems in engineering applications.

2 Numerical Analysis

Lattice Boltzmann method appears as a powerful mesoscopic tool for solving Energy problems in complex geometries. Modelling different transport phenomena that occur inside energetic systems have been gaining interest during the last years. The most realistic model has to be a 3-dimensional, non-steady state and with the coupling of the different transport phenomena over all the range of scales from the micro- to the macroscale. When modelling energetic systems at micro or macro scale, it is important to deeply understand the behaviour of the fluids throughout the media present in the different layers of the energetic configuration geometry. Then solving transport phenomena in more realistic complex geometries is considered one of the problems to deal with. Lattice Boltzmann method (LBM) can handle with problems at different scales and has proven to be suitable for solving problems in wide range of energetic configurations media, and modelling different transport phenomena in such complex area of energy research. The aim of this work is to show the solution of physical problems using the LBM.

3 Conduction Radiation

The unsteady energy conservation equation consisting of conduction and radiation can be expressed as

$$\rho c_p \frac{dT}{dt} = \nabla.(k\nabla T - \overrightarrow{q_R})$$ (1)

It is assumed that the thermal conductivity k of the emitting, absorbing, and scattering medium is independent of temperature. ρ is the density, c_p is the specific heat, and $\overrightarrow{q_R}$ represents the radiative heat flux given by:

$$\overrightarrow{q}_R = \int_{4\pi} I\overrightarrow{\Omega} d\Omega$$ (2)

where I is the radiative intensity which can be obtained by solving the Radiative Transfer Equations (RTE).

The divergence of radiative heat flux is given by

$$\overrightarrow{\nabla}.\overrightarrow{q}_R = k_a(4\pi I_b - G)$$ (3)

$I_b = \sigma T^4/\pi$ is the blackbody intensity, G is the incident radiation and k_a is the absorption coefficient.

For the RTE, an absorbing, emitting, and scattering grey medium can be written as

$$\overrightarrow{\nabla}.(I(s, \overrightarrow{\Omega}).\overrightarrow{\Omega}) = -(k_a + k_d)I(s, \overrightarrow{\Omega}) + k_a I_b(s)$$
$$+ (k_d/4\pi) \int_{\Omega'=4\pi} I(s, \overrightarrow{\Omega'})\Phi(\overrightarrow{\Omega'} \to \overrightarrow{\Omega})d\Omega'$$ (4)

where $I(s, \overrightarrow{\Omega})$ is the radiative intensity, which is a function of position s and direction $\overrightarrow{\Omega}$; k_d is the scattering coefficient, and $\Phi(\overrightarrow{\Omega'} - \overrightarrow{\Omega})$ is the scattering phase function from the incoming $\overrightarrow{\Omega'}$ direction to the outgoing direction $\overrightarrow{\Omega}$.

The term on the left-hand side represents the gradient of the intensity in the direction. The three terms on the right-hand side represent the changes in intensity due to absorption and out-scattering, emission, and in-scattering, respectively [6–9]. The radiative boundary condition for Eq. (4), when the wall bounding the physical domain is assumed grey and emits and reflects diffusely, can be expressed as

$$I_w(\overrightarrow{\Omega}) = (\varepsilon_w \sigma T_w^4/\pi)$$
$$+ ((1 - \varepsilon_w)/\pi) \int_{\overrightarrow{\Omega'}.\overrightarrow{n}_w<0} I_w(\overrightarrow{\Omega'})\left|\overrightarrow{\Omega'}.\overrightarrow{n}_w\right| d\Omega' \text{ if } \overrightarrow{\Omega'}.\overrightarrow{n}_w > 0$$ (5)

$\overrightarrow{n}_w$ is the unit normal vector on the wall, and ε_w represents the wall emissivity [10, 11].

In the LBM, the equation describing transient conduction-radiation heat transfer [12–19] is:

$$f_i(\overrightarrow{r} + \overrightarrow{c_i}\,\Delta t, t + \Delta t) = f_i(\overrightarrow{r}, t) - \frac{\Delta t}{\tau}[f_i(\overrightarrow{r}, t) - f_i^{(0)}(\overrightarrow{r}, t)]$$

$$- (\frac{\Delta t}{\rho c_p})w_i(\nabla.\overrightarrow{q_R}(\overrightarrow{r}, t)) \quad i = 0, .., 18 \qquad (6)$$

$$\tau = \frac{3\alpha}{|\overrightarrow{e_i}|^2} + \frac{\Delta t}{2} \qquad (7)$$

The velocities $\overrightarrow{e_i}$ and their corresponding weights ω_i in the D3Q19 (Fig. 1) lattice are the following:

$$\overrightarrow{e}_0 = (0, 0, 0), \ \overrightarrow{e}_{1,2} = (\pm 1, 0, 0).C, \ \overrightarrow{e}_{3,4} = (0, \pm 1, 0).C,$$
$$\overrightarrow{e}_{5,6} = (0, 0, \pm 1).C, \ \overrightarrow{e}_{7...10} = (\pm 1, \pm 1, 0).C,$$
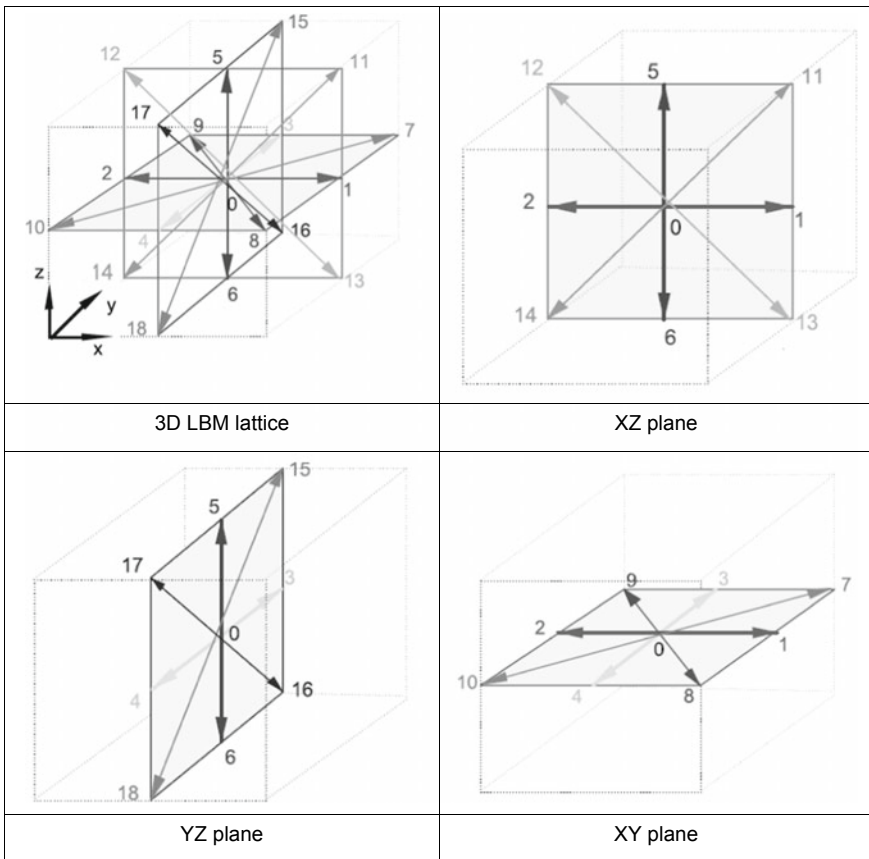
Fig. 1 D3Q19 LBM projection discretisation scheme

$$\overrightarrow{e}_{11\ldots14} = (\pm1, 0, \pm1).C, \ \overrightarrow{e}_{15\ldots18} = (0, \pm1, \pm1).C \tag{8}$$

$$\omega_0 = \frac{1}{6}, \ \omega_{1\ldots6} = \frac{1}{18}, \ \omega_{7\ldots18} = \frac{1}{36} \tag{9}$$

In the present problem, temperature is computed from

$$T(\overrightarrow{r}, t) = \sum_{i=0}^{b} f_i(\overrightarrow{r}, t) \tag{10}$$

To process Eq. (6), the required equilibrium distribution $f_i^{(0)}$ is given by

$$f_i^{(0)}(\overrightarrow{r}, t) = \omega_i T(\overrightarrow{r}, t) \tag{11}$$

The energy equation is subjected to Dirichlet boundary condition. To express this condition, the bounce-back concept in the LBM in which particle fluxes are balanced at any point on the boundary was used. For 1D and 2D geometries, implementations of the temperature boundary conditions in the LBM have been explained in the literature [12]. In the present work, procedures described in [12] have been followed.

4 Free Convection

The geometry and the coordinate system are illustrated in Fig. 2. The enclosure is simply represented by a rectangular prism with the height H, width, and length L.

Fig. 2 The geometry and the coordinate system of cubic enclosure
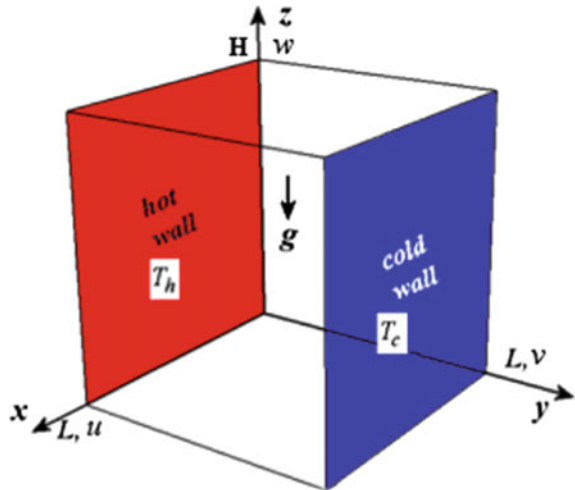
The left and right lateral walls, as shown in Fig. 12, are kept at uniform T_h and T_c, respectively. Other walls are assumed to be adiabatic. The temperature difference between the hot and cold surfaces promotes the buoyancy driven flow inside the enclosure. The temperature difference is also assumed to be small enough so that the Boussinesq approximation is valid.

The known CFD steady state equations for a Newtonian fluid for continuity, the momentum equations, and the energy equation will be simulated by the mesoscopic approach (LBM).

For computation of density and velocity fields, the governing lattice Boltzmann equation is given by [1, 16, 17].

$$
\begin{aligned}
f_k(\overrightarrow{r} + \overrightarrow{c_k}\,\Delta t, t + \Delta t) &= f_k(\overrightarrow{r}, t) \\
&\quad - \frac{\Delta t}{\tau_v}[f_k(\overrightarrow{r}, t) - f_k^{\mathrm{eq}}(\overrightarrow{r}, t)] + \Delta t\, F, \quad k = 0, .., 8
\end{aligned}
\tag{12}
$$

where f_k are the particle distribution function defined for the finite set of the discrete particle velocity vectors $\overrightarrow{c_k}$. The collision term Ω_k on the right-hand side of Eq. (12) uses the so-called BGK approximation [18].

Where f_k^{eq} is the local equilibrium distribution function that has an appropriately prescribed functional dependence on the local hydrodynamic properties and τ_v is the relaxation time defined as:

$$
\tau_v = \frac{1}{2} + \frac{3\nu}{c^2 \Delta t}
\tag{13}
$$

F represents the external force term given by:

$$
F = \left[\frac{(\rho \beta_T g (T - T_m) \overrightarrow{j}).(\overrightarrow{c_k} - \overrightarrow{u})}{RT} \right] f_k^{\mathrm{eq}}
\tag{14}
$$

where the unit vector $\overrightarrow{j}$ is in a direction opposite to gravity, T_m is the mean temperature, g is the gravity acceleration, β_T is the volumetric thermal expansion coefficient and ρ is the density of the fluid at the mean temperature.

The macroscopic density ρ and the velocity $\overrightarrow{u}$ are calculated as follow:

$$
\rho(\overrightarrow{r}, t) = \sum_k f_k(\overrightarrow{r}, t)
\tag{15}
$$

$$
\overrightarrow{u}(\overrightarrow{r}, t) = \sum_k \overrightarrow{c}_k f_k(\overrightarrow{r}, t) / \rho(\overrightarrow{r}, t)
\tag{16}
$$

5 Results and Discussions

5.1 Validation with Pure 3D Transient Conductive Case

In a pure transient heat conduction transfer problems, a 3D cubical enclosure of unit length is considered. With a D3Q19 lattice Boltzmann method, steady state conditions were assumed to have been achieved when the temperature difference between two consecutive time levels at each lattice centre did not exceed 10^{-6}. Non-dimensional time was defined as $(\xi = \alpha\beta^2 t)$, and $\Delta\xi$ was taken as 10^{-4}. To check the accuracy of the present D3Q19 LBM algorithm, results are compared with results of literature using a D3Q15 LBM algorithm [19]. In this case, initially the initial condition is $T(x, y, z, 0) = T_0$.

The imposed boundaries conditions are $T(x, y, Z, t) = T(0, y, z, t) = T(0, y, z, t) = T(0, y, z, t) = T(X, y, z, t) = T(x, 0, z, t) = T(x, Y, z, t) = T_0$ and $T(x, y, 0, t) = T_{hot}$.

In the present D3Q19 LBM algorithm, boundary temperatures $T_{hot} = T_{ref}$ and other walls are at $T_i = 0.25 T_{ref}$. In Fig. 3, results are generated for $31 \times 31 \times 31$ lattices.

In Fig. 3, the T/T_{ref} results of the steady state D3Q19 LBM algorithm and the reference's ones have been compared along the centreline $(y/Y = 1/2)$ in the $y - z$ plane at $(x/X = 1/2)$. A good agreement is found as seen from the transient non-dimensional temperature plots at different instants $\xi = 0.001$, $\xi = 0.01$, $\xi = 0.05$, and $\xi = \infty$. A given semi-transparent medium (SMT) can have a volumetric heat generation source, so effects of heat generation are compared and shown in Fig. 4.

Fig. 3 Centreline temperature along (z/Z) direction, validation with [19]
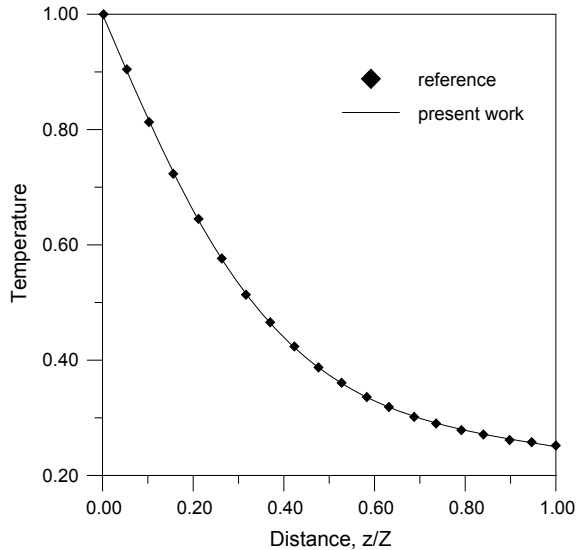
Fig. 4 Effect of heat
generation on centreline
non-dimensional
temperature distribution in a
3D enclosure
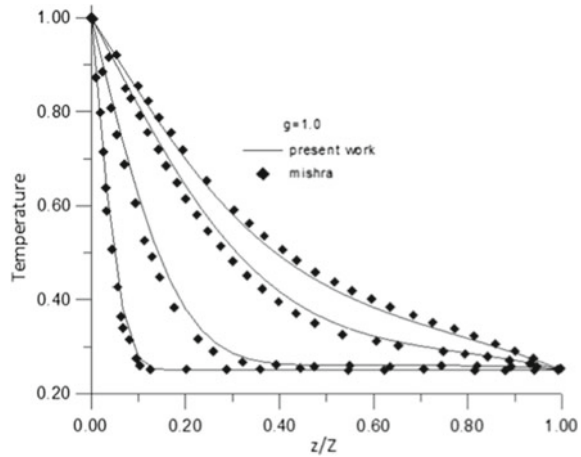
Results are plotted for the case of unity value of the non-dimensional heat generation for different time ξ levels including the transient and the steady state. Results were compared with literature [19]. It can be seen that the proposed algorithm presents an accurate result.

5.2   Validation with Pure 3D Radiative Case

In order to assess the CVFEM algorithm with basic reliable cases, the numerical approach was implemented for a cubical enclosure in which the medium is absorbing-emitting with an emissive power of unity. All the walls are black and cold (0 K). Solutions were obtained with ($11 \times 11 \times 11$) control volumes and (8×6) control angles. Figure 5 shows the non-dimensional surface radiative flux along the centreline of a wall. It compare the predicted flux distribution with that of the exact solution in literature [11] and their benchmark code for $ke = 1$ m^{-1} and $ke = 10$ m^{-1}. It can be seen that the proposed algorithm presents good results.

The second test case is made of a black-walled square box–shaped furnace enclosure (1 m × 1 m × 1 m). The walls are cold and the medium is grey with $\beta = 1$ m^{-1},$\omega = 0.5$. The results were obtained with ($11 \times 11 \times 11$) control volumes and (8×6) control angles. The wall heat flux for absorbing-emitting and isotropically scattering medium in the cubic enclosure is shown in Fig. 4b. The obtained results are in good agreement with the reference result [19].

After validation with pure 3D conductive case (Figs. 3 and 4) and radiative case (Figs. 5 and 6), the 3D transient conduction-radiation heat transfer problems considered in the present work is highlighted based on the variation of the transient and the steady temperature for various extinction coefficients (Fig. 7), conduction-radiation parameters (Fig. 8), and scattering albedos (Fig. 9). One hot boundary is

Fig. 5 Wall heat flux for absorbing-emitting in the cubic enclosure $\beta = 0.1, \ \beta = 1, \ \beta = 10$ [11]
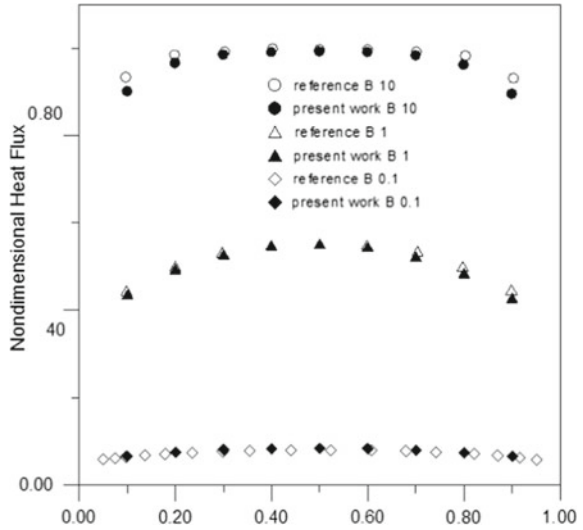
Fig. 6 Wall heat flux for absorbing-emitting and isotropically scattering medium in the cubic enclosure $\beta = 0.1, \ \beta = 1, \ \beta = 10$ [11]
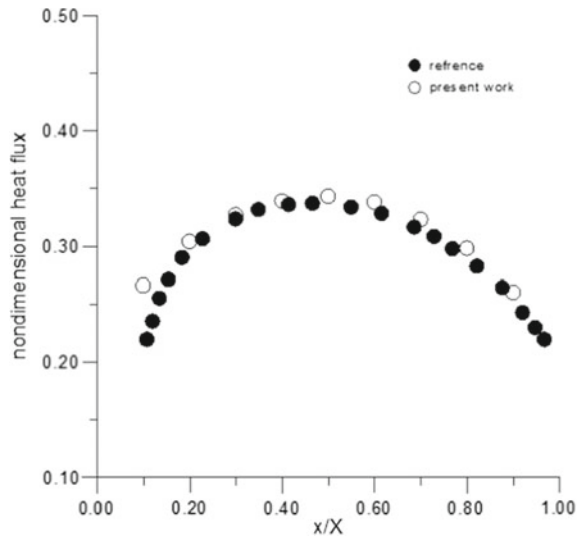
at $\theta = T/T_{hot} = 1$, and others are at the same lower temperature $\theta = 1/2$. Results of temperature distributions along z/Z direction at $x/X = 1/2$ and $y/Y = 1/2$ are presented in Figs. 7, 8, and 9. A $15 \times 15 \times 15$ grid points and 8×6 rays are considered for all the cases. Results are presented in graphical form rather than tabular form so as to explain the physical trend more effectively.

In those figures, at different time levels, centreline ($x/X = 1/2$ and $y/Y = 1/2$) temperature distributions along the z/Z direction obtained from LBM-CVFEM have been highlighted for the effects of different radiative parameters.
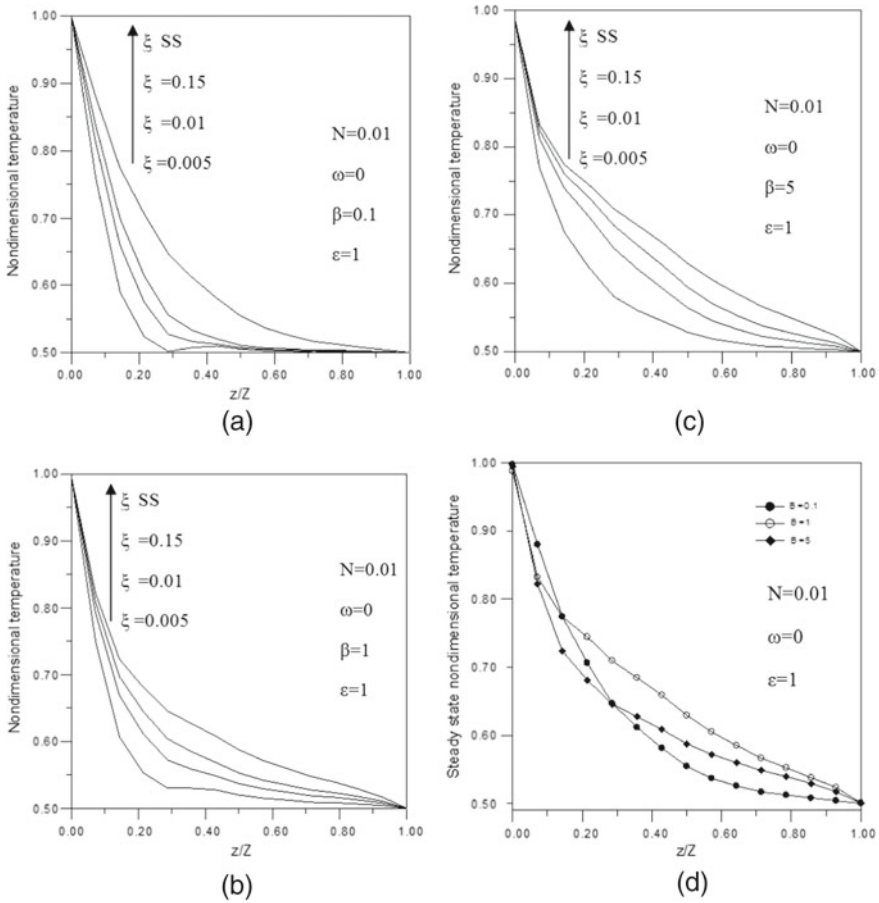
Fig. 7 Transient (**a–c**) and steady state (**d**) centreline ($x/X = y/Y = 1/2$) temperature: effect of the extinction coefficient

For black boundaries and for no scattering ($\omega = 0$), the effect of the extinction coefficient β is shown in Fig. 7 for $N = 0.01$. The temperature profile (Fig. 7a) for lower $\beta = 0.1$ approaches the pure conduction profile.

The influence of the conduction to radiation parameter $N = k\beta/4\sigma T_{hot}^3$ that characterizes the relative importance of conduction in regard to radiation is presented for temperature response in Fig. 8 for black boundaries and for no scattering.

It is shown (Fig. 8c) that the temperature profile is near to a pure conduction profile for $N = 1$ because it display a conduction-dominated situation showing higher temperature gradient. For $N = 0.01$(Fig. 8a), a comparatively flat profile is seen as medium temperature increases with lower temperature gradient.
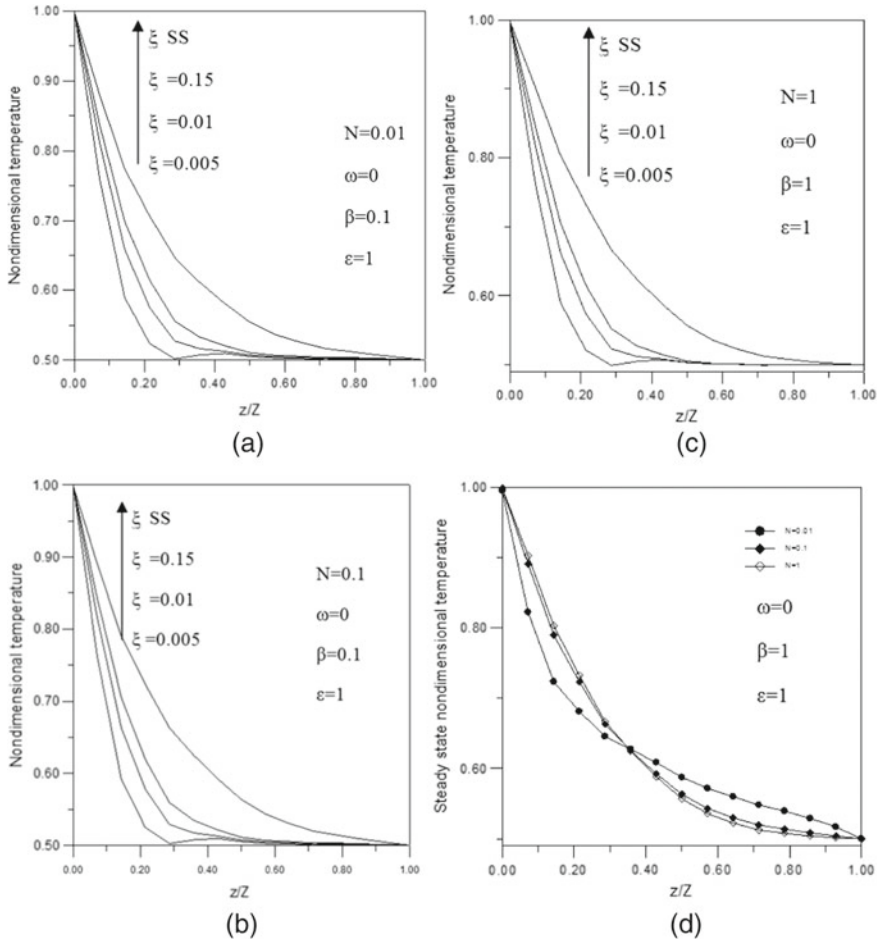
Fig. 8 Transient (**a**–**c**) and steady state (**d**) centreline ($x/X = y/Y = 1/2$) temperature: effect of the conduction-radiation parameter coefficient

For $N = 0.01$, $\beta = 1$, and perfectly black boundaries, the parametric study for the effect of the scattering albedo ω is highlighted in Fig. 9. The medium temperature comparatively increases for an absorbing-emitting medium ($\omega = 0$).

The computer code for the present 3D problem has been extended for transient convection and validated against the results given in literature [20] (Fig. 10); unsteady convection problem in a 3D real cubical enclosure has been considered. The continuity, momentum, and the energy equations are solved using the Lattice Boltzmann mesoscopic approach.

In Fig. 11, with $Ra = 10^3 - Ra = 10^6$ along z/Z and x/X direction at $y/Y = 0.5$ the centreline non-dimensional temperature has been highlighted. For a cubical medium undergoing transient convection, grid independence results are studied and Figs. 8,
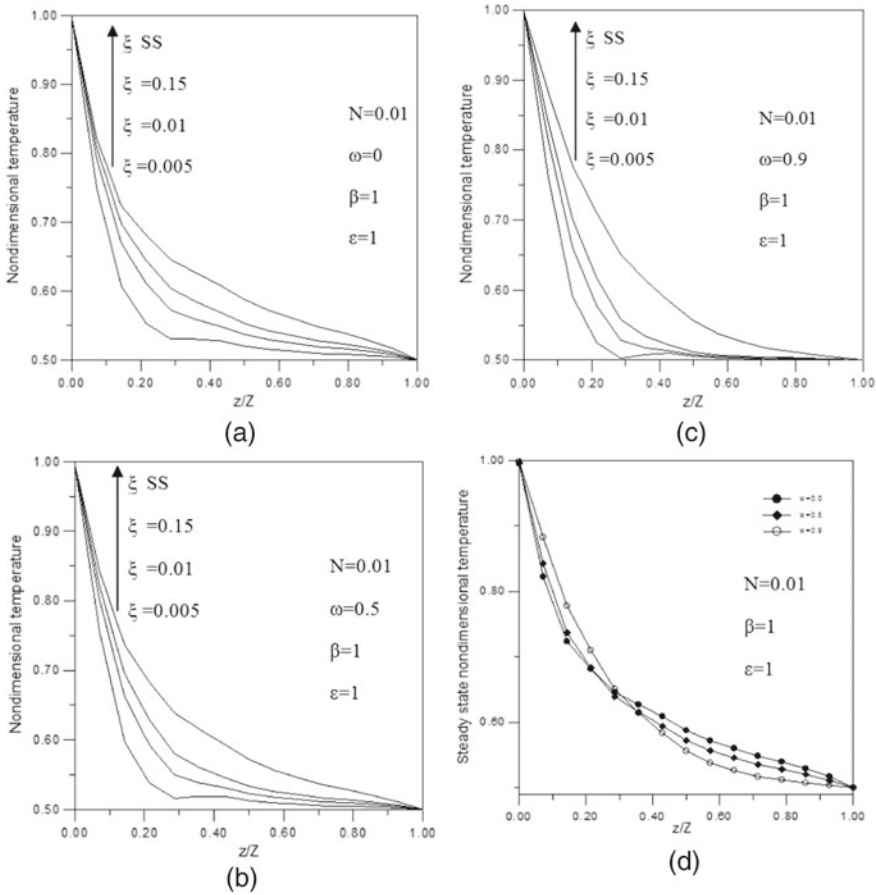
Fig. 9 Transient (**a–c**) and steady state (**d**) centreline ($x/X = y/Y = 1/2$) temperature: effect of the scattering albedo coefficient

9, and 10, respectively, show centreline temperature along z/Z direction at $x/X = 0.5$ and $y/Y = 0.5$ of the cubical medium for 155 * 155 * 155 lattices and iso-surfaces of temperature for $Ra = 10^6$ (Figs. 12 and 13).

6   Conclusions

LBM-CVFEM was used for the solution of unsteady combined conduction-radiation problems in a 3D cubical absorbing, emitting, and isotropically enclosure. Centreline temperature distributions were obtained for various parameters. The convective results presented in this study highlight the efficiency and the robustness of LBM and
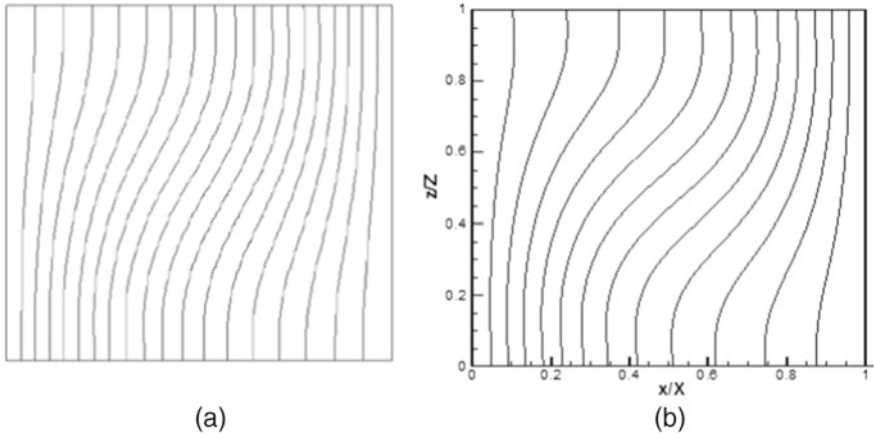
Fig. 10 Isotherms for Ra $= 10^3$ **a** [20] **b** present work
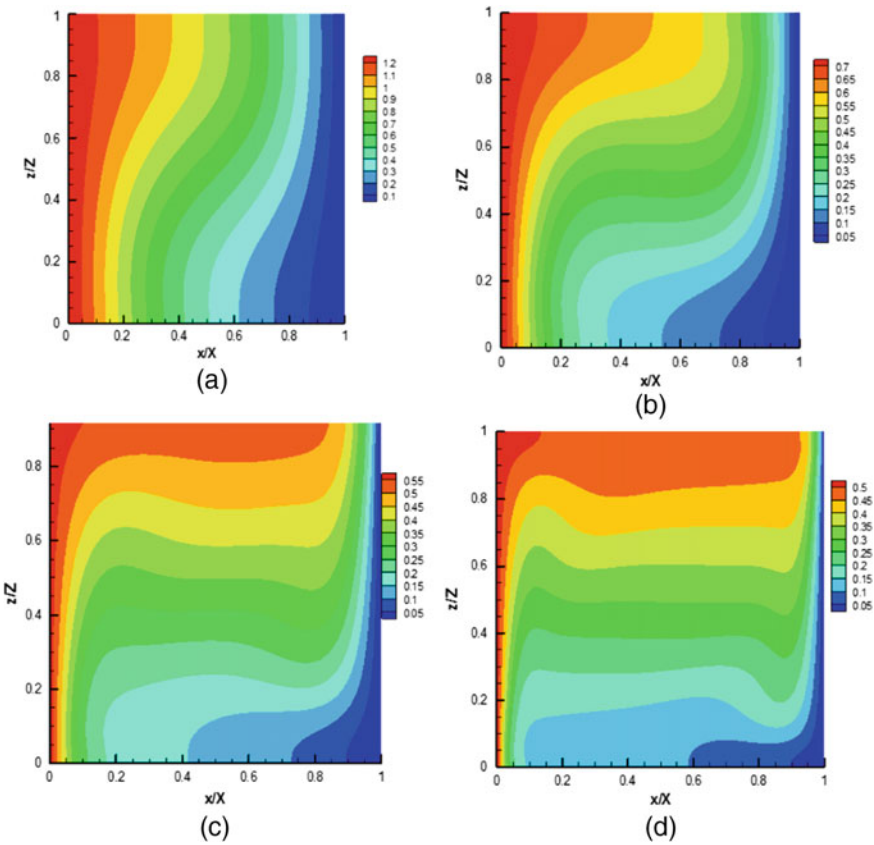
Fig. 11 The predicted temperature contours on the plane of symmetry at different values of Ra: **a** 10^3, **b** 10^4, **c** 10^5, **d** 10^6
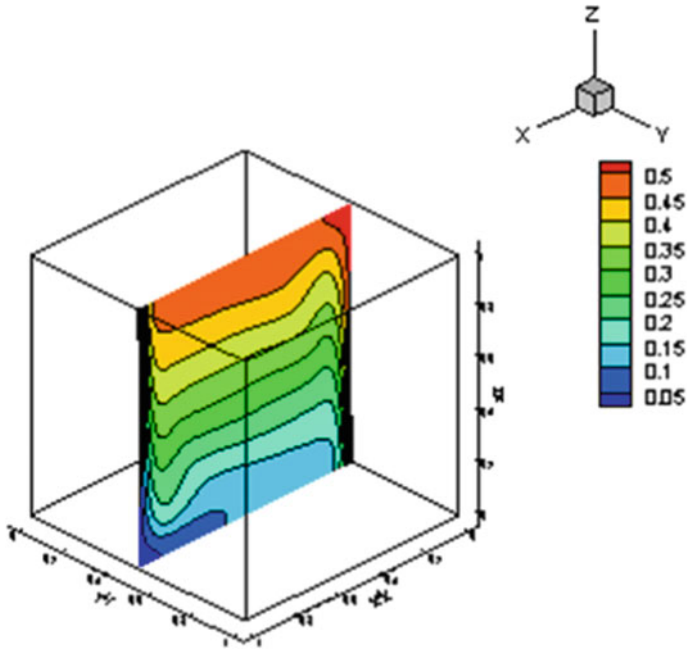
Fig. 12 The contours of temperature in the x–z plane of $y/Y = 0.5$ in the cubic cavity for flows of $Ra = 10^6$
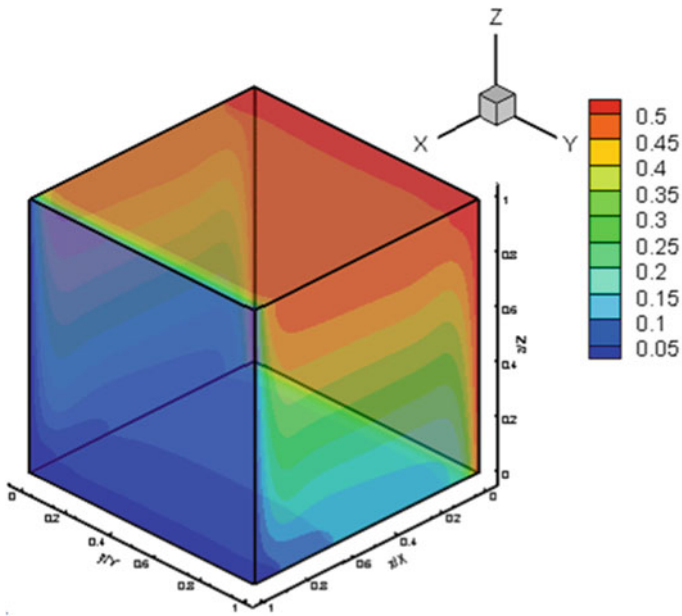
Fig. 13 Iso-surfaces of temperature for $Ra = 10^6$

allow the expectation that LBM has advantages over conventional energy (convection) equation solvers, especially for problems with complex geometry in multi-dimensional enclosures with axisymmetric or non-axisymmetric diffusive-radiative problems in different multi-mode engineering areas such as multiphase flow and complex fluid phenomena.

References

1. Lee KH, Viskanta R (2001) Two-dimensional combined conduction and radiation heat transfer: comparison of the discrete coordinates method and the diffusion approximation methods. Numer Heat Transf A 39:205–225
2. Razzaque MM, Howell JR, Klein DE (1984) Coupled radiative and conductive heat transfer in a two dimensional enclosure with gray participating media using finite elements. J Heat Transf 106(3):613–619
3. Ho CH, Owisik MN (1988) Combined conduction and radiation in a two-dimensional rectangular enclosure. Numer Heat Transf 13:229–239
4. Rousse DR, Gautier G, Sacadura JF (2000) Numerical prediction of two-dimensional conduction, convection and radiation heat transfer. II-validation Int J ThermSci 39:332–353
5. Wellele O, Orlande HRB, Ruperti N Jr, Colaco MJ, Delmas A (2006) Coupled conduction-radiation in semi-transparent materials at high temperatures. J PhysChem Solids 67:2230–2240
6. Chaabane R, Askri F, Narallah SB (2011) Parametric study of simultaneous transient conduction and radiation in a two-dimensional participating medium. Commun Nonlinear Sci Num Simul 16:4006–4020
7. Chaabane R, Askri F, Narallah SB (2011) A new hybrid algorithm for solving transient combined conduction radiation heat transfer problems. J Thermal Sci 15:649–662
8. Chaabane R, Askri F, Narallah SB (2011) Analysis of two-dimensional transient conduction-radiation problems in an anisotropically scattering participating enclosure using the lattice Boltzmann method and the control volume finite element method. J Comput Phys Commun 182:1402–1413
9. Chaabane R, Askri F, Narallah SB (2011) Application of the lattice Boltzmann method to transient conduction and radiation heat transfer in cylindrical media. J Quant Spectrosc Radiat Transf 112:2013–2027
10. Sakami M, Charette M, Le Dez V (1998) Radiative heat transfer in three dimensional enclosures of complex geometries by using the discrete ordinates method. J Quant Spectrosc Radiat Transf 59:117–136
11. Kang SH, Song T-H (2008) Finite element formulation of the first- and second-order discrete ordinates equations for radiative heat transfer calculation in three-dimensional participating media. J Quant Spectrosc Radiat Transf 109:2094–2107
12. Mishra SC, Lankadasu A, Beronov K (2005) Application of the lattice Boltzmann method for solving the energy equation of a 2-D transient conduction-radiation problem. Int J Heat Mass Transf 48:3648–3659
13. Mishra SC, Roy Hillol K (2007) Solving transient conduction and radiation heat transfer problems using the lattice Boltzmann method and the finite volume method. J Comput Phys 223: 89–107
14. Mishra SC, Mondal B, Kush T, Siva Rama Krishna B (2009) Solving transient heat conduction problems on uniform and non-uniform lattices using the lattice Boltzmann method. Int Commun Heat Mass Transf 36:322–328
15. Mishra SC, Lankadasu A (2005) Analysis of transient conduction and radiation heat transfer using the lattice Boltzmann method and the discrete transfer method. Numer Heat Transf A 47:935–954

16. Mondal B, Mishra SC (2009) Simulation of natural-convection in the presence of volumetric radiation using the lattice Boltzmann method. Numer Heat Transf As 55:18–41
17. Mondal B, Li X (2010) Effect of volumetric radiation on natural convection in a square cavity using lattice Boltzmann method with non-uniform lattices. Int J Heat Mass Transf 5:4935–4948
18. Benzi R, Succi S, Vergassola M (1992) The lattice Boltzmann equation: theory and applications. Phys Rev 222:145–197
19. Mondal B, Siva Rama Krishna B, Mishra SC, Kush T (2009) Solving transient heat conduction problems on uniform and non-uniform lattices using the lattice Boltzmann method. Int Commun Heat Mass Transf 36:322–328
20. NorAzwadi CS, Tanahashi T (2007) Three-dimensional thermal lattice Boltzmann simulation of natural convection in a cubic cavity. Int J Mod Phys B 21:87–96

2D Numerical Simulation of Downburst Simulator in the Wall of Wind

Guillaume Levieux, Amal Elawady, Arindam Chowdhury, and Fethi Aloui

Abstract Downbursts are extremely spontaneous and dangerous phenomena that have been shown to be responsible for failures of many structural systems. The Wall of Wind team is currently in the process of developing a large-scale downburst simulator that could facilitate research to improve the resistance of building envelopes and lifeline infrastructures. For this purpose, four setups have been numerically simulated in order to recreate downburst-like wind characteristics while the height of the maximum velocity can be controlled. Consequently, three different roughness elements have been added, and the results demonstrate that the roughness elements have a positive impact on the height of the maximum velocities.

Keywords Downburst · Wall of wind · Simulator · Computational fluid dynamics CFD · Thunderstorms

Nomenclature

St	Strouhal number (dimensionless)
f	Shedding frequency (Hz)
D	Opening height of the gate (m)
V	Horizontal velocity (m s^{-1})
Z^*	Corrected height ($Z - Z_{\text{roughness}}$) (m)

G. Levieux · F. Aloui (✉)
Université Polytechnique Hauts-de-France (UPHF), LAMIH CNRS UMR 8201, INSA
Hauts-de-France, 59313 Valenciennes, France
e-mail: Fethi.Aloui@uphf.fr

G. Levieux · A. Elawady · A. Chowdhury
Department of Civil and Environmental Engineering (CEE), Florida International University,
11200 SW 8th St, Miami 33199, USA
e-mail: Aelawady@fiu.edu

1 Introduction

The United States often faces natural hazards such as thunderstorms or hurricanes. These extreme weather conditions are a huge threat to human beings and infrastructures. Thunderstorms can give rise to tornadoes but more frequently to downbursts which are believed to be the most destructive winds in inland North America [1, 2].

In 1990, Dr. Theodore Fujita defined these events as non-stationary, short duration, and strong downdrafts which upon reaching the ground surface develop intense gusts near the soil. This definition highlights the two main features of downburst winds. First, a downburst is a transient event where the horizontal velocity near the ground peaks during 1–5 min after a ramp-up. This characteristic associated with wind is called non-synoptic wind when everyday winds or even hurricane winds are synoptic winds. Secondly, the everyday wind has low velocity near the ground surface and it increases with altitude. This phenomenon is ruled by the atmospheric boundary layer ABL. On the other hand, during a downburst, the maximum velocity occurs underneath 50 m from the ground [3, 4]. It explains why downbursts velocity profiles are often compared to nose shape. These last characteristics highlight the dangerousness of downbursts because the velocities can be considerable near the ground, and they are also highly unpredictable events. Thus, full-scale measurements represent a challenging task which has motivated researchers to study downbursts either experimentally or computationally [1, 2, 5–7]. These benchmark research have greatly contributed to developing a better understanding of downbursts and have also led to the development of experimental facilities. There are two main categories of downburst simulator. The first category of simulator is using jet impingement to model the entire downburst event where spatial variation is considered. Thus, the downdraft must be formed. The second category of simulator is only focused on the downburst gust front created in the wake of the downdraft impact. The spatial variation is not considered for this second category of downburst simulator. Nevertheless, it allows studying the effect of the outflow on infrastructures. The first category of simulators can be small-scale facilities in order to study the downburst wind field only. Structural analyses require larger facilities because the downburst and the studied structure need to be simulated using the same scale [8]. The second category of simulator does not recreate the downdraft. Wind tunnels with a particular impediment are often used to create downburst-like winds. Louvers at the outlet of a wind tunnel have been used by Matsumoto [9] in order to study the effect of downburst on trains. Moreover, [5] used two techniques to redirect horizontal wind tunnel flow and recreate a downburst typical gust front. Only a few research works have been found to deal with multi-blade system at the exit of a wind tunnel [10, 11]. The latest system shows good results using multiple louvers capable of rotating to different angles which is very similar to the Wall of Wind.

This study aims to numerically confirm that the Wall of Wind is able to recreate downburst-like winds in order to conduct structural testing. A sensible height of the maximum horizontal velocity is needed during these assays. With this aim in mind, different rough terrains will be studied in order to control this height.

2 Experimental Facility

2.1 The Wall of Wind Facility

The Wall of Wind (WOW) is one of the experimental facilities designated by the national science foundation (NSF) to help prevent natural hazards from becoming social disasters. The Wall of Wind is a large-scale experimental facility that allows testing full-scale, large-scale, and small-scale models for various civil structures. The WOW is powered by a combined 12-fan electric system capable of repeatable testing in up to 250 km/h wind speeds with wind-driven rain simulation which is equivalent to category five hurricane according to Saffir-Simpson scale. The flow created by each fan is gathered inside a plenum that converges into a flow management box. This box guides the flow along 9.75 m (Fig. 1). Then, the wind reaches the turntable which corresponds to the testing area. Finally, the flow is getting out on the north side of the facility. Inside the flow management box, roughness elements have been added in order to imitate the unevenness of a natural terrain. Thus, it creates a more realistic turbulent flow upstream to the testing area.

The WOW team has started to think about adding a downburst simulator to the existing facility, as this addition could be a great opportunity to extend WOW possibilities. The downburst simulator at the WOW facility will belong to the second category since a wind tunnel is already existing. Karen and Butler (2007) studies have been reused to develop a system capable of turning ABL winds into downburst-like winds. In order to do this, a blockage gate with louvers has been added at the flow management box outlet.

However, several gates must be tested in order to comply with constraints and recreate a typical downburst gust front. In light of the large dimensions of the facility, it would be time-consuming and extremely costly to test the gates on the large-scale simulator. Thereby, numerical simulations have been conducted in addition to experimental tests on a 1:15 model.

Fig. 1 Dimensions of the wall of wind facility
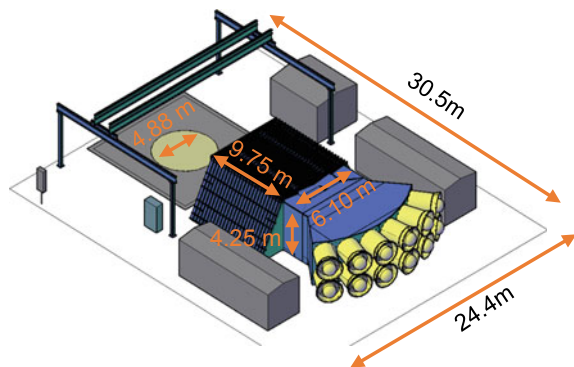
2.2 Small-Scale Wall of Wind

The small-scale Wall of Wind has been developed in order to facilitate testing before it is set up on the full-scale simulator. The length scale is 1:15 compared with the full-scale simulator which, according to Aboutabikh [10], does not allow structural testing. However, this model is able to reproduce the flow topology created by the full-scale facility. Since the beginning of the study, several gates have been tested as it is shown in Fig. 2.

In order to validate or dismiss a gate, the following criteria must be respected:

– The height of the maximum radial velocity must occur between 10 and 100 cm (large-scale dimensions)
– The simulator has to reproduce a nose-shape velocity profile
– The wind speed time history must show a peak with the signature ramp-up and ramp-down
– The vertical velocity must be low in comparison to the radial velocity in the testing area.

This development has led to a simple gate with two opening louvers (f) shown in Fig. 2. The following study is focused on this very last system. Downstream the gate, several types of terrain are tested. It allows showing the influence of roughness on the velocity profile. The data are measured at the beginning, at the center, and at the end of the testing area. The data obtained at the center of the turntable (Fig. 3) are compared to the literature [3, 6, 7, 12, 13]. Both axes are normalized. The abscissa is normalized with the maximum velocity, and the ordinate is normalized with the height where the maximum velocity occurs.

The two experimental results show good agreement with literature results, especially with short grass. Indeed, the slop appears to be equivalent to the other full-scale data. It is important to note that the stiffer is the slop, the higher is the maximum velocity which means that the height of the maximum velocity is increased by using roughness elements.

Due to the Pitot tubes, measuring data near the ground is a challenging task and it explains why experimental data are unavailable for $Z/Z_{max} < 0.5$.

Fig. 2 Evolution of the blockage gates
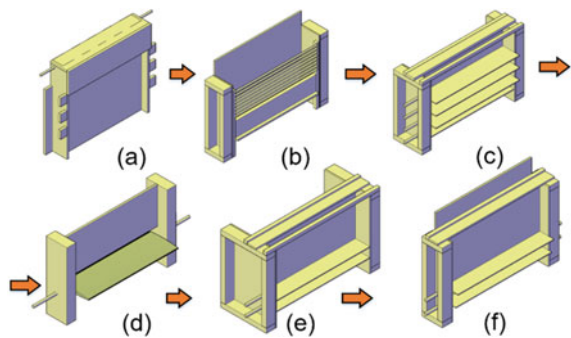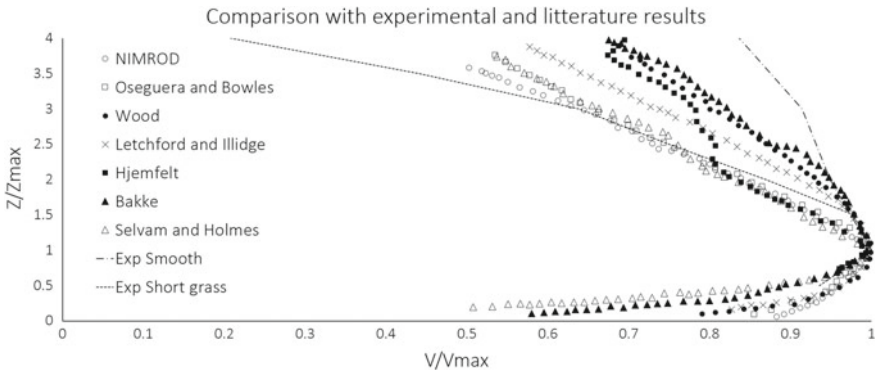
Fig. 3 Velocity profiles' comparison between literature and experimental results

Numerical simulations allow solving this issue in addition to providing better visualization and flexibility.

3 Numerical Model Description

3.1 Objectives

The previous experimental and CFD studies have shown the low height of the maximum velocity. However, it is essential for the maximum velocity to be high enough during structural testing. Thus, adding roughness elements could not only solve this issue, but it could also allow monitoring the height of the maximum velocity.

The main objective of this study is to demonstrate the influence of the roughness on the height of the maximum velocity while creating downburst-like winds. For this purpose, four different cases have been studied. First a smooth terrain and then three different rough terrains. Bin [14] showed that roughness elements can be mimicked by geometrical forms such as rectangles or triangles. This method has been chosen to recreate the rough terrains that have been experimentally studied on the 1:15 model. The dimensions of these roughness elements will be further discussed in the next part 3.2.

We will be focusing on a very critical angle of 60° from the horizontal axis. This kind of angle creates a huge reduction of the cross-section which triggers high velocities and a high-pressure gradient between the lower surface and the upper surface of the slats.

3.2 Geometry

Considering the computational costs, a 2D axisymmetric geometry has been chosen. It has already been proved by reference [15, 16] that 2D CFD modeling is accurate enough to simulate downburst-like winds.

These numerical simulations are the link between experimental results on the 1:15 model and the large-scale simulator. Therefore, the large-scale dimensions shown in Fig. 1 are used to numerically recreate the Wall of Wind facility. The geometry has been created by using ANSYS Design Modeler and the exact dimensions are shown in Fig. 4. The pressure outlet 1 has been slightly taken away in order to measure phenomena independently of boundary conditions.

Note that Fig. 4 shows the geometry without roughness elements, it represents the smooth terrain.

The first roughness is chosen to be equivalent to a 0.508 cm high roughness used on the 1:15 model. This height must be multiplied by 15 to fit the full-scale simulator. The characteristics of this roughness element are available in Table 1.

The second roughness element retains the same width and, consequently, the same gap between each triangle, but on the other hand, the height is doubled. However, this second roughness occupies twice more surface than the previous roughness elements. Thus, the third roughness is designed to retain the same surface occupied. For this purpose, the height is multiplied by 2, but the width is divided by 2 in the meantime (Fig. 5).
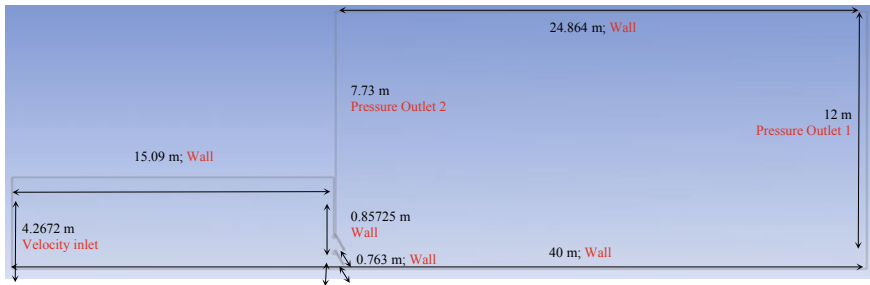
Fig. 4 Dimensions of the 2D Wall of Wind created in ANSYS design modeler

Table 1 Characteristics of the roughness elements

	Shape	Height (cm)	Width (cm)	Gap (cm)
Roughness 1	Triangle	7.62	6	4
Roughness 2	Triangle	15.24	6	4
Roughness 3	Triangle	15.24	3	7

Fig. 5 Roughness elements visualization; **a** roughness 1 on the left; **b** roughness 2 in the middle; **c** roughness 3 on the right
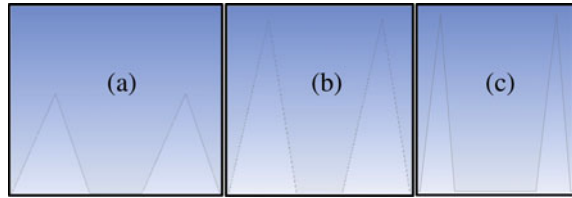
Table 2 Characteristics of the mesh for each case

	Cells	Skewness	y^+ min	y^+ max
Smooth	137,051	$4.02.10^{-2}$	5.46	69.02
Roughness 1	123,300	$9.09.10^{-2}$	6.06	41.41
Roughness 2	142,241	$9.69.10^{-2}$	5.37	31.91
Roughness 3	146,028	$9.91.10^{-2}$	5.38	32.55

3.3 Mesh

In order to reduce the computational cost, a coarse mesh has been chosen with refinement around the part of interest. Note that ANSYS Meshing has been used to develop the following mesh.

First, a body of influence is used to refine the mesh around the testing area. Indeed, the body of influence allows reducing the maximum size of a cell inside a given area (0.2 m inside the domain; 0.05 m inside the body of influence). Then, the mesh is refined around the slats because they are redirecting the flow and they are subject to high gradients (0.005 m).

Finally, the flow is redirected toward the ground which must be refined. A $k_{-\varepsilon}$ realizable turbulence model is used, and this choice will be further discussed in the following part (3.4). However, this turbulence model demands a range of y^+ included between 5 and 300. Thus, a boundary layer mesh is added on the bottom wall. The first cell is 5.10^{-4} m high, and the boundary layer is composed of 20 layers. Table 2 allows checking the mesh quality for each case. The skewness evaluates the asymmetry of the cells across the domain, a skewness close to 0 is a quality factor.

3.4 Choice of the Numerical Model

Three numerical models can be used for downburst simulations. The first one is direct numerical simulation (DNS) which requires very fine mesh and it is also tremendously time-consuming. Abd-Elaal et al. (2017) used this approach to numerically simulate downburst. The second approach, the most commonly used in the industry, is the reynolds averaged navier–Stokes (RANS). All the turbulent are modeled, but the plethora of turbulence models makes RANS approach very versatile, and it is

proven to be a satisfactory compromise between precision and computational time. References [5, 7, 16] chose a RANS method to simulate downburst-like winds. The third method is the large eddy simulation (LES). This approach is a balance between the previous models as it solves the large turbulent scales and models the smaller scales. The LES is still time-consuming but gives excellent results. For instance, this method has been used by Aboutabikh et al. [10].

Unfortunately, LES and DNS are unavailable for 2D simulations. However, [17] Li et al. [18] concluded that the RANS model is reasonable for downburst simulations. More precisely, a $k_{-\varepsilon}$ realizable turbulence model is used in concordance with the study of Selvam and Holmes [7]. An enhanced wall is employed because this wall treatment is multipurpose and allows capturing the viscous sublayer ($y^+ < 5$).

The inlet velocity is set to 8 m/s. The time step has been set to 0.005 s in order to accurately catch the evolution of the rolling vortex. For this simulation, a Strouhal number of 0.2 is considered according to the topology of the gate (1).

$$St = \frac{fD}{V} \rightarrow f = \frac{St.V}{D} \tag{1}$$

The characteristic dimension D is the opening height of the gate which is equal to 1.61 m. Thus, the shedding frequency is found to be 1 Hz, so the period is 1 s. Using the Nyquist-Shannon sampling theorem, the transient simulation time has been set to 2 s. Thereby, the number of time steps is equal to 400.

4   Numerical Results

In this part, we will be mainly focused on four specific locations. The position where the maximum horizontal velocity occurs is studied and will be called $P_{\max}$. The three other locations refer to the turntable (Fig. 1). The measures are done at the front of the turntable, at the center of the turntable, and finally at the end of the turntable. Particular attention is given to the center of the turntable because the structural tests are most likely to take place at this very location (Fig. 6).

Fig. 6 Positions of interest inside the fluid domain, $P_{\max}$ is not represented because its location is variable

First of all, the downburst event must show a peak of the horizontal velocity. This is why Fig. 8 shows the time histories of the horizontal velocity for the four cases at each location. All the curves are showing a maximum velocity after a characteristic ramp-up, proper to downburst events. However, it is clear in Fig. 8b that the ramp-down is less distinct because the slats are motionless [10]. Indeed, the flow accelerated by the reduction of the cross-section maintains a high velocity inside the domain even if the downburst event is gone. In Fig. 8, it appears that the maximum velocity occurs after the same amount of the time regardless of the roughness. On the other hand, from the front to the end of the turntable table, the maximum horizontal velocity is delayed because of the roughness elements. This trend is more conspicuous in Fig. 7 which represents the time when the maximum velocity occurs as a function of the position. It is shown that the rough terrains are postponing the maximum velocity downstream in P_{max}.
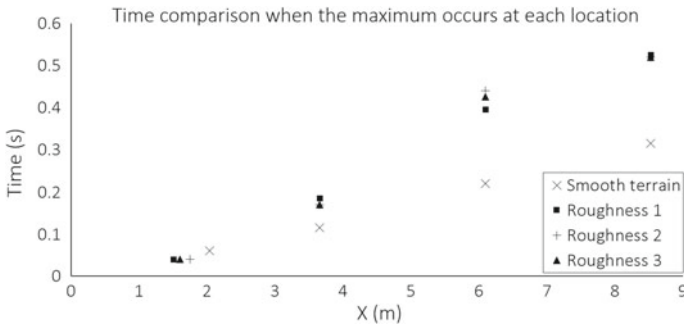
Fig. 7 Time comparison of the four cases when the maximum occurs at each location
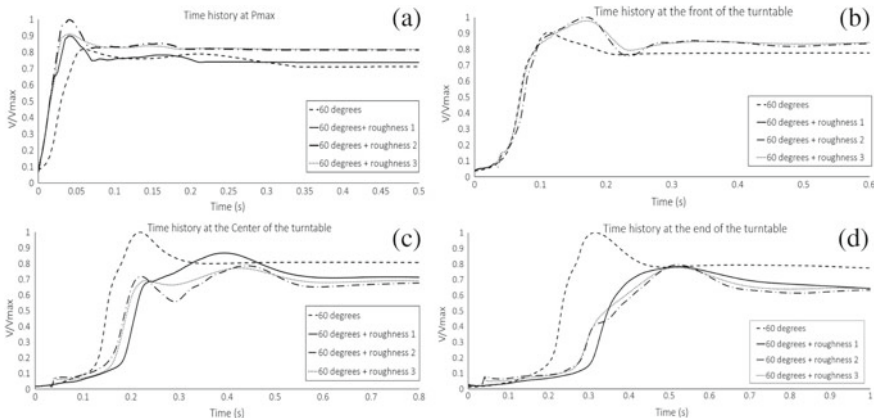
Fig. 8 Time histories of the horizontal velocity at 4 different locations; **a** P_{max}; **b** front of the turntable; **c** center of the turntable; **d** end of the turntable

This phenomenon is explainable by the fact that the roughness elements are introducing much more energy dissipation due to the unevenness of the ground and the increase of the wall shear stress. The energy dissipation provokes a significant decrease in velocity.

The main feature of downbursts, i.e. jet impingement, is the creation of vortex that spreads radially in all the directions. This rolling vortex is clearly identifiable in Figs. 9 and 10, and as the vortex is moving forward, its height also increasing until a point where the eddy disappears. In fact, Fig. 10 shows that the vortex is higher with roughness elements. The center of the vortex is 2.13 m high at end of the turntable for
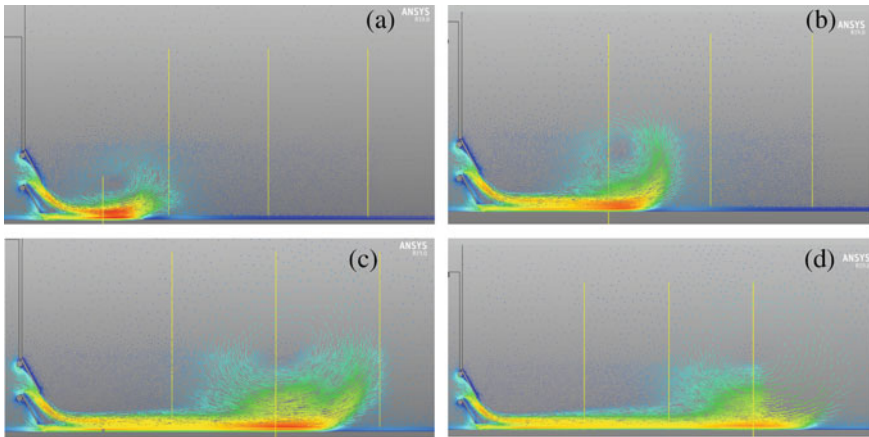
Fig. 9 Development of the vortex throughout the domain (smooth terrain); (**a**) $t = 0.06$ s; **b** $t = 0.115$ s; **c** $t = 0.22$ s; **d** $t = 0.315$ s
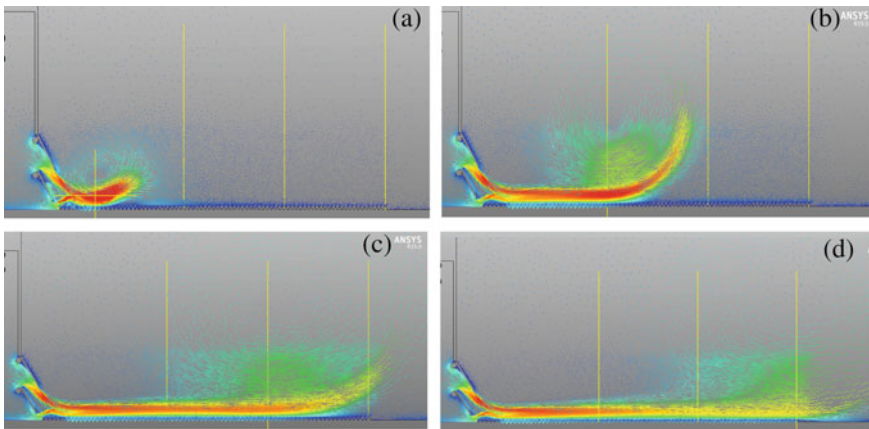
Fig. 10 Development of the vortex throughout the domain (roughness 1); **a** $t = 0.04$ s; **b** $t = 0.185$ s; **c** $t = 0.395$ s; **d** $t = 0.525$ s

smooth terrain. On the other hand, the center of the vortex is located at 3.43 m for the first rough terrain. Once again, it can be explained by the fact that the rough terrain is the origin of turbulence and loss of energy. The eddy is widening due to losing energy and disappears to give rise to smaller eddies (Richardson 1920; Kolmogorov 1940). Moreover, the substantial velocities appear to be close to the ground which is essential for downburst-like winds simulations.

The vectors are mostly oriented toward the x-axis which is the horizontal axis. It proves that the vertical velocity is low compared to the horizontal velocity. Indeed, at the locations where the maximum horizontal velocities occur, the vertical velocities range from 1 to 5% of the horizontal velocity. Finally, it is important to note that the addition of roughness is increasing the overall velocity inside the domain. Actually, at P_{max}, the difference of horizontal velocity amounts 9.9% between the smooth terrain and the first roughness. When the roughness surface is doubled (roughness 2), the difference between smooth and roughness 2 amounts 22.4%. While the roughness height is extended, the cross-section is shrinking. Thus, the mass flow conservation involves acceleration.

Figure 11 shows the velocity profiles of the four cases at the four different locations of interest. The abscissa is normalized with the maximum velocity of each case. Therefore, when $V/V_{max} = 1$, it corresponds to the height of the maximum horizontal velocity. The different zero-crossings are consistent with the previous explanations because along the domain, the height is increasing. Moreover, the difference between smooth terrain and rough terrains is widening throughout the turntable.

The slops are also interesting as we can see an inflection point in Fig. 11b, c at $V/V_{max} = 0.6$, especially for the first roughness elements. This observation results from the combination of two phenomena. The very stiff slop is created by the downburst gust front and also by the two jets coming from the slats. At a certain height, above the jets, the vortex is the only origin of velocity which explains a less stiff
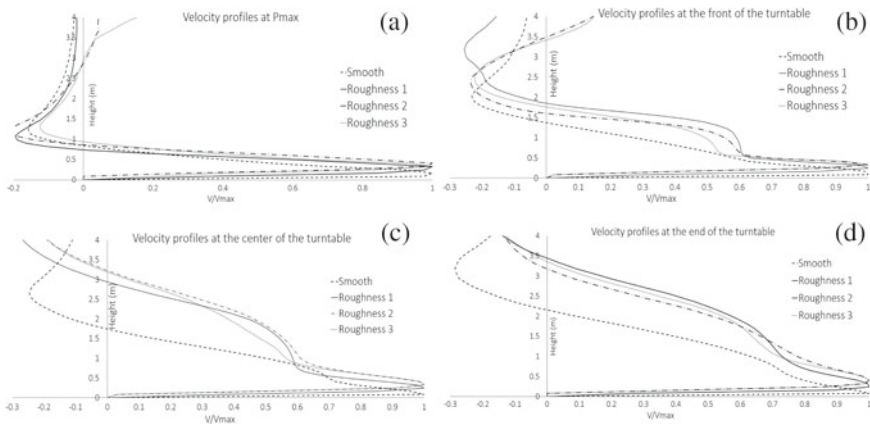
Fig. 11 Velocity profiles at 4 different locations: **a** P_{max}; **b** front of the turntable; **c** center of the turntable; **d** end of the turntable

slop. This phenomenon is less and less marked throughout the domain as the jet is losing energy and has less impact on the overall flow. For instance, the inflection point is non-existent at the end of the turntable and the slop remains almost constant. Thus, the characteristic nose shape is well depicted at the end of the turntable. A softer angle (45°) for the slats has been shown to reduce this effect as the jets are less energetic.

The velocity profiles (Fig. 14) ensure to see the evolution of the height where the maximum velocity (Z_{max}) occurs depending on the roughness. At P_{max}, the smooth terrain gives the highest Z_{max} which is not the purpose of adding roughness elements. However, at this specific location, the downburst event is beginning and the influence of the jets is more important. On the other hand, when the downburst event is ongoing inside the turntable, the smooth terrain gives the smallest Z_{max} value. Therefore, Fig. 11b, c, and d and Table 3 are revealing the smallest values for the smooth terrain, then the rough terrain 1 increases Z_{max}. Finally, the two last terrains are increasing even more Z_{max}, but the difference between those two cases is null because they both have the same height. Figure 11 allows a quick overview of the phenomenon but shows some limits when it comes to comparing the roughness influence. Indeed, the Z_{max} values are also including the height of the roughness elements; thus, these results are valid only if the testing structure is installed on the ground and is surrounded by the roughness elements. Then, $Z*_{max}$ is added in order to evaluate the real height of the maximum velocity:

$$Z*_{max} = Z_{max} - \text{Roughness height} \qquad (2)$$

Table 4 shows a different influences of the rough terrains. The first roughness allows to raise the height compared to the smooth terrain, but then the roughness enlargement has no impact on the front of the turntable. The same observation can

Table 3 Heights of the maximum velocity for each case

	z P_{max} (m)	z Front (m)	z Centre (m)	z End (m)
Smooth	0.163	0.081	0.085	0.084
Roughness 1	0.327	0.25	0.244	0.25
Roughness 2	0.408	0.326	0.327	0.408
Roughness 3	0.339	0.326	0.327	0.398

Table 4 Corrected heights of the maximum velocities

	z* P_{max} (m)	z* Front (m)	z* Centre (m)	z* End (m)
Smooth	0.163	0.081	0.085	0.084
Roughness1	0.250	0.174	0.168	0.174
Roughness2	0.255	0.174	0.175	0.255
Roughness3	0.187	0.174	0.175	0.246

be made for the center of the turntable because the gain between the first roughness and the other roughness is very low (7 mm). Finally, the roughness height has an impact at the end of the turntable as there is a gain of 8.1 cm between roughness 1 and roughness 2 and a gain of 7.2 cm between roughness 1 and toughness 3. This disparity is due to the energy dissipation throughout the domain that increases the height of the vortex. The maximum velocities are staying close to the ground surface while the flow is still energetic, but once the energy is not sufficient, the heights of the maximum velocities are following the same path than the center of the vortex. These results with the corrected heights Z^*_{max} are interesting if the testing structure is placed on the roughness elements. Adding roughness elements has been shown to be interesting for increasing Z_{max} or Z^*_{max}. The first roughness is interesting as the heights are sensible and it creates less loss of energy than the two other roughness. However, roughness 2 and 3 are increasing consequently Z_{max} which is very interesting despite important loss of energy. The third roughness has shown to produce the same heights, but it creates slightly less dissipation of energy which makes this case attractive.

5 Validation

CFD results must always be validated with experimental or literature data. Thus, Fig. 12 shows experimental, literature, and CFD comparison with the normalized height Z/Z_{max} function of the normalized velocity V/V_{max}. These data are taken at the center of the turntable, and every data are scaled in order to show a consistent comparison.

First, the analytical smooth result is included between the experimental smooth result and literature results [12], and its slope shows good agreement with literature results. Thus, it demonstrates that ANSYS Fluent's results give consistent heights of the maximum velocities in addition to the characteristic nose shape. Moreover,
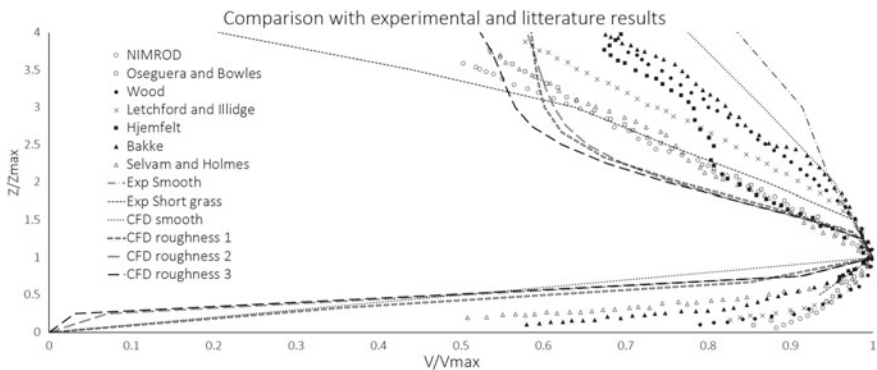
Fig. 12 CFD validation using literature [3, 7, 12, 13, 19] and experimental data

underneath $Z/Z_{max} = 2.5$, the numerical smooth results are fitting nearly perfectly the literature results.

The results including roughness are showing stiffer slopes than experimental and literature results, even though their shapes are in good agreement. A stiff shape means that the maximum velocity is happening relatively high. Indeed, the experimental short grass result gives a curve with a stiffer slope than the literature review. This observation proves that the analytical slopes are coherent because the objective of adding roughness elements is precisely to obtain stiffer slopes.

6 Improvement

Results presented above are consistent with previous studies, but the velocities created by this system are significant. For instance, the maximum velocity at the center of the turntable for the first roughness reaches 107 m/s. However, the velocity inlet is 8 m/s, consequently, there is a 13.75 ratio between the inlet velocity and the maximum found at the center of the turntable. Naturally, slats with a 60° angle represent the worst case because the cross-section is reduced and as a result, the flow is accelerated. However, the Wall of Wind is designed for higher speed than 8 m/s. The ratio has to decrease in order to obtain a better inlet velocity range. Thus, the 12-fans system can produce reasonable velocities without exceeding the compressibility limit inside the testing area. Such an issue can be solved by introducing another outlet above the gate (Fig. 13) which will limit significant and unwanted accelerations.

The first and the third roughness have been numerically studied while none of the parameters have been changed. The gate geometry, the turbulence model, and the mesh are exactly identical.

The purpose of this study is to ensure that the velocities are reduced while the previous results are preserved. The following results are taken at the center of the turntable.

Fig. 13 Opening above the gate on the full-scale Wall of Wind

0.5025 m
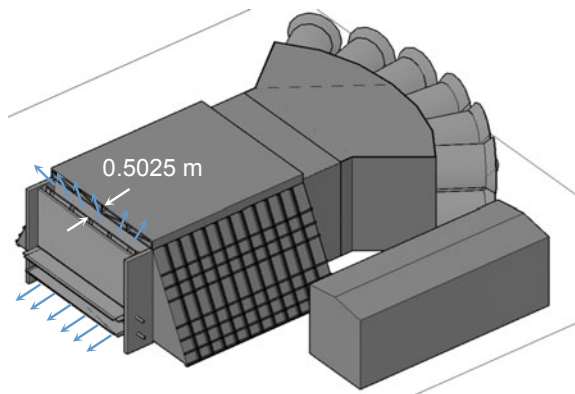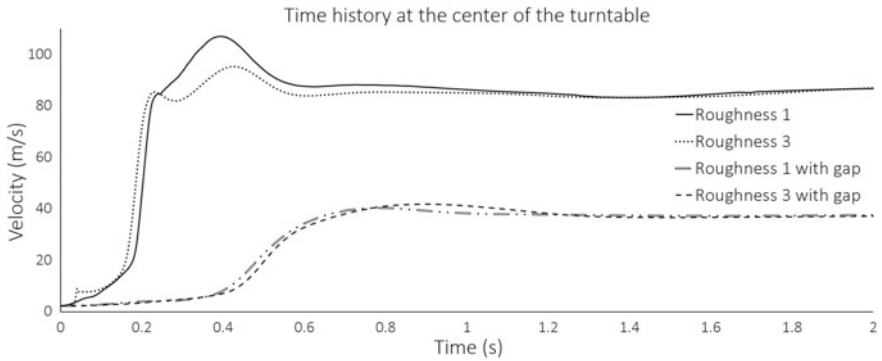
Fig. 14 Time history of the maximum velocity at the center of the turntable

As it could be seen previously, the characteristic ramp-up is clear and the ramp-down is less marked.

The new curves (Fig. 14) are shifted to the right. It means that the maximum velocity happens later because the velocities are lower so the vortex takes more time to spread throughout the domain. Indeed, the maximum velocities amount to 41 m/s and give a ratio equal to 5.125 which is much more satisfactory.

It is important to check that the system is still able to create the downburst-like winds as it has been presented previously. Figure 15 shows a comparison between the results with and without the opening above the gate. Besides 0.87 m, the curves with and without gap are combined for each roughness. It is satisfactory because most of the structures will be tested underneath this height. It shows that the roughness elements still have the same impact on the height of the maximum velocity than previously. Above 0.87 m, some differences are shown mostly because the addition of this gap changes the topology in the upper part of the gate. However, these differences are not significant and the nose shape is still visible for each curve.
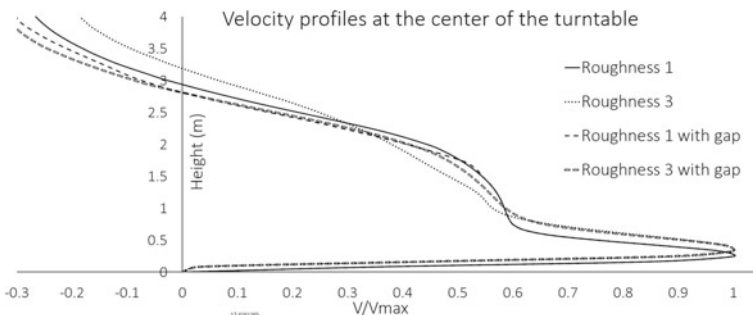
Fig. 15 Velocity profiles at the center of the turntable

This addition is interesting because it gives more flexibility to control the flow inside the facility. Indeed, the inlet flow can be controlled by the 12 fans and it can also be controlled by the width of this gap above the gate.

7 Conclusions

The aim of this work is to numerically simulate downburst-like winds simulator (WOW) and examining the influence of roughness elements addition. The validation of the numerical smooth terrain proves that the first aim of this study has been successfully completed. Different roughness elements were tested to examine the height of the maximum velocity at four locations. The ongoing study using triangles as rough elements shows promising results. Indeed, a reasonable roughness height allows to substantially raise the maximum velocities. Higher roughness elements demonstrate the rise of maximum velocities. Therefore, variable roughness element heights can be an interesting solution in order to control the flow inside the Wall of Wind facility. Continued work seeks to give a better understanding of the roughness influence in addition to a study of dynamic slats.

References

1. Fujita TT (1990) Downbursts: meteorological features and wind field characteristics. J Wind Eng Ind Aerodyn 36(1):75–86. https://doi.org/10.1016/0167-6105(90)90294-M
2. Holmes J, Hangan H, Schroeder J, Letchford C, Orwig K (2008) A forensic study of the Lubbock Reese downdraft of 2002. Wind Struct 11(2):137–152
3. Oseguera RM, Bowles RL (1988) A simple, analytic 3-dimensional downburst model based on boundary layer stagnation flow. NASA Technical Memrandum 100632, Hampton, Virginia, VA, USA
4. Wilson JW, Roberts RD, Kessinger C, McCarthy J (1984) Microburst wind structure and evaluation of Doppler radar for airport wind shear detection. J Clim Appl Meteorol 23(6):898–915
5. Butler K, Kareem A (2007) Physical and numerical modeling of downburst generated gust fronts. In: Proceedings of the 12th international conference on wind engineering, pp 791–98, Cairns, Australia
6. Fujita TT (1985) The downburst-microburst and macroburst. Technical Report 198518, Projects NIMROD and JAWS. University of Chicago, Department of Geophysical Sciences, Chicago, IL, USA
7. Panneer SR, Holmes JD (1992) Numerical simulation of thunderstorm downdrafts. J Wind Eng Ind Aerodyn 44(1–3):2817–2825. https://doi.org/10.1016/0167-6105(92)90076-M

8. Elawady AH, Aboshosha A, Damatty El, Bitsuamlak G, Hangan H, Elatar A (2017) Aero-elastic testing of multi-spanned transmission line subjcted to downbursts. J Wind Eng Ind Aerodyn 169:194–216. https://doi.org/10.1016/j.jweia.2017.07.010
9. Matsumoto M (1984) Study on unsteady aerodynamic in unsteady wind flow. Kyoto University, Japan
10. Moustafa A, Tarek G, Jiaxiang C, Sameh E, Haitham A (2019) Designing a blade-system to generate downburst outflows at boundary layer wind tunnel. J Wind Eng Ind Aerodyn 186:169–191. https://doi.org/10.1016/j.jweia.2019.01.005
11. Cao S, Nishi A, Kikugawa H, Matsuda Y (2002) Reproduction of wind velocity history in a multiple fan wind tunnel. J Wind Eng Ind Aerodyn 90:1719–1729. https://doi.org/10.1016/S0167-6105(02)00282-9
12. Bakke P (1957) An experimental investigation of a wall jet. J Fluid Mech 2(5):467–472. https://doi.org/10.1017/S0022112057000270
13. Letchford CW, Illidge G (1999) Turbulence and topographic effects in simulated thunderstorm downdrafts by wind tunnel jet. In: 10th International conference on wind engineering, June 21–24, 1999, Copenhagen, Denmark
14. Bin R, Syaifullah M, Basit A, KuShaar KuZilati, Keong LK (2014) Study of the effect of surface roughness on droplet spreading behavior using CFD modeling. Appl Mech Mater 625:378–381. https://doi.org/10.4028/www.scientific.net/AMM.625.378
15. Mason MS, Wood GS, Fletcher DF (2009) Numerical simulation of downburst winds. J Wind Eng Ind Aerodyn 97:523–539. https://doi.org/10.1016/j.jweia.2009.07.010
16. Wang JW, Qu WL, Ji BF (2009) Numerical analysis of factors influencing the downburst wind profiles. In: The Seventh Asia-Pacific conference on wind engineering, November 8–12, 2009, Taipei, Taiwan
17. Wilcox DC (1994) Turbulence modelling for CFD. DCW Industries, Inc.
18. Li C, Xiao YQ, Li QS, Ou JP (2009) CFD simulation of impinging jet with application to stationary downburst. In: Proceedings of the symposium of the 14th national wind engineering conference, Beijing, China
19. Fujita TT, Wakimoto RM (1981) Five scales of airflow associated with a series of downbursts on July 1980. Mon Weather Rev 109:1438–1455

CFD Aided Design: Case Studies

Mohamed Sadok Guellouz, Kaouther Ghachem, Abdelmajid Jemni, and Maher Ben Chiekh

Abstract Computational Fluid Dynamics, CFD, has evolved from a scientific interest to a practical engineering tool that can assist engineers in the design and optimization of equipment of different types and for different applications. The present work introduces two case studies where CFD analyses are employed as a tool for design evaluation and optimization. These include the case of designing dust extraction devices for the wood industry and the case of improving the uniformity of the air inlet velocity distribution in a convective dryer. The methodologies and typical results are presented in each studied case. The importance of the simulations in the design and optimization was demonstrated as they allowed the calculation of the equipment behavior in situations that are otherwise hard to foresee, either because of the unpredictable combined effects of different features or because of the counterintuitive results.

Keywords CFD · Design · Optimization · Case studies · Dust extraction · Dryer

1 Introduction

Computational Fluid Dynamics, CFD, has evolved from a scientific interest to a practical engineering tool that can assist engineers in the design and optimization of equipment of different types and for different applications. This is the result of the enhanced computer memory and speed performances and the profusion and development

M. S. Guellouz (✉) · A. Jemni · M. Ben Chiekh
Laboratory of Thermal and Energy Systems Studies LESTE, University of Monastir, ENIM, LR99ES31, 5000 Monastir, Tunisia
e-mail: mohamedsadok.guellouz@enib.ucar.tn

M. S. Guellouz
University of Carthage, National Engineering School of Bizerte, 7035 Bizerte, Tunisia

K. Ghachem
Princess Nourah Bint Abd Rahman University, College of engineering, Riadh, Saudi Arabia

of commercial CFD codes. The latter decreased significantly the prohibitive over-head investment in programming and code testing, while the computers' progresses allowed the solution of problems that were otherwise impossible to tackle, either because of the required memory storage or due to the excessively long simulation times. As a result, many design and development projects adopted the CFD aided design approach.

The use of CFD as a design tool, was conceivably initiated in the Aerodynamic design field, where it was realized that the traditional "cut and try" design method had reached its limits and that continued improvements were becoming much more difficult to attain. In fact, the aerodynamic expertise of the designer is no longer sufficient for the selection of truly optimal shape modification, because of the subtle and complex fluid dynamics phenomena. The need for design techniques that involve the detailed calculations of the fluid flow was felt quite soon. Examples of the adoption of this approach in the optimum aerodynamic design and in the closely related field of ship engineering are presented respectively in [1] and [2].

The use of CFD as a design tool extended quickly to the development of a variety of other applications such as prosthetic cardiovascular devices [3], water jet cutting systems [4], and even the more established applications like the design of indoor ventilation systems [5], farming [6] and the many food industry processes e.g. drying, sterilization, refrigeration and mixing [7, 8].

The present work introduces two case studies where CFD analyses are employed as a tool for design evaluation and optimization. These include the case of designing dust extraction devices for the wood industry and the case of improving the uniformity of the air inlet velocity distribution in a convective dryer. The focus is put on the design approach, employing CFD to optimize the technical solutions.

2   CFD Aided Design of Dust Extraction Devices for the Wood Industry

Wood dust accumulation in the wood-working shops interferes with maneuvers near machines, impedes good machining and can cause pathologies such as cancer of the respiratory tract (ethmoidonasal cancer) and allergic-type pathologies (eczema and asthma) [9]. Improving working conditions involves the extraction of the wood dust injected into the air during machining. Several studies dealing with this problem have been carried out in France (efforts of INRS and CRAM), Finland, Germany, Switzerland and the USA and have led to several interesting results [10] and [11]. In Tunisia, a research and innovation project was launched to address these air quality problems in the workshops of the wood industry. It involved our laboratory, a prominent company in the field and the CETIBA (the technical centre of the wood and furniture industry).

Observations and inspective studies were organized during visits to the workshops of our industrial partner, where several machines were considered during their use.

The "T130N SCM router" was identified as one of the dustiest machine tools. This machine allows the modification of the profile of rectilinear or curvilinear workpieces by material removal. It also allows tenoning and calibration operations to be carried out. The "wood rejection" phenomenon is the main source of dust production by the router. The quantity, nature and rejection (speed and direction) of this dust are controlled by the following parameters: the router action mode, the number of teeth, the protrusion of the tooth from the body of the tool, the settings (cutting height, depth of cut), cutting speed, type of wood in addition to the conditions of use of the router and its maintenance conditions [12].

Some operations require varying the cutting direction in order to achieve specific geometries, which causes dust to be ejected in all directions. In addition, these machining operations require that the cover be removed from the original vacuum system, which makes it unable to capture most of the dust emitted. Therefore, a new method of dust extraction must be developed that maximizes the dust collection, minimizes the suction pumping demand without affecting the efficiency and functionality of the machine. The best system design must optimize these conflicting conditions and constraints.

Pollutant dispersion or capture requires an understanding of fluid mechanics and a good tool for calculating flow details. It is for these reasons that the design method used is based on "CFD optimization". This technique promises to lead to designs far superior to those based on conventional methods.

2.1 Methodology

2.1.1 Configuration

In order to simplify the mathematical problem while keeping most of the parameters of the physical problem, certain configuration related assumptions must be adopted.

The present work addresses the dust suction problem for the "T130N SCM router" machine tool during a machining operation where the cover around the tool is removed and the operator is forced to change the tool cutting direction. This results in dust ejection in all directions.

Except for the machine table, the geometric configuration of the problem is essentially axisymmetric around the axis of the router. As the end of the table is far enough away from the particle injection and suction field, the problem is considered insensitive to the exact shape of the table. The table will, therefore, be considered cylindrical in shape having the same axis of symmetry as the top. According to this assumption, the configuration to be studied is axisymmetric around the vertical axis going through the center of the router tool (Fig. 1).

The model's second hypothesis concerns the injection of the particles, which is considered to be done uniformly over the entire lateral surface of the router and with a speed in the radial direction. In reality, the dust emission is neither uniform over the entire surface of the router, nor in the radial direction. Actually, the particles leave

Fig. 1 Computational
domain and boundary
definitions (dimensions in m)
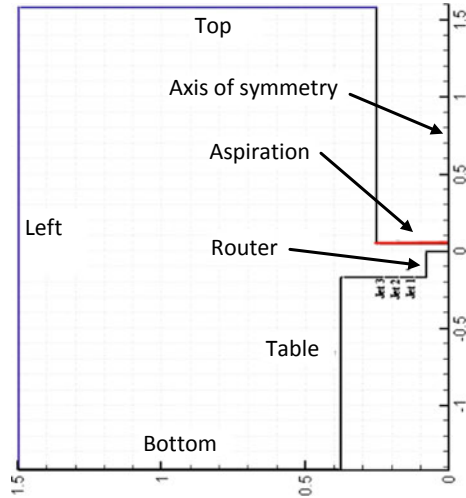
the router at a certain angle to the radius and only in areas where there is contact
between the tool and the machined wood. These areas change position continuously
during the machining operation. The second hypothesis was introduced to simplify
the problem and take advantage of its geometric symmetry. Its justification is that it
is conservative, i.e. it is more demanding from the point of view of dust collection.

2.1.2 Governing Equations

The studied domain consists of two phases: a continuous phase (air at atmospheric
pressure) and a solid phase (wood dust). The continuous phase obeys the equations
of continuity and momentum. Using the turbulence closure assumptions helps deter-
mine the unknown terms of the correlations that appear in the averaged equations.
The solid or discrete phase is treated by writing the equation of motion, for a spher-
ically shaped particle, which expresses the balance between the acceleration of the
particle and the forces it experiences.

The problem governing equations are based on the following assumptions: (i) the
fluid flow is stationary, two-dimensional and axisymmetric; (ii) the gas constituting
the continuous phase is incompressible; (iii) the injected particles are solid spheres;
(iv) the particle size is calculated from Schlessinger's empirical relation for rotating
tools [13]. It is evaluated at 35 μm for typical cutting conditions i.e. a 16 cm diameter
router, a tool rotational speed of 10,000 revolutions per minute, a workpiece feed
rate equal to 2.5 m/min and a depth of cut equal to 5 cm.

The motion of the continuous phase is governed by the continuity equation

$$\frac{\partial \overline{U_i}}{\partial x_i} = 0 \tag{1}$$

and the momentum equations

$$-\frac{\partial \overline{P}}{\partial x_i} + \frac{\partial}{\partial x_j}\left[\mu\left(\frac{\partial \overline{U_i}}{\partial x_j} + \frac{\partial \overline{U_j}}{\partial x_i}\right) - \rho\overline{u_i u_j}\right] = \rho\overline{U_j}\frac{\partial \overline{U_i}}{\partial x_j} \tag{2}$$

The standard $k - \varepsilon$ turbulence model is adopted to achieve turbulence closure.

To solve for the discrete phase motion, a Lagrangian approach is adopted. In this approach the particles are tracked individually during their movements and the behavior of the discrete phase is obtained from a statistical processing carried out on a sample of trajectories which takes into account at each instant the variations of the velocity fields that they meet. The statistical processing applied to all the trajectories makes it possible to obtain an estimate of the various specific average quantities such as the average speeds and concentrations. The limits of the validity of this approach require that the volume fraction i.e. the ratio of the introduced solid phase volume to the domain volume, should not exceed 12% [14].

The trajectory of a discrete phase particle is predicted by integrating the particle equation of motion, written in a Lagrangian reference frame. This equation of motion is based on the equation developed by Maxey and Riley [15] with the introduction of simplifications and empirical relations to model some of the forces. The reduced vectorial equation is

$$\frac{d\overrightarrow{U_{\mathrm{P}}}}{dt} = \varphi_{\mathrm{D}}\left(\vec{V} - \overrightarrow{U_{\mathrm{P}}}\right) + (\rho_{\mathrm{P}} - \rho)\vec{g} \tag{3}$$

The term $\varphi_{\mathrm{D}}\left(\vec{V} - \overrightarrow{U_{\mathrm{P}}}\right)$ represents the drag force applied on the particle. V and U_{P} are respectively the local fluid velocity and the particle speed, and $\varphi_{\mathrm{D}} = 3\mu/\left(4\rho_{\mathrm{P}} D_{\mathrm{P}}^2\right).C_{\mathrm{D}}.Re_{\mathrm{P}}$ where the particle relative Reynolds number is $Re_{\mathrm{P}} = (\rho D_{\mathrm{P}}/\mu)\left|\vec{V} - \overrightarrow{U_{\mathrm{P}}}\right|$, and the drag coefficient evaluated using $C_{\mathrm{D}} = \frac{K_1}{Re_{\mathrm{P}}} + \frac{K_2}{Re_{\mathrm{P}}^2} + K_3$. The values of the constants K_i are given by Morsi and Alexander [16] for different particle relative Reynolds numbers.

2.1.3 Resolution Method

Solving this problem involves few steps. First, calculating the field of the continuous phase and then the trajectories of the discrete particles according to the Lagrangian approach. In a subsequent step, the continuous phase velocities are recalculated taking into account the dynamic effects of the solid phase. In fact, as a particle passes through a control volume, there is a momentum exchange between the particle and the surrounding continuous phase.

The finite volume method is used to discretize the continuous phase equations. A first order upwind scheme is employed and the pressure—velocity coupling is based on the SIMPLE algorithm. The typical values of under-relaxation are fixed to 0.3

for the pressure and 0.5 for the discrete phase. The Convergence criterion was set to 0.1%.

A non-uniform mesh is used, with a refined mesh close to the aspiration mouth ($\Delta p = 0.0025$ m) and at the router tool level ($\Delta p = 0.0017$ m). In the rest of the domain, the mesh is more loose ($\Delta p = 0.03$ m). The domain has 62,731 triangular node centered cells.

The boundary conditions (nomenclature according to Fig. 1) for the continuous phase are as follows: the vertical axis going through the center of the router tool is an axis of circular symmetry: except for the top and left boundaries where the pressure is taken as constant, the Dirichlet boundary conditions are applied for other boundaries, specifically constant specified velocities at the aspiration surface and jet outlet (will be proposed as a solution below); and the wall condition (no slip and no penetration) for remaining boundaries. The particles are assumed to be injected uniformly over the entire lateral surface of the router and with a speed in the radial direction. In reality, the dust emission is neither uniform, nor in the radial direction. It is done at a certain angle to the radius and only in areas where there is contact between the tool and the machined wood. This hypothesis was introduced to simplify the problem and take advantage of its geometric symmetry. Its justification is that it is conservative i.e. it is more demanding from the point of view of dust collection. The particle injection speed, corresponding to typical machining operations, was specified as 83 m/s.

2.2   Results

The work presented here was prompted by the need to develop a new method of dust extraction for special machining operations on the router that require varying the cutting direction in order to achieve specific geometries. This entails removing the cover from the original dust aspiration system, which makes it unable to capture most of the dust emitted. In addition to this constraint, the nature of the machining operation causes dust to be ejected in all directions. Therefore, a new dust extraction method must be developed that maximizes the dust collection, minimizes the suction pumping demand without affecting the efficiency and functionality of the machine. The best system design must optimize the conflicting conditions and constraints.

Since the machining operation requires that the vacuum system cover, normally placed around the tool, be removed and since the operator is continually changing the cutting direction, resulting in dust ejection in all areas. directions, and given that dust suction must not interfere with the functionality of the machine, dust collection can only be achieved using systems placed above the machine or systems placed at the end of the machine table without protruding above the table level. This last alternative proved to be limited according to preliminary calculations.

In view of the above, the configuration, adopted as a starting point for the design, consists of a circular aspirating duct placed at a height H above the router.

For the first tests, it was decided to consider a circular aspiration duct with an aspiration velocity of 20 m/s, a maximum value generally used for safety reasons, having a radius Ra = 0.25 m, and placed at a height H = 0.05 m from the top of the router tool. This is the minimum height that would insure visual access to the tool for an operator that is 1.80 m tall or less, standing in front of the machine table.

Figure 2 shows the streamlines obtained for this first tests configuration. Note that the suction is not very efficient as most of the suction flow comes from areas where you would expect to have a low concentration of wood particles. In fact, when the particles are considered, it is clear that for this configuration not all particles are drawn towards the aspiration duct (Fig. 3). This finding is confirmed by the percentage of particles captured. This is computed as the ratio of the number of particles that cross the aspiration boundary to the number of injected particles. In

Fig. 2 Streamlines of the continuous phase flow due to aspiration
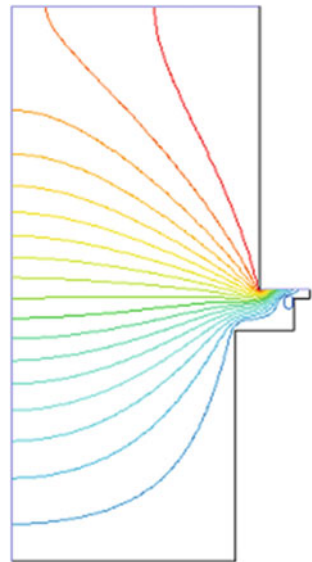
Fig. 3 Calculated particle trajectories, colored according to the local particle speeds (m/s). The dashed ellipse shows the particles that escape suction
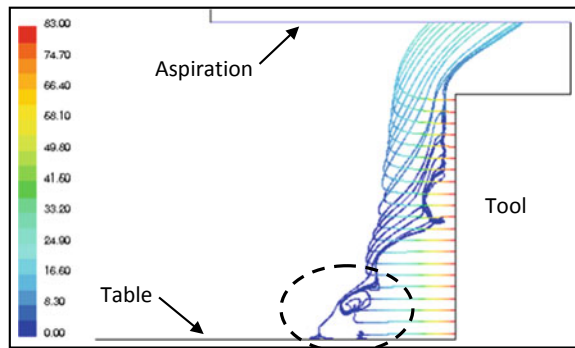
fact, for this configuration, only 62% of the particles ejected by the router during machining end up in the aspiration duct, the rest is dispersed in the workshop.

An effort to increase the suction efficiency by modifying the aspiration geometry (for example, by installing flanges) or the configuration (for example, using two concentric aspirations of different velocities) has been undertaken. However, no appreciable improvement was observed.

The alternative developed here is to use an air curtain with the aim of stopping the dispersion of dust beyond the suction zone. The air curtain is a jet formed by the vertical injection of air through a circular slot, at the level of the table, of thickness, e, and radius, R, coaxial with the router.

Three radial positions (R1 = 13 cm (position 1); R2 = 18 cm (position 2) and R3 = 23 cm (position 3, nearly aligned with the edge of the aspiration duct)) of this air curtain, with at each position three different jet velocities, V_j (20, 30 and 40 m/s), are studied. All the slits have a thickness $e = 2$ mm. Figure 4 shows the percentage of captured particles for each case. It can be seen that, for position 1 of the air curtain i.e. the closest position to the tool, this percentage reaches 100% for all jet velocities. This is also confirmed by the particle trajectories of Fig. 5. The decrease in particle aspiration at jets further from the tool can be explained by examining the velocity field of the continuous phase. Figure 6 shows samples, for different jet positions, of the streamlines in the vicinity of the tool and the aspiration duct. The formation of a fairly large circulation zone for the no-jet case is observed (Fig. 6a). This zone blocks the movement of the fluid below it and prevents it from reaching the aspiration duct. Since, the majority of the wood particles are injected in the resulting stagnation zone, the aspiration is therefore less likely to act on these particles and direct them upwards. In Fig. 6b, the air curtain reduces the size of the circulation area and therefore the particles are subjected to an upward flow as soon as they are injected, which would eventually entrain them upward, facilitating their guidance to the aspiration duct (see the particle trajectories of Fig. 5). When the jet of the air curtain is placed further from the tool, it can be seen (see for example Fig. 6c) that the sizes of the circulation

Fig. 4 Percentage of captured particles by the aspiration system for different jet positions and velocities (aspiration duct 0,05 m above the tool)
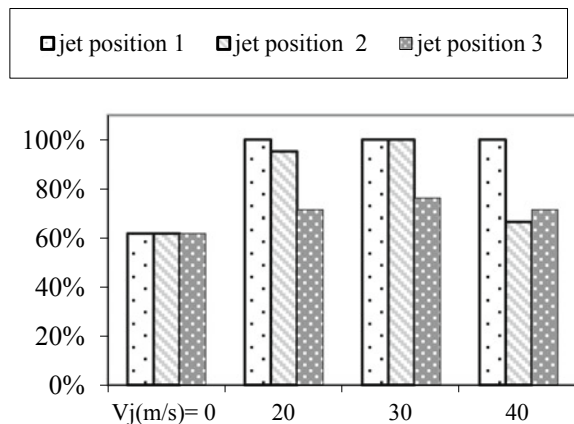
Fig. 5 Calculated particle trajectories, colored according to the local particle speeds (m/s) for jet at position 1 and $V_j = 20$ m/s
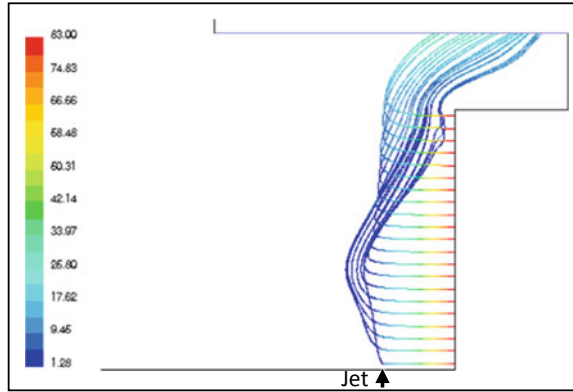
Fig. 6 Streamlines for the cases **a** no-jet; **b** jet in position 1, $V_j = 20$ m/s; **c** jet in position 3, $V_j = 20$ m/s
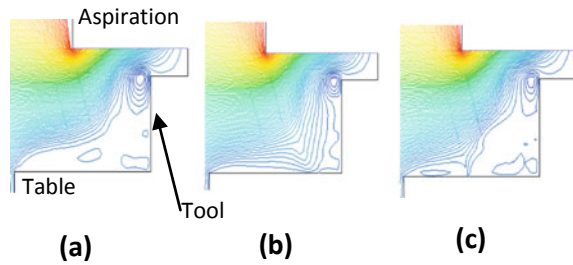
and stagnation zones increase and therefore the flow situation becomes similar to the one without an air curtain. Furthermore, it is seen in Fig. 5 that increasing the speed of the jet will resolve the suction problem for the case of jet at position 2, but not for the case of the jet at position 3. This is due to the fact that the jet serves only to drive the dust particles towards the aspiration duct but it cannot alone, and even at a speed equal to 40 m/s (when it is far from the injection zone) deviate their trajectories. Actually, very few particles would reach the position of jet 3. They are either entrained towards the aspiration duct or are precipitated down on the table at locations ahead of the jet position. Hence, the limited effect of the jet, no matter what its velocity is.

The effect of the location of the air curtain is also illustrated in Fig. 7 that presents the particle concentration profiles at a height halfway between the tool and the entrance to the aspiration duct. The increase in captured particles, when an air jet is introduced at position 1, is obvious. It is also clear that for position 3 of the jet, the number of captured particles is reduced. However, it is not as easy to interpret the profile for a jet at position 2. Indeed, there is a decrease in captured particles for this configuration (Fig. 4), although we see a larger peak in the concentration profile. The explanation lies in the fact that the y-axis represents a radius, so for the same concentration the quantity of particles is greater when the radius is larger (it corresponds to the integral over the area). Other observations related to Fig. 7 concern the position

Fig. 7 The discrete phase
mass, DPM, concentration
profiles for different jet
positions with a jet velocity
of 20 m/s
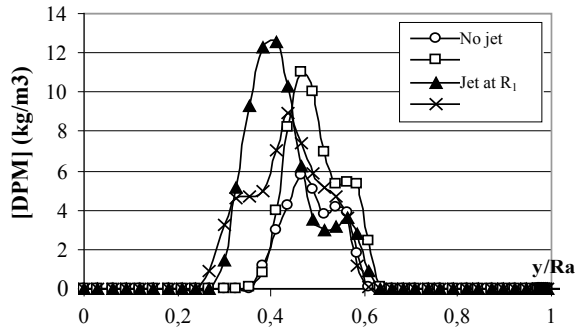
of the maximum concentration. The latter is expected intuitively to occur at larger
radial positions when the jet is moved outward. This is not the case (Fig. 7). This
observation is consistent with the streamlines of Fig. 6, as the particles entrained
towards the aspiration duct follow streamlines that are closer to the axis of symmetry
when the jet position is moved further away from the tool.

In the above simulations, the aspiration duct's diameter and position were kept
constant. However, as stated earlier, the duct position in that configuration represents,
for the duct and tool diameters, the minimum height that would insure visual access
to the tool for an operator that is 1.80 m tall or less, standing in front of the machine
table. It is therefore, opportune to examine higher duct positions in order to select a
position that would allow better visual access and yet insures a full dust extraction.
Two other heights, in addition to the 0.05 m already presented, namely 0.1 and 0.25 m
above the tool top, are considered.

Based on the results for 0.05 m duct entrance height, the simulations were
conducted for an arrangement proven efficient previously i.e. an air curtain jet at posi-
tion 1. Three different jet velocities were considered. Figure 8 presents the calculated

Fig. 8 Percentage of
captured particles by the
aspiration system for
different jet velocities (jet at
position 1 and aspiration
duct 0.10 m above the tool)
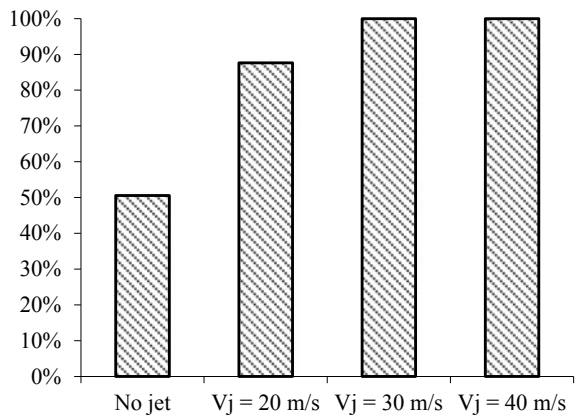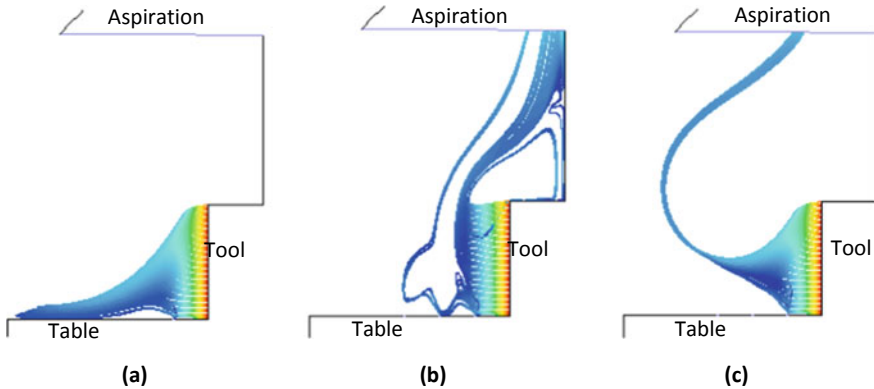
Fig. 9 Particle trajectories when the aspiration duct is placed 0.25 m above the tool for (**a**) a single jet at position 1 with $V_j = 20$ m/s; (**b**) three jets operated simultaneously with $V_j = 30$ m/s; and (**c**) three jets operated simultaneously with $V_j = 40$ m/s (legend as in Fig. 3)

percentages of captured particles for each of these velocities. There are two differences between the case with h $= 0.05$ m and the case with h $= 0.10$ m. For the latter, only 51% extraction is obtained when there is no jet and a jet velocity of 20 m/s is no longer sufficient to capture 100% of the injected particles. This is obtained for jet velocities of 30 and 40 m/s.

For h $= 0.25$ m, no particles reach the aspiration duct even for the highest jet velocities (Fig. 9a). For this reason, it was decided to examine the effects of operating all three jets simultaneously and seeing their effects on the efficiency of the suction.

The analysis of the percentages of the dust particles collected show that only 89.7% of the particles are captured for a simultaneous operation of the three jets with a velocity of 20 m/s, 98.5% for a velocity of 30 m/s, and 100% of the particles injected are captured for 40 m/s. The trajectories of the discrete particles of the last two cases are presented in Fig. 9b and c. It is obvious that, for $V_j = 30$ m/s (Fig. 9b), the first and second jets are not able to direct all the particles toward the aspiration duct. Some particles reached the table prior to the third jet. For a velocity of 40 m/s (Fig. 9c), the two first jets succeeded in preventing the precipitation of the particles. However, it took the third jet to direct the particles towards the aspiration. Nevertheless, the solution involving an aspirating duct position at h $= 0.25$ m, is to be excluded since operating 3 jets simultaneously at 40 m/s is neither practical nor cost effective. In addition to the fact that a 40 m/s velocity can have safety implications.

By examining the particle trajectories and the particle concentration profiles e.g. in Figs. 5 and 7, it was obvious that not all the cross-section of the aspiration duct receives particles. This prompted us to study the effect of diminishing the duct radius, Ra, to 0.20 m. The simulations confirmed that for h $= 0.10$ m, for a jet at position 1 and having a velocity of 20 m/s, 100% of the particles are captured for Ra $= 0.20$ m. This last result is opposite to what one would expect intuitively, since only 88% of the particles were captured for the same configuration but with a larger duct radius
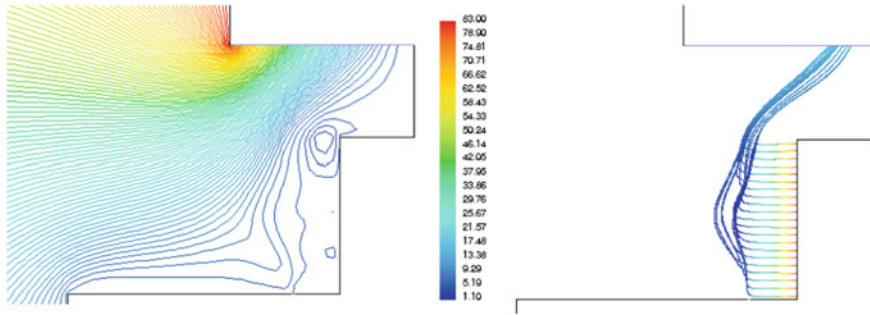
Fig. 10 Streamlines and particle trajectories (colored according to the local particle speeds, m/s) for an aspiration duct radius of 0.20 m, placed 0.10 m above the tool and with a jet at position 1 with a velocity of 20 m/s

(Ra = 0.25 m). This perplexing result can be explained by studying the streamlines of Fig. 10. It can be seen that the reduction of the duct radius, combined with jet flow, pushed the upward streamlines towards the tool. Thus, the suction flow could act earlier on the particles and direct them into the aspiration duct.

In conclusion, dust extraction is most efficient when the jet is placed close to the tool e.g. at a radius of 13 cm. A jet velocity of 20 m/s is sufficient to extract 100% of the wood dust. The aspiration duct is to have a radius of 0.20 m and is to be placed at a height of 0.10 m from the top of the tool. Selecting a smaller duct would cost less, allow a better visual access, and would require a reduced suction flow rate e.g. the flow rate for a 0.20 m duct radius corresponds to 64% of that for Ra = 0.25 m.

3 CFD Aided Design of a Convective Dryer

Drying of Agricultural products is industrially conducted in tray dryers where the products to be dried are spread and subjected to convective heat and mass transfer. For example, our industrial partner's dryer consists of a chamber housing a number of trays over which parallel airflow, emanating from a side inlet, passes. To insure product quality and minimize the drying time and its corresponding energy consumption, it is desirable to obtain uniform drying of the product. This is difficult to obtain in industrial tray dryers because of the uneven distribution of the airflow. In fact, a coarse air velocity measurement in the industrial partner's dryer showed that the velocity distribution varied vertically over the tray cart from 0.70 to 1.65 m/s with much higher velocities above the trays (these represent a by-pass flow that does not contribute to the drying). Several features can be implemented in a dryer design to obtain uniform velocities over the trays and thus improve the dryer performance [17]. The flow uniformity can be improved by acting on the geometry and the dimensions of different parts of the dryer. However, the quantitative influence of each of these features and especially the fine tuning of their combined effects requires accurate

prediction of the flow in the dryer. Thus, the use of CFD numerical simulations as a tool to assist in the selection and dimensioning of the dryer components and features required to insure the sought flow distribution in the drying chamber. An example for the use of this approach is provided in [18], where it was employed for the prediction of drying uniformity in tray dryer systems. In addition to improving the performance of the dryer, this CFD aided design can help optimize the dryer size in order to minimize the use of materials, and hence the cost of the installation. All the interior walls of the dryer have to be made of expensive food grade stainless steel, which makes size minimization even more crucial.

The objective of this work is to study the effect of the variations of the dryer's geometrical features and dimensions on the flow uniformity. The objective is to optimize the industrial dryer in terms of size while obtaining the best flow uniformity.

3.1 Dryer Description

The industrial dryer to be improved is presented schematically in Fig. 11. Its operation can be described as follows. Air (actually a mixture of fresh and recycled air) is drawn into a hybrid heating compartment (comprising a gas burner and a heat exchanger with solar heated water) placed on top of the dryer. The hot air is then blown by fans into a 30 cm deep plenum, occupying the entire left side of the dryer. It enters subsequently the drying chamber through a 3 mm thick perforated plate. The latter has uniformly distributed perforations, with a porosity of 69%, from a height above the ground of 0.25 m (corresponds to the level of the bottom tray) to a height of
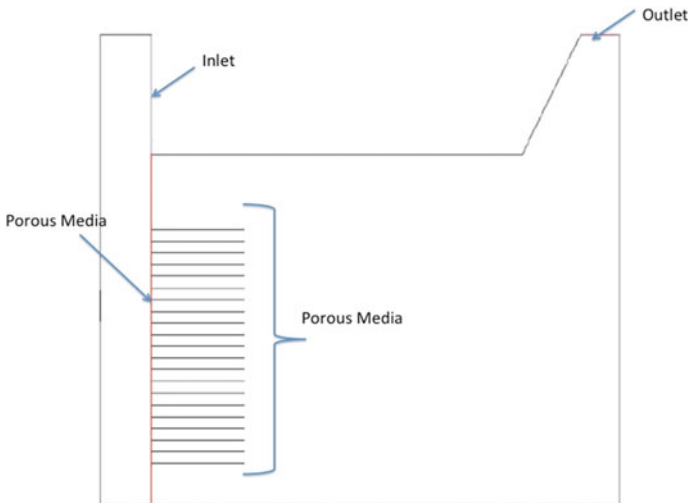
Fig. 11 The numerical flow configuration corresponding to the actual industrial dryer

1,85 m. The purpose of the plenum and the perforated plate is to produce horizontal uniform flow over the trays. The drying chamber, where the exchanges between the air and the product to be dried take place, has a length, in the flow direction, of 3.64 m, a width of 2.00 m and a height of 2.82 m. The drying air leaves the chamber from the top right corner.

The drying chamber contains three carts located right at the perforated plate and placed next to each other so that they occupy the entire width of the chamber. Each cart contains 21 trays over which the products to be dried are laid. The trays are 90 cm long and 60 cm wide wire racks. The vertical tray separation is 6 cm.

3.2 Methodology

The numerical simulations were conducted for a 2D model of the dryer in steady state condition. Unstructured 2D mesh was employed. The initial geometrical configuration is shown in Fig. 11 with the following boundary conditions:

- Velocity inlet: 3 m/s normal to the air inlet to insure a velocity of 1.6 m/s over the trays
- Pressure outlet: Assuming a zero gauge pressure at the outlet.
- Porous media: The trays and the perforated plate were assumed as porous media
- Walls: no-slip and no penetration boundary condition

The finite volume method is employed to solve the equations of the conservation of mass and momentum (Eqs. 1 and 2) in combination with the standard k-ε turbulence model.

The simulations were carried out for the initial geometry of Fig. 11, corresponding to the existing dryer, then gradually the geometries and relative sizes of the dryer components were modified and the resulting effects investigated. The geometrical parameters of the cases presented in the next section are summarized in Table 1. The velocity profile at a vertical line located just at the exit of the trays was selected to study and analyze the uniformity of the velocity in the drying chamber.

Table 1 Summary of the geometrical variation of the studied cases

Case number	Perforation height (m)	Chamber length (m)	Plenum depth (cm)	End walls inclination angle (°)
Case 1	1.85	3.64	30	0
Case 2	1.55	3.64	30	0
Case 3	1.55	3.64	70	0
Case 4	1.55	2.00	70	0
Case 5	1.55	2.00	30	8

3.3 Results

For the initial flow configuration i.e. the geometry of Fig. 11, hereafter referred to as case 1, the simulations yielded the velocity contours of Fig. 12 and the velocity profile of Fig. 13. It is obvious that the velocity over the trays (heights between 0.25 and 1.55 m) is not uniform. It actually varies between 1.0 and 1.5 m/s. A quite large variation which would result in uneven drying of the products. A high bypass flow, reaching 2.75 m/s, occurs above the trays. This is a large portion of the total flow rate that does not participate in the drying. This large flow velocity is the result of the reduced flow resistance above the trays. It can also be seen in Fig. 13 that at the bottom of the profile, there is a flow reversal due to the upstream flow stagnation region below the bottom tray. Based on these results, flow improvement is needed. It can be achieved by modifying the plenum size and/or geometry and the perforated plate porosity distribution and/or extent.

The large flow bypass above the carts can be reduced and eventually eliminated by limiting the perforations to the part of the plate that is in front of the carts. Figure 14 presents the velocity magnitude profile when the plate perforations are limited to heights between 0.25 and 1.55 m (case 2). It shows that not only the flow bypass was eliminated, but also the flow over the trays became more uniform. Varying the porosity of the perforated plate to improve the flow uniformity was explored. However, it revealed to be quite tedious to obtain in practice and much better results were obtained by acting on the plenum depth.

The larger the plenum, the better it can play the role of a settling chamber, or pressurized box, that would yield more uniform velocity into the drying chamber.
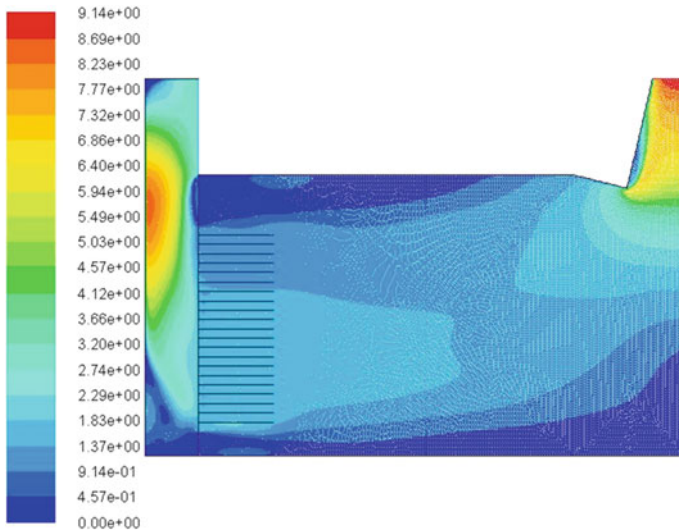
Fig. 12 Calculated iso-velocity contours for the actual industrial dryer configuration (case 1)
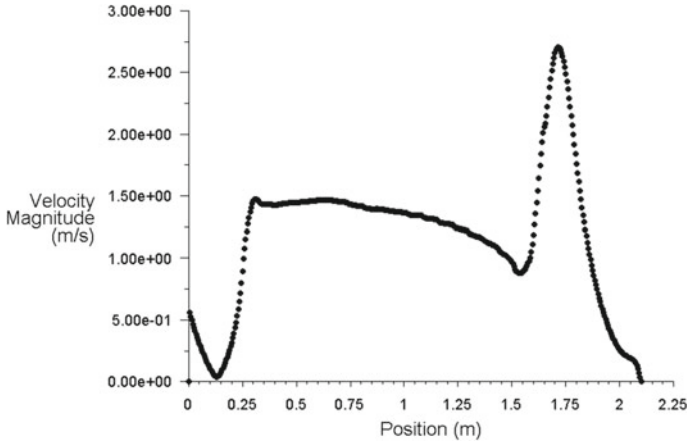
Fig. 13 Profile, along a vertical line at the tray exit, of velocity magnitude for the actual industrial dryer configuration (case 1). The axis origin is at the ground level
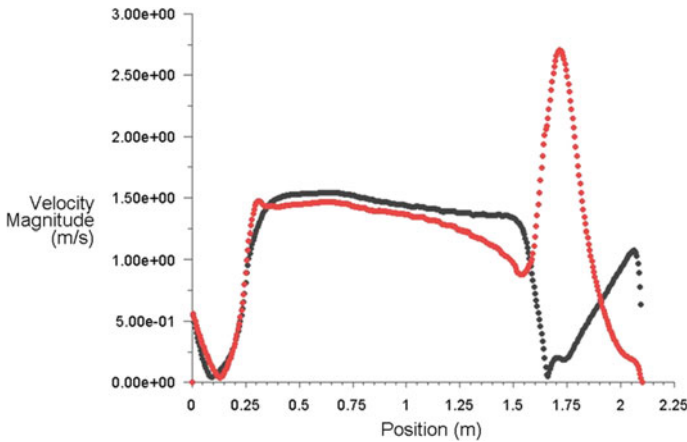
Fig. 14 Profile, along a vertical line at the tray exit, of velocity magnitude for the modified dryer configuration (case 2), black curve. For comparison the profile of Fig. 13 (case1) is presented in red

So, to further improve the profile of Fig. 14, the plenum depth was increased from 30 to 70 cm (case 3). Figure 15 shows that such a change does improve the velocity uniformity. It also removed the flow reversal in the bottom and reduced the size of the recirculation zone in the top.

In order to reduce the construction cost of the dryer, by reducing the use of material, we've examined the effect of reducing the streamwise length of the chamber, while keeping the perforated plate and plenum configurations corresponding to case 3. Several lengths were tested. It was found that the chamber length can be reduced from 3.64 to 2.5 m (case 4) without modifying the profile (in Fig. 16, the velocity
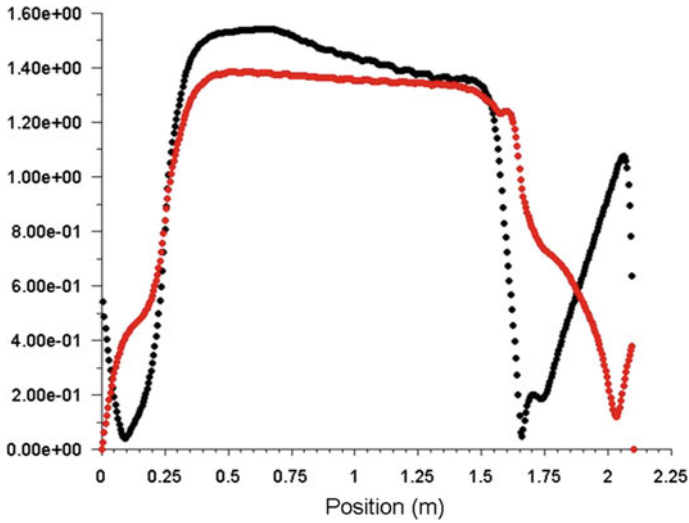
Fig. 15 Profiles, along a vertical line at the tray exit, of velocity magnitude for cases 2 (black curve) and 3 (red curve) showing the effect of increasing the plenum depth from 30 to 70 cm
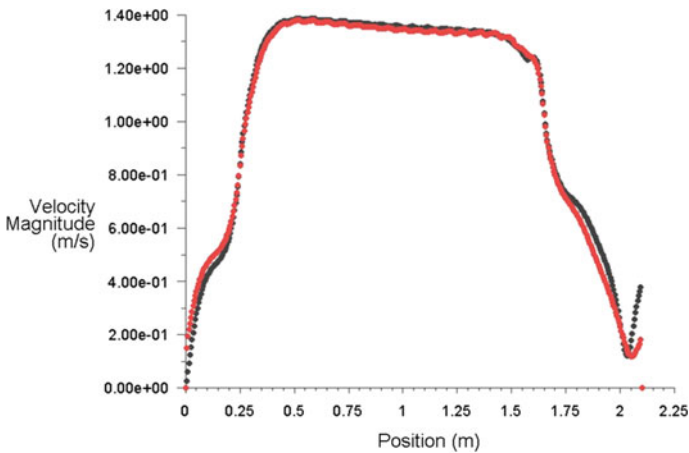
Fig. 16 Profiles, along a vertical line at the tray exit, of velocity magnitude for cases 3 (black curve) and 4 (red curve) showing the effect of reducing the chamber length from 3.64 to 2.5 m

profile remains essentially the same for cases 3 and 4). However, reducing the length further, alters the profile by increasing its nonuniformity.

In an effort to further reduce the size of the dryer, it was decided to examine the possibility of reducing the plenum depth to its initial value i.e. 30 cm, while maintaining the dryer length equal to 2.50 m. This would be achieved by studying the effect of inclining the plenum left wall and the chamber right wall, as shown
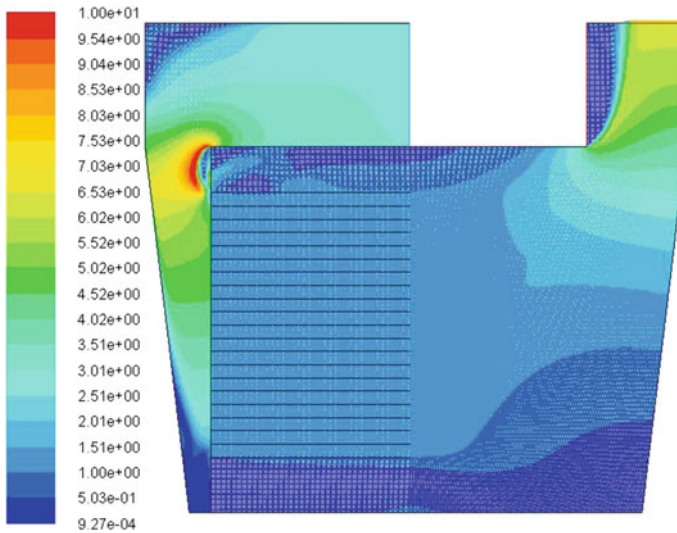
Fig. 17 Calculated iso-velocity contours for the optimized dryer configuration (case 5)

in Fig. 17, on the uniformity of the velocity profile. Several inclination angles were tested. An inclination angle of 8° with respect to the vertical for both walls (case 5) was found to yield a practically uniform velocities over the trays (Fig. 18).

In recapitulation, starting with an existing dryer design and varying some of its features' geometries and dimensions, we were able to obtain an optimized dryer i.e. the smallest, and thus the least expensive, that still insures a uniform drying convective velocities over all trays. This the configuration of case 5.

4 Conclusion

In this work, we have presented two case studies where Computational Fluid Dynamics, CFD, is employed as a tool to assist in the design and optimization of equipment involving fluid flows.

In the first case, a dust extraction equipment for the router tool machine was designed and its dimensions optimized according to criteria related to dust extraction capacity, visual access, operability of the machine, safety and aspiration flow rate. The equipment consists of an aspiration duct placed above the tool and an air curtain formed by the vertical injection of air through a circular slot around the tool, at the level of the table.
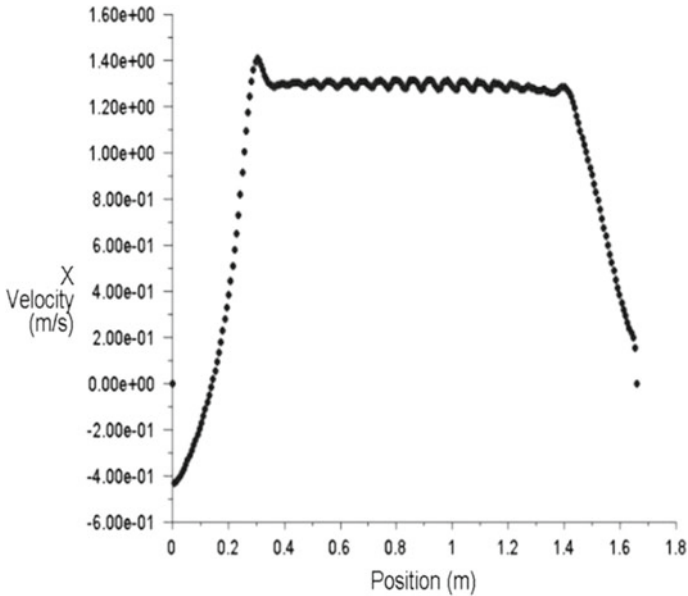
Fig. 18 Profile, along a vertical line at the tray exit, of velocity magnitude for the optimized dryer configuration (case 5)

In the second case, a convective dryer configuration and dimensions were optimized in order to insure uniform drying with the smallest dryer dimensions possible, thus minimizing its cost.

The simulations, in both study cases, were instrumental in the design and optimization as they allowed the prediction of the equipment behavior that is otherwise hard to foresee, either because of the unpredictable combined effects of different features or because of the counterintuitive results. The two study cases are proof of the usefulness of the CFD aided design approach. Further development would be to incorporate the CFD calculations in an optimization routine to automatically reach the optimum values.

References

1. Jameson A (1995) Optimum aerodynamic design using CFD and control theory, American Institute of aeronautics and astronautics 12th computational fluid dynamics conference, San Diego, CA, U.S.A. (19–22 June 1995). doi:https://doi.org/10.2514/6.1995-1729

2. Zhang Z, Liu H, Zhu S, Zhao F (2006) Application of CFD in ship engineering design practice and ship hydrodynamics. J Hydrodyn Ser B 18(3-supp-S):315–322. doi:https://doi.org/10.1016/s1001-6058(06)60072-3

3. Fraser KH, Taskin ME, Griffith BP, Wu ZJ (2011) The use of computational fluid dynamics in the development of ventricular assist devices. Med Eng Phys 33(3):263–280. https://doi.org/10.1016/j.medengphy.2010.10.014

4. Annoni M, Arleo F, Malmassari C (2014) CFD aided design and experimental validation of an innovative air assisted pure water jet cutting system. J Mater Process Technol 214:1647–1657

5. Zhai Z, Xue Y, Chen Q (2014) Inverse design methods for indoor ventilation systems using CFD-based multi-objective genetic algorithm. Build Simul 7(6):661–669

6. Bartzanas T, Kacira M, Zhu H, Karmakar S, Tamimi E, Katsoulas N, Lee IB, Kittas C (2013) Computational fluid dynamics applications to improve crop production systems. Comput Electron Agric 93:151–167. https://doi.org/10.1016/j.compag.2012.05.012

7. Xia B, Sun DW (2002) Applications of computational fluid dynamics (CFD) in the food industry: a review. Comput Electron Agric 34(1–3):5–24. https://doi.org/10.1016/s0168-1699(01)00177-6

8. Norton T, Sun DW (2006) Computational fluid dynamics (CFD)—an effective and efficient design and analysis tool for the food industry: a review. Trends Food Sci Technol 17(11):600–620. https://doi.org/10.1016/j.tifs.2006.05.004

9. INRS (1993) Maladies professionnelles, INRS ED 486, Juillet

10. Muller JP, Lamoureux P (1996) Amélioration des dispositifs d'aspiration localisée: étude sur quatre machines à bois traditionnelles, INRS, cahier de note documentaire n° 163, 2° trimestre

11. Möcklinghoff K, Fricke HH, Wermer W (1999) Holzstaub messen, bewerten und vermindern Ein Erfahrungsbericht. Gefahrstoffe-Reinhaltung der Luft 7–8:273–280

12. L'Huilier JC, Otter B, Obrecht P (2004) Toupie verticales simples. INRS, ED 589, mise à jour Mars 19–21

13. Groupe de travail CRAM et INRS, Conception des dispositifs de captage sur machines à bois, INRS, Paris, 2002, ED 841, p 9

14. FLUENT 6.0 User's Guide, Fluent Inc, Lebanon, NH, USA, 2001, Vol 1–5

15. Maxey M, Riley J (1983) Equation of motion for a small rigid sphere in a nonuniform flow. Phys Fluid 26(4):883–889

16. Morsi SA, Alexander AJ (1972) An investigation of particle trajectories in two phase flow systems. J Fluid Mech 55:193–208

17. Misha S, Mat S, Ruslan MH, Sopian K, Salleh E (2013) Review on the application of a tray dryer system for agricultural products. World Appl Sci J 22(3):24–433

18. Misha S, Mat S, Ruslan MH, Sapian K, Salleh E (2013) The prediction of drying uniformity in tray dryer system using CFD simulation. Int J Mach Learn Comput 3(5):419–423

Advancement in Refrigeration Systems

Energy Efficient Automobile Air Conditioning System Through Effective Condenser Cooling

Rohith Thotakura, Lakshmi Supraja, S. Vineeth Raj, Anjali Damodaram, and M. Mohamed Musthafa

Abstract An air conditioning system was built in all deluxe vehicles. The air conditioning fit in vehicles will give higher fuel consumption because of power absorbed to run the compressor from engine output. The main drawback of reduction in mileage will be improved in this study by increasing the heat removal rate, thereby decreasing the compressor power absorption. This study was depicted with experimental test rig consists of various components such as compressor, condenser, evaporator, expansion device, and electric motor were put together. The modifications were made on the existing system viz., the compressor was run by an electric motor instead of engine power. Inbuilt condenser fan was replaced by an evaporative cooling method using exhaust fan was surrounded by a cooling pad. Cool water is supplied to the cooling pad using a pump. The test was conducted on conventional cooling and evaporative cooling methods to obtain a similar cooling effect. The result showed that a higher coefficient of performance (COP) for the evaporative cooling system compared to the conventional system due to an increase in heat removal rate.

Keywords Compressor · Condenser · Electric motor · Evaporative cooling · Heat removal rate · Performance

Nomenclature

CoP	Coefficient of performance
p–h	Pressure-enthalpy
Q	Heat removal rate (W)
rpm	Revolution per minute
VCR	Vapour compression refrigeration

R. Thotakura (✉) · L. Supraja · S. V. Raj · A. Damodaram · M. M. Musthafa
School of Mechanical Engineering, SASTRA Deemed University, Thirumalaisamudram, Thanjavur 613401, India
e-mail: rohiththotakura6997@gmail.com

1   Introduction

The air conditioning system in the vehicle refers to providing and maintaining desirable temperature and humidity for passenger comfort irrespective of external conditions. The working substance which is used in the air conditioning system to absorb and liberate the heat alternatively is called refrigerant. The name of refrigerant used is R134a [1]. An automobile air conditioning system works on the principle of vapour compression refrigeration (VCR) system [2]. In this system, a refrigerant R134a undergoes alternatively a change of phase from vapour to liquid and liquid to vapour during the working of the cycle. The refrigerant is circulated in a closed circuit through a compressor, condenser, expansion valve, and evaporator. The power required to run the compressor is given from engine power. It will increase fuel consumption and reduce the mileage of the vehicle by up to 35% [3]. The system should give a higher CoP in the working temperature range. This is necessary to reduce the running cost of the system in terms of reducing fuel consumption. The CoP is defined as the ratio of heat extracted from the cabin to the work done on the system [4]. The heat removal rate in the evaporator depends on the refrigerant temperature at the condenser exit. The evaporative cooling gives a decrease in exit temperature of refrigerant by additional removal of heat than the inbuilt air cooling condenser. Hence, CoP of the system increases for the same amount of compressor work [5]. This was understood from the p–h chart as shown in Fig. 1. In this Fig. 1, 3–3′ is the decrease in exit temperature of the refrigerant in the condenser due to evaporative cooling, and 4–4′ is corresponding to the increase in heat removal rate in the evaporator for the same compressor work of 1–2. Hence, the CoP of the system increases [6].

Many kinds of research [7] on VCR system are focussed to increase the CoP through either increase in heat removal rate (refrigeration effect) by subcooling or a decrease in compressor work input by superheating. Subcooling has a simple and more effective method rather than superheating [8]. Removing extra heat from the

Fig. 1   p–h chart of VCRS
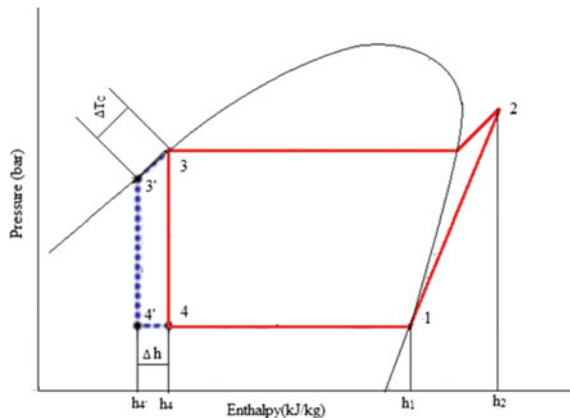
condenser through any method allows a higher amount of heat absorption in the next stages of the cycle. Hence, the CoP of the system increases with the same compressor work. Subcooling by liquid-suction method has been used in the past years to achieve better performance of the system [9]. These methods necessitate the exact and optimised design of the heat exchanger. The research gap of improving performance on the air conditioning system is to be fulfilled in this study through evaporative cooling of the condenser.

2 Experimental Facility

2.1 Evaporative Cooler Setup

The evaporative cooler was fabricated as shown in Fig. 2, and it consists of exhaust fan runs at 1300 rpm, three cooling pad of size 60 cm × 40 cm and a water pump. The steel frame was fabricated in such a way that to accommodate the fan and cooling pads. A separate water pump was used to supply water over the cooling pads through the multi-drilled PVC pipe at a different flow rate such as 0.03, 0.07, 0.08, and 0.1 kg/s, and the corresponding reduction of atmospheric air temperature was measured and found 4 °C temperature reduction from 31 to 27 °C at 0.08 kg/s flowrate. The velocity of cooled air blow over the surface of the condenser was measured using an anemometer. The distance between the cooler and condenser was adjusted to obtain a maximum reduction in condenser surface temperature. At a gap of 20 cm, the maximum decrease in surface temperature of the condenser was attained at 5.5 m/s velocity of air blow.
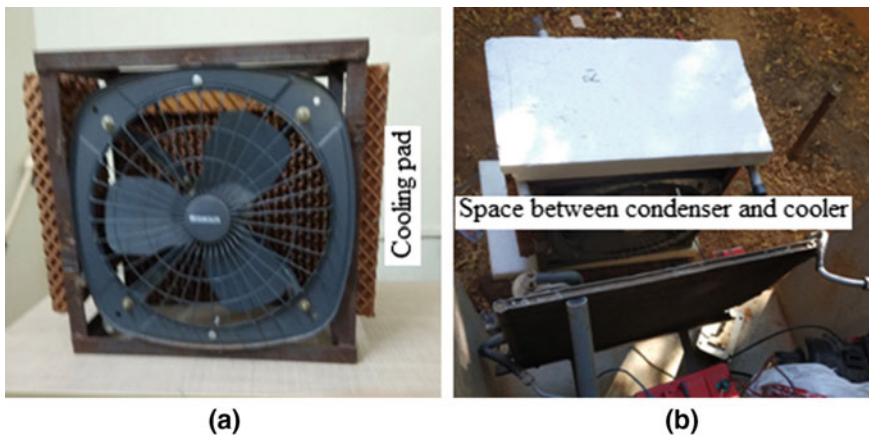
Fig. 2 **a** Fabricated evaporative cooler. **b** Distance between cooler fan and the condenser
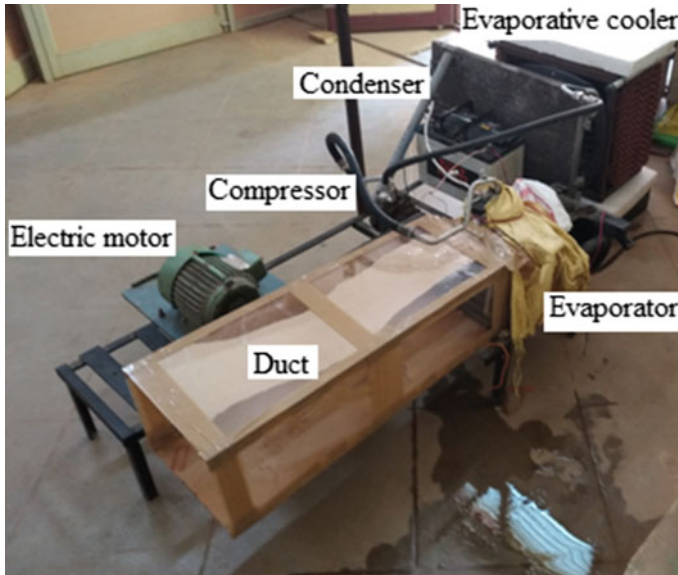
Fig. 3 Test rig setup

2.2 Test Rig Setup

The experiment test rig was fabricated as shown in Fig. 3 using Hyundai, i-10 variant car air conditioning parts. A 1.5 HP three-phase induction motor was attached to the test rig set up to drive the compressor through the belt and pulley assembly. The electric power consumption was measured using an energy metre. The evaporator is enclosed by a rectangular duct of size 25 cm × 18 cm and 80 cm made up of a 3 mm thick acrylic sheet to prevent heat loss to the surrounding. The inbuilt condenser fan was replaced by an evaporative cooler fan. The velocity of cooled air blows in the duct was measured as 0.5 m/s.

2.3 Experimental Tests

The experiment was conducted on the test rig at three various cases viz., 1. using inbuilt fan, 2. exhaust fan, and 3. evaporative cooler. During the test trial, the amount of heat removed from one kg of water in the aluminium jug which is kept inside the duct at a regular interval of 10 min was measured. Besides that suction and delivery pressure of compressor; condenser and evaporator inlet and exit temperatures; and energy metre readings were noted for CoP calculation.

Fig. 4 Condenser exit temperature with a running time
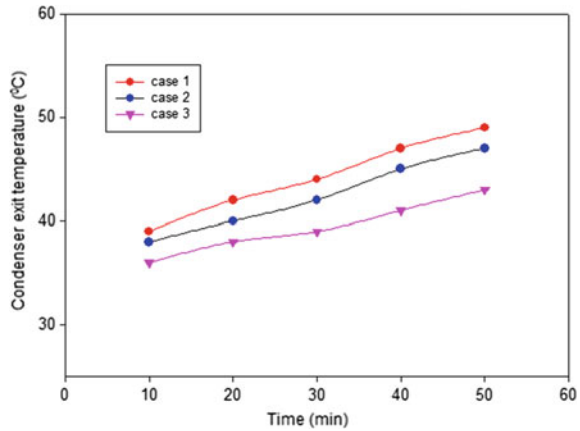
3   Results and Discussion

3.1   Condenser Exit Temperature

Figure 4 represents the exit temperature of the condenser against the running time of the system for the three cases. When running time increases, the exit temperature of the condenser increases in all trails. The increasing excess temperature for an entire test run was reduced in the case 2 and 3 compared to case 1. Most reduction in condenser exit temperature in case 3 was observed by blowing the cooled air over the entire surface of the condenser and placing the cooler at an optimised distance from the condenser. Trail 2 also reduces the exit temperature of the condenser to some extent compared to Trail 1 due to reduction of bypass volume of air blows over condenser surface even the exhaust fan speed (1300 rpm) is lower than inbuilt fan speed (1700 rpm).

3.2   Heat Removal Rate

Figure 5 illustrates the amount of heat removed with running time for three trails. The amount of heat removed from the water was calculated using the formula $m\, c_p\, \Delta T$. Where m is mass of water, c_p is the specific heat of water and ΔT is the decrease in temperature of the water after 10 min. An increasing trend of heat removal rate was observed in three cases. The more amount of heat was removed in case 3 followed with case 2 and case1. It is evident from Graph 4; there is a small drop of exit temperature of condenser give more amount of heat removal rate in case 3 due to evaporative cooling.

Fig. 5 Amount of heat
removed with a running time
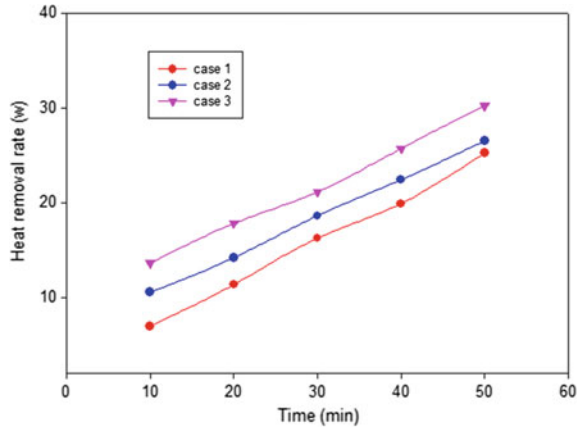
3.3 Coefficient of Performance

As explained in the introduction section, the higher CoP of the system reduces the
running cost. The actual CoP of the three cases was calculated against the running
time using the ratio between heat removal rate and electric power consumption for the
motor. Theoretical CoP was also calculated using p–h chart of R134a and found that
the actual CoP of three cases was lower than theoretical CoP. Figure 6 represents the
comparison of the coefficient of performance with running time. From the calculation,
the deviations of the power consumption of the compressor in the three trails are very
small. Hence, work input was assumed as constant. But the variation of heat removal
rate, the CoP has varied. The higher CoP was noted in case 3 during the test run due
to more amount of heat was removed, it is evident from Graph 5.

Fig. 6 Coefficient of
performance with a running
time
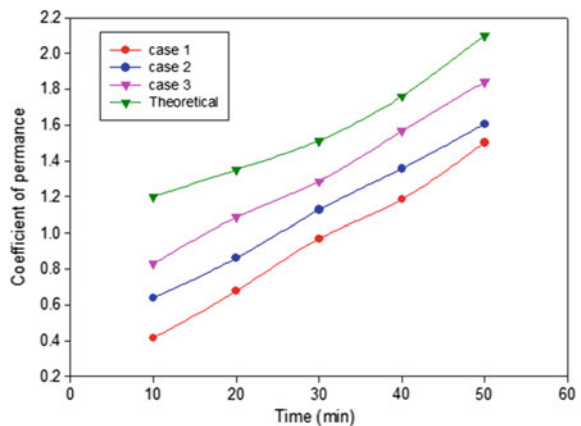
4 Conclusion

Through experimental study, it was proved that the evaporative cooling process in the condenser increases the heat removal rate for the same compressor work which results in higher CoP of the system. The test results point out the following.

- Through the fabricated evaporative cooler reduce the atmospheric air temperature up to 4 °C
- By reducing the bypass of air blows over the condenser surface using an evaporative cooler increases the amount of heat removed rate up to 35%
- A 5 °C temperature drop of the liquid refrigerant at condenser exit due to evaporative cooler increases the CoP system up to 22.5%
- This method will put into operation in the vehicle reduces fuel consumption considerably.

References

1. Boloji and Bukola Olalekan (2010) Effects of sub-cooling on the performance of R12 alternatives in a domestic refrigeration system. Int Sci Technol 15(1):12–19
2. Ashish Kumar P, Gupta RC (2013) Effect of sub cooling and super-heating on vapour compression refrigerant systems using R-22 alternative refrigerants. Int J Emerg Trends Eng Develop 1(3):521–531
3. Mohammed Sajid NK, Ram KS, Shafi KA (2012) Performance improvement of an air conditioning system using matrix heat exchanger. Int J Eng Res Develop 2(11):66–70
4. Poltker G, Predrag Hrnjak S (2012) Effect of condenser sub-cooling of the performance of vapour compression systems: experimental and numerical investigation. In: International refrigeration and air conditioning conference, Purdue
5. She X, Yonggao, Zhang X (2014) A proposed sub-cooling method for vapour compression refrigeration cycle based on expansion power recovery. Int J Refrig 43:50–61
6. Hajidavalloo E, Eghtedari H (2009) Performance improvement of air-cooled refrigeration system by using evaporatively cooled air condenser. Int J Refrig 33:982–988
7. Christian JL, Hermes (2014) Refrigerant charge reduction in vapour compression refrigeration cycle via liquid-to-suction heat exchanger. Int J Refrig 52:93–99
8. Upadhyay and Neeraj (2014) To study the effect of sub-cooling and diffuser on the coefficient of performance of vapour compression refrigeration system. Int J Res Aeronaut Mech Eng 2(6):40–44
9. Upadhyay N (2014) Analytical study of vapour compression refrigeration system using diffuser and sub-cooling. J Mech Civil Eng 11(3):92–97

A Comparative Analysis of Solar-Assisted ORC and Refrigeration System for Supercritical Working Fluids

Onder Kizilkan and Hiroshi Yamaguchi

Abstract In present study, a comparative thermodynamic assessment of a solar-driven organic Rankine cycle integrated with an absorption refrigeration system was performed. During the analyses, parabolic trough solar collectors were used to meet the necessary thermal energy for the power and refrigeration cycles. For the absorption refrigeration, the H_2O-LiBr cycle was proposed for the integrated system in order to maintain chilled water. The analysis was carried out for three supercritical working fluids: carbon dioxide (R744), ethane (R170), and fluoromethane (R41). For specified parabolic trough collector parameters, energetic and exergetic performances of the cycles were determined for constant turbine inlet pressure and constant pressure ratio. A parametrical study was also implemented for determining the effect of the system parameters on cycle performances. According to the results, the best performance was achieved using R41 with a net energy production rate of 32.54 kW, followed by R170 and R744. Based on the results of the exergy analysis, the leading exergy destruction rate was estimated for the integrated cycle working with R744. Additionally, the necessary collector length and area were determined for specific net power generation and refrigeration duties.

Keywords Organic Rankine cycle · Supercritical fluid · PTSC · Absorption refrigeration

1 Introduction

In the past several decades, a great amount of the world's power generation requirement is satisfied by facilities that are based on fossil fuels. On the other hand, the

O. Kizilkan (✉)
Department of Mechanical Engineering, Faculty of Technology, Isparta University of Applied Sciences, 32200 Isparta, Turkey
e-mail: onderkizilkan@isparta.edu.tr

H. Yamaguchi
Department of Mechanical Engineering, Doshisha University, Kyo-Tanabeshi, Kyoto 610-0321, Japan

excavated fossil-based fuels are utilized for generating heat energy or converted into practical industrial equipment. Due to the fact that these resources are being depleted, exhausting fossil-based fuels give rise to a severe energy crisis. Accordingly, sustainable and clean energy resources that are renewable and more environmentally friendly to substitute fossil fuels are being pursued by many investigators and industrial sectors [1]. Within renewable resources, solar thermal energy certainly has the greatest potential. When the environmental costs are taken into account, solar energy can be financially competitive with fossil fuel-based electricity generation. However, without taking into account such environmental costs, solar-based energy generation systems are not cost competitive currently due to the high capital investments. On the other hand, it is possible to reduce the investment costs by improving the performance of solar thermal power systems [2]. Among the solar thermal applications, parabolic trough solar collectors regarded as the most developed technology for electricity generation from solar thermal power [3]. This kind of collectors has been utilized in bigger power plants for the last four decades, exhibiting a promising future [4].

One of the major ways to generate energy from low and medium-temperature energy resources, such as solar energy, is utilizing the organic Rankine cycle (ORC). Although it has got many advantages, the major problem of these kinds of power plants is the relatively lower energy efficiency. A possible solution for increasing the energy production efficiency of the Rankine cycle may be the utilization of supercritical working fluid in order to create a supercritical cycle, which is widely known and has been implemented satisfactorily in a wide range of applications [5].

Supercritical natural fluids are becoming the most promising working fluids, especially in low-temperature power generation with organic Rankine cycles (ORCs). Among these, carbon dioxide (CO_2), as a supercritical fluid, has received increasing attention in low-temperature power generation applications of Rankine cycles for the last decades [6–8]. As an environmentally benign working fluid, without ozone depletion potential and insignificant global warming potential, CO_2 is non-flammable, poisonous, and inexpensive, which is a naturally occurring substance and abundant in the atmosphere. In addition, the heat transfer properties of CO_2 are quite satisfactory, and the specific volume of CO_2 is reasonably lower, which leads to a reduction in the component dimensions for the same operational states. On the other hand, there two major problems appear during the operation of the CO_2 cycles. The first one is the operating pressure which is relatively higher when compared to the other cycles, and the second one is the somewhat lower efficiency [9]. One of the other proper working fluids to be utilized in a supercritical cycle is possibly ethane (R170) due to its lower critical temperature and pressure. However, one crucial drawback of ethane as a working fluid is its cracking and chemical decomposition at high temperatures. Ethane is utilized as a refrigerant at low temperatures, while it is cracked to produce ethylene at high temperatures [10]. Another working fluid with lower critical properties such as CO_2 is fluoromethane (R41). R41 is a non-toxic, liquefiable, and flammable gas at reference conditions, but its ignition lower limit is high. Since it does not contain chlorine, it is not destructive to the ozone layer. Thus, owing to its properties, it can be used in supercritical cycles likewise [11].

Air conditioning demands occur mainly during summertime when the solar radiation is very high, and this facilitates generating electric power along with cooling utilizing the solar thermal energy [12]. A solar-powered absorption refrigeration system is one of the most common ways of utilizing solar energy [13]. Today, water–lithium bromide (H_2O-LiBr) is the most common working fluid commercially available for most industrial absorption systems. These systems serve for mainly air-conditioning applications [14].

In this study, a comparative thermodynamic analysis is carried out for evaluating the performance of the parabolic trough solar collector-based (PTSC) ORC integrated with the absorption refrigeration system. The proposed system is powered by solar energy using PTSC. For the ORC, three different supercritical working fluids are used for performance comparison, which are CO_2 (R744), ethane, and fluoromethane. For refrigeration purposes, an absorption refrigeration system (ARS) working with H_2O-LiBr is integrated into the system. Additionally, exergy analysis is carried out in order to determine the exergy destructions.

2   Integrated Power and Refrigeration System

The schematic representation of the PTSC-based ORC integrated with the vapor absorption refrigeration cycle is shown in Fig. 1. Referring to Fig. 1, there are four sub-cycles, PTSC, ORC, ARS, and cooling tower (CT) cycle. In the PTSC cycle, the heat transfer fluid (HTF) enters the pump and is pumped to the PTSC field. While the HTF passes through the PTSC, it is heated up and enters to the vaporizer of ORC, where it gives some amount of its thermal energy to the working fluid. After passing the vaporizer, HTF enters the generator of ARS, and it gives the rest of its energy to
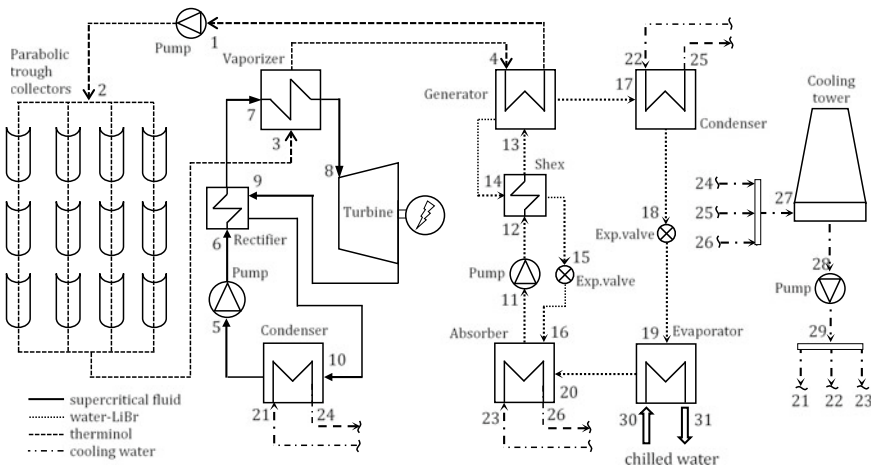
Fig. 1 Schematic representation of the PTSC-assisted ORC-ARS

the H$_2$O-LiBr couple. The ORC system consists of a turbine, a vaporizer, a condenser, a rectifier, and a pump. The superheated vapor needs to be cooled to a saturated liquid before entering the feed pump. In ORC, the saturated fluid is pumped to the rectifier, where it is preheated before the vaporizer. In the vaporizer, it reaches a supercritical temperature and pressure and enters the turbine. While passing through the turbine, some amount of thermal energy of the working fluid is converted to mechanical energy, and it exits the turbine with lower pressure. After, it enters the condenser, where it becomes a saturated liquid and pumped again by the feed pump. The ARS is working with the H$_2$O-LiBr couple. The fluid pair is pumped by the feed pump of ARS and enters the generator after preheated by the solution heat exchanger (Shex). In the generator, the fluid pair is heated up, and due to low pressure, some amount of water evaporates below 100 °C. The vapor water then enters the condenser, becomes saturated liquid, passes from the expansion valve, while its pressure is decreased and enters the evaporator. In the evaporator, the water becomes saturated vapor under very low pressure, while it cools down the coolant water for air-conditioning purposes. After exiting the evaporator, it reaches the absorber, and in the absorber, it is mixed with the fluid pair coming from the generator by rejecting some amount of heat. Additionally, the integrated system includes a CT system for absorbing the reject heat energy from the cycles. For the analysis, the main design parameters of the PTSC are given in Table 1.

Three supercritical fluids are selected for the performance analysis of the solar energy-driven ORC: R744, R170, and R41. These fluids were selected because of their low critical temperature and pressures. The working fluids with lower critical properties execute well for supercritical cycles, but the chemical stability of these kinds of working fluids utilized in supercritical cycles also relies on their critical properties, especially critical temperature due to the fact that with a high degree of superheat, they tend to degenerate [16]. As can be seen from Table 2, all three selected fluids have critical temperatures between 30 and 45 °C.

3 Methodology

In order to assess the thermodynamic performance of the solar energy-powered integrated system explained previously, energy and exergy analyses are performed. The assumptions listed below are made throughout the analyses:

- The system is in steady-state flow conditions.
- Kinetic and potential energies are ignored.
- No heat transfers from the heat exchangers and turbine to the environment.
- No pressure drops during the operation.
- The dead-state temperature T_0 is taken to be 20 °C, while the pressure P_0 is assumed as 101.325 kPa.

Table 1 General design x of the combined system [15]

PTSC	Inner diameter of receiver	0.08 m
	Outer diameter of receiver	0.09 m
	Outer diameter of cover	0.15 m
	PTSC length	100 m
	HTF mass flow rate	2 kg/s
	Emissivity of receiver	0.92
	Emissivity glass cover	0.87
	Temperature of the sun	5739 K
	Solar radiation	750 W/m^2
	Wind velocity	5 m/s
	Sun temperature	5739 K
ORC	Inlet pressure of turbine	9000 kPa
	Inlet temperature of turbine	140 °C
	Condenser temperature	25 °C
	Isentropic efficiency of turbine	0.88
	Isentropic efficiency of pump	0.92
ARS	Generator temperature	90 °C
	Condenser temperature	35 °C
	Absorber temperature	35 °C
	Evaporator temperature	5 °C
	Pump isentropic efficiency	0.95
	Shex effectiveness	0.83

Table 2 Properties of supercritical fluids studied [17]

	M (g/mol)	T_{bp} (°C)	T_c (°C)	P_c (MPa)	safety[1]	ALT[2]	ODP	GWP
R41	34.03	−78.12	44.13	5.8	NA	2.4	0	92
R170	30.07	−88.60	32.18	4.8	A3	0.21	0	~20
R744	44.01	−78.40	30.98	7.3	A1	>50	0	1

[1]ASHRAE 34 safety group
[2]Atmosphere life time

3.1 PTSC Modeling

In order to determine the solar energy amount absorbed by the parabolic trough collectors, the model given in Ref. [18] is used. The absorbed useful solar energy from the sun is determined by:

$$\dot{Q}_u = F_R[SA_a - A_r U_L(T_{in} - T_0)] \tag{1}$$

Here, S is the solar radiation; F_R is the heat removal factor; U_L is the heat loss coefficient of solar collector; A_a and A_r are collector aperture area and receiver area, respectively. The useful energy can also be calculated from:

$$\dot{Q}_u = \dot{m}c_p(T_{out} - T_{in}) \tag{2}$$

In Eq. (1), the heat removal factor F_R is described as:

$$F_R = \frac{\dot{m}C_p}{A_r U_L}\left[1 - \exp\left(\frac{-A_r U_L F'}{\dot{m}C_p}\right)\right] \tag{3}$$

In Eq. (3), F′ denotes the efficiency factor of collector and determined as:

$$F' = \frac{U_0}{U_L} \tag{4}$$

where U_0 represents the overall heat transfer coefficient. Since the receiver is encircled by an evacuated glass cover, the effects of convection heat transfer inside the receiver can be neglected. Thus, the heat loss coefficient can be calculated as:

$$U_L = \left[\frac{A_r}{(h_{c,c-a} + h_{r,c-a})A_g} + \frac{1}{h_{r,r-c}}\right]^{-1} \tag{5}$$

In the above equation, $h_{c,c-a}$ is the heat convection heat coefficient between the glass cover and surroundings; $h_{r,c-a}$ is the radiation heat transfer coefficient between the glass cover and surroundings, and the radiation coefficient between receiver and glass cover is denoted by $h_{r,r-c}$. These coefficients are described below:

$$h_{c,c-a} = \frac{Nu_{air}k_{air}}{D_g} \tag{6}$$

$$h_{r,c-a} = \varepsilon_g \sigma\left(T_g + T_a\right)\left(T_g^2 + T_a^2\right) \tag{7}$$

$$h_{r,r-c} = \frac{\sigma\left(T_r + T_g\right)\left(T_r^2 + T_g^2\right)}{\frac{1}{\varepsilon_r} + \frac{A_r}{A_g}\left(\frac{1}{\varepsilon_g} - 1\right)} \tag{8}$$

In the above equations, k is the thermal conductivity; Nu is the Nusselt number; σ is Stefan–Boltzmann constant; ε is the emissivity. In addition, subscripts r and g represent glass cover and receiver, respectively. In Eq. (7), the Nusselt number is determined as a function of Reynolds number with the equations given below:

$$Nu_{air} = 0.4 + 0.54\,Re^{0.52}(0.1 < Re < 1000) \tag{9a}$$

$$Nu_{air} = 0.3\,Re^{0.6}(1000 < Re < 50000) \tag{9b}$$

The temperature of glass cover T_g can be determined from the equation below:

$$T_g = \frac{A_r h_{r,r-c} T_r + A_g (h_{r,c-a} + h_w) T_a}{A_r h_{r,r-c} + A_g (h_{r,c-a} + h_w)} \tag{10}$$

Finally, the overall heat transfer coefficient of the collector is determined by;

$$U_0 = \left[\frac{1}{U_L} + \frac{D_o}{h_{fi} D_i} + \left(\frac{D_o \ln\left(\frac{D_o}{D_i}\right)}{2k} \right) \right]^{-1} \tag{11}$$

In the above equation, D represents diameter; h_{fi} denotes heat transfer coefficient of HTF flowing inside the pipes; subscripts i and o represent inner and outer, respectively. The convection heat transfer coefficient of the heat transfer fluid is calculated from the equation given below:

$$h_{fi} = \frac{Nu_{fi} k_{fi}}{D_i} \tag{12}$$

$$Nu_{fi} = 0.023\,Re^{0.8}\,Pr^{04}(Re > 2300) \tag{13a}$$

$$Nu_{fi} = 4.364(Re < 2300) \tag{13b}$$

3.2 Thermodynamic Modeling

The governing equations of mass and energy balance can be written as [19];

$$\sum \dot{m}_{in} = \sum \dot{m}_{out} \tag{14}$$

$$\sum (\dot{m} X)_{in} = \sum (\dot{m} X)_{out} \tag{15}$$

$$\sum \dot{E}_{in} = \sum \dot{E}_{out} \tag{16}$$

Here, $\dot{m}$ is the mass flow rate; $\dot{E}$ is the energy; subscripts in and out represent inlet and outlet streams, respectively. Moreover, X in Eq. (15) stands for the concentration ratio for the H_2O-LiBr cycle. The energy balance equation can be expressed more clearly as;

$$\dot{Q} + \sum \dot{m}_{\text{in}} h_{\text{in}} = \dot{W} + \sum \dot{m}_{\text{out}} h_{\text{out}} \tag{17}$$

where Q represents heat transfer, h is the enthalpy, and $\dot{W}$ is the work. In order to carry out thermodynamic modeling of vapor absorption cycle, the effectiveness method is used as a practical way of specifying the fluid temperatures entering and exiting the solution heat exchanger. If the effectiveness is known, other thermodynamic properties can be calculated from the definition of the heat exchanger effectiveness, which is given below [20];

$$\varepsilon = \frac{\dot{Q}_{\text{actual}}}{\dot{Q}_{\text{max}}} \tag{18}$$

In Eq. (18), the maximum heat transfer rate for given conditions can be written as:

$$\dot{Q}_{\text{max}} = \left(\dot{m} C_{\text{p}} \right)_{\text{min}} \Delta T_{\text{max}} \tag{19}$$

Here, $(\dot{m}C_{\text{p}})_{\text{min}}$ is the smaller one of the hot and cold fluids of the Shex where ΔT_{max} is the temperature difference between higher and lower temperatures of the streams entering the heat exchanger. For the exergy analysis, the exergy balance equation is given below [21]:

$$\dot{E}x_{\text{Q}} - \dot{E}x_{\text{W}} = \sum \dot{m}_{\text{out}} e_{\text{out}} - \sum \dot{m}_{\text{in}} e_{\text{in}} + \dot{E}x_{\text{dest}} \tag{20}$$

In above equation, $\dot{E}x$ is the exergy flow; e is the flow exergy of the stream, and $\dot{E}x_{\text{dest}}$ is the exergy destruction rate. The exergy of heat, work and flow exergy terms are defined below:

$$\dot{E}x_{\text{Q}} = \dot{Q} \left(\frac{T - T_0}{T} \right) \tag{21}$$

$$\dot{E}x_{\text{W}} = \dot{W} \tag{22}$$

$$e = (h - h_0) - T_0(s - s_0) \tag{23}$$

For the calculation of the exergy of solar, the formula defined by Ref. [22] is used:

$$\dot{E}x_{\text{solar}} = SA_{\text{a}} \left(1 + \frac{1}{3} \left(\frac{T_0}{T_{\text{sun}}} \right)^4 - \frac{4}{3} \left(\frac{T_0}{T_{\text{sun}}} \right) \right) \tag{24}$$

Finally, the energy efficiency, coefficient of performance (COP) value of absorption refrigeration system, and exergy efficiency terms are described below:

$$\eta_{en} = \frac{\dot{E}_{out}}{\dot{E}_{in}} \quad (25)$$

$$COP = \frac{\dot{Q}_{evap}}{\dot{Q}_{gen}} \quad (26)$$

$$\eta_{ex} = \frac{\dot{E}x_{out}}{\dot{E}x_{in}} \quad (27)$$

4 Results and Discussions

For the energy and exergy analyses of solar-assisted integrated power and refrigeration system, the thermodynamic properties of the working fluids are determined using EES software (Klein 2018). Energy and exergy efficiencies, refrigeration capacity, as well as the net power generated for different supercritical fluids, required heat input, and the exergy destructions are calculated using the equations given in the previous section. Since the working pressure of CO_2 is relatively high with that of the R170 and R41, the analysis is made for constant turbine inlet pressure and constant pressure ratio (r_P). The calculated power generation and refrigeration capacities are given in Fig. 2 for constant turbine inlet pressure for different fluids. As seen from the figure, the maximum power generation is achieved by R170 with a value of 32.54 kW, followed by R41 and R744. This result is because of the higher pressure ratio of R170 and R41. Also, the pressure ratios are displayed in the figure. It must be noted
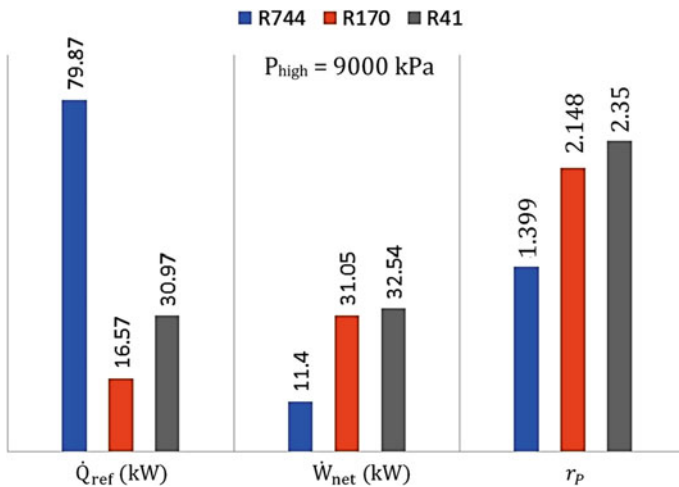
Fig. 2 Calculated refrigeration and power generation with pressure ratio for constant turbine inlet pressure
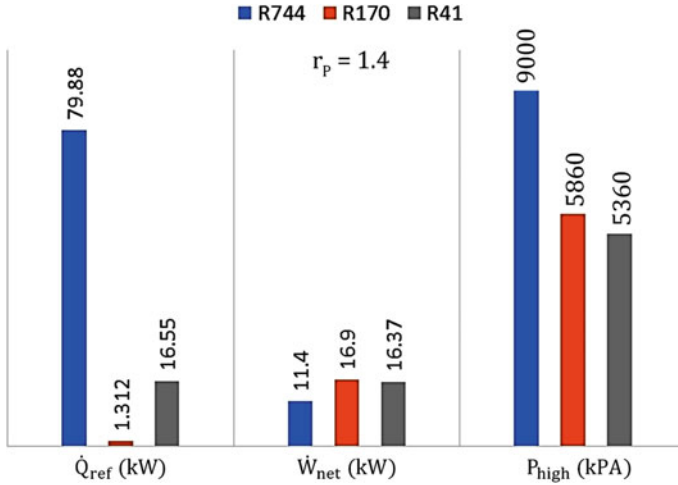
Fig. 3 Calculated refrigeration and power generation with turbine inlet pressure constant pressure ratio

that the turbine outlet pressure is the saturation pressure at condenser temperature, while inlet pressure is 9000 kPa.

For the refrigeration capacity, the integrated ORC working with R744 has the highest capacity value with 79.87 kW, while for the others, the capacities are calculated to be very low. This is mainly due to the solar energy gained by the cycles. For power generation, ORC working with R170 and R41 absorbs the major part of the solar energy with the remaining less solar heat for ARS. For R744, the power generation is low, with remaining more solar energy for ARS. This will be explained in detail next. In Fig. 3, the calculations are given for constant r_P. This means the turbine inlet pressure was calculated by multiplying condenser saturation pressure with r_P. As expected, the power generation rates decrease since the turbine inlet pressure decrease for R170 and R41. Also, the refrigeration capacities are lower than previous calculations since most of the heat energy was used for power generation. As seen from the figure, for R170, the refrigeration capacity is very close to zero. Also, the difference between the high pressure of R744 with R170 and R41 is noteworthy.

The main reason lying under the previous two results is depending on the specific heat capacity and specific volume of the fluids. In Fig. 4, the variation of these values with temperature is displayed for pressure of 9000 kPa. For all fluids, there is a bounce which is very sharp for R744 and relatively slight for the others. This is because the pressure is close to critical pressure for R744 and far for the others. After this bounce, all the lines become nearly flat. The other reason which is more meaningful is the difference between C_p values. R170 has the highest C_p followed by R41 and R744. This means the amount of energy required for heating of R170 is much more than the others, which leads to remaining less heat energy for ARS.
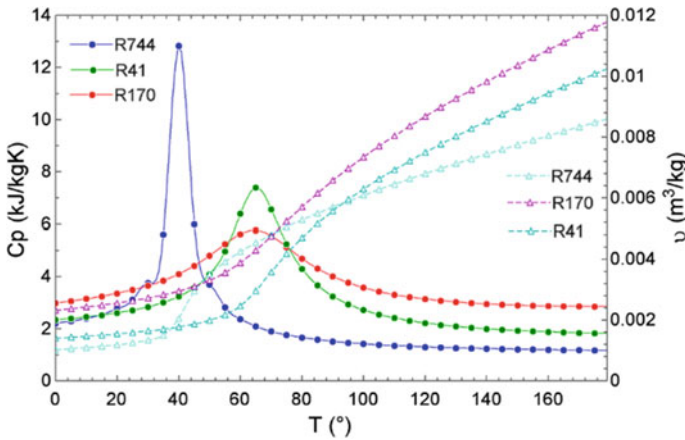
Fig. 4 Variation of specific heat and volume as a function of temperature ($P = 9000$ kPa)

Additionally, the right-hand side of Fig. 4 shows the variation of specific volumes. R170 has the highest specific volume that explains the reason for the highest power generation rate.

On the contrary to these results, R744 has the highest exergy destruction rate, followed by R170 and R41 (Fig. 5). The calculations were made for constant high pressure. It must be noted that the figure was plotted by excluding the exergy destruction rate of the solar collectors, which remains constant for all calculations. This is because the HTF and the PTSC are independent of the other cycle parameters. The collector, exergy destruction rate is 294 kW which is mainly due to the temperature
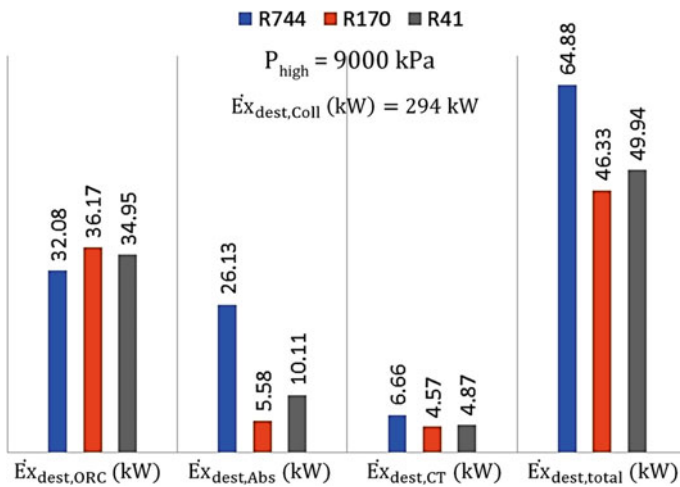
Fig. 5 Exergy destruction rates for constant turbine inlet pressure

difference between the sun and the receiver of the PTSC. The results of the individual cycle are also given in the figure. For ORC, R744 has the lowest destruction rate due to absorbing a low amount of heat for power generation, as explained before.

For the thermal processes, the exergy destruction rates mainly occur during heat transfer operations; the higher heat transfer rate causes higher exergy destruction rates. As evidence, the exergy destruction rate of ARS integrated with the R744 cycle is the highest because of much more heat energy utilization. In Fig. 6, the results are given for constant r_P. As previously declared, the power generation rated decreases for R170 and R41, which means higher exergy destruction rates.

Figures 7 and 8 show the efficiencies of the cycles for two conditions. In Fig. 7, for high pressure of 9000 kPa, the energy and the exergy efficiencies have got the same trend as for the power generation except for overall efficiency. The overall efficiency calculated here is the rate of total power generation and refrigeration to absorbed solar energy. Although cycle working with R744 has the lowest energy production rate, it has a remarkable refrigeration capacity which leads to higher overall efficiency.

In Fig. 8, the energy efficiency of ORC working with R744 is higher than the others. The reason for that is R41 and R170 cycles require more thermal energy for the power generation, as explained before, and this results in lower energy efficiency. Additionally, in Figs. 7 and 8, the COP of ARS is constant and calculated as 0.785, which is adequate for solar applications. The efficiency of the solar collector is found to be 73.15%, and it is also constant since it is not affected by the working fluid type and cycles.

For the analysis, parametrical studies were also carried out to determine the effect of working parameters on system performance. Figures 9 and 10 show the variation of net power generation and the energy efficiency of ORC with turbine inlet pressure and temperature, respectively. As expected, with the increase of turbine inlet pressure,
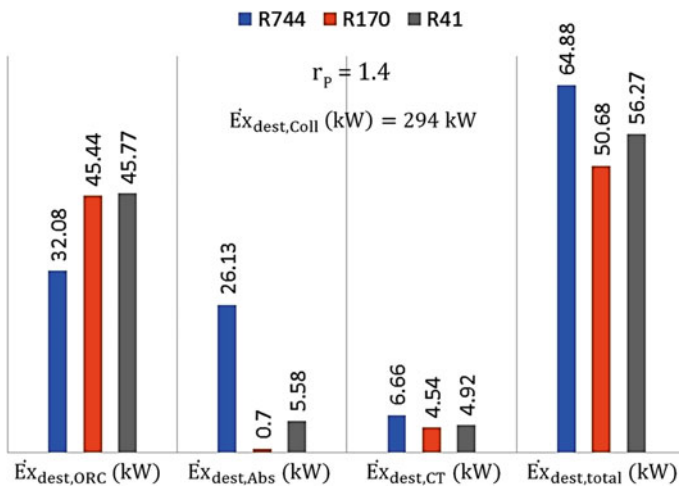
Fig. 6 Exergy destruction rates for constant pressure ratio
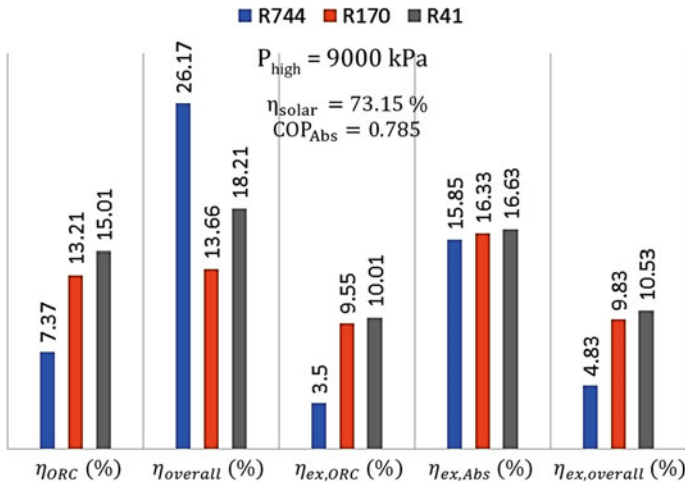
Fig. 7 Efficiencies for constant turbine inlet pressure
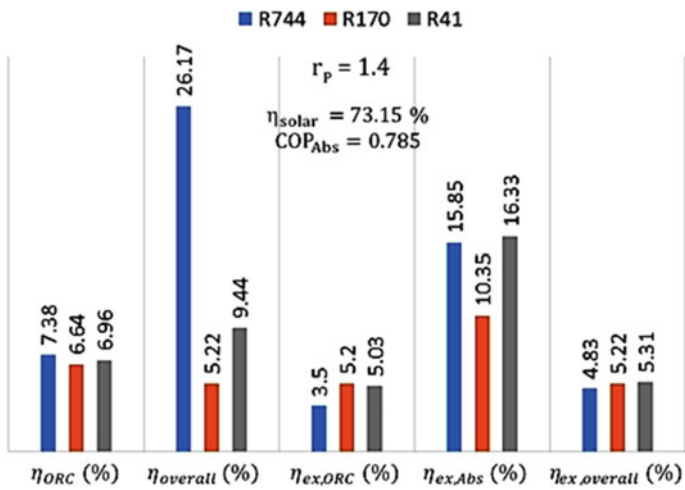
Fig. 8 Efficiencies for constant pressure ratio

power generation and energy efficiency increase for all working fluids. Also, turbine inlet temperature has got the same effect on these outputs.

The effect of the turbine inlet pressure on the exergy destruction rate and exergy efficiency of ORC is given in Fig. 11. On the contrary to power generation, with the increase of high pressure, the exergy destruction rates decrease for all supercritical working fluids. Also, from the figure, it can be seen that the lowest exergy destruction occurs in the system working with R170. The trend for the exergy efficiency is the opposite of this result, as expected. With the increasing turbine inlet pressure, exergy
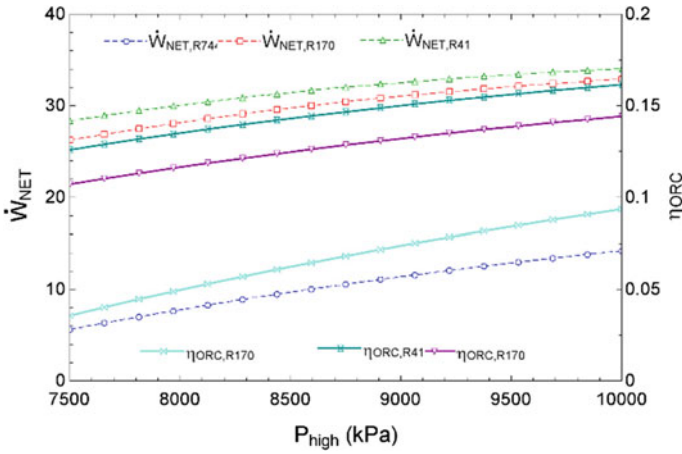
Fig. 9 Variation of power generation and energy efficiency of ORC with turbine inlet pressure
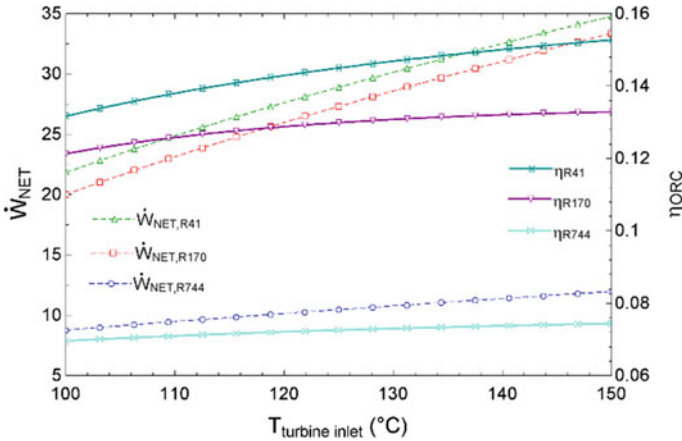
Fig. 10 Variation of power generation and energy efficiency of ORC with turbine inlet temperature

efficiency increases for all fluids. The increment ratio is slightly higher for R744 than the others.

The effect of the turbine inlet temperature is more evident than the pressure, as seen from Fig. 12. With the increase of temperature, the destruction rate decreases substantially for all fluids. The decrement ratio is higher for R170, followed by R41 and R744. The exergy efficiency acts the same as the turbine inlet temperature. The increment ratio R41 and R170 is higher than R744. This mainly depends on specific heat and the specific volume of the fluids.

Finally, a calculation was carried out for determining the necessary PTSC length and is for a given power and refrigeration duty as displayed in Fig. 13. Calculations
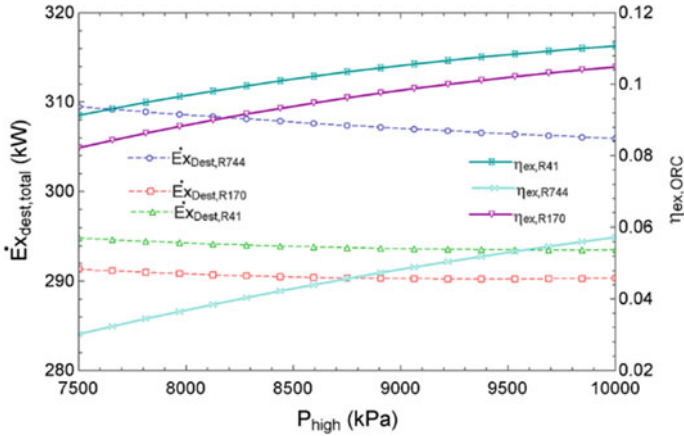
Fig. 11 Variation of exergy destruction rate and exergy efficiency of ORC with turbine inlet pressure
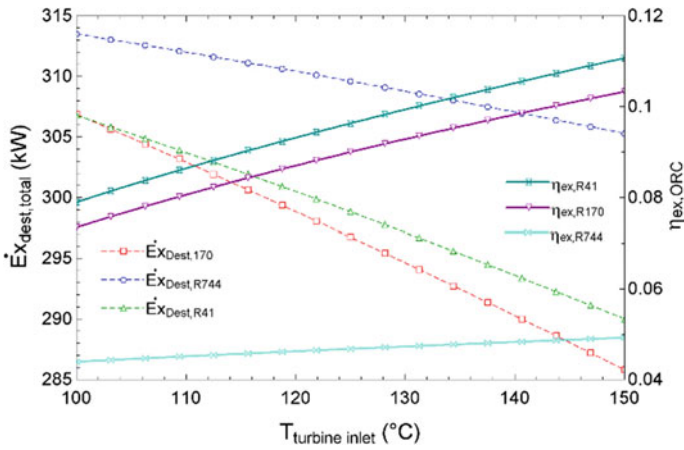
Fig. 12 Variation of exergy destruction rate and exergy efficiency of ORC with turbine inlet temperature

were made for a turbine net power generation of 50 kW for ORC and a refrigeration capacity of 50 kW for ARS. The necessary PTSC dimensions were determined for all cycles individually. As seen from the figure, an ORC working with R744 requires 265.3 m of PTSC, which corresponds to an area of 1234 m^2. For the same power generation, an ORC working with R170 requires 148.1 m PTSC, while it is 130.3 m for R41. Also, it must be noted that the calculations were made for a turbine inlet pressure of 9000 kPa.

Fig. 13 Required PTSC
length and area for 50 kW
net power generation or
refrigeration
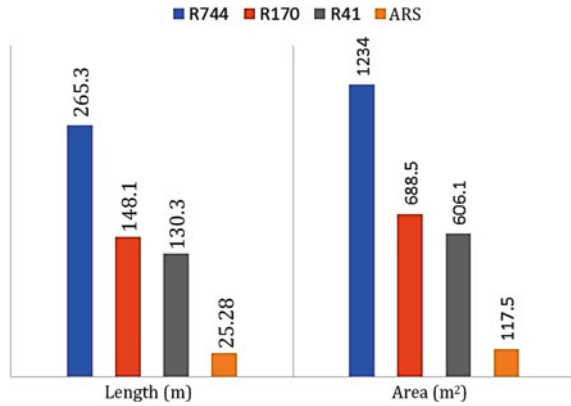
5   Conclusions

Comprehensive energy and exergy analyses were carried out to evaluate the perfor-
mance of PTSC-assisted ORC integrated with absorption refrigeration. The calcula-
tions were made for three different working fluids: R744, R170, and R41. According
to the results, the followings were concluded:

- ORC working with R41 has the highest power generation rate with 32.54 kW for
  a turbine inlet pressure of 9000 kPa.
- For the constant pressure ratio, R41 again has the lowest net power generation of
  16.37 kW, while the turbine inlet pressure of the cycle is 5360 kPa.
- The maximum refrigeration capacity for ARS is obtained for the integrated system
  working with R744 with a value of 79.88 kW due to higher remaining solar energy
  after vaporizer.
- According to the exergy analysis, R744-integrated system has the highest
  destruction rates for both cases, constant pressure and constant pressure ratio.
- Turbine inlet pressure and temperature have remarkable effects on system
  performances for all working fluids.
- The best working fluid for both power generation and refrigeration is R41 even
  though with relatively lower refrigeration capacity. If the refrigeration capacity is
  more important than power generation, the system with R744 can be preferable
  due to its very high refrigeration capacity.
- The minimum PTSC length for a power generation of 50 kW is calculated for the
  cycle using R41 with 130.3 m.
- The specific heat capacity and specific volume of the working fluid are very
  important for the power cycles as well as the other parameters.

References

1. Zhang XR, Yamaguchi H, Fujima F, Enomoto M, Sawada N (2005) A Feasibility study of CO_2-based Rankine cycle powered by solar energy. JSME Int J Ser B 48(3):540–547
2. Zhang XR, Yamaguchi H, Uneno D, Fujima K, Enomoto M, Sawada N (2006) Analysis of a novel solar energy-powered Rankine cycle for combined power and heat generation using supercritical carbon dioxide. Renewable Energy 31:1839–1854
3. Singh H, Mishra RS (2018) Performance analysis of solar parabolic trough collectors driven combined supercritical CO_2 and organic Rankine cycle. Eng Sci Technol Int J 21(3):451–464
4. Al-Sulaiman FA (2013) Energy and sizing analyses of parabolic trough solar collector integrated with steam and binary vapor cycles. Energy 58:561–570
5. Mocarski S, Gozdur AB (2015) Selected aspects of operation of supercritical (transcritical) organic Rankine cycle. Arch Thermodyn 36(2):85–103
6. Yamaguchi H, Zhang XR, Fujima K, Enomoto M, Sawada N (2006) Solar energy powered Rankine cycle using supercritical CO_2. Appl Therm Eng 26:2345–2354
7. Garg P, Srinivasan K, Dutta P, Kumar P (2014) Comparison of CO_2 and steam in transcritical Rankine cycles for concentrated solar power. Energy Procedia 49:1138–1146
8. Sarkar S (2015) Review and future trends of supercritical CO2 Rankine cycle for low-grade heat conversion. Renew Sustain Energy Rev 48:434–451
9. Wang D, Lu Y, Tao L (2017) Thermodynamic analysis of CO2 blends with R41 as an azeotropy refrigerant applied in small refrigerated cabinet and heat pump water heater. Appl Therm Eng 125:1490–1500
10. Nemati A, Mohseni R, Yari M (2018) A comprehensive comparison between CO_2 and Ethane as a refrigerant in a two-stage ejector-expansion transcritical refrigeration cycle integrated with an organic Rankine cycle (ORC). J Supercrit Fluids 133(1):494–502
11. Liao J, Zheng Q (2014) Thermodynamic analysis of low-temperature power generation transcritical rankine cycle with R41 And CO2. In: Proceedings of ASME turbo expo 2014: turbine technical conference and exposition GT2014
12. Khaliq A, Kumar R, Mokheimer EMA (2018) Investigation on a solar thermal power and ejector-absorption refrigeration system based on first and second law analyses. Energy 164:1030–1043
13. Crepinsek Z, Goricanec D, Krope J (2009) Comparison of the performances of absorption refrigeration cycles. WSEAS Trans Heat Mass Transfer 3(4):65–76
14. Fathi R, Ouaski S (2001) Performance of a Solar LiBr—water absorption refrigerating systems. Rev Energ Ren Journées de Thermique 73–78
15. Kizilkan O (2018) Exergetic performance assessment of solar driven combined CO2 power and refrigeration system. Int J Exergy 27(2):147–164
16. Babatunde AF, Sunday OO (2018) A review of working fluids for organic rankine cycle (ORC) applications. IOP Conf Ser Mater Sci Eng 413
17. Shengjun Z, Huaixin W, Tao G (2011) Performance comparison and parametric optimization of subcritical organic Rankine cycle (ORC) and transcritical power cycle system for low-temperature geothermal power generation. Appl Energy 88(8):2740–2754
18. Kalogirou SA (2009) Solar energy engineering: processes and systems. Academic Press, Oxford
19. Cengel YA, Boles MA (2006) Thermodynamics: an engineering approach. McGraw-Hill, New York, USA
20. Herold KE, Radermacher R, Klein SA (2016) Absorption Chillers and heat pumps. CRC Press, Boca Raton, FL, p 346
21. Dincer I, Rosen MA (2013) Exergy: energy, environment and sustainable development. Elsevier Science, p 576
22. Petela R (2005) Exergy analysis of the solar cylindrical-parabolic cooker. Sol Energy 79:221–233

Thermodynamic Analysis of a Combined Vapor Compression Refrigeration Cycle and Organic Rankine Cycle via a Sharing Heat Exchanger

Debanjan Ghata, Anirban Majumder, Mirza Adnan Beig, Madasu Anjali, and Bijan Kumar Mandal

Abstract In this paper, an attempt has been made to carry out thermodynamic investigation of an integrated organic Rankine cycle for waste heat recovery from a vapor compression refrigeration cycle (VCRC). The heat rejected by the vapor compression cycle is utilized and converted into electrical energy by running an organic Rankine cycle (ORC). A sharing heat exchanger (SHX) is used to transfer the heat from VCRC to the ORC. It works as the condenser in VCRC as well as the evaporator in ORC. Six refrigerants are selected as the working fluids for the refrigeration subsystem, which are R134a, R407C, R404A, R407C, R600a, and R410A. Four different working fluids (R123, R227ea, R600, and R245fa) are chosen as the candidates for the ORC subsystem. Coefficient of performance (COP), the energy output, and the thermal efficiency of the combined arrangement consisting of ORC and VCRC are considered as main performance parameters for this numerical work. For the present investigation, total of 24 working fluid combinations are considered, and the system performances with these combinations are analyzed and compared. Results show that the maximum COP of about nearly 3.5 is obtained when R134a is taken as the working fluid in the VCR cycle, and R600 is taken as the working fluid in the ORC. The maximum thermal efficiency and the maximum energy output are obtained when R123 and R245fa are used as working fluid in the ORC, respectively. The corresponding values are 3.1% and 3.5 kW for a 10-ton capacity refrigeration plant.

Keywords Organic Rankine cycle · VCR cycle · SHX · COP · Combined thermal efficiency

Nomenclature

a	: Plate area of heat exchangers (m^2)
E	: Electric power output (kW)

D. Ghata (✉) · A. Majumder · M. A. Beig · M. Anjali · B. K. Mandal
Department of Mechanical Engineering, IIEST Shibpur, Shibpur, Howrah 711103, India
e-mail: debanjanghata332@gmail.com

h	: Specific enthalpy (kJ kg^{-1})
m	: Mass flow of the working fluid (kg)
p	: Pressure (Nm^{-2})
Q	: Heat flow (kW)
U	: Heat transfer coefficient (kW m^2)
W	: Work input (kW)

Greek letters

η_g :Thermal efficiency

Superscripts

*	: Dimensionless
.	: Rate of change

Subscripts

comp	: Compressor
turb	: Turbine
evap	: Evaporator
ini	: Initial
reco	: Recovered

1   Introduction

One of the largest amounts of energy generated in the world is used to operate air conditioning and refrigeration appliances. Vapor–compression refrigeration cycle is the most commonly used refrigeration system. In this VCR cycle, the mechanical compressor consumes energy in the form of electrical energy, and it increases the refrigerant pressure. With a steady rise in world energy consumption, alternative systems that use lesser electricity or use other forms of energy have been urged.

The abundance of low-grade energy sources such as geothermal resources, biomass energy, solar energy, and power plant waste heat has attracted attention to utilize this kind of low-grade energy because of its low contribution to environmental pollution and also it reduces the usage of fossil fuel.

With a rise in the use of refrigeration and air conditioning appliances, electricity consumption has increased. Since most of this electricity is generated by burning fossil fuels, it has a significant effect on Global Warming. According to Li et al. [1], AC application surges 30–50% of the total electricity consumption in urban areas in summer accelerating the deterioration of urban micro-climate due to the rejected waste heat. So, promoting waste heat recovery (WHR) has great importance, by the same means to prolong micro-environmental protection and saving of energy.

This low-temperature waste heat cannot be recovered by using conventional steam power cycles, so an organic Rankine cycle (ORC) is proposed to generate power from this waste heat.

The ORC is preferred to use to recover low-grade waste heat because of few advantages, like smaller systems, economical utilization of energy resources, and reduced emissions of NOx, CO, CO_2, and other atmospheric pollutants. However, its superior performance in recovering waste heat available at low temperatures is the main advantage of the ORC.

In the paper Aphornratana and Sriveerakul [2], a plan of combined VCRC-ORC system has been suggested. Many studies have stated that to optimize the performance of the ORC system, the crucial thing is the selection of working fluid. In the paper, Wang et al. [3] isentropic and dry fluids like R245fa, R141b, and butane are investigated and found that these show attractive performance for low-grade waste heat recovery. On the choice of working fluids and the performance analysis of the ORC, many efforts have been made. In these studies, the exergetic and energetic analyzes were taken as key parametric indicators and effective approaches Chen et al. [4], Kaska [5], Heberl and Bruggemann [6].

In recent times, there has been a shift in focus toward maximizing the utilization of low-grade energy sources, namely biomass energy, solar energy, geothermal energy as well as waste heat coming out from utility stations to reduce environmental pollution and fossil fuel consumption.

Hung et al. [7] have performed experiments related to ORC systems with benzene group fluids which showed that nearly isentropic fluids can be considered as candidates for the ORC working fluids. Mago et al. [8] studied the behavior of various working fluids and concluded the better performance of drier ones compared to wet fluids. Chen et al. [4] investigated the various criteria for working fluid for their selection like density, specific heat, latent heat, critical point, thermal conductivity, and so on. Li et al. [1] tried to optimize the evaporation temperature of ORC fluids through numerical computation at various conditions. Guo et al. [3] investigated the parameters like power output of CO_2-based transcritical Rankine cycle and R245a-based subcritical ORC. Manolakos et al. [9] computed the mechanical work output of a low-temperature solar ORC for reverse osmosis desalination under different conditions.

Dai et al. [10] analyzed the effect of various parameters of a combined power and ejector refrigeration system on the net power output. Wei et al. [11] investigated the system optimization of an ORC with R245fa and concluded that it improves the system performance and efficiency and maximizes the waste heat recovery. Baik et al. [12] tried to compare the efficiencies of the transcritical cycle with CO2 and

R125 for a low-grade heat source. The above-mentioned brief review points to the necessity of choosing the best working fluid to optimize system performance.

2 Mathematical Modeling

2.1 Setup

In this study, the heat rejected by the vapor compression refrigeration cycle is utilized. So by implementing an organic Rankine cycle (ORC), the waste heat is utilized and converted into some power output in the form of electrical energy. As shown in Fig. 1, the VCRC-ORC system is a combination of vapor compression refrigeration cycle (VCRC) on the left side and an ORC on the right side. Here, a sharing heat exchanger (SHX) is used to transfer the heat from VCRC to the ORC. It works as the condenser in VCRC as well as the evaporator in ORC.

Counter-flow type of heat exchangers is used in this analysis. Also the method logarithmic mean temperature difference (LMTD) is used to calibrate it. Here, each exchanger is distributed in some regions, like boiling, condensation, and single-phase flow based on different fluid phases. By taking into account two convective heat transfer resistances of the fluid on both sides of the heat exchanger, the heat transfer coefficient U_i and heat exchange area A_i of each zone are calculated
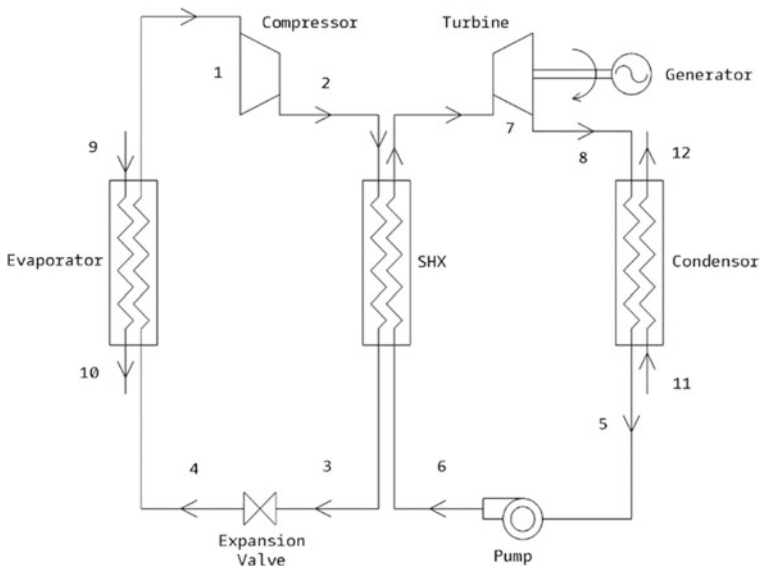
Fig. 1 Experimental installation

$$\frac{1}{U_i} = \frac{1}{a_{i,hf}} + \frac{1}{a_{i,ef}}$$

(1)

The heat transfer coefficient for a single-phase flow can be estimated by non-dimensional relationship developed by Wanniarachchi and Chisholm [13]. Similarly, Hsieh and Lin[14] correlation and Han, Lee, and Kim[15] correlation are employed for boiling and condensation processes, respectively.

2.2   A Selection of Working Fluid

Six refrigerants are chosen as the potential working fluids for the VCR subsystem, which are R134a, R290, R404a, R407c, R600a, and R410a. Considering properties like isentropic and dry behavior four working fluids are chosen as candidates for the ORC subsystem; those are R600, R123, R227ea, and R245fa. According to Badr et al. [15] and Maizza and Maizza [16], optimum pressure values are in the range of 0.1–2.5 MPa, and a pressure ratio (PR) of about 3.5 is appreciable. Ozone depletion potential (ODP) and global warming potential (GWP) become necessary factors to decide the working fluid for any cycle these days as environmental concerns have been a major issue.

2.3   Assumptions

In this paper, the modeling equations on energetic and thermodynamic analyzes are developed. Here, the equations are developed and programmed in engineering equation solver (EES). Some assumptions are considered to complete the computational modeling, those are.

1. Steady state conditions are assumed for the system.
2. Slight energy losses due to friction, kinetic, potential, and heat losses are neglected.
3. The negligible drop in pressure heads across the tubes of heat exchangers are not considered as they are well within estimated errors.
4. Saturated vapor and liquid states are approximated at the compressor inlet and condenser outlet, respectively.
5. Adiabatic expansion is assumed in the refrigeration process.
6. The ORC subsystem does not affect the pre-designed condensation temperature of the refrigeration subsystem.
7. Saturated liquid and vapor conditions are assumed for the fluids exiting the condenser and entering the turbine, respectively.
8. The entire refrigerant is assumed to have expanded in the cylinder.

Table 1 Parameters proposed for the setup of the VCRC-ORC system

Item	Value
Return chilled water temperature	16.5 °C
Cooling water temperature	30 °C
Designed AC condensation temperature	48.5 °C
ORC condensation temperature	35 °C
Pinch point temperature difference in AC evaporator	5.0 °C
Pinch point temperature difference in the SHX	1.5 °C
Pinch point temperature difference in the condenser	2.4 °C
Return chilled water pressure	0.101 MPa
Inlet cooling water pressure	0.101 MPa
Compressor efficiency	70%
Pump efficiency	80%
Turbine efficiency	80%
Generator efficiency	95%
Mass flow rate of chilled water	1.7 kg/s
Cooling capacity of the AC subsystem	10 TR

9. All of the refrigerant is assumed to have compressed during the compression process (Table 1).

3 Numerical Scheme

Based on the assumptions mentioned above, the energy analysis is performed as follows.

The cooling capacity (Q_{evap}) of the VCRC subsystem can be written as

$$Q_{evap} = \dot{m}_{VCR}(h_1 - h_4) \qquad (2)$$

The compressor work (W_{comp}) is given as

$$W_{comp} = \dot{m}_{comp}(h_2 - h_1) \qquad (3)$$

The rejected waste heat ($Q_{rejected}$) is calculated as

$$Q_{rejected} = \dot{m} \rightarrow_{rejected} (h_2 - h_3) \qquad (4)$$

The COP of the VCRC subsystem can be expressed as

$$COP_{\text{ini}} = \frac{Q_{\text{evap}}}{W_{\text{comp}}} \tag{5}$$

In the ORC subsystem, the recovered waste heat rate (Q_{reco}) is in equilibrium with the rejected waste heat rate (Q_{rejected}). Hence, in order to recover the entire waste heat via the SHX, full condensing method needs to be applied. Thus, one can write

$$Q_{\text{reco}} = \dot{m}_{\text{ORC}}(h_7 - h_6) \tag{6}$$

The turbine power output (W_{turb}) and the pump work (W_{pump}) are expressed as

$$W_{\text{turb}} = \dot{m}_{\text{ORC}}(h_7 - h_8) \tag{7}$$

$$W_{\text{pump}} = \dot{m}_{\text{ORC}}(h_6 - h_5) \tag{8}$$

The net electricity output (E_{net}) and thermal efficiency (η_{thermal}) of the ORC subsystem can be calculated as

$$E_{\text{net}} = W_{\text{turb}}\eta_{\text{g}} - W_{\text{pump}} \tag{9}$$

$$\eta_{\text{thermal}} = \frac{E_{\text{net}}}{Q_{\text{reco}}} \times 100 \tag{10}$$

where η_{g} is the generator efficiency.

Hence, by applying waste heat rate recovery, the combined COP of the VCRC-ORC system can be defined as

$$COP_{\text{combined}} = \frac{Q_{\text{evap}}}{W_{\text{comp}} - E_{\text{net}}} \tag{11}$$

4 Results and Discussion

Various performance parameters such as preliminary COP of the VCRC subsystem, thermal efficiency, total COP of the VCRC-ORC arrangement, and net electricity output with different fluid pair combinations are presented in Tab. 2. The computation is performed by maintaining the condensation temperature of the VCRC subsystem at 48.5 °C. To compare the performances of various fluid pair combinations, overall UA values of the heat exchangers are considered to be temperature independent.

The overall changes appearing on the system have been examined by changing the return chilled water temperature and by changing the cooling water temperature. Figure 2 shows the variation of both initial COP and combined COP of the

Table 2 Performances of different fluid pairs

VCRC fluids	ORC fluids	COP_{ini}	Thermal efficiency	COP_{comb}	E_{net}
R134a	R123	3.067	3.061	3.505	3.452
	R600	3.067	3.011	3.507	3.483
	R227ea	3.067	2.873	3.474	3.319
	R245fa	3.067	3.023	3.499	3.496
R290	R123	2.978	3.061	3.185	3.452
	R600	5.987	3.011	3.182	3.483
	R227ea	2.978	2.873	3.171	3.319
	R245fa	2.978	3.023	3.182	3.496
R404a	R123	2.469	3.061	2.908	3.542
	R600	2.469	3.011	2.899	3.483
	R227ea	2.469	2.873	2.876	3.319
	R245fa	2.469	3.023	2.901	3.496
R407c	R123	2.413	3.061	2.679	3.452
	R600	2.413	3.011	2.674	3.483
	R227ea	2.413	2.873	2.66	3.319
	R245fa	2.413	3.023	2.675	3.496
R600a	R123	3.134	3.061	3.375	3.452
	R600	3.314	3.011	3.370	3.483
	R227ea	3.134	2.873	3.358	3.319
	R245fa	3.134	3.023	3.371	3.496
R410a	R123	2.705	3.061	3.029	3.452
	R600	2.705	3.011	3.023	3.483
	R227ea	2.705	2.873	3.007	3.319
	R245fa	2.705	3.023	3.007	3.452

VCRC-ORC system with changing return chilled water temperature. R-134a–R600 is selected as the optimal fluid pair to analyze the effect of return chilled water temperature. From the plot, it is observed that both the initial COP of the VCRC subsystem and combined COP of the VCRC-ORC arrangement increase almost linearly with increasing return chilled water temperature. It is quite prominent that the combined COP of the VCRC-ORC system reaches 3.57 when the return chilled water temperature reaches 18 °C. Along with this, the utilization of the waste heat from the VCRC system is done, and an electrical output of nearly 3.5 kW can be generated, which partially compensates the electricity requirement for the operation of the VCRC subsystem. However, the efficiency of the organic Rankine cycle is only about 3%.

Figure 3 shows the variation of combined COP of the VCRC subsystem with cooling water temperature. Six fluid pair combinations are considered for this analysis out of which R134a–R600 shows maximum combined COP for a given cooling water temperature while the fluid pair R600a–R245fa shows minimum combined COP. It

Fig. 2 Variation of initial and combined COP of VCRC-ORC system with return chilled water temperature
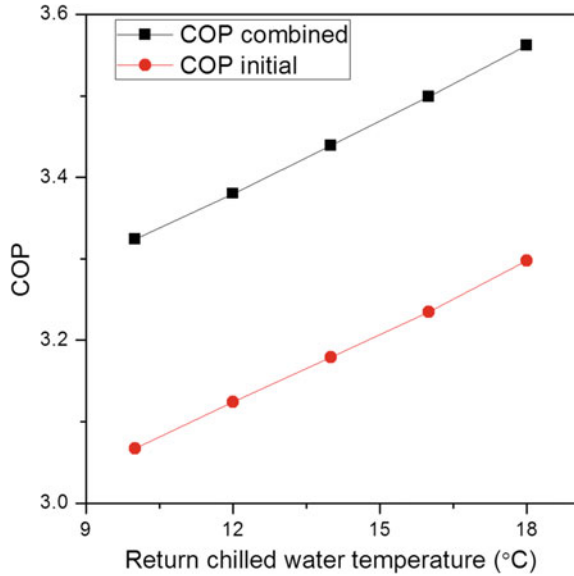
Fig. 3 Variation of combined COP of VCRC-ORC system with temperature of cooling water
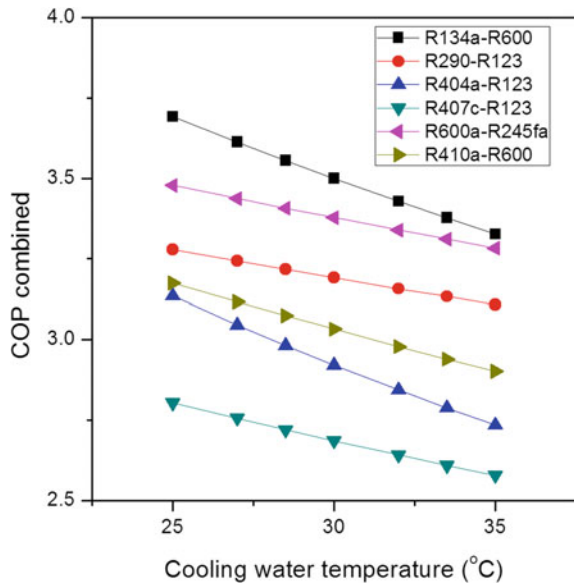
is also evident that the combined COP of all the six fluid pair combinations degrades as the cooling water temperature increases. Moreover, for the fluid pair R404a–R123, the rate of decrement of combined COP is maximum compared to the other five combinations, while the combination R290–R123 shows a lot slower rate of decrement of COP.

Fig. 4 Variation of thermal efficiency with respect to cooling water temperature
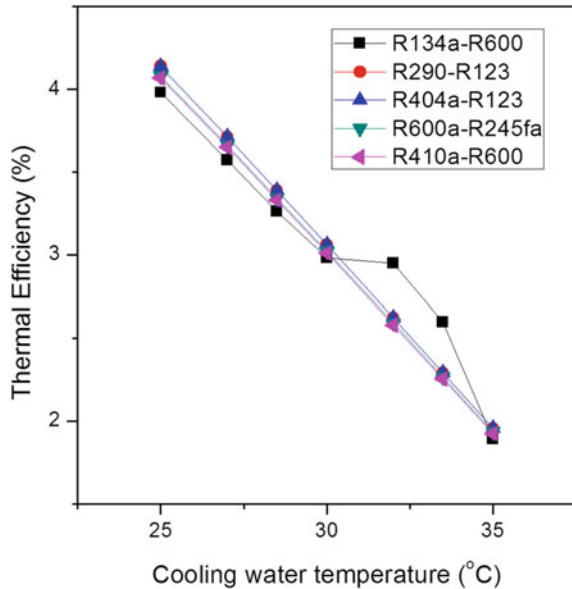
Figure 4 represents the variation of thermal efficiency of the VCRC-ORC system with cooling water temperature, and Fig. 4 represents the variation of net electricity produced with cooling water temperature. Five fluid pair combinations are chosen for the analysis out of which R404a–R123 shows maximum thermal efficiency as well as it produces maximum electric output for a given cooling water temperature.

5 Conclusion

In this paper, analyzation of a VCRC-ORC system has been done, also suggested for waste heat restoration. For the present investigation, combinations of 24 working fluid are considered and the arrangement result response with these amalgamations are studied and correlated. On the basis of thermodynamic analysis, the following conclusions can be drawn:

1. The initial performance of the VCRC subsystem has a great effect on performance of the VCRC-ORC arrangement. Integration of the ORC subsystem with a VCRC subsystem with better performance results toward comparatively enhanced overall performance.
2. Considering the COP combined R134a can take as working fluid of VCRC, and R600 can be taken as the working fluid of ORC. Due to flammability of R600a, it is chosen as the working fluid for the ORC subsystem only when the operation is under restrict safety control.
3. R245fa can be taken as working fluid of the ORC considering the energy output.

4. The maximum COP of about nearly 3.5 is obtained when R134a is taken as the working fluid in the VCR cycle, and R600 is taken as the working fluid in the ORC.
5. The maximum thermal efficiency and the maximum energy output are obtained when R123 and R245fa are used as working fluid in the ORC, respectively. The corresponding values are 3.1% and 3.5 kW for a 10-ton capacity refrigeration plant.

References

1. Li J, Pei G, Ji J (2010) Optimization of low temperature solar thermal electric generation with Organic Rankine cycle in different areas. Appl Energy 87:3355–3365
2. Aphornratana S, Sriveerakul T (2010) Analysis of a combined Rankine-vapour-compression refrigeration cycle. Energy Convers Manag 51:2557–2564
3. Guo T, Wang HX, Zhang SJ (2010) Comparative analysis of CO2-based transcritical Rankine cycle and HFC245fa-based subcritical organic Rankine cycle using low-temperature geothermal source. Sci China 53:1638–1646
4. Chen HJ, Goswami DY, Stefanakos EK (2010) A review of thermodynamic cycles and working fluids for the conversion of low-grade heat. Renew Sustain Energy Rev 14:3059–3067
5. Kaşka Ö (2014) Energy and exergy analysis of an organic Rankine for power generation from waste heat recovery insteel industry. Energy Convers Manag 77:108–117
6. Heberle F, Brüggemann D (2010) Exergy based fluid selection for a geothermal Organic Rankine cycle for combined heat and powergeneration. Appl Therm Eng 30:1326–1332
7. Hung TC, Wang SK, Kuo CH, Pei BS, Tsai KF (2010) A study of organic working fluids on system efficiency of an ORC using low-grad energy sources. Energy 35:1403–1411
8. Mago PJ, Chamra LM, Somayaji C (2007) Performance analysis of different working fluids for use in organic Rankine cycles. Proc Inst Mech Eng Part A J Power Energy 221:255–264
9. Manolakos D, Kosmadakis G, Kyritsis S, Papadakis G (2009) On site experimental evaluation of a low-temperature solar organic Rankine cycle system for RO desalination. Sol Energy 83:646–656
10. Dai YP, Wang JF, Lin G (2009) Exergy analysis, parametric analysis and optimization for a novel combined power and ejector refrigeration cycle. Appl Therm Eng 29:1983–1990
11. Wei DH, Lu XS, Lu Z, Gu JM (2007) Performance analysis and optimization of organic Rankine cycle (ORC) for waste heat recovery. Energy Convers Manage 48:1113–1119
12. Baik YJ, Kim MS, Chang KC, Kim SJ (2011) Power-based performance comparison between carbon dioxide and R125 transcritical cycles for a low-grade heat source. Appl Energy 88:892–898
13. Wanniarachchi S, Chisholm D (1990) Plate heat exchangers: plate selection and arrangement. AIChE Meeting, Orlando, Florida, pp 18–22
14. Hsieh YY, Lin TF (2002) Saturated flow boiling heat transfer and pressure drop of refrigerant R-410A in a vertical plate heat exchanger. Int J Heat Mass Transf 45:1033–1044
15. Badr O, Oallaghan PW et al (1990) Rankine-cycle systems for Harnessing power from low-grade waste heat. Appl Energy 36:263–292

16. Maizza V, Maizza A (2001) Unconventional working fluids in organic Rankine-cycles for waste energy recovery systems. Appl Therm Eng 21:381–390
17. Kim YS (1999) An experimental study on evaporation heat transfer characteristics and pressure drop in plate heat exchanger. Diss. MS thesis, Yonsei University
18. Li JZ, Cao Y, Zhong J, Liu Y, Kang C, Tan Y (2014) Interaction between urban microclimate and electric air-conditioning energy consumption during high temperature season. Appl Energy 117,149–156

Performance Optimization of Chiller Used for Commercial Building Air-Conditioning

Aaliya Azeem, C. Chiranjeevi, Y. Raja Sekhar, M. Natarajan, and T. Srinivas

Abstract The energy efficiency of buildings is highly affected by heating, ventilation, and air-conditioning (HVAC) systems being more energy intensive. The paper aims in providing an energy-efficient cooling solution by analyzing and modeling the cooling load requirement of a commercial building and optimizing the chiller system. Design Builder software integrated with Energy plus simulation software is used for predicting the scope of improvement by energy simulation modeling. The study also focuses on analyzing the performance improvement achieved with the optimized chiller system and by integrating it with efficient control strategies at the component level. With the energy-efficient optimization, along with the assessment of energy cost savings, the reduction in carbon emissions is also interpreted. About 50% energy savings is achieved with the water-cooled chiller retrofit, and with improved control strategies, energy consumption is reduced by 62%. An added advantage of reduced energy consumption is the reduction in carbon footprint, which is analyzed in the study. This reduction contributes to the global aim of reducing carbon dioxide emissions and controlling global warming.

Keywords Cooling load · Heating ventilation and air-conditioning (HVAC) · Chiller system · Energy simulation modeling · Energy consumption reduction · Carbon dioxide emission

A. Azeem (✉)
Department of Civil Engineering, Indian Institute of Technology Bombay, Mumbai, Maharashtra, India
e-mail: aaliyaazeem95@gmail.com

C. Chiranjeevi · M. Natarajan
School of Mechanical Engineering, VIT, Vellore, Tamil Nadu, India

Y. R. Sekhar
Center for Disaster Mitigation and Management, VIT, Vellore, Tamil Nadu, India

T. Srinivas
Department of Mechanical Engineering, Dr. B. R. Ambedkar National Institute of Technology, Jalandhar, Punjab, India

509

1   Introduction

With the increase in population growth and demand for comfort needs, the energy usage has increased rapidly in the world. The energy usage of buildings is quite high, accounting to almost 40% of world's energy consumption. In buildings, more than 60% of energy consumption is by heating, ventilation, and air-conditioning (HVAC) systems followed by lighting systems and others [5]. The main aim of this paper is to lower the energy consumption of HVAC systems in a building by providing an energy-efficient cooling solution. The required cooling load for the building is modeled by cooling analysis of the building and necessary calculations. By obtaining the cooling load required, the cooling system can be designed accordingly to meet the optimum cooling requirements of the building. With the proposed chiller system, reduction in chiller energy consumption was predicted, and scope of improvement in effectiveness was analyzed using the energy simulations done through Design Builder software, which is integrated with Energy plus simulation software generated by US Department of Energy's (DOE) Building Technologies Office (BTO) [15].

By literature survey, different air cooling methods, its energy and economic analysis, etc., were studied [7], and this paper has focused on reducing the overall cost spent in chillers, by financial analysis. Studies about savings obtained through cooling equipment of different capacities in office building with its simulation analysis were also studied [8]. Also, by literature survey, the chiller effectiveness improvement through retrofit process was studied [9], and in this paper, the analysis also focuses on the monthly energy consumption reduction of the energy-efficient chiller system. Along with the retrofit of energy-efficient optimized chiller, the chiller components were also optimized by efficient mechanical control strategies. The importance of control system at the component level in improving the chiller effectiveness was also studied [3]. With these optimized efficient strategies, it means that the power consumption reduction was achieved, either by retrofit of the components or by automated controls [16]. This included replacement of pumps with variable drive pumps controlled by VFD, replacement of belt-driven blowers with efficient EC fans, etc. With the retrofit of less energy consuming EC fans with inbuilt speed controls, the energy consumption in air handling units (AHUs) is also reduced. By variable air volume (VAV) system, with advanced dampers and efficient controllers, volume of supply air can be varied, by which, demand-based cooling is achieved. For better chiller efficiency and heat transfer in the condenser side, auto-tube cleaning system (ATCS) is also implemented to remove condenser scaling. By integrating these control strategies with the energy-efficient chiller system, the energy savings and energy efficiency improvement is quantitatively validated with the real chiller plant studied here. Also, a financial analysis is done, in which scope of generating savings in total energy cost spent in chillers will also be estimated. Energy-efficient chiller system with its control measures helps in reducing the kW/TR that leads to better cooling results with high energy and cost savings.

Studies prove that the carbon emissions have a linear relationship with the electricity usage [18]. Therefore, with less chiller energy consumption and reduced electricity usage, CO_2 emissions can also be decreased. The reduction in CO_2 emissions due to less electricity usage is also calculated. Reduction in CO_2 emissions and lowering energy consumption leads to more energy-efficient sustainable buildings.

2 Methodology

2.1 Optimization of Chiller System—Cooling Load Analysis and Retrofit

In this paper, a corporate office building located in Bangalore, India, is taken as the case study here, in which the HVAC system optimization has to be done [12]. The building has six floors and two blocks, namely A-wing and B-wing. The building was already facilitated with three air-cooled chillers of 180 TR capacity (Screw compressor) in both the wings with a chilled water supply temperature of 7–9 °C. The chillers in A and B-wing support the base load and work for 12 h a day. The various zones in the office building are air-conditioned through 28 nos. of air handling units (AHUs). All the required details of existing chiller system were collected including the readings from energy meters for calculating the current chiller energy consumption. After analyzing the current load profile of the chiller and the data obtained from the existing system, we find the need to optimize the chiller. The existing system is short of many energy saving possibilities due to deterioration of chiller and lack of sophisticated technology and limitation of automated BMS system. Optimization of the chiller system and its components was highly essential. The chiller system has to be retrofitted with an energy-efficient chiller system, which can meet the present cooling load requirement [1]. For this, an efficient chiller system of capacity equivalent or more than the existing chiller capacity was preferred, meeting the cooling load requirement of the building.

Here, the cooling load requirement of the building was modeled using heat load calculations and Design Builder software, in which all the heat load factors were accounted for cooling analysis. This means that the factors contributing to heat generation in the building need to be considered. These factors include:

- Construction and orientation of the building,
- Number of people occupied in the building that contributes to sensible and latent heat load,
- U-value of the walls and windows exposed,
- Other loads, i.e., load of equipment or components like computers, etc.

For the 4054.72 m^2 floor area office building with six floors of ceiling height 4 m, the necessary considerations and factors were considered in the calculations for

Table 1 Factors for accessing the cooling load requirement

Sl. No.	Description	Values
1	Area of the building (m^2)	4054.72
2	No of people/employees occupied	1500
3	Occupancy density (people/m^2)	0.37
4	Computers power density (W/m^2)	4.72
5	Power density of other office equipment (W/m^2)	11.72
6	Window to wall (%)	40%

estimating the cooling load and for simulations in Design Builder software [14] as listed in the following Table 1.

The number of people occupied was observed to be 1500, which is needed for considering people heat load calculations. For solar heat gain through walls and windows, wall area and window area of the building in each orientation are accounted. Relative temperature difference is also accounted in heat gain for walls. The solar heat gains for walls, floor, and roof were calculated by using the formula:

$$Q = UA\Delta T \tag{1}$$

While in case of windows other than window area (A), the shading coefficient (SC) and solar heat gain factor (SHGF) of glass were also considered for calculating the solar heat gain factor (Q). The solar heat gain for windows is calculated by using the equation:

$$Q = A * SC * SHGF \tag{2}$$

For other heat load factors, U-values of walls and windows, solar heat gain coefficients, equipment power density (W/m^2), etc., were taken as according to the standard values specified in ISHRAE Data book. All the latent and sensible heat load factors were accounted, and the total effective room heat load was obtained by summing up the effective sensible heat load and effective latent heat load.

$$ERHL = E.S.H.L + E.L.H.L \tag{3}$$

By modeling the cooling load requirement for the building using heat load calculations and Design Builder software, the cooling capacity was estimated to be 320TR. The existing 3 nos. 180 TR air-cooled chillers in both the wings are replaced with 2 nos. (1 no. working and 1 no. standby) 320 TR water-cooled chillers in one of the wing and 1 no. air-cooled chiller in the other. Also, the chiller systems of both the wings are proposed to be integrated. This means that, the energy-efficient water-cooled chiller is proposed to be the main chiller system for the whole building, while the air-cooled chiller to be used as standby. The interconnection of both the wings helps in sharing of load during peak time.

2.2 *Energy Simulations by Design Builder Software*

The commercial building was modeled and simulated using Design Builder software which is integrated with the Energy plus simulation software, generated by US Department of Energy [4]. By energy simulations, energy consumption of the chiller system is derived for peak summer months (March, April, and May) from which, the efficient cooling system, reduction in energy consumption, etc., were determined. This software uses the built-in templates, in which simulations were done based on the COP, and all the heat load factors of the building were considered. The office building under case study is modeled in the Design Builder software as shown in Fig. 1.

By Design Builder software, the energy consumption results were generated for both the wings. After the retrofit of water-cooled chiller, the chiller effectiveness was decreasing over months. So, for proposed 320 TR water-cooled chiller (WCC) installed, the measured energy consumption was compared with the simulated results. The scope of reducing energy consumption and improving its effectiveness to the rated efficiency is studied by mitigating the cause for increase in kW/TR. By comparing energy consumption of installed water-cooled chiller during its installation and that of present condition, the condenser scaling was assumed to be a major cause for decrease in efficiency. Also, for the 300 TR air-cooled chiller to be installed as standby, the future energy consumption is simulated, and the reduction in energy consumption caused by the retrofit is predicted.

Fig. 1 Office building model generated in design builder software
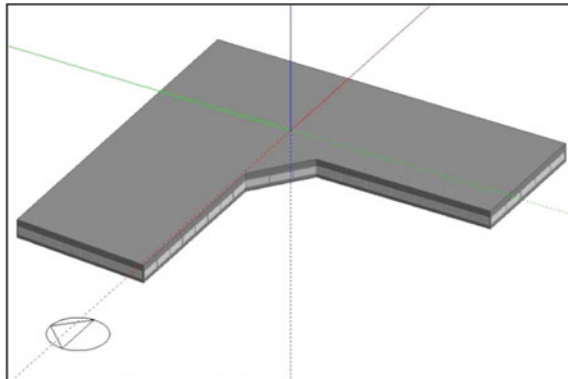
2.3 Performance Improvement with Efficient Control Strategies

Other than the chiller replacement, the efficiency of chiller can be even more improved at the component level by optimizing the chiller components with efficient mechanical control strategies. With these optimized efficient integrated control strategies, it means that the power consumption reduction is achieved either by retrofit of the components or by automated controls [11].

This includes replacement of primary-constant and secondary-variable pumps with variable-driven primary pumps, replacement of belt-driven blowers with efficient electronically commutative fans, etc. Variable air volume (VAV) system with advanced dampers and efficient controllers automated by the building automation or building management system (BMS) helps in achieving demand-based cooling. After comparing energy consumption of water-cooled chiller during its installation and that of present condition, the condenser scaling was assumed to be a major cause for decrease in efficiency. For better chiller efficiency and heat transfer in the condenser side, auto-tube cleaning system (ATCS) is also implemented to remove condenser scaling, in order to improve chiller effectiveness.

2.3.1 Variable Primary Flow System

The initial system in both the wings had 4 nos. of primary pumps and 3 nos. secondary-variable pumps in chilled water system. The primary pumps were working with constant speed, and the secondary pumps were variable pumps in which the speed was varied according to the load. This system was proposed to be replaced with energy-efficient variable primary flow system without affecting the flow requirement. By proposed system, the secondary pumps were removed, and the constant flow primary pumps were replaced with variable primary pumps. With variable primary-driven system, the flow through the chillers can be increased slowly from zero to minimum required rate by controlling the speed at which the isolation valve opens. This helps in lowering the rate of change in chilled water flow through operating chillers. Also, the number of operating pumps need not match the number of operating chillers [17]. With variable speed drives (VSDs) provided in the primary pumps, it improves the pumping efficiency and lowers the pump energy cost due to reduced pump full load power requirement. It also contributes to huge energy savings and cost savings by eliminating the secondary pumps, its associated fittings and controls.

The inefficient primary–secondary-variable system is replaced with variable primary pumping system in both the wings, that included 4 nos. primary variable pumps, in which 2 nos. running and 2 nos. standby and 3 nos. of condenser pumps with 2 nos. working and 1 no. standby, for the main 320 TR water-cooled chiller. And for the air-cooled chiller, three primary variable pumps (in which 2 nos. running and 1 no. standby) were retrofitted.

2.3.2 Electronically Commutative Fans (EC Fans)

The existing variable frequency drive (VFD) fans are replacedwith energy-efficient electronically commutative (EC) fans with inbuilt speed controls [16]. EC fans can give 18–20% energy saving at full load operation, >30% energy saving during part load operations. EC fans are direct drive fans that are integrated into the cooling unit by replacing the centrifugal fans and motor assemblies. EC fans have permanent magnet motors with inbuilt speed controls. They are inherently more efficient than traditional centrifugal fans because of their unique design, which uses a brushless EC motor in a backward curved motorized impeller. EC fans achieve speed control by varying the DC voltage delivered to the fan. One of the main differences between VFDs and EC fans is that VFDs save energy when the fan speed can be operated below full speed. VFDs do not reduce energy consumption when the airflow demands require the fans to operate at or near peak load. Conversely, EC fans typically require less energy even when the same quantity of air is flowing [10]. With EC fans, higher energy efficiency, efficient air quality, and less maintenance are achieved.

With 27 nos. AHUs and 2 nos. EC fans per AHU, total of 54 nos. EC fans are installed. After installing EC fans, the static pressure can be measured using measuring devices behind the fans. With the measured static pressure and with high efficiency of 75%, the air flow in cfm and power consumption (kW) can be calculated.

Than the existed belt-driven blowers, more air flow (cfm) was achieved with EC fans with:

- Reduction in static pressure
- Increased efficiency and
- Less power consumption.

2.3.3 Variable Air Volume (VAV) Systems

The optimized chiller system can be operated more efficiently in terms of energy consumption if the whole system can be automated by controls and by integrating it to building automation or building management system (BMS) [13]. With advanced dampers and efficient VAV controllers, supply air volume can be varied in AHUs according to cooling demand. Normally, a variable air volume (VAV) system contains a damper, a damper actuator, controller, a digital thermostat (fixed in the room). The required temperature set in the room is achieved by thermostat and maintained; the airflow will be allowed just to maintain the set temperature. The controller and actuator works according to the feedback from the thermostat.

The main benefit of VAV controllers is that the power consumption is highly reduced and works according to the need by which more precise temperature control is achieved. Also, it helps in lowering the energy consumption of system fans. VAV units can respond to environmental changes such as increased occupancy or cooling demand and adjust air flow according to signals from a local or central control system providing good air quality. Better performance and constant temperature profile is

achieved in the work place. With advanced dampers and effective controllers integrated with efficient automated control system, better cooling with improved efficiency is achieved. Implementation of VAV system with precision control actuators and BMS compatibility, i.e., completely automated, energy savings is obtained.

2.3.4 Auto-Tube Cleaning System (ATCS)

After comparing energy consumption of installed water-cooled chiller during its installation and that of present condition, the condenser scaling was assumed to be a major cause for decrease in efficiency. ATCS cleans the tubes, removing scaling, and the chiller works in full capacity. The water and balls are injected under controlled water pressure into the condenser removes accumulating residue every few minutes, before it can adhere to the tube walls. It also avoids the difficulty involved in manual cleaning. Auto-tube cleaning system (ATCS) was introduced to remove condenser scaling and to improve chiller efficiency. Energy consumption was simulated by Design Builder software for peak months with rated 0.5 kW/TR and present 0.7 kW/TR measured. On comparing the energy consumption before and after scaling, 28.57% increase in energy consumption was observed, as shown in Table.2.

From the literature studies [2], there is a linear relationship between percentage increase in chiller energy consumption and condenser scale thickness. Scale thickness of 0.76 mm was analyzed from 28.57% increase in energy consumption, as from case studies. With auto-tube cleaning system (ATCS), 20% energy savings can be achieved. Performance improvement with ATCS system was evaluated. Energy consumption reduction was realized by comparison of chiller system with and

Table 2 Increase in chiller energy consumption with condenser scaling

Sl. No.	Description	Value	Unit
Before scaling			
1	Design kW/TR	0.5	kW/TR
2	Chiller load	320	TR
3	Power consumption	160	kW
4	Operating hours	2880	h
5	Energy consumption	460,800	kWh
After scaling—present condition			
1	Measured kW/TR	0.7	kW/TR
2	Chiller load	320	TR
3	Power consumption	224	kW
4	Operating hours	2880	h
5	Energy consumption	645,120	kWh
	Percentage increase in energy consumption	28.57	%

without ATCS. Avoiding or decreasing the scale lowers the condenser approach temperature and increases COP, thereby chiller efficiency gets improved.

2.4   Financial Studies and Carbon Analysis

In HVAC chiller system optimization, with the reduction in energy consumption, energy costs can also be saved. The energy costs in INR per unit value of energy consumption kWh are 8 Rs. Therefore, energy costs are obtained by multiplying the energy consumption kWh with 8 Rs. The energy consumption of initial chiller system was calculated. With very high kW/TR, the annual energy consumption of 180 TR chiller system was 13,47,840 kWh. With energy cost of about 8 Rs. per unit kWh, annual chiller energy cost was 107.83 lakhs.

For the proposed 300 TR air-cooled chiller system with specific energy consumption of 0.7 kW/TR, the energy consumption was 210 kW. With 12 operating hours in a day, 20 operating days in a month, the annual operating hours was estimated to be 2880 h. Annual chiller energy consumption and annual chiller energy costs were estimated to be 6,04,800 kWh and 48.384 lakhs. As compared to the initial chiller system, annual energy savings and cost savings calculated were 7,43,040 kWh/annum and 59.44 lakhs (INR/annum). Therefore, with the retrofit of proposed 300 TR air-cooled chiller in A-wing, the chiller energy consumption and energy costs are expected to decrease by 55.12%.

In B-wing, for the proposed 320 TR water-cooled chiller system with specific energy consumption of 0.5 kW/TR, the energy consumption was 160 kW. With 12 operating hours in a day, 20 operating days in a month, the annual operating hours were estimated to be 2880 h. Annual chiller energy consumption and annual chiller energy costs were estimated to be 4,60,800 kWh and 36.86 lakhs. As compared to the initial chiller system, annual energy savings and cost savings calculated were 8,87,040 Kwh/annum and 70.96 lakhs (INR/annum). Therefore, with the retrofit of proposed 320 TR water-cooled chiller in B-wing, the chiller energy consumption and energy costs were expected to decrease by 65.81%.

For carbon analysis, studies proves that with carbon emissions have a linear relationship with electricity usage. Therefore, with less chiller energy consumption and reduced electricity usage, CO_2 emissions can also be decreased [6]. The reduction in CO_2 emissions due to less electricity usage is also calculated by multiplying 0.89 to energy consumption (kWh). The carbon emissions are derived with the measured chiller energy consumption values for each month and are compared [6].
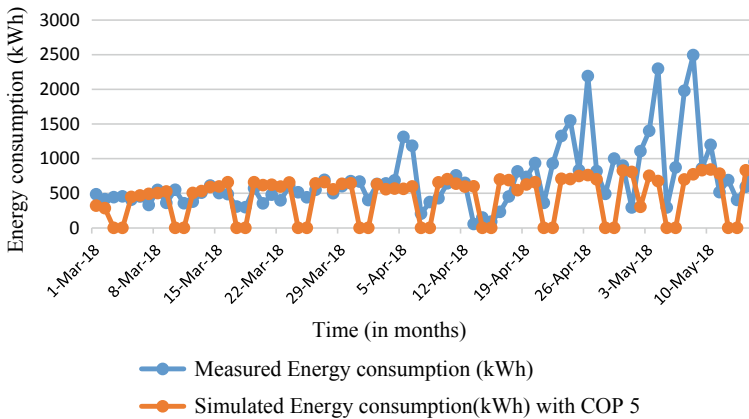
Fig. 2 Comparison of measured and simulated energy consumption of water-cooled chiller

3 Results and Discussion

3.1 Simulation Results for the Modeled Office Building

For the proposed main 320 TR water-cooled chiller (WCC) installed, the measured energy consumption was compared with the simulated results. The simulations template assumed weekends to be holidays, but practically, the chiller energy consumption on Saturdays and Sundays never went zero. Also, for the 300 TR air-cooled chiller to be installed as standby, the future energy consumption is simulated for the peak summer months, i.e., (for March, April, and May), and the reduction in energy consumption caused by the retrofit is predicted. The energy consumption is predicted to decrease by more than 70%. The graphical results as shown in Figs. 2 and 3.

3.2 Performance Improvement-Energy-Efficiency by Retrofit of Water-Cooled Chiller

By optimization of chiller and making it energy efficient, the building energy consumption decreased. The performance improvement obtained is studied, by comparing the monthly energy consumption before and after the retrofit. With the replacement of 180 TR air-cooled chillers by 320 TR energy-efficient water-cooled chillers, up to 50% energy consumption reduction is achieved, as shown in Fig. 4.
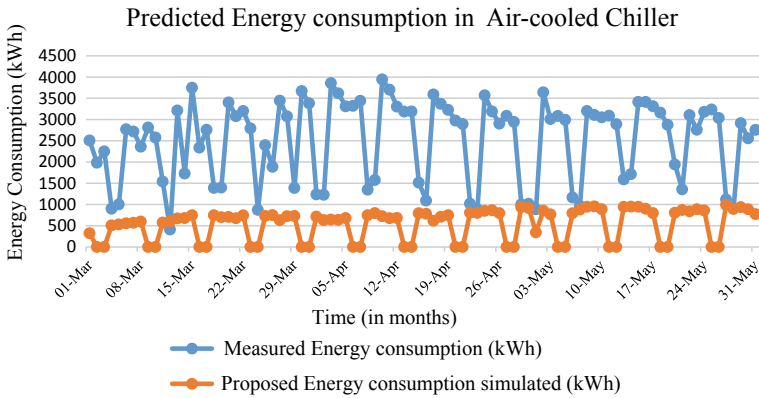
Fig. 3 Predicted chiller energy consumption reduction with proposed chiller
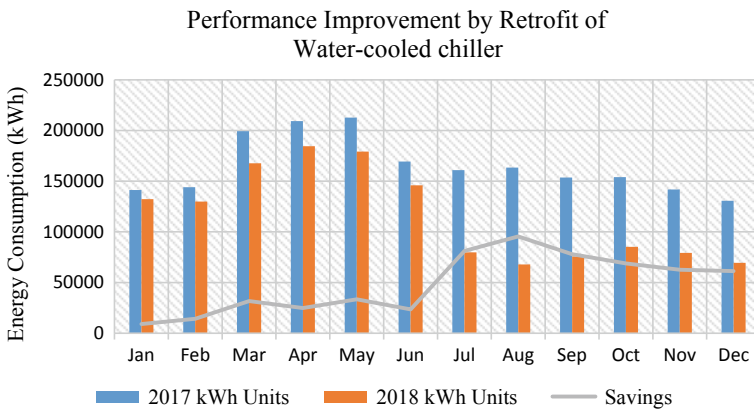
Fig. 4 Performance improvement with the retrofit

3.3 Reduction in Overall Chiller Plant Energy Consumption with Optimized Chiller and Efficient Control Strategies

Other than retrofit of energy-efficient water-cooled chiller, the chiller efficiency can be more improved by bringing energy efficiency at its component level. This is done by integrating the chiller system with efficient control strategies, i.e., by replacing its components with more efficient ones and also by automated controls. With the integration of energy-efficient control strategies at the component level, the chiller energy consumption is reduced by more than 60%. (as shown in Fig. 5).

Overall Energy consumption reduction with
Chiller optimization & efficient control strategies
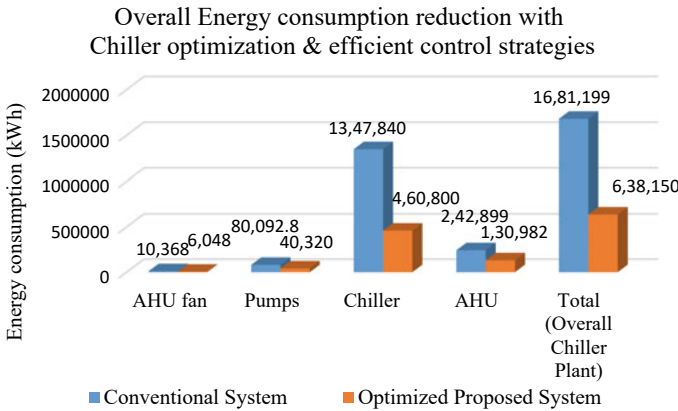
Fig. 5 Energy consumption reduction with efficient control strategies

3.4 Financial Studies: Energy Cost Savings with Energy-Efficient Chiller Retrofit

The energy cost savings achieved with both the proposed main water-cooled chiller and standby air-cooled chiller are studied, by calculating the energy costs caused due to old chiller system and that caused due to energy-efficient chiller system. With retrofit of air-cooled chiller to be used as standby, reduction in energy costs achieved is about 55%. While with the main operating energy-efficient water-cooled chiller installed which act as the main chiller for the whole building, the cost savings of more than 60% achieved, as in Fig. 6.
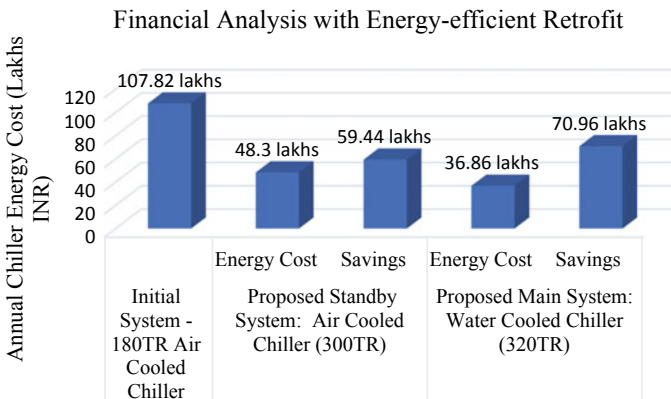
Fig. 6 Energy cost savings with the energy-efficient chiller retrofit
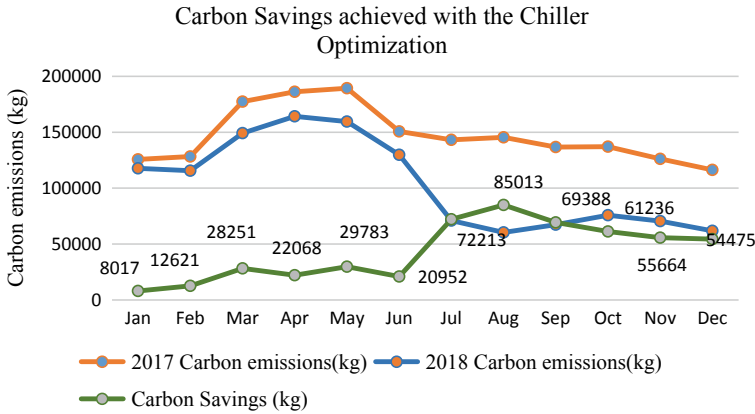
Fig. 7 Carbon emission savings with chiller optimization

3.5 Carbon Savings Analysis with Chiller Optimization

By calculating the carbon emissions from energy consumption values measured before and after the retrofit of energy-efficient water-cooled chiller, the monthly carbon savings achieved are analyzed. Since, the carbon emissions (in kg) are assumed to vary linearly with the energy consumption (kWh), as in Fig. 7, about 40–50% carbon savings are also achieved.

4 Conclusion

The air-conditioning system of the commercial building was analyzed and modeled meeting its cooling requirements. Energy savings of almost 50% are achieved by replacing the inefficient chiller system with energy-efficient water-cooled chiller. Also, with the increase in energy consumption observed for water-cooled chillers due to condenser, scaling was mitigated by auto-tube cleaning system. With the integrated control strategies at chiller component level, the chiller efficiency was improved by 62%. By financial studies, energy cost savings of about 55 and 65% were obtained with the proposed standby and main chillers, respectively. Along with decrease in chiller energy consumption (kWh), the carbon emissions also decreased by 40–50%.

References

1. Arya JS, Chavda DK (2014) Design and performance analysis of water chiller—a research. Int J Eng Res Appl 4(6):19–25
2. Beitelman AD, McInerney MK (2014) Demonstration of noncorrosive, capacitance based water-treatment technology for chilled water cooling systems. US Army Corps of Engineers
3. Chen CW, Lee CW, Chen CY (2010) To enhance the energy efficiency of chiller plants with system optimization theory. Energy Environ 409–424
4. Chowdhury AA, Rasul M, Khan M (1923) Modelling and simulation of building energy consumption. A case study on an institutional building in central Queensland, Australia. Build Simul 1916–1923
5. Chua KJ, Chou SK, Yang WM (2013) Achieving better energy-efficient air conditioning—a review of technologies and strategies. Appl Energy 104:87–104
6. Congradac V, Kulic F (2009) HVAC system optimization with CO_2 concentration control using genetic algorithms. Energy Build 41(5):571–577
7. Dashtebayaz MD, Najafabad PK (2018) Energy, Exergy, Economic, and Environmental analysis for various inlet air cooling methods on Shahid Hashemi-Nezhad gas turbines refinery. Energy Environ 1–18
8. Entchev E, Kangb EC, Lee EJ (2015) Future energy paradigm of microgeneration technologies for decentralized smart home and office buildings. Energy and Environ 67–81
9. Kumar CV, Marjanovic-Halburd D (2014) An investigation into retro-commissioning effectiveness in tropical climates. ASHRAE Trans 120(L1)
10. Lelkes A (2003) Electronically commutated motors. In: Proceedings of the international intelligent motion conference. INTERTEC International, Inc., pp 167–172
11. Liu Z, Song F, Jiang Z, Chen X (2014) Optimization based integrated control of building HVAC system. Build Simul 7(4):375–387
12. Lu L, Cai W, Xie L, Li S, Soh YC (2005) HVAC system optimization—in-building section. Energy Build 37:11–22
13. Ma K, Zhao T, Shen D, Liu M (2017) Web based chiller plant optimal control-a case study. Proc Eng 205:967–974
14. National Renewable Energy Laboratory (2011) Saving energy in commercial buildings-plug load assessment guidelines. Colorado:National Renewable Energy Laboratory (NREL)
15. Pan Y, Yin R, Huang Z (2008) Energy modeling of two office buildings with data center for green building design. Energy Build 40(7):1145–1152
16. Saidur R, Mekhilef S, Ali M, Safari A, Mohammed H (2012) Applications of variable speed drive (VSD) in electrical motors energy savings. Renew Sustain Energy Rev 16(1):543–550
17. Shaikh PH, Nor NB, Nallagownden P, Elamvazuthi I, Ibrahim T (2014) A review on optimized control systems for building energy and comfort management of smart sustainable buildings. Renew Sustain Energy Rev 34:409–429
18. Taylor ST, E P (2002) Primary-only versus primary-secondary variable flow systems. ASHRAE J 25–29
19. Wang X, Huang C, Zou Z (2016) The analysis of energy consumption and greenhouse gas emissions of a large-scale commercial building in Shanghai China. Adv Mech Eng 8(2):1–8

Exergetic Investigations of a Multistage Multi-evaporator Vapour Compression Refrigeration System

Prateek Malwe, Bajirao Gawali, Juned Shaikh, and Mahmadrafik Choudhari

Abstract Energy is the ability to cause a change in a system. It is usually available as exergy and anergy. Exergy is a useful part of energy, also known as available energy. Anergy is the counterpart of exergy, also known as unavailable energy. Thermodynamics is the science associated with energy and exergy, thereby ensuring both laws of thermodynamics—the first and the second by incorporating energy and exergy efficiencies. Refrigeration is a technology to preserve commodities at lower temperatures than their surroundings. One of the most widely used refrigeration systems is a vapour compression refrigeration system whose basic objective is to produce a refrigerating effect at the desired location. Commercial large capacity plants consist of the preservation of a different variety of food items requiring different preservation temperatures. It needs to maintain the evaporators correspondingly at different required temperatures. It requires multi-staging in compressors to save the compressor energy consumption. Exergy efficiency governs the actual performance of the system by knowing its deviation from the ideal one, and thus, is a true measure of any system performance. In this paper, an exergetic investigation of a multistage multi-evaporator vapour compression refrigeration system with individual expansion valves using R22 refrigerant is carried out. A shell and helical type

P. Malwe (✉) · M. Choudhari
Research Scholar under the AICTE NDF scheme, Department of Mechanical Engineering, Walchand College of Engineering, Sangli, Shivaji University, Sangli, Maharashtra 416415, India
e-mail: prateek.malwe@walchandsangli.ac.in

M. Choudhari
e-mail: rafikmith@gmail.com

B. Gawali · J. Shaikh
Department of Mechanical Engineering, Walchand College of Engineering, Sangli, Shivaji University, Sangli, Maharashtra 416415, India
e-mail: bajirao.gawali@walchandsangli.ac.in

J. Shaikh
e-mail: juned.shaikh@walchandsangli.ac.in

P. Malwe
Department of Mechanical Engineering, Dr. D. Y. Patil Institute of Technology, Pimpri, Pune, Maharashtra 411014, India

heat exchanger is inbuilt as an intercooler between two compression stages comprises of refrigerant on both—shell and tube side. The two evaporators are maintained at $-10\,°C$ and $10\,°C$. Various parameters like exergy destruction and exergy efficiency are computed. Compressor consumes the maximum exergy destruction among all the components. Variation of exergy efficiency with different parameters is represented in graphical forms. Exergy analysis is a well-known technique and proved to be an alone tool for evaluating and comparing systems more meaningfully. It also helps to improve and optimize the design and analysis of a system.

Keywords Energy · Thermodynamics · Refrigeration · Exergy efficiency · Exergy destruction

Nomenclature

W	Work input
m	Mass flow rate
h	Enthalpy
Q	Heat load
V	Voltage
I	Current
COP	Coefficient of performance
T	Temperature
RE	Refrigerating effect
N	Number of revolutions
t	Time
EX	Exergy
S	Entropy
EP	Exergy of the product
EDR	Exergy destruction ratio

Greek Letters

η	Efficiency

Subscripts

LP	Low-pressure compressor
HP	High-pressure compressor
e1	Evaporator 1

e2	Evaporator 2
r	Refrigerant
carnot	Carnot
theo	Theoretical
act	Actual
L	Low-temperature side
H	High-temperature side
Heater,ip	Input to the heater
comp,ip	Input to the compressor
h	Heater
c	Compressor
D	Destruction
0	Dead state condition
cond	Condenser
cap	Capillary tube
tex	Thermostatic expansion valve
ex	Exergy

1 Introduction

The energy crisis is the most critical issue in today's era. The first law of thermodynamics indicates the analysis, design, and evaluation of a given system, and it governs the quantity of energy only and not the quality. It is insufficient and incapable of dealing with practicalities associated with any system. As a corollary to this, the second law of thermodynamics is introduced which makes accountability for losses, irreversibilities, and exergy destructions in any system. Entropy generation creates disturbances within the system making it inefficient. Therefore, exergy is a tool in second law analysis. System exergy is the most attainable work to be pulled out from a system at a specified state under a given environment. Thus, it is a property of both: the system as well as the surroundings. 'Exergy' term is derived from Greek words: 'ex' means 'form' and 'ergon' means 'work'. Unlike conserved energy, exergy is always destroyed in all irreversible processes and is a boundary phenomenon. A dead state (normally referred to as environment) is a condition of complete equilibrium of both system and surroundings, and exergy at a dead state is always zero.

Exergy analysis overcomes the inadequacies that remain with energy analysis. It shows that degradation of exergy occurs when a system reaches a complete equilibrium state with surroundings; thereby no further work can be performed at all. Exergy analysis has the following characteristics: It quantifies true locations, the magnitude of losses, irreversibilities, and destructions along with inefficiencies. It also enables to have maximum availability or usefulness of a system to become more efficient. Exergy efficiency is a tool to measure the approach to idealness, which is not the case

with often misleading energy efficiencies. Recently, exergy is used in conjunction with exergoeconomic terms wherein cost calculations, environmental impacts, and sustainability assessment are incorporated.

2   Literature Survey

Dincer [1] suggested different methods to perform an exergy analysis of some thermal systems. It focuses on various features of refrigeration, power production, and cryogenic intentions, etc. Exergy analysis case studies of various thermal systems are done involving their basic concepts. It is a research-oriented textbook that covers almost all features including theory and practice in an easily understandable format. It enlightens various latest techniques for viewing the exergy analysis all along together with their applications and recent information. It incorporates basic information to conduct an exergy analysis of any particular thermodynamic system like the principle of entropy generation, various practical case studies of energy, and exergy analysis, etc. It is the most widely referred book for exergy analysis of any particular system [1]. It also explained the basics of thermodynamic concepts for the analysis purpose. Moreover, examples of exergy concepts are illustrated with simple concepts [2]. A study includes the method to enhance the thermal functioning of the refrigeration system by using analysis tools like energy and exergy. The system considered is multiple evaporators with multistage compressors and multiple expansion valves including flash chambers. R134a finds its suitability for various commercial and practical applications. After going through numerical computations, an increase of 22% is obtained in both—the first and second law efficiencies. Among all the components, the worst thermal performance is shown by the expansion valve followed by the condenser, evaporator, and compressor. With the increase in ambient temperature, the corresponding decrease in exergy destruction ratio takes place with an increase in exergy efficiency [3].

A cascade (ammonia/carbon dioxide) vapour compression refrigeration system is simulated using the Energy Equation Solver tool. Exergy analysis provides a good look for system design, its analysis, and its exergy assessment. The overall plant exergy efficiency of 42.13% is suggesting scope for improvement from an energy point [4]. An EES tool is used for COP maximization with consideration of different variables and parameters. Interpretation predicts that with an increase in the subcooling phenomenon, COP increases. Also, R717 gives the best outcomes among all other refrigerants selected [5].

A simulation of high temperature and multistage compression using R1234ze(Z) as refrigerant of a heat pump including exergy analysis is done with hot water as supply from waste heat recovery. Exergy destruction for the compressor is higher in comparison with the evaporator and condenser of a single-stage system. The multistage system shows an increase of 9.1% and 14.6% in COP for two- and three-stage vapour compression refrigeration systems, respectively. COP increases proportionately with an increase in temperature of the source of waste heat. Among all the

combinations, three-stage refrigeration systems offer various thermal performance advantages over others [6].

A thermodynamic analysis of waste heat extraction using ammonia as a refrigerant using an intercooler of a multistage refrigeration system is performed [7]. Heat recovery can be boosted by ensuring optimum operating conditions like water flow rate, water temperatures, use of suitable working fluid, etc. A 20 kW of waste heat recovery is achieved which thereby causes a 4–5% increase in COP value. Maximum COP of 3.087 for − 40 °C evaporator temperature is obtained. However, COP decreases with an increase in the condenser and a decrease in evaporator temperatures.

The thermal performance analysis of a multi-evaporator and multi-compressor refrigeration system using eco-friendly refrigerants is presented [8]. It includes both combinations of individual and multi-expansion valves by using different low GWP refrigerants. Mathematical formulae and expressions to interpret component-wise exergy destructions, etc., are presented. Results reveal that for the same operating conditions, multiple evaporator systems with multiple expansion valves give better performance than that with individual expansion valves. The highest exergy destruction is found for condenser and lowest for throttling valves. Experimental investigation of dual evaporator vapour compression refrigeration system shows there is an increase in COP, exergy efficiency, and exergetic performance coefficient with a drop in condenser temperature and an increase in evaporator temperature. Also, it summarizes a systematic procedure regarding designing a refrigeration system [9].

A systematic first and second law evaluation of a refrigeration system using a liquid vapour heat exchanger along with various low GWP refrigerants is carried out [10]. Results show that up to a 20% increase in exergy efficiency is achieved by adding a liquid vapour heat exchanger. Among all refrigerants used, R717 gives a better experimental performance with 5% accuracy for the same values. Due to practical difficulties and flammable properties of R600, R152A, R600A. R290 finds limitations in its applications from a safety point of view. An exergy assessment of a refrigeration system is involving mixtures of different refrigerants of hydrocarbons [11]. Exergy depends upon temperatures and pressures of condenser and evaporator, environmental conditions, etc. Among all components, the compressor has the largest exergy destructions. An exergy method using exergy—enthalpy charts with R11, R12 as refrigerants for analysing a vapour compression refrigeration system is used. System conditions include cold room maintained at − 15 °C and heat rejection at 30 °C. Exergy efficiencies of 49 and 50% are obtained for R11 and R12, respectively. Improvements in exergy efficiency may be possible by having a brief study of economic considerations [12, 13]. The waste heat rejected from the condenser of a refrigeration system can be used to drive an Organic Rankine Cycle to have energy conservation [14, 15]. Phase change materials are used nowadays to store/tap the waste heat energy [16]. Exergy analysis is a very powerful tool to examine the analysis of various thermal systems like single stage refrigeration systems [17, 18], multi-stage refrigeration systems [19], internal combustion engines [20], cryocoolers [21–24], etc. Nowadays, recent advancements in the exergy analysis domain involves

the use of statistical approach [25], artificial intelligence [26], latent heat storage systems [27], materials characterizations [28], etc.

3 Exergy Analysis Methodology

It includes everything like the impact of environmental conditions, needs and procedure to carry out exergy analysis, the principle of increase of entropy, the exergy of system, mathematical expressions for exergy change, exergy balance, etc. Exergy analysis involves the use and concepts of energy and exergy balances, enthalpy, entropy, and exergy calculations at various stages in the system. To perform an exergetic investigation of any thermal system, certain specific assumptions are required to be made by considering practical difficulties which may be encountered during the actual analysis. Given this, it requires subdividing a given system into multiple subsystems. Exergy destruction is examined for the individual component. The outcome of this gives the area of major exergy destruction among all components, which can further be subjected to its minimizations. During exergy analysis of a system, certain things like having standard dead state conditions, negligible pressure drops in pipes, negligible potential, and kinetic energy changes, etc., associated with the system are assumed.

4 Experimental Facility

It consists of a two-stage open type reciprocating compressor with a shell and helical coil type intercooler, two evaporators each of 1.2 and 0.8 TR capacities are maintained at -10 and $10\ ^{\circ}$C with individual expansion valves as shown in Fig. 1. Loading on evaporators is done by heating elements placed inside them. Refrigerant from
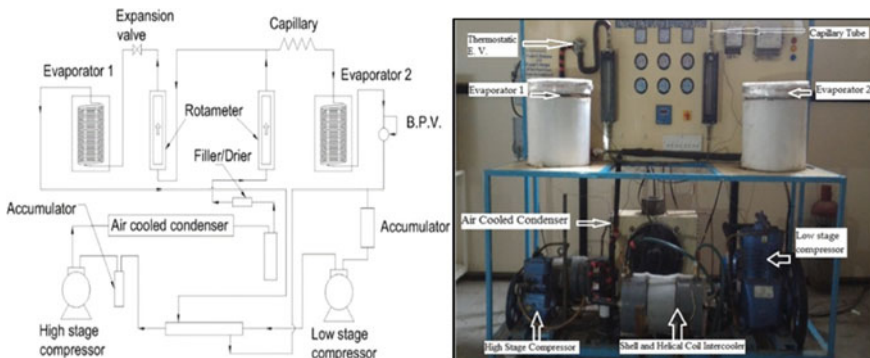
Fig. 1 Diagrammatic demonstration and real picture of the experimental setup
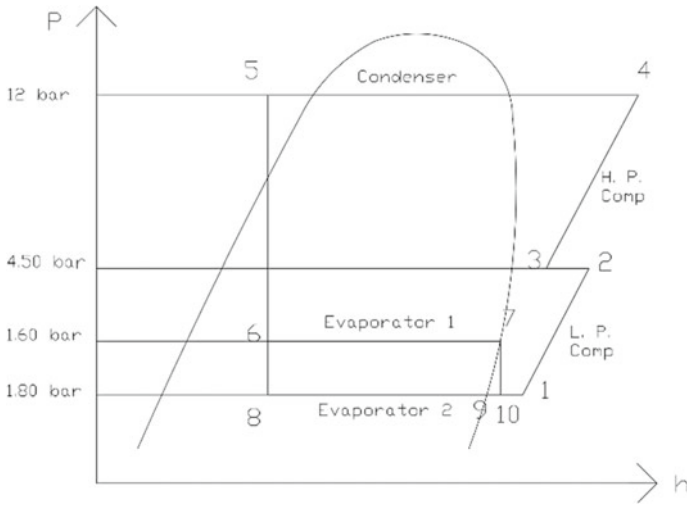
Fig. 2 Representation of system on P–h chart

evaporator 1 enters on the shell side of the intercooler to cool the refrigerant coming from the LP compressor. It is then clubbed with return line refrigerant coming from evaporator 2, to feed the mixture to LP compressor to repeat the cycle.

4.1 *Measurements*

As explained earlier, this refrigeration system works at 12 bar condenser pressure with 1.6 and 1.8 bar pressures of evaporator 1 and 2, respectively, as shown in Fig. 2.

The system is allowed to come under steady-state conditions after which corresponding readings were taken as shown in Table 1.

4.2 *Calculations*

The following formulae are used for performing energy and exergy analysis of the system:

Power input to LP compressor (kW)

$$W_{LP} = m_r \times (h_2 - h_1) \tag{1}$$

Power input to HP compressor (kW)

$$W_{HP} = m_r \times (h_4 - h_3) \tag{2}$$

Table 1 Experimental readings of setup at steady-state condition

Parameter	Unit	Value
Inlet pressure of LP compressor	bar	1.80
Intercooler pressure	bar	4.50
Condenser pressure	bar	12
Evaporator 1 pressure	bar	1.60
LP compressor—inlet temperature	°C	18
LP compressor—outlet temperature	°C	58
HP compressor—inlet temperature	°C	45
Condenser inlet temperature	°C	80
Condenser outlet temperature	°C	38
Evaporator 1 inlet temperature	°C	−12
Outlet temperature—evaporator 1	°C	−06
Inlet temperature—evaporator 2	°C	05
Evaporator 2 outlet temperature	°C	11

Load on evaporator—1 and 2 (kW)

$$Q_{e1} = V \times I_1 \text{ and } Q_{e2} = V \times I_2 \tag{3}$$

Carnot COP

$$(COP)_{carnot} = \frac{T_L}{T_H - T_L} \tag{4}$$

Theoretical COP

$$(COP)_{theo} = \frac{RE}{W_{c1} + W_{c2}} \tag{5}$$

Actual COP

$$(COP)_{act} = \frac{W_{heater,ip}}{W_{comp,ip}} = (\frac{N_h \times 3600}{t_h \times 1200})/\left(\frac{N_c \times 3600}{t_c \times 3200}\right) \tag{6}$$

Exergy destruction in LP compressor (kW)

$$EX_{D\_LP} = m_r \times T_0(S_2 - S_1) \tag{7}$$

Exergy destruction in HP compressor (kW)

$$EX_{D\_HP} = m_r \times T_0(S_4 - S_3) \tag{8}$$

Exergy destruction in condenser (kW)

$$EX_{D\_cond} = m_r \times [(h_4 - h_5) - T_0(S_4 - S_5)] \qquad (9)$$

Exergy destruction in the capillary tube (kW)

$$EX_{D\_cap} = m_r \times T_0(S_6 - S_5) \qquad (10)$$

Exergy destruction in TEX (kW)

$$EX_{D\_tex} = m_{r2} \times T_0(S_8 - S_5) \qquad (11)$$

Exergy destruction in evaporator—1 (kW)

$$EX_{D\_e1} = m_{r1}[(h_6 - h_7) - T_0(S_6 - S_7)] - \left[-Q_{e1}\left(1 - \frac{T_O}{T_{L1}}\right)\right] \qquad (12)$$

Exergy destruction in evaporator—2 (kW)

$$EX_{D\_e2} = m_{r2}[(h_8 - h_9) - T_0(S_8 - S_9)] - \left[-Q_{e2}\left(1 - \frac{T_O}{T_{L2}}\right)\right] \qquad (13)$$

Exergy of the product (kW)

$$EP = \left[-Q_{e1}\left(1 - \frac{T_O}{T_{L1}}\right)\right] + \left[-Q_{e2}\left(1 - \frac{T_O}{T_{L2}}\right)\right] \qquad (14)$$

Exergy efficiency of the system (%)

$$\eta_{ex} = \frac{EP}{W_{c1} + W_{c2}} \qquad (15)$$

Exergy destruction ratio

$$EDR = \left(\frac{1}{\eta_{ex}} - 1\right) \qquad (16)$$

5   Results and Discussion

The outcomes of the analysis are tabulated in Tables 2 and 3 as shown.

From Fig. 3a, due to an increase in evaporator temperature, exergy efficiency decreases because of an increase in exergy of cooling load. Also, at lower temperatures, exergy losses are less, thus the evaporator works effectively. As condenser temperature increases, the enthalpy of refrigerant increases while exergy efficiency

Table 2 Energy analysis of system

Parameter	Unit	Value
Power input to LP compressor	kW	0.433
Power input to HP compressor	kW	0.692
Load on evaporator—1	kW	1.225
Load on evaporator—2	kW	0.245
Carnot COP	–	5.25
Theoretical COP	–	3.068
Actual COP	–	1.053

Table 3 Exergy analysis of system

Parameter	Unit	Value
Exergy destruction of LP compressor	kW	0.052
Exergy destruction of HP compressor	kW	0.051
Exergy destruction of the condenser	kW	0.493
Exergy destruction of the capillary tube	kW	0.156
Exergy destruction of TEX	kW	0.182
Exergy destruction of evaporator—1	kW	0.134
Exergy destruction of evaporator—2	kW	0.124
Exergy of product	kW	0.226
Exergy efficiency of the system	%	20.06
Exergy destruction ratio	–	3.985
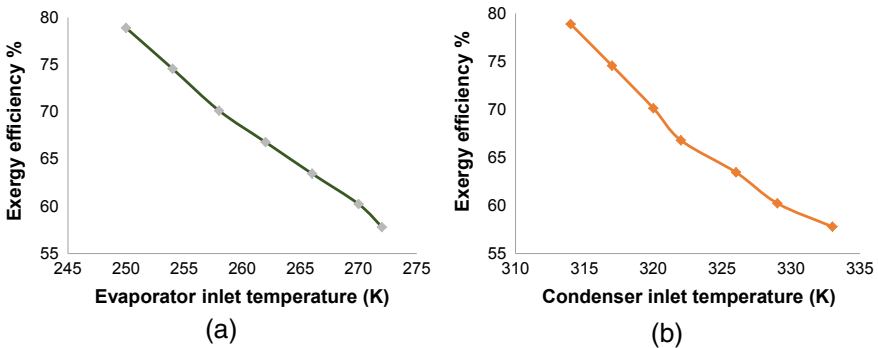
Fig. 3 Behaviour of exergy efficiency with **a** the evaporator inlet temperature and **b** the condenser inlet temperature

decreases as shown in Fig. 3b. The compressor works more effectively at lower condenser pressure; because at higher pressure, it has to deal with highly superheated refrigerant; needs to handle more volume and correspondingly require more work.

6 Conclusion

Exergy efficiency always gives a true representation of the index of system performance with the ideal one. A 20% overall system exergy efficiency is obtained for the system considered. The highest exergy efficiency is found for the evaporator and the lowest for the compressor. Major contributors to exergy losses include loss due to entropy generation, refrigeration piping leaks, systems irreversibility, and so on. These exergy destructions should be reduced to enhance the system performance and to boost the life of components; which ultimately reduces the operational and running cost. A lot of heat is wasted from the condenser which can be effectively utilized as waste heat recovery for certain applications. An effort is going on these areas that inherently have the highest margins for exergy efficiency improvement.

References

1. Kotas TJ (1985) The exergy method of thermal plant analysis. Elsevier Ltd., London, pp 1–296
2. Dincer, Rosen MA (2012) Exergy: energy, environment and sustainable development, 2nd ed. Amsterdam: Elsevier Ltd., pp 576
3. Cengel YA, Boles MA, Kanoglu M (2019) Thermodynamics: an engineering approach, 9th edn. McGraw-Hill Education, New York, pp 1–1009
4. Mishra RS (2018) Energy and exergy analysis of multiple evaporators and compressors with individual or multiple expansion valves vapour compression refrigeration system using ecofriendly refrigerants. Int J Res Eng Innov 2(6):572–580
5. Gholamian E, Hanafizadeh P, Ahmadi P (2018) Advanced exergy analysis of a carbon dioxide ammonia cascade refrigeration. Appl Thermal Eng 137:689–699
6. Baakeem SS, Orfi J, Alabdulkarem A (2018) Optimization of a multistage vapor-compression refrigeration system for various refrigerants. Appl Thermal Eng 136:84–96
7. Hu B, Wu D, Wang RZ (2017) Performance simulation and exergy analysis on multi-stage compression high temperature heat pumps with R1234ze(Z) refrigerant. In: 2017 proceedings of 12th IEA heat pump conference, Rotterdam
8. Anjum A, Gupta M, Ansari NA, Mishra RS (2017) Thermodynamic analysis of a two stage vapour compression refrigeration system utilizing the waste heat of the intercooler for water heating. J Fundam Renewable Energ Appl 7:232–238
9. Mishra RS (2013) Irreversibility analysis of multi-evaporators vapour compression refrigeration systems using new and refrigerants: R134a, R290, R600, R600a, R1234yf, R502, R404a and R152a, and R12, R502. Int J Adv Res Innov 1:188–200
10. Dwinanto MM, Suhanan, Prajitno P (2017) Exergy analysis of a dual-evaporator refrigeration systems. In: 2017 AIP conference proceedings, international conference on engineering, science and nanotechnology, Solo

11. Mishra RS (2014) Methods for improving exergetic efficiency of multi-evaporators single compressor and single expansion valve in vapour compression refrigeration systems using thirteen ecofriendly refrigerants for reducing global warming and ozone depletion. Int J Latest Res Sci Technol 3(2):191–196

12. Ahamed JU, Saidur R, Masjuki HH (2011) A review on exergy analysis of vapor compression refrigeration system. Renew Sustain Energ Rev 15(3):1593–1600

13. Kumar S, Prevost M, Bugarel R (1988) Exergy analysis of a compression refrigeration system. Heat Recovery Syst CHP 9(2):151–157

14. Malwe P, Gawali B, Shaikh J, Deshpande M, Dhalait R, Kulkarni S, Shindagi V, Panchal H, Sadasivuni KK (2021) Exergy assessment of an organic rankine cycle for waste heat recovery from a refrigeration system: a review. Chem Eng Commun 1–29. https://doi.org/10.1080/009 86445.2021.1980396

15. Malwe PD, Gawali BS, Choudhari MS, Dhalait RS, Deshmukh NS (2021) Energy and exergy analysis of an organic rankine cycle integrated with vapour compression refrigeration system. Adv Appl Math Sci 20(10):2137–2150

16. Ganesh S, Wahile Prateek D, Malwe Ajay V, Kolhe (2020) Waste heat recovery from exhaust gas of an engine by using a phase change material. Mater Today: Proc 28:2101–2107. https:// doi.org/10.1016/j.matpr.2020.03.247

17. Malwe PD, Gawali BS, Thakre SD (2014) Exergy analysis of vapour compression refrigeration system. Inter J Therm Technol 4(2):54–57

18. Malwe PD, Gawali BS (2014) Exergy management of vapour compression refrigeration system. Inter J Eng Assoc 3(1):33–36

19. Malwe PD, Shaikh J, Gawali BS (2022) Exergy assessment of a multistage multi-evaporator vapor compression refrigeration system using eighteen refrigerants. Energy Rep 8153–162. https://doi.org/10.1016/j.egyr.2021.11.072

20. Malwe PD, Gawali BS, Wahile GS (2018) Exergy analysis of a four stroke diesel engine. In: Pawar PM, Ronge BP, Balasubramaniam R, Vibhute AS, Apte SS (eds) Techno-Societal, Vol 2. Springer International Publishing, Maharashtra, 885–894. https://doi.org/10.1007/978-3-030-16962-6_88

21. Malwe PD, Gawali BS, Choudhari MS, Dhalait RS, Deshmukh NS (2021) Performance analysis and exergy assessment of an inertance pulse tube cryocooler. J Therm Eng

22. Choudhari M, Gawali B, Malwe P, Deshmukh N, Dhalait R (2022) Second order cyclic analysis of counter flow pulse tube refrigerator. J Therm Eng 9:1–8

23. Choudhari M, Gawali B, Momin M, Malwe P, Deshmukh N, Dhalait R (2021) Numerical analysis of double inlet two-stage inertance pulse tube cryocooler. Inter J Advan Technol Eng Explor 8(79):766–779. https://doi.org/10.19101/IJATEE.2021.874108

24. Choudhari MS, Gawali BS, Malwe P (2021) Numerical analysis of inertance pulse tube refrigerator. In: IOP Conference Series: Mater Sci Eng 1104(1):012008. https://doi.org/10.1088/1757-899X/1104/1/012008

25. Borikar SA, Gupta MM, Alazwari MA, Malwe PD, Moustafa EB, Panchal H, Elsheikh A (2021) A case study on experimental and statistical analysis of energy consumption of domestic refrigerator. Case Stud Thermal Eng 28101636. https://doi.org/10.1016/j.csite.2021.101636

26. Kolhe AV, Malwe PD, Wahile GS (2021) Artificial intelligence for prediction of performance and emission parameters of CI engine using bio-fuel. In: AIP Conf Proc National Conf Phys Chem Mater. https://doi.org/10.1063/5.0060862

27. Wahile GS, Malwe PD, Aswalekar U (2022) Latent heat storage system by using phase change materials and their application. Mater Today: Proc 52:513–517. https://doi.org/10.1016/j.matpr.2021.09.268

28. Raushan R, Dhande KK, Jamadar NI, Malwe PD (2022) Material characterization design and analysis of CF/PA66 drive shaft with high strength carbon steel. Mater Today: Proc. https://doi.org/10.1016/j.matpr.2022.03.512

Experimental Analysis of Freeze Drying and Estimating the Transient Moisture Contents of Food Products

V. P. Chandramohan ⓘ

Abstract Freeze drying is an advanced dehydration technology with many advantages over other traditional drying methods. The present work deals with development of an experimental model for freeze drying. The sample products used were skimmed milk and egg white. Experiments were performed with skimmed milk and egg white to estimate the transient moisture content. The experiments were performed with a laboratory lyophilizer setup and deep freezing was performed using a domestic refrigerator. The milk lost its 50% mass during the first 2.5 h freeze-drying process. It took 12 h to reach its solid powdered state. The egg white lost its mass very vigorously in the first 6 h of drying, and after that, a constant drying rate was noticed. The constant drying time continued up to 10 h. The egg white reached its solid state at 10 h. The obtained results were compared with existing numerical study, and a reasonable match was observed.

Keywords Freeze drying · Skimmed milk · Egg white · Lyophilizer · Transient moisture content

1 Introduction

Freeze drying is a hygienic process of dehydration which is used to protect food, medicines and biological applications. During the freeze-drying process, the water content in the material frozen and thereafter a high vacuum is applied on the product. Therefore, the frozen ice is sublimed to vapour directly without reaching the liquid state and hence the product is dried. Though it is an expensive process, the dried product can be saved for years without any action of micro-organisms through perfect air tight package. Whenever this freeze-dried product is used, enough water is added; therefore, the food regain its original aroma, flavour and colour [1, 2].

V. P. Chandramohan (✉)
Mechanical Engineering Department, National Institute of Technology Warangal, Warangal, Telangana 506004, India
e-mail: vpcm80@nitw.ac.in

Considerable numbers of researches were made on freeze drying though both experiments and numerical estimations. Toei et al. [3] conducted freeze-drying experiments with a building material and found that a sublimation layer was formed during drying which was dividing the dried and frozen layer. The drying rate was low in the dried region as this region's thermal conductivity is low comparatively the frozen region. The stability criterion of the sublimation front was explained by the concept of zone sublimation. This experimental analysis found that the plane sublimation front was unstable, and it was broken into several zone sublimation regions.

Another study on the freeze-drying process used a sorption-sublimation model [4]. During the low pressure drying, the shortest drying time was estimated. Also, it was estimated that for small size samples, the bound water was more than the free moisture existing in the product. Also, it was proved that continuous freeze drying during the secondary drying led to undesirable effect in the solid food product.

A parameter called 'collapse phenomenon' was analysed by Pikal and Shah [5] though their experiments on moxalactam di-sodium with 12% mannitol. At high chamber temperature, the sublimation happens quickly, but during overheating, there was a loss of pore structure and it was called as a 'collapse phenomenon' which deteriorates the product quality. The product temperature depends on the chamber temperature and the pressure applied in the chamber and it could not be controlled directly during the drying process. In practice, trial-and-error experimental approach is used to find the suitable chamber temperature and pressure [6].

There is a detailed study on the effects of glass transition temperature that is one of the most important parameter which is responsible for the deterioration mechanism. It also determines the stability of the food product [7]. Glass transition temperature is the temperature at which the amorphous system changes to rubbery state from the glassy state. Glass transition temperature was experimentally determined for different products by variation of some thermodynamic or dielectric properties as a function of temperature. It also determined the quality of the food product. An easy approach to the glass transition phenomenon was presented by Genin and Rene [8] explaining its influence to different food products and reviewed several methods to determine it experimentally.

Time-scale modelling has been applied by Quiroga et al. [9] on freeze-drying process which is capable of describing freeze drying at the time scales. The model has been solved by finite element method. This model constitutes the core of the proposed optimal control approach, which defines the operation conditions for minimizing freeze–drying cycle time. A mathematical model was developed by Sadikoglu and Liapis [10] to describe quantitatively the dynamic behaviour of freeze-drying stages of pharmaceuticals in trays. The theoretical approaches were based on classical mass and heat transfer equations and simulated freeze-drying processes for the industry. Finite element analysis in two dimensional axisymmetric space has been considered by Mascarenhas et al. [11]. This model calculated the variation of partial pressure of water vapour, the temperature and the concentration of sorbed water. Lagarangian–Eulerian method was used to model the sublimation front of freeze-drying process which is the surface which separates the frozen and dried region. The developed

finite element practice provided valuable information on primary and secondary drying stages.

Trelea et al. [12] developed a software tool for interactive selection of operating condition for freeze-drying process in order to maximize the efficiency in terms of productivity and product quality (obtaining of the highest quality in the shortest cycle time), and it was found that the product temperature was the most determinant one. The model was validated in a wide range of operating conditions: −25 to + 25 °C shelf temperature and 10–34 Pa chamber pressure. Hammami and Rene [13] worked on the production of high-quality freeze-dried strawberry pieces by the response surface method which is a quadratic model. This method was used to predict optimal solution from the fitting surfaces obtained from trial experiments. It is found that the processing conditions have an influence on both the quality of the strawberries and freeze-drying time. The freezing rate has no significant effect on the product quality or the freeze-drying time.

Few works are available on numerical solution of freeze drying as the complexity of governing equations is high. The proper handling of the product temperature is very important as it allows the maintenance of product quality and also reducing the process cycle time. Different boundary conditions were used by mathematical models [10, 14], where a product is set in chamber and sublimation is done by heating from the top with heating by radiation and by receiving conductive heat from the bottom of the chamber. There were other heating options available like microwave heating [15, 16] in which internal heat generation was considered. A mathematical model of vacuum freeze drying of random solids at microwave heating was explained by Nastaj and Witkiewicz [16]. Even for materials having considerable porosity, primary drying was not sufficient to remove entire moisture content. Secondary drying was necessary to remove the remaining residual moisture (more than 7%) after primary drying stage.

There were not many detailed studies on freeze drying experimentally and numerically as both ways have their own practical complexities. The specific results and its explanations were not observed to come out with definite conclusions. There were few studies on experimental analysis on freeze drying [17–19]. The transient mass transfer data is not found in any literature.

Hence, the main objectives of the present work are as follows: (i) to develop an experimental setup for freeze drying, (ii) perform experiments with the food products such as milk and egg white and (iii) to estimate the drying time and the moisture content of the products from the experiments.

2 Methodology

The experimental setup, selection of materials, sample preparations and experimental procedures are mentioned in this section.

2.1 Selection of Materials

The experiments on freeze drying were done on milk and egg white. Packaged milk from the local market is taken for the experiment. Two sets of experiments were performed. In the first set, three samples of 20 ml milk was used. In the second set, 20 ml sample of egg white was taken. The yolk (the yellow part of an egg) was separated from the egg and the egg white was taken for experiment. Again three samples of egg white were taken for the experiment. Milk and egg white were selected for the experiment because these come under food category, and also they have organic substance and have rich protein.

2.2 Experimental Setup

The experimental setup is a laboratory lyophilizer which consists of a vacuum chamber, in which the pressure is continuously maintained by the help of a vacuum pump. There is a condenser which is used to catch the water vapour and preventing it to enter into the vacuum pump. The block diagram of the experimental setup is shown in Fig. 1. The external and important device which is required is a deep freezer to pre-freeze the sample. The accessories and attachments used for the experiment are conical flasks, rubber tubes, glass connectors and rubber cork. The conical flask acts as a container to place the sample, and when it is attached to the vacuum chamber, it acquires the vacuum pressure. The rubber tubes are used to connect the vacuum chamber with the glass connectors which fit in the cork. The cork makes
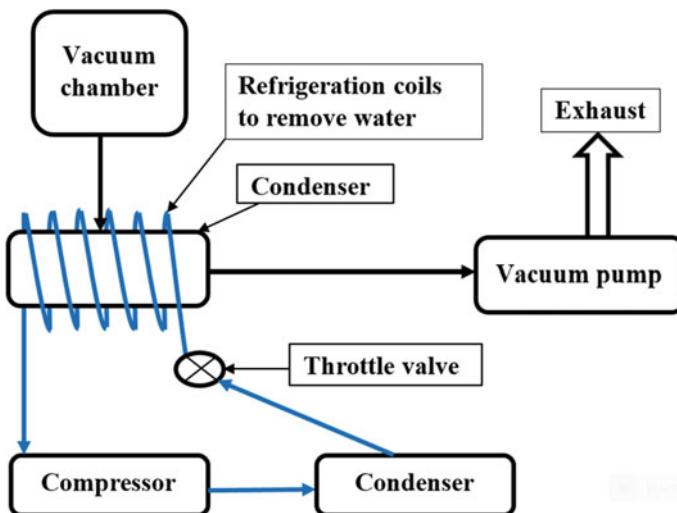

Fig. 1 Block diagram of lyophilizer

the conical flask sealed to the atmosphere and connects to the vacuum chamber. The main features of the lyophilizer are: safety cut-off for the vacuum pump, well arranged ports for placement of flasks, dual stage rotary vane vacuum pump.

2.3   Sample Preparation

Three conical flasks were taken, washed properly and dried. The flasks were fitted with cork and the combined mass of the flask and cork were taken. The combined mass was taken because it is convenient to measure the combined mass during the experiment. Later, for calculation of the mass of the sample, the mass of conical flask and the cork was subtracted from the total mass. For the first experiment, three samples of 20 ml milk were taken, and for the second experiment, three samples of 20 ml egg white were taken in three flasks. The respective corks were tightly put on the flask. The mass of each flask and cork with sample was taken again and noted down. The flasks with the sample were taken to freeze in a deep freezer of a domestic refrigerator. Before putting it inside the deep freezer, the mouth of the flask was sealed tightly so that any loss of moisture can be prevented from the sample. The deep freezer was set to its maximum freezing capacity to freeze it to the lowest possible temperature available with the refrigerator. Once the samples were frozen, they were taken outside, and now, the samples were ready for experiments in the lyophilizer.

2.4   Experiments and Calculations

The lyophilizer was turned ON. The condenser was allowed to reach a stable temperature of −80 °C. The vacuum pump was switched ON and allowed to run the lyophilizer idle for some time till the pressure indicator showed a value of 10 Pa or less. The frozen sample was taken and loaded in the ports available in the vacuum chamber. After waiting for 30 min, the ports were closed, and the sample with the flask and cork was weighed in the weighing balance in least possible time. The samples were again loaded in the lyophilizer. This process was repeated again and again in every 30 min till the reading in the weighing balance shows nearly the same values for last three consecutive readings. The flask and cork masses were subtracted from the raw data to get the actual mass of the sample with time.

The percentage of water loss can be calculated with the tabulated values, and moisture content is calculated by plotting as moisture content versus time.

The moisture content of the sample is calculated by the given simple using the procedures mentioned below.

The mass of sample (m_s) was estimated using,

$$m_s = (m_{sc} + m_c) - (m_{co} + m_c) \tag{1}$$

where, m_{sc} is mass of sample with conical flask, m_c is mass of cork and m_{co} is mass of conical flask.

Total mass of water in the sample (m_T) was estimated using,

$$m_T = m_i - m_d \tag{2}$$

where, m_i is initial mass of sample and m_d is final dried mass of sample.

The mass of water at any given time (m_t) was estimated by subtracting the m_d from mass of sample at a given time.

Moisture content of sample on dry basis (M_{db}) was calculated using,

$$M_{db} = \frac{m_t}{m_d} \tag{3}$$

3   Results and Discussion

The average mass of the sample from three samples was estimated with time in order to reduce any experimental error. The mass loss data, average mass, moisture content on dry basis and total moisture percentage of skimmed milk are calculated and tabulated in Table 1.

The results were plotted and shown in Fig. 2a–c. From Table 2, it can be seen that the moisture decreased with time for 9 h, and after that, there is not much reduction in mass. It shows that the mass reaching its constant value implies that the sample is completely dried. The average mass for the milk with time is plotted in Fig. 2a. The initial mass of the sample (m_i) was 21.3352 g which was reduced to 2.5872 g after 9 h. At the end of 12 h, the complete dried mass (m_d) remained was 2.4625 g. At the end of the drying process, when major part of water content is removed, the process gets slowed because the final water content is adsorbed with the solid matrix. Once the mass was obtained, the moisture content of the sample in terms of dry basis was calculated and shown in Fig. 2b. The initial moisture content in dry basis (db) was 7.6642 kg/kg of db. After 9 h of drying, the moisture content is reduced to 0.66 kg/kg of db. After 10 h of time, the moisture content was almost same, and it is assumed to be dried. The moisture content in terms of total per cent of water content was plotted in Fig. 2c. The moisture content of the milk is reduced to half (50%) in just 2.5 h; it remains 23% after 5 h, 0.66% at 9 h and 0.16% after 10 h of drying time.

Table 2 presents the similar data of egg white, and it consists of the data of three experiments and its average mass. Finally, the moisture content in kg/kg of db and moisture percentage were estimated.

The average mass of the sample, moisture content on dry basis and total moisture percentage are calculated for egg white and tabulated in Table 2 and plotted in Fig. 3a–c. From Table 2, it can be seen that the moisture decreased with time for the first 6 h,

Table 1 Experimental results from three sample of 20 ml milk

Time (h)	Sample-1 (g)	Sample-2 (g)	Sample-3 (g)	Average (g)	kg of water/kg of db	Moisture (%)
0	21.3362	21.3337	21.3357	21.3352	7.6642	100
0.5	18.3519	18.6102	18.613	18.525	6.5229	85.1097
1.0	16.5454	16.5134	16.7606	16.6065	5.7438	74.9442
1.5	14.6539	14.8935	15.1115	14.8863	5.0453	65.8295
2.0	13.1628	13.437	13.6493	13.4164	4.4484	58.0410
2.5	11.4027	11.8318	12.2922	11.8422	3.8091	49.6998
3.0	10.1953	10.5	10.8245	10.5066	3.2667	42.6229
3.5	8.9966	9.5034	9.7165	9.4055	2.8195	36.7886
4.0	7.97	8.4173	8.5975	8.3283	2.3821	31.0809
4.5	7.3686	7.6724	7.8489	7.63	2.0985	27.3808
5.0	6.5538	6.8438	7.0358	6.8111	1.7660	23.0417
5.5	5.7959	6.0338	6.2478	6.0258	1.4471	18.8807
6.0	5.2418	5.447	5.7089	5.4659	1.2197	15.9140
6.5	4.5524	4.7913	4.8947	4.7461	0.9274	12.1000
7.0	3.8849	4.1097	4.3199	4.1048	0.6669	8.7020
7.5	3.4563	3.6385	3.7965	3.6304	0.4743	6.1883
8.0	2.9511	3.1833	3.2842	3.1395	0.2749	3.5872
8.5	2.6414	2.8915	3.001	2.8446	0.1552	2.0246
9.0	2.4353	2.5857	2.7407	2.5872	0.0507	0.6607
9.5	2.434	2.4812	2.6582	2.5245	0.0252	0.3285
10.0	2.433	2.4783	2.5667	2.4927	0.0123	0.1600
10.5	2.4312	2.4761	2.4938	2.467	0.0018	0.0238
11.0	2.4303	2.4753	2.4902	2.4653	0.0012	0.0148
11.5	2.4299	2.474	2.4897	2.4645	0.0008	0.0106
12.0	2.4301	2.473	2.4843	2.4625	0.0000	0.0000

and after that, there is not much reduction in mass. The initial mass (m_i) of 20 ml egg white is estimated as 21.2677 g. As time progresses, the mass reduced due to the removal of water. The mass of the sample becomes 2.7566 g after 6 h of drying. At the end of drying, the final mass of the dried product (m_d) is 2.6127 g. From 6 to 10 h, the curve is flattening which indicates that the product is almost dried after 6 h of drying. The moisture content in dry basis is plotted in Fig. 3b. The initial moisture content is 7.1401 kg of water/kg of db which is reduced to 0.0551 kg of water/kg of db after 6 h of drying. The moisture percentage with time is plotted in Fig. 3c. The moisture content is reduced to 53.6% in the first hour of drying, and it reduced to 23.67% at 2.5 h. After 6 h of drying, it is reduced to 0.77%. The complete drying time to produce solid egg powder is estimated as 10 h.
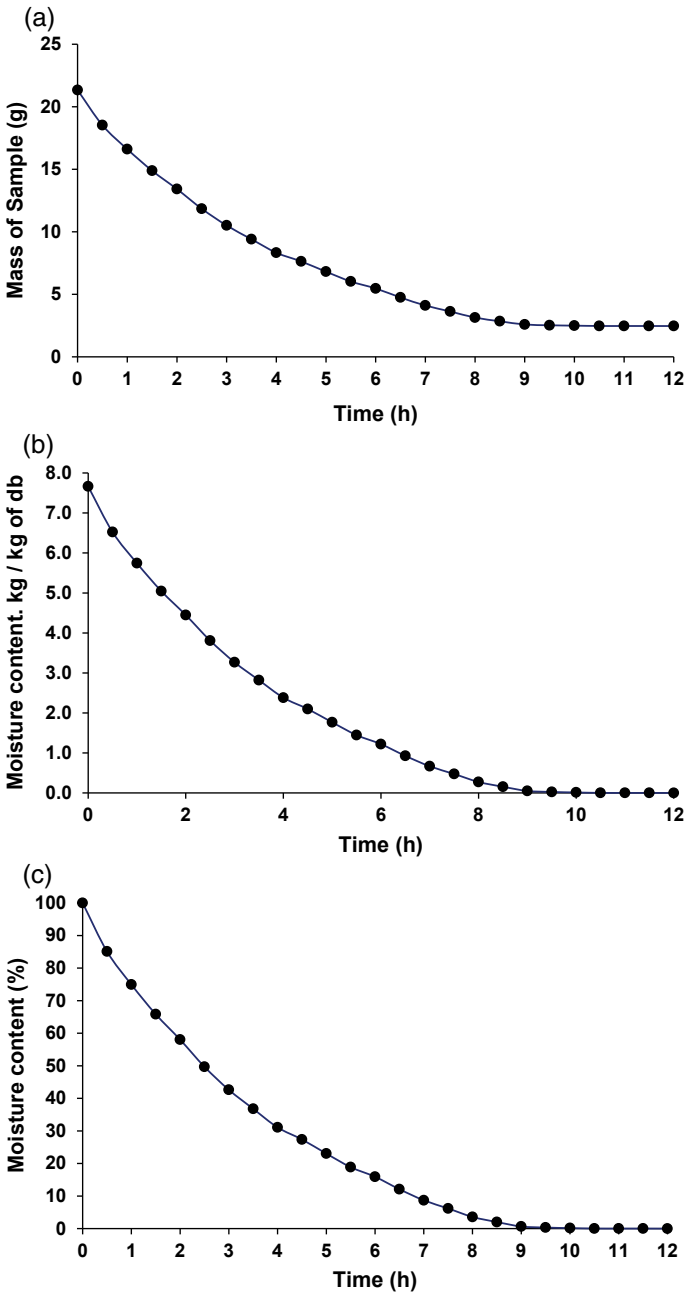
Fig. 2 A **a** Mass of the milk measured during experiment, **b** moisture content of milk in terms of dry basis and **c** moisture content of milk in percentage

Table 2 Experimental results from three samples of 20 ml egg white

Time (h)	Sample-1 (g)	Sample-2 (g)	Sample-3 (g)	Average (g)	kg of water/kg of solid	Moisture (%)
0.0	21.2335	21.4365	21.1332	21.2677	7.1401	100
0.5	16.3785	16.4274	16.5723	16.4594	5.2998	74.2250
1.0	12.5799	12.6272	12.6325	12.6132	3.8276	53.6075
1.5	9.9787	9.7227	9.6336	9.7783	2.7426	38.4113
2.0	8.4093	8.3165	8.4123	8.3794	2.2072	30.9121
2.5	7.0279	6.9373	7.1253	7.0302	1.6908	23.6798
3.0	6.031	5.9792	6.1332	6.0478	1.3148	18.4138
3.5	5.0413	4.9276	5.1375	5.0355	0.9273	12.9872
4.0	4.1764	4.0174	4.3417	4.1785	0.5993	8.3934
4.5	3.7729	3.6725	3.7276	3.7243	0.4255	5.9589
5.0	3.2672	3.2584	3.2731	3.2662	0.2501	3.5033
5.5	2.9696	2.8295	2.9894	2.9295	0.1213	1.6982
6.0	2.7558	2.7521	2.7619	2.7566	0.0551	0.7714
6.5	2.7385	2.7363	2.8384	2.7711	0.0606	0.8489
7.0	2.7094	2.7217	2.7139	2.7150	0.0392	0.5484
7.5	2.6726	2.7032	2.7021	2.6926	0.0306	0.4285
8.0	2.6623	2.6743	2.6927	2.6764	0.0244	0.3416
8.5	2.6598	2.6242	2.6782	2.6541	0.0158	0.2217
9.0	2.6591	2.5929	2.6329	2.6283	0.0060	0.0836
9.5	2.6588	2.5892	2.6272	2.6251	0.0047	0.0663
10.0	2.6587	2.571	2.6084	2.6127	0.0000	0.0000

The experimental results obtained for skimmed milk are compared with the numerical results of Naik et al. [6] and are shown in Fig. 4. It is seen that there is a slight deviation in the moisture content. A maximum deviation of 10% is noticed at t = 4 h. The deviation increased and again the deviation decreased toward the end of the process. From the numerical result, it is found that the total drying time at 10 Pa and 313 K (40 °C) was 9.25 h. From the experiment, it is found that the drying time is about 10 h.

There may be various reasons for these deviations. As discussed earlier in literature review, at higher chamber temperature, there is slight distortion in the frozen sample and a small amount of froth is formed. Hence, a change in shape occurred and the numerical results are purely calculated on basis of fixed shape. Therefore, the numerical results could not be able to produce the real values.
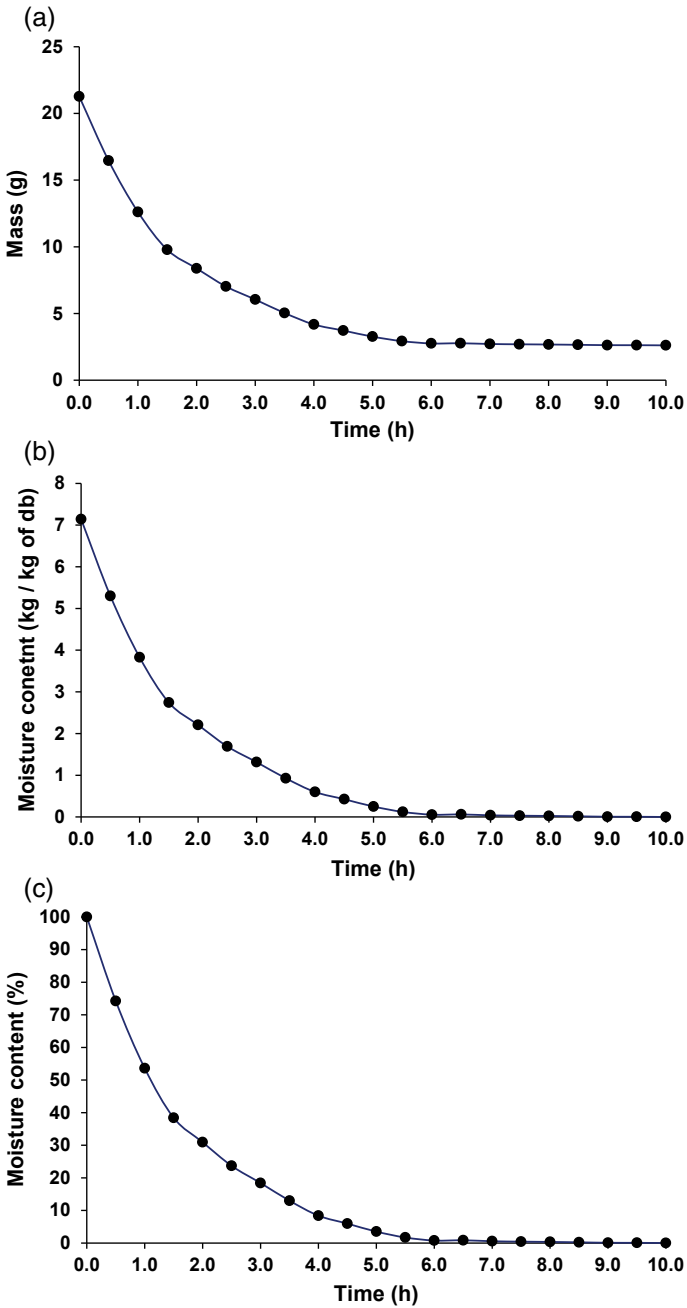
.

Fig. 3 **a** Mass of the egg white, **b** moisture content of egg white and **c** moisture content in percentage
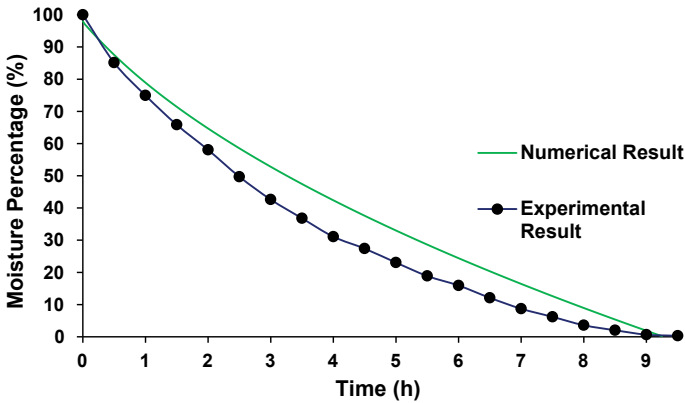
Fig. 4 Numerical results of moisture percentage of skimmed milk [6] compared with present results

4 Conclusion

An experimental analysis of freeze drying was made in this analysis. Milk and egg white were used as sample objects. A table top lyophilizer was used for freeze-drying experiments. A domestic deep freezer was used to freeze the food materials. The following important conclusions were obtained.

The average initial mass of milk was 21.3352 g, and the same of egg white was 21.2677 g. The mass of the samples was reduced when the drying time was increased for both experiments with milk and egg white. The moisture content was reduced to 50% during the first 2.5 h drying time. It reached to 25% approximately at 4.75 h. At 9 h, the change of mass was almost vanished, but the moisture percentage of 0% was obtained at 12 h. Therefore, it is concluded that at 12 h, the milk reached its solid powdered state.

The moisture percentage of egg white was reduced to 74% within 0.5 h. It reached to 53% at 1 h, 31% at 2 h and 3.5% at 6 h. A constant drying rate was noticed from 6 to 10 h of drying time. The moisture percentage reached to 0% at 10 h, and therefore, it is concluded that the egg white reached its solid powdered state at 10 h. The results were compared with existing numerical case and found a good agreement.

References

1. I. Liapis, R. Bruttini (2006) Freeze drying in handbook of industrial drying. In: Mujumdar AS (ed) CRC Press, Taylor and Francis group, 257–281
2. Thijssen HAC (1971) Flavour retention in drying preconcentrated food liquids. J Appl Chem Biotech 21:372–377
3. Toei R, Okazaki M, Asaeda M (1975) The stability of plane sublimation and a model of zone sublimation in freeze-drying of porous bodies. J Chem Eng Jpn 8:282–288

4. Millman MJ, Liapis AI, Marchello JM (1985) An analysis of the lyophilization process using a sorption-sublimation model and various operational policies. AIChE J 31:1594–1604

5. Pikal MJ, Shah S (1990) The collapse temperature in freeze–drying: dependence on measurement methodology and rate of water removal from the glassy state. Int J Pharm 62:165–186

6. Naik R, Arun SG, Chandramohan VP (2017) Numerical simulation for freeze drying of skimmed milk with moving sublimation front using tri diagonal matrix algorithm. J Appl Fluid Mech 10(3):813–818. https://doi.org/10.18869/acadpub.jafm.73.240.27054

7. Roos YH (1992) Phase transitions and transformations in food systems, in handbook of food engineering. In: Heldman DR, Lund DB Marcel Dekker, New York, 145–197

8. Genin N, Rene F (1995) Analyse du Role de la transition vitreuse dans les procedes de conservation agroalimentaires. J Food Eng 26:391–408

9. Quiroga EL, Antelo LT, Alonso AA (2012) Time-scale modeling and optimal control of freeze–drying. J Food Eng 111:655–666

10. Sadikoglu H, Liapis AI (1997) Mathematical modelling of the primary and secondary drying stages of bulk solution freeze-drying in trays: parameter estimation and model discrimination by comparison of theoretical results with experimental data. Drying Technol 15:791–810

11. Mascarenhas WJ, Akay HU, Pikal MJ (1997) A computational model for finite element analysis of the freeze–drying process. Comput Methods Appl Mech Eng 148:105–124

12. Trelea C, Passot S, Fonseca F, Michele M (2007) An interactive tool for the optimization of freeze–drying cycles based on quality criteria. Drying Technol 25:741–751

13. Hammami, Rene F (1997) Determination of freeze-drying process variables for strawberries. J Food Eng 32:133–154

14. Nakagawa K, Ochiai T (2015) A mathematical model of multi-dimensional freeze-drying for food products. J Food Eng 161:55–67

15. Duan X, Zhang M, Mujumdar AS, Wang S (2010) Microwave freeze drying of sea cucumber (Stichopus japonicus). J Food Eng 96:491–497

16. Nastaj JF, Witkiewicz K (2009) Mathematical modeling of the primary and secondary vacuum freeze drying of random solids at microwave heating. Int J Heat Mass Transf 52:4796–4806

17. Crank J (1984) Free and moving boundary problems. Clarendon Press, Oxford, UK

18. Liapis R, Bruttini A (1994) Theory for the primary and secondary drying stages of the freeze-drying of pharmaceutical crystalline and amorphous solutes: comparison between experimental data and theory. Sep Technol 4:144–155

19. Pikal MJ, Roy ML, Shah S (1984) Mass and heat transfer in vial freeze-drying of pharmaceuticals: role of the vial. J Pharm Sci 73:1224–1237